Transactions of the ASME®

Transactions of the ASME, Journal of Heat Transfer (ISSN 0022-1481) is published quarterly (Feb., May, Aug., Nov.) for $165.00 per year by The American Society of Mechanical Engineers, 345 East 47th Street, New York, NY 10017. Second class postage paid at New York, NY and additional mailing offices. POSTMASTER: Send address changes to Transactions of the ASME, Journal of Heat Transfer, c/o THE AMERICAN SOCIETY OF MECHANICAL ENGINEERS, 22 Law Drive, Box 2300, Fairfield, NJ 07007-2300.
CHANGES OF ADDRESS must be received at Society headquarters seven weeks before they are to be effective. Please send old label and new address.
PRICES: To members, $40.00, annually; to nonmembers, $165.00. Add $15.00 for postage to countries outside the United States and Canada.
STATEMENT from By-Laws. The Society shall not be responsible for statements or opinions advanced in papers or . . . printed in its publications (B7.1, para. 3).

INDEXED by Applied Mechanics Reviews and Engineering Information, Inc.
Canadian Goods & Services Tax Registration #126148048

Journal of Heat Transfer

Published Quarterly by The American Society of Mechanical Engineers

VOLUME 114 • NUMBER 3 • AUGUST 1992

ANNOUNCEMENTS

TECHNICAL PAPERS

(Contents continued)

TECHNICAL NOTES

J. M. Houghton

D. B. Ingham

Department of Applied Mathematical Studies,
University of Leeds,
Leeds, LS2 9JT, United Kingdom

P. J. Heggs

Department of Chemical Engineering,
University of Bradford,
Bradford, BD7 1DP, United Kingdom

The One-Dimensional Analysis of Oscillatory Heat Transfer in a Fin Assembly

Studies of the transient heat transfer within extended surfaces have so far considered the fins in isolation. The isolated fin model is not representative of the physical boundary conditions within an extended surface heat exchanger since it does not account for the thermal effects of the supporting interface. The aim of this study is to extend the work on transient heat transfer within finned surfaces by incorporating the supporting wall in the problem. A mathematical one-dimensional solution for harmonic oscillatory heat transfer in a fin assembly is derived. It is concluded that, unlike steady-state situations, the transient heat transfer in a fin assembly can only be found by considering both the wall and the fins simultaneously.

Introduction

Studies of the transient heat transfer within extended surfaces have so far considered the fins in isolation, e.g., Yang (1972), Aziz (1975), Suryanarayana (1975), Chu et al. (1983), Ju et al. (1989), and Houghton et al. (1990), and so far no attempt has yet been made to include the supporting interface (wall) in the problem. For the case of steady-state heat transfer, there have been numerous investigations of both the isolated fin and the complete assembly of fins and wall, e.g., Heggs and Stones (1980a), Manzoor et al. (1981, 1982a, 1982b, 1983). For the one-dimensional approximation of the assembly, it has been shown rigorously by Manzoor et al. (1983) that the results for isolated fins can be combined with the wall heat transfer by the "sum of resistances" method. This approach is currently the design technique using the fin efficiency concept, i.e., ratio of the heat flow through the isolated fin to the heat flow if all the fin surface was at the base temperature of the isolated fin. The heat flow through the fin is calculated by considering either the heat flux through the base of the fin, or the heat flow from or to the fin surfaces exposed to the surrounding environment. Both of these values will be identical for steady-state conditions.

Investigations have been performed for harmonic oscillatory heat transfer in an isolated fin. An oscillatory temperature was applied at the base of the fin (Yang, 1972; Aziz, 1975; Houghton et al., 1990). Yang and Aziz evaluated the rate of heat transfer from the fin surface in terms of the temperature gradient at the base. However, this rate at any particular time is not equal to the rate of heat transfer from the fin surface at the same point in time; see Houghton et al. (1990). The integrated point rates of heat transfer over a complete cycle at the base and from the fin surface will be equal as in the case of the steady-state but not the point rates. The authors have presented results for the temporal variation of the fin heat transfer for a rectangular fin (see Houghton et al., 1990), subjected to an oscillatory temperature applied to the base. It is not possible to define and evaluate a fin efficiency using the steady-state definition, because the base temperature is oscillatory. The heat flow through the fin oscillated but the frequency and amplitude were different from those of the oscillatory temperature at the base. The differences depended upon the fin dimensions as well as the thermal properties of the fin: thermal diffusivity, thermal conductivity, and the fin heat transfer coefficient.

The aim of this present study is to extend the previous investigation so that the complete assembly of fins and supporting wall is considered. Additionally the oscillatory temperature is now that of the fluid in contact with the unfinned side of the supporting wall, and account is taken of the convection from the fluid to the wall.

Assumptions and Model

Consider a fin surface assembly comprising equally spaced, rectangular fins attached to a plane wall. It is only necessary to examine the section OABCDEO of the assembly due to geometric symmetry and this is shown pictorially in Fig. 1. The following assumptions are made:

1 The materials of the fins and walls are isotropic and have constant, but possibly different, physical properties.
2 There is perfect contact between the wall and the fins.
3 The heat transfer coefficients at the wall and over the fin surface are constant.

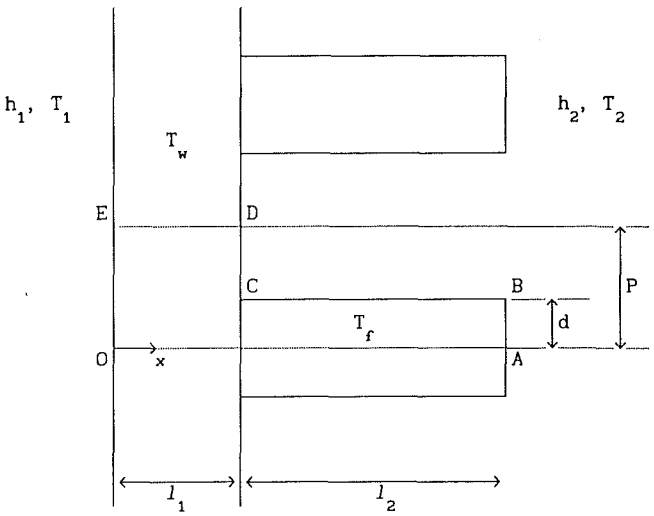

Fig. 1 Fin assembly geometry

Contributed by the Heat Transfer Division for publication in the JOURNAL OF HEAT TRANSFER. Manuscript received by the Heat Transfer Division February 1991; revision received December 1991. Keywords: Finned Surfaces, Heat Exchangers, Transient and Unsteady Heat Transfer.

4 The transverse variation of the temperature distribution within the wall and fin is negligible.

The surrounding temperature, T_1, on the side of the unfinned wall, oscillates around a mean temperature, T_m, which is greater than the surrounding temperature on the side of the finned side, T_2, and is described by the equation:

$$T_1 - T_m = (T_m - T_2) A \cos(\omega t) \tag{1}$$

where A is the dimensionless amplitude parameter and $\omega/2\pi$ is the frequency of the temperature distribution.

Mathematical Analysis

In dimensionless form the governing equations and boundary conditions are as follows:

Within the wall region

$$\frac{\partial^2 \theta_w}{\partial X^2} = \frac{\partial \theta_w}{\partial \tau} \tag{2}$$

Within the fin region

$$\frac{\partial^2 \theta_f}{\partial X^2} - N^2 \theta_f = \frac{1}{\alpha} \frac{\partial \theta_f}{\partial \tau} \tag{3}$$

At $X = 0$

$$\frac{\partial \theta_w}{\partial X} = \mathrm{Bi}_1(\theta_w - 1 - A \cos(B\tau)) \tag{4}$$

At $X = L_1$

$$\frac{\partial \theta_w}{\partial X} = \kappa D \frac{\partial \theta_f}{\partial X} - \kappa(1 - D)\mathrm{Bi}_2 \theta_w \tag{5}$$

and

$$\theta_w = \theta_f \tag{6}$$

At $X = L_3$

$$\frac{\partial \theta_f}{\partial X} = -\mathrm{Bi}_2 \theta_f \tag{7}$$

where $N^2 = h_2 P^2 / d k_f$.

After a large number of cycles it may be assumed that the assembly has reached a pseudo-cyclic steady state and a solution may be obtained by considering the wall and fin temperatures, to comprise the sum of a steady component and an oscillatory component, i.e.,

$$\theta_w = \theta_{w1}(X) + \theta_{w2}(X, \tau) \tag{8}$$

and

$$\theta_f = \theta_{f1}(X) + \theta_{f2}(X, \tau) \tag{9}$$

Applying the steady-state components $\theta_{w1}(X)$ and $\theta_{f1}(X)$ of Eqs. (8) and (9) to the set of Eqs. (2)–(7) results in a new set of equations, which is identical except for Eq. (4), which becomes:

At $X = 0$

$$\frac{d\theta_{w1}}{dX} = \mathrm{Bi}_1(\theta_{w1} - 1) \tag{10}$$

This set of equations can be readily solved to give:

$$\theta_{w1} = \theta_1 X + \theta_2 \tag{11}$$

and

$$\theta_{f1} = \zeta_3 \cosh[N(L_3 - X)] + \zeta_4 \sinh[N(L_3 - X)] \tag{12}$$

$$\zeta_2 = \mathrm{Bi}_1 \left(L_1 + \frac{\phi_2 \phi_4}{D\phi_1} \right) \Bigg/ \left(1 + \mathrm{Bi}_1 L_1 - \frac{\phi_2 \phi_3}{D\phi_1} \right) \tag{13}$$

$$\zeta_1 = \mathrm{Bi}_1(\zeta_2 - 1) \tag{14}$$

$$\zeta_3 = (\zeta_2 \phi_3 + \mathrm{Bi}_1 \phi_4)/D\phi_1 \tag{15}$$

$$\zeta_4 = \mathrm{Bi}_2 \zeta_3 / N \tag{16}$$

$$\phi_1 = N \sinh(NL_2) + \mathrm{Bi}_2 \cosh(NL_2) \tag{17}$$

$$\phi_2 = \cosh(NL_2) + \frac{\mathrm{Bi}_2}{N} \sinh(NL_2) \tag{18}$$

$$\phi_3 = \mathrm{Bi}_2(D - 1)(\mathrm{Bi}_1 L_1 + 1) - \mathrm{Bi}_1/\kappa \tag{19}$$

$$\phi_4 = 1/\kappa + \mathrm{Bi}_2 L_1 (1 - D) \tag{20}$$

To find the solution for the oscillatory components $\theta_{w2}(X, \tau)$ and $\theta_{f2}(X, \tau)$ of Eqs. (8) and (9), it is assumed that they can be written in the form:

$$\theta_{w2}(X, \tau) = \mathrm{Re}(A\psi_w(X)e^{iB\tau}) = A[\mathrm{Re}(\psi_w)\cos(B\tau) - Im(\psi_w)\sin(B\tau)] \tag{21}$$

$$\theta_{f2}(X, \tau) = \mathrm{Re}(A\psi_f(X)e^{iB\tau}) = A[\mathrm{Re}(\psi_f)\cos(B\tau) - Im(\psi_f)\sin(B\tau)] \tag{22}$$

Applying Eqs. (21) and (22) to the set of Eqs. (2)–(7) provides a further set of equations and boundary conditions, which may be formulated for the functions ψ_w and ψ_f and solved to give:

$$\psi_w = \beta_1 \cosh[\mu(L_1 - X)] + \beta_2 \sinh[\mu(L_1 - X)] \tag{23}$$

$$\psi_f = \beta_3 \cosh[\lambda(L_3 - X)] + \beta_4 \sinh[\lambda(L_3 - X)] \tag{24}$$

in which

Nomenclature

A = dimensionless amplitude parameter
B = dimensionless frequency parameter $= \omega P^2/\alpha_w$
Bi_1 = Biot number $= h_1 P/k_w$
Bi_2 = Biot number $= h_2 P/k_f$
c_p = specific heat capacity
d = half-fin thickness
D = dimensionless half-fin thickness $= d/P$
F = instantaneous augmentation factor
h_1 = heat transfer coefficient on the side of the unfinned wall
h_2 = heat transfer coefficient on the side of the finned wall
k = thermal conductivity
l_1 = wall thickness
l_2 = fin length
L_1 = dimensionless wall thickness $= l_1/P$
L_2 = dimensionless fin length $= l_2/P$
L_3 = $L_1 + L_2$
N = dimensionless fin parameter $= (h_2 P^2/dk_f)^{1/2} = (\mathrm{Bi}_2/D)^{1/2}$
P = half-fin spacing
$\tilde{q}$ = heat flow rate per unit depth
t = time
T = temperature
T_1 = ambient temperature at the side of the unfinned wall
T_2 = ambient temperature at the side of the finned wall
T_m = a constant mean temperature
x = coordinate
X = dimensionless displacement $= x/P$
α_w = wall thermal diffusivity
α_f = fin thermal diffusivity
α = ratio $= \alpha_f/\alpha_w$
θ = dimensionless temperature $= (T - T_2)/(T_m - T_2)$
κ = ratio $= k_f/k_w$
ρ = density of wall or fin material
τ = dimensionless time $= \alpha_w t/P^2$
ω = angular frequency of the ambient temperature oscillation t_1

Subscripts

f = fin
w = wall

$$\beta_3 = \mathrm{Bi}_1/(\Omega_1\Omega_3 + \Omega_2\Omega_5), \quad \beta_1 = \beta_3\Omega_3, \quad \beta_2 = \Omega_5\beta_3,$$
$$\beta_4 = \mathrm{Bi}_2\beta_3/\lambda,$$
$$\Omega_1 = \mathrm{Bi}_1 \cosh(\mu L_1) + \mu \sinh(\mu L_1),$$
$$\Omega_2 = \mathrm{Bi}_1 \sinh(\mu L_1) + \mu \cosh(\mu L_1),$$
$$\Omega_3 = \cosh(\lambda L_2) + \frac{\mathrm{Bi}_2}{\lambda}\sinh(\lambda L_2),$$
$$\Omega_4 = \sinh(\lambda L_2) + \frac{\mathrm{Bi}_2}{\lambda}\cosh(\lambda L_2),$$
$$\Omega_5 = \frac{\kappa}{\mu}(D\lambda\Omega_4 + (1-D)\mathrm{Bi}_2\Omega_3), \quad \mu^2 = iB, \ \lambda^2 = N^2 + \frac{iB}{\alpha}. \tag{25}$$
$$\mu = u^* + iu^*, \quad \lambda = u + iv, \quad u^* = \left(\frac{B}{2}\right)^{1/2},$$
$$u = \left(\frac{1}{2}\left[N^2\left(N^4 + (B/\alpha)^2\right)^{1/2}\right]\right)^{1/2},$$
$$v = \left(\frac{1}{2}\left[-N^2\left(N^4 + (B/\alpha)^2\right)^{1/2}\right]\right)^{1/2}$$

Fin Assembly Heat Transfer Rate

The instantaneous heat flow through the fin assembly is obtained by calculation of the point rate of heat flow by convection from the fin-side surfaces. This is expressed in nondimensional form as follows:

$$\tilde{q} = \frac{q}{h_2 P(t_m - t_2)} = \int_D^1 \theta_w(X = L_1)dY + \int_{L_1}^{L_3} \theta_f dX + \int_0^D \theta_f(X = L_3)dY \tag{26}$$

$$\begin{aligned} &= (1-D)[(\zeta_1 L_1 + \zeta_2) + A\cos(B\tau)\mathrm{Re}(\beta_1) - A\sin(B\tau)Im(\beta_1)] \\ &+ \frac{1}{N}[\zeta_3 \sinh(NL_2) + \zeta_4(\cosh NL_2) - 1)] \\ &+ A\cos(B\tau)\mathrm{Re}(C) - A\sin(B\tau)Im(C) \\ &+ \zeta_3 D + AD(\mathrm{Re}(\beta_3)\cos(B\tau) - Im(\beta_3)\sin(B\tau)\sin(B\tau)) \end{aligned} \tag{27}$$

where

$$C = [\beta_3 \sinh(\lambda L_2) + \beta_4(\cosh(\lambda L_2) - 1]/\lambda \tag{28}$$

Results and Discussion

It is more convenient to represent the results in the form of an instantaneous augmentation factor (Heggs et al., 1980a, 1980b), which is a direct indication of the advantage of adding fins to a surface in order to augment the heat transfer. This is defined as the ratio of the heat flow through the assembly to the steady-state heat flow through the plain wall. This is obtained from the dimensionless heat flow rate Eqs. (26) and (27) as follows:

$$F = \tilde{q}h_2/U \tag{29}$$

where

$$\frac{1}{U} = \frac{1}{h_1} + \frac{l_1}{k_w} + \frac{1}{h_2} \tag{30}$$

Values of the instantaneous augmentation factor have been obtained for a wide range of heat transfer coefficients h_1 and h_2, oscillatory parameters A and ω, and fin assembly dimensions. Results are presented here, showing variations of F as a function of $B\tau$, for the dimensions of Integron High-Fin Tubing, i.e., $L_1 = 0.888$, $L_2 = 7.63$, $D = 0.555$, and $P = 1.35 \times 10^{-3}$ m. The wall material was steel [$k = 15$ W/mK and $\alpha = 0.5 \times 10^{-5}$ m^2/s], the fin material was copper [$k = 386$ W/mK and $\alpha = 11.234 \times 10^{-5}$ m^2/s] and the frequency, ω, was taken to be 0.5.

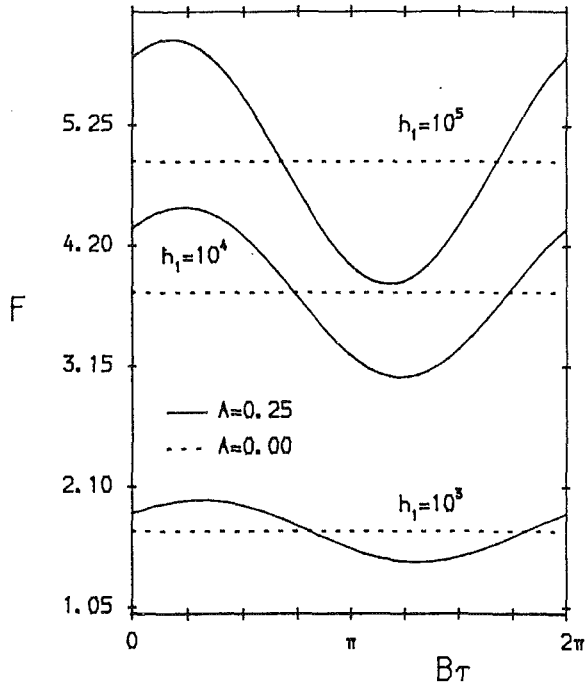

Fig. 2 Effect of heat transfer coefficient at unfinned wall, h_1

The heat transfer rate from the fin-side surfaces, and therefore F, consists of a steady component, which is independent of A, and an oscillatory component, which is dependent upon A. The heat flux oscillates periodically around a mean value, which is the heat transfer rate at steady state. The amplitude of the heat flow oscillation increases with A.

The effect on F produced by varying the heat transfer coefficient at the unfinned wall, h_1, is shown in Fig. 2 for $h_2 = 10^3$ W/m^{2}K and $h_1 = 10^5$, 10^4, and 10^3 W/m^{2}K. The value of F and the amplitude of the oscillation both increase as h_1 increases. Also as h_1 increases, the phase difference between the oscillation of F and the oscillation of the temperature T_1 on the side of the unfinned wall decreases.

In Fig. 3 the effect produced on F by varying the heat transfer coefficient at the finned surface, h_2, is illustrated. For this figure $h_1 = 10^3$ Wm^2/K and $h_2 = 10^3$, 10^2, and 10 W/m^{2}K. Although the value of the instantaneous heat transfer rate from the fin-side surfaces, $\tilde{q}$, increases with increasing values of h_2, the opposite effect can be seen to occur for F, thus indicating that the addition of the fins has a more beneficial effect on the heat transfer rate through the assembly for larger values of the ratio h_1/h_2.

The effect of varying the angular frequency, ω, is illustrated in Fig. 4 in which variations of F are presented as a function of τ and where $h_1 = 10^5$ W/m^{2}K and $h_2 = 10^3$ W/m^{2}K. As in the case of oscillatory heat transfer in the isolated fin (Houghton et al., 1990), the amplitude of the heat flux oscillation is greatly affected by ω, increasing as ω decreases. At a fixed time, τ, as $\omega \to 0$ the heat flow rate approaches a constant value. This is because as $\omega \to 0$ the surrounding temperature at the unfinned wall, T_1 approaches a constant value, i.e.,

$$T_1 \to T_m + A(T_m - T_2) \qquad \text{as } \omega \to 0$$

and this new constant temperature is greater than the mean temperature T_m.

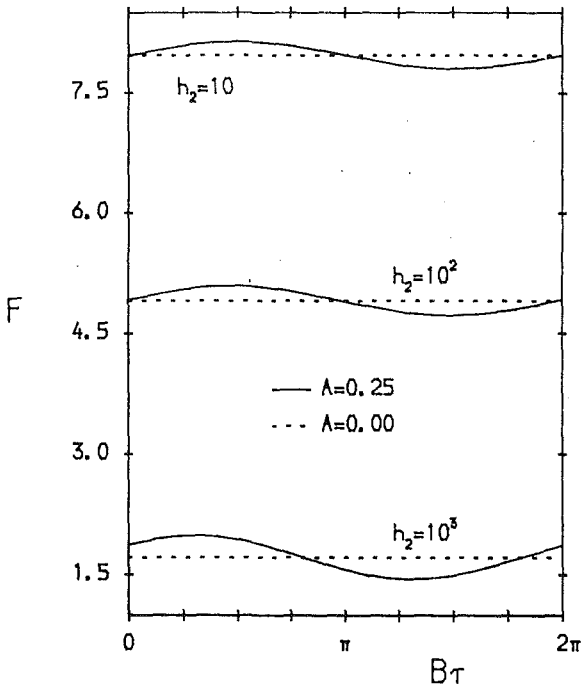

Fig. 3 Effect of heat transfer coefficient at unfinned wall, h_2

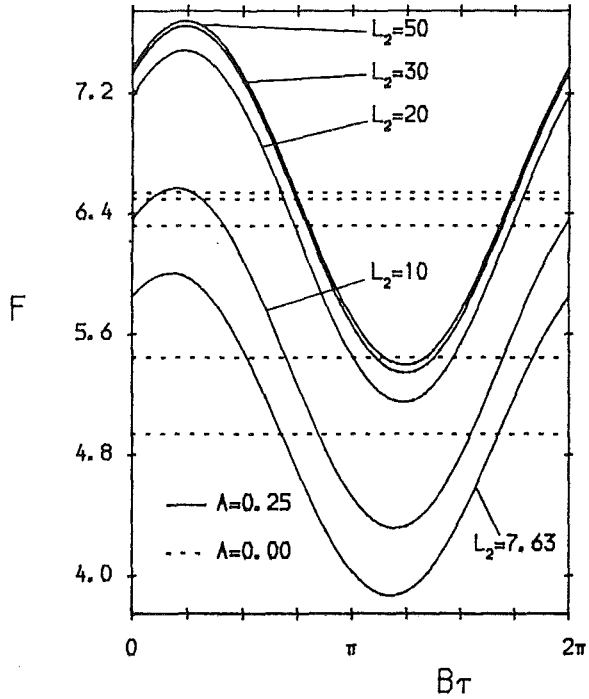

Fig. 5 Effect of fin length on F

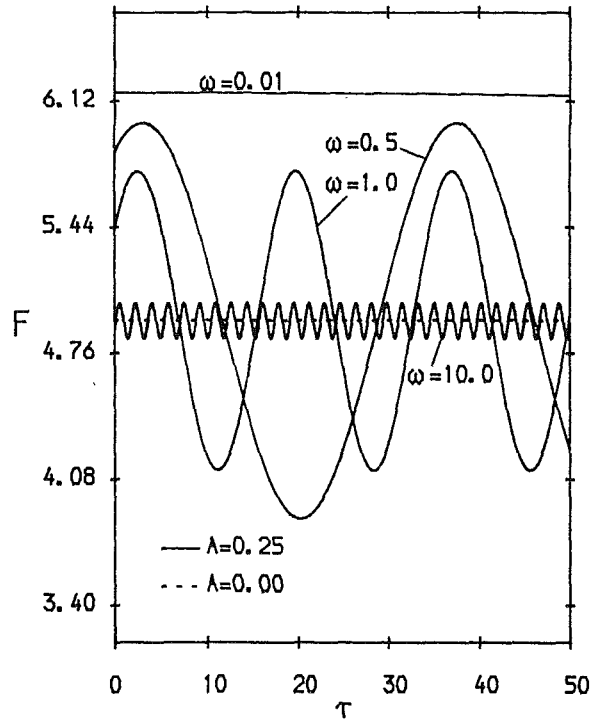

Fig. 4 Effect of angular frequency ω on F

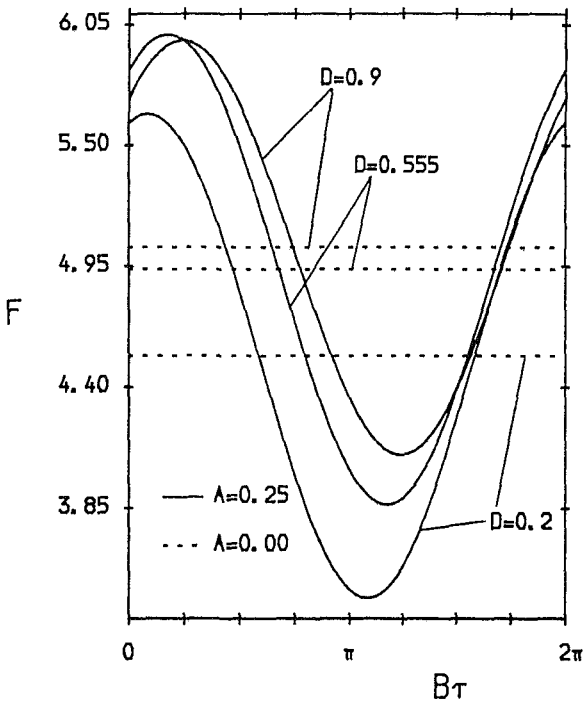

Fig. 6 Effect of half-fin thickness d on F

Increasing the fin length, L_2, increases the surface area available for heat transfer by convection. This corresponds to an increase in the instantaneous heat transfer rate and therefore F, as L_2 increases. As $L_2 \to \infty$ the heat oscillations of F converge to a single oscillation. This is illustrated in Fig. 5. Here $h_1 = 10^5$ W/m^{2}K and $h_2 = 10^3$ W/m^{2}K.

The effect produced on F by varying the half-fin thickness, d, is illustrated in Fig. 6, where $h_1 = 10^5$ W/m^{2}K and $h_2 = 10^3$ W/m^{2}K. The steady component of F increases with increasing D ($= d/P$) but the amplitude of the oscillation of F decreases with increasing values of D.

Due to the thermal heat capacities of the wall and fin materials, the forcing function of temperature at the side of the unfinned wall is damped, resulting in the amplitude of the fin-side surface heat flux being considerably smaller than the heat flux at the unfinned wall. The damping effect of both the wall and the fin is illustrated in Fig. 7 in which the heat flux from the fin-side surfaces and the heat flux at the unfinned wall are presented together. This damping effect is greater for larger frequencies, ω. For steady-state heat transfer the heat flow rate at the unfinned wall is equal to the heat flow rate from the fin-side surfaces.

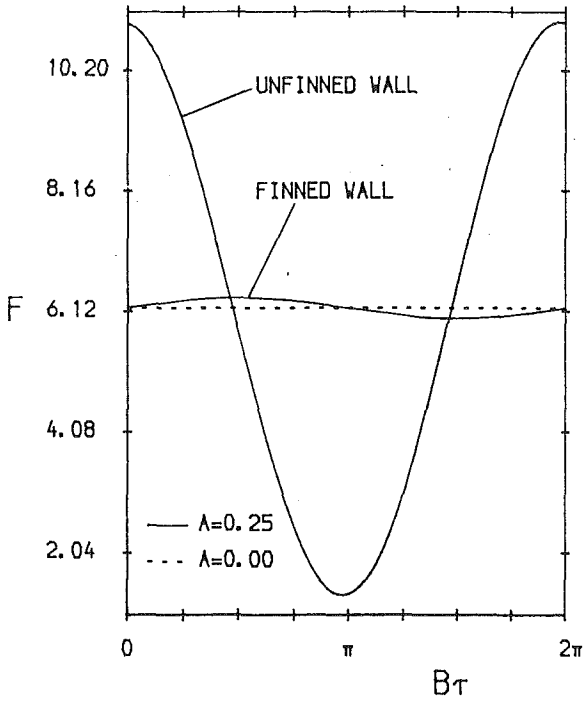

Fig. 7 Damping effect of wall and fin

The results present in this paper have been chosen so as to represent the important phenomena. Numerous other calculations have been performed by the authors and these may be obtained from the authors.

Conclusions

A one-dimensional analytical solution has been developed to determine the oscillatory heat transfer in a fin assembly comprising equally spaced rectangular fins. As in the case of oscillatory heat transfer in the isolated fin (see Houghton et al., 1990), the heat flow rate by convection from the fin-side surfaces is found to oscillate periodically about a mean value, which is the heat flow rate at steady state.

For the isolated fin subjected to an oscillating base temperature, which was investigated by Houghton et al. (1990), it was found that the instantaneous heat flow rate from the fin surface increased with increasing heat transfer coefficient, increasing fin length, and fin thickness. Varying A and the angular frequency of the base temperature oscillation, ω, greatly affects the amplitude of the heat flow oscillation, which becomes greater with larger values of A and smaller values of B $(=\omega P^2/\alpha_w)$.

Similar results have been found for the case of oscillatory heat transfer in a fin assembly. The instantaneous heat flow rate by convection from the fin-side surfaces is found to oscillate periodically about a mean value, which is the fin assembly steady-state heat flow rate. For a fixed value of the fin spacing, the heat flow rate increased in magnitude with greater values of the heat transfer coefficients and larger fin lengths. The greatest augmentation of the heat transfer through the assembly occurs for larger values of the ratio h_1/h_2. The amplitude of the heat flow oscillation is again greatly affected by varying the amplitude, A, and the angular frequency of the ambient temperature oscillation, increasing with increasing values of A and decreasing values of ω. Considerable damping of the heat flow was found to occur due to the presence of the wall and fin. The damping is greater than that observed in the single fin.

For transient heat transfer in a fin assembly the "sum of resistances" method is no longer applicable due to the effects of the thermal capacities of the wall and the fin. Hence the heat transfer rate for transient heat transfer in a fin assembly can only be found by considering the wall and fins simultaneously, i.e., as a complete assembly.

Acknowledgments

This work was performed with the financial support of the Science and Engineering Research Council.

References

Aziz, A., 1975, "Periodic Heat Transfer in Annular Fins," ASME JOURNAL OF HEAT TRANSFER, Vol. 97, pp. 302–303.

Chu, H. S., Weng, C. I., and Chen, C. K., 1983, "Transient Response of a Composite Straight Fin," ASME JOURNAL OF HEAT TRANSFER, Vol. 105, pp. 307–311.

Heggs, P. J., and Stones, P. R., 1980a, "The Effect of Dimensions on the Heat Flowrate Through Extended Surfaces," ASME JOURNAL OF HEAT TRANSFER, Vol. 102, pp. 180–182.

Heggs, P. J., and Stones, P. R., 1980b, "Improved Design Methods for Finned Tube Heat Exchangers," *Transactions of the Institution of Chemical Engineers*, Vol. 58, pp. 147–154.

Houghton, J. M., Ingham, D. B., and Heggs, P. J., 1990, "Oscillatory Heat Transfer in Extended Surfaces," *Heat Transfer 1990*, Vol. 4, Hemisphere Publishing Corporation, New York, pp. 111–116.

Integron Fin Tubes, 1999, *Design Data*, IMI Yorkshire Alloys Ltd., P. O. Box 166, Leeds, United Kingdom.

Ju, Y. H., Chou, Y. S., and Hsiao, C. C., 1989, "A New Approach to the Transient Conduction in a 2-D Rectangular Fin," *International Journal of Heat and Mass Transfer*, Vol. 32, No. 9, pp. 1657–1661.

Manzoor, M., Ingham, D. B., and Heggs, P. J., 1981, "Boundary Integral Element Analysis of Fin Assembly Heat Transfer," *Numerical Heat Transfer*, Vol. 4, pp. 285–301.

Manzoor, M., Ingham, D. B., and Heggs, P. J., 1982a, "The Analysis of Fin Assembly Heat Transfer by a Series Truncation Method," ASME JOURNAL OF HEAT TRANSFER, Vol. 104, pp. 210–212.

Manzoor, M., Ingham, D. B., and Heggs, P. J., 1982b, "The Two-Dimensional Analysis of Fin Assembly Heat Transfer. A Comparison of Solution Techniques," *Proceedings of the 2nd National Conference on Numerical Methods in Heat Transfer*, Hemisphere, Washington, DC.

Manzoor, M., Ingham, D. B., and Heggs, P. J., 1983, "The One-Dimensional Analysis of Fin Assembly Heat Transfer," ASME JOURNAL OF HEAT TRANSFER, Vol. 105, pp. 646–651.

Suryanarayana, N. V., 1975, "Transient Response of Straight Fins," ASME JOURNAL OF HEAT TRANSFER, Vol. 97, pp. 417–423.

Yang, J. W., 1972, "Periodic Heat Transfer in Straight Fins," ASME JOURNAL OF HEAT TRANSFER, Vol. 94, pp. 310–314.

T. R. Hsu
Professor.
Mem. ASME

N. S. Sun

G. G. Chen

Z. L. Gong

San Jose State University,
San Jose, CA 95192-0087

Finite Element Formulation for Two-Dimensional Inverse Heat Conduction Analysis

This paper presents a finite element algorithm for two-dimensional nonlinear inverse heat conduction analysis. The proposed method is capable of handling both unknown surface heat flux and unknown surface temperature of solids using temperature histories measured at a few discrete point. The proposed algorithms were used in the study of the thermofracture behavior of leaking pipelines with experimental verifications.

1 Introduction

In contrast to the direct heat conduction analysis in which the temperature history of the interior of a solid is evaluated by satisfying a set of specified boundary conditions, the inverse heat conduction analysis determines the transient surface temperature or heat flux across the surface using temperature histories specified, or measured at certain discrete points in the solid. The temperature or heat flux at the surfaces of the solid so determined would then be used as the necessary boundary condition for the computation of temperature field in the entire solid, including those on the boundary surfaces, by means of conventional heat conduction analysis. Generally speaking, the inverse heat conduction analysis provides the user with a great advantage in many experimental investigations in which direct measurements of surface conditions are not possible.

Various solution methods have been published to handle the inverse heat conduction problems. These solution methods include graphic (Hartee, 1952), polynomial (Hills and Mulholland, 1979; Frank, 1963; Mulholland et al., 1975; Arledge and Haji-Sheikh, 1977), Laplace transform (Krzystof et al., 1981), exact solution (Stolz, 1960; Sparrow et al., 1964; Burggraf, 1964; Deverall and Channapragada, 1966; Koveryanov, 1967), dynamic programming (Trujillo, 1978; Busby and Trujillo, 1985), finite difference (Beck, 1970; Fidelle and Zinsmeister, 1968; D'Souza, 1975) and finite element methods (Krutz et al., 1978; Bass, 1980). Almost all these methods are restricted to one-dimensional analysis.

There are generally two approaches for the inverse heat conduction analysis. These are: (1) to find the unknown surface heat flux, and (2) to determine the unknown surface temperature. While most of the proposed inverse techniques are applicable for the prediction of the surface heat flux, a few methods (Hills and Mulholland, 1979; Imber, 1974) can be used to determine the surface temperature.

In practice, algorithms developed to determine surface temperature in a one-dimensional analysis can readily lead to the solution of heat flux, or vice versa, as these two quantities can be correlated by a single Fourier law of heat conduction. This simple correlation, however, ceases to exist for multidimensional cases. Formulations derived for the determination of vectorial quantities such as heat flux cannot be used to determine the corresponding surface temperature without additional conversion as temperature is a scalar quantity. Likewise, the inverse heat conduction formulations derived for the surface temperature cannot be readily correlated to the surface heat flux for the same reason. The situation can be better illustrated by examining a hypothetical case related to a two-dimensional heat conduction problem as depicted in Fig. 1. The solid with a semicircular geometry has its curved surface thermally insulated while the temperature at the straight boundary is maintained at a uniform temperature. It is entirely conceivable that the corresponding heat flux across various parts of this boundary has different magnitudes. Correlation between the surface temperature to the corresponding heat flux vectors is much more complicated than that in the one-dimensional analysis. Separated formulations for these two quantities in two-dimensional geometries thus become necessary (Hensel, 1986).

This paper presents two unified finite element algorithms for the solution of general two-dimensional nonlinear inverse heat conduction analysis. One algorithm was derived on the basis of boundary heat flux while the other on the surface temperature. In some way this method may be perceived as an extension of Beck's method (Beck et al., 1982). Either algorithm is capable of evaluating both surface heat flux and surface temperatures. The mathematical framework of this method is so general that a variety of inverse heat conduction problems involving solids of planar and axisymmetric geometries can be treated. Other inherent complexities such as material nonlinearity and the number and locations of the data points have all been included in the algorithm.

A numerical example is included to demonstrate the application of the algorithm. This application relates to the determination of the temperature of the surfaces of a crack in a leaking pipe using measured temperature at five nearby locations. The computed temperature drop on the crack surfaces was then used to assess the temperature field in the pipeline near the crack tip. The resulting temperature distribution was then used to assess the thermofracture behavior of the leaking pipeline.

2 Determination of Unknown Surface Heat Fluxes

A two-dimensional body subjected to unknown heat fluxes $q_1(t), q_2(t), \ldots, q_m(t)$ on respective boundary surfaces $S_1, S_2,$

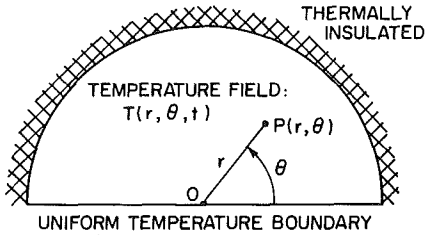

Fig. 1 A solid with semicircular cross section

Contributed by the Heat Transfer Division for publication in the JOURNAL OF HEAT TRANSFER. Manuscript received by the Heat Transfer Division August 1990; revision received February 1992. Keywords: Conduction, Numerical Methods. Technical Editor: R. Viskanta.

..., S_m is illustrated in Fig. 2. Let the measured temperature histories at some interior points a_1, a_2, ..., a_r in the body be $d_1(t)$, $d_2(t)$, ..., $d_r(t)$. The following derivation will be presented to determine the unknown transient heat fluxes $q_1(t)$, $q_2(t)$, ..., $q_m(t)$ corresponding to the above conditions.

The partial differential equation that describes the temperature distribution in a two-dimensional region defined by the x–y coordinate system takes the form:

$$\frac{\partial}{\partial x}\left(k_x \frac{\partial T}{\partial x}\right)+\frac{\partial}{\partial y}\left(k_y \frac{\partial T}{\partial y}\right)=\rho C \frac{\partial T}{\partial t} \tag{1}$$

in which T denotes the temperature field $T(x, y, t)$. The notations k_x and k_y are the thermal conductivities of the material in the respective x and y directions, ρ is the density, and C is specific heat of the material. The variable t denotes time. The physical parameters k_x, k_y, and ρC may be regarded as temperature dependent. The boundary conditions considered in this case can be expressed as:

$$k \frac{\partial T}{\partial n}\bigg|_{S_1}=q_1(t),\ k \frac{\partial T}{\partial n}\bigg|_{S_2}=q_2(t),\ \ldots,\ k \frac{\partial T}{\partial n}\bigg|_{S_m}=q_m(t) \tag{1a}$$

and the initial condition is

$$T(x, y, 0)=T_o(x, y) \tag{1b}$$

By the conventional finite element procedure, Eq. (1) can be converted to the following discrete form:

$$\mathbf{K}^* \mathbf{T}_{t+\Delta t}=\mathbf{K}^{**} \mathbf{T}_t+\mathbf{Q} \tag{2}$$

with the initial condition

$$\mathbf{T}(0)=\mathbf{T}_o \tag{3}$$

By using the Crank–Nicholson integration scheme, the coefficient thermal force matrices in Eq. (2) may be expressed as (Zienkiewicz, 1977; Hsu, 1986):

$$\mathbf{K}^*=\frac{2\mathbf{C}}{\Delta t}+\mathbf{K} \tag{4a}$$

$$\mathbf{K}^{**}=\frac{2\mathbf{C}}{\Delta t}-\mathbf{K} \tag{4b}$$

$$\mathbf{Q}=\mathbf{Q}_t+\mathbf{Q}_{t+\Delta t} \tag{4c}$$

in which $\mathbf{C}$ is the capacity matrix, $\mathbf{K}$ is the conductivity matrix and $\mathbf{Q}_t$ and $\mathbf{Q}_{t+\Delta t}$ denote the respective thermal force vectors at time t and $t+\Delta t$.

If the change in the material properties with temperature is small or moderate within the time step size Δt, it is reasonable to assume that the thermal properties can be regarded constant within the time interval between t and $t+\Delta t$. This approximation justifies the linearization of the analysis. Thus, by differentiating both sides of Eq. (2) with respect to q_i ($i=1,\ldots,m$) as indicated in Eq. (1a), one may obtain the following expression:

$$\mathbf{K}^* \frac{\partial \mathbf{T}_{t+\Delta t}}{\partial q_i}=\int_{S_i} \mathbf{N}^T dS \quad (i=1,\ldots,m) \tag{5}$$

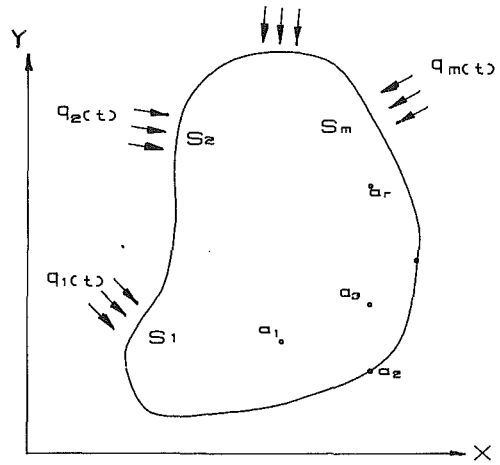

Fig. 2 A two-dimensional solid with unknown boundary heat fluxes

in which $\mathbf{N}$ is the interpolation function matrix, which relates the temperature in the element to its corresponding nodes.

It is obvious that the temperature $\mathbf{T}$ is a function of $\mathbf{q}$, and the Taylor expansion about $\mathbf{T}$ in the time period Δt provides:

$$\mathbf{T}_{t+\Delta t}=\mathbf{T}^*_{t+\Delta t}+\frac{\partial \mathbf{T}_{t+\Delta t}}{\partial \mathbf{q}} \cdot \Delta \mathbf{q}_{t+\Delta t} \tag{6}$$

$$(n\times 1) \qquad (n\times 1) \qquad (n\times m) \qquad (m\times 1)$$

The quantities included in the parentheses in the above equation denote the dimension of matrices. The matrix $\Delta \mathbf{q}_{t+\Delta t}$ is the increment of heat flux across the boundary. Let us define a diagonal matrix $\mathbf{A}$ with entries a_1, a_2,...,a_r, such that:

$$\mathbf{Y}(t)=\mathbf{A}\mathbf{T}(t) \tag{7}$$

where $\mathbf{Y}$ is a $(r\times n)$ matrix, which represents the temperatures measured at the discrete points a_1, a_2,...a_r. Multiplying both sides of Eq. (6) by matrix $\mathbf{A}$ will yield:

$$\mathbf{Y}_{t+\Delta t}=\mathbf{Y}^*_{t+\Delta t}+\frac{\partial \mathbf{Y}_{t+\Delta t}}{\partial \mathbf{q}} \Delta \mathbf{q}_{t+\Delta t} \tag{8}$$

If the increment of heat flux $\Delta \mathbf{q}_{t+\Delta t}$ is to be determined by a least-square criterion then the inherent error can be expressed as:

$$E(\mathbf{q})=(\mathbf{Y}_{t+\Delta t}-\mathbf{d}_{t+\Delta t})^T \mathbf{W}(\mathbf{Y}_{t+\Delta t}-\mathbf{d}_{t+\Delta t}) \tag{9}$$

in which $\mathbf{d}_{t+\Delta t}=\{d_{1,t+\Delta t} \quad d_{2,t+\Delta t}\ldots d_{r,t+\Delta t}\}^T$ represents the measured temperature at corresponding data points a_1, a_2,...,a_r. The weighting matrix $\mathbf{W}$ is a diagonal matrix.

Upon minimizing the above least-square function $E(\mathbf{q})$, the following set of simultaneous equations is obtained:

$$\frac{\partial E(\mathbf{q})}{\partial \mathbf{q}}=0 \tag{10}$$

Substituting Eqs. (8) and (9) into Eq. (10) will lead to:

$$\mathbf{D}_1 \Delta \mathbf{q}_{t+\Delta t}=\mathbf{P}_1 \tag{11}$$

Nomenclature

C = specific heat
$\mathbf{C}$ = heat capacitance matrix
k_x, k_y = thermal conductivities of material in respective x and y directions
k_{ij} = elements of thermal conductivity matrix
$\mathbf{K}$ = thermal conductivity matrix
$\mathbf{N}$ = interpolation function matrix
q_i = elements of heat flux matrix
$\mathbf{q}$ = heat flux matrix
$\mathbf{Q}$ = thermal force matrix
S = boundary surfaces of an element
t = time
T = temperature
$\mathbf{T}$ = temperature matrix
$\mathbf{W}$ = weighting diagonal matrix
$\mathbf{Y}$ = temperature matrix involving measured values at discrete points
ρ = density

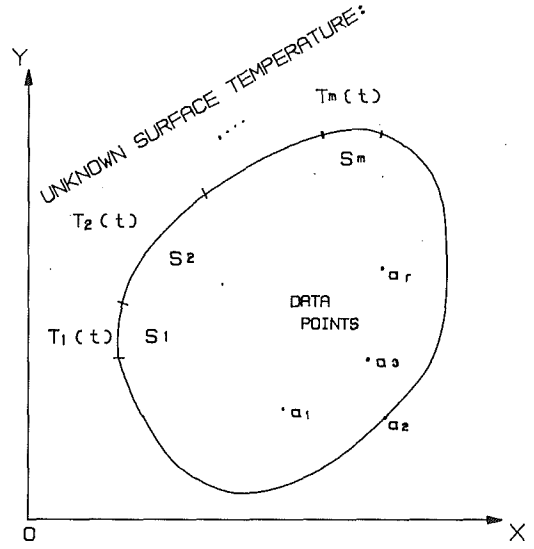

Fig. 3 A two-dimensional solid with unknown boundary temperatures

where $\mathbf{D}_1$ is a $(r\times m)$ matrix and $\mathbf{P}_1$ is a $(m\times 1)$ matrix with the forms:

$$\mathbf{D}_1=\left(\frac{\partial \mathbf{Y}}{\partial \mathbf{q}}\right)^T \mathbf{W}\frac{\partial \mathbf{Y}}{\partial \mathbf{q}}$$

$$\mathbf{P}_1=\left(\frac{\partial \mathbf{Y}}{\partial \mathbf{q}}\right)^T \mathbf{W}(\mathbf{d}_{t+\Delta t}-\mathbf{Y}^*_{t+\Delta t}) \tag{12}$$

Thus, the increment of heat flux $\Delta\mathbf{q}_{t+\Delta t}$ can readily be solved from Eq. (11) and the heat flux $\mathbf{q}_{t+\Delta t}$ at time $t+\Delta t$. The temperature $\mathbf{T}_{t+\Delta t}$ at all nodes, including those at $a_1,\ldots,a_r$, can be evaluated from Eq. (6).

3 Determination of Unknown Surface Temperatures

Let us assume that the temperature variations on the boundaries $S_1, S_2,\ldots,S_m$ of a solid follow a set of unknown functions, $T_1^\circ(t), T_2^\circ(t),\ldots,T_m^\circ(t)$, as illustrated in Fig. 3. The following derivation will lead to the solution of the unknown surface temperature functions $T_1^\circ(t), T_2^\circ(t),\ldots,T_m^\circ(t)$, from the measured values $d_1(t), d_2(t),\ldots,d_r(t)$.

The discrete form of the partial differential equation for this case is similar to Eq. (2) with the absence of thermal forces, or:

$$\mathbf{K}^*\mathbf{T}_{t+\Delta t}=\mathbf{K}^{**}\mathbf{T}_t \tag{13}$$

in which $\mathbf{K}^*$ and $\mathbf{K}^{**}$ are defined in Eqs. (4*a*) and (4*b*). Let us assign the numbers of the nodes in the region in the following way:

$1, 2,\ldots,L_1$	on the surface S_1
$L_1+1, L_1+2,\ldots,L_2$	on the surface S_2
.	.
.	.
.	.
.	.
.	.
.	.
.	.
$L_{m-1}+1, L_{m-1}+2,\ldots,L_m$	on the surface S_m

and $L_{m+1},\ldots,L_n$ for the remaining nodes in the region, where the subscript n denotes total number of nodes. Equation (13) can be expressed in a differential form after introducing the above numbering system for the nodes:

$$\sum_{j=1}^{L_n} k^*_{ij}T_{j,t+\Delta t}=\sum_{j=1}^{L_n} k^{**}_{ij}T_{j,t}\quad (i=1,\ldots,L_n) \tag{14}$$

and the boundary conditions become:

$$T_{1,t+\Delta t}=T_{2,t+\Delta t}=\ldots=T_{L_1,t+\Delta t}=T^\circ_{1,t+\Delta t}$$

$$T_{L_1+1,t+\Delta t}=T_{L_1+2,t+\Delta t}=\ldots=T_{L_2,t+\Delta t}=T^\circ_{2,t+\Delta t}$$

$$T_{L_{m-1},t+\Delta t}=\ldots=T_{L_m,t+\Delta t}=T^\circ_{m,t+\Delta t} \tag{15}$$

The vector quantities k^*_{ij} and k^{**}_{ij} in Eq. (14) denote the respective elements in matrices $\mathbf{K}^*$ and $\mathbf{K}^{**}$.

By substituting Eq. (15) into Eq. (14), and differentiating both sides of the resulting equation with respect to $\mathbf{T}^o_s$ $(s=1,2,\ldots,m)$, one obtains the following set of equations:

$$\sum_{j=L_m+1}^{L_n} k^*_{ij}\frac{\partial T_{j,t+\Delta t}}{\partial T^\circ_1}=-\sum_{j=1}^{L_1}k^*_{ij}$$

$$\sum_{j=L_m+1}^{L_n} k^*_{ij}\frac{\partial T_{j,t+\Delta t}}{\partial T^\circ_2}=-\sum_{j=L_1+1}^{L_2}k^*_{ij}$$

$$\vdots \qquad\qquad \vdots$$

$$\sum_{j=L_m+1}^{L_n} k^*_{ij}\frac{\partial T_{j,t+\Delta t}}{\partial T^\circ_m}=-\sum_{j=L_{m-1}+1}^{L_m}k^*_{ij}\quad (i=L_m+1,\ldots,L_n) \tag{16}$$

The temperatures $\mathbf{T}_{t+\Delta t}$ can be expressed in the following form by the Taylor expansion:

$$\mathbf{T}_{t+\Delta t}=\mathbf{T}^*_{t+\Delta t}+\frac{\partial \mathbf{T}_{t+\Delta t}}{\partial \mathbf{T}^\circ}\Delta\mathbf{T}^\circ_{t+\Delta t} \tag{17}$$

The $\mathbf{T}^*_{t+\Delta t}$ in Eq. (17) denotes the temperatures $\mathbf{T}$ with $\mathbf{T}^\circ_{t+\Delta t}$ being replaced by $\mathbf{T}^\circ_t$. Multiplying both sides of Eq. (17) by the matrix $\mathbf{A}$ as defined in Eq. (7), the following relation will yield:

$$\mathbf{Y}_{t+\Delta t}=\mathbf{Y}^*_{t+\Delta t}+\frac{\partial \mathbf{Y}_{t+\Delta t}}{\partial \mathbf{T}^\circ}\Delta\mathbf{T}^\circ_{t+\Delta t} \tag{18}$$

The error in the least-square approximation can be expressed in the usual form as:

$$E(\mathbf{T}^\circ)=(\mathbf{Y}_{t+\Delta t}-\mathbf{d}_{t+\Delta t})^T\mathbf{W}(\mathbf{Y}_{t+\Delta t}-\mathbf{d}_{t+\Delta t}) \tag{19}$$

from which the increment of the surface temperature $\Delta\mathbf{T}^\circ_{t+\Delta t}$ can be solved by minimizing the error function, $E(\mathbf{T}^\circ)$ as shown in Eq. (19) by letting:

$$\frac{\partial E(\mathbf{T}^\circ)}{\partial \mathbf{T}^\circ}=0$$

or in a compact form:

$$\mathbf{D}_2\Delta T^\circ_{t+\Delta t}=\mathbf{P}_2 \tag{20}$$

in which

$$\mathbf{D}_2=\left(\frac{\partial \mathbf{Y}}{\partial \mathbf{T}^\circ}\right)^T\mathbf{W}\frac{\partial \mathbf{Y}}{\partial \mathbf{T}^\circ}$$

$$\mathbf{P}_2=\left(\frac{\partial \mathbf{Y}}{\partial \mathbf{T}^\circ}\right)^T\mathbf{W}(\mathbf{d}_{t+\Delta t}-\mathbf{Y}^*_{t+\Delta t}) \tag{21}$$

Once $\Delta\mathbf{T}^\circ_{t+\Delta t}$ is solved from Eq. (20), the surface temperatures $\mathbf{T}^\circ_{t+\Delta t}$ can be calculated, and the temperature $\mathbf{T}^\circ_{t+\Delta t}$ can be determined by using Eq. (17).

4 Computer Implementation

Normal procedures for nonlinear heat conduction analysis were followed. In the case of temperature-independent material

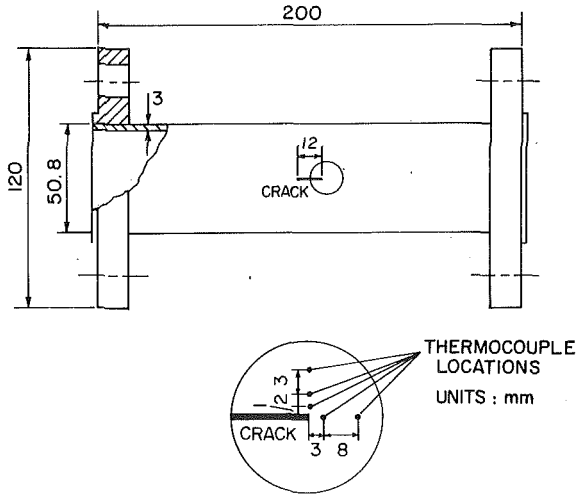

Fig. 4 Dimensions of a test pipe section and the locations of thermocouples

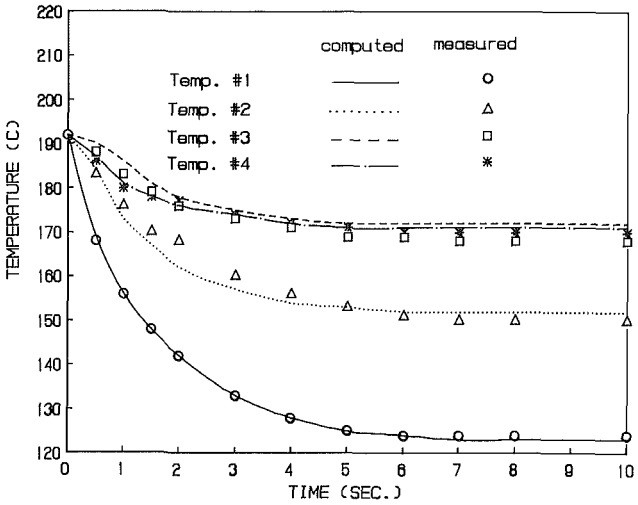

Fig. 5 Correlations of measured and computed temperatures at four thermocouple locations

properties, the matrices $\mathbf{K}^*$ and $\mathbf{D}_1$ (or $\mathbf{D}_2$ in the case of surface temperatures) need to be formed only once. Otherwise, these two matrices would have to be formed after every time step according to temperature values at the last step. The matrix $\mathbf{T}^*_{t+\Delta t}$ is solved by back-substitution. This procedure is noniterative and takes little more computer time than direct solution in which boundary conditions are specified. It is thus computationally efficient.

Another unique advantage of this method is that the present algorithm is consistent with the semidiscretization approach for the direct transient heat conduction analysis (Zienkiewicz, 1977; Hsu, 1986). Hence it can be readily implemented into existing finite element program such as TEPSAC code (Hsu, 1986).

5 Numerical Illustration

The inverse heat conduction algorithm presented in the preceding sections has been implemented into an existing finite element code, TEPSAC (Hsu, 1986). It is applied to solve a practical problem related to the assessment of thermal fracture behavior of a leaking pipe containing a high-temperature pressure medium.

The authors have demonstrated in a previous paper (Hsu et al., 1986) that when pressurized saturated water leaks through

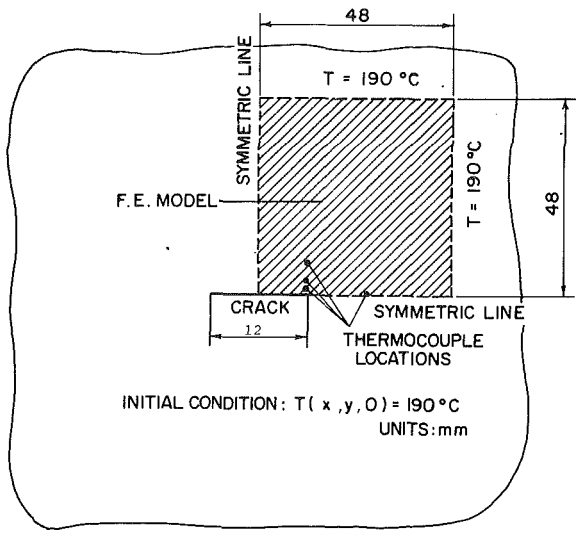

Fig. 6 Finite element model region

a slit or crack in a pipeline, a significant temperature drop could occur at the crack surfaces. This phenomenon can be attributed to the well-known thermal throttling effect. This local cooling effect has shown to substantially increase the value of the J-integral that characterizes the stress field near the crack.

In order to evaluate the J-integral associated with this local cooling effect and hence the fracture behavior of the leaking pipe, a thermal stress analysis had to be performed. The major difficulty involved in this analysis is that the thermal boundary condition on the crack surfaces is not available. Since the direct measurement of the temperature or heat flux across the leaking crack surface cannot be made, the inverse theory as presented in the previous section become the only practical solution. An experiment was carried out in the authors' laboratory to demonstrate the feasibility of such an approach. A detailed description of the experiment is presented by Sun et al. (1989).

The dimensions of the test pipe section are indicated in Fig. 4 in which the locations of five thermocouples are designated. The temperature variations measured at the four locations (No. 1–4) during the leaking process have been shown in Fig. 5. The temperature at location 5 was virtually unchanged during the entire test period.

The measured temperatures were used to determine the crack surface temperature by the inverse algorithm presented in Section 3. The unknown temperature of the crack surface was assumed to be uniform during the leaking process. This hypothesis is considered to be reasonable as the mixture of vapor and water ejected from the crack is at a high velocity. Consequently, little variation of temperature along the crack surface is expected during the leaking process.[1] The modeled zone used in the analysis is illustrated in Fig. 6. The originally curved surface of the pipe wall was treated as a flat plate.

Figure 7 shows the computed temperature history of the crack surface as the result of the inverse analysis. Comparisons between the computed and measured temperature at data points 1–4 are depicted in Fig. 5. Agreement between these sets of values is excellent. The computed temperature distribution near the crack surface at various instants was computed as shown in Fig. 8. The associated thermal stress and fracture analysis is described by Hsu et al. (1986).

[1]The heat flux across the crack surface, however, is not constant. The case with maximum heat flux was calculated to vary from 1.5 W/mm at the center to 0.1 W/mm toward the tip of the crack.

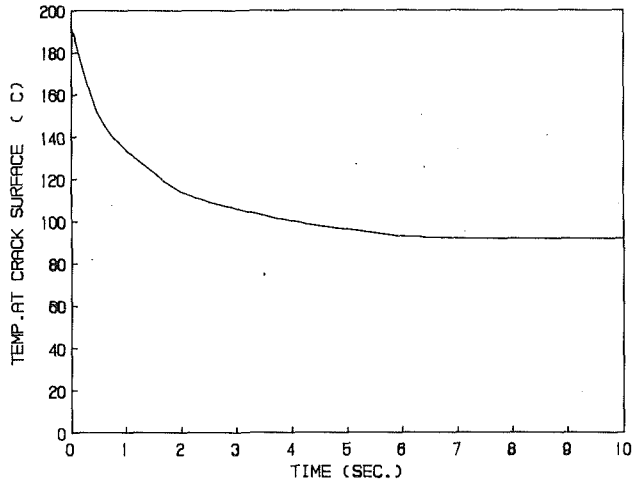

Fig. 7 Computed temperature variation at crack surfaces

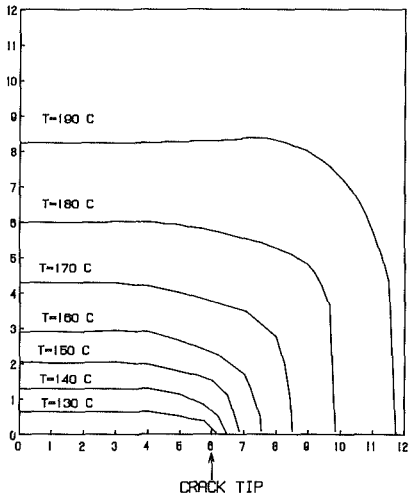

Fig. 8 Computed temperature distribution near crack at $t = 1.5$ s

6 Concluding Remarks

Two finite element algorithms for two-dimensional inverse heat conduction analysis have been presented. The unique feature of the proposed algorithms is that either algorithm can be used to treat both cases with unknown surface heat flux and surface temperature in a unified way. It thus provides a great flexibility in solving general two-dimensional inverse heat conduction problems.

The value of the proposed two-dimensional inverse method has been demonstrated in a case study involving the thermal fracture of a pipeline. The excellent correlation of the computed temperature histories and those measured at selected points in the pipe wall as shown in Fig. 5 provides a clear indication of the credibility of the proposed formulations.

Numerical studies on several other cases by using the present method also indicate that the number of input data has a significant effect on the accuracy of predicted surface conditions in two-dimensional inverse analyses, whereas one data point is usually sufficient for a one-dimensional analysis. The number of required input data becomes even more critical when the input temperatures used in the analysis are not very accurate. In such cases input from a large number of data points are required to yield accurate results.

Another unique advantage of the present formulation is that it is noniterative and can be easily adapted to existing finite element programs. Nonlinear material properties can also be readily accommodated.

Acknowledgments

The authors gratefully acknowledge the financial support to this research by the Natural Sciences and Engineering Research Council of Canada.

References

Arledge, R. G., and Haji-Sheikh, A., 1977, "An Iterative Approach to the Solution of Inverse Heat Conduction Problem," ASME Paper No. 77-WA/TM-2.

Bass, B. R., 1980, "Application of the Finite Element Method to the Nonlinear Inverse Heat Conduction Problem Using Beck's Second Method," ASME *Journal of Engineering for Industry*, Vol. 102, pp. 168–176.

Beck, J. V., 1970, "Non-linear Estimation Applied to the Non-linear Inverse Heat Conduction Problem," *Int. J. Heat Mass Transfer*, Vol. 13, pp. 703–716.

Beck, J. V., Litkouki, B., and St. Clair, C. R., Jr., 1982, "Efficient Sequential Solution of the Nonlinear Inverse Heat Conduction Problem," *Num. Heat Transfer*, Vol. 5, pp. 275–286.

Burggraf, O. R., 1964, "An Exact Solution of the Inverse Problem in Heat Conduction Theory and Applications," ASME JOURNAL OF HEAT TRANSFER, Vol. 86, pp. 373–382.

Busby, H. R., and Trujillo, D. M., 1985, "Numerical Solution to a Two-Dimensional Inverse Heat Conduction Problem," *Int. J. Num. Meth. Eng.*, Vol. 21, pp. 349–359.

Deverall, L. I., and Channapragada, R. S., 1966, "A New Integral Equation for Heat Flux in Inverse Heat Conduction," ASME JOURNAL OF HEAT TRANSFER, Vol. 88, pp. 327–328.

D'Souza, N., 1975, "Numerical Solution of One-Dimensional Inverse Transient Heat Conduction by Finite Difference Method," ASME Paper No. 75-WA/HT-81.

Fidelle, T. P., and Zinsmeister, G. E., 1968, "A Semi-Discrete Approximate Solution of the Inverse Problem of Transient Heat Conduction," ASME Paper No. 68-WA/HT-26.

Frank, I., 1963, "An Application of Least Squares Method to the Solution of the Inverse Problem of Heat Conduction," ASME JOURNAL OF HEAT TRANSFER, Vol. 85, pp. 378–379.

Hartree, D. R., 1952, *Numerical Analysis*, Oxford University Press, London, United Kingdom.

Hensel, E., 1986, "Multi-dimensional Inverse Heat Conduction," Ph.D. Thesis, New Mexico University.

Hills, R. G., and Mulholland, G. P., 1979, "The Accuracy and Resolving Power of One Dimensional Transient Inverse Heat Conduction Theory as Applied to Discrete and Inaccurate Measurements," *Int. J. Heat Mass Transfer*, Vol. 22, pp. 1221–1229.

Hsu, T. R., 1986, *The Finite Element Method in Thermomechanics*, George Allen & Unwin Ltd., London, United Kingdom.

Hsu, T. R., Chen, G. G., Gong, Z. L., and Sun, N. S., 1986, "On Thermofracture Behavior of Leaking Thin-Wall Pipes," *Int. J. Pres. Ves. & Piping*, Vol. 24, pp. 269–281.

Imber, M., 1974, "A Temperature Extrapolation Mechanism for Two-Dimensional Heat Flow," *AIAA J.*, Vol. 12, pp. 1087–1093.

Incropera, F. P., and De Witt, D. P., 1981, *Fundamentals of Heat Transfer*, Wiley, New York.

Koveryanov, A. V., 1967, "Inverse Problem of Nonsteady State Thermal Conductivity," *High Temperature*, Vol. 5, pp. 121–127.

Krutz, G. W., Schoenhals, R. J., and Hore, P. S., 1978, "Application of Finite Element Method to the Inverse Heat Conduction Problem," *Num. Heat Transfer*, Vol. 1, pp. 489–498.

Krzystof, G., Cialkowski, M. J., and Kaminski, H., 1981, "An Inverse Temperature Field Problem of the Theory of Thermal Stresses," *Nucl. Eng. Des.*, Vol. 64, pp. 169–184.

Mulholland, G. P., Gupta, B. P., and San Martin, R. L., 1975, "Inverse Problem of Heat Conduction in Composite Media," ASME Paper No. 75-WA/HT-83.

Sparrow, E. M., Haji-Sheikh, A., and Lundgren, T. S., 1964, "The Inverse Problem in Transient Heat Conduction," ASME *Journal of Applied Mechanics*, Vol. 86, pp. 369–375.

Stolz, G., Jr., 1960, "Numerical Solutions to an Inverse Problem of Heat Conduction for Simple Shapes," ASME JOURNAL OF HEAT TRANSFER, Vol. 82, pp. 20–26.

Sun, N. S., Hsu, T. R., Gong, Z. L., and Chen, G. G., 1989, "An Experimental Study of Thermofracture Behaviour of Leaking Pipes," *Experimental Techniques*, Sept., pp. 16–20.

Trujillo, D. M., 1978, "Application of Dynamic Programming to the General Inverse Problem," *Int. J. Num. Meth. Eng.*, Vol. 12, pp. 613–624.

Zienkiewicz, O. C., 1977, *The Finite Element Method*, 3rd ed., McGraw-Hill, New York.

D. Kundu
IMCOA, Inc.,
Haltom City, TX 76117

A. Haji-Sheikh

D. Y. S. Lou

Department of Mechanical Engineering,
University of Texas at Arlington,
Arlington, TX 76019-0023

Heat Transfer in Crossflow Over Cylinders Between Two Parallel Plates

The heat transfer coefficient and pressure drop are measured for laminar and turbulent incompressible flow over an in-line cylinder array (eight copper tubes) between two parallel plates. Data are given using two different aspect ratios for the intermediate range of the Reynolds number between 220 to 2800. A criterion is defined for flow transition from laminar to turbulent. The pressure and heat transfer data are compared to numerically computed data obtained for laminar flow and the results exhibit reasonably good agreement.

Introduction

Experimental data are presented for heat transfer from an array of in-line cylinders (eight copper tubes) centrally located and placed equidistant between two parallel plates. Similar measurements of Nusselt numbers for constant wall heat flux are reported by Oyakawa and Mabuchi (1981, 1983). Oyakawa and Mabuchi (1981) measured the heat transfer coefficient for the fully developed turbulent fluid flow between two parallel plates with a single cylinder for cylinder-diameter to duct-height ratio of 0.4 to 0.8. Later, Oyakawa and Mabuchi (1983) reported heat transfer for turbulent flow in a parallel plate channel with two rows of staggered circular cylinders. They used an H/D ratio of 2.5 where H is the spacing between plates and D is the diameter of the cylinder.

The heat exchanger studied is shown in Fig. 1. It approximates a coil heat exchanger, Fig. 2, with industrial applications. The heat transfer for Heat Exchanger Modules (HEMs), shown in Fig. 1, is measured and results are reported. A HEM is a section of the heat exchanger designated by dashed lines in Fig. 1. It is a section of duct between two parallel plates, having a length L. Each HEM contains one cylinder. The heat transfer coefficient and pressure drop for two aspect ratios are measured. All cylinders and both plates are at the same constant temperature. The Nusselt number that represents the heat transfer coefficient is measured as a function of the Reynolds number.

The experimental data are primarily for transition and turbulent regimes. It is inefficient to use the apparatus described in this study for Reynolds numbers significantly higher or lower. Data for higher Reynolds numbers require redesign of the experimental setup with larger dimensions. However, a scheme is introduced to provide a first-order estimation when empirical data are unavailable. The scheme is based on physical reasoning and uses information available for heat transfer from a bank of aligned cylinders and heat transfer for flow in a parallel plate channel.

Apparatus

The experimental apparatus consists of two compressors, venturi, settling chamber and entrance section, test section, and wooden mixing chamber. A schematic of the apparatus is shown in Fig. 3.

Two compressors operating in a parallel arrangement supply the required air flow rate: a water-cooled rotary compressor delivers 0.3 m^3 of air per minute at 0.34 M Pa (50 psi), and a two-stage air compressor delivers 0.11 m^3 of air per minute at 1.2 M Pa (175 psi).

A venturi tube, with 0.0214 m inlet and 0.0107 m throat diameters, is used to measure the velocity and the flow rate of air. Air enters a settling chamber 0.276 m wide, 0.1 m high, and 0.158 m long. Air from the settling chamber then passes through a long rectangular duct to provide fully developed flow. The 0.0095-m-thick Plexiglas duct is 1.83 m long, and inside dimensions are 0.149 m by 0.0254 m. All joints are sealed and the duct is attached flush with the test section.

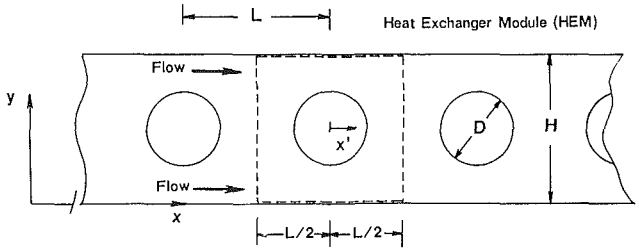

Fig. 1 Heat exchanger and heat exchanger module (HEM)

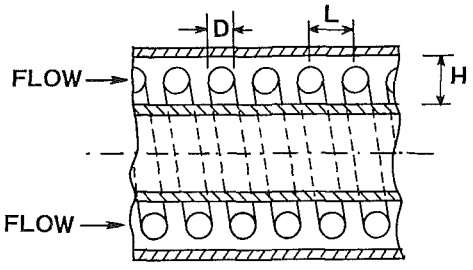

Fig. 2 Schematic of a coil heat exchanger

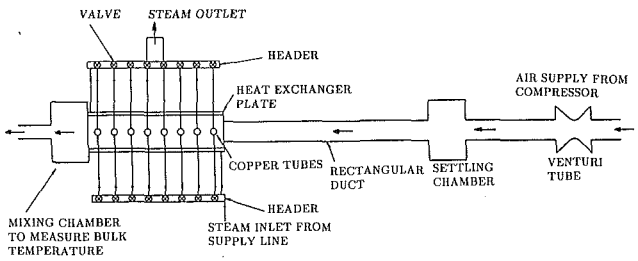

Fig. 3 Schematic of apparatus

Contributed by the Heat Transfer Division for publication in the JOURNAL OF HEAT TRANSFER. Manuscript received by the Heat Transfer Division January 1991; revision received February 1992. Keywords: Augmentation and Enhancement, Forced Convection, Heat Exchangers. Associate Technical Editor: J. H. Kim.

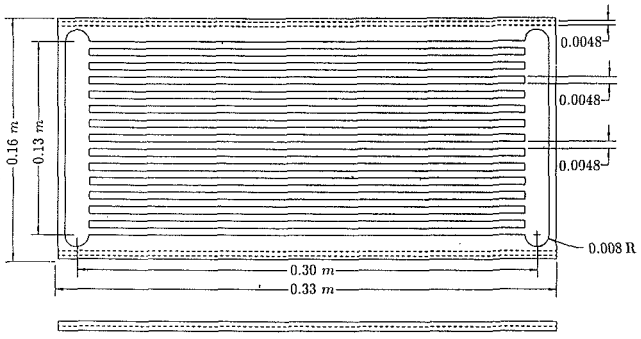

Fig. 4 Steam passages in upper and lower plates

The test section is designed to measure the heat transfer coefficient and the pressure drop, and to maintain a constant wall temperature. It is 0.33 m long, 0.16 m wide, and 0.0254 m high. It has an upper plate and a lower plate placed parallel to the bulk flow direction. Eight parallel copper tubes with outside diameter of 0.0127 m form the cylinder array; each tube is centrally located between the parallel plates and perpendicular to the bulk flow direction. However, the word "tube" in this study is used for reference to internal flow or to describe materials used, and "cylinder" for reference to crossflow of air. The upper and lower aluminum plates are 0.33 m long and 0.16 m wide. Each plate is a heat exchanger comprised of two aluminum parts, a 0.0065-mm-thick main plate and a cover plate, welded together. Steam heats the upper and lower plates. The upper and lower plates are similarly constructed; details are given below.

The steam passages shown in Fig. 4 have two headers, each 0.0111 m wide, 0.13 m long, and 0.3 m apart, milled along the width of the main aluminum plate. The header near the entry side of the steam passage has two inlet ports. The header near the exit has two outlet ports. The headers are connected by 14 steam passages, 0.0048-m-wide and 0.29-m-long grooves milled perpendicular to the headers and along the length of the main aluminum plate, shown in Fig. 4.

The test section has Plexiglas side walls. Each main plate has two 0.00325-m-deep channels milled on the external side to hold the side walls. The Plexiglas pieces are 0.33 m long, 0.032 m high, and 0.0045 m thick. Each piece has eight 0.0127-m-dia holes, 0.038 m apart, along the length and centered midway between the two main aluminum plates. Eight 0.0127-m-dia copper tubes, press fitted into these holes, form the cylinder array. Type L copper is chosen because of its high thermal conductivity and rigidity.

Each copper cylinder in the test section is connected to a separate gate valve at the inlet side. A gate valve at the outlet side prevents back flow of steam into the copper cylinders. The valves are connected to the cylinders via Teflon tubing, as shown in Fig. 3, to reduce unwanted heat conduction to and from the test section. The inlet valves regulate the steam supply through preselected copper cylinders. All eight valves at the inlet side are connected to a main supply pipe (Fig. 3). The main supply line is connected to the steam service line. The outlet side valves are connected to a collection pipe and drain. Steam from the service line branches into two different supply lines: One supply line provides steam to the cylinders and the other one is connected to the inlet ports of the upper and lower plates.

A labyrinth mixing chamber, made of 0.0048-m-thick balsa wood and located after the test section, mixes the air when it leaves the test section. The mixing chamber, shown in Fig. 3, is 0.2 m long, 0.152 m wide and 0.051 m high, with two baffles in tandem, each 0.1 m long and 0.076 m high. Copper meshes (scouring pads) inside the mixing chamber keep the temperature gradient of the air uniform.

Instrumentation

The instrumentation is implemented to measure temperature, pressure difference, and flow rate. The temperature is measured at various sections of the heated plate to monitor the constant wall temperature condition. Thermocouples in the mixing chamber provide the final bulk temperature. Pressure measurements taken at different points along the test section are used to calculate the pressure coefficient.

The incoming air flow rate from the compressor is measured by a calibrated venturi, constructed according to ASME standards. The estimated error of flow measurement is typically ± 1 percent. The upstream static pressure and the pressure difference between the inlet and the throat are measured by U-tube water manometers. When necessary, a traveling optical microscope reads the difference in the water level.

Sixteen copper-constantan thermocouples monitor the plate temperature at various points in the test section. One thermocouple in the mixing chamber before the entrance to the rectangular duct measures air inlet temperature. Another thermocouple in the rectangular duct just before the entrance to the test section monitors the temperature of the incoming air. Two thermocouples measure the steam temperature as it passes through the tubes, and the upper and lower plates: one at the inlet side and another at the outlet side. Two more thermocouples are placed in the mixing chamber to measure the bulk temperature of the air leaving the test section. The two thermocouples in the mixing chamber ensure that no significant temperature gradient exists between two preselected points in the mixing chamber and that the mixing process is satisfactory. The remaining thermocouples are placed in holes drilled in the lower plate. All thermocouples are connected to a data acquisition system (scanner, voltmeter, and controller). The scanner reads temperature at 200-ms intervals, i.e., five readings per second, and sends a signal to the digital voltmeter. The resolution of the voltmeter is 1 μV and accuracy ± 0.1°C.

Pressure taps were centrally located on the upper plate to measure pressure drop across the HEMs. The first pressure tap is between the first and second cylinders and the last pressure tap is between the seventh and eighth cylinders. A Barocell

Nomenclature

A = area, m^2
c_p = specific heat, J/kg•K
D = diameter of cylinder, m
De = equivalent hydraulic diameter $= 2(H - D)$
$\bar{h}$ = heat transfer coefficient, W/m^2•K
H = distance between plates, m
k = thermal conductivity, W/m•K
L = spacing between cylinders, m
$\dot{m}$ = mass flow rate, kg/s
$\overline{Nu}_H$ = Nusselt number $= \bar{h}H/k$
$\overline{Nu}_i$ = Nusselt number $= \bar{h}_iH/k$
p = pressure, Pa
p^* = dimensionless pressure $= p/\rho u_m^2$
Pr = Prandtl number $= \mu c_p/k$
Re_H = Reynolds number $= u_mH/\nu$
T = temperature, K
u_m = average velocity, m/s
u_{max} = $u_m \times H/(H - D)$
μ = viscosity coefficient, N•s/m^2
ν = kinematic viscosity, m^2/s
ρ = density, kg/m^3

Subscripts

b = bulk temperature
i = ith HEM
m = mean bulk temperature
p = plate
s = at surface temperature
t = tube

pressure sensor measures pressure at pressure tap sites in the test section. The electrical signal from the Barocell goes to the data acquisition system. The Barocell measures the differential pressure from 1 mm Hg to less than 0.001 mm Hg with accuracy and repeatability of ± 0.05 percent and ± 0.01 percent of voltage reading (manufacturer's data). The output signal is between 0 and 6.804 volts d-c linearly proportional to the pressure. The transducer was calibrated by the manufacturer prior to the experiments. The overall device accuracy is ± 0.5 percent of the voltage signal.

Measurement Procedure

The pressure data are used to find the pressure coefficient. Condensing steam is used to maintain a constant wall temperature condition. Bulk temperature values are measured and used to calculate the Nusselt number. The measurement procedure is described later.

Pressure Measurements. The pressure drop measurement along the upper surface of the test section is independent of the temperature measurement. A Barocell differential pressure transducer, described in the instrumentation section, measures the pressure difference. Unlike the temperature readings, the pressure readings do not require a long stabilization period and the compressors can supply a steady flow of air for a short time. Therefore, it is possible to measure the pressure and calculate the coefficient for much higher Reynolds numbers than for the heat transfer.

Sixteen different flow rates corresponding to sixteen different Reynolds numbers are selected for $L/D = 3$. The pressure drop between the first and second pressure taps is for the second HEM, between the second and third is for the third HEM, and so on, until the seventh HEM where the pressure drop between the sixth and seventh taps is used. Generally, a mean voltage value is recorded because there is a small low-frequency voltage fluctuation at high Reynolds numbers.

The same procedure is followed to find the pressure drop for the aspect ratio of $L/D = 6$. There are only four cylinders in this case and the pressure difference is measured across the first and third, third and fifth, and fifth and seventh pressure taps for the second, third, and fourth cylinders. The first cylinder is ignored because the flow is spatially periodic after the first cylinder.

Temperature Measurement. The thermocouples used for measuring the temperature were described earlier. The data acquisition system reads the temperature every 200 ms for visual monitoring but temperatures are recorded at 15-min intervals.

The first test uses eight copper cylinders for aspect ratios $H/D = 2$ and $L/D = 3$. The air flow rate is adjusted for a particular Reynolds number. The flow rate is monitored to ensure that it does not change throughout the experiment. All the inlet valves to the cylinders are closed and steam passes through the top and bottom plates. The temperatures are recorded at 15-min intervals until steady state is reached. It usually takes about two hours to reach the steady-state condition. Next, the steam is introduced into the eighth cylinder and through the top and bottom plates. Again, the temperatures are measured and recorded until steady state is reached. The variation of the plate temperature in the flow direction is within ± 0.3°C. The steady-state bulk or mixed fluid temperature is recorded after a cylinder is heated. This process continues until all cylinders, one at a time in descending order, are heated during the measurement process. The duration of an experiment for one Reynolds number is 18 to 20 hours. The procedure for calculating the heat transfer coefficient from the bulk temperature data is discussed later. A total of thirteen experiments are carried out for thirteen different air flow rates. Some experiments are repeated to verify the reproducibility of the data. The maximum Reynolds number at which the Nusselt number could be measured in 2161. Two compressors working in parallel could not maintain steady flow for higher Reynolds numbers.

The experimental procedures are repeated for aspect ratios of $H/D = 2$ and $L/D = 6$. Four of the eight copper tubes from the test section are removed and wooden rods plug the holes in the Plexiglas side walls. The wooden plugs must be flush with the inside surface of the side walls to prevent artificial disturbances in the flow, and sealed to prevent leakage. Fifteen experiments are conducted for the above aspect ratios, each using different air flow rates. The tests are run as described for $L/D = 3$. Again, the data are checked for reproducibility with satisfactory results. It took eight to ten hours to complete one set of tests for $L/D = 6$.

Results

The heat transfer coefficient and pressure drop are calculated using the experimental data for selected H/D and L/D. The calculation procedure and the results for the pressure drop and the heat transfer coefficient are discussed. The calculation of the heat transfer coefficient for different heat exchanger modules from the bulk temperature data requires a unique strategy. Data reduction for the pressure coefficient is routine and will be discussed first.

Pressure Coefficient. Pressure on the top plate of the test section is measured for two cases: $H/D = 2$, $L/D = 3$ and $H/D = 2$, $L/D = 6$. The pressure coefficient or the dimensionless pressure difference is $\Delta p/\rho u_m^2$, where u_m is the mean velocity upstream from the blockage and ρ is the density of the air. For $H/D = 2$ and $L/D = 3$, a total of 16 data sets are recorded for Reynolds numbers ranging from 275 to 2767. The pressure transducer did not respond reliably to pressure difference at Reynolds numbers lower than 275. Each data set consists of the pressure drop for all modules except the first and the last. The pressure drop of the first and last modules is not measured because they are influenced by the entrance and exit effects. Table 1 shows the dimensionless pressure drop across different modules for four preselected Reynolds numbers. The data in Table 1 are nearly uniform. Also, the numerical calculation for laminar flow (Kundu et al., 1991a) shows that, after the first cylinder, the pressure drop for all HEMs is constant.

Figure 5(*a*) shows the pressure coefficient for the sixth module plotted against the Reynolds number. The primary cause for pressure drop in the test section is the presence of the cylinder array; the plates have less influence. The pressure coefficient first decreases between Reynolds numbers of 275 and 400, increases until the Reynolds number is 700, then assumes a near-constant value of 1.55. At low Reynolds numbers the experimental data are in good agreement with the numerical data (Kundu et al., 1991a). Clearly, the experimental data depart from the numerical data because the numerical data for laminar flow do not include the turbulent mixing effect. The Reynolds number at which the experimental data departs from the numerical result is interpreted as the transition Reynolds number. Based on pressure data, transition Reynolds number is ~350.

Table 1 Differential pressure coefficient $\Delta p/\rho u_m^2$ across HEMs when $L/D = 3$

Re	$i=2$	$i=3$	$i=4$	$i=5$	$i=6$	$i=7$
510	1.40	1.41	1.39	1.37	1.35	1.38
1166	1.47	1.51	1.53	1.54	1.51	1.49
1345	1.55	1.53	1.55	1.52	1.51	1.50
1614	1.54	1.51	1.53	1.50	1.52	1.55

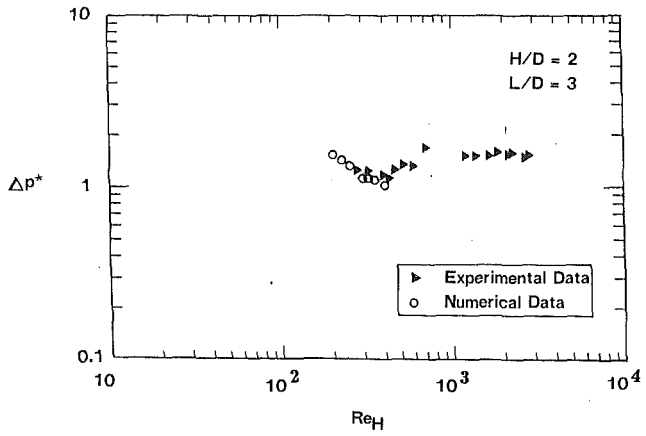

Fig. 5(*a*) Pressure drop across the sixth HEM, *L/D* = 3

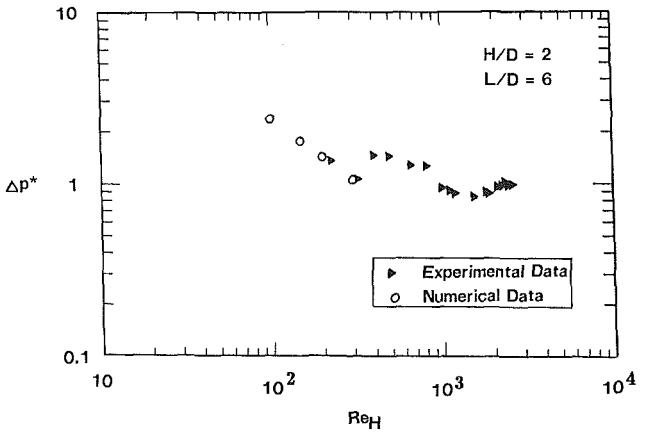

Fig. 5(*b*) Pressure drop across the third HEM, *L/D* = 6

For $H/D = 2$ and $L/D = 6$, there are only four cylinders in the test section. A total of 17 data sets are obtained for Reynolds numbers ranging from 223 to 2557. Each set of data consists of pressure coefficients for all modules except the first. Samples of pressure coefficients for the second, third, and fourth modules at four different Reynolds numbers are in Table 2. Note that, at a given Reynolds number, the pressure coefficient changes slightly from module to module. The third module data are plotted versus the Reynolds number in Fig. 5(*b*). The first two pressure coefficient data points agree well with the numerical data for laminar flow (Kundu et al., 1991a). Flow becomes unstable when the Reynolds number is larger than 350. When the Reynolds number is less than 350, the pressure coefficient decreases as the Reynolds number increases; the pressure coefficient increases until the Reynolds number is 500, and then decreases. At Reynolds numbers larger than 1000, the pressure coefficient is nearly constant. The slight reduction of pressure drop at Reynolds numbers higher than 500 is not fully understood. One can hypothesize that, due to a large L/D ratio and while the Reynolds number is below the critical limit for simple channel flow, the flow tends to decay the wake disturbances before getting to the next cylinder. Notice that the pressure coefficient is approximately equal to 1.5 when $L/D = 3$ and $\mathrm{Re}_H = 1500$. When $L/D = 6$, it is about 0.9 for the same Reynolds number; that is, for a higher pitch, the resistance to the flow is much less compared to the smaller pitch. Although the ratio L/D is doubled, the pressure coefficient is less for $L/D = 6$ than for $L/D = 3$.

Heat Transfer Coefficient. The heat transfer coefficient and the Nusselt number are calculated from the temperature data recorded during the experiment. The temperature of the air entering and exiting the test section is recorded, and the plate temperature is monitored continuously. From these data and theoretical considerations, the average heat transfer coefficient and the average modular Nusselt number are calculated. Using an energy balance between the entrance and exit to each module of the test section one can write

$$\dot{m}c_p(T_{b,i}-T_{b,i-1}) = 2A_p\bar{h}_{p,i}(T_p-T_{m,i}) + A_t\bar{h}_{t,i}(T_t-T_{m,i}) \quad (1)$$

where

$T_{m,i}$ = $0.5\,(T_{b,i-1}+T_{b,i})$
$\dot{m}$ = mass flow rate of air
c_p = specific heat of air
$T_{b,i}$ = bulk temperature of the air at exit from the ith module
$T_{b,i-1}$ = bulk temperature of the air at the inlet to the ith module
$\bar{h}_{p,i}$ = heat transfer coefficient of the plate for ith HEM
$\bar{h}_{t,i}$ = heat transfer coefficient of the cylinder for ith HEM
A_p = surface area of the plate for one HEM
A_t = surface area of the cylinder
T_p = plate temperature equal to steam temperature
T_t = steam temperature in the tube

Throughout the duration of the test, the plates are at the temperature of the steam. However, there are two possible cases: (1) a cylinder is at constant temperature but the net heat flux from that cylinder is zero, (2) the temperature of the cylinder is considered uniform and equal to T_t when it is heated. For the former case, the second term on the right side of Eq. (1) is zero. Equation (1) is rewritten for both cases as

$$T_{b,i} = BT_p + CT_{b,i-1} \quad (2)$$

where

$$B = \frac{2A_p\bar{h}_{p,i} + A_t\bar{h}_{t,i}}{\dot{m}c_p + A_p\bar{h}_{p,i} + 0.5A_t\bar{h}_{t,i}} \quad (3a)$$

$$C = \frac{\dot{m}c_p - A_p\bar{h}_{p,i} - 0.5A_t\bar{h}_{t,i}}{\dot{m}c_p + A_p\bar{h}_{p,i} + 0.5A_t\bar{h}_{t,i}} \quad (3b)$$

However, when cylinder i is unheated

$$B = \frac{2A_p\bar{h}_{p,i}}{\dot{m}c_p + A_p\bar{h}_{p,i}} \quad (4a)$$

$$C = \frac{\dot{m}c_p - A_p\bar{h}_{p,i}}{\dot{m}c_p + A_p\bar{h}_{p,i}} \quad (4b)$$

Equation (2) holds for every module. Since $T_{b,i}$ is the outlet bulk temperature of the ith module, it becomes the inlet bulk temperature of the $(i+1)$th module. The entrance and the exit temperatures of the test section are $T_{b,0}$ and $T_{b,8}$ respectively. It it shown by Kundu et al. (1991b) that for heated plates, the modular heat transfer coefficient at the plate rapidly attains its fully developed value and is unaffected by the temperature of the cylinders. Therefore, when the plate is heated and the cylinders are unheated, the plate heat transfer coefficient, $\bar{h}_p = \bar{h}_{p,i}$, is nearly constant and obtained from equation

$$\bar{h}_p = \frac{\dot{m}c_p(T_{b,8}-T_{b,0})}{16A_p[T_p - 0.5(T_{b,8}+T_{b,0})]} \quad (5)$$

Table 2 Differential pressure coefficient $\Delta p/\rho u_m^2$ across HEMs when $L/D = 6$

Re	$i=2$	$i=3$	$i=4$
483	1.43	1.45	1.44
799	1.28	1.27	1.30
1503	0.83	0.84	0.88
2452	1.01	0.99	1.01

Table 3 The Nusselt number, $\overline{Nu}_i$, across HEMs when $L/D = 3$ and $H/D = 2$

Re	$i=1$	$i=2$	$i=3$	$i=4$	$i=5$	$i=6$	$i=7$	$i=8$
865	16.8	16.9	19.5	20.3	21.6	22.4	22.3	22.5
1079	21.2	21.5	24.5	25.1	25.4	26.4	26.7	26.9
1324	25.4	26.4	29.4	30.1	30.2	30.5	30.6	30.7
1708	29.2	32.2	35.5	36.5	36.8	37.1	37.1	37.1

One can hypothesize for the subsequent calculations that $\bar{h}_p$ rapidly takes its fully developed value and remains unaffected when the cylinders are heated. This is justified when the thermophysical properties are independent of temperature (Kundu et al., 1991b).

It is difficult to measure simultaneously and directly the heat transfer coefficient for all eight cylinders. The numerical calculations by Kundu et al. (1991b) suggest a procedure for measuring the heat transfer coefficient for individual cylinders. First, cylinders 1–7 are unheated and the eighth cylinder and plates are heated. Equation (2) yields $T_{b,1}$, $T_{b,2}$, . . . , $T_{b,7}$, with B and C coefficients obtained from Eqs. (4*a*) and (4*b*). After $T_{b,8}$ is measured, Eq. (2) yields the value of $\bar{h}_{t,8}$ using B and C coefficients taken from Eqs. (3*a*) and (3*b*). Next, the experiment is repeated with cylinders 1–6 unheated and the seventh and eighth cylinders and the plates heated. The new exit bulk temperature of the test section, $T_{b,8}$, increases. The newly measured $T_{b,8}$ and the previously calculated $\bar{h}_p$ and $\bar{h}_{t,8}$ are used to calculate the new heat transfer coefficient for cylinder 7. Two strategies are possible: first, assume $\bar{h}_{t,8}$ remains the same and calculate $\bar{h}_{t,7}$; second, assume $\bar{h}_{t,8}$ is the heat transfer coefficient for the 7th cylinder, then recalculate the new $\bar{h}_{t,8}$. The results from the first strategy are in Table 3. Because the calculated values for the 7th and 8th HEMs shown in Table 3 are nearly the same, one can infer that both strategies yield similar results. The procedure is repeated with unheated cylinders 1–5, and heated cylinders 6, 7, 8, and the plates. The heat transfer coefficient $\bar{h}_{t,6}$ is then calculated using Eqs. (2)–(5). The measurement and calculation process is continued, one cylinder at a time, until all cylinders and plates are heated and all modular heat transfer coefficients are computed.

The average heat transfer coefficient for ith HEM (Fig. 1) is defined as

$$\bar{h}_i = \frac{2A_p\bar{h}_{p,i} + A_t\bar{h}_{t,i}}{2A_p + A_t} \tag{6}$$

The average Nusselt number for a particular module i is

$$\overline{Nu}_i = \bar{h}_i H/k \tag{7}$$

where H is the distance between the plates and k is the thermal conductivity of air.

Table 3 shows the Nusselt number for each of the eight HEMs at four preselected Reynolds numbers when $H/D = 2$ and $L/D = 3$. The Nusselt number for the last four modules remains nearly constant; there are some differences between the first two HEMs and the third HEM, due to measurement errors. The change in $T_{b,8}$ becomes very small as i decreases toward 1. The Nusselt number for the sixth HEM is used here because it is far enough from the entrance and the influence of the measurement errors for modules 6, 7, and 8 is small.

Figure 6(*a*) shows the Nusselt numbers versus the Reynolds numbers for the sixth module and for $L/D = 3$. Thirteen data sets are presented. As seen in Fig. 6(*a*), there are two regions: one for Reynolds numbers 300 to 550, and the other for Reynolds numbers 550 and larger. In both regions, the Nusselt number increases as the Reynolds number increases. The slope is steeper at larger Reynolds numbers because the total heat transfer is affected by the flow regime. Based on pressure measurement and numerical calculations, the flow attains turbulent characteristics when the Reynolds number is larger than 400.

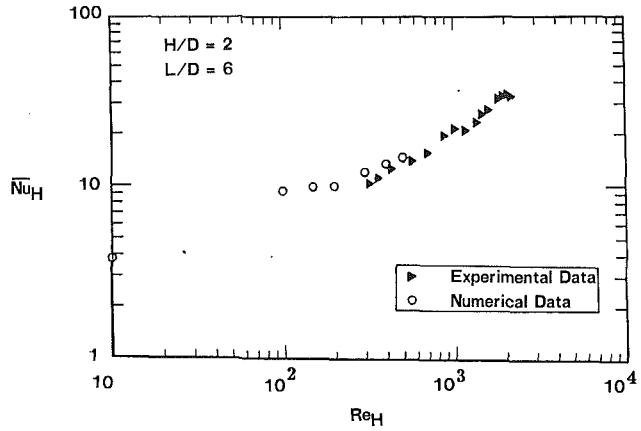

Fig. 6(*a*) Nusselt number of the sixth HEM, $L/D = 3$

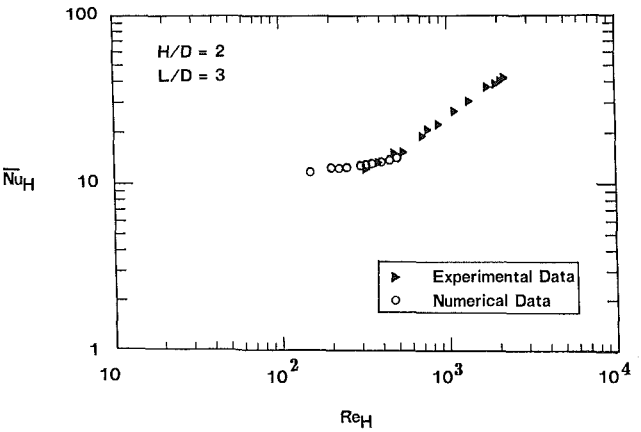

Fig. 6(*b*) Nusselt number of the third HEM, $L/D = 6$

Table 4 The Nusselt number, $\overline{Nu}_i$, across HEMs when $L/D = 6$ and $H/D = 2$

Re	$i=2$	$i=3$
318	10.3	10.2
690	15.5	15.5
865	19.5	19.0
1154	20.9	20.4
1345	23.3	22.5
1921	33.1	32.1

The results for the Nusselt number as a function of the Reynolds number when $L/D = 6$ and $H/D = 2$ are also shown in Fig. 6(*b*). In this case, there are only four aligned cylinders in crossflow. The third module is chosen as the representative module because the end effects are small. Fifteen data sets are presented. Similar to the previous case, the Nusselt number increases as the Reynolds number increases. The first region extends from a Reynolds number of 300 to a Reynolds number of ~550. The second region is for Reynolds numbers larger than 550. Table 4 provides the Nusselt number for selected Reynolds numbers for the second and third HEMs.

Generally, the magnitude of the heat transfer coefficient is influenced by the velocity of the fluid in the recirculatory zone near the cylinders. Clearly, there is a transition at the Reynolds number, $u_m(H - D)/\nu \approx 700$ corresponding to $Re_H \approx 350$. This is less than the transition Reynolds number for flow between two parallel plates $H - D$ apart. The factor $(H - D)/H$ accounts for the flow displacement and higher average fluid velocity, u_{max}, in the gap between a plate and a cylinder.

A comparison between the Nusselt numbers for $L/D = 3$ and $L/D = 6$ indicates that as the pitch, L/D, decreases from

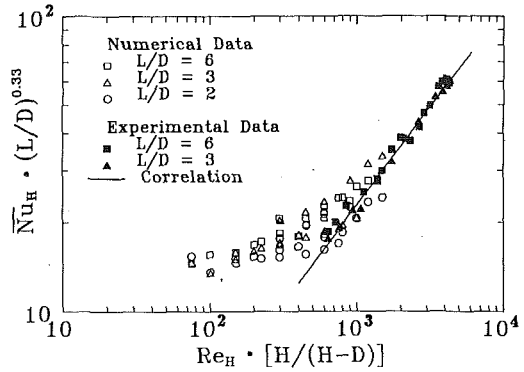

Fig. 7 Correlation of the experimental heat transfer results and comparison with the numerical data

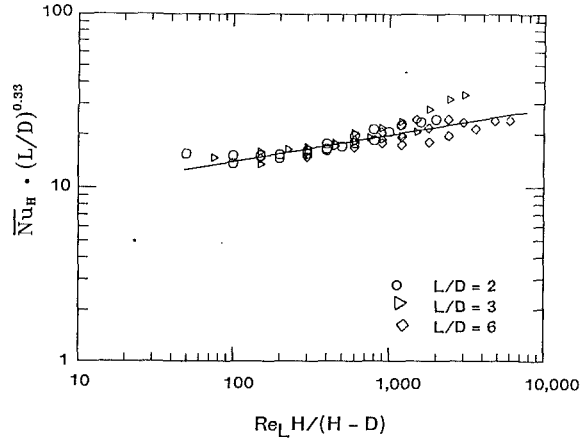

Fig. 8 Correlation of the numerical heat transfer data for laminar flow (Kundu et al., 1991b)

6 to 3, the fluid circulation in the vortex region intensifies, and the heat transfer coefficient increases. Obviously, there is a close relationship between the pitch of the cylinder array and the modular heat transfer coefficient. The results of a numerical study of this tendency are reported by Kundu et al. (1991a).

Comparison of Numerical and Experimental Results

The pressure coefficient and the heat transfer coefficient obtained from the numerical analysis are reported by Kundu (1989) for low Reynolds numbers ranging from 10 to 500. The experimental data are for an intermediate range of Reynolds numbers from 300 to 3000; therefore, the range in which the analytical and experimental data can be compared is between Reynolds numbers from 300 to 500. The data from both numerical and experimental investigations are useful over a wide range of Reynolds numbers.

The numerical data reported by Kundu et al. (1991a) are for nine different combinations of H/D and L/D ratios. However, the experimental data reported here are for two sets of aspect ratios: $H/D = 2$, $L/D = 3$, and $H/D = 2$, $L/D = 6$. All comparisons between the numerical and experimental results are for two geometric configurations.

Comparison of Pressure Coefficients. The numerical calculation of pressure at the top plate, reported by Kundu et al. (1991a), is compared with the measured data in Figs. 5(*a*) and 5(*b*). When $H/D = 2$ and $L/D = 3$, Fig. 5(*a*), the numerical and experimental pressure coefficient agree closely in the range of Reynolds numbers from 275 to 425. However, as the Reynolds number further increases, the experimental data begins to deviate from the numerical results. While the numerical pressure coefficient continues to decrease, the experimental pressure coefficient first increases slightly and then assumes a nearly constant value.

Figure 5(*b*) compares the numerical and experimental pressure coefficient when $H/D = 2$ and $L/D = 6$. The data agree well in a range of Reynolds numbers from 200 to 300; however, for larger Reynolds numbers the numerical and experimental pressure coefficients begin to deviate from each other. The precision of Barocell differential pressure transducer did not permit reliable data acquisition below those reported. As the Reynolds number further increases, the vorticity in the flow becomes more intense than the low Reynolds number flow, and consequently, the flow becomes unstable. The numerical modeling for low Reynolds numbers cannot simulate the high Reynolds number flow because the numerical model of Kindu et al. (1991a) does not consider the turbulence. As expected, the pressure coefficient decreases as the Reynolds number increases up to the Reynolds number of ~350. At higher Reynolds numbers, the mixing effect causes the pressure coefficient to increase.

Comparison of Heat Transfer Results. The numerical data and the experimental results for $H/D = 2$ and $L/D = 3$ are plotted in Fig. 6(*a*). In this case, the experimental results include three Reynolds numbers, and the numerical results have six data points between Reynolds numbers 300 and 500. As seen from Fig. 6(*a*), the numerical and experimental data closely agree in this range. Figure 6(*b*) shows the numerical and experimental Nusselt numbers versus the Reynolds number when $H/D = 2$ and $L/D = 6$. Each of the numerical and experimental results have three data points between the Reynolds numbers of 300 and 500. As seen in Fig. 6(*b*), the numerical and experimental Nusselt number data also agree closely within this range. For Reynolds numbers noticeably lower than those reported here, the temperature in the mixing chamber rapidly approaches the wall temperature. This causes the measured temperature changes to approach the measurement errors and produce unreliable heat transfer coefficient data.

The numerical data (Kundu et al., 1991a) and the experimental data are included in a single graph in Fig. 7. The experimental data are curve fitted by the equation

$$\overline{Nu}_H = 0.24\left(\frac{Re_H H}{H-D}\right)^{0.66}\left(\frac{L}{D}\right)^{-0.33} \tag{8}$$

for $Re_H H/(H - D) > 600$. When $Re_H H/(H - D) > 700$, the flow exhibits turbulent characteristics. Also, the numerical calculation (Kundu et al., 1991a) shows that there is severe vortex shedding in the laminar regime for $L/D = 3$ and some vortex shedding for $L/D = 6$. The experimental data are only for $H/D = 2$; however, the numerical data in Fig. 7 are for $H/D = 1.5$, 2, and 3. Experimental data for other H/D ratios are needed to confirm or amend the correlation give by Eq. (8). In the laminar regime, the numerical data are influenced by H/D and L/D ratios, and the vortex shedding behind the cylinder. For example, when $L/D = 2$, open circles in Fig. 7, the vortices are stable (no shedding) and the Nusselt number is relatively small. Kundu et al. (1991b) provided a different correlation for numerical data obtained for laminar flow regime (Fig. 8). Their data are closely approximated by the relation

$$\overline{Nu}_H = 7.11\left(\frac{Re_L H}{H-D}\right)^{0.144}\left(\frac{L}{D}\right)^{-0.33} \tag{9}$$

where $Re_L = u_m L/\nu$. For the experimental and numerical data, the heat transfer coefficient is defined using the mean bulk temperature of HEMs; see Eq. (1).

Discussion

It is of interest to compare the experimental data with those

Table 5 Comparison of experimental data for $\overline{Nu}_H$ with Eq. (10) and percent deviation

$L/D = 3$				$L/D = 6$			
Re	Table 3	Eq. (10)	Dev. %	Re	Table 4	Eq. (10)	Dev. %
865	22.4	17.9	20.0	865	19.0	14.6	23.0
1079	26.4	20.9	20.8	1154	20.4	17.9	12.3
1324	30.5	24.1	21.0	1345	22.5	20.0	11.1
1708	37.1	28.7	22.6	1921	32.1	25.8	19.6

for aligned cylinders in crossflow within an infinite medium. Equation (6) can be written in the following form:

$$\overline{Nu}_H = \frac{\left(\frac{H}{H-D}\right)\overline{Nu}_{p,De} + \pi\left(\frac{H}{L}\right)\overline{Nu}_{t,D}}{2+\pi D/L} \tag{10}$$

where $\overline{Nu}_{p,De} = \bar{h}_p De/k$, $De = 2(H - D)$ is the hydraulic diameter of the gap between cylinder and plate, and $\overline{Nu}_{t,D} = \bar{h}_t D/k$. The first and second terms in the numerator are the contribution of the plate and cylinder in a HEM to the Nusselt number. An estimated value of $\overline{Nu}_{p,De}$ suggested here is for flow between two parallel plates $H - D$ apart (Kays and Perkins, 1973),

$$\overline{Nu}_{p,De} \simeq 0.027(Re_{De})^{0.8}Pr^{1/3} \tag{11}$$

where $Re_{De} = u_{max}De/\nu$ and $u_{max} = u_m \times H/(H - D)$. Also, the estimated value of $\overline{Nu}_{t,D}$ for an array of aligned cylinders (Zhukauskas, 1972, p. 144) is

$$\overline{Nu}_{t,D} \simeq 0.27(Re_{D,max})^{0.63}Pr^{1/3}\left(\frac{Pr}{Pr_s}\right)^{0.25} \tag{12}$$

where $Re_{D,max} = u_{max}D/\nu$. The minor adjustment for temperature dependent thermophysical properties is small (~0.5 percent); hence, it does not appear in Eq. (11).

Equation (10), when $\overline{Nu}_{p,De}$ and $\overline{Nu}_{t,D}$ are calculated using Eqs. (11) and (12), underestimates the experimental data. One can visualize that there is a separation zone between two adjacent cylinders in Fig. 1, and one half of the flow moves above the separation zone and the other half below. For this reason, it is hypothesized that the maximum velocity is at a distance $(H - D)/2$ away from the wall and flow near the flat walls is similar to flow between two parallel plates $H - D$ apart. Using Eqs. (10)–(12), the data for module 6 in Table 3 and for module 3 in Table 4, when $Re_H \geq 865$, are calculated and presented in Table 5. Equations (10)–(12) underestimate the measured values by as much as 23 percent. An examination of data used for entries in Table 3 shows that the measured values of $\overline{Nu}_{t,D}$ are 15.5, 18.3, 20.3, and 25.6 for Reynolds numbers, $Re_{D,max}$, equal to 865, 1079, 1324, and 1708 ($Re_{D,max} = Re_H$ for $H/D = 2$). Equation (12) yields slightly higher values of 17.1, 19.7, 22.4, and 26.3 for the corresponding Nusselt numbers with deviations of 10, 6, 10, and 5 percent, respectively. Equation (12) also yields slightly higher values at the lower range of Reynolds numbers for aligned cylinders in an infinite flow field (Zhukauskas, 1972, p. 143). The experimental values of $\overline{Nu}_{p,De}$ for the same entries in Table 3 are 17.8, 21.6, 25.2, and 29.7, respectively; however, Eq. (11) underestimates these values by as much as 80 percent. Therefore, the primary cause for the differences shown in Table 5 is the high turbulence generated by the cylinders that penetrates the boundary layers near the flat walls. The high turbulence intensity is likely responsible for the Nusselt numbers higher than predicted by Eq. (11). For a better understanding of this effect, heat transfer data at higher Reynolds numbers and for a broader range of L/D ratios are needed.

Equation (10) uniformly underestimates the measured data for $L/D = 3$ in Table 5 by ~21 percent. However, the experimental data for $L/D = 6$ show more erratic deviations. Equation (10) can be adjusted to account for the deviations listed in Table 5. For parameters beyond the range of this study, it is reasonable to use Eq. (10) to obtain a preliminary estimation of $\overline{Nu}_H$, and then multiply that by 1.27.

Conclusion and Remarks

The experimental data presented here are for two aspect ratios. The transition from laminar to turbulent flow is defined using the pressure data. The Reynolds number at which the numerical and experimental data depart from each other is the transition Reynolds number. Figures 5(*a*) and 5(*b*) show that when $Re_H < 350$, the agreement between laminar flow data and numerical results is very good. The heat transfer data correlate well for $Re_H H/(H - D) > 700$. The laminar flow numerical data are for $H/D = 1.5$, 2, and 3, while the correlation of experimental data is for $H/D = 2$. A separate correlation for laminar flow numerical data that includes the effect of H/D ratio is given by Eq. (9).

The estimated measurement error for the pressure coefficient is 5 percent. It was stated that the accuracy of the pressure transducer is ±0.5 percent of the signal. However, when the differential pressure is small, the error rapidly increases and becomes unmanageable. All reported pressure data are for signals that have errors less than 5 percent. Except at the lower range of Reynolds numbers, the error in pressure data is much less than 5 percent and the measured value of the flow rate is the primary contributor to the error in Δp^*. The error in the heat transfer coefficient is difficult to predict. Many factors are responsible for error in the heat transfer coefficient data, namely: conduction through the side walls, theoretical model, thermocouples, flowmeter, dimensional variations, nonuniformity of the wall temperature, etc. However, the major cause of the errors is conduction losses through side walls. Based on the estimation of conduction losses and the reproducibility of the data, the uncertainty in the heat transfer coefficient is approximately 10 percent. This estimated error is for modules near the mixing chamber and as one moves away from the mixing chamber the errors increase because the conduction losses occur across a larger heat transfer area. This can be inferred from the data in Table 5 where the deviations for $L/D = 3$ are more uniform than those for $L/D = 6$.

References

Kays, W. M., and Perkins, H. C., 1973, "Forced Convection, Internal Flow in Ducts," in: *Handbook of Heat Transfer*, W. M. Rohsenow and J. P. Harnett, eds., McGraw-Hill, New York, Section 7, p. 122.

Kundu, D., 1989, "Computational and Experimental Studies of Flow Field and Heat Transfer From a Row of In-line Cylinders Centered Between Two Parallel Plates," Ph.D. Thesis, The University of Texas at Arlington, Dec.

Kundu, D., Haji-Sheikh, A., and Lou, D. Y. S., 1991a, "Pressure and Heat Transfer in Cross Flow Over Cylinders Between Two Parallel Plates," *Numerical Heat Transfer*, Part A, Vol. 19, pp. 345–360.

Kundu, D., Haji-Sheikh, A., and Lou, D. Y. S., 1991b, "Heat Transfer Predictions in Cross Flow Over Cylinders Between Two Parallel Plates," *Numerical Heat Transfer*, Part A, Vol. 19, pp. 361–377.

Oyakawa, K., and Mabuchi, I., 1981, "Fluid Flow and Heat Transfer in Parallel Plate Duct Containing a Single Cylinder," *Bulletin of JSME*, Vol. 24, No. 196.

Oyakawa, K., and Mabuchi, I., 1983, "Heat Transfer in Parallel Plate Duct With Circular Cylinders Inserted in Staggered Arrangement," *Bulletin of JSME*, Vol. 26, No. 214.

Zhukauskas, A., 1972, "Heat Transfer From Tubes in Cross Flow," in: J. P. Hartnett and T. F. Irvine, Jr., eds., *Advances in Heat Transfer*, Vol. 8, Academic Press, New York, pp. 142–144.

Developing Heat Transfer and Friction in a Ribbed Rectangular Duct With Flow Separation at Inlet

Tong-Miin Liou
Professor.

Jenn-Jiang Hwang
Ph.D. Candidate.

Power Mechanical Engineering Department,
National Tsing Hua University,
Hsinchu, Taiwan

The local heat transfer and pressure drop characteristics of developing turbulent flows in a rectangular duct with an abrupt-contraction entrance and repeated square-rib pairs on the two opposite walls have been investigated experimentally. Both entrance-region and periodic-fully-developed-region results were obtained. Laser holographic interferometry was employed in the local and average heat transfer measurements. The Reynolds number was varied from 5.0 × 10^3 to 5.0 × 10^4; the rib pitch-to-height ratios were 10, 15, and 20; and the rib height-to-duct height ratio was kept at a value of 0.13. The results allowed the entry length to be determined and the regions susceptible to hot spots to be located. Semi-empirical heat transfer and friction correlations for the periodic fully developed region were developed. Moreover, performance comparisons between the ribbed and smooth ducts were made under two types of constraint, namely equal mass flow rate and equal pumping power. Finally, the effect of thermal entry length on the length mean Nusselt number was also investigated. The results showed that the length mean Nusselt number ratio was a function of only the duct length and independent of PR and Re, and could be further correlated by an equation of the form $\overline{Nu}_m / \overline{Nu}_p = 1 + 1.844/(X/De)$.

Introduction

A well-known method to improve the heat transfer from a surface is to apply turbulence promoters or roughness elements to the surface. A number of reports (Dipprey and Sabersky, 1963; Webb et al., 1971; Lewis, 1975; Han et al., 1985) have been published on the heat transfer characteristics in channels or pipes with roughness elements on the walls for forced convection. However, these investigations consider the fully developed heat transfer situation only and actually most practical applications include not only the fully developed region, but also the developing region, where the development of hydrodynamic and thermal boundary layers is very strongly influenced by the character of the typical duct entrance. For example, in typical turbine-airfoil cooling passage applications the entrance, far from being a nozzle, is a nearly abrupt contraction. In this case there is a separated flow at the entrance with sufficient vorticity shedding into the mainstream that the heat transfer rate is very much higher than what would be obtained in a developing turbulent boundary layer where the turbulence originates from the surface. In addition, the configurations of the internal cooling passages of the turbine airfoils are relatively short (typically L/D_e = 10–15). Thus, the effect of thermal entry length on the length mean Nusselt number ($\overline{Nu}_m$) of the ribbed channel with an abrupt-contraction entrance may be significant. However, there is no report of such a study in the open literature. In this paper, the effects of the thermal entry length, the rib parameter, and the flow parameter on the length mean Nusselt number will be investigated for the first time. Furthermore, it is of importance whether the hot spots occurring in a long ribbed duct with periodically fully developed flows (Lockett and Collins, 1990; Liou and Hwang, 1992) still hold in the case of developing flows. This has not been reported before and will be studied in this work.

To provide perspective for the foregoing paragraph, the relevant literature about turbulent flows of ribbed ducts with abrupt-contraction entrances will be briefly reviewed. Sparrow and Tao (1983, 1984) systematically investigated the effects of the Reynolds number ($1.0 \times 10^4 \le Re \le 4.5 \times 10^4$), the rib pitch-to-height ratio (PR = 9.15, 18.3, and 36.6), and the rib-to-duct height ratio ($H/2B$ = 0.082 and 0.164) on the mass transfer coefficients and friction factors for developing and periodic fully developed duct flows with ribs arranged both on the two opposite walls and on one wall only. The duct inlet was sharp edged. The local as well as cyclic average Sherwood numbers (Sh) were determined by using the naphthalene sublimation technique. The rib turbulators were of a circular cross section, and the rib angle of attack (α) was kept at 90 deg. It was found that the fully developed Sherwood numbers for two-sided ribbed duct exceeded those for a one-sided ribbed duct, typically by about 40 percent; and higher performance (under the same pumping power) was attained with two-sided ribs than with one-sided ribs. Han (1988) reported experiments to determine the effect of the channel aspect ratio (W/B = 1/4, 1/2, 2, and 4) on the distributions of local heat transfer coefficients in rectangular channels with two opposite ribbed walls for turbulent flows under sudden entrance conditions. Both the local and the average Nusselt numbers were measured by the thermocouple technique and the resistance (stainless foil) heating method. The ribs were of a square cross section. The results showed that the increased ribbed-side-wall heat transfer with a smaller aspect ratio channel was higher than that in a larger aspect ratio channel for a constant pumping power; however, the increased average heat transfer was slightly lower. Another important finding in his work showed the local Nusselt numbers became uniformly periodic between ribs in the axial direction at about $X/D_e \ge 3$. Employing the same measurement technique and method, Han and Park (1988) further investigated the combined effects of the rib angle of attack (α = 90, 60, 45, and 30 deg) and the channel aspect ratio (W/B = 1, 2, and 4) on the local heat transfer coefficients for the same flow patterns as used by Han (1988). In their study, it was found that the best heat transfer performance in the square channel (W/B = 1) with angled ribs (α = 30–45 deg) was about 30 percent higher than with the transverse ribs (α = 90 deg) for a constant pumping power; however, that in the rectangular ducts (W/H = 2 and 4) at α = 30–45 deg was only about 5 percent higher than at α = 90 deg. Metzger et

Contributed by the Heat Transfer Division for publication in the JOURNAL OF HEAT TRANSFER. Manuscript received by the Heat Transfer Division April 1991; revision received February 1992. Keywords: Augmentation and Enhancement, Measurement Techniques, Turbines. Associate Technical Editor: D. M. McEligot.

al. (1990) performed an experimental study on the local convection heat transfer characteristics in square cross-sectional channels containing roughness ribs set at various angles and orientations to produce single- and double-cell secondary flows superposed on the main streamwise flow. The ribs were of a square cross section. In their work the authors utilized the melting patterns of thin replaceable coatings on the test surfaces in the presence of a heated air stream to determine local surface heat transfer rates. The most prominent features of the results in their study were the superior heat transfer performance associated with rib patterns producing a two-cell secondary flow and the significantly superior performance of the 60 deg, two-cell pattern. Note that in their study the performance was under the constraint of constant mass flow rate.

The present investigation is concerned with the heat transfer enhancement and friction characteristics in an abrupt-contraction-entrance rectangular duct with two opposite ribbed walls. The ribs are of a square cross section. The experimental technique used in this work is the laser holographic interferometry (LHI), which is in contrast to the conventional methods of aforementioned thermocouple, naphthalene sublimation, and melting point surface coating techniques, and has not been applied to such a problem. This technique not only is noninvasive and whole-field in character, but it also allows direct determination of the convection heat transfer to the working fluid. Thus, the heat losses (containing conductive and radiative losses) that usually exist in the heat transfer experiments can be characterized, quantified, and corrected. The study will be focused on two regions of the duct, namely: (1) the entrance region where the velocity and temperature profiles are simultaneously developing, and (2) the periodic fully developed region far away from the inlet of the duct. The geometric and flow parameters are the rib pitch-to-height ratio (PR) and the Reynolds number (Re). This study has three objectives: First, experiments are carried out to determine both the entrance and the fully developed local heat transfer and pressure coefficient distributions, which yields the evaluation of periodic average Nusselt numbers and friction factors so that compact correlations can be developed in terms of rib and flow parameters. Detailed measurements of local pressure coefficient distributions of developing associated with fully developed flows for the problem studied have not been made previously. Then, by employing the basic heat transfer and pressure drop data, a performance analysis is made, which yields comparisons between the ribbed ducts investigated and the classical smooth duct. The analysis is carried out for two sets of constraints, namely for (1) equal mass flow rate, and (2) equal pumping power. These comparisons enable definitive conclusions to be drawn about the effectiveness of the periodic ribs as an enhancement technique. Finally, of importance, the effects of thermal entry length on the length mean Nusselt number of the ribbed duct, which is highly desired for the design of turbine airfoils, and has not been studied before, will be investigated.

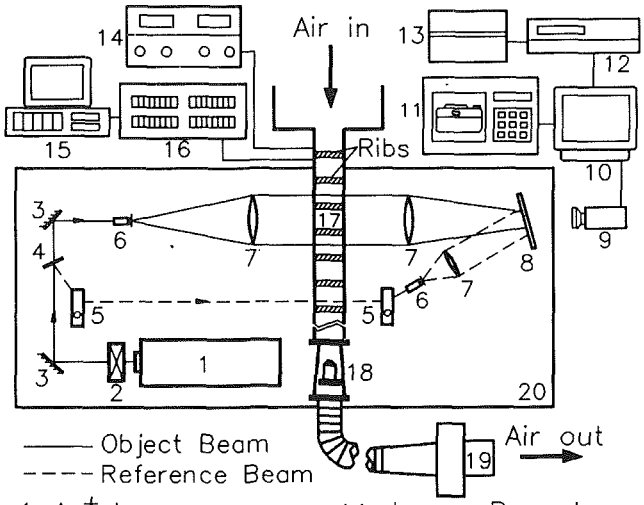

Fig. 1 Schematic drawing of overall experimental system

The Experiments

Flow System. The open-loop flow circuit shown in Fig. 1 was operated in the suction mode and oriented horizontally. Air was drawn into the test section from the temperature-controlled laboratory room. After traversing of the test section, the air flowed subsequently through a flow straightener, a rotameter, and a bellows, and then was exhausted by a 3 hp

Nomenclature

B = half height of channel
C = Gladstone Dale constant
C_f = pressure drop coefficient $= 2(P_x - P_0)/(\rho U^2)$
c_p = specific heat at constant pressure
D_e = hydraulic diameter
f = average friction factor
G = mass flux
g = gravitational acceleration
H = rib height
h = heat transfer coefficient $= q''/(T_w - T_m)$
k_f = air conductivity
L_h = wetted length in one pitch
$\overline{\mathrm{Nu}}$ = local Nusselt number
$\overline{\mathrm{Nu}}_p$ = average Nusselt number
$\overline{\mathrm{Nu}}_m$ = length mean Nusselt number
P_0 = ambient pressure
P = pressure
P_i = rib pitch
PR = rib pitch-to-rib height ratio $= P_i/H$
Pr = Prandtl number
Q = quantity of heat given to air from entrance to the considered cross section of the duct
q'' = local wall heat flux
Re = Reynolds number $= U \cdot D_e/\nu$
Re* = smooth-duct Reynolds number, Eq. (9)
S = fringe shift
Sh = Sherwood number
T_m = local bulk mean temperature of air
$\overline{T}_m$ = average bulk mean temperature of air
T_w = local wall temperature
$\overline{T}_w$ = average wall temperature
U = axial mean velocity
W = half-width of channel
w = rib width
X = axial coordinate
Y = transverse coordinate
Z = spanwise coordinate
α = rib angle of attack
λ = wavelength of laser light
ν = kinetic viscosity of air
ρ = air density

Subscripts

i = fringe order index
p = periodicity
r = reference
s = smooth duct
w = wall

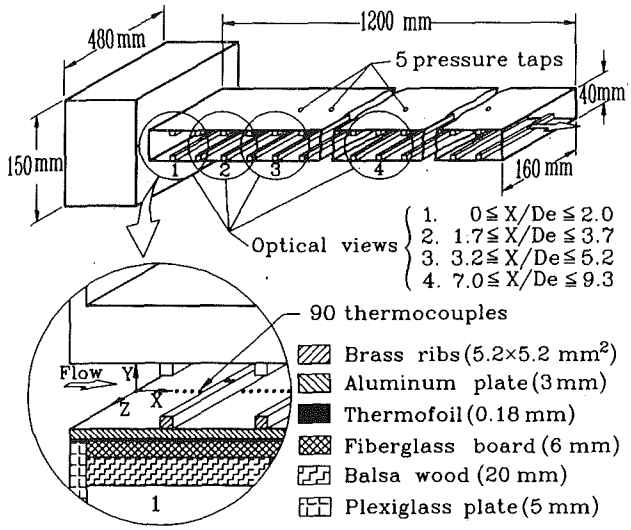

Fig. 2 Sketch of configuration, coordinate system, and dimensions of the test section

blower. The blower was situated in a service corridor outside the laboratory to insulate the vibration, and its discharge (heated air) was vented outside the building. The upstream end of the test section was connected with a plexiglass plenum, which ensured the air entering the test duct had an abrupt-contraction-entrance condition. The contraction area ratio between the pleum and the test duct was 11.25. This inlet condition was arbitrarily selected (Han, 1988) to simulate turbine cooling channels because the actual turbine cooling channels may have a wide range of inlet configurations, which depend on the specific design.

Instrumentation. The optical circuit of the laser holographic interferometry (Fig. 1) and its experimental procedure were described in detail by Liou and Hwang (1992), and will not be further elaborated on in the present paper. It is noteworthy that a combination of a holographic film plate holder and a liquid gate was used to provide in-place development of film plate as required for subsequent real-time work. The photographic emulsion 8E56, made by Agfa-Gevaert Limited, was found to be a suitable material for the present work. Through a CCD camera, the instantaneous interference field was monitored on a multisync monitor and recorded on a VHS videocassette recorder for storage and further image processing.

In addition to flow field temperature measured by LHI, the wall temperature of the heated duct was further measured by thermocouples. A Yokogawa DA-2500 hybrid recorder and a PC-AT were used for temperature readings and recordings. To measure static pressure, a microdifferential transducer (Kyowa, PDL-40B, ±0.1 percent) was connected to each pressure tap on the duct wall. The measured pressure signal was subsequently amplified by a Kyowa WGA-200A amplifier and read from a digital readout.

Test Section. The configuration, coordinate system, and dimensions of the test duct and the associated plenum are sketched in Fig. 2. The test duct consisting of two principal walls (the top and bottom walls of the duct) and two side walls was 1200 mm long and had a rectangular cross section 160 × 40 mm² (X-Y plane), i.e., an aspect ratio of 4:1. Each principal wall, fabricated from a highly polished aluminum plate, was covered by brass ribs with size of 5.2 × 5.2 mm². Aluminum plates and brass ribs were adopted in this work for their high conductivity and easy machinability. Two thermofoils of thickness 0.18 mm emit heat to the top and bottom walls of the test section, respectively. Each thermofoil was adhered uniformly between the aluminum plate and fiberglass board, and could be controlled individually by a 60-W d-c power supply for controllable electrical heating to the test section. Additionally, the heated plates were insulated by 20-mm-thick balsa wood to prevent heat loss. The side walls of the entire heated test duct were made of plexiglass plates to provide optical access for laser holographic interferometry measurements. The construction of the ribbed walls was displayed in detail in Fig. 2.

Experimental Conditions. As shown in Fig. 2, the interferograms were taken for the regions of $0 \le X/D_e \le 2.0$, $1.7 \le X/D_e \le 3.7$, $3.2 \le X/D_e \le 5.2$, and $7.0 \le X/D_e \le 9.3$, respectively. The first three were situated in the developing region and the last one was situated in the fully developed region. It was one rib pitch (P_i) from the duct entrance to the first rib pair. The entire test section was mounted on a modified milling machine with four vibration-isolation mounts to allow vertical and horizontal movement, and hence successive scanning of the expanded object beam. Additionally, for wall temperature measurements the regions corresponding to the interferometric measurements were instrumented with 90 copper-constantan thermocouples (68 for the developing region and 22 for the fully developed region) distributed along the centerline of the heated plate and ribs. The junctions 0.2 mm in diameter were cemented into small holes drilled into the back side of the heated plate approximately 1.0 mm from the front surface.

The measurements of centerline pressure distributions for the developing flows were carried out by a Pitot tube, which was inserted from the side wall of the test duct to transverse across and along the flow direction. Also, five pressure taps were used for static pressure drop measurements across the fully developed region of the test duct. The pressure taps were drilled at intervals of 10.4 cm, with the first tap 45 cm from the duct inlet. The pressure drop of the present study was based on the adiabatic conditions.

Further, to study the effects of various parameters on the fluid flow and heat transfer characteristics of ribbed ducts, the Reynolds number (Re) in this study, based on the duct hydraulic diameter and bulk mean velocity, extended from 5.0×10^3 to 5.0×10^4; the ratios of rib pitch to height (PR) were 10, 15, and 20; while the rib-to-duct-height ratio ($H/2B$) was kept at a value of 0.13.

Data Reduction and Uncertainty Analysis

The distributions of the centerline pressure drop for the developing ribbed-duct flows were normalized by the fluid dynamic pressure as

$$C_f = (P_x - P_0)/(\rho U^2/2) \tag{1}$$

where P_0 is the ambient pressure, and P_x, the static pressure of channel spanwise midpoint at axial station of X from duct entrance. It is of interest to note that the variance of pressure difference in the channel spanwise (Z) and transverse (Y) directions is very slight (about 6 percent in scatter). This observation coincides with that pointed out by Han et al. (1985), which states that the pressure difference is almost the same when measured from the pressure taps, either on the ribbed wall or on the smooth side wall.

The following equation is used to calculate the friction factors in the fully developed region of the duct:

$$f = (-dP/dX)D_e/(\rho U^2/2) \tag{2}$$

In this expression, dP/dX is an axial pressure gradient, which is evaluated by taking the ratio of the pressure difference ΔP between corresponding points (pressure taps) of successive cycles and the rib pitch. The maximum uncertainties of C_f and f are estimated to be less than 6.2 and 7.1 percent, respectively,

by the uncertainty estimation method of Kline and McClintock (1953).

It is necessary to insure that the temperature distributions along the test section width (Z direction) in the flow field are two dimensional because the holographic interferometry is based on the integral of the spanwise refractive-index change. The significant errors usually encountered in the interferometric experiments are not only due to the end effect, which is caused by deviation from two dimensionality of the actual temperature field, but also due to the refraction effect. The refraction-effect error is caused by a bend of the light beam, which results from the presence of a density gradient normal to the light beam. It increases with increasing disturbed length (Z direction). Thus, if an experimental apparatus is designed to minimize the end-effect error (increasing the optical path length), the refraction-effect error may be large, and vice versa. For a reasonable combination of the end-effect and refraction-effect errors, the channel aspect ratio employed in this work is 4:1. The same aspect ratio is used by Walklate (1981) for the study of two-dimensional thermal boundary layers and by Lockett and Collins (1990) and Liou and Hwang (1992) for the studies of rib-roughness channel flows. By using the interferometry error analysis suggested by Goldstein (1976), it is found that the resulting errors in the fringe (or temperature) shift due to the end effect and the refraction effect are about 8 and 4.2 percent, respectively. Nevertheless, the two dimensionality of spanwise temperature profile of the flow field is checked by thermocouple probing in this study. The scatters in spanwise direction are less than 6 and 9 percent of the channel spanwise average temperature for the fully developed and developing regions, respectively. To determine the temperature field described by the interferogram, the equation of interferometry for a two-dimensional incompressible flow is as follows (Hauf and Grigull, 1970):

$$S_i - S_{i-1} = 2T_r \cdot \rho_r \cdot C \cdot W \cdot (1/T_{S_i} - 1/T_{S_{i-1}})/\lambda \qquad (3)$$

where $S_i - S_{i-1}$ is the fringe shift, S_i the fringe order, C the Gladstone Dale constant, and ρ_r the air density evaluated at reference temperature T_r. By setting $S_i - S_{i-1} = 1$, the temperature differences $T_{S_i} - T_{S_{i-1}}$ associated with each fringe are determined. A list of typical $T_{S_i} - T_{S_{i-1}}$ versus $S_i - S_{i-1}$ was given by Liou and Hwang (1992). Knowledge of at least one temperature and the temperature difference in the region of interest will provide the approximate heat transfer feature from wall to air.

The convection heat transfer coefficient can be presented in terms of the local Nusselt number Nu, which is defined as $\mathrm{Nu} = h \cdot D_e/k_f$. Also, the local heat transfer coefficient h may be expressed in terms of the measured temperature gradient at the heated wall and the wall temperature. Thus,

$$\mathrm{Nu} = h \cdot D_e/k_f = -(dT/dY)_w \cdot D_e/(T_w - T_m) \qquad (4)$$

The local wall-temperature gradient, $(dT/dY)_w$, was obtained by using a second-order, least-square curve fit to the measured temperature field. The local wall temperature of the heated plate and ribs, T_w, was read from the output of the thermocouples. The local bulk mean air temperature is calculated from $T_m = T_{in} + Q/(Gc_p)$, where Q is the quantity of heat given to air from the entrance to the considered cross section of the duct and can be obtained by the integrated form of $\int_0^x [k_f(dT/dY)_w \cdot 2W]dX$. The Nu thus obtained is estimated to have an uncertainty less than 6.5 percent. It is worthwhile to notice that the heat input into the fluid is highly localized, due to the existence of ribs, and the idealized circumstance of perfectly isothermal or isoflux over the heated wall, with uniform heat flux over the thermofoil, clearly does not arise in the experiments. Further, the average Nusselt number $\overline{\mathrm{Nu}}_p$ for the periodically fully developed region can be evaluated by two independent methods. In the first approach, $\overline{\mathrm{Nu}}_p$ is defined in terms of the average wall temperature $\overline{T}_w$ as:

$$\overline{\mathrm{Nu}}_p = \overline{h}D_e/k_f = q_{\mathrm{conv}} \cdot D_e/[k_f(\overline{T}_w - \overline{T}_m)] = \int_0^{L_h} (dT/dY)_w dX \cdot D_e/[L_h(\overline{T}_w - \overline{T}_m)] \qquad (5)$$

where L_h is the wetted length of heated surface in one rib pitch, $\overline{T}_w$ is the average wall temperature in one pitch, and the average bulk mean air temperature, $\overline{T}_m$, is evaluated as $(\int_0^{L_h} T_m dX)/L_h$. In the second method, the average Nusselt number, $\overline{\mathrm{Nu}}_p$, is determined by a simple area-weighted average of the local Nusselt number. In other words, $\overline{\mathrm{Nu}}_p = \int_0^{L_h} \mathrm{Nu} \cdot dX/L_h$. The availability of the above approach is because the local wall-to-mean temperature difference, $(T_w - T_m)^{-1}$ in Eq. (4), is substantially identical and nearly independent of axial station (X) in one rib pitch. A close agreement (about 5 percent in difference) is obtained between the average Nusselt numbers determined by the two methods. This fact suggests that the Nusselt number for the turbulent ribbed-duct flows at Pr = 0.7 (or higher) is relatively insensitive to a variation of surface temperature and heat flux in the flow direction. The conclusion was also addressed by Kays and Crawford (1980) for the turbulent smooth-duct flows. The maximum uncertainties of $\overline{\mathrm{Nu}}_p$ obtained by the two methods are estimated to be less than 9.6 and 9.9 percent, respectively. It is interested to note that the net convective heat transfer rate, q_{conv}, can also be estimated by subtracting the heat losses (containing conductive and radiative losses) from the supplied electrical input. The values of q_{conv} obtained by interferometry and the energy balance method are found to agree closely with each other, typically about 12 percent in difference.

Results and Discussion

Pressure Distribution. In a periodic ribbed duct as is considered here, the flow patterns (containing mean velocity and turbulence intensity) repeat themselves cyclically in the fully developed region, and this was verified by Liou and Lin (1988) by using LDA. Similarly, the pressure has certain periodic characteristics. In the periodic region the pressure differences between X_1 and $X_1 + P_i$, $X_1 + P_i$ and $X_1 + 2P_i$, $X_1 + 2P_i$ and $X_1 + 3P_i$, ..., etc., are identical. That is, if the pressures at points X_1, $X_1 + P_i$, $X_1 + 2P_i$, $X_1 + 3P_1$, ..., are plotted, they will fall on a straight line. This is shown in Fig. 3, which is a plot of centerline pressure coefficient (C_f) versus nondimensional axial station (X/H) for PR = 10, 15, and 20. In considering Fig. 3, it is helpful to take note of the solid-square symbols along the abscissa of each graph, which serve to indicate the axial positions of the ribs. It could be seen from this figure that the hydrodynamic development length was rather short (about X/D_e = 2.5, 2.5, and 3 for PR = 10, 15, and 20, respectively). Downstream of a hydrodynamic development length, the measured centerline pressures for the axial stations of rib situation (solid circle) fell on a straight line and those $7H$ downstream of rib (open triangle) fell on another straight line, with the two lines being parallel. That is, different straight lines correspond to different choices of X_1 within a pitch, but all straight lines have the same slope. Within a given pitch, the pressure distribution along the axial station of the pitch is not linear. Note should also be taken that the greater the value of PR, the flatter (although slightly) the straight line. Further, the data of Fig. 3 may suggest that the flow development is almost immediate for small PR and the entrance region can probably be neglected. With regard to the thermal development, however, the effect of the thermal entry length on the mean heat transfer coefficient is substantial because of the high conductance in the developing region. This will be demonstrated below.

Isotherm Patterns. Owing to space limitations, only four representative interferograms are presented here. Figures 4(a)

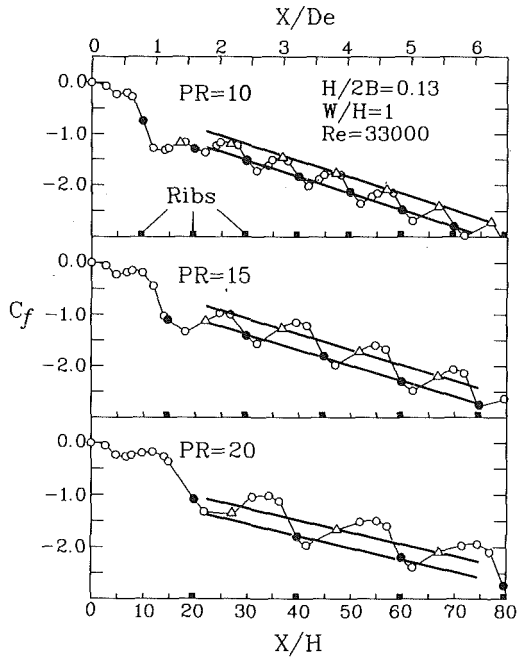

Fig. 3 Measured centerline pressure coefficient distribution for *PR* = 10, 15, and 20

and 4(*b*) illustrate the effect of Reynolds number on the development of thermal boundary layer in the entrance region. In these figures, isothermal lines are shown for a fixed rib pitch, $PR = 10$, and two values of the Reynolds number, Re = 12,600 and 33,000. It is qualitatively observed from these two pictures that the thermal boundary layer thickness is inversely related to the mass flow rate. Both pictures also show that the effects of flow separation, recirculation, and reattachment caused by the abrupt-contraction inlet of the duct appears in the form of the dome-shaped isotherm patterns near the duct inlet. The effect of *PR* on the development of thermal boundary layer of the ribbed-duct flow is seen from Figs. 4(*a*) and 4(*c*). The Reynolds number is kept at a value of 12,600. The aforementioned dome-shaped isotherm patterns caused by the duct inlet do not seem to be affected by *PR*. Figure 4(*d*) is a typical interferogram of the periodic fully developed region of the ribbed-duct flow for $PR = 10$ and Re = 12,600. From Fig. 4(*d*) it is found that the cyclic isotherm patterns happen between the successive rib pairs. From the information of complete air temperature distributions given by the interferograms, the local heat transfer coefficients of the heated walls can be calculated, and this will be discussed below.

Local Heat Transfer. Before initiating experiments with ribbed ducts, the local Nusselt numbers were measured for a smooth duct and compared with the results given in the literature, as shown in Fig. 5(*a*). In Sparrow and Cur (1982), the data were based on the local measurements of the flow in a high-aspect-ratio rectangular channel ($W/B = 18$) with a sharp entrance by using the naphthalene sublimation technique. In Han (1988), the results were obtained for a turbulent flow in a rectangular duct with a sharp entrance by using the thermocouple technique. The local heat transfer results are presented as the streamwise distributions of the Nusselt number ratio, $Nu/\overline{Nu}_s$. An overall examination of the figure reveals a familiar trend, namely, large heat transfer coefficients near the leading edge of the duct inlet followed by a rapid decrease, then an increase up to a local maximum, finally a decrease approaching the fully developed values. The relatively large initial values of $Nu/\overline{Nu}_s$ are due to the large temperature gradients near the leading edge of the duct inlet. The direct impingement of the reattaching flow from the duct inlet on the duct wall produces the second peak values of $Nu/\overline{Nu}_S$, while the growth of thermal boundary layer and resulting decrease in temperature gradients are responsible for the subsequent lower values of $Nu/\overline{Nu}_S$. It is interesting to note that all of the three studies show that the flow reattachment is attained at about $0.35 \pm 0.05\ D_e$ (or $4.3 \pm 0.6H$) from the duct entrance. In the developing region with $1 < X/D_e < 4$, the present data agree qualitatively with those of Sparrow and Cur (1982) and Han (1988). In the region about $X/D_e = 8$, the present data agree fairly well with those of Sparrow and Cur (1982) and Han (1988). It should be noted that both the present results and Han's data (1988) reveal that the maximum values of heat transfer coefficient happen both at the point near the leading edge of the duct and near reattachment. The smooth-duct results prove that the test sections are reliable to reproduce data for the cases when the periodic ribs are applied.

The distributions of the local Nusselt number ratio of the ribbed-duct flows along the axial direction are presented in Fig. 5(*b*) for Re = 12,600 and $PR = 10$, 15, and 20. In the regions of optical views (Fig. 2), the local Nusselt numbers are determined at up to 12 stations for every rib pitch (3 stations on rib top and 9 stations in interrib) along the axial line for

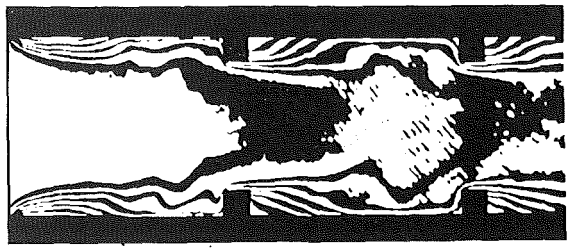

Fig. 4(*a*) Re = 12,600, $PR = 10$, $0 \le X/D_e \le 2.0$

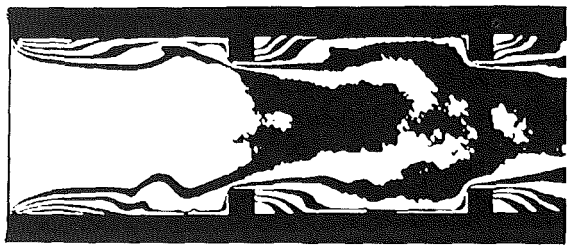

Fig. 4(*b*) Re = 33,000, $PR = 10$, $0 \le X/D_e \le 2.0$

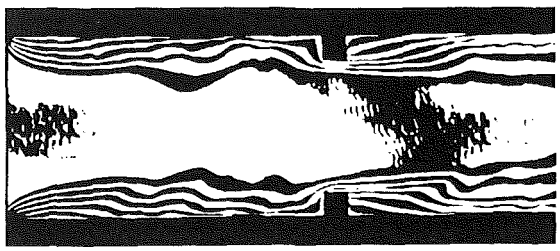

Fig. 4(*c*) Re = 12,600, $PR = 15$, $0 \le X/D_e \le 2.0$

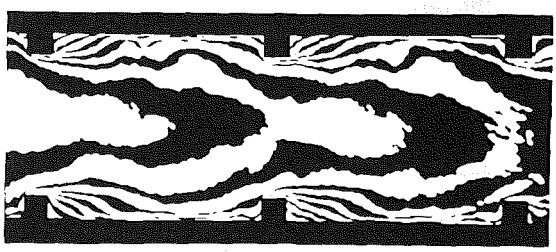

Fig. 4(*d*) Re = 12,600, $PR = 10$, $7.0 \le X/D_e \le 9.3$

Fig. 4 Examples of holographic interferometry of developing and periodic fully developed duct flows

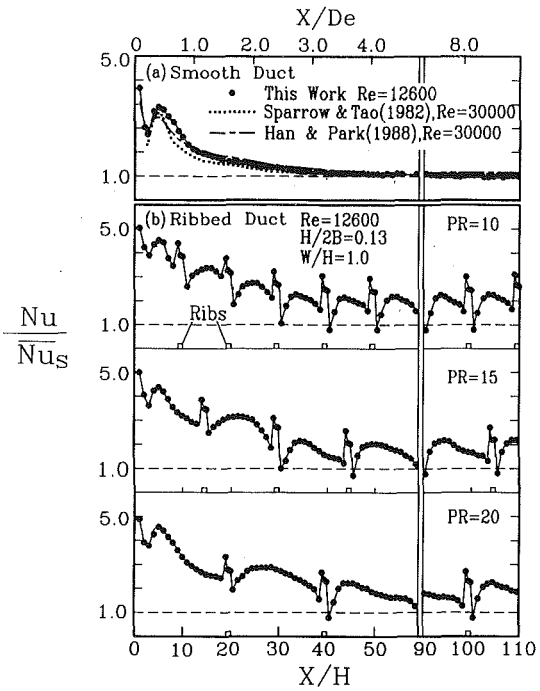

Fig. 5 Local Nusselt number ratio versus *X/H* in smooth and ribbed ducts

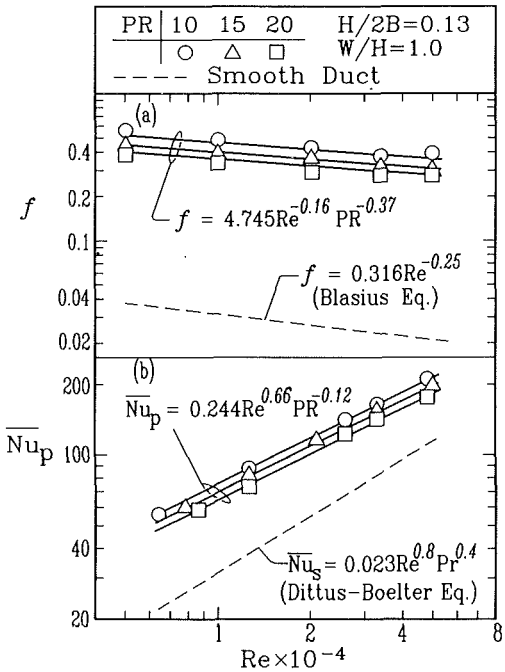

Fig. 6 Heat transfer and friction versus Re for *PR* = 10, 15, and 20

the cases of $PR = 10$ (17 and 22 stations for the cases of $PR = 15$ and 20, respectively). The open-square symbols along the abscissa of each graph in Fig. 5(*b*) indicate the axial positions of the ribs. It is useful to address the general feature of the distribution of $Nu/\overline{Nu}_S$ before comparing the three graphs in Fig. 5(*b*). In the upstream portion of the first rib, the general behavior of the three curves affected by the abrupt-contraction inlet of the duct is similar to that of the entrance region of a smooth duct. While in the downstream portion of the first rib, the distributions of $Nu/\overline{Nu}_S$ decrease slowly with increasing distance, settling into a periodic pattern just after the first few ribs. The periodically fully developed region can be defined as after the onset of the periodicity of the local Nusselt number distribution (Han, 1988; Sparrow and Tao, 1984). From Fig. 5(*b*), it is seen that the periodicity of the local Nusselt number ratio is encountered after about $X/D_e = 3$ (or $X/H = 40$), and the corresponding regions are after the third, second, and second rib pairs from the abrupt-contraction inlet of the duct for $PR = 10$, 15, and 20, respectively. Similar trends were observed by Han (1988). The periodic distribution of $Nu/\overline{Nu}_S$ is shaped and controlled by the presence of the ribs. The nature of the periodic pattern is that the flow separates from the wall when it encounters a rib and then reattaches to the wall in the interrib region. After reattachment, the flow tends to redevelop with a consequent decrease in $Nu/\overline{Nu}_S$ that is arrested when the next rib is encountered. With regard to the *PR*, the Nusselt number distribution is virtually unaffected but stretched or contracted along the streamwise direction. However, the average values of $Nu/\overline{Nu}_S$ will decrease slightly with *PR*, as will be seen later from the $\overline{Nu}_p$ correlation (Eq. (7)).

The identification of poor heat transfer regions, which are called hot spots if $Nu/\overline{Nu}_S < 1$, is important to the design of the internal cooling passages of turbine blades. Under periodic fully developed conditions, the experimental studies of Lockett and Collins (1990) for single-ribbed-wall duct flows and Liou and Hwang (1992) for two-opposite-ribbed-wall duct flows had shown the hot spots often occurring in the regions around the rib's rear corners formed by the intersection of ribs and duct wall. However, whether the abovementioned hot spots still hold in the case of developing flows has not been addressed previously and is of practical importance since the turbine blades are usually rather short. Figure 5(*b*) clearly reveals that the hot spots do not arise in the regions of flow development ($X/D_e \leq 3$).

Average Friction and Heat Transfer. Based on the local heat transfer and pressure distributions, it is found that the local Nusselt numbers have a periodic distribution and the pressure coefficients become linear between successive axial stations separated by a distance of rib pitch after $X/H > 40$. Therefore, the heat transfer and friction data in the region with $X/H > 40$ are used to provide the average Nusselt numbers and average friction factors. In the present study the average Nusselt numbers and average friction factors are based on the average values in the region between $X/H = 90$ and $X/H = 110$.

The Reynolds number dependence of average friction factor and Nusselt number for fully developed ribbed-duct flows with different rib pitches is depicted in Fig. 6, where the results of smooth ducts are also included for comparison. As expected, the average friction factor decreases with increasing Reynolds number, whereas the average Nusselt number increases with increasing Reynolds number. The results also show that, for a given Reynolds number, both the average friction factor and the Nusselt number decrease with increasing *PR*. In Fig. 6, a comparison of f and $\overline{Nu}_p$ distributions between the smooth-duct flow and the ribbed-duct one reveals that the extent of increased toll in f is a factor of 6–11, while the level of heat transfer augmentation is approximately 1.6–2.5 times $\overline{Nu}_S$ for $H/2B = 0.13$, and the test ranges of *PR* and Re. The results shown in Fig. 6 generally agree with the previous data of fully developed ribbed-duct flows without the flow separation at inlet reported by Liou and Hwang (1992).

The effects of Reynolds number ($5.0 \times 10^3 \leq Re \leq 5.0 \times 10^4$) and rib pitch ($PR \geq 10$) on the average friction factor and Nusselt number can be well correlated by the power law:

$$f = 4.745 \cdot Re^{-0.159} \cdot PR^{-0.369} \quad (6)$$

$$\overline{Nu}_p = 0.244 \cdot Re^{0.656} \cdot PR^{-0.121} \quad (7)$$

The maximum deviations of the measured data from the

above correlations are 4.2 and 5.5 percent, respectively, for the friction factor and the Nusselt number.

In general, the increase in the friction factor due to the ribbing is much greater than the increase of the Nusselt number, and f is more sensitive to the geometric parameters than is $\overline{Nu}_p$. To assess the net benefit of using a periodically ribbed duct instead of a smooth one, performance analyses are appropriate, and will be illustrated below.

Performance Analysis. The performance comparisons now presented are aimed basically at determining when it is useful to employ ribbed ducts (instead of smooth ducts) in practical applications. As mentioned before, comparisons under two different sets of constraint are undertaken.

First, a comparison between the heat transfer performance of smooth and ribbed ducts is made for equal mass flow rate. This type of comparison is meaningful for an allocation where the pressure drop due to the heat exchanger is small compared to the overall pressure drop in the flow circuit or the pressure drop is not as important as heat transfer augmentation.

The other set of constraints employed is equal pumping power. In situations where the cost of pumping power is a factor and the pressure drop across the heat exchanger is comparable to the pressure drop in the remainder of the installation or the pressure drop is substantially as important as the heat transfer augmentation, the constraint of equal mass flow rate is not appropriate. In this case, it is more meaningful to fix the pumping power consumed in the two types of ducts under comparison.

In order to impose the constraint of equal pumping power, it is necessary to find the relationship between the Reynolds number relative to the ribbed duct (Re) and the corresponding Reynolds number for the smooth duct (Re*) that yield the same pumping power. Intuitively, since the pressure drop in the ribbed ducts is large, it is expected that it takes a higher Reynolds number in the smooth duct to dissipate the same pumping power as in a ribbed duct.

The relationship of the ribbed and smooth ducts for the same pumping power is directly obtained by the expressions $G\Delta P/\rho = (G\Delta P/\rho)^*$. For fixed duct dimensions and equal thermophysical properties, it is readily shown that the constraint of equal pumping power is reduced to

$$f \cdot \mathrm{Re}^3 = f^* \cdot (\mathrm{Re}^*)^3 \tag{8}$$

Further, by combining the experimentally determined friction factors of the enhanced configurations and those of the well-known Blasius equation for the smooth duct, Eq. (8) is a relation between Re and Re*:

$$\mathrm{Re}^* = f^{1/3} \cdot \mathrm{Re} \cdot [0.316 \cdot (\mathrm{Re}^*)^{-0.25}]^{1/3} \tag{9}$$

The numerical results obtained from the solution of Eq. (9) are presented in Fig. 7(*a*). From Fig. 7(*a*), it is shown that, as expected, a ribbed duct has to be operated at a lower Reynolds number than smooth duct in order to achieve equal pumping power. It is interesting to note in this figure that the difference between the two Reynolds numbers is only slightly dependent on the pitch ratio PR.

With Re* and Re information of Fig. 7(*a*), the corresponding Nusselt numbers of smooth ducts can be evaluated, and then the ratios $\overline{Nu}_p/\overline{Nu}_S$ and $\overline{Nu}_p/\overline{Nu}_S^*$ determined and plotted in Fig. 7(*b*). Note that $\overline{Nu}_S$ corresponds to Re, and $\overline{Nu}_S^*$ corresponds to Re*. In this plot, the ratio $\overline{Nu}_p/\overline{Nu}_S$ for the case of equal mass flow rate is much higher than the ratio $\overline{Nu}_p/\overline{Nu}_S^*$ for the case of equal pumping power. Moreover, it can be seen that, regardless of the set of constraints employed, the improvement in Nusselt number ratios of the ribbed duct is more pronounced at low Reynolds numbers than at high Reynolds numbers, ranging from factors of 1.6–2.5 and 1.08–1.5 for the constraints of equal mass flow rate and equal pumping power, respectively. Furthermore, at the same rib height the dependence of $\overline{Nu}_p/\overline{Nu}_S^*$ on PR is very mild, whereas the dependence of $\overline{Nu}_p/\overline{Nu}_S$ on PR is significant.

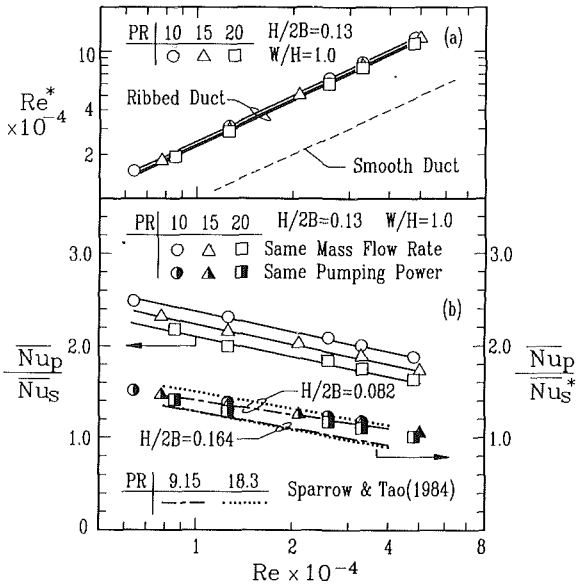

Fig. 7(*a*) Relationship between Re for ribbed ducts and Re* for smooth ducts (equal pumping power constraint); (*b*) comparison of constant-mass-flow-rate and constant-pumping-power fully developed heat transfer coefficients for the ribbed and smooth ducts

At the constraint of equal pumping power, a comparison of the present data with Sparrow and Tao's (1984) data is also made in Fig. 7(*b*). In their work the PR is 9.15 and 18.3, and the $H/2B$ is 0.082 and 0.164; in the present work the PR is 10, 15 and 20, and the $H/2B$ is 0.13. Although the rib pitch and height between the two works are different, the qualitative trend is in reasonable agreement.

Length Mean Nusselt Number. In turbine blade design, a mean conductance with respect to duct length, and thus a length mean Nusselt number, is generally of more utility than the local conductance and Nusselt number and has not been addressed in the past. As mentioned before, the local Nusselt number ratios maintain the same periodic distribution after $X/D_e \geq 3$. Thus, for ducts with lengths greater than the entry length, it should be possible to express the length mean Nusselt Number in the form

$$\overline{Nu}_m = [3D_e \cdot \overline{Nu}_d + (X - 3D_e)\overline{Nu}_p]/X \tag{10}$$

where $\overline{Nu}_d$ is the mean Nusselt number obtained by the integration of Nu from $X = 0$ to $X = 3D_e$ and can be further correlated by an equation of the form

$$\overline{Nu}_d = 0.352 \cdot \mathrm{Re}^{0.663} \cdot PR^{-0.106} \tag{11}$$

Furthermore, in combining the periodic fully developed results and the above equation, Eq. (10) becomes

$$\overline{Nu}_m/\overline{Nu}_p = 1 + 3 \cdot (1.443 \cdot \mathrm{Re}^{0.007} \cdot PR^{0.015} - 1)/(X/D_e) \tag{12a}$$

$$\cong 1 + 1.844/(X/D_e) \tag{12b}$$

The length mean Nusselt number ratios are also presented as a function of duct length (X/D_e) for various Reynolds numbers and pitch ratios in Figs. 8 and 9, respectively. In these figures, the results of the smooth ducts with nozzlelike and abrupt-contraction entrance are also included for comparison. The former is solved by direct numerical integration of the energy differential equation for a circular tube with constant surface temperature (Sleicher and Tribus, 1956). The latter is an experimental result that was carried out by Boelter et al.

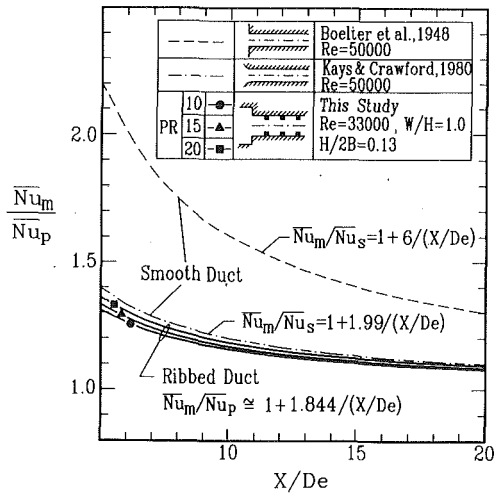

Fig. 8 Effect on *PR* on the length mean Nusselt number distributions

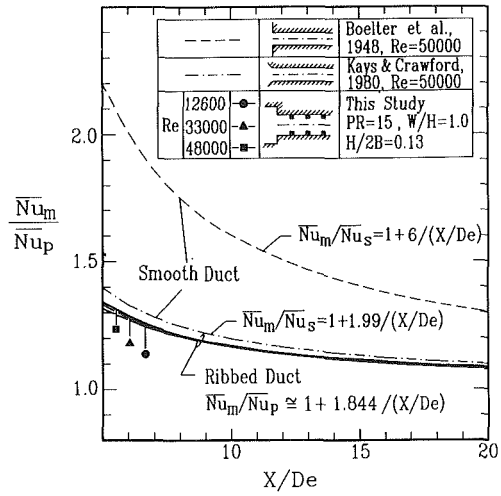

Fig. 9 Effect of Re on the length mean Nusselt number distributions

(1948) for flow in a circular tube with a sharp entrance and heated by condensing stream. It is seen that the behavior of these curves, which result from the ribbed duct with an abrupt-contraction entrance, is similar to that of a smooth duct with a nozzlelike entrance; that is, the effect of the abrupt-contraction entrance of the ribbed duct on the length mean Nusselt number ratio is not as substantial as that of the smooth duct with the same inlet condition. In fact, the mechanism that is responsible for large heat transfer coefficients near the abrupt-contraction inlet of the duct, i.e., flow separation, recirculation, and redevelopment, occurs everywhere throughout the duct due to the presence of the periodic turbulence promoters on the walls. Therefore, the magnitude of $\overline{Nu}_p$ is comparable to the values of $\overline{Nu}_d$ in the developing region near the duct inlet. Thus, the distribution of length mean Nusselt number ratio of the ribbed duct with an abrupt-contraction entrance, which is normalized by the asymptotic value, is similar to that of the smooth one with a nozzlelike rather than with an abrupt-contraction entrance. Moreover, Figs. 8 and 9 show that there is little influence of *PR* and Re on $\overline{Nu}_m/\overline{Nu}_p$. This is because the dependence of $\overline{Nu}_p$ and $\overline{Nu}_d$ on the *PR* and the Re are largely identical. With regard to the effect of Re, a similar trend was obtained by Kays and Crawford (1980) for a smooth duct with a nozzlelike entrance in which the distributions of local as well as length mean Nusselt numbers are nearly independent of Reynolds number for Pr = 0.7. As a last comment on these figures, it is worth noting that for a ribbed duct 10–15 hydraulic diameters in length with an abrupt-contraction inlet, which simulates a typical internal cooling passage of turbine airfoils, the length mean Nusselt number is 12–18 percent above the asymptotic value; that is, there is a 12–18 percent effect of the entry length.

Summary and Conclusions

Turbulent developing heat transfer in a ribbed duct with an abrupt-contraction inlet has been studied by using laser holographic interferometry. The duct has hot gas flowing outside and is cooled from the inside. The main contributions of the present work are: (1) to identify the fact that the local hot spots do not occur in the developing region of ribbed-duct flow, and (2) to investigate the effects of thermal entry length, flow parameter, and rib parameter on the length mean Nusselt number of the ribbed duct. The key conclusions are drawn from the data presented:

1 Both axial distributions of the local Nusselt numbers and pressure coefficients revealed that the establishment of periodic fully developed regime was about after $X/H = 40$ (or $X/D_e = 3$), whereas the former showed cyclic repetition of local Nusselt number and the latter showed linear pressure distributions between successive axial stations, which were separated by one-pitch distance, as $X/H \geq 40$.

2 The hot spots occurring in the regions around the downstream concave corners of the ribs for the periodic fully developed flows did not arise in the corresponding regions for the developing flows. This finding was not reported in the past.

3 From the performance analysis, enhancements of the order of 60 to 150 percent were obtained with the ribbed ducts when compared with the smooth ducts at equal mass flow rate. When the comparison was at equal pumping power, enhancements in the range 8–50 percent were encountered. Moreover, the dependence of $\overline{Nu}_p/\overline{Nu}_S^*$ on *PR* was very mild, while the dependence of $\overline{Nu}_p/\overline{Nu}_S$ on *PR* was significant.

4 A compact correlation for the length mean Nusselt number was obtained for the first time for the developing flows in a ribbed duct with an abrupt-contraction entrance. The behavior of $\overline{Nu}_m/\overline{Nu}_p$ distribution for the ribbed duct with an abrupt-contraction entrance was found to be similar to that of a smooth duct with a nozzlelike entrance, and was nearly independent of *PR* and Re.

5 For a ribbed duct with 10–15 hydraulic diameters of length, which was a typical length of the internal cooling passages of turbine airfoils, the length mean Nusselt number for the abrupt-contraction entrance revealed a 12–18 percent effect of the entry length.

Acknowledgment

Support for this work was provided by the National Science Council of the Republic of China under contract NSC 80-04101-E007.

References

Boelter, L. M. K., Young, G., and Iversen, H. W., 1948, "An Investigation of Aircraft Heaters—Distribution of Heat-Transfer Rate in the Entrance Section of a Circular Tube," NACA Technical Note No. 1451. Data reported by Kays and Crawford, 1980, in: *Convective Heat and Mass Transfer*, 2nd ed., p. 269, McGraw-Hill, New York.

Dipprey, D. F., and Sabersky, R. J., 1963, "Heat and Momentum Transfer in Smooth and Rough Tubes at Various Prandtl Number," *Int. J. Heat Mass Transfer*, Vol. 6, pp. 329–353.

Goldstein, R. J., 1976, "Optical Measurement of Temperature," *Measurements in Heat Transfer*, 2nd ed., E. R. G. Eckert, and R. J. Goldstein, eds., Hemisphere, Washington, DC, pp. 241–294.

Han, J. C., Park, J. S., and Lei, C. K., 1985, "Heat Transfer Enhancement in Channels With Turbulence Promoters," ASME *Journal of Engineering for Gas Turbines and Power*, Vol. 107, pp. 628–635.

Han, J. C., 1988, "Heat Transfer and Friction Characteristics in Rectangular

Channels With Rib Turbulators," ASME JOURNAL OF HEAT TRANSFER, Vol. 110, pp. 321-328.

Han, J. C., and Park, J. S., 1988, "Developing Heat Transfer in Rectangular Channels With Rib Turbulators," *Int. J. Heat Mass Transfer*, Vol. 31, No. 1, pp. 183-195.

Hauf, W., and Grigull, U., 1970, "Optical Methods in Heat Transfer," *Advances in Heat Transfer*, Vol. 6, J. P. Hartnett and T. F. Irvine, Jr., eds., Academic, New York, pp. 133-136.

Kays, W. M., and Crawford, M. E., 1980, *Convection Heat and Mass Transfer*, 2nd ed., p. 269, McGraw-Hill, New York.

Kline, S. J., and McClintock, F. A., 1953, "Describing Uncertainties in Single-Sample Experiments," *Mechanical Engineering*, Vol. 75, Jan., pp. 3-8.

Lewis, M. J., 1975, "An Elementary Analysis for Predicting the Momentum and Heat Transfer Characteristics of a Hydraulically Rough Surface," ASME JOURNAL OF HEAT TRANSFER, Vol. 97, pp. 249-254.

Liou, T. M., and Lin, J., 1988, "Measurements of Turbulent Flow in a Duct With Repeated Ribs Applied to Two Opposite Walls," *Journal of the Chinese Institute of Engineers*, Vol. 11, No. 4, pp. 319-326.

Liou, T. M., and Hwang, J. J., 1992, "Turbulent Heat Transfer and Friction in Periodic Fully Developed Channel Flows," ASME JOURNAL OF HEAT TRANSFER, Vol. 114, pp. 56-64.

Lockett, J. F., and Collins, M. W., 1990, "Holographic Interferometry Applied to Rib-Roughness Heat Transfer in Turbulent Flow," *Int. J. Heat Mass Transfer*, Vol. 33, No. 11, pp. 2439-2449.

Metzger, D. E., Fan, C. S., and Yu, Y., 1990, "Effects of Rib Angle and Orientation on Local Heat Transfer in Square Channels With Angled Roughness Ribs," *Compact Heat Exchangers*, A Festschrift for A. L. London, Hemisphere.

Rowley, G. J., and Patankar, S. V., 1984, "Analysis of Laminar Flow and Heat Transfer in Tubes With Internal Circumferential Fins," *Int. J. Heat Mass Transfer*, Vol. 27, No. 4, pp. 553-560.

Sleicher, C. A., and Tribus, M., 1956, *J. Heat Transfer Fluid Mechanics Institute*, Stanford, CA, p. 59. Data reported by Kays and Crawford, 1980, in: *Convective Heat and Mass Transfer*, 2nd ed., p. 264, McGraw-Hill, New York.

Sparrow, E. M., and Cur, N., 1982, "Turbulent Heat Transfer in a Symmetrically or Asymmetrically Heated Flat Rectangular Duct With Flow Separation at Inlet," ASME JOURNAL OF HEAT TRANSFER, Vol. 104, pp. 82-89.

Sparrow, E. M., and Tao, W. Q., 1983, "Enhanced Heat Transfer in a Flat Rectangular Duct With Streamwise-Periodic Disturbances at One Principal Wall," ASME JOURNAL OF HEAT TRANSFER, Vol. 105, pp. 851-861.

Sparrow, E. M., and Tao, W. Q., 1984, "Symmetric vs. Asymmetric Periodic Disturbances at the Walls of a Heated Flow Passge," *Int. J. Heat Mass Transfer*, Vol. 27, No. 11, pp. 2133-2144.

Walklate, P. J., 1981, "A Two Wavelength Holographic Technique for the Study of Two-Dimensional Thermal Boundary Layers," *Int. J. Heat Mass Transfer*, Vol. 24, pp. 1051-1057.

Webb, R. L., Eckert, E. R. G., and Goldstein, R. J., 1971, "Heat Transfer and Friction in Tubes With Repeated-Rib Roughness," *Int. J. Heat Mass Transfer*, Vol. 14, pp. 601-617.

Laminar Heat Transfer and Fluid Flow in the Entrance Region of a Rotating Duct With Rectangular Cross Section: The Effect of Aspect Ratio

T.-C. Jen

A. S. Lavine

Mechanical, Aerospace, and Nuclear Engineering Department,
University of California, Los Angeles
Los Angeles, CA 90024-1597

A numerical calculation has been performed for the simultaneously developing laminar velocity and temperature fields in the entrance region of an isothermal rectangular duct rotating about an axis perpendicular to the duct axis. The present paper particularly addresses the effect of the aspect ratio of the rectangular duct. The vorticity-velocity method with the power law scheme is employed to solve the governing equations for the flow and heat transfer. It is seen that pairs of counterrotating vortices appear in the cross section of the duct. The number of vortex pairs depends on the aspect ratio of the duct. Under some circumstances, the number of vortex pairs varies with axial position. The numerically calculated stability boundary points for small aspect ratio show excellent agreement with the neutral stability curve, which was obtained by linear stability analysis. Friction factor and Nusselt number are presented as functions of axial position, and it is seen that they are strongly affected by the vortices. Comparisons with existing theoretical and experimental results are also presented.

Introduction

The analysis of heat transfer and fluid flow in channels subject to a spanwise rotation is important in the prediction of cooling requirements for the rotor blades in gas turbines and other rotating machineries (Dakin et al., 1978; Metzger et al., 1982). It is also relevant to a variety of geophysical problems (Hart, 1979; Pedlosky, 1982). Qualitative similarity is also found to the heat transfer and fluid flow in a curved channel by Dennis and Ng (1982). Although some of these applications, such as gas turbine blade cooling, would be turbulent flows, the present analysis addresses the laminar case. This is relevant in some applications (e.g., Hart, 1979; Speziale, 1986) and is also of fundamental interest. A detailed literature review for rotating ducts is given by Jen et al. (1992a). Only the papers closely relevant to the present study are reviewed here.

Hart (1971) employed linear stability analysis for the laminar flow regime, and made experimental measurements of critical conditions required for the onset of instabilities. He found that there existed a weak double-vortex secondary flow at small rotation speeds, and an instability existed in the form of longitudinal rolls of nondimensional wave number 5 at moderately high rotation speeds. Lezius and Johnston (1976) studied the Taylor-type roll-cell instability for the laminar and turbulent flow in a rotating parallel plate channel. They used the linear stability analysis to predict the critical Reynolds number for which instability occurs, as a function of Rossby number. They found the critical value for laminar plane Poiseuille flow occurred at a Reynolds number of 88.53 and a Rossby number of 0.5 with a wave number of 4.9. Jen et al. (1992b) presented a numerical analysis of the fully developed region in a rotating isothermal isosceles triangular duct with three different aspect ratios. For large apex angles the results would be expected to approach the parallel plate case. In fact, it was found that their numerical calculations of stability limit curves for large apex angles did lie close to the stability curve obtained by Lezius and Johnston (1976) for laminar Poiseuille flow. Speziale (1982, 1986) and Speziale and Thangan (1983) studied the laminar flow in rotating rectangular ducts extensively. For constant axial pressure gradient, they calculated the velocities and showed the flow pattern qualitatively. According to the flow characteristics, Smirnov (1978) divided the channel cross section into four regions, and used an asymptotic analysis to obtain the drag coefficient formula. This formula is in good agreement with experimental data for Rossby number up to order unity. However, a more restricted condition (i.e., $E^{1/4} \ll \gamma$) was imposed, thus it is only valid for ducts with large aspect ratios. Hwang and Jen (1990) and Jen (1987) studied the fully developed laminar flow and heat transfer problem in rectangular ducts. The friction factor and Nusselt number were reported for a large range of parameters, and showed qualitative agreement with experiment. They also investigated the effect of axial conduction for a fluid with small Peclet number.

The earlier works almost all concentrated on the hydrodynamically and thermally fully developed region. Reports of developing flows are very scarce, as indicated by Mori and Nakayama (1984). The available entrance region data, closely relevant to the present analysis, from both theoretical and experimental studies are now reviewed. Heat transfer measurements were carried out by Hwang and Soong (1988) in a rotating isothermal square duct for Reynolds number ranging from 717 to 16,000 and rotational Reynolds number from 20 to 320, and by Soong et al. (1991) in rectangular ducts for aspect ratios 0.2, 0.5, 1, 2, and 5. Jen at al. (1992a) studied the heat transfer and flow field in the entrance region of a rotating isothermal square duct numerically by the vorticity-velocity formulation.

So far, little information is available for a rectangular duct in the simultaneously developing entrance region. The purpose

Contributed by the Heat Transfer Division for publication in the JOURNAL OF HEAT TRANSFER. Manuscript received by the Heat Transfer Division March 1991; revision received February 1992. Keywords: Forced Convection, Numerical Methods, Rotating Flows. Associate Technical Editor: R. J. Simoneau.

of the present investigation is to extend the previous work on square ducts (Jen et al., 1992a) to channels of aspect ratios $\gamma = 0.2$, 0.5, 2, and 5 to examine the effect of aspect ratio on the flow and heat transfer characteristics. It will be shown that pairs of counterrotating vortices appear in the cross section of the duct. The number of vortex pairs depends on the aspect ratio of the duct. Under some circumstances, the number of vortex pairs varies with axial position, and it will be seen that they are strongly affected by the vortices.

In addition to these results, a slender duct (i.e., $\gamma = 0.1$) is employed to find the boundary points of the stability curve. The results are found to be in excellent agreement with linear stability analysis. Comparisons with existing theoretical and experimental results are also presented.

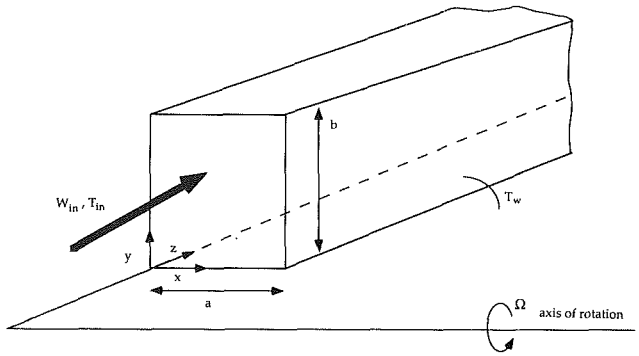

Fig. 1 Physical configuration and coordinate system

Theoretical Analysis

Consider the steady, laminar, developing forced convection flow in an isothermal rectangular channel rotating at a constant angular speed about an axis perpendicular to the channel longitudinal direction as shown in Fig. 1. A uniform inlet axial velocity $W_{in} = \overline{W}$ and a constant inlet temperature T_{in} are imposed at $Z = 0$. The duct wall temperature is held constant at T_w. The flow is assumed to be steady, constant property, and incompressible, and axial diffusion, viscous dissipation, compression work, and buoyancy are neglected. It is worth noting that centrifugal-buoyancy forces may not be neglected when the speed of rotation is large. Therefore, the present calculations will cover low to moderate rotational speed where centrifugal-buoyancy forces are relatively small. Note that once centrifugal-buoyancy force is neglected, the distance from the axis of rotation to the duct inlet is irrelevant.

The axial and cross-sectional pressure gradients may be decoupled by making the usual parabolic assumption (Patankar and Spalding, 1972). A modified pressure P, which includes the centrifugal force, may be defined as

$$P(X, Y, Z) = \overline{P}(Z) + P^*(X, Y) + \frac{1}{2}\rho(Z^2 + Y^2)\Omega^2 \tag{1}$$

where $\overline{P}(Z)$ is the pressure averaged over the cross section at each axial location, and $P^*(X, Y)$ is the pressure variation in the X, Y direction, which drives the secondary flow. Now, having made the parabolic assumption, the nondimensional axial pressure gradient depends only on z, that is:

$$\frac{\partial p}{\partial z} = f(z) \tag{2}$$

where $f(z)$ is determined by the constant flow rate constraint.

The following dimensionless variables and parameters are introduced:

$$x = \frac{X}{D_e},\ y = \frac{Y}{D_e},\ z = \frac{Z}{\mathrm{Re}D_e},\ u = \frac{U}{U_c},\ v = \frac{V}{U_c},\ w = \frac{W}{W_c},$$

$$p = \frac{P}{P_c},\ \theta = \frac{(T - T_w)}{(T_{in} - T_w)}, \tag{3}$$

$$\mathrm{Re} = \frac{\overline{W}D_e}{\nu},\ \mathrm{Re}_\Omega = \frac{\Omega D_e^2}{\nu},\ \mathrm{Pr} = \frac{\nu}{\alpha},\ \mathrm{Ro} = \frac{\mathrm{Re}}{2\mathrm{Re}_\Omega} = \frac{\overline{W}}{2\Omega D_e}$$

where

$$P_c = \rho \mathrm{Re}\mathrm{Re}_\Omega\left(\frac{\nu}{D_e}\right)^2,\ U_c = \mathrm{Re}\mathrm{Re}_\Omega\left(\frac{\nu}{D_e}\right),$$

$$W_c = \overline{W}\mathrm{Re}\mathrm{Re}_\Omega,\ D_e = \frac{4A}{S}$$

The following governing equations can be obtained as in Jen et al. (1992a):

$$\xi = \frac{\partial u}{\partial y} - \frac{\partial v}{\partial x} \tag{4}$$

$$\nabla^2 u = \frac{\partial \xi}{\partial y} - \frac{\partial^2 w}{\partial x \partial z} \tag{5}$$

Nomenclature

A = cross-sectional area
a = width of duct
b = height of duct
D_e = hydraulic diameter $= 4A/S$
E = Ekman number $= [16\gamma^2/(1+\gamma)^2](1/\mathrm{Re}_\Omega)$
f = friction factor $= \bar{\tau}_w / \frac{1}{2}\rho\,\overline{W}^2$
k = wave number
Nu = peripherally averaged Nusselt number
n = dimensionless normal direction coordinate
P, p = pressure and dimensionless pressure
Pr = Prandtl number $= \frac{\nu}{\alpha}$
Re = Reynolds number $= \frac{\overline{W}D_e}{\nu}$
Re_Ω = rotational Reynolds number $= \frac{\Omega D_e^2}{\nu}$
Ro = Rossby number $= \frac{\mathrm{Re}}{2\mathrm{Re}_\Omega}$
S = perimeter
T = temperature
U, V, W = velocity components in X, Y, Z directions
u, v, w = dimensionless velocity components in x, y, z directions
X, Y, Z = rectangular coordinates
x, y, z = dimensionless rectangular coordinates
α = thermal diffusivity of fluid
γ = aspect ratio $= b / a$
θ = dimensionless temperature defined in Eq. (3)
λ = wavelength
ν = kinematic viscosity
ξ = vorticity defined in Eq. (4)
ρ = density
τ_w = wall shear stress
Ω = angular speed

Subscripts

c = characteristic quantity
in = inlet quantity condition
L = parameters defined by Lezius and Johnston (1976)
m = bulk mean quantity
o = condition without rotation
w = condition at wall

Table 1 Grid convergence tests for various aspect ratios

γ	0.2	0.5	2.0	5.0
Grid used	67 x 19	46 x 22	22 x 46	19 x 67
Grid test	97 x 28	67 x 31	31 x 67	28 x 97
Changes in				
fRe	2.6%	0.7%	0.8%	1.2%
Nu	2.5%	1.0%	0.9%	0.8%
at $z = 1.89 \times 10^{-3}$				
Maximum error by halving Δz				
fRe	2.2%	1.3%	1.5%	2.1%
Nu	3.2%	1.7%	2.4%	3.5%

$$\nabla^2 = -\frac{\partial \xi}{\partial x} - \frac{\partial^2 w}{\partial y \partial z} \tag{6}$$

$$\mathrm{ReRe}_\Omega \left[u\frac{\partial \xi}{\partial x} + v\frac{\partial \xi}{\partial y} + w\frac{\partial \xi}{\partial z} + \xi\left(\frac{\partial u}{\partial x} + \frac{\partial v}{\partial y}\right) + \left(\frac{\partial w \partial u}{\partial y \partial z} - \frac{\partial w \partial v}{\partial x \partial z}\right)\right] = \frac{\partial^2 \xi}{\partial x^2} + \frac{\partial^2 \xi}{\partial y^2} + 2\mathrm{ReRe}_\Omega \frac{\partial w}{\partial x} \tag{7}$$

$$\mathrm{ReRe}_\Omega \left(u\frac{\partial w}{\partial x} + v\frac{\partial w}{\partial y} + w\frac{\partial w}{\partial z}\right) = -f(z) + \frac{\partial^2 w}{\partial x^2} + \frac{\partial^2 w}{\partial y^2} + \frac{v}{\mathrm{Ro}} \tag{8}$$

$$\mathrm{PrReRe}_\Omega \left(u\frac{\partial \theta}{\partial x} + v\frac{\partial \theta}{\partial y} + w\frac{\partial \theta}{\partial z}\right) = \frac{\partial^2 \theta}{\partial x^2} + \frac{\partial^2 \theta}{\partial y^2} \tag{9}$$

The solution depends on three independent parameters: Prandtl number (Pr), a combined Reynolds and rotational Reynolds number (ReRe_Ω), and Rossby number (Ro). The reasons for choosing this group of parameters were explained by Jen et al. (1992a). An additional constraint that will be used to determine $f(z)$ is that global mass conservation must be satisfied:

$$\int_0^{\frac{1+\gamma}{2}} \int_0^{\frac{1+\gamma}{2\gamma}} w_t \, dx dy = \frac{(1+\gamma)^2}{4\gamma} \tag{10}$$

where $w_t = \frac{W}{\overline{W}}$ has been defined for convenience.

The boundary conditions are:

$$u = v = w = \theta = 0 \text{ at walls,}$$
$$u = v = \xi = 0, \text{ and } w_t = \theta = 1 \text{ at } z = 0 \tag{11}$$

Following the usual definitions, the expression for the product of the peripherally averaged friction factor and Reynolds number, $f\mathrm{Re}$, can be written based on the axial velocity gradient at the wall:

$$f\mathrm{Re} = 2\left(\frac{\overline{\partial w_t}}{\partial n}\right)_{\text{wall}} \tag{12}$$

The peripherally averaged Nusselt number, Nu, can be written based on the temperature gradient at the wall:

$$\mathrm{Nu} = -\frac{1}{\theta_m}\left(\frac{\overline{\partial \theta}}{\partial n}\right)_{\text{wall}} \tag{13}$$

where the overbar in Eqs. (12) and (13) means average around the perimeter. The quantity θ_m is defined as

$$\theta_m = \frac{(T_m - T_w)}{(T_{in} - T_w)} = \frac{4\gamma}{(1+\gamma)^2} \int_0^{\frac{1+\gamma}{2}} \int_0^{\frac{1+\gamma}{2\gamma}} w_t \theta \, dx dy \tag{14}$$

where T_m is the mean temperature.

Method of Solution

The governing equations are solved numerically by the vorticity–velocity method for three-dimensional parabolic flow, along with the power law scheme (Patankar, 1980). The numerical procedures were described by Jen et al. (1992a) and will not be repeated here.

Computational Tests and Details

The uniform cross-sectional meshes used for the different aspect ratios are shown In Table 1. The full domain of the cross section is used, since some asymmetric flow patterns are observed and will be discussed later. The axial step size Δz was varied from 10^{-5} near the duct entrance to about 2.56×10^{-3} near the fully developed region; about 130 forward steps are needed to reach the fully developed region. Grid independence tests both in the cross-sectional direction and axial direction have been performed for denser grids, at moderately high rotational speed (i.e., $\mathrm{ReRe}_\Omega = 10^4$, Ro = 1.0, which is equivalent to Re = 141.7 and $\mathrm{Re}_\Omega = 70.0$) for various aspect ratios. The changes in predicted heat transfer and friction coefficients for various aspect ratios are also shown in Table 1. The errors are seen to be small at $z = 1.89 \times 10^{-3}$, and become smaller further downstream. As an additional verification of the computational procedure, the hydrodynamically developing flow was calculated without rotation. The results were compared with Shah and London (1978) and Curr et al. (1972). The apparent friction factors were found to agree within 2 percent at all axial stations for all aspect ratios.

Results and Discussion

In the presentation that follows, the secondary flow patterns and isotherms will be examined closely. Typical developing flow and single pair secondary flow patterns have been reported in a previous investigation (Jen et al., 1992a), and will not be repeated here. The roll-cell instability phenomenon will be discussed, and the comparison with linear stability analysis will be presented. The friction factors and Nusselt numbers for low and moderately high rotation speeds are shown, and comparisons with both theoretical and experimental data are presented.

As shown in Fig. 1, a rectangular channel is rotating at a constant speed about the X axis. The fluid in the core region is driven in the negative Y direction by the Coriolis force. The downward flow in the core region forces the fluid near the side walls to flow in the positive Y direction and a pair of counterrotating vortices is generated. There exist two kinds of boundary layers, Ekman layers at the side walls, and Stewartson layers at the top and bottom walls (Bennetts and Hocking, 1974). This makes a perturbation analysis possible for a single pair of vortices, which will be discussed later. In the present study, multiple pairs of vortices are observed for the high ReRe_Ω and moderate Ro regime, and changes in flow and heat transfer characteristics are also found as a result. The two-pair vortex phenomenon was reported by Jen et al. (1992a) for a square duct. Similar results are also observed for aspect ratios of 0.5 and 2, and are not repeated here. However, in order to demonstrate the asymmetric flow patterns, Fig. 2 shows examples of this phenomenon for both $\gamma = 0.5$ and 2.0. The asymmetry of the second pair of vortices is quite

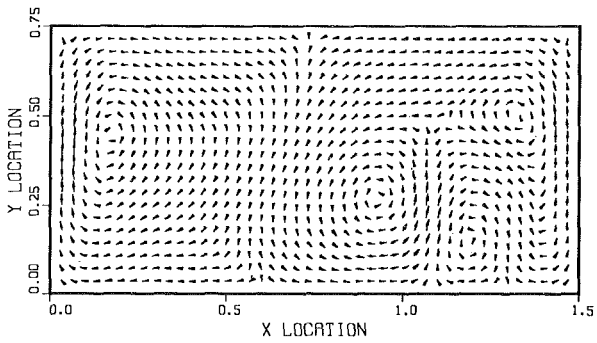

Fig. 2(*a*) Secondary flow map for $\gamma = 0.5$ with $ReRe_\Omega = 10^5$, Ro = 10 at $z = 1.4077 \times 10^{-1}$

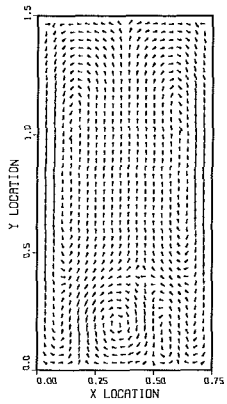

Fig. 2(*b*) Secondary flow map for $\gamma = 2.0$ with $ReRe_\Omega = 2 \times 10^5$, Ro = 10 at $z = 7.165 \times 10^{-2}$

Fig. 2 Asymmetric secondary flow maps for $\gamma = 0.5$ and 2.0

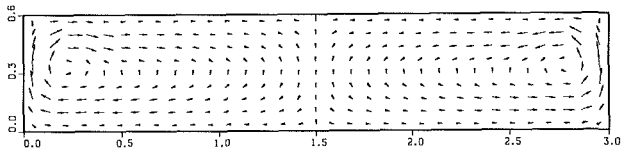

Fig. 3(*a*) Secondary flow map at $z = 2.173 \times 10^{-2}$

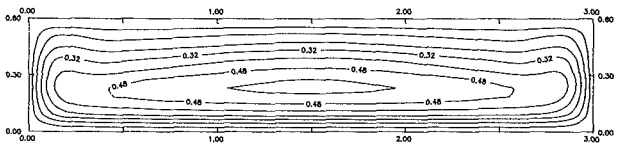

Fig. 3(*b*) Isotherm map at $z = 2.173 \times 10^{-2}$

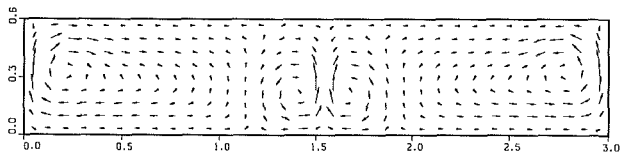

Fig. 3(*c*) Secondary flow map at $z = 6.013 \times 10^{-2}$

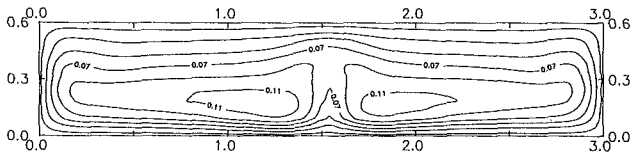

Fig. 3(*d*) Isotherm map at $z = 6.013 \times 10^{-2}$

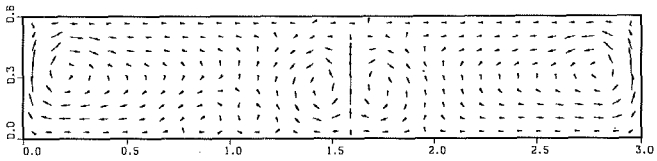

Fig. 3(*e*) Secondary flow map at $z = 1.062 \times 10^{-1}$

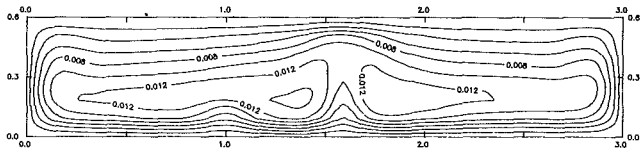

Fig. 3(*f*) Isotherm map at $z = 1.062 \times 10^{-1}$

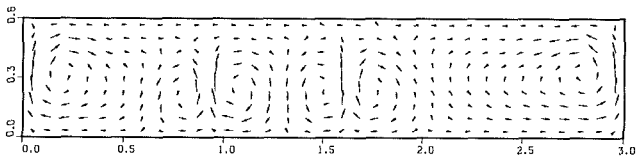

Fig. 3(*g*) Secondary flow map at $z = 1.177 \times 10^{-1}$

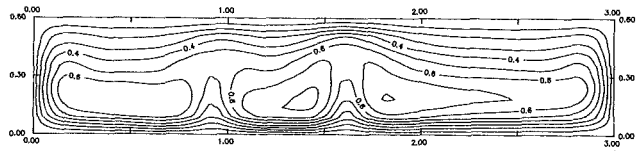

Fig. 3(*h*) Isotherm map at $z = 1.177 \times 10^{-1}$ ($\theta \times 10^2$)

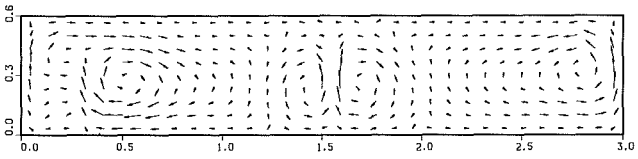

Fig. 3(*i*) Secondary flow map at $z = 1.561 \times 10^{-1}$

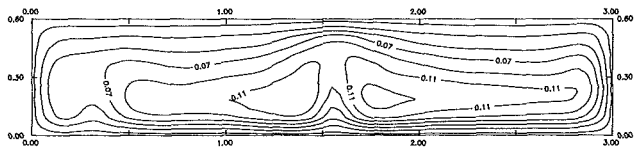

Fig. 3(*j*) Isotherm map at $z = 1.561 \times 10^{-1}$ ($\theta \times 10^2$)

Fig. 3 The development of secondary flow and isotherm maps for $\gamma = 0.2$ at $ReRe_\Omega = 10^5$, Ro = 10.

apparent. Further downstream, the flow will revert to one pair of vortices, resulting in a pronounced drop of friction factor and Nusselt number, which will be discussed later. It is worth noting that in general, Taylor-type instabilities exhibit streamwise oscillation in certain supercritical states, as shown by Coles (1965). The linear stability analysis usually assumes disturbance without dependence on the z direction. This oscillatory behavior of vortices has its origin in the nonlinear inertia term. Therefore, in order to fully understand such effects, the nonlinear Navier-Stokes equation must be solved without any linearization.

Axial Development of Secondary Flow and Temperature

The detailed development of secondary flow and temperature for $\gamma = 0.2$ is presented in Fig. 3. The parameters are $ReRe_\Omega = 10^5$, Ro = 10. The first pair of figures (3*a*, *b*) shows the "rotational developing" region (Jen et al., 1992a), in which

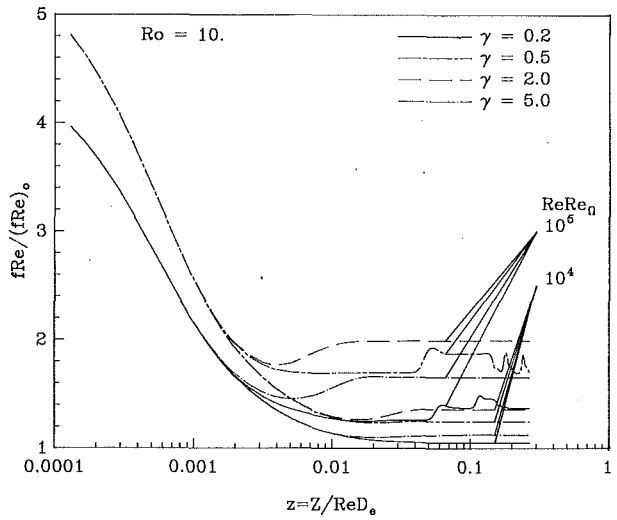

Fig. 4(*a*) Friction factor ratio for Ro = 10

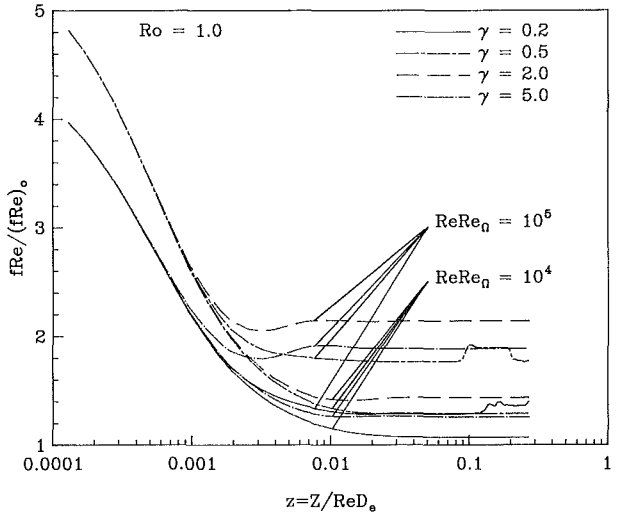

Fig. 4(*b*) Friction factor ratio for Ro = 1.0

Fig. 4 $fRe/(fRe)_o$ versus z for Ro = 10 and 1 in rectangular channels

the single pair of vortices is formed. The growth of the second pair of vortices is shown in the second pair of figures (3*c*, *d*). The distortion of the isotherms is pronounced. The cooler fluid flowing down in the center divides the high-temperature center core into two isolated halves. (It is noted that the imposed wall boundary condition $\theta = 0$ means the walls are "cold.") The heat transfer rate increases due to the mixing of the core hot fluid with the cold fluid near the wall. The third pair of figures (3*e*, *f*) presents the most interesting results. Note that a third pair of counterrotating vortices appears at $x = 1.0$ near the bottom of the channel. This flow shows a nonsymmetric distribution of vortices, and suggests that the two-dimensional rolls are unstable. The following two pairs of figures (3*g*–*j*) make it clear that the longitudinal mode cannot be neglected. The growth and shifting of the third pair of vortices and isotherms are clearly seen. There is an oscillatory instability superimposed on the longitudinal rolls that is similar to the oscillatory instability of Taylor vortices (Coles, 1965). These results are further supported by Ravi Sankar et al. (1988). Their analysis showed that spatially periodic three-dimensional solutions are possible, and can be asymmetric about the midplane in a square curved duct. Due to the similarity of flow behavior between curved ducts and rotating ducts, it is therefore expected that similar results can also be obtained in the rotating duct case.

Axial Variation of the Friction Factor and the Nusselt Number

The wall shear stress is presented in terms of the friction factor ratio $f\mathrm{Re}/(f\mathrm{Re})_o$, where the subscript o denotes the quantity for fully developed forced convection without rotation. In the presentation that follows, chosen results for high Ro and moderately low Ro are given separately for various aspect ratios. Figures 4(*a*), 4(*b*) show the values of $f\mathrm{Re}/(f\mathrm{Re})_o$ versus dimensionless axial distance z for the cases of Ro = 10, 1 with $\mathrm{ReRe}_\Omega = 10^4$ and 10^5. Figure 4(*a*) presents the axial variation of $f\mathrm{Re}/(f\mathrm{Re}_o)$ for $\mathrm{ReRe}_\Omega = 10^4$ and 10^5 with Ro = 10, which indicates a large ratio of Re to Re_Ω. From the definitions of Re, Re_Ω, and Ro, it is seen that holding Ro fixed while increasing ReRe_Ω is like simultaneously increasing the Reynolds number Re and rotational Reynolds number Re_Ω at a fixed ratio of Re and Re_Ω. Informally speaking, higher Ro means lower rotation speed, and vice versa. Four different types of line represent the different aspect ratios. In the absence of rotation, the friction factor would depend on the aspect ratio, with $\gamma = 0.5$ and 2.0 yielding one curve, and $\gamma = 0.2$ and 5.0 yielding another. In the present calculations, the Coriolis force effect is insignificant near the inlet, and it can be seen that the results do indeed fall along one of two curves (depending on aspect ratio), which correspond to the case of no rotation. As the Coriolis force becomes important, at about $z = 10^{-3}$ or later, the $f\mathrm{Re}/(f\mathrm{Re})_o$ curves rise above the single curve for their respective aspect ratios. The "rotational developing" (Jen et al., 1992a) flow region is then observed. Finally, a nominally constant friction factor is reached, which will be referred to as the fully developed flow region. It is obvious that larger ReRe_Ω values increase the friction factor. For some cases, the roll-cell instability phenomenon is observed, and the corresponding increase in $f\mathrm{Re}/(f\mathrm{Re})_o$ is significant. There are two curves for which this phenomenon is observed, both for $\mathrm{ReRe}_\Omega = 10^5$, and $\gamma < 1$. The friction factor ratio increases are 18 and 14 percent, for $\gamma = 0.2$ and 0.5, respectively. It is also worth noting that a strong oscillation in friction factor ratio is observed for the curve of $\gamma = 0.5$. This is because of the appearance and disappearance of the second pair of vortices. The other curve for $\gamma = 0.2$ shows a double step increase in friction factor ratio. The first and second steps are due to the generation of the second and third pair of vortices, respectively.

Figure 4(*b*) demonstrates the friction factor ratio for Ro = 1. If we examine both figures closely, it is easy to see that the stronger rotation (i.e., smaller Rossby number) forces the flow to develop much faster. For example, for the $\gamma = 5.0$ curves at $\mathrm{ReRe}_\Omega = 10^5$, for Ro = 10 it takes abut 2.2 D_e to enter the rotational developing region, but for Ro = 1 it only takes about 0.22 D_e to reach the same region. Similarly, for the fully developed region, it takes about 28 and 4.5 D_e for Ro = 10 and 1, respectively. It is also noted that stronger rotation speed tends to diminish the increase of the friction factor ratio due to the generation of the second pair of vortices. For Ro = 1, the increases in friction factor ratios for $\gamma = 0.2$ and 0.5 are only 9 and 7 percent respectively. This is because higher rotation speed tends to stabilize the flow (Hart, 1971; Lezius and Johnston, 1976).

Hwang and Jen (1990) show that aspect ratio $\gamma = 0.5$ yields higher values of friction factor ratio than aspect ratio $\gamma = 5.0$ for the same value of ReRe_Ω. However, that calculation is only valid for small rotation speeds (i.e., Ro $\rightarrow \infty$). The present study agrees with this result for Ro = 10, but for Ro = 1 the $f\mathrm{Re}/(f\mathrm{Re})_o$ curve for $\gamma = 5.0$ at $\mathrm{ReRe}_\Omega = 10^5$ lies above the curve for $\gamma = 0.5$. It seems that as rotation speed increases the larger aspect ratio tends to have a higher friction factor ratio.

Figures 5(*a*), 5(*b*) show the values of $\mathrm{Nu}/(\mathrm{Nu})_o$ versus dimensionless axial distance z/Pr for the cases of Ro = 10, 1

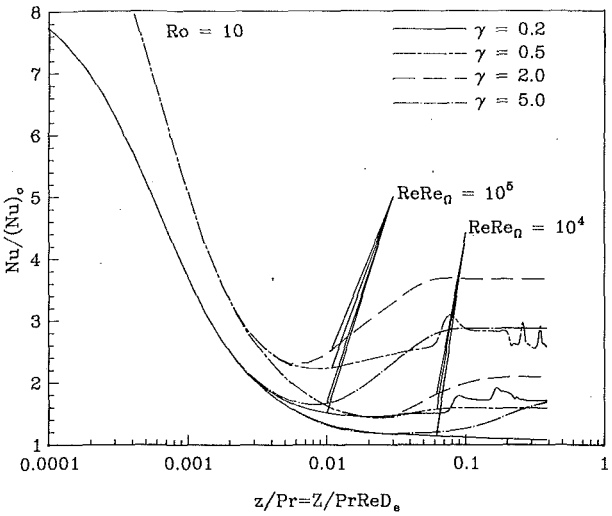

Fig. 5(*a*) Nusselt number ratio for Ro = 10

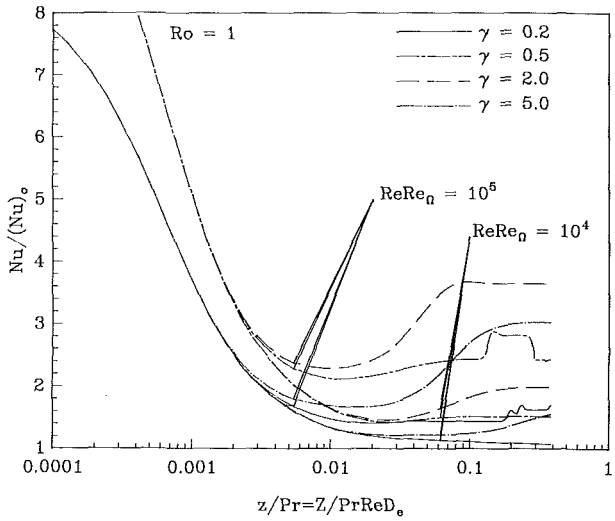

Fig. 5(*b*) Nusselt number ratio for Ro = 1.0

Fig. 5 Nu/(Nu)$_o$ versus *z*/Pr for Pr = 0.7 fluid rectangular channels

with ReRe$_\Omega$ = $10^4$and 10^5. The Prandtl number used in the present analysis is 0.7. The effect of higher Prandtl number fluid was investigated by Jen et al. (1992a). As demonstrated by Jen et al. (1992a), the increases in Nusselt number in the fully developed region are significant in comparison with the no-rotation case. This shows that the rotation effect is strong. However, the use of the fully developed flow Nusselt number will tend to overpredict the heat transfer rate if the flow is in the thermal rotational developing region. A simple estimate of flow development length is performed for the channel of γ = 2.0. It takes about 50 D_e and 25 D_e to reach the thermally fully developed region for ReRe$_\Omega$ = 10^5 and Ro = 10 and 1, respectively. In comparison, the flow becomes hydrodynamically fully developed in only 15 D_e and 3 D_e for the same parameters (see Figs. 4*a* and 4*b*). This means that the flow development region is considerably shorter than the thermal development region. This reveals that the entrance effect for heat transfer is very important, especially when the duct length is not very large. This is particularly true for turbine blade cooling channels, in which the length of the cooling channels is usually less than 50 D_e. Although the flow in the turbine blade cooling channels is typically in the turbulent flow regime, the conclusions made here concerning the thermal development length are still valid (e.g., Wagner et al., 1991).

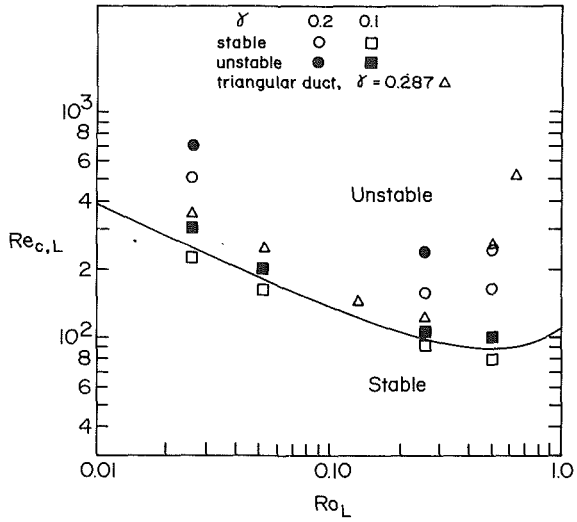

Fig. 6 Comparison with linear stability analysis (Lezius and Johnston, 1976)

It was shown by Hwang and Jen (1990) that γ = 0.5 yields higher values of Nusselt number than γ = 5.0 for the same value of ReRe$_\Omega$, as Ro → ∞. However, as shown in Figs. 5(*a*, *b*), the curves of γ = 5.0 lie above the curves of γ = 0.5 for both Ro = 10 and 1 in the fully developed region.

From the curves shown in Figs. 4(*a*) to 5(*b*), the advantage of rotation is then very obvious: the stronger the rotation,the faster the flow and temperature fields develop. Due to the Ekman suction and Coriolis force effects, large velocity and temperature gradients are formed at side and bottom walls. These cause substantial increases in heat transfer rate.

Comparison With Linear Stability Analysis

A comparison with the neutral stability curve (Lezius and Johnston, 1976), which was obtained by linear stability analysis for laminar Poiseuille flow, is presented in Fig. 6. This analysis was for parallel plates, that is, γ → 0. A higher instability curve would be expected for a finite-aspect-ratio channel. A similar situation was also demonstrated by Jen et al. (1992b) for an isosceles triangular channel with γ = 0.287 (i.e., with apex angle equal to 120 deg). These neutral stability points are indicated with triangles in the figure. Their results showed the tendency of approaching the laminar Poiseuille flow case as γ → 0.

In the present numerical analysis, the flow is defined to be unstable when more than two vortices appear in the cross section of the duct. For the channel aspect ratio γ = 0.2, the discrete points of the numerical simulation indicate that the neutral stability curve is far above the laminar Poiseuille flow case, as expected. However, the results for γ = 0.1 (a more slender duct) are in excellent agreement with the results of Lezius and Johnston (1976). Note that the black square signifies that the point is unstable, and the empty square signifies that the point is stable. In particular, we obtain a critical point that lies between Re$_L$ = 110 and 80 at Ro$_L$ = 0.5. These values bound the value of the critical Reynolds number, Re$_{c,L}$ = 88.53 at Ro$_L$ = 0.5 obtained by them. The subscript L denotes the parameters defined by Lezius and Jonston (1976). Their critical wave number (i.e., $k = 2\pi/\lambda$) was then found to be 4.9, in comparison to the present computation of 4.6. The wave number in the present analysis is based on the number of vortex pairs in the cross section of the duct. The corresponding average wavelength is then found to compute the wave number. Note that the presence of the side walls of the duct tends to stabilize the flow; thus a lower wave number is expected. Exploratory runs for smaller aspect ratio (i.e., γ = 0.05) have

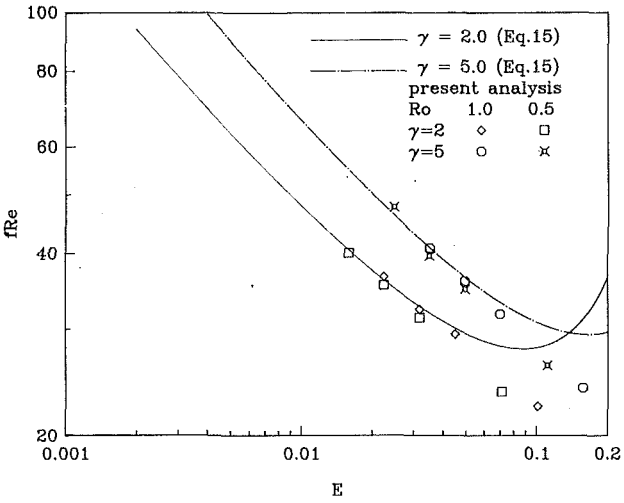

Fig. 7 Comparison with asymptotic analysis (Smirnov, 1978)

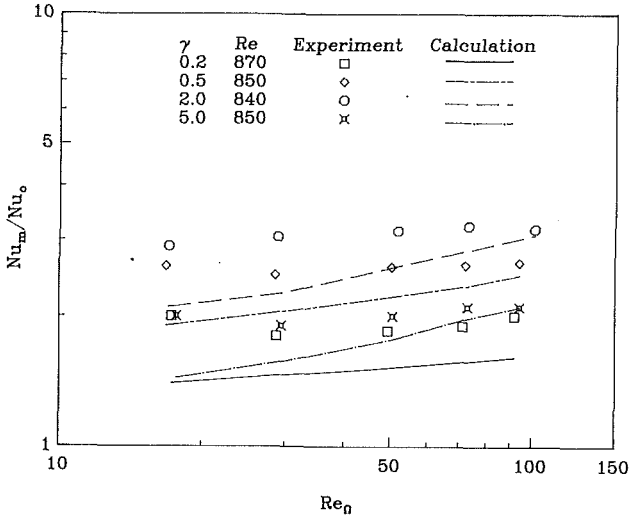

Fig. 8 Comparison of Nu_m/Nu_o with experimental data

been performed. The boundary points of the stability curve are still bounded by the same values of Re and Ro that were obtained at $\gamma = 0.1$. The critical wave number for $\gamma = 0.05$ is then found to be 4.8. This shows the critical wave number does approach the value of 4.9 obtained by Lezius and Johnston (1976). From the data shown in this figure, we feel that the results are quite encouraging and highly support the accuracy of the results obtained by the present numerical scheme.

Comparison With Theoretical and Experimental Results

The first comparison to theoretical results is a qualitative assessment of the thickness of the Ekman and Stewartson layers. In the fully developed flow region, the cross section can be divided into four regions. The central region is the constant-velocity core, with dimension O(1). The regions near the side wall are the Ekman layers with thickness of $O(E^{1/2})$. The regions near the upper and lower walls have Stewartson layers with characteristic thicknesses $O(E^{1/4})$ and $O(E^{1/3})$ (Bennetts and Hocking, 1974; Hocking, 1967). In the present study, the layer thicknesses are determined as the distance from the wall to the location of maximum velocity. It is observed that the orders of magnitude of the thicknesses of these layers are in agreement with these theoretical analyses.

Smirnov (1978) employed the asymptotic method with known characteristic layer thicknesses to obtain the axial velocity distribution and then found the drag coefficient formula for fully developed flow. After transformation to the present parameters, the final form for the friction factor is

$$f\mathrm{Re} = \frac{8\gamma^2}{(1+\gamma)^2 E^{1/2}(1 - E^{1/4}/\gamma - E^{1/2} + O(E^{3/4})/\gamma)} \quad (15)$$

where E is the Ekman number. This formula is in good agreement with experimental data for Ro of order up to unity. However, a more restricted condition was imposed on the value of E at which this formula is valid, as follows:

$$E^{1/4} \ll \gamma \quad (16)$$

Thus, this equation is valid only for large aspect ratios. The present computations of fRe in the fully developed region for aspect ratios $\gamma = 2$, 5 at Ro = 0.5 and 1.0 are shown in Fig. 7. These results are in excellent agreement with this analytic formula except for large E values. This is simply because of the restriction of Eq. (16). It is seen that Eq. (15) predicts unrealistic behavior when Ekman number exceeds around 0.1. Experimental evidence has also shown that this formula overpredicts fRe as the Ekman number becomes large, or the rotation speed is small (Smirnov, 1978).

Because of the lack of experimental data in both the fully developed and developing regions of isothermal rectangular ducts, the present numerical computation is compared with the only existing rectangular duct data presented by Soong et al. (1989) at $L/D = 30$. Figure 8 shows the values of Nu_m/Nu_o versus Re_Ω at different Reynolds numbers. The solid lines in the figure denote the present numerical analysis. The analysis and experiment show the same trend of nonmonotonic dependence on aspect ratio. The Nusselt number increases with increasing γ up to $\gamma = 2.0$, and then decreases for $\gamma = 5.0$. However, the analysis does not show precise quantitative agreement with the experimental data, especially when the rotational Reynolds number is small (small rotational speed). This may be due to the unknown inlet condition (Mori and Nakayama, 1984). As indicated by Jen et al. (1992a), the experimental data may have entrance swirling or local turbulence effects, which will increase heat transfer coefficients substantially in the entrance region (Soong, 1990). Some exploratory runs have shown that the centrifugal-buoyancy effect is small for the experimental conditions in Fig. 8, except possibly for the largest value of Re_Ω.

Concluding Remarks

1 The equations governing the simultaneously developing laminar forced convection in the entrance region of a rotating isothermal rectangular duct have been solved using a three-dimensional parabolic computational technique. The vorticity-velocity method along with the power law scheme successfully solved the Navier-Stokes equations and energy equation.

2 Oscillatory behavior of the vortices in the axial direction is observed. This may be due to the general Taylor-type instabilities in certain supercritical states in which streamwise oscillation is possible (i.e., three-dimensional steady flow).

3 The numerically obtained stability boundary points for low γ are in excellent agreement with the results obtained by linear stability analysis. Comparisons with existing theoretical results for the friction factor are quite favorable. However, there exist some discrepancies in comparison with experimental results for the Nusselt number. This may be due to the unknown inlet condition of the experiments.

4 Since the thermal development length is much longer than the flow development length, the entrance effect for heat transfer rate may be important if the channel is not very long.

5 Further studies are needed to investigate the centrifugal-buoyancy effect when rotational speed is large.

References

Bennetts, D. A., and Hocking, L. M., 1974, "Pressure-Induced Flows at Low Rossby Numbers," *Phys. Fluids*, Vol. 17, No. 9.

Coles, D., 1965, "Transition in Circular Couette Flow," *J. Fluids Mech.*, Vol. 21, pp. 385–425.

Curr, R. M., Sharma, D., and Tatchell, D. G., 1972, "Numerical Prediction of Some Three-Dimensional Boundary Layers in Ducts," *Comput. Methods Applied Mech. and Engg.*, Vol. 1, pp. 143–158.

Dakin, J. T., Horner, M. W., Piekarski, A. J., and Triandafyllis, J., 1978, "Heat Transfer in the Rotating Blades of a Water-Cooled Gas Turbine," General Electric Report No. 78CRD150.

Dennis, S. C. R., and Ng, M., "Dual Solutions for Steady Laminar Flow Through a Curved Tube," *Q. J. Mech. Appl. Math.*, Vol. 35, pp. 305–324.

Hart, J. E., 1971, "Instability and Secondary Motion in Rotating Channel Flow," *J. Fluid Mech.*, Vol. 45, Part 2, pp. 341–351.

Hart, J. E., 1979, "Finite Amplitude Baroclinic Instability," *Ann. Rev. Fluid Mech.*, Vol. 11, pp. 147–172.

Hocking, L. M., 1967, "Boundary and Shear Layers in a Curved Rotating Pipe," *J. Math. Phys. Sci.*, Vol. 1, Nos. 1–2, pp. 123–136.

Hwang, G. J., and Soong, C. Y., 1988, "Experimental Automation and Heat Transfer Measurement on a Rotating Thermal System," *Proc. 3rd Int. Symp. on Transport Phenomena in Thermal Control*, pp. 665–678.

Hwang, G. J. and Jen, T. C., 1990, "Convective Heat Transfer in Rotating Isothermal Ducts," *Int. J. Heat Mass Transfer*, Vol. 33, No. 9, pp. 1817–1828.

Jen, T. C., 1987, "Convective Heat Transfer in Rotating Isothermal Rectangular Ducts," MS. Thesis, National Tsing Hua University, Hsinchu, Taiwan.

Jen, T. C., Lavine, A. S., and Hwang, G. J., 1992a, "Simultaneously Developing Laminar Convection in Rotating Isothermal Square Channels," *Int. J. Heat Mass Transfer*, Vol. 35, No. 1, pp. 239–254.

Jen, T. C., Hwang, G. J., and Lavine, A. S., 1992b, "Fully Developed Laminar Convection in Rotating Isothermal Isosceles Triangular Channels With the Effect of Axial Conduction," in preparation.

Lezius, F. K., and Johnston, J. P., 1976, "Roll-Cell Instabilities in Rotating Laminar and Turbulent Channel Flows," *J. Fluids Mech.*, Vol. 77, Part 1, pp. 153–175.

Metzger, D. E., Fan, Z. X., and Shepard, W. B., 1982, "Pressure Loss and Heat Transfer Through Multiple Rows of Short Pin Fins," *Proc. 7th Int. Heat Transfer Conf.*, No. FC24, Hemisphere, New York, pp. 137–142.

Mori, Y., and Nakayama, W., 1984, "Secondary Flows and Enhanced Heat Transfer in Rotating Pipes and Ducts," in: *Heat and Mass Transfer in Rotating Machinery*, D. E. Metzger and N. H. Afgan, eds; pp. 3–24.

Patankar, S. V., and Spalding, D. B., 1972, "A Calculation Procedure for Heat, Mass and Momentum Transfer in Three-Dimensional Parabolic Flows," *Int. J. Heat Mass Transfer*, Vol. 15, pp. 1787–1806.

Patankar, S. V., 1980, *Numerical Heat Transfer and Fluid Flow*, Hemisphere, New York.

Pedlosky, J., 1982, *Geophysical Fluid Dynamics*, Springer-Verlag, New York.

Ravi Sankar, S., Nandakumar, K., and Masliyah, J. H., 1988, "Oscillatory Flows in Coiled Square Ducts," *Phys. Fluids*, Vol. 31, pp. 1348–1359.

Shah, R. H., and London, A. L., 1978, *Laminar Flow Forced Convection in Ducts*, Academic Press, New York.

Smirnov, E. M., 1978, "Asymptotic Drag Formulas for Rapidly Rotating Radial Channels of Rectangular Cross Section," *Izv. Akad. Nauk. SSSR Mekh. Zhidk. Gaza*, No. 6, p. 42.

Soong, C. Y., 1990, private communication.

Soong, C. Y., Lin, S. T., and Hwang, G. J., 1991, "An Experimental Study of Convective Heat Transfer in Radially Rotating Rectangular Ducts," ASME JOURNAL OF HEAT TRANSFER, Vol. 113, pp. 604–611.

Speziale, C. G., 1982, "Numerical Study of Viscous Flow in Rotating Rectangular Ducts," *J. Fluid Mech.*, Vol. 122, pp. 251–271.

Speziale, C. G., and Thangan, S., 1983, "Numerical Study of Secondary Flow and Roll-Cell Instabilities in Rotating Channel Flow," *J. Fluid Mech.*, Vol. 130, pp. 377–395.

Speziale, C. G., 1986, "The Effect of the Earth's Rotation on Channel Flow," *Journal of Applied Mechanics*, Vol. 53, pp. 198–202.

Wagner, J. H., Johnson, B. V., and Hajek, T. J., 1991, "Heat Transfer in Rotating Passages With Smooth Walls and Radial Outward Flow," ASME *Journal of Turbomachinery*, Vol. 113, pp. 42–51.

Heat Transfer in the Non-Newtonian Axisymmetric Flow in the Neighborhood of a Sudden Contraction

M. S. Carvalho

P. R. Souza Mendes[1]

Department of Mechanical Engineering,
Pontificia Universidade Católica—RJ,
Rio de Janeiro, RJ 22453, Brazil

The flow pattern at low Reynolds number in the neighborhood of a sudden contraction is very sensitive to the mechanical behavior of the flowing fluid. A large extensional viscosity leads to vortex enhancement in the corner region of the flow of a non-Newtonian fluid in such geometry. In the corresponding flow of a Newtonian fluid, these vortices are much weaker and smaller. Moreover, the extension-thickening behavior of most polymeric liquids leads to higher viscous dissipation effects in the predominantly extensional flow, as compared to typical shear flows. The flow and temperature fields for this problem have been obtained from numerical integration of the conservation equations, aiming at applications related to extrusion and capillary rheometry of polymeric liquids. To account for the flow dependence of the stress tensor, a generalized Newtonian model has been employed, including the dependence of the viscosity function on both the second and the third invariants of the rate-of-deformation tensor. The numerical solutions have been obtained via a finite-volume method. The case of a 4:1 circular contraction was investigated, with uniform temperature distribution at the solid boundaries. The fluid inlet temperature is equal to the temperature at the walls, so that thermal gradients in the fluid are due to viscous dissipation effects only. Comparisons between Newtonian and non-Newtonian results showed that the combined effect of viscous dissipation and enhancement of vortex activity significantly affects the temperature field. The practical significance of the results is discussed for extrusion processes and capillary rheometry.

Introduction

An important idealization of the flow of a polymeric liquid through a die found in extrusion processes is the flow in a sudden contraction. It also represents well the flow in a capillary rheometer. For this reason, this flow has been studied in the recent past by a number of authors. Because this is a very complex flow, it also provides an important test for constitutive models (Boger and Binnington, 1990). Fairly recent reviews addressing this interesting problem are available from White et al. (1987) and Boger (1987).

Boger and Nguyen (1978) reported important experimental results where a viscoelastic test fluid with special rheological properties, the so-called Boger fluid, was developed and characterized. Flow visualizations of the Boger fluid flowing through a sudden contraction are also presented. Several reports of numerical simulations of this flow are found in the literature, and one usual basis for comparison is the results of Boger and Nguyen (1978). Generally, these simulations are aimed at the validation of constitutive mechanical models and of numerical formulations (e.g., Crochet et al., 1984; Dupret et al., 1985; Debbaut et al., 1988; Dupont and Crochet, 1988; and many others).

Winter (1977) presented a comprehensive treatise on viscous dissipation effects in shear flows of molten polymers. Vergnes (1985) reported different studies of flows in extrusion dies, including heat transfer and viscous dissipation effects. In these studies, however, the lubrication approximation has been employed, which is appropriate to shear flows in dies with narrow passages only. It is interesting that, although a prediction of the temperature rise due to viscous dissipation is important in extrusion applications and especially in (shear) viscosity measurements with the capillary rheometer, no heat transfer information for the flow through the sudden contraction could be found in the literature.

Perhaps the main reason for the dearth of heat transfer studies on the flow analyzed here resides in the fact that the velocity field is greatly affected by the non-Newtonian behavior of the polymeric liquid. Therefore, constitutive models such as (*i*) the Newtonian model, and (*ii*) the well-known generalized Newtonian model with a power-law (shear thinning) viscosity function, do not predict the flow field observed experimentally by a number of authors (e.g., Boger and Nguyen, 1978).

This paper reports an investigation of heat transfer in axisymmetric, two-dimensional, laminar flow through a sudden contraction. The flow field has been obtained with the aid of a generalized Newtonian model proposed by Debbaut and Crochet (1988), whose viscosity depends on both the second and third invariants of the rate-of-deformation tensor. This model yields a qualitatively correct flow field, and it will be shown that the temperature field is a strong function of the non-Newtonian behavior of the flowing fluid. However, it is important to state at the outset that the sole purpose here is to provide a qualitative assessment of the role of the non-Newtonian behavior on the thermal problem. A quantitatively accurate description of the flow field should not be expected, because the Debbaut model employed here also has its limitations, as discussed below.

[1] Presently on sabbatical leave at the Department of Chemical Engineering and Materials Science, University of Minnesota, Minneapolis, MN 55455.

Contributed by the Heat Transfer Division for publication in the JOURNAL OF HEAT TRANSFER. Manuscript received by the Heat Transfer Division March 1991; revision received December 1991. Keywords: Materials Processing and Manufacturing Processes, Non-Newtonian Flows and Systems. Associate Technical Editor: H. R. Jacobs.

Analysis

The problem under study is shown in Fig. 1. The geometry consists of a tube of inner radius r_1 whose downstream end is attached to another tube of smaller radius r_0. The length of the downstream tube is $2r_0$, and it is positioned such as to share the same axis with the upstream tube.

At the inlet cross section, a parabolic axial velocity profile and uniform temperature are imposed, i.e.,

$$\text{at } x=0, \quad \begin{cases} \dfrac{u}{\bar{u}}=\dfrac{2}{\alpha^2}\left[1-\left(\dfrac{r}{r_1}\right)^2\right] \\ v=0 \\ T=T_0 \end{cases} \tag{1}$$

In this equation, $\alpha \equiv r_1/r_0$, and $\bar{u}$ is the average axial velocity at the downstream tube.

At the solid boundaries, the no-slip condition ($u=v=0$) is assumed, and temperature is uniform and equal to the inlet flow temperature, T_0. Symmetry boundary conditions are imposed at the centerline, namely, $\partial u/\partial r=\partial T/\partial r=0$ and $v=0$. At the outflow boundary, it is assumed that the flow is locally parabolic, i.e., $\partial u/\partial x=0$, $\partial v/\partial x=0$, $\partial T/\partial x=0$.

Equations of Motion and Constitutive Model. The flow is assumed to be two dimensional, laminar, and steady. It is further hypothesized that the flowing fluid is incompressible and that its thermophysical properties (including the viscosity function) do not depend on temperature.

The mass conservation equation may be written in cylindrical coordinates as

$$\frac{\partial u}{\partial x}+\frac{\partial v}{\partial r}+\frac{v}{r}=0 \tag{2}$$

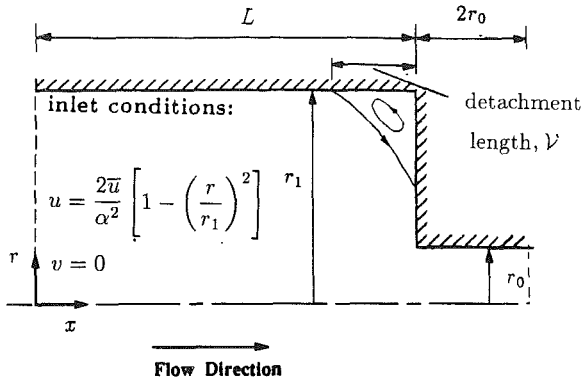

Fig. 1 Schematic of the problem

For a generalized Newtonian fluid, the extra-stress tensor τ is related to the motion in the following manner:

$$\tau \equiv \sigma + p\mathbf{1} = \eta\dot{\gamma}, \tag{3}$$

where $\dot{\gamma}$ is the rate-of-deformation tensor and η is the viscosity function. In principle, η depends on the scalar invariants of $\dot{\gamma}$, namely, $\mathrm{I} \equiv \mathrm{tr}\dot{\gamma}$, $\mathrm{II} \equiv \mathrm{tr}\dot{\gamma}^2$, and $\mathrm{III} \equiv \mathrm{tr}\dot{\gamma}^3$. Assuming this type of fluid behavior, the momentum conservation equations become

$$\rho\left\{u\frac{\partial u}{\partial x}+v\frac{\partial u}{\partial r}\right\} = -\frac{\partial p}{\partial x}+\frac{1}{r}\frac{\partial}{\partial r}\left[r\eta\left(\frac{\partial u}{\partial r}+\frac{\partial v}{\partial x}\right)\right]+\frac{\partial}{\partial x}\left[2\eta\frac{\partial u}{\partial x}\right] \tag{4}$$

and

Nomenclature

$\mathbf{1}$ = unit or identity tensor
I = first invariant of $\dot{\gamma} \equiv \mathrm{tr}\dot{\gamma}$, s^{-1}
II = second invariant of $\dot{\gamma} \equiv \mathrm{tr}\dot{\gamma}^2$, s^{-2}
III = third invariant of $\dot{\gamma} \equiv \mathrm{tr}\dot{\gamma}^3$, s^{-3}
c_p = specific heat, J/kg K
$h(\chi)$ = local heat transfer coefficient at curved wall $\equiv -\{(\kappa\partial T/\partial r)_{r=r_1}\}/(\bar{u}^2\eta_0/\kappa)$, W/m^2K
$h(R)$ = local heat transfer coefficient at plane wall $\equiv -\{(\kappa\partial T/\partial x)_{x=L}\}/(\bar{u}^2\eta_0/\kappa)$, W/m^2K
L = axial length of upstream tube, m
$\mathrm{Nu}(\chi)$ = local Nusselt number at curved wall $\equiv 2h(\chi)r_1/\kappa$
$\mathrm{Nu}(R)$ = local Nusselt number at radial wall $\equiv 2h(R)r_1/\kappa$
p = pressure, N/m^2
P = dimensionless pressure, Eq. (10)
Pe = Peclet number $\equiv$ RePr
Pr = Prandtl number $\equiv \eta_0 c_p/\kappa$
r = radial coordinate, m
r_0 = radius of downstream tube, Fig. 1, m
r_1 = radius of upstream tube, Fig. 1, m
R = dimensionless radial coordinate, Eq. (10)
Re = Reynolds number $\equiv \rho\bar{u}r_0/\eta_0$
T = temperature field, K
T_0 = inlet flow and wall temperature, K
$T_{\max}$ = maximum value of T, K
u = axial component of $\mathbf{u}$, m/s
$\mathbf{u}$ = velocity field, m/s
$\bar{u}$ = mean axial velocity at downstream tube, m/s
U = dimensionless axial velocity, Eq. (10)
v = radial component of $\mathbf{u}$, m/s
V = dimensionless radial velocity, Eq. (10)
$\mathcal{V}$ = detachment length, Fig. 1, m
We = Weissenberg number $\equiv 4\lambda\dot{\gamma}_0$
x = axial coordinate, m
α = contraction ratio $\equiv r_1/r_0$
$\dot{\gamma}$ = shear rate, Eq. (7), s^{-1}
$\dot{\gamma}_0$ = characteristic value of $\dot{\gamma} \equiv \bar{u}/r_0$, s^{-1}
$\dot{\gamma}$ = rate-of-deformation tensor $\equiv \mathrm{grad}\,\mathbf{u} + (\mathrm{grad}\,\mathbf{u})^T$, s^{-1}
$\Delta\chi$ = average control-volume width in axial direction
$\overline{\Delta R}$ = average control-volume width in radial direction
$\dot{\epsilon}$ = elongation rate, Eq. (7), s^{-1}
$\dot{\mathcal{E}}$ = dimensionless elongation rate, Eq. (10)
η = viscosity function, kg/ms
η_0 = zero elongation rate viscosity, kg/ms
η^* = dimensionless viscosity function, Eq. (10)
θ = dimensionless temperature field $\equiv (T-T_0)/(\bar{u}^2\eta_0/\kappa)$
$\theta_{\max}$ = maximum value of θ
κ = thermal conductivity, W/m K
λ = characteristic time of fluid, s
λ_1 = Maxwell relaxation time of the fluid $\equiv \Psi_1/2\eta_0$, s
ρ = fluid density, kg/m^3
σ = stress tensor field, N/m^2
τ = extra-stress tensor field $\equiv \sigma + p\mathbf{1}$, N/m^2
$\bar{\tau}_w$ = average wall shear stress, N/m^2
Φ = dimensionless dissipation function, Eq. (17)
χ = dimensionless axial coordinate, Eq. (10)
Ψ_1 = first normal stress coefficient, kg/m

$$\rho\left\{u\frac{\partial v}{\partial x}+v\frac{\partial v}{\partial r}\right\}=-\frac{\partial p}{\partial r}+\frac{1}{r}\frac{\partial}{\partial r}\left[2r\eta\frac{\partial v}{\partial r}\right]+\frac{\partial}{\partial x}\left[\eta\left(\frac{\partial u}{\partial r}+\frac{\partial v}{\partial x}\right)\right]-2\frac{\eta v}{r^2} \quad (5)$$

Since for incompressible fluids $I=0$, and for shearing and plane flows $III=0$ everywhere in the flow, it is a rather common practice among users of the generalized Newtonian fluid model to assume that the viscosity function η depends solely on the second invariant II, even for flows whose third invariant, III, is not zero throughout the flow. This assumption leads to a prediction of a flow field qualitatively different from the experimental observations of Boger and Nguyen (1978). In fact, the dependence of η on II alone decreases the vortex size and intensity compared to the small Newtonian vortex (Kim-E et al., 1983).

As mentioned earlier, Debbaut and Crochet (1988) showed that the inclusion of the third invariant, III, on the viscosity function leads to qualitatively realistic predictions of the generalized Newtonian model for this flow. The functional relationship was chosen so that the generalized Newtonian model yields the same behavior in uniaxial extension as the upper-convected Maxwell model:

$$\eta(\dot{\epsilon})=\frac{\eta_0}{1-\lambda\dot{\epsilon}-2(\lambda\dot{\epsilon})^2} \quad (6)$$

where

$$\dot{\gamma}\equiv\sqrt{\frac{1}{2}\mathrm{II}};\quad \dot{\epsilon}\equiv\frac{\mathrm{III}}{\mathrm{II}} \quad (7)$$

$$\mathrm{II}=4\left[\left(\frac{\partial v}{\partial r}\right)^2+\left(\frac{\partial u}{\partial x}\right)^2+\frac{1}{2}\left(\frac{\partial u}{\partial r}+\frac{\partial v}{\partial x}\right)^2+\left(\frac{v}{r}\right)^2\right] \quad (8)$$

and

$$\mathrm{III}=\frac{12v}{r}\left\{2\frac{\partial v}{\partial r}\frac{\partial u}{\partial x}-\frac{1}{2}\left(\frac{\partial u}{\partial r}+\frac{\partial v}{\partial x}\right)^2\right\} \quad (9)$$

The quantities η_0 and λ are rheological constants of the model; η_0 is the viscosity at zero elongation rate, whereas the characteristic time λ represents the sensitivity of the viscosity function to the elongation rate. Some dimensionless quantities are now defined:

$$\chi\equiv\frac{x}{r_0};\quad R\equiv\frac{r}{r_0};\quad U\equiv\frac{u}{\bar{u}};\quad V\equiv\frac{v}{\bar{u}};\quad P\equiv\frac{p}{\eta_0\dot{\gamma}_0};\quad \eta_*\equiv\frac{\eta}{\eta_0};\quad \mathcal{E}\equiv\frac{\dot{\epsilon}}{4\dot{\gamma}_0} \quad (10)$$

where $\dot{\gamma}_0\equiv\bar{u}/r_0$ is a characteristic deformation rate for the flow.

Using the above definitions, the governing equations of the flow are rewritten in the following dimensionless form:

$$\frac{\partial U}{\partial\chi}+\frac{\partial V}{\partial R}+\frac{V}{R}=0 \quad (11)$$

$$\mathrm{Re}\left\{U\frac{\partial U}{\partial\chi}+V\frac{\partial U}{\partial R}\right\}=-\frac{\partial P}{\partial\chi}+\frac{1}{R}\frac{\partial}{\partial R}\left[R\eta_*\left(\frac{\partial U}{\partial R}+\frac{\partial V}{\partial\chi}\right)\right]+\frac{\partial}{\partial\chi}\left[2\eta_*\frac{\partial U}{\partial\chi}\right] \quad (12)$$

$$\mathrm{Re}\left\{U\frac{\partial V}{\partial\chi}+V\frac{\partial V}{\partial R}\right\}=-\frac{\partial P}{\partial R}+\frac{1}{R}\frac{\partial}{\partial R}\left[2R\eta_*\frac{\partial V}{\partial R}\right]+\frac{\partial}{\partial\chi}\left[\eta_*\left(\frac{\partial U}{\partial R}+\frac{\partial V}{\partial\chi}\right)\right]-2\frac{\eta_* V}{R^2} \quad (13)$$

where $\mathrm{Re}\equiv\rho\bar{u}r_0/\eta_0$ is the Reynolds number. The dimensionless version of the viscosity function is

$$\eta_*(\mathcal{E})=\frac{1}{1-\mathcal{E}\mathrm{We}-2(\mathcal{E}\mathrm{We})^2} \quad (14)$$

where $\mathrm{We}\equiv4\lambda\dot{\gamma}_0$ is the Weissenberg number.

Energy Equation. For highly viscous liquids such as polymer melts, the dissipation rate of mechanical energy is generally important, and should be taken into account in the energy balance. Considering this effect and employing the previously stated assumptions, the energy equation becomes

$$\rho\left\{u\frac{\partial T}{\partial x}+v\frac{\partial T}{\partial r}\right\}=\frac{\kappa}{c_p}\left\{\frac{1}{r}\frac{\partial}{\partial r}\left[r\frac{\partial T}{\partial r}\right]+\frac{\partial^2 T}{\partial x^2}\right\}+\frac{2\eta}{c_p}\dot{\gamma}^2 \quad (15)$$

Defining $\theta\equiv(T-T_0)/(\bar{u}^2\eta_0/\kappa)$, the dimensionless version of this equation is written as

$$\mathrm{Pe}\left\{U\frac{\partial\theta}{\partial\chi}+V\frac{\partial\theta}{\partial R}\right\}=\frac{1}{R}\frac{\partial}{\partial R}\left[R\frac{\partial\theta}{\partial R}\right]+\frac{\partial^2\theta}{\partial\chi^2}+\eta_*\Phi \quad (16)$$

where $\mathrm{Pe}\equiv\mathrm{Re}\,\mathrm{Pr}$ is the Peclet number, and $\mathrm{Pr}\equiv\eta_0 c_p/\kappa$ is the Prandtl number. The dissipation function Φ is defined as

$$\Phi\equiv2\left(\frac{\dot{\gamma}}{\dot{\gamma}_0}\right)^2 \quad (17)$$

The local Nusselt numbers at the curved wall and at the radial plane wall are given respectively by

$$\mathrm{Nu}(\chi)=-2\alpha\left.\frac{\partial\theta}{\partial R}\right|_{R=1} \quad (18)$$

and

$$\mathrm{Nu}(R)=-2\alpha\left.\frac{\partial\theta}{\partial\chi}\right|_{\chi=L/r_0} \quad (19)$$

The parameters that govern the present problem are (*i*) the diameter ratio α; (*ii*) the length ratio L/r_0; (*iii*) the Reynolds number Re; (*iv*) the Weissenberg number We; and (*v*) the Peclet number Pe. Since the present study is mainly concerned with the non-Newtonian effects on heat transfer, only the influence of the Weissenberg number has been investigated.

According to Boger and Binnington (1990), inertial effects in this flow may be of importance even for Re values as low as 10^{-4} for non-Newtonian fluids. For this reason, solutions of the complete momentum equations were obtained to check the dependence of the dimensionless velocity field on Re, but evidence of inertial effects was only observed for $\mathrm{Re}>\sim0.1$. The results presented in this paper pertain to $\mathrm{Re}\to0$, which is normally the case in polymer processing applications. It is worth noting, however, that the advection term in the energy equation is expected to be of importance, because the Prandtl number is very high for polymeric liquids.

The other parameters have been held constant at the following values: $\alpha=4$, $L/r_0=13$, and $\mathrm{Pe}=800$.

Method of Solution

The finite-volume method described by Patankar (1980) has been employed to integrate numerically the governing equations presented earlier. The power-law scheme was adopted to account properly for convection-diffusion effects, and the coupling of continuity and momentum equations was handled using the SIMPLE algorithm. The line-by-line Thomas Algorithm was employed in successively alternating directions to solve the resulting discretization equations, in conjunction with the block correction suggested by Prakash and Patankar (1981).

A nonuniform grid was employed, with 50×26 nodal points in the axial and radial directions, respectively, concentrated in the region where the recirculation occurs. Because the flow region of interest is in the upstream tube up to the contraction plane, the only reason for extending the computational domain

downstream by means of the downstream tube was to ensure that the outflow boundary conditions have no appreciable effect on the flow in the region of interest. A length of $2r_0$ for the downstream tube was found to be satisfactory in this regard. Of course, the presence of the downstream tube length introduces an irregularity in the computational domain, which was handled via a region blockage, as explained by Patankar (1980).

To obtain a converged solution for the velocity field, difficulties in convergence caused by the nonlinearity related to the viscosity function were treated as follows: (*i*) First the flow field is obtained for $\dot{\mathcal{E}} = 0$ (Newtonian solution); (*ii*) with this velocity field, a $\dot{\mathcal{E}}$ field and hence a viscosity field are evaluated; (*iii*) without correcting the viscosity field during iterations, a new converged velocity field is obtained; (*iv*) steps (*ii*) and (*iii*) are repeated until full convergence. Typically final convergence was achieved in a total of about one hundred iterations, including those needed in the along-the-way convergencies of step (*iii*).

It can be seen that the viscosity function as given in Eq. (14) yields infinite or negative viscosity values of $\dot{\mathcal{E}}\mathrm{We} \geq 0.5$, which are not realistic. To avoid too large or negative viscosities during iterations, whenever the calculated $\dot{\mathcal{E}}$ was such that $\dot{\mathcal{E}}\mathrm{We} > 0.49$, the viscosity value used was that obtained from Eq. (14) for $\dot{\mathcal{E}}$ We $= 0.49$. In this manner, convergence was facilitated. However, the Weissenberg numbers investigated here were low enough so that the converged value of $\dot{\mathcal{E}}$We is always less than 0.49.

Numerical Uncertainty. The accuracy of the results obtained with the grid distribution utilized in the final runs was assessed using a grid-dependence test that is now described. It is helpful at this point to define average control-volume widths, $\overline{\Delta\chi}$ and $\overline{\Delta R}$, in the axial and radial directions, respectively, as the control-volume widths of a uniform grid with the same number of grid points. These widths are employed as parameters for comparison among the solutions pertaining to different grids. The solutions needed in the grid test were obtained with nonuniform grids, with a distribution similar to the one employed in the final grid.

For a typical case, the dependence of the detachment length, $\mathcal{V}$ (defined in Fig. 1), and also of the average wall shear stress, $\bar{\tau}_w$, on the grid size have been investigated. The uncertainty of the numerical results was estimated as follows. An estimate of the *exact* value of $\mathcal{V}$ (or $\bar{\tau}_w$), i.e., the solution for $\overline{\Delta\chi} = 0$ and $\overline{\Delta R} = 0$, was obtained with the aid of a two-variable ($\overline{\Delta\chi}$ and $\overline{\Delta R}$) Taylor series expansion up to the second-order terms:

$$\mathcal{V}(0,0) = \mathcal{V}(\overline{\Delta\chi}, \overline{\Delta R}) - \overline{\Delta\chi}\frac{\partial\mathcal{V}}{\partial(\overline{\Delta\chi})} - \overline{\Delta R}\frac{\partial\mathcal{V}}{\partial(\overline{\Delta R})} + \frac{1}{2}\left\{\overline{\Delta\chi}^2\frac{\partial^2\mathcal{V}}{\partial(\overline{\Delta\chi})^2} + \overline{\Delta R}^2\frac{\partial^2\mathcal{V}}{\partial(\overline{\Delta R})^2} + \overline{\Delta\chi\Delta R}\frac{\partial^2\mathcal{V}}{\partial(\overline{\Delta R})\partial(\overline{\Delta\chi})}\right\} \quad (20)$$

The evaluation of the five partial derivatives involved was done via finite differences, which required extra computer runs to obtain solutions for eight other combinations of $\overline{\Delta\chi}$ and $\overline{\Delta R}$ in the *vicinity* of the result pertaining to 50×26 grid points.

Using this extrapolated result as a basis for comparison, it was found that the numerical uncertainty of the result for the typical case analyzed is 0.4 percent for the detachment length and 4.3 percent for the average wall shear stress.

Results and Discussion

The formulation and numerical procedure described in the preceding sections yielded results that are now presented and discussed. It will be seen that the non-Newtonian nature of the fluid affects both the flow and the temperature fields.

Before proceeding, it is important to emphasize that in the present analysis the Weissenberg number has an unusual physical meaning, namely, it represents the sensitivity of the fluid viscosity to extension. In principle, it has no relation to the Weissenberg number that usually appears in experimental papers on the present flow. Therefore, quantitative comparisons between the results to be presented here and experimental results available in the literature cannot be performed directly. Meaningful comparisons would only be possible if extensional data were available for the fluids employed in the reported experiments. Only upon evaluation of the parameter λ of Eq. (6) with a basis in extensional experimental data would it be possible to determine at which values of We the published experiments were run. Unfortunately, data on steady extensional viscosity are very scarce in the literature. This is particularly true for polymer melts in the range of extension rates typical in engineering applications of contraction flows. Moreover, presently there is no reliable means of obtaining steady extensional viscosity data, especially in the range of viscosities of the Boger fluids and other dilute polymeric solutions (Jones et al., 1987; Binding and Walters, 1988). However, it is still possible qualitatively to assess the role of the non-Newtonian fluid behavior on heat transfer for the present problem, as it will be shown.

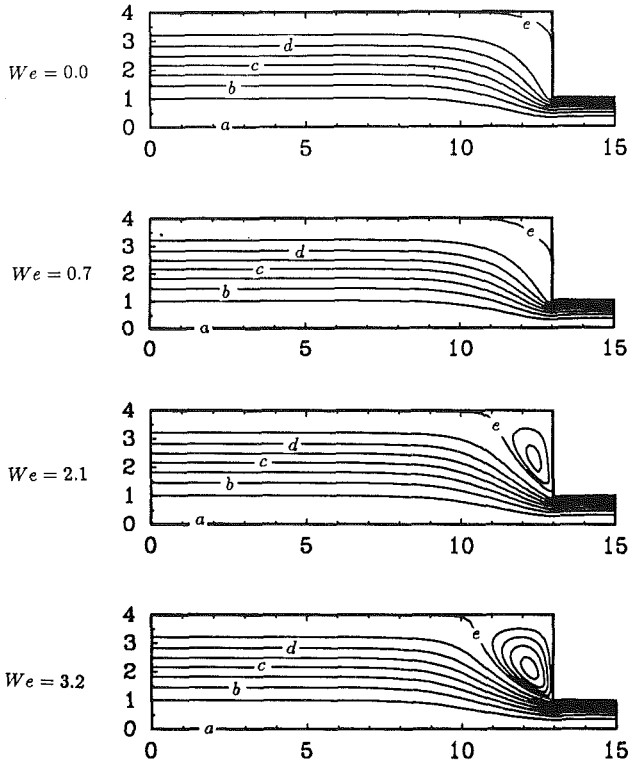

Fig. 2 The flow field: The labels *a*, *b*, *c*, *d*, and *e* correspond respectively to stream function values of 0.0, 1×10^{-4}, 2×10^{-4}, 3×10^{-4}, and 4×10^{-4}

Figure 2 shows streamlines for four different values of the Weissenberg number We. For a Newtonian fluid (We = 0), only a weak and small vortex (not shown in Fig. 2) appears at the corner. A small increase in the Weissenberg number to We = 0.7 does not significantly alter the flow field. However, when the Weissenberg number is further increased to We = 2.1, the non-Newtonian effect of the fluid on the flow becomes clear. A larger vortex is observed, and the streamlines start converging toward the centerline farther upstream of the contraction plane. Increasing the Weissenberg number to We = 3.2 makes the vortex even larger and stronger.

It is worth noting that, because velocities are much lower in the vortex region than in the main flow, the difference between stream function values of adjacent streamlines (i.e.,

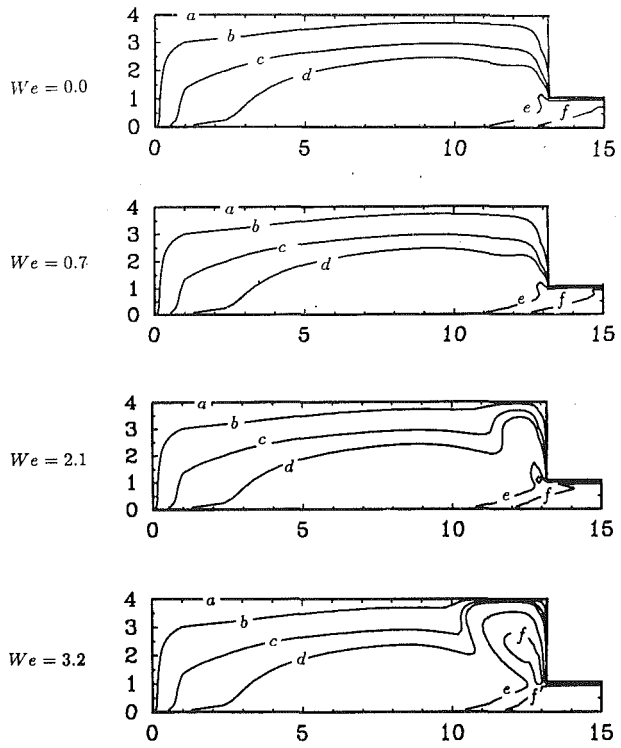

Fig. 3 The temperature field: The labels *a*, *b*, *c*, *d*, *e*, *f*, and *g* correspond respectively to θ values of 0.0, 1×10^{-4}, 5×10^{-4}, 1×10^{-3}, 5×10^{-3}, 1×10^{-2}, and 5×10^{-2}

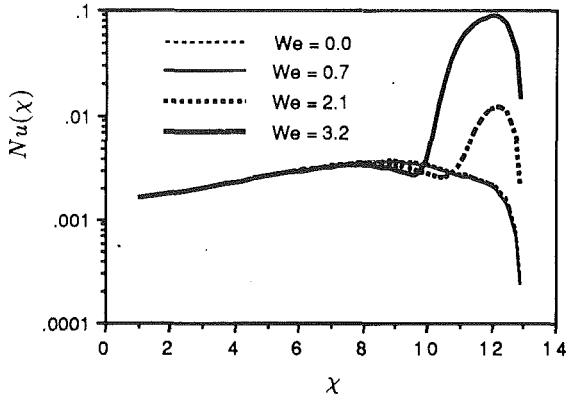

Fig. 4 Local Nusselt number at curved wall

the volume flow rate between streamlines) was chosen not to be the same in these two regions, otherwise no vortices would appear in Fig. 2.

One interesting contribution of Debbaut and Crochet (1988) is to provide further evidence, by means of a quite ingenious numerical investigation, that the non-Newtonian effects observed in this flow are related not to rheological quantities measured in shear viscometric flows, but to the non-Newtonian behavior of the fluid's extensional viscosity. Indeed, the inclusion of elastic prediction capability on the model is shown by Debbaut and Crochet (1988) to decrease the vortex size and intensity for moderate values of elasticity.

The qualitative success of such a simple model is perhaps better understood with the aid of the conclusions of a comprehensive study by Boger and Binnington (1990), which included flow visualizations and numerical simulations. Their results led them to postulate that the difference between Newtonian and non-Newtonian flow fields is essentially due to a solidlike core of non-Newtonian fluid that is formed immediately upstream of the contraction entrance, as a result of the strong extensional flow (and hence large extensional viscosity) in that region.

In spite of efforts of the ongoing research, a complete understanding of the fluid mechanics of this flow is far from being achieved. There is a number of basic issues that clearly need further clarification. For instance, it is presently accepted that the non-Newtonian effects mentioned earlier are closely related to the fluid behavior on extension (e.g., Boger, 1987; White et al., 1987). However, it is common practice to use as non-Newtonian parameter in experiments a Weissenberg number that is proportional to $\lambda_1 \dot{\gamma}_0$, where $\dot{\gamma}_0$ is a characteristic shear rate and λ_1 is the Maxwell relaxation time of the fluid. The latter is defined as a ratio between two rheological quantities measured in shear flows, namely, the first normal stress coefficient Ψ_1 and the shear viscosity η_0 (i.e., $\lambda_1 = \Psi_1/2\eta_0$). Due to experimental difficulties, typically the fluids are not characterized as far as their extensional behavior is concerned, and no parameter representing this fluid characteristic is specified. As a result, for two different fluids, completely different flow patterns may be observed for the same Weissenberg number (see Boger et al., 1986).

Attention is now turned to the temperature field illustrated in Fig. 3. For all values of the Weissenberg number We, it can be seen that the viscous dissipation of mechanical energy plays a major role on the temperature field. In terms of the dimensionless temperature θ, the fluid enters the domain at $\theta = 0$, which is the same temperature at which the solid boundaries are maintained.

Figure 3 shows that temperature increases toward the centerline and in the downstream direction for all We, with the highest values occurring in the neighborhood of the contraction entrance. This behavior agrees with expectations, since the highest elongation rates $\dot{\varepsilon}$ occur exactly in the region close to the outflow boundary, and it is clear from Eq. (16) that the rate of heat generation (as a result of viscous dissipation of mechanical energy) at a given location increases with the extension-thickening viscosity η_*. It is further observed from Fig. 3 that axial diffusion of heat is virtually absent in all cases, due to the high Peclet number employed here.

For $We = 0$, the fluid viscosity is constant and equal to η_0 (Newtonian fluid). Although in this case the rate of viscous dissipation varies throughout the flow due to the shear rate distribution only, values of θ as high as 1.1×10^{-2} are observed (this value can yield important dimensional temperature rises, depending upon the fluid viscosity and average velocity; see Eq. (21)). As We is increased, higher values of θ occur at the exit region, the region where the highest elongation rates, $\dot{\varepsilon}$, occur. This yields high values for the viscosity function, and consequently for the rate of viscous dissipation. The result is that a significant temperature rise is observed in the exit region, especially for $We = 3.2$, when it turns out to be typically over three times the temperature rise encountered in the Newtonian case.

Further, Fig. 3 shows that, as the Weissenberg number is increased, major qualitative changes on the temperature field occur due to the increasing vortex size and intensity. The vortex activity serves to transport heat from the exit region, significantly distorting the isothermals at the corner region. This convective action of the non-Newtonian vortex causes the isothermals to approach the curved wall near the corner.

In Fig. 4, the local Nusselt number at the curved wall $Nu(\chi)$ is given as a function of the axial position for four different values of the Weissenberg number. The Nusselt number increases gently with χ, up to $\chi \simeq 8$, as a result of the viscous heating, which increases the temperature gradient at the wall. It is seen that the Weissenberg number has no effect on heat transfer at the wall up to this axial location, because the flow

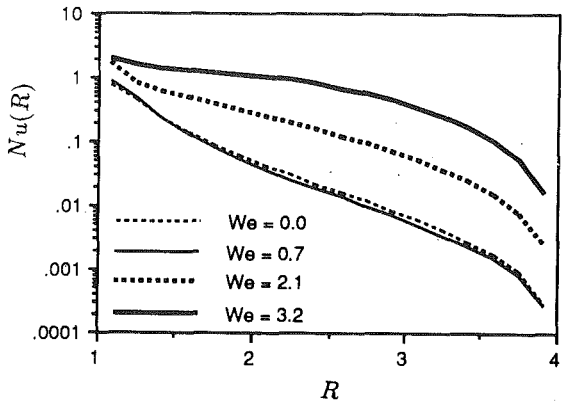

Fig. 5 Local Nusselt number at radial wall

away from the exit region is nearly a shear flow, and hence the elongation rate $\dot{\varepsilon}$ is close to zero.

Farther downstream ($\simeq 8 \leq \chi \leq 13$), however, the Weissenberg number strongly influences heat transfer at the curved wall, increasing the Nusselt number significantly for We = 3.2. This is due to the convective action of the vortex, which conveys hot liquid from the exit region to the neighborhood of the curved wall near the corner. As We is increased, viscous heating increases and the corner vortex gets larger and more intense. Both effects combine to increase the Nusselt number at the curved wall in this region. A maximum value of $\mathrm{Nu}(\chi)$ occurs for We = 2.1 and 3.2 at $\chi \simeq 12$, which roughly corresponds to the axial location where the hot fluid convected from the exit region by the vortex gets the closest to the curved wall.

Figure 5 shows the local Nusselt number at the wall of the contraction plane, $\mathrm{Nu}(R)$, as a function of radial position for four values of the Weissenberg number. For all cases, $\mathrm{Nu}(R)$ is extremely high in the neighborhood of $R = 1$, due to the presence of the hot fluid in the exit region, which impinges on the surface as a result of the vortex activity. Since the fluid temperature in the exit region and the vortex activity both increase as We is increased, so does $\mathrm{Nu}(R)$ in the neighborhood of $R = 1$.

It is also clear (Fig. 5) that $\mathrm{Nu}(R)$ decreases sharply with the radial position R, especially for lower We. The vortices on Fig. 2 indicate that the recirculating fluid closely approaches the plane wall in the neighborhood of $R = 1$, but soon departs from the surface as it flows in the positive radial direction. A nearly stagnant fluid fills the region close to the walls in the neighborhood of the corner, yielding very poor heat transfer at the walls.

As discussed above, the non-Newtonian behavior of the fluid causes two different effects on the present flow: (*i*) a dramatic change in the flow pattern, and (*ii*) extra viscous heating due to the "elongation-thickening" characteristic of the viscosity function. Both effects are seemingly important as far as heat transfer is concerned. In order to help understand the relative importance of these two effects, three extra solutions of the energy equation were obtained for We = 0.7, 2.1, and 3.2, for the same non-Newtonian flow fields as previously, but replacing the viscosity function η by the Newtonian viscosity η_0, in the viscous dissipation term of the energy equation only.

These additional results (pertaining to $\eta_* = 1$ in the energy equation) showed that the non-Newtonian change in flow pattern alone has the same qualitative influence on the temperature field (and on the Nusselt number) as before. Due to a stronger vortex activity, the main effect of the non-Newtonian flow field is to promote more heat exchange between the exit region and other regions around the vortex (i.e., it promotes mixing). Therefore, (dimensionless) temperatures in the exit region are slightly lower than in the purely Newtonian case (about 5 percent), whereas at the other regions around the vortex a mild temperature increase is observed. Quantitatively, however, the temperature fields for the three nonzero values of We investigated are very close to the one obtained for We = 0, as expected. Therefore, it becomes clear that the elongation-thickening characteristic of the viscosity function and the non-Newtonian flow pattern are both responsible for the significant changes in Nusselt number and temperature field behavior.

Practical Significance. Padmanabhan (1992) measured shear and extensional viscosities for a low-density polyethylene melt (LDPE, grade DOW4012) at 180°C, the latter using the method based on Cogswell's analysis (Cogswell, 1972). These recent experimental data are now used to assess the viscous dissipation effect in typical practical applications of this flow. The measured values of interest here are, respectively, $\eta_0 \simeq 2 \times 10^3$ Pa s and $3\eta \simeq 1.5 \times 10^4$ Pa s at $\dot{\epsilon} = 17\ \mathrm{s}^{-1}$. These data allow an estimate of the parameter λ in Eq. (6) for this material, viz $\lambda \simeq 2.07 \times 10^{-2}$ s. The thermal diffusivity for LDPE and other polymer melts is typically $\kappa/\rho c_p \simeq 10^{-7}\ \mathrm{m}^2/\mathrm{s}$ (e.g., Agassant et al., 1991).

Attention is now focused on the flow of this LDPE melt in a four-to-one abrupt contraction, such that We = 3.2 and Pe = 800. The corresponding values of the average exit velocity and downstream radius are respectively $\bar{u} = 5.56 \times 10^{-2}$ m/s and $r_0 = 1.44 \times 10^{-3}$ m. These are typical numbers found in extrusion processes. From the dimensionless temperature field obtained for this case (Pe = 800, We = 3.2) and illustrated in Fig. 3, the maximum value of θ is found at the exit region, namely, $\theta_{\max} = 3.6 \times 10^{-2}$. Therefore,

$$T_{\max} - T_0 = \frac{\eta_0 \bar{u}^2}{\kappa} \theta_{\max} = 1.1^\circ\mathrm{C} \tag{21}$$

Such temperature rise may be large enough to cause important changes in the velocity field in some extrusion applications, due to viscosity sensitivity to temperature, affecting the quality of the final product.

Reducing now the radius to $r_0 = 5.0 \times 10^{-4}$ m, which is often used in commercial capillary rheometers, a Peclet number of Pe = 800 means that the average velocity is now $\bar{u} = 1.6 \times 10^{-1}$ m/s. This value is also within the range of velocities that is typical in capillary rheometry. However, it implies a Weissenberg number of We = 26.5, being outside the range of applicability of the present viscosity model (Eq. (14)). It seems reasonable to expect, however, that the maximum dimensionless temperature $\theta_{\max}$ will be higher for this larger value of We, since in the range investigated here θ was shown to be a monotonically increasing function of We. Therefore, a conservative estimate for the maximum temperature rise $T_{\max} - T_0$ may be obtained by using the value of $\theta_{\max}$ pertaining to We = 3.2. The temperature rise obtained in this manner is $T_{\max} - T_0 = 9.2^\circ\mathrm{C}$.

The above sample calculations suggest that neglecting viscous dissipation effects may lead to large errors in viscosity measurements with the capillary rheometer, because the shear and elongation viscosities of polymer melts are strong functions of temperature (e.g., Laun and Schuch, 1989). However, the above numbers should be regarded with caution, because the viscosity function employed here is an oversimplified representation of the real behavior (Barnes et al., 1989; Laun and Schuch, 1989). Moreover, other possibly important effects such as shear thinning behavior are not accounted for in the present analysis.

Conclusions

A numerical investigation of heat transfer in the axisymmetric, two-dimensional, laminar flow through a sudden contraction is examined. To relate the stress tensor field to the fluid motion, a generalized Newtonian model whose viscosity

depends on both the second and third invariants of the rate-of-deformation tensor was used. The non-Newtonian nature of the fluid significantly affects both the flow and the temperature fields.

The governing equations have been integrated numerically with the aid of a finite-volume method. The power-law scheme was adopted to account properly for convection-diffusion effects, and the coupling of continuity with the momentum equations was treated with the SIMPLE algorithm.

The results showed that, whereas for a Newtonian fluid only a small weak vortex appeàrs at the corner, when the Weissenberg number is increased, a larger vortex is observed, and the streamlines converge to the centerline farther upstream from the contraction plane. The observed non-Newtonian effects are related to the primarily extensional flow kinematics in conjunction with the non-Newtonian behavior of the fluid's extensional viscosity.

It is held that the difference between Newtonian and non-Newtonian flow fields is due primarily to a solidlike core of fluid that is formed immediately upstream of the contraction entrance, as a result of the strong extensional flow (and hence large extensional viscosity) in that region.

Viscous dissipation of mechanical energy plays a major role on the dimensionless temperature field, and its importance increases with the Weissenberg number. For the Newtonian fluid, the rate of viscous dissipation varies throughout the flow due to the shear rate distribution only, and the thermal effect is mild. As We is increased, the dimensionless temperature θ reaches much higher values at the exit region, due to intense viscous heating in this region. Major effects on the temperature field are restricted to the exit region and corner regions, due to the low thermal conductivity (high Pr) of the liquid. In the neighborhood of the solid boundaries, the isotherms are mildly pushed toward the walls as We is increased. This effect is stronger in the corner region, where (*i*) higher temperature gradients enhance diffusion, and (*ii*) vortex-induced convection promotes additional heat transfer from the exit region to the corner region.

The local Nusselt number at the curved wall, $\mathrm{Nu}(\chi)$, increases slightly up to $\chi \simeq 8$ as a result of the viscous heating, with no effect of the Weissenberg number. Farther downstream ($\simeq 8 \leq \chi \leq 13$), however, the Weissenberg number strongly influences heat transfer at the curved wall, increasing the Nusselt number significantly for $\mathrm{We} = 3.2$. This is due to combined viscous heating augmentation and strong vortex activity. A maximum value of $\mathrm{Nu}(\chi)$ occurs for all values of We at $\chi \simeq 12$, which roughly corresponds to the axial location where the hot fluid convected from the exit region by the vortex gets the closest to the curved wall.

The local Nusselt number at the wall of the contraction plane, $\mathrm{Nu}(R)$, is very large in the vicinity of $R = 1$, due to the influence of the hot fluid of the exit region and to the vortex motion toward the surface. Since both the fluid temperature in the exit region and the vortex activity increase as We is increased, $\mathrm{Nu}(R)$ in the neighborhood of $R = 1$ also increases with We. It is also seen that $\mathrm{Nu}(R)$ decreases rapidly with radial position, R, due to the presence of a nearly stagnant fluid filling the region close to the walls in the neighborhood of the corner, causing very poor heat transfer there.

Sample calculations using the present results and experimental viscosity data available in the literature suggest that if certain ranges of process parameters are not avoided, significant temperature rise may occur due to extension-thickening viscous dissipation during extrusion processes, leading to defective or lower quality products.

Acknowledgments

This research was supported by a grant from the Secretaria de Ciência de Tecnologia da Presidência da República, of the Brazilian Federal Government. Additional support in the form of a scholarship was provided by CNPq to M. S. Carvalho during his master's program at PUC—Rio. The authors wish to thank Dr. Padmanabhan for kindly sharing with them his keen expertise on the sudden contraction flow.

References

Agassant, J.-F., Avenas, P., Sergent, J.-Ph., and Carreau, P. J., 1991, *Polymer Processing*, Oxford University Press, New York.

Barnes, H. A., Hutton, J. F., and Walters, K., 1989, *An Introduction to Rheology*, Elsevier, Amsterdam.

Binding, D. M., and Walters, K., 1988, "On the Use of Flow Through a Contraction in Estimating the Extensional Viscosity of Mobile Polymer Solutions," *Journal of Non-Newtonian Fluid Mechanics*, Vol. 30, pp. 233–250.

Boger, D. V., and Nguyen, H., 1978, "A Model Viscoelastic Fluid," *Polymer Engineering and Science*, Vol. 18, No. 13, pp. 1037–1043.

Boger, D. V., Hur, D. H., and Binnington, R. J., 1986, "Further Observations of Elastic Effects in Tubular Entry Flows," *Journal of Non-Newtonian Fluid Mechanics*, Vol. 20, pp. 31–49.

Boger, D. V., 1987, "Viscoelastic Flows Through Contractions," *Ann. Rev. Fluid Mech.*, Vol. 19, pp. 157–182.

Boger, D. V., and Binnington, R. J., 1990, "Circular Entry Flows of Fluid M1," *Journal of Non-Newtonian Fluid Mechanics*, Vol. 35, pp. 339–360.

Cogswell, F. N., 1972, "Converging Flow of Polymer Melts in Extrusion Dies," *Polym. Eng. Sci.*, Vol. 12, pp. 64–73.

Crochet, M. J., Davies, A. R., and Walters, K., 1984, *Numerical Simulation of Non-Newtonian Flow*, Rheology Series, Vol. 1, Elsevier, Amsterdam.

Debbaut, B., and Crochet, M. J., 1988, "Extensional Effects in Complex Flows," *Journal of Non-Newtonian Fluid Mechanics*, Vol. 30, pp. 169–184.

Debbaut, B., Marchal, J. M., and Crochet, M. J., 1988, "Numerical Simulation of Highly Viscoelastic Fluids Through an Abrupt Contraction," *Journal of Non-Newtonian Fluid Mechanics*, Vol. 29, pp. 119–146.

Dupont, S., and Crochet, M. J., 1988, "The Vortex Growth of a K.B.K.Z. Fluid in an Abrupt Contraction," *Journal of Non-Newtonian Fluid Mechanics*, Vol. 29, pp. 81–91.

Dupret, F., Marchal, J. M., and Crochet, M. J., 1985, "On the Consequence of Discretization Errors in the Numerical Calculation of Viscoelastic Flow," *Journal of Non-Newtonian Fluid Mechanics*, Vol. 18, pp. 173–186.

Jones, D. M., Walters, K., and Williams, P. R., 1987, "On Extensional Viscosity of Mobile Polymer Solutions," *Rheologica Acta*, Vol. 26, pp. 20–30.

Kim-E, M. E., Brown, R. A., and Armstrong, R. C., 1983, "The Roles of Inertia and Shear-Thinning in Flow of an Inelastic Liquid Through an Axisymmetric Sudden Contraction," *Journal of Non-Newtonian Fluid Mechanics*, Vol. 13, pp. 341–363.

Laun, H. M., and Schuch, 1989, "Transient Elongational Viscosities and Drawability of Polymer Melts," *Journal of Rheology*, Vol. 33, No. 1, pp. 119–175.

Padmanabhan, M., 1992, "In-Line Measurement of Shear-Elastic and Extensional Rheological Material Functions of Food Doughs," Ph.D. thesis, University of Minnesota, Minneapolis, MN.

Patankar, S. V., 1980, *Numerical Heat Transfer and Fluid Flow*, Hemisphere Publishing Company, New York.

Prakash, C., and Patankar, S. V., 1981, "Combined Free and Forced Convection in Vertical Tubes With Radial Internal Fins," ASME JOURNAL OF HEAT TRANSFER, Vol. 103, pp. 566–572.

Vergnes, B., 1985, "Calcul des Ecoulements de polymeres fondus dans les filières d'extrusion," Docteur D'Etat Es-Sciences thesis, Université de Nice, France.

White, S. A., Gotsis, A. D., and Baird, D. G., 1987, "Review of the Entry Flow Problem: Experimental and Numerical," *Journal of Non-Newtonian Fluid Mechanics*, Vol. 24, pp. 121–160.

Winter, H. H., 1977, "Viscous Dissipation in Shear Flows of Molten Polymers," *Advances in Heat Transfer*, Vol. 13, pp. 205–267.

Numerical Calculation of Convective Heat Transfer Between Rotating Coaxial Cylinders With Periodically Embedded Cavities

T. Hayase
The Institute of Fluid Science,
Tohoku University,
Sendai, Japan

J. A. C. Humphrey

R. Greif

Department of Mechanical Engineering,
University of California at Berkeley,
Berkeley, CA 94720

A numerical study has been performed for the flow and heat transfer in the space between a pair of coaxial cylinders with the outer one fixed and the inner one rotating. Of special interest is the case where either one of the cylinders has an axially grooved surface resulting in twelve circumferentially periodic cavities embedded in it. The ends of the cylinder are bounded by flat impermeable walls that are either fixed to the outer cylinder or rotate with the inner one. Such a geometry is common in electric motors where an improved understanding of thermophysical phenomena is essential for analysis and design. Discretized transport equations are solved for two-dimensional and three-dimensional, steady, constant property laminar flow using a second-order accurate finite volume scheme within the context of a SIMPLER-based iterative methodology. The two-dimensional calculations reveal a shear-induced recirculating flow in the cavities. For supercritical values of the Reynolds number, the three-dimensional calculations show how the flow in a cavity interacts with Taylor vortices in the annular space to enhance heat transfer. Relative to coaxial cylinders with smooth surfaces, for the conditions of this study the transport of momentum and heat is raised by a factor of 1.2 in the case of cavities embedded in the inner cylinder and by a factor of 1.1 in the case of cavities embedded in the outer cylinder.

1 Introduction

The understanding of the flow field in an electric motor is an essential consideration in the analysis and design of motors in relation to their heat transfer characteristics. Most electric motors have a configuration that may be approximated by a fixed outer cylinder and a rotating inner cylinder, and are characterized by axially grooved surfaces of the cylinders (see Fig. 1). The grooves give rise to circumferentially periodic distributions of cavities on the cylinder surfaces. The air flow induced between the cylinders is expected to possess two features: namely, a complicated recirculating flow region in the cavities and a Couette-like shear flow region in the annulus. At a critical value of the Taylor number, the shear flow in the annulus undergoes a Taylor instability, which results in axial- or spanwise-periodic axisymmetric vortices.

In an earlier communication (Hayase et al., 1990a) the authors performed a numerical analysis for the case of a grooved inner cylinder and found that, at a supercritical value of the Reynolds number, the Taylor vortex flow in the annulus interacts with the recirculating flow in the cavities to enhance the heat transfer between the cylinders by as much as 20 percent. In the present study further numerical analysis is performed over a range of the Reynolds number for two typical configurations in which either surface of the cylinders is axially grooved. The effects of these cavities on the Taylor instability and the resultant heat transfer are investigated.

Since the work of Taylor (1923), the flow between corotating cylinders has attracted considerable interest. This geometric configuration is deceivingly simple, since it is known to possess a range of complex flow structures the characteristics of which depend on the relevant dimensionless parameters. Coles (1965) made a detailed experiment for the flow between a pair of concentric cylinders whose rotation speeds were independently varied over a wide range. He observed two quite different processes for the transition from laminar Couette flow to turbulent flow: (1) a catastrophic transition, corresponding to a dominating outer cylinder rotation; and (2) a transition by spectral evolution, corresponding to a dominating inner cylinder rotation. Within the periodic and doubly periodic stages of the latter transition process, he also pointed out that a variety of different flows, characterized by different combinations of axial and tangential wave numbers, can exist at a given speed of the inner cylinder. The nonuniqueness of solutions for the Taylor vortex flow was also shown numerically for the case of axisymmetric spanwise-periodic waves by Alziary de Roque-

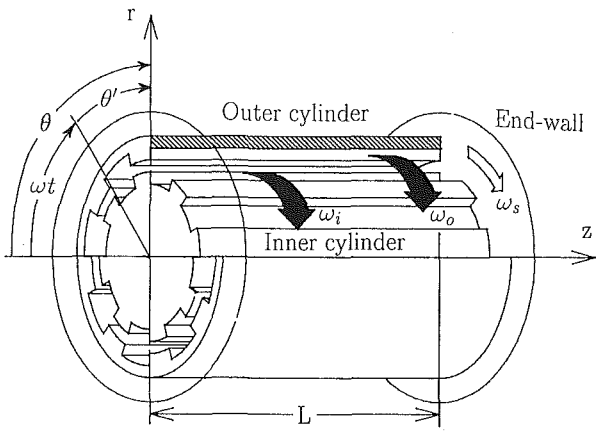

Fig. 1 Sketch of the general flow configuration showing two coaxial cylinders in relative rotational motion. Axial grooves result in circumferentially periodic distributions of cavities on either one of the facing cylinder surfaces.

Contributed by the Heat Transfer Division for publication in the JOURNAL OF HEAT TRANSFER. Manuscript received by the Heat Transfer Division September 1991; revision received March 1992. Keywords: Electronic Equipment, Numerical Methods, Rotating Flows. Associate Technical Editor: R. J. Simoneau.

fort and Grillaud (1978). Related topics, including chaotic behavior and its connection to transition to turbulence, have been discussed by Di Prima and Swinney (1981).

In spite of its technological importance, little work has been done on the flow and heat transfer in an annulus where the cylinders do not have a continuous smooth surface. Patankar and Murthy (1984) performed a numerical study showing that axisymmetrically arranged fins on a rotating inner cylinder enhance the heat transfer between the cylinder surfaces. In their experimental study, Lee and Minkowycz (1989) systematically investigated the effects on the flow and heat transfer resulting from axially arranged grooves embedded in the inner or outer cylinder. In that work either cylinder could be rotated and an axial flow was imposed in the annulus. Heat transfer between corotating cylinders with an axially grooved inner cylinder was also experimentally investigated by Hwang et al. (1990).

The shear-driven cavity flow configuration is commonly used as a test case in computational fluid mechanics because of the simplicity of the geometry and the strong elliptic character of the flow. Studies using different numerical schemes have been summarized for the two-dimensional configurations by Tuann and Olsen (1978). Recently, the present authors also presented accurate numerical solutions for the two-dimensional problem (Hayase et al., 1992). The structure of the flow in a three-dimensional cavity has been investigated by Perng and Street (1989). The problems of heat transfer in sheared cavity flows have been reviewed by Chen et al. (1985) and Humphrey and To (1986). In particular, the latter calculated the variation of the cavity Nusselt number as a function of the Grashof number and the Reynolds number.

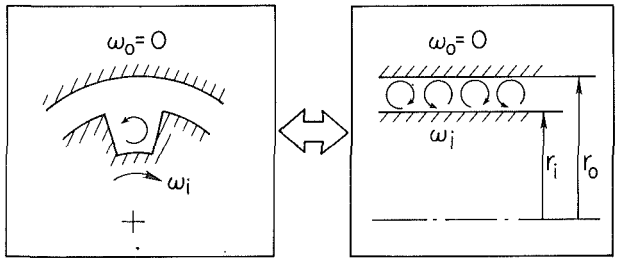

Cavity flow (r, θ plane) Taylor vortex flow (r, z plane)

Fig. 2 Schematic emphasizing the appearance of flow recirculation in the r, θ plane of the cavity and Taylor vortices in the r, z plane of the annulus

The problem of interest in this work involves elements from both the annulus and cavity flow configurations, since it consists of a pair of concentric cylinders in relative rotation with a periodic array of cavities embedded in the inner or outer cylinder (see Fig. 2). The steady flow for this configuration has been investigated here via numerical calculation. Section 2 of the paper presents the conservation equations and boundary conditions describing the flow cases of interest. This section also contains a summary of the numerical algorithm employed. The calculated results are presented and discussed in section 3. These include tests performed to verify the numerical accuracy of the calculation procedure. [Additional tests, relating to the physical accuracy of the algorithm, are reported by Hayase et al. (1990a, 1992).] The effects on the Taylor instability and heat transfer resulting from the presence of cavities on the inner or outer cylinder surfaces are then presented and

Nomenclature

A = area
$\tilde{C}_p$ = specific heat
$d(\cdot, \cdot)$ = distance in $\mathbf{V}_{X_n}$ (Eq. (10))
$d\mathbf{x}$ = $(dr, rd\theta, dz)$
$\tilde{k}$ = thermal conductivity
L = length of the cylinders
n_r, n_θ, n_z = number of cells in the r, θ, z directions, respectively
$\underline{\mathrm{Nu}}$ = local Nusselt number
$\overline{\mathrm{Nu}}$ = mean Nusselt number
p = pressure
Pr = Prandtl number (Eq. (5))
q = heat flux
r = radial coordinate
$\tilde{r}_i, \tilde{r}_o$ = radius of inner and outer cylinder, respectively
Re = $\tilde{\omega}_i \tilde{r}_i (\tilde{r}_o - \tilde{r}_i)/\tilde{\nu}$ = Reynolds number Eq. (6)
Re^* = critical Reynolds number for Taylor instability
Re_o = $\tilde{\omega}_i \tilde{r}_o^2/\tilde{\nu}$ (used only in Eqs. (3) and (4))
s = distance along the surface of inner cylinder projected in (r, θ') plane
S_h = heat generation term
t = time
T = temperature
$\tilde{T}_i, \tilde{T}_o$ = inner and outer cylinder temperature, respectively
T_a = $4R_e^2(1-r_i)/(1+r_i)$ = Taylor number (Eq. (6))
$\tilde{T}_s$ = $(\tilde{T}_i - \tilde{T}_o)$ = reference value of temperature
u, v, w = radial, circumferential and axial velocity components, respectively
$\mathbf{v}_n$ = discrete velocity vector field on the grid system $X_n \subset \Omega$
$\mathbf{V}_{X_n}$ = normed linear vector space consisting of $\mathbf{v}_n$
x_i = point in the grid system X_n
z = axial coordinate
$\|\cdot\|$ = norm in $\mathbf{V}_{X_n}$ (Eq. (9))
X_n = $\{x_1, x_2, \cdots, x_n\} \subset \Omega$ (grid system)
$\Delta_r, r\Delta_\theta, \Delta_z$ = grid spacing in the r, θ, z direction, respectively
θ = circumferential coordinate
$\theta_0, \theta_{\mathrm{in}}, \theta_{\mathrm{out}}$ = angles determining the cavity configuration (Fig. 3)
$\tilde{\lambda}$ = wavelength of Taylor vortices in z direction
$\tilde{\lambda}^*$ = critical wavelength for Taylor instability
$\tilde{\mu}$ = dynamic viscosity
$\tilde{\nu}$ = kinematic viscosity
$\tilde{\rho}$ = density
ϕ = dummy variable in Eq. (11)
$\tilde{\omega}_i$ = angular velocity of inner cylinder
$\tilde{\omega}_o$ = angular velocity of outer cylinder
$\tilde{\omega}_s$ = angular velocity of end wall
Ω = domain

Superscripts

$\tilde{}$ = dimensional values
$'$ = values with respect to the coordinate system fixed to the cavities
$*$ = critical values for Taylor instability
$\overline{}$ = mean values

Subscripts

e = east surface of a control volume (Fig. 4)
i = denotes cell location (Fig. 4)
w = west surface of a control volume (Fig. 4)

discussed for a range of the Reynolds number. Section 4 summarizes the conclusions of this work.

2 Formulation

2.1 Governing Equations and Boundary Conditions. The geometry shown in Fig. 1 is described by the cylindrical coordinate system (r, θ, z) with the corresponding velocity components (u, v, w). The typical case for an electric motor has a fixed outer cylinder $(\omega_o = 0)$ and a rotating inner cylinder $(\omega_i \geq 0)$. As previously mentioned, the present study deals with the cases where cavities are periodically embedded in either the inner or the outer cylinder surface. By adopting a coordinate system (r, θ', z) fixed to the cylinder with cavities, the boundary configuration is time-invariant and, therefore, a steady flow solution is expected unless the Reynolds number exceeds a critical value.

The two coordinate systems are related by:

$$\theta = \theta' + \omega t \qquad v = v' + \omega r \tag{1}$$

where the angular velocity ω of the relative rotation between the coordinate systems is equal to ω_i or ω_o depending on whether the cavities are embedded in the inner cylinder or the outer cylinder. Hereafter, we refer to the variables in the new coordinate system (r, θ', z) by means of a prime.

The pertinent equations in this study describe the conservation of mass, momentum, and energy for a fluid with constant physical properties. Buoyancy, viscous heating, and pressure work are assumed to be negligible. The nondimensional form of the equations is given below for the (r, θ', z) coordinate system.

Mass:

$$\frac{\partial u}{\partial r} + \frac{u}{r} + \frac{1}{r}\frac{\partial v'}{\partial \theta'} + \frac{\partial w}{\partial z} = 0 \tag{2}$$

Momentum (r, θ', z):

$$u\frac{\partial u}{\partial r} + \frac{v'}{r}\frac{\partial u}{\partial \theta'} + w\frac{\partial u}{\partial z} - \frac{v'^2}{r} - 2\omega v' - r\omega^2 = -\frac{\partial p}{\partial r} + \frac{1}{\mathrm{Re}_o}\left(\frac{\partial^2 u}{\partial r^2} + \frac{1}{r}\frac{\partial u}{\partial r} - \frac{u}{r^2} + \frac{1}{r^2}\frac{\partial^2 u}{\partial \theta'^2} - \frac{2}{r^2}\frac{\partial v'}{\partial \theta'} + \frac{\partial^2 u}{\partial z^2}\right)$$

$$u\frac{\partial v'}{\partial r} + \frac{v'}{r}\frac{\partial v'}{\partial \theta'} + w\frac{\partial v'}{\partial z} + \frac{uv'}{r} + 2\omega u = -\frac{1}{r}\frac{\partial p}{\partial \theta'} + \frac{1}{\mathrm{Re}_o}\left(\frac{\partial^2 v'}{\partial r^2} + \frac{1}{r}\frac{\partial v'}{\partial r} - \frac{v'}{r^2} + \frac{1}{r^2}\frac{\partial^2 v'}{\partial \theta'^2} + \frac{2}{r^2}\frac{\partial u}{\partial \theta'} + \frac{\partial^2 v'}{\partial z^2}\right)$$

$$u\frac{\partial w}{\partial r} + \frac{v'}{r}\frac{\partial w}{\partial \theta'} + w\frac{\partial w}{\partial z} = -\frac{\partial p}{\partial z} + \frac{1}{\mathrm{Re}_o}\left(\frac{\partial^2 w}{\partial r^2} + \frac{1}{r}\frac{\partial w}{\partial r} + \frac{1}{r^2}\frac{\partial^2 w}{\partial \theta'^2} + \frac{\partial^2 w}{\partial z^2}\right) \tag{3}$$

Energy:

$$u\frac{\partial T}{\partial r} + \frac{v'}{r}\frac{\partial T}{\partial \theta'} + w\frac{\partial T}{\partial z} = \frac{1}{\mathrm{Pr}\,\mathrm{Re}_o}\left(\frac{\partial^2 T}{\partial r^2} + \frac{1}{r}\frac{\partial T}{\partial r} + \frac{1}{r^2}\frac{\partial^2 T}{\partial \theta'^2} + \frac{\partial^2 T}{\partial z^2}\right) + S_h \tag{4}$$

The dimensionless variables are defined using the outer radius $\tilde{r}_o$, the angular velocity of the inner cylinder $\tilde{\omega}_i$, density of the fluid $\tilde{\rho}$, and a reference temperature $\tilde{T}_s$ for scaling. (The definition of nondimensional temperature, T, is given by Eq. (14) in Section 3.3.) In the above equations:

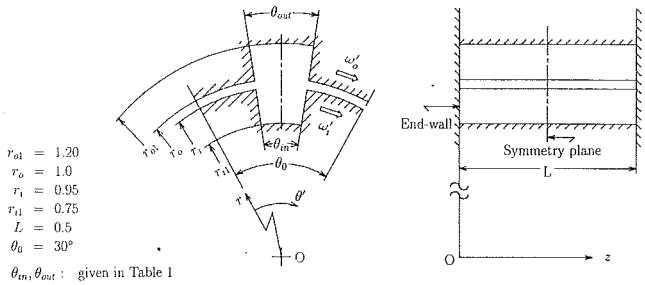

Fig. 3 Geometry from *(r, θ')* and *(r, z)* coordinate views

$$r = \tilde{r}/\tilde{r}_o, \quad z = \tilde{z}/\tilde{r}_o,$$

$$u = \tilde{u}/(\tilde{\omega}_i\tilde{r}_o), \quad v' = \tilde{v}'/(\tilde{\omega}_i\tilde{r}_o), \quad w = \tilde{w}/(\tilde{\omega}_i\tilde{r}_o), \quad p = \tilde{p}/(\tilde{\rho}\tilde{\omega}_i^2\tilde{r}_o^2),$$

$$\mathrm{Re}_o = \tilde{\omega}_i\tilde{r}_o^2/\tilde{\nu}, \quad \mathrm{Pr} = \tilde{\mu}\tilde{C}_p/\tilde{k}, \quad S_h = \tilde{S}_h/\tilde{C}_p\tilde{T}_s \tag{5}$$

For subsequent discussion, it is convenient to define two additional nondimensional parameters using the annular separation, $(\tilde{r}_o - \tilde{r}_i)$, for a length scale and $\tilde{\omega}_i\tilde{r}_i$ as the velocity scale. These are the Reynolds number Re and the Taylor number Ta (Di Prima and Swinney, 1981):

$$\mathrm{Re} = \tilde{\omega}_i\tilde{r}_i(\tilde{r}_o - \tilde{r}_i)/\tilde{\nu} \quad \text{and} \quad \mathrm{Ta} = 4\mathrm{Re}^2(1 - r_i)/(1 + r_i) = \mathrm{Re}_o\tilde{r}_i(\tilde{r}_o - \tilde{r}_i)/\tilde{r}_o^2 \tag{6}$$

We now consider a grid system X_n in the relevant domain Ω:

$$X_n = \{x_1, x_2, \cdots, x_n\} \subset \Omega \tag{7}$$

and a linear vector space $\mathbf{V}_{X_n}$ whose element is a discrete velocity vector field $\mathbf{v}_n$ on X_n:

$$\mathbf{v}_n(x_i) = (u(x_i), v(x_i), w(x_i)); \quad x_i \in X_n \tag{8}$$

One possible choice for the norm in this linear vector space $\mathbf{V}_{X_n}$ is

$$\|\mathbf{v}_n\| = \sum_{x_i \in X_n} \sqrt{u(x_i)^2 + v(x_i)^2 + w(x_i)^2}\,\rho_{x_i}\Delta x_i \Big/ \sum_{x_i \in X_n} \rho_{x_i}\Delta x_i \tag{9}$$

This value represents the average magnitude of the velocity vectors over the grid system X_n. Then a distance $d(\cdot, \cdot)$ between two elements $\mathbf{v}_n$ and $\mathbf{w}_n$ of $\mathbf{V}_{X_n}$ is derived from the norm

$$d(\mathbf{v}_n, \mathbf{w}_n) = \|\mathbf{v}_n - \mathbf{w}_n\| \tag{10}$$

These definitions satisfy the axiom of the norm and the distance in a general normed space theory (Dieudonne, 1969). The norm is later used to evaluate the strength of the flow field, while the distance is used to qualify the difference between velocity vector fields derived from two-dimensional and three-dimensional calculations.

Detailed drawings of the geometries of interest are shown in Fig. 3. Twelve cavities are arranged at 30 deg intervals along either the inner or the outer cylinder surface. (The cavities are shown on both cylinders for economy of presentation.) In the spanwise direction the flow field is confined by end walls that can be fixed or made to rotate with the inner cylinder. By assuming periodicity in the circumferential direction, the calculations are confined to a 30 deg sector in the (r, θ') plane. Based on the coordinate system (r, θ', z), which is fixed to the cylinder with cavities, the cylinder without cavities rotates with nondimensional angular velocity of unity. Assuming symmetry about the spanwise midplane, the calculations are carried out in one half of the physical domain. For velocity, no-slip, impermeable wall boundary conditions were used on the solid boundaries, while periodicity and symmetry were assumed at the circumferentially periodic boundary planes and the spanwise midplane, respectively. The boundary conditions for the heat transfer problem are described below in section 3.3. We note that while it is reasonable to assume circumferential pe-

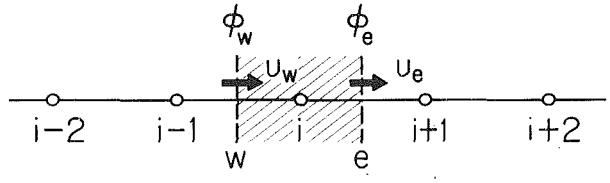

Fig. 4 One-dimensional staggered grid system for the control volume method illustrating nodes required for the QUICK scheme

riodicity of the flow, as a result of geometry periodicity, the symmetry plane assumption needs stronger justification. We are concerned here with stable (meaning time-independent) solutions of the conservation equations and their associated fixed patterns of motion. As a result we expect to find only an even number of Taylor vortices in the three-dimensional calculations. This is because an odd number would pose an unstable flow condition. Thus, the symmetry plane condition is consistent with the notion of time-independent motions with an even number of cross-stream cells.

Linear stability analysis gives a critical Taylor number of Ta = 3510 (Roberts, 1965) for a pair of infinitely long concentric cylinders, the outer one fixed and the inner one rotating, with the same gap/radius ratio as the present study. The corresponding critical Reynolds number is Re* = 185, corresponding to a rotation speed of the inner cylinder of 1410 rpm when inner and outer radii are $\tilde{r}_i = 2$ cm and $\tilde{r}_o = 2.11$ cm, respectively, for example.

Calculations have been carried out for the three-dimensional case and two supplemental two-dimensional cases referred to as two-dimensional (r, θ) and two-dimensional (r, z). In the first two-dimensional (r, θ) case the domain is the same as the three-dimensional case but the variation of the flow field in the spanwise direction is ignored. In the second two-dimensional (r, z) case, the annulus flow field is investigated assuming invariance in the θ direction. This is a special case of the present study in that cavities are not present on the cylinder surfaces.

2.2 Numerical Procedure. In order to obtain the numerical solution of the velocity and temperature fields, an equally spaced staggered grid system is first defined in each coordinate direction. The discretized representation of the relevant Eqs. (2)–(4) is obtained through the control volume method. The resulting finite-difference equations are solved by an iterative algorithm similar to the SIMPLER method due to Patankar (1980). The Thomas algorithm generally used to solve the algebraic equations was replaced with the MSI method of Schneider and Zedan (1981). This pentadiagonal matrix solver significantly improves the efficiency of the computation. The present solution procedure (Hayase et al., 1990b) is essentially that used in the earlier study (Hayase et al., 1990a). The only difference lies in the discretization of the convective terms of the Navier–Stokes equation; the reformulated QUICK scheme (Hayase et al., 1992) is employed in place of the Hybrid scheme (combination of upwind and central differencing). By reference to Fig. 4, the value of any quantity ϕ at a control volume boundary is expressed by means of a three-point interpolation:

$$U_e > 0,\ U_w > 0$$

$$\phi_e = \phi_i + \underline{1/8(-\phi_{i-1} - 2\phi_i + 3\phi_{i+1})}$$

$$\phi_w = \phi_{i-1} + \underline{1/8(-\phi_{i-2} - 2\phi_{i-1} + 3\phi_i)}$$

$$U_e < 0,\ U_w < 0$$

$$\phi_e = \phi_{i+1} + \underline{1/8(3\phi_i - 2\phi_{i+1} - \phi_{i+2})}$$

$$\phi_w = \phi_i + \underline{1/8(3\phi_{i-1} - 2\phi_i - \phi_{i+1})} \qquad (11)$$

where U_e and U_w denote the velocity components of the flow at the e and w surfaces of a ϕ control volume cell in the coordinate direction of interest. In these expressions the underlined terms are evaluated as source terms whose values are calculated using the results of the previous iteration. It is the treatment of these source terms that differentiates the present QUICK formulation from Leonard's original version (Leonard, 1979) and its revisions discussed in full detail by Hayase et al. (1992). The reformulated QUICK scheme assures the physical consistency of the numerical solution procedure and therefore greatly improves its numerical stability.

Table 1 Calculation cases; the definitions of θ_{in} and θ_{out} are given in Fig. 3

Case	A	B	C
Sketch	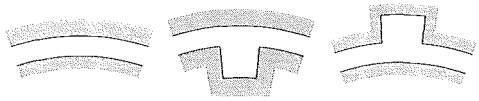		
θ_{in}	0°	10°/20°	0°
θ_{out}	0°	0°	10°/20°
End-wall	Fixed/ Rotating	Rotating	Fixed

3 Results and Discussion

The calculations were carried out using a relaxation factor of 0.8 for the momentum equations to avoid the divergence of solutions. Typical computational times were of order 300 s for the three-dimensional case, and 4 s for the corresponding two-dimensional cases on the Cray X-MP/14. Test calculations were first carried out to confirm the validity of the numerical procedure. Then the isothermal flow field and the heat transfer problems were carefully investigated. The three-dimensional characteristics of the flow due to the interaction between the Taylor vortices and cavity flow are presented and discussed.

Two- and three-dimensional calculations were performed for geometries shown in Table 1: concentric cylinders with smooth surfaces (case A) and cylinders with cavities on the inner cylinder (case B) or on the outer cylinder (case C).

3.1 Test Calculations. The present computer code, ROTFLO2, is a variant of the code validated in detail in the earlier study (Hayase et al., 1990a). The only difference between the codes lies in the discretization scheme of the convective terms in the Navier–Stokes equation (see section 2.2). The convergence of the numerical solution as a function of the grid refinement has already been examined by Hayase et al. (1992) where detailed comparisons are made between the QUICK and Hybrid schemes. Additional results especially pertinent to the present problem are discussed below.

Test calculations were performed for the two-dimensional (r, θ) case B ($\theta_{in} = 20$ deg; see Table 1) with Re = 218 for several grids $(n_r \times n_\theta) = (20 \times 22)$, (40×44), (80×88). The circumferential velocity distribution along the symmetry line ($\theta' = 15$ deg) is shown in Fig. 5. The region inside the cavity embedded in the inner cylinder corresponds to $0.75 \le r \le 0.95$, while the annular region corresponds to $0.95 \le r \le 1.0$ (most of the velocity distribution in the annular region is omitted in the figure). A comparison between the (40×44) and (80×88) QUICK results shows the grid independence of the latter. The (20×22) QUICK result is very close to the (80×88) QUICK solution, while the (20×22) Hybrid result deviates substantially. This demonstrates the superiority of the QUICK scheme over the Hybrid scheme in predicting the detailed variation of the flow field.

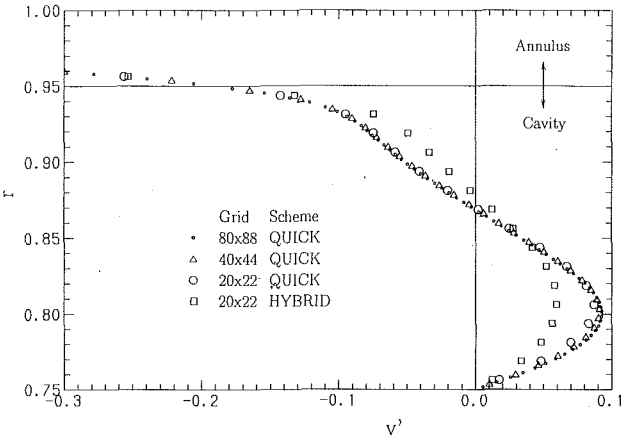

Fig. 5 Nondimensional circumferential velocity distribution along the symmetry plane with $\theta' = 15$ deg for case B in Table 1 ($\theta_{in} = 20$ deg). Comparison among different grids and discretization schemes for a two-dimensional (r, θ) calculation with Re = 218.

By simultaneously considering the discretization error, the computer storage and computational time requirements, the grid system for the three-dimensional calculations was fixed to:

$$(n_r \times n_\theta \times n_z) = (20 \times 22 \times 20),$$
$$(\Delta_r,\ r_o\Delta_\theta,\ \Delta_z) = (0.0125,\ 0.0238,\ 0.0125), \tag{12}$$

3.2 Flow Field. Three-dimensional isothermal flow calculations were carried out first for the configurations listed in Table 1. The interaction between the Taylor vortices in the annulus and the flow in the cavities on the inner or outer cylinder surface is investigated here. Results were obtained for several subcritical and supercritical Reynolds numbers. The flow field, including the two-dimensional calculation case, is characterized by the overall values of the norm and the distance (Eqs. (9) and (10)). For three-dimensional calculations of cases B and C, the end wall was fixed to the cylinder with cavities. The flow in a cavity is driven only by the shear at its opening, having more of a two-dimensional character in the (r, θ') plane than for the case where the end walls are in motion relative to the cavity (Hayase et al., 1990a).

Figures 6(a) and 6(b) show the results for three-dimensional calculations of case B with a supercritical Reynolds number of Re = 218 (Re/Re* = 1.18). This is one of the sequential solutions for $70 \le \mathrm{Re} \le 250$, every one of which was used as the initial condition of the next solution for an increased Reynolds number. (Simple shear flow in the annulus and solid body rotation in the cavity were assumed as the initial guess of the solution for Re = 70.) The upper part of each figure shows the velocity field with components (u, v') in the (r, θ') symmetry plane ($z = 0.25$), while the lower part shows the velocity vector field (u, w) at two (r, z) planes marked as (I) and (II) in the upper part of the figure. Figure 6(a) shows a steady solution for a cavity opening of $\theta_{in} = 10$ deg. Taylor vortices comprising a total of 10 cells appear in the annular region (I) (only one half of the z domain is shown in the figure). These vortices interact with the flow in the cavity, resulting in a complicated three-dimensional flow structure. Starting from an artificial initial condition with 12 vortices, a second steady solution with 12 Taylor vortices ($\tilde{\lambda}/(\tilde{r}_o - \tilde{r}_i) = 1.6$) was obtained for the same boundary conditions. The nonuniqueness of steady flow solutions for corotating cylinders with smooth surfaces has already been pointed out (Coles, 1965; Alziary de Roquefort and Grillaud, 1978). Figure 6(b) corresponds to numerical results for a large cavity opening of $\theta_{in} = 20$ deg. In this case the calculation converged not to a steady state, but to a numerically oscillating solution. The figure shows an instant in the calculation sequence during which the Taylor vortices in the annulus interact strongly with the recirculating flow in the cavity.

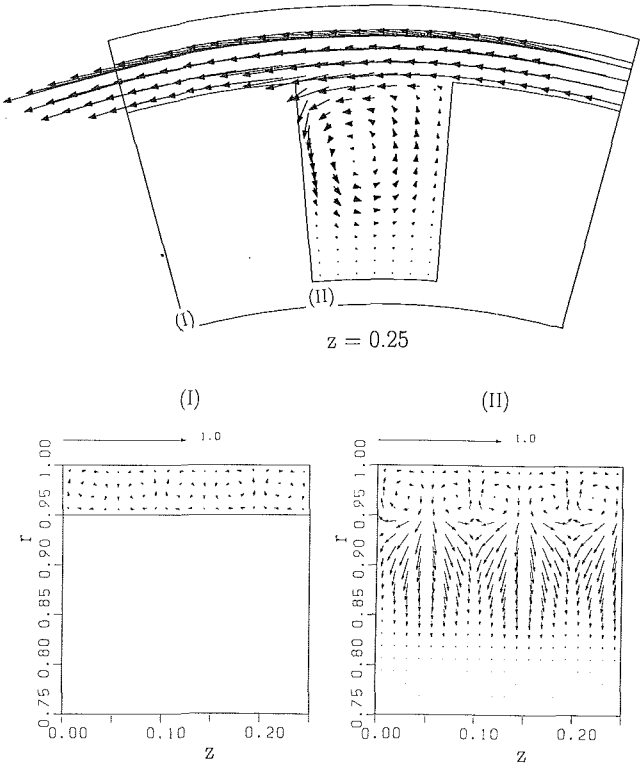

Fig. 6(a) $\theta_{in} = 10$ deg, 10 cells, $\tilde{\lambda}/(\tilde{r}_o - \tilde{r}_i) = 2.0$

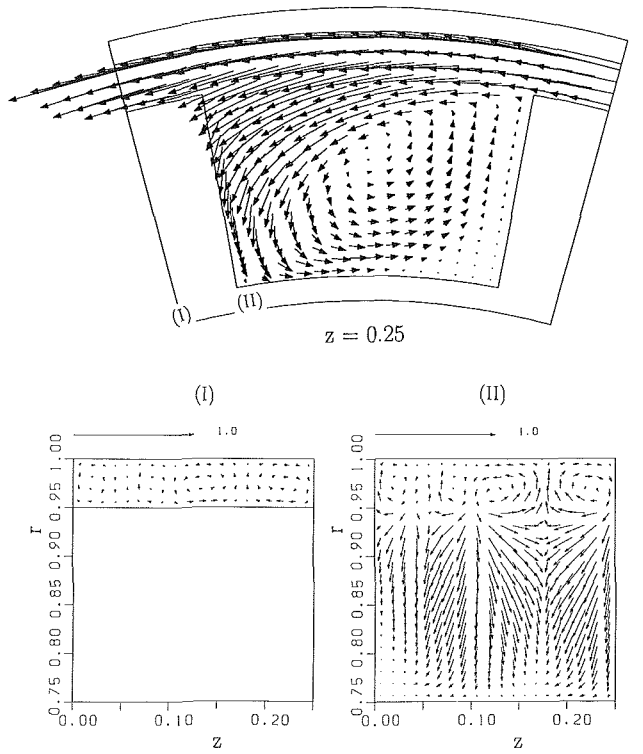

Fig. 6(b) $\theta_{in} = 20$ deg, 10 cells, $\tilde{\lambda}/(\tilde{r}_o - \tilde{r}_i) = 2.6$

Fig. 6 Three-dimensional flow field for case B with supercritical Reynolds number Re = 218 (Re/Re* = 1.18)

A possible range of wavelengths for the Taylor vortices in

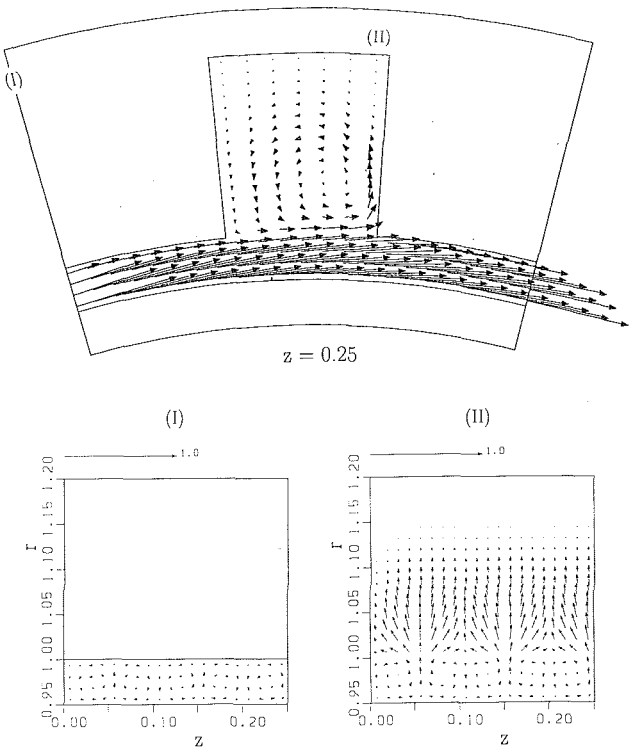

Fig. 7(*a*) $\theta_{out} = 10$ deg, 10 cells, $\tilde{\lambda}/(\tilde{r}_o - \tilde{r}_i) = 2.1$

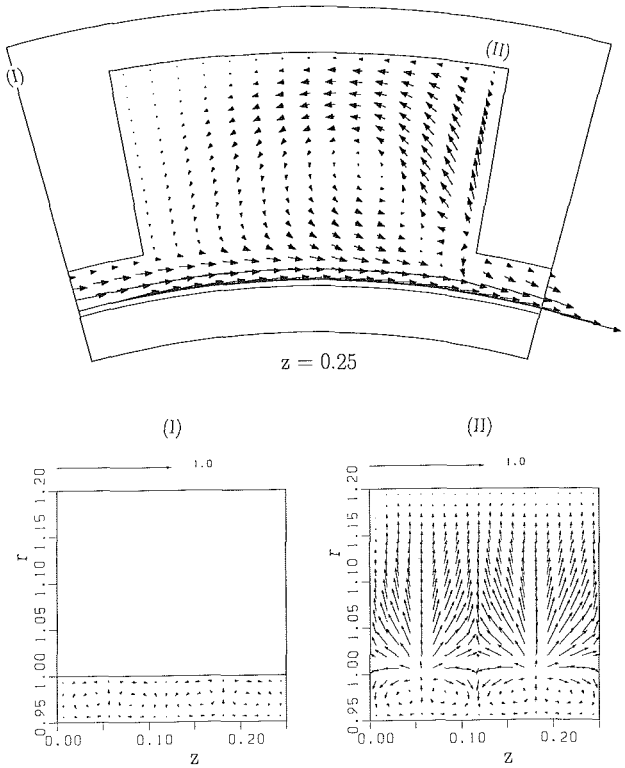

Fig. 7(*b*) $\theta_{out} = 20$ deg, 8 cells, $\tilde{\lambda}/(\tilde{r}_o - \tilde{r}_i) = 2.4$

Fig. 7 Three-dimensional flow field for case C with supercritical Reynolds number Re = 218 (Re/Re* = 1.18)

an infinitely long annulus is given by Kogelman and Di Prima (1970) through a nonlinear stability analysis. They find:

$$1.52 \leq \tilde{\lambda}/(\tilde{r}_o - \tilde{r}_i) \leq 2.51 \qquad (13)$$

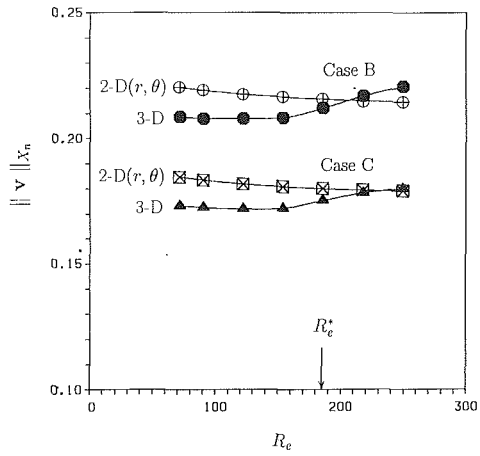

Fig. 8(*a*) Norm of two-dimensional (r, θ) and three-dimensional solutions

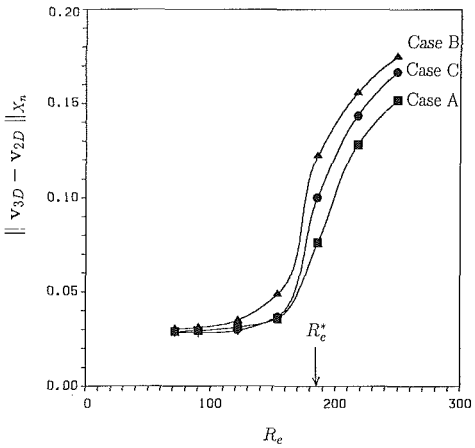

Fig. 8(*b*) Distance between two-dimensional (*r*, θ) and three-dimensional solutions

Fig. 8 Norm and distance as a function of the Reynolds number. Comparison between two-dimensional (*r*, θ) and three-dimensional solutions; Re* = 185

The wavelengths obtained in the present calculations are shown in Fig. 6. The results are within the range of inequality (13) for the small cavity opening ($\theta_{in} = 10$ deg), but out of the range for the large cavity opening ($\theta_{in} = 20$ deg).

Figures 7(*a*) and 7(*b*) show the results of three-dimensional calculations for case C. The conditions are the same as for Fig. 6, except that the cavity is now embedded in the outer cylinder surface. Figure 7(*a*) shows a steady solution comprising 10 cells for the small cavity opening ($\theta_{out} = 10$ deg). Another steady solution with eight cells ($\tilde{\lambda}/(\tilde{r}_o - \tilde{r}_i) = 2.4$) was obtained for this case. A numerically oscillating solution was also obtained for the large cavity opening ($\theta_{out} = 20$ deg), but the recirculating flow in the cavity was not as strong as in the former case B. The wavelengths of the Taylor vortices shown in Fig. 7 are all within the theoretical range predicted by the inequality (13).

Results have been obtained for cases B and C with a small cavity opening ($\theta_{in} = 10$ deg, $\theta_{out} = 10$ deg) for different Reynolds numbers using the two-dimensional (r, θ) and three-dimensional formulations. The norm and the distance defined in Eqs. (9) and (10) were calculated for the quantitative evaluation of these flows. Figure 8(*a*) shows the norms of the velocity fields as a function of the Reynolds number (all the results are referred to the (r, θ', z) coordinate system as mentioned before). For subcritical Reynolds numbers (Re/Re* < 1, Re* = 185), the norms of the three-dimensional results

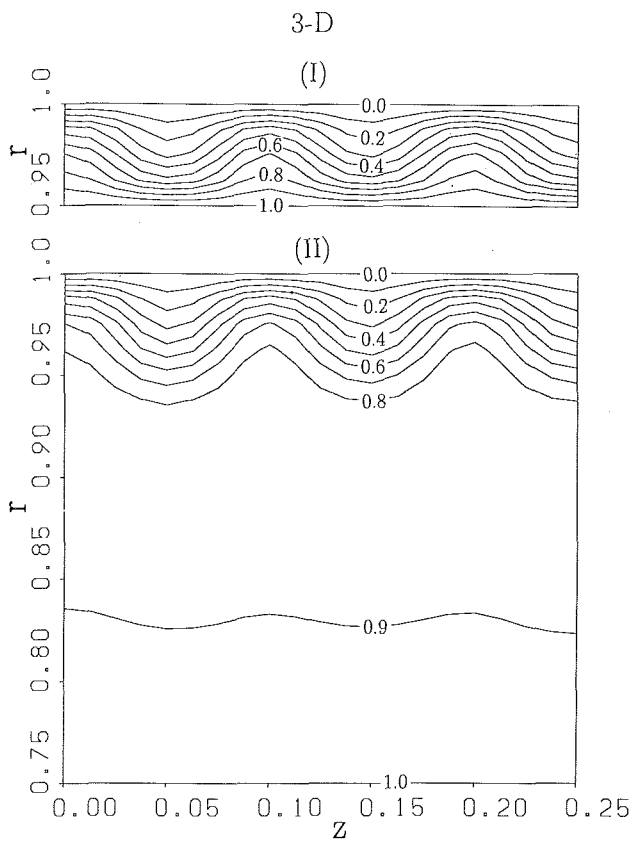

Fig. 9(*a*) Three-dimensional

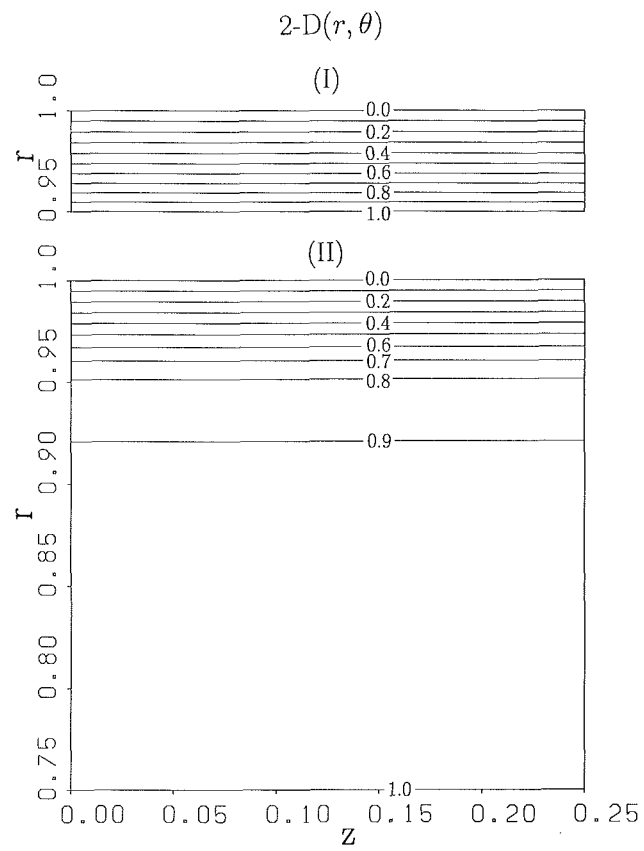

Fig. 9(*b*) Two-dimensional (*r*, *θ*)

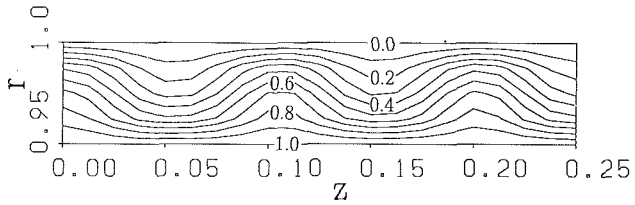

Fig. 9(*c*) Two-dimensional (*r*, *z*)

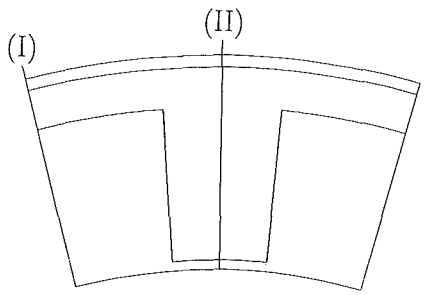

Fig. 9(*d*) Locations of planes (I) and (II)

Fig. 9 Isotherms for case B ($\theta_{in} = 10$ deg) with Re = 218. Comparison among three-dimensional, two-dimensional (*r*, *θ*) and two-dimensional (*r*, *z*) results along planes (I) and (II) in the figure.

are smaller than those of the two-dimensional (r, θ) cases for both cases B and C. A comparison of the solutions reveals that the two-dimensional (r, θ) and three-dimensional subcritical flow fields are identical except in regions near the walls. The difference of the norms, therefore, is ascribed to the friction effect at the end walls in the three-dimensional case. Above the critical Reynolds number ($\mathrm{Re}/\mathrm{Re}^* > 1$), Taylor vortices appear in the three-dimensional solutions and, as a result, the magnitudes of the norms gradually increase. It is noted that the norms of the two-dimensional (r, θ) and three-dimensional solutions for case C are very close in magnitude in the supercritical region, although the two flow patterns are completely different. The difference between the solutions should be evaluated by the distance $d(\cdot, \cdot)$ rather than their norms.

For the cases A, B, and C, the distance between the two-dimensional (r, θ) and three-dimensional solutions were obtained by evaluating Eq. (10) over the annular region as the domain Ω. Figure 8(*b*) shows the result as a function of the Reynolds number. For subcritical Reynolds numbers the magnitudes of the distances are small, implying that the flow field is essentially two dimensional. Above the critical Reynolds number, however, the distance value significantly increases, showing the strong three-dimensionality of the flow. A comparison among the cases A, B, and C reveals that the existence of cavities on either cylinder surface intensifies flow three dimensionality and that this effect is stronger for the cavities on the inner cylinder (case B) than on the outer cylinder (case C).

3.3 Heat Transfer. The heat transfer problem was investigated for some of the flow fields obtained in the preceding section assuming a constant physical property fluid. While this rules out predicting the effects of body forces on fluid motion through variable density, the results correspond to a forced convection condition (small temperature differences). Constant temperature $\tilde{T}_i$ and $\tilde{T}_o$ ($\tilde{T}_i > \tilde{T}_o$) boundary conditions were assumed over the inner and the outer cylinder, respectively. For three-dimensional calculations, the adiabatic condition was applied at the end wall and the symmetry plane, in order to facilitate comparisons with the two-dimensional (r, θ) case. The nondimensional temperature was defined as:

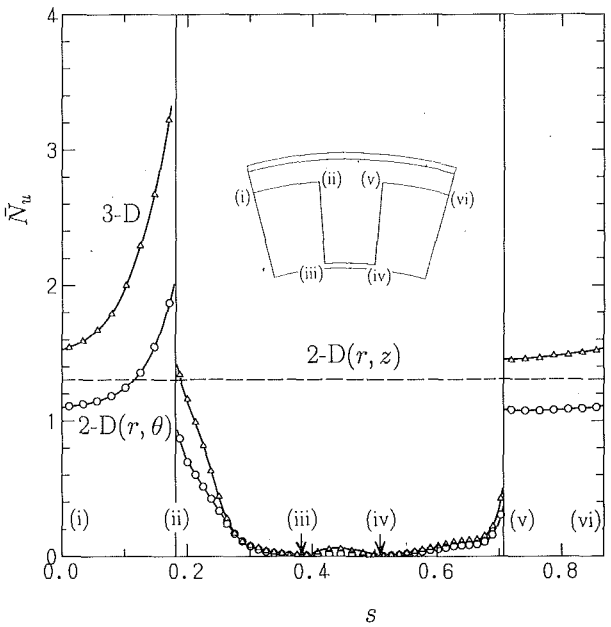

Fig. 10 Surface distribution of mean Nusselt number averaged in z direction over the inner cylinder surface with Re = 218. Three-dimensional calculation for Case B (θ_{in} = 10 deg).

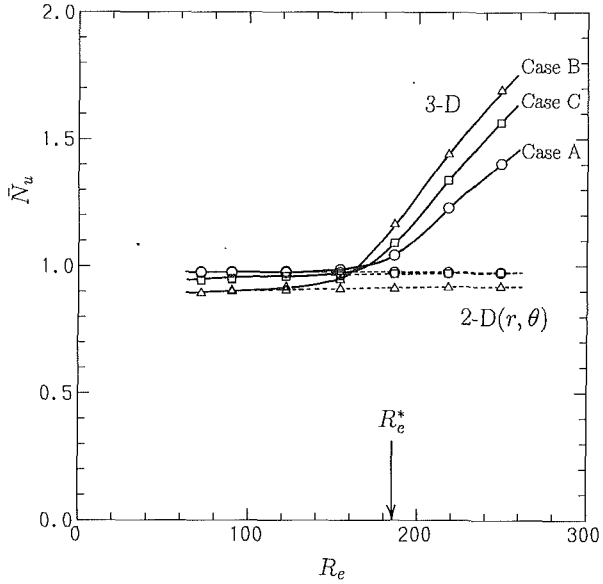

Fig. 11 Variation of mean Nusselt number with Reynolds number. Comparison among different geometries and between two-dimensional and three-dimensional calculations (θ_{in} = 10 deg for Case B, θ_{out} = 10 deg for Case C). Nusselt number was averaged over the outer cylinder surface for Cases A and B, and over the inner cylinder surface for Case C.

$$T = \frac{\tilde{T} - \tilde{T}_o}{\tilde{T}_i - \tilde{T}_o} \tag{14}$$

The heat transfer characteristics are presented in terms of a surface integral of the local Nusselt number defined as:

$$\overline{\mathrm{Nu}} = \frac{1}{A}\int_A \mathrm{Nu}\, dA$$

where

$$\mathrm{Nu} = \frac{\tilde{q}(\tilde{r}_o - \tilde{r}_i)}{\tilde{k}(\tilde{T}_i - \tilde{T}_o)} \tag{15}$$

Figure 9 shows the isotherms for case B (θ_{in} = 10 deg) at the supercritical Reynolds number Re = 218 for the three-dimensional, two-dimensional (r, θ) and two-dimensional (r, z) calculations. The presence of the Taylor vortices accounts for the wavy pattern observed in the annulus region in the three-dimensional and two-dimensional (r, z) cases. As discussed below, this leads to larger values of $\overline{\mathrm{Nu}}$ than in the two-dimensional (r, θ) case.

The values of $\overline{\mathrm{Nu}}$ averaged along the z-direction on the inner cylinder surface for the supercritical Reynolds number of 218 are shown in Fig. 10 as a function of location on the surface projected in the (r, θ') plane. The distribution for the three-dimensional flow of case B is similar to the corresponding two-dimensional (r, θ) result but the heat transfer magnitudes are different, especially in the annular zone. The figure shows that $\overline{\mathrm{Nu}}$ increases from (i) to (ii) along the surface of the cylinder, toward the cavity. The maximum value of $\overline{\mathrm{Nu}}$ for the three-dimensional case at point (ii) is more than twice that for the two-dimensional (r, z) Taylor vortex case. On the other hand $\overline{\mathrm{Nu}}$ is very small in the cavity except along surface (ii) to (iii), which is sheared by the flow that penetrates from the annular space.

The overall heat transfer property was evaluated by averaging the Nusselt number over the cylinder with a smooth surface: the outer cylinder for Cases A and B, and the inner cylinder for Case C. The results are plotted in Fig. 11 for the two-dimensional (r, θ) and three-dimensional calculations. It is well known that the Taylor vortices in the supercritical region enhance the heat transfer in the annulus (Case A). The present results reveal that the effect of cavities embedded in the cylinders is to further intensify the heat transfer for supercritical Reynolds numbers by a factor of 1.1 for Case C and by a factor of 1.2 for Case B.

4 Conclusions

Numerical calculations have been performed for two-dimensional and three-dimensional laminar flow and heat transfer between concentric cylinders with the inner cylinder rotating. Specifically, the influence of cavities embedded in either the inner or the outer cylinder has been studied. For supercritical values of the Reynolds number, the three-dimensional calculations reveal a spanwise-dependent Taylor vortex flow in the annulus. These vortices interact with the recirculating flow in the cavity along its aperture plane and enhance the heat transfer. Present results show that larger effects, both on the flow and heat transfer, arise when the cavities are located on the inner cylinder rather than on the outer cylinder.

Acknowledgments

The authors are grateful to Professor K. J. Binns of the University of Liverpool for pointing out the importance of the cooling of electric motors and providing initial guidance in terms of configuration choice and relative dimensions. The authors gratefully acknowledge the support received from the University-wide Energy Research Group of the University of California. The authors also thank Professor Y. Suematsu of Nagoya University for useful discussions, and graduate students A. Kikuchi and N. Yoshioka for conducting some of the calculations. The calculations were performed on the Cray X-MP/14 at the Computer Center of the University of California at Berkeley with a grant received from the Cray Corporation, on the Cray Y-MP/8 at the Institute of Fluid Science in Tohoku University, and on the FACOM M780/20 at the Nagoya University Computational Center.

References

Alziary de Roquefort, T., and Grillaud, G., 1978, "Computation of Taylor Vortex Flow by a Transient Implicit Method," *Computers and Fluids*, Vol. 6, pp. 259-269.

Chen, K. S., Humphrey, J. A. C., and Sherman, F. S., 1985, "Free and Mixed Convective Flow of Air in a Heated Cavity of Variable Rectangular Cross Section and Orientation," *Phil. Trans. R. Soc. Lond.*, Vol. A 316, pp. 57–84.

Coles, D., 1965, "Transition in Circular Couette Flow," *J. Fluid Mech.*, Vol. 21, pp. 385–425.

Dieudonne, J., 1969, *Foundations of Modern Analysis*, Academic Press, New York.

Di Prima, R. C., and Swinney, H. L., 1981, "Instabilities and Transition in Flow Between Concentric Rotating Cylinders," *Hydrodynamic Instabilities and the Transition to Turbulence*, H. L. Swinney and J. P. Gollub, eds., Springer, pp. 139–180.

Hayase, T., Humphrey, J. A. C., and Greif, R., 1990a, "Numerical Study of Three-Dimensional Flow and Heat Transfer Between a Fixed Outer Cylinder and a Rotating Inner Cylinder with Cavities," *3rd Int. Symp. on Transport Phenomena and Dynamics of Rotating Machinery*, Vol. 1, pp. 216–231.

Hayase, T., Humphrey, J. A. C., and Greif, R., 1990b, "Mini-manual for ROTFLO2," Dept. Mech. Eng. Report #FM-90-1, Univ. Calif. Berkeley.

Hayase, T., Humphrey, J. A. C., and Greif, R., 1992, "A Consistently Formulated QUICK Scheme for Fast and Stable Convergence Using Finite-Volume Iterative Calculation Procedures," *J. Comp. Physics*, Vol. 98, pp. 108–118.

Humphrey, J. A. C., and To, W. M., 1986, "Numerical Simulation of Buoyant, Turbulent Flow—II. Free and Mixed Convection in a Heated Cavity," *Int. J. Heat Mass Transfer*, Vol. 29-4, pp. 593–610.

Hwang, G. J., Lin, D. K., and Chen, L. T., 1990, "Heat Transfer Between Rotating Cylinders," *3rd Int. Symp. on Transport Phenomena and Dynamics of Rotating Machinery*, Vol. 1, pp. 143–155.

Kogelman, S., and Di Prima, R. C., 1970, "Stability of Spatially Periodic Supercritical Flows in Hydrodynamics," *Phys. Fluids*, Vol. 13, pp. 1–11.

Lee, Y. N., and Minkowycz, W. J., 1989, "Heat Transfer Characteristics of the Annulus of Two Coaxial Cylinders With One Cylinder Rotating," *Int. J. Heat Mass Transfer*, Vol. 32-4, pp. 711–722.

Leonard, B. P., 1979, "A Stable and Accurate Convective Modelling Procedure Based on Quadratic Interpolation," *Comp. Meths. Appl. Mech. Engrg.*, Vol. 19, pp. 59–98.

Patankar, S. V., 1980, *Numerical Heat Transfer and Fluid Flow*, McGraw-Hill, New York.

Patankar, S. V., and Murthy, J. Y., 1984, "Analysis of Heat Transfer From a Rotating Cylinder With Circumferential Fins," *Heat and Mass Transfer in Rotating Machinery*, D. E. Metzger and N. H. Afgan, eds., Springer-Verlag, New York, pp. 155–166.

Perng, C., and Street, R., 1989, "Three-Dimensional Unsteady Flow Simulations: Alternative Strategies for a Volume-Integrated Calculation," *Int. J. Numer. Meth. Fluids*, Vol. 9, pp. 341–362.

Roberts, P. H., 1965, "Appendix: The Solution of the Characteristic Value Problem," *Proc. R. Soc.*, Vol. A283, pp. 550–556.

Schneider, G. E., and Zedan, M., 1981, "A Modified Strongly Implicit Procedure for the Numerical Solution of Field Problems," *Numerical Heat Transfer*, Vol. 4, pp. 1–19.

Taylor, G. I., 1923, "Stability of a Viscous Liquid Contained Between Two Rotating Cylinders," *Phil. Trans. R. Soc. London*, Vol. A223, pp. 289–343.

Tuann, S., and Olson, M., 1978, "Review of Computing Methods for Recirculating Flows," *J. Comp. Physics*, Vol. 29, pp. 1–19.

Direct Numerical Simulation of Passive Scalar Field in a Turbulent Channel Flow

N. Kasagi
Professor.
Mem. ASME

Y. Tomita
Graduate Student.

A. Kuroda[1]
Graduate Student.

Department of Mechanical Engineering,
The University of Tokyo,
Bunkyo-ku, Tokyo, 113 Japan

A direct numerical simulation (DNS) of the fully developed thermal field in a two-dimensional turbulent channel flow of air was carried out. The isoflux condition was imposed on the two walls so that the local mean temperature increased linearly in the streamwise direction. With any buoyancy effect neglected, temperature was considered as a passive scalar. The computation was executed on 1,589,248 grid points by using a spectral method. The statistics obtained were root-mean-square temperature fluctuations, turbulent heat fluxes, turbulent Prandtl number, and dissipation time scales. They agreed fairly well with existing experimental and numerical simulation data. Each term in the budget equations of temperature variance, its dissipation rate, and turbulent heat fluxes was also calculated. It was found that the temperature fluctuation θ' was closely correlated with the streamwise velocity fluctuation u', particularly in the near-wall region. Hence, the distribution of budget terms for the streamwise and wall-normal heat fluxes, $\overline{u'\theta'}$ and $\overline{v'\theta'}$, were very similar to those for the two Reynolds stress components, $\overline{u'u'}$ and $\overline{u'v'}$.

Introduction

The fundamental turbulent transport mechanism is of great importance from both scientific and engineering viewpoints. Up to the present, a number of experimental and numerical studies have been devoted to better understanding of the near-wall turbulence, because it must play a predominant role in convective momentum, heat and mass transfer (see, e.g., Kline and Afgan, 1990). However, the current knowledge on the transport mechanism in the wall region is neither complete nor satisfactory, owing to various difficulties in measuring fluctuating turbulent quantities in a very thin layer adjacent to the wall. In the meantime, recent advances in large-scale computers have made it possible to simulate numerically simple turbulent shear flows at moderate Reynolds numbers (Moin and Spalart, 1989). Simulation data bases are superior to experimental data in permitting thorough analysis of the turbulent flow structures with all the instantaneous flow variables. They are also very useful for engineering turbulence modeling, since they provide quantitative data that cannot be obtained experimentally with confidence, e.g., each budget term in the transport equations of the Reynolds stresses.

Recently, Kim (1988) and Kim and Moin (1989) numerically simulated the turbulent thermal field in a two-dimensional channel. They confirmed experimentally observed features of turbulent heat transfer such as a high correlation between steamwise velocity and temperature fluctuations (Perry and Hoffman, 1976) and existence of the thermal streaky structures near the wall (Iritani et al., 1984). Their database is valuable for modeling turbulent heat transfer and can be used in analyzing heat transfer mechanisms near a solid wall. However, they have used a thermal boundary condition somewhat uncommon to practical heat transfer problems: a passive scalar is generated uniformly in the fluid and removed from the isothermal walls.

The aim of this investigation is to offer new information on turbulent heat transfer under a more practical heating condition. Hence, we simulate the fully developed turbulent thermal field in a two-dimensional channel of which two walls are heated with a constant time-averaged heat flux (i.e., isoflux condition). In this paper, some of the thermal turbulence statistics are presented and compared with previous experimental and numerical results. In addition, the detailed budgets for the temperature variance, its dissipation rate, and the turbulent heat fluxes are calculated and discussed.

Numerical Procedures

The flow geometry and the coordinate system are shown in Fig. 1. Note that y denotes the distance from the bottom wall normalized by the channel half width δ; i.e., $y = 0$ and 2 at the two walls. The Reynolds number Re_τ based on the wall friction velocity u_τ and δ was set to be 150. The resultant bulk Reynolds number Re_m was 4580. Referring to the numerical procedure used by Kim et al. (1987), a fourth-order partial differential equation for v, a second-order partial differential equation for the wall-normal component of vorticity ω_y, and the continuity equation were used to solve the flow field. A spectral method with Fourier series in the x and z directions and a Chebyshev polynomial expansion in the wall-normal direction was used. The computational periods were chosen to be 5π and 2π (2356 and 942 in wall units) in the x and z directions, respectively. 128 × 128 Fourier modes and Chebyshev polynomials up to the order 96 in wave number space were used in order to resolve all essential turbulent scales on the computation grid. The collocation grid used to compute the nonlinear terms in physical space had 1.5 times finer resolution in each direction to remove aliasing errors. This resulted in the effective grid spacings of $\Delta x^+ \simeq 18.4$, $\Delta y^+ = 0.08 \sim 4.9$, and $\Delta z^+ \simeq 7.4$ in the three directions, respectively. They are almost equivalent to $\Delta x^+ \simeq 17.7$, $\Delta y^+ = 0.05 \sim 4.4$, and $\Delta z^+ \simeq 5.9$ in Kim and Moin (1989) who simulated turbulent thermal fields for Pr = 0.1, 0.71, and 2.0 at $\mathrm{Re}_\tau = 180$. For time integration, the second-order Adams-Bashforth and Crank-Nicolson schemes were adopted for the nonlinear and viscous terms, respectively. The time increment was $0.12\, u_\tau^2/\nu$.

Once the velocity field was calculated at each time step, the scalar field was obtained by integrating the energy equation.

[1]Present address: Department of Mechanical Engineering, Hokkaido University, Kita-ku, Sapporo 060, Japan.

Contributed by the Heat Transfer Division and presented at the Third ASME/JSME Thermal Engineering Joint Conference, Reno, Nevada, March 1991. Manuscript received by the Heat Transfer Division March 12, 1991; revision received January 6, 1992. Keywords: Forced Convection, Numerical Methods, Turbulence.

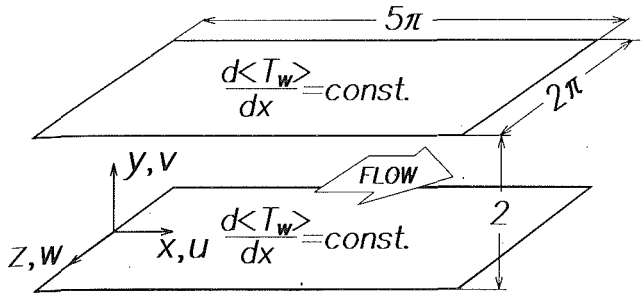

Fig. 1 Flow geometry and coordinate system

This calculation was done by the spectral method with the same grid system used for the velocity field. Air was chosen as a test fluid, and the Prandtl number Pr was 0.71. Any buoyancy effect was neglected, and hence temperature was considered as a passive scalar.

When a flow is unsteady, there occur unsteady temperature and heat-flux fluctuations on the wall surface. In reality, these fluctuating quantities are determined by the coupled unsteady heat conduction inside the wall so that they cannot be specified without knowing the wall material and its thickness. This conjugate heat transfer problem was studied by Kasagi et al. (1989). With a deterministic kinematic turbulence model in which streamwise vortical fluid motions were assumed, they found that in the case of an air flow (Pr = 0.71) the wall temperature fluctuation would be very small for most wall materials. Hence, the wall can be assumed to be locally isothermal. On the other hand, the isoflux condition conventionally means that the time-averaged wall heat flux does not change in the streamwise direction in a two-dimensional flow. Presently, this heating condition is equivalent to an assumption that the wall temperature ensemble-averaged over the z-direction and time, $\langle T_w \rangle$, should increase linearly in the x direction because of the global heat balance for a fully developed thermal field. As a result, the bulk mean temperature $\langle T_m \rangle$ should also increase linearly in the x direction, i.e., $\partial\langle T\rangle/\partial x = \partial\langle T_m\rangle/\partial x = \partial\langle T_w\rangle/\partial x$ = const.

The dimensionless temperature is defined as:

$$\theta^+(x, y, z; t) = \{\langle T_w \rangle - T(x, y, z; t)\}/T_\tau, \quad (1)$$

and periodic boundary conditions for θ^+ are used in the x and z directions. Hence, the governing equation for the thermal field is given as follows:

$$\frac{\partial\theta^+}{\partial t} + u^+\frac{\partial\theta^+}{\partial x} + v^+\frac{\partial\theta^+}{\partial y} + w^+\frac{\partial\theta^+}{\partial z} - \frac{2}{\int_0^2 \overline{u}^+ dy}u^+ = \frac{1}{\mathrm{Re}_\tau \mathrm{Pr}}\nabla^2\theta^+, \quad (2)$$

where the velocities are nondimensionalized by u_τ. The last term on the left-hand side of Eq. (2) corresponds to $-u^+\{\partial\langle T_w\rangle^+/\partial x\}$. As mentioned above, the temperature fluctuation is assumed to be zero on the wall and the wall thermal boundary condition is given as follows:

$$\theta^+(x, 0, z; t) = \theta^+(x, 2, z; t) = 0. \quad (3)$$

As the initial condition, an instantaneous velocity field at the fully developed state was supplied by the numerical simulation of turbulent channel flow performed by Kuroda (1990), while the initial thermal field was given as:

$$\theta^+(x, y, z; 0) = \mathrm{Pr}\, u^+(x, y, z; 0). \quad (4)$$

The time integration was repeated for about 2500 ν/u_τ^2 until the thermal field was judged to be fully developed, and then the computation was further continued for about 2100 ν/u_τ^2 (17,500 time steps) in order to calculate turbulence statistics as ensemble averages over space and time. The data sampling was started when we observed stationary time histories of the statistics, i.e., zeroth to fourth-order moments of temperature fluctuation and two turbulent heat fluxes averaged over every 500 time steps. However, there were very low frequency changes in these time histories although their amplitudes were very small. Thus, the statistically stationary state was judged with some arbitrariness. The computation was carried out on a HITAC-S-820/80 super-computer system at the Computer Center of the University of Tokyo. For one time step advancement, 5.26 second CPU time was required.

A program code, which consists of about 4000 FORTRAN statement lines, was presently developed from the DNS code

Nomenclature

c_p = specific heat at constant pressure
F = flatness factor
h = heat transfer coefficient
k = turbulent kinetic energy $= \overline{u_i' u_i'}/2$
k_θ = temperature variance $= \overline{\theta'^2}/2$
Nu = Nusselt number $= 2h\delta/\lambda$
Pr = Prandtl number $= \nu/\alpha$
Pr_t = turbulent Prandtl number $= \nu_t/\alpha_t$
p = pressure
Q_{ij} = two-point correlation coefficient, $= \overline{u_i'(r) u_j'(r+\Delta r)}/u_{i\mathrm{rms}} u_{j\mathrm{rms}}$
q_w = time-averaged wall heat flux
R = time-scale ratio $= \tau_\theta/\tau_u$
R_{ij} = correlation coefficient $= \overline{u_i' u_j'}/u_{i\mathrm{rms}} u_{j\mathrm{rms}}$
Re_m = Reynolds number $= 2u_m\delta/\nu$
Re_τ = Reynolds number $= u_\tau\delta/\nu$
S = skewness factor
T = temperature
T_m = bulk mean temperature
T_τ = friction temperature $= q_w/\rho c_p u_\tau$
t = time normalized by δ/u_τ
u_m = bulk mean velocity
u_τ = friction velocity $= \sqrt{\tau_w/\rho}$
u, v, w = velocity components in the x, y, and z directions
u_i = velocity component in the ith direction; u_1, u_2, and u_3 denote u, v, and w, respectively
x, y, z = streamwise, wall-normal, and spanwise coordinates normalized by δ
x_i = coordinate in the ith direction; x_1, x_2, and x_3 denote x, y, and z, respectively
α = thermal diffusivity $= \lambda/\rho c_p$
α_t = eddy diffusivity for heat, $-\overline{v'T'}/(\partial\overline{T}/\partial y)$
δ = channel half width or pipe radius or boundary layer thickness
ϵ = dissipation rate of k
ϵ_θ = dissipation rate of k_θ
θ = local temperature difference $= (\langle T_w\rangle - T)$
κ = Von Karman constant
κ_θ = Von Karman constant of temperature field
λ = thermal conductivity
ν = kinematic viscosity
ν_t = eddy diffusivity, $= -\overline{u'v'}/(\partial\overline{u}/\partial y)$
ρ = density
τ_w = time-averaged wall shear stress
τ_u = velocity dissipation time scale $= k/\epsilon$
τ_θ = temperature dissipation time scale, k_θ/ϵ_θ

Superscripts and Subscripts

$(\ )'$ = fluctuating component
$(\ )^+$ = normalized by the wall variables, u_τ, ν, and T_τ
$\overline{(\ )}$ = ensemble average over the x–z plane and time
$\langle\ \rangle$ = ensemble average over the z direction and time
$(\ )_{\mathrm{rms}}$ = root-mean-square value
$(\ )_w$ = value at the wall

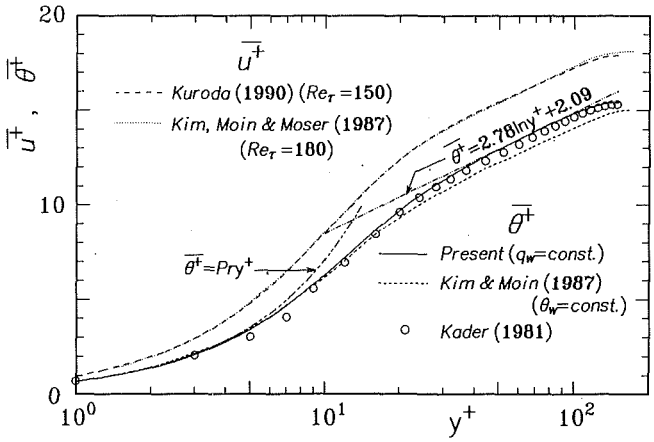

Fig. 2 Dimensionless mean velocity and temperature distributions

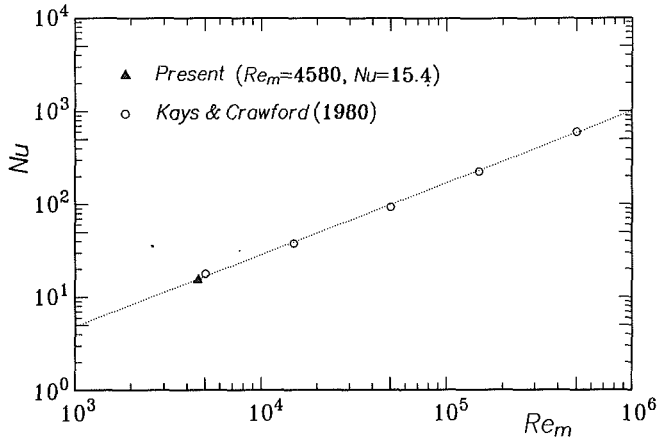

Fig. 3 Nusselt number for the fully developed turbulent channel flow with a constant wall heat flux

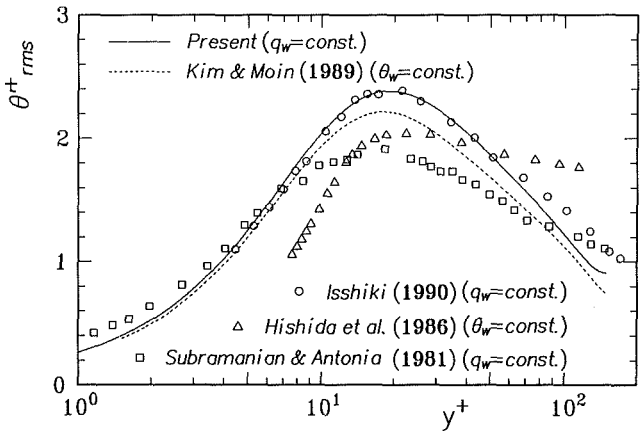

Fig. 4 Distribution of rms temperature fluctuation

of Kuroda (1990) for channel flow simulation. The accuracy of the numerical code developed was first tested by computing the evolution of a laminar flow with an arbitrary initial velocity distribution. The steady parabolic profiles reached were confirmed to be accurate enough. Because of an extremely heavy computational load, the computation was not repeated with changing the number of numerical grids systematically. However, the statistics and instantaneous flow patterns of the turbulent velocity field were extensively compared to the available experimental and simulation data by Kuroda (1990). In general, the agreement was very good and the Reynolds number dependence of statistics was confirmed to be consistent. As for the thermal field, global parameters such as the heat transfer coefficient and the mean temperature profile were confirmed to be in good agreement with the available experimental data as shown later. It is finally noted that, in the energy spectra of velocity and temperature fluctuations, there has not been observed any noticeable energy accumulation at high wave numbers that should be evidence of insufficient numerical resolution.

Results and Discussion

Turbulence Statistics. The dimensionless mean velocity and temperature profiles are shown as a function of y^+ ($=u_\tau y/\nu$) in Fig. 2. The mean velocities obtained by Kim et al. (1987) and Kuroda (1990) agree closely despite a slight difference in the Reynolds numbers. The temperature profile at Re_τ = 180 and Pr = 0.71 was obtained by Kim and Moin (1989) and is also included in Fig. 2. In their case, a passive scalar is created uniformly in the fluid and removed from the isothermal walls. Owing to the difference in the thermal boundary conditions, agreement between these two results is moderate. Both agree with the linear profile, $\overline{\theta}^+ = \mathrm{Pr}\, y^+$, in the conductive sublayer ($y^+ \lesssim 5$). However, the present result in the logarithmic region is in better agreement with the profile given by Kader's empirical formula (1981), which is a function of the Reynolds and Prandtl numbers. The Von Karman constant of the thermal field determined by the slope at $y^+ = 70$ is $\kappa_\theta = 0.360$ and is appreciably smaller than the value generally accepted for high Reynolds numbers, e.g., $\kappa_\theta \simeq 0.47$ (Kader, 1981) and $\kappa_\theta = 0.48 \pm 0.02$ (Subramanian and Antonia, 1981). This discrepancy must be mainly because the present Reynolds number is much smaller than those in the experiments.

The Nusselt number obtained by the present simulation is 15.4 and compared with the values at $Re_m > 5000$ recommended by Kays and Crawford (1980) in Fig. 3. The agreement is excellent.

The root-mean-square temperature fluctuation normalized by the friction temperature is compared with previous results in Fig. 4. The experimental data of Subramanian and Antonia (1981) was obtained in a boundary layer flow at $Re_\tau \simeq 370$, while Hishida et al. (1986) and Isshiki (1990) measured fully developed pipe flows at Re_τ = 879 and 203, respectively. Subrananian and Antonia, and Isshiki used an electrically heated stainless-steel foil as a wall surface, which realized the isotherlux boundary condition on the wall. The present result shows good agreement with these experimental data, particularly with those of Isshiki. The data of Hishida et al., which was obtained in an isothermal pipe, indicates somewhat different asymptotic behavior toward the wall. Both in the present and Kim and Moin's simulations, the maximum temperature fluctuations are located at $y^+ \simeq 18$. The present result, however, gives slightly larger temperature fluctuations in the near-wall region. This must be due to a difference in the production rate of temperature fluctuation, which is given as a product of the turbulent heat flux and the mean temperature gradient (see Eq. (8)); the temperature gradient in the buffer layer is steeper in the present simulation as seen in Fig. 2.

Figure 5 shows the distribution of streamwise turbulent heat flux. Its maximum is located between the point of the maximum u'_{rms} at $y^+ = 14$ and that of θ'_{rms} at $y^+ = 18$. There is again a slight difference between the two DNS results.

The wall-normal turbulent heat flux is shown in Fig. 6. Over the channel cross section, the wall-normal heat flux is smaller by an order of magnitude than the streamwise one. In addition, the maximum wall-normal heat flux is obtained farther away from the wall than the maximum streamwise heat flux, because the wall-normal velocity fluctuation, which is damped strongly by the wall, has its maximum at $y^+ = 53$. When plotted against y^+, the difference between the two DNS results is large in the central region of the channel owing to the difference in the

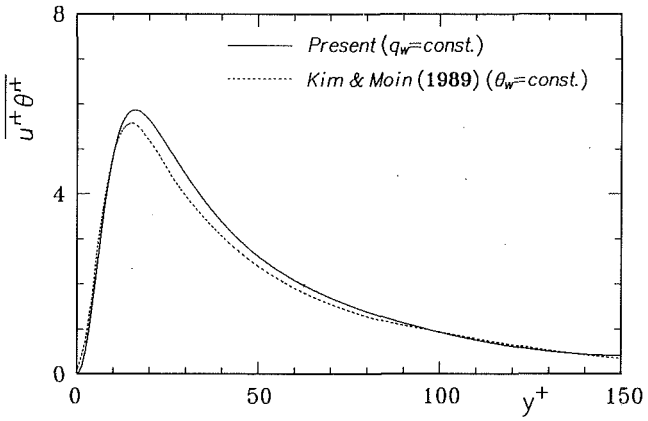

Fig. 5 Distribution of streamwise turbulent heat flux

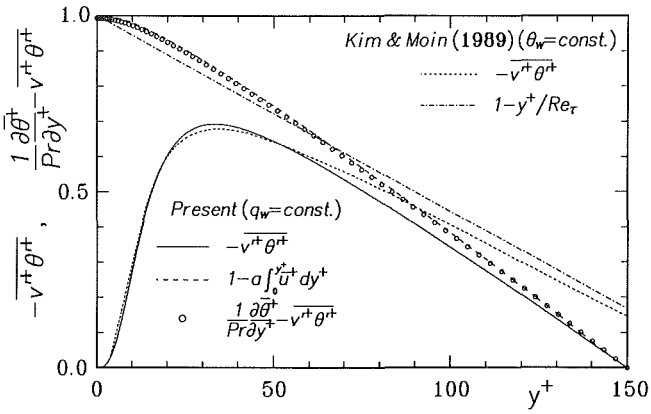

Fig. 6 Total and turbulent wall-normal heat fluxes

Reynolds number, while against y/δ they appear similar in that region, although it is not shown here.

For the fully developed channel flow between the isoflux walls, the wall-normal heat flux balance can be deduced from the averaged energy equation as follows:

$$1-a\int_0^{y^+}\overline{u}^+\,dy^+=\frac{1}{\mathrm{Pr}}\frac{\partial\overline{\theta}^+}{\partial y^+}-\overline{v'^+\theta'^+},\qquad(5)$$

where

$$a=1/\int_0^{\mathrm{Re}_\tau}\overline{u}^+\,dy^+.\qquad(5a)$$

Equation (5) gives a local total heat flux, which consists of conductive and turbulent heat fluxes. The values of both sides of Eq. (5) are also plotted in Fig. 6. They agree closely, but there is a small difference, less than 0.018, which may be caused by very low-frequency components of turbulent fluctuations. In the case of the flow with uniform heat generation between the isothermal walls simulated by Kim and Moin (1989), a similar balance equation is derived as follows:

$$1-\frac{y^+}{\mathrm{Re}_\tau}=\frac{1}{\mathrm{Pr}}\frac{\partial\overline{\theta}^+}{\partial y^+}-\overline{v'^+\theta'^+}.\qquad(6)$$

The two different thermal conditions result in a difference between the second terms on the left-hand side of Eqs. (5) and (6), and this difference is appreciable even in the near-wall region; this must also have influenced slight differences in the foregoing results.

The cross-correlation coefficients, which are indicative of the degree of similarity in waveforms and differences in phase, are shown in Fig. 7. The cross-correlation coefficient $R_{u\theta}$ is as large as 0.96 near the wall. This maximum $R_{u\theta}$ is not located at the wall, but at $y^+ \simeq 8$. At the channel centerline, $R_{u\theta}$ does

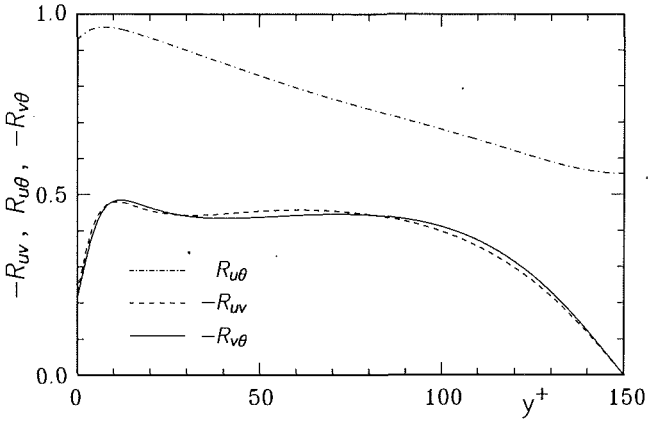

Fig. 7 Cross-correlation coefficients between velocity and temperature fluctuations

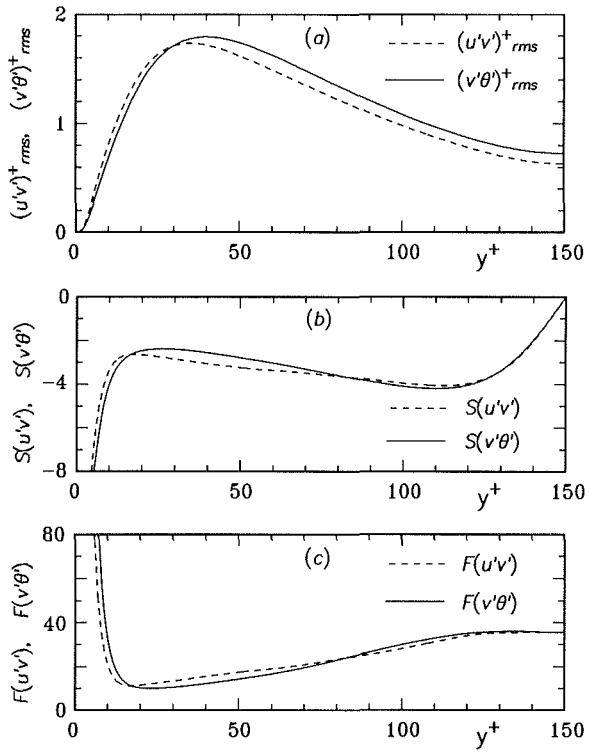

Fig. 8 Statistics of the shear stress product $u'v'$ and the heat flux product $v'\theta'$: (a) rms fluctuations, (b) skewness factors, (c) flatness factors

not vanish, unlike the cross-correlation coefficients of R_{uv} and $R_{v\theta}$; this is in good agreement with the measurement in a turbulent pipe flow of Hishida et al. (1986). Note that the correlation coefficient R_{uv} agrees quite well with $R_{v\theta}$. For pipe flow turbulence, Bremhorst and Bullock (1973) obtained $R_{v\theta} = -0.47$ and $R_{uv} = -0.43$. For boundary layer flows, Subramanian and Antonia (1981) reported $R_{v\theta} = -0.49$ and $R_{uv} = -0.47$. These values are in close agreement with the present data in the logarithmic region.

The close agreement between $R_{v\theta}$ and R_{uv} reveals that the wall-normal turbulent heat flux and the Reynolds shear stress are generated by similar turbulence mechanisms. Similarities between these turbulence properties are also found in the root-mean-square fluctuations, skewnesses, and flatnesses of the instantaneous products, $v'\theta'$ and $u'v'$, as shown in Fig. 8. Their skewness and flatness factors do not change remarkably in the logarithmic region; they are about -3 to -4 and about 10 to 35, respectively. However, they show steep changes when

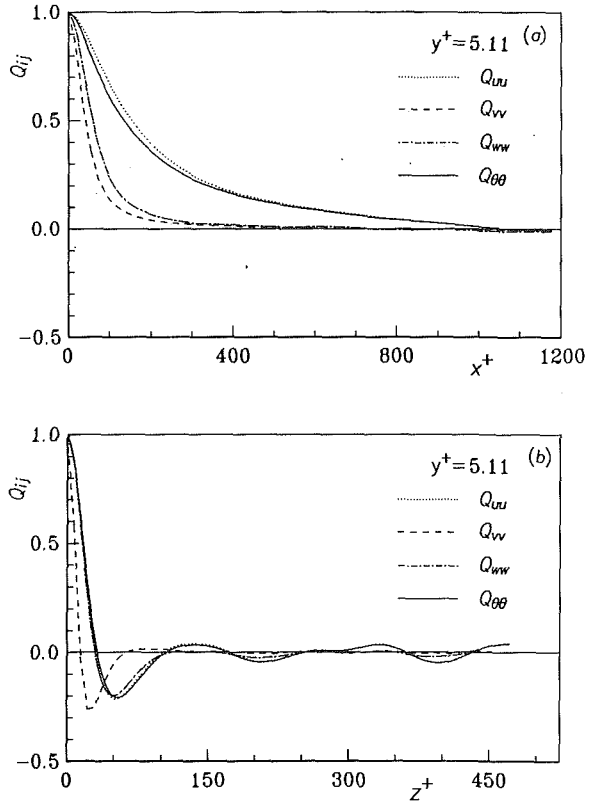

Fig. 9 Two-point correlation coefficients of velocity and temperature fluctuations at $y^+ = 5.11$: (*a*) streamwise correlation coefficients, (*b*) spanwise correlation coefficients

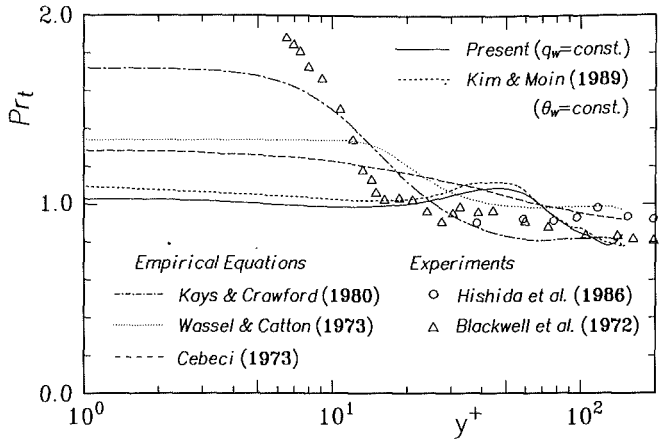

Fig. 10 Distribution of turbulent Prandtl number

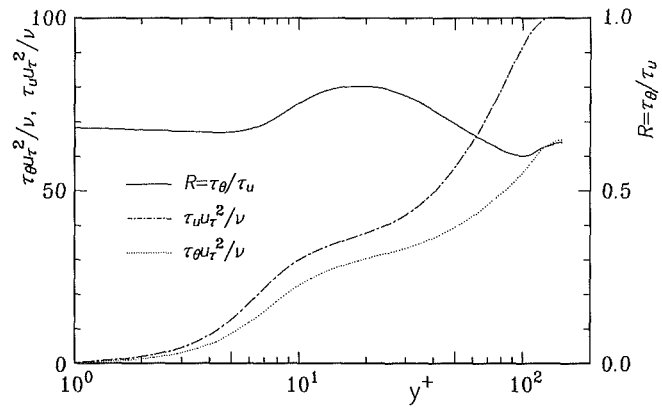

Fig. 11 Distributions of dissipation time scales and their ratio

approaching the wall. The skewness and flatness factors of $v'\theta'$ calculated at the first grid point from the wall are about -25 and 3000, respectively. Although these higher order moments may not be accurate enough, the extremely large flatness factor suggests an intermittent nature of the Reynolds shear stress and the wall-normal turbulent heat flux near the wall.

Figures 9(*a*) and 9(*b*), respectively, show the streamwise and spanwise two-point correlations of velocity and temperature fluctuations at $y^+ = 5.11$. At this y^+ location, the profile of $Q_{\theta\theta}$ closely agrees with that of Q_{uu}; it has a long tail over a streamwise distance 1000 ν/u_τ and shows weak periodicity in the spanwise direction. This fact must result from the thermal streaky structures, which resemble the sublayer streaky structures in the velocity field, as was found by Iritani et al. (1984).

Turbulent Prandtl Number and Time-Scale Ratio. The turbulent Prandtl number, which is defined as the ratio between the eddy diffusivities for momentum and heat, is shown in Fig. 10 together with empirical equations (Cebeci, 1973; Wassel and Catton, 1973; Kays and Crawford, 1980) and experimental data (Blackwell et al., 1972; Hishida et al., 1986). Although the profile of Pr_t in the vicinity of the wall has been a matter of conjecture, the two numerical simulations do not show a marked increase toward the wall that is seen in the empirical and experimental results. The present value is 1.02 on the wall. It has a maximum of about 1.1 at $y^+ \simeq 50$ and then decreases gradually away from the wall. It is noticeably different from the constant value of 0.9, which is often assumed in the turbulent heat transfer calculations. In the logarithmic layer, Pr_t can be roughly estimated as:

$$Pr_t = \kappa/\kappa_\theta = 0.388/0.360 = 1.078, \quad (7)$$

which is nearly equal to the values at $y^+ = 35 \sim 60$.

The velocity dissipation time scale $\tau_u = k/\epsilon$, the temperature dissipation time scale $\tau_\theta = k_\theta/\epsilon_\theta$, and their ratio $R(=\tau_\theta/\tau_u)$ are often used in modeling the eddy diffusivity of heat α_t on the basis of the temperature variance and its dissipation rate (see, e.g., Nagano and Kim, 1988; Yoshizawa, 1988). This means that, with the above quantities, one can avoid using empirically specified values for the turbulent Prandtl number and may reach more general thermal turbulence modeling. Their distributions are shown in Fig. 11. Both velocity and temperature dissipation time scales increase monotonically with the distance from the wall, but τ_u is always larger than τ_θ; for $Pr < 1$, the temperature fluctuation dissipates faster than the velocity fluctuation. As for the time-scale ratio, Launder (1976) claimed that the prescription of a constant time-scale ratio should not be sufficiently general, while Béguier et al. (1978) deduced that R was nearly uniform with a value close to 0.5 in thin shear layers. The present result shows that the change in the time-scale ratio across the channel is modest, although it has a local maximum of about 0.8 at $y^+ \simeq 20$. It is noted that the value should be equal to Pr at the wall theoretically.

Budgets for Temperature Variance, Its Dissipation Rate, and Turbulent Heat Fluxes. Current engineering turbulent heat transfer computations rely on various one-point closure turbulence models. Among them, those based on the second-moment equations are of great interest for many researchers (see, e.g., Launder, 1988). For example, the transport equations of $\overline{u_i'u_j'}$, ϵ, $\overline{u_i'\theta'}$ and ϵ_θ are numerically solved with the averaged momentum and energy equations. In those second-moment equations, there are several terms of unknown correlations and of higher order moments, which must be modeled with known variables. Hence, the budget data obtained by DNS should be useful for testing and developing existing closure models (Mansour et al., 1988). In the following, each term, which appears in the budget equations of temperature

variance, its dissipation rate and turbulent heat fluxes, is presented in order to establish a data base of convective heat transfer for thermal turbulence modeling.

The fully developed turbulent thermal field in a two-dimensional channel is homogeneous in both the x and z directions, and under the condition of $d\langle T\rangle/dx = \text{const}$, the budget equation for the temperature variance $\overline{\theta'^2}/2$ leads to:

$$0 = \underbrace{\overline{u'^+\theta'^+}\frac{\partial\langle T\rangle^+}{\partial x^+}}_{\text{Production}} - \overline{v'^+\theta'^+}\frac{\partial\bar{\theta}^+}{\partial y^+} \underbrace{-\frac{1}{\text{Pr}}\overline{\frac{\partial\theta'^+}{\partial x_j^+}\frac{\partial\theta'^+}{\partial x_j^+}}}_{\text{Dissipation}}$$

$$\underbrace{-\frac{\partial}{\partial y^+}\left\{\frac{\overline{v'^+\theta'^{+2}}}{2}\right.}_{\text{Turbulent diffusion}} \underbrace{\left.-\frac{1}{\text{Pr}}\frac{\partial}{\partial y^+}\frac{\overline{\theta'^{+2}}}{2}\right\}}_{\text{Molecular diffusion}}. \tag{8}$$

Figure 12 shows each term included in Eq. (8). Also included in this figure are the data taken by Krishnamoothy and Antonia (1987). Away from the wall ($y^+ > 40$), the production rate balances with the dissipation rate. Note that the first term of the production in Eq. (8) is negligibly small compared with the second term, because $\partial\langle T\rangle^+/\partial x^+ \ll \partial\bar{\theta}^+/\partial y^+$. With the wall approached, the turbulent diffusion plays an important role. In the viscous sublayer, the molecular diffusion and the dissipation are dominant; the same tendency is found in the budget for the turbulent kinetic energy (Mansour et al., 1988; Kuroda, 1990). The dissipation rate has a local minimum at $y^+ \simeq 8$. This is contrary to the experimental data of Krishnamoothy and Antonia (1987), but is in qualitative agreement with an analysis based on conceptual streamwise vortical fluid motions near the wall (Kasagi et al., 1989). Among three components of the dissipation in Eq. (8), the term $\overline{(\partial\theta'/\partial y)^2}$ is dominant in the viscous sublayer while at $y^+ > 20$ both $\overline{(\partial\theta'/\partial y)^2}$ and $\overline{(\partial\theta'/\partial z)^2}$ are important, but the term $\overline{(\partial\theta'/\partial x)^2}$ remains relatively very small over the channel cross section. This fact suggests that ϵ_θ is highly correlated with the streamwise vortical motions as suggested by Kasagi et al. (1989).

The equation of the dissipation rate of temperature variance can be obtained by taking the derivative of Eq. (2) with respect to x_ℓ, multiplying by $2(\partial\theta'^+/\partial x_\ell^+)/\text{Pr}$ and ensemble averaging. The resultant equation is written as:

$$0 = \underbrace{-\frac{2}{\text{Pr}}\overline{\frac{\partial\theta'^+}{\partial x_\ell^+}\frac{\partial u_j'^+}{\partial x_\ell^+}\frac{\partial\bar{\theta}^+}{\partial x_j^+}}}_{\text{Mean gradient production}} \underbrace{-\frac{2}{\text{Pr}}\overline{\frac{\partial\theta'^+}{\partial x_\ell^+}\frac{\partial\theta'^+}{\partial x_j^+}\frac{\partial\bar{u}_j^+}{\partial x_\ell^+}} - \frac{2}{\text{Pr}}\overline{\frac{\partial\theta'^+}{\partial x_\ell^+}\frac{\partial u'^+_j}{\partial x_\ell^+}\frac{\partial\theta'^+}{\partial x_j^+}}}_{\text{Turbulent production}}$$

$$\underbrace{-\frac{2}{\text{Pr}}\overline{u'^+_j\frac{\partial\theta'^+}{\partial x_\ell^+}}\frac{\partial^2\bar{\theta}^+}{\partial x_j^+\partial x_\ell^+}}_{\text{Gradient production}} \underbrace{-\frac{2}{\text{Pr}^2}\left(\overline{\frac{\partial^2\theta'^+}{\partial x_\ell^+\partial x_j^+}}\right)^2}_{\text{Dissipation}}$$

$$\underbrace{-\frac{1}{\text{Pr}}\frac{\partial}{\partial x_j^+}\left(\overline{\frac{\partial\theta'^+}{\partial x_\ell^+}\frac{\partial\theta'^+}{\partial x_\ell^+}u'^+_j}\right)}_{\text{Turbulent diffusion}} \underbrace{+\frac{1}{\text{Pr}^2}\frac{\partial^2}{\partial x_j^{+2}}\left(\overline{\frac{\partial\theta'^+}{\partial x_\ell^+}\frac{\partial\theta'^+}{\partial x_\ell^+}}\right)}_{\text{Molecular diffusion}}. \tag{9}$$

The various terms in Eq. (9) are shown in Fig. 13. The present results indicate that the turbulent production rate and the dissipation rate are dominant in the central region of the channel; this fact is in agreement with Tennekes and Lumley's analysis (1972) of the ϵ equation for high Reynolds number flows. Near the wall, these terms remain large, but the mean gradient production rates become more dominant. Note that the production by the mean temperature gradient is larger than that by the mean velocity gradient in the close vicinity of the wall. The diffusive terms and the gradient production are generally small except in the viscous sublayer. Very close to the wall, i.e., $y^+ < 1$, the profile of the dissipation goes through a local maximum at $y^+ = 0.3$ and then reaches -0.01 at the wall. Although not shown here, there is some appreciable imbalance in the presently calculated budget at the wall, but it is less than 1 percent of the dissipation rate at $y^+ > 2$.

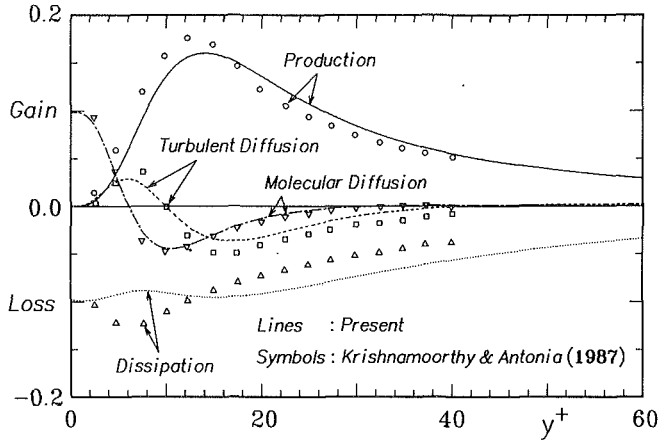

Fig. 12 Budget of the temperature variance k_θ in the near-wall region

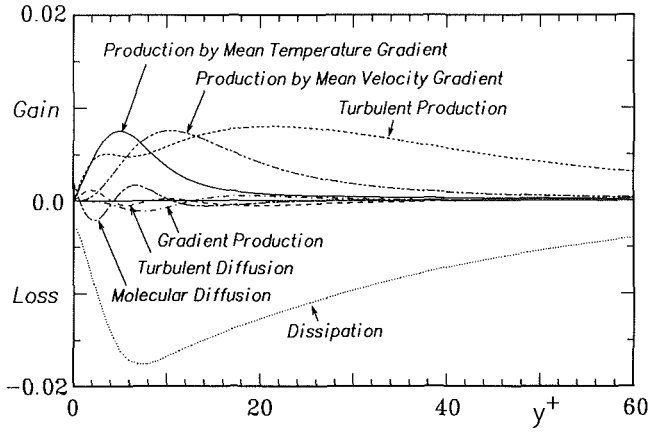

Fig. 13 Budget of the dissipation rate of the temperature variance ϵ_θ in the near-wall region

The following are the budget equations for the two Reynolds stress components, $\overline{u'^+u'^+}$ and $\overline{u'^+v'^+}$, and the streamwise and wall-normal turbulent heat fluxes, $\overline{u'^+\theta'^+}$ and $\overline{v'^+\theta'^+}$, respectively:

$$0 = \underbrace{-2\overline{u'^+v'^+}\frac{\partial\bar{u}^+}{\partial y^+}}_{\text{Production}} \underbrace{-2\overline{\frac{\partial u'^+}{\partial x_j^+}\frac{\partial u'^+}{\partial x_j^+}}}_{\text{Dissipation}} \underbrace{-2\overline{u'^+\frac{\partial p'^+}{\partial x^+}}}_{\text{Velocity pressure-gradient correlation}}$$

$$\underbrace{-\frac{\partial}{\partial y^+}\left\{\overline{u'^+u'^+v'^+}\right.}_{\text{Turbulent diffusion}} \underbrace{\left.-\frac{\partial}{\partial y^+}(\overline{u'^+u'^+})\right\}}_{\text{Molecular diffusion}}, \tag{10}$$

$$0 = \underbrace{-\overline{v'^+v'^+}\frac{\partial\bar{u}^+}{\partial y^+}}_{\text{Production}} \underbrace{-2\overline{\frac{\partial u'^+}{\partial x_j^+}\frac{\partial v'^+}{\partial x_j^+}}}_{\text{Dissipation}} \underbrace{-\left\{\overline{u'^+\frac{\partial p'^+}{\partial y^+}}+\overline{v'^+\frac{\partial p'^+}{\partial x^+}}\right\}}_{\text{Velocity pressure-gradient correlation}}$$

$$\underbrace{-\frac{\partial}{\partial y^+}\left\{\overline{u'^+v'^+v'^+}\right.}_{\text{Turbulent diffusion}} \underbrace{\left.-\frac{\partial}{\partial y^+}\overline{(u'^+v'^+)}\right\}}_{\text{Molecular diffusion}}, \tag{11}$$

$$0 = -\overline{u'^+v'^+}\frac{\partial\bar{\theta}^+}{\partial y^+} + \overline{u'^+u'^+}\frac{\partial\langle T\rangle^+}{\partial x^+} - \overline{v'^+\theta'^+}\frac{\partial\bar{u}^+}{\partial y^+}$$

Production

$$-\left(1+\frac{1}{\mathrm{Pr}}\right)\overline{\frac{\partial u'^+}{\partial x_j^+}\frac{\partial\theta'^+}{\partial x_j^+}} - \overline{\theta'^+\frac{\partial p'^+}{\partial x^+}}$$

Dissipation Temperature pressure-gradient correlation

$$-\frac{\partial}{\partial x_j^+}\left\{\overline{u'^+\theta'^+u_j'^+} - \left(\overline{\theta'^+\frac{\partial u'^+}{\partial x_j^+}} + \frac{1}{\mathrm{Pr}}\overline{u'^+\frac{\partial\theta'^+}{\partial x_j^+}}\right)\right\}, \quad (12)$$

Turbulent diffusion Molecular diffusion

$$0 = \overline{u'^+v'^+}\frac{\partial\langle T\rangle^+}{\partial x^+} - \overline{v'^+v'^+}\frac{\partial\bar{\theta}^+}{\partial y^+}$$

Production

$$-\left(1+\frac{1}{\mathrm{Pr}}\right)\overline{\frac{\partial v'^+}{\partial x_j^+}\frac{\partial\theta'^+}{\partial x_j^+}} - \overline{\theta'^+\frac{\partial p'^+}{\partial y^+}}$$

Dissipation Temperature pressure-gradient correlation

$$-\frac{\partial}{\partial x_j^+}\left\{\overline{v'^+\theta'^+u_j'^+} - \left(\overline{\theta'^+\frac{\partial v'^+}{\partial x_j^+}} + \frac{1}{\mathrm{Pr}}\overline{v'^+\frac{\partial\theta'^+}{\partial x_j^+}}\right)\right\}. \quad (13)$$

Turbulent diffusion Molecular diffusion

The budget terms for the streamwise turbulent heat flux $\overline{u'^+\theta'^+}$ are shown in Fig. 14(a) along with those obtained by Kim (1988). The two data sets agree very well despite the difference in the thermal boundary conditions. There are three major terms in the logarithmic region: the production, the dissipation, and the temperature pressure-gradient correlation. The temperature pressure-gradient correlation always lies in the loss side. Both turbulent and molecular diffusion terms are appreciable only in the region of $y^+ < 30$. The production, dissipation, and molecular diffusion terms in Eq. (12) are further decomposed and shown in Fig. 14(b). In the production term, the component due to the streamwise temperature gradient is negligibly small over the whole cross section, while the two other components make almost the same contribution to the budget of $\overline{u'^+\theta'^+}$. In both dissipation and diffusion terms, two kinds of molecular effects are comparable, but the conductive ones are slightly stronger because of $\mathrm{Pr} < 1$. Note that the profile of each term in the $\overline{u'^+u'^+}$ budget is quite similar to the corresponding term in the $\overline{u'^+u'^+}$ budget equation (10), which is shown in Fig. 15. This must have arisen from the high correlation between u' and θ' mentioned previously.

The budget for the wall-normal turbulent heat flux given by Eq. (13) is shown in Figs. 16(a), 16(b), and 16(c). Figure 16(a) shows that the agreement between the present and Kim's results is again fairly good. In the $\overline{v'^+\theta'^+}$ budget, the production and the temperature pressure-gradient correlation are dominant. The latter term can be split into two terms as follows:

$$-\overline{\theta'^+\frac{\partial p'^+}{\partial y^+}} = -\frac{\partial}{\partial y^+}\overline{(p'^+\theta'^+)} + \overline{p'^+\frac{\partial\theta'^+}{\partial y^+}}, \quad (14)$$

which are called a pressure diffusion term and a pressure temperature-gradient correlation term, respectively. As shown in Fig. 16(b), these two terms behave almost contrary to each other and more drastically than their sum. It is noted that the sign of the pressure temperature-gradient term reverses near the wall; this happens also in the $\overline{u'v'}$ budget and is considered due to the splatting effect (Moin and Kim, 1982). Figure 16(b) also shows that the production by the streamwise temperature gradient is again negligible if compared with that by the wall-normal temperature gradient. The dissipation and molecular terms are generally very small, and they are effective only in the viscous sublayer as shown in Fig. 16(a). Their component terms are represented in Fig. 16(c), where the conductive terms are again slightly larger than the viscous ones as in Fig. 14(b).

In general, the budget of $\overline{v'^+\theta'^+}$ is very similar to that of the Reynolds shear stress given by Eq. (11), which is shown in Fig. 17.

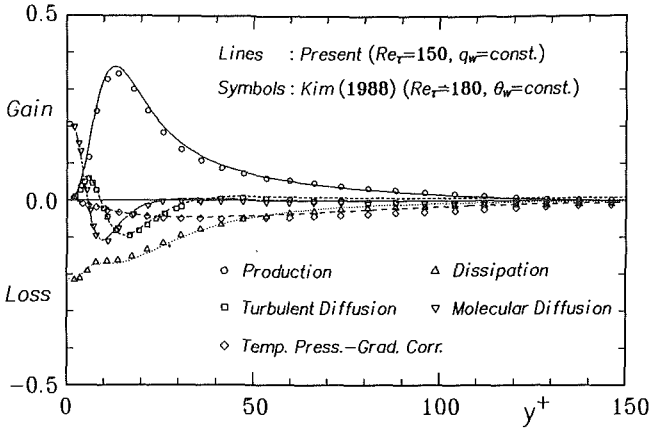

(a)

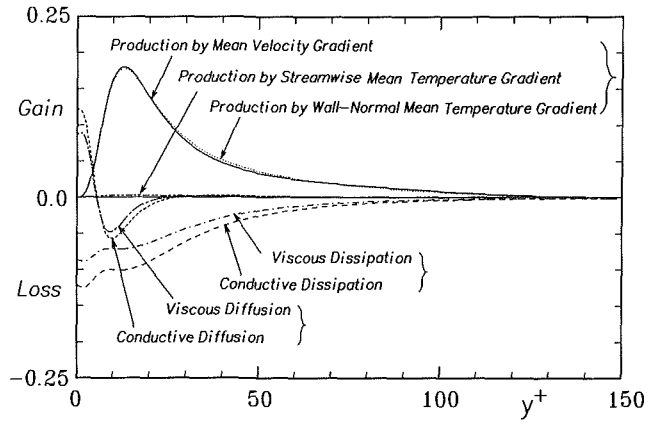

(b)

Fig. 14 Budget of the streamwise turbulent heat flux $\overline{u'\theta'}$: (*a*) comparison with the data of Kim (1987), (*b*) decomposition of the production, dissipation, and diffusion terms

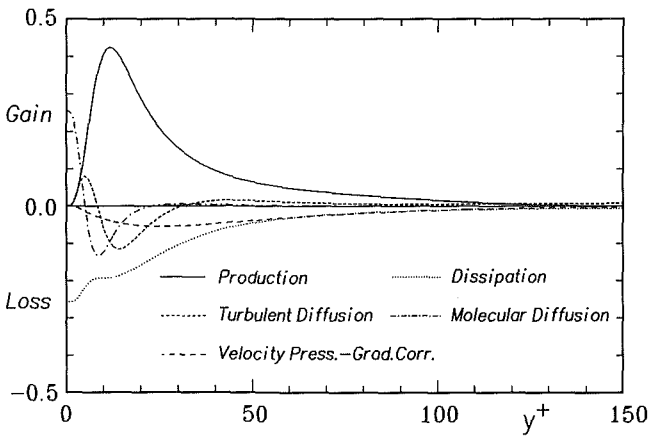

Fig. 15 Budget of the Reynolds stress $\overline{u'u'}$ (Kuroda, 1990)

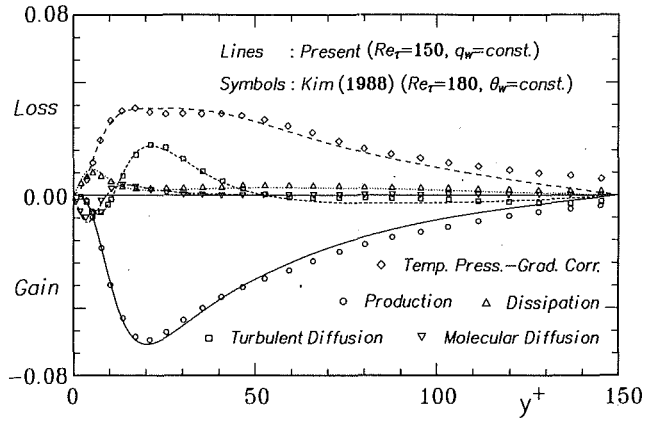

(a)

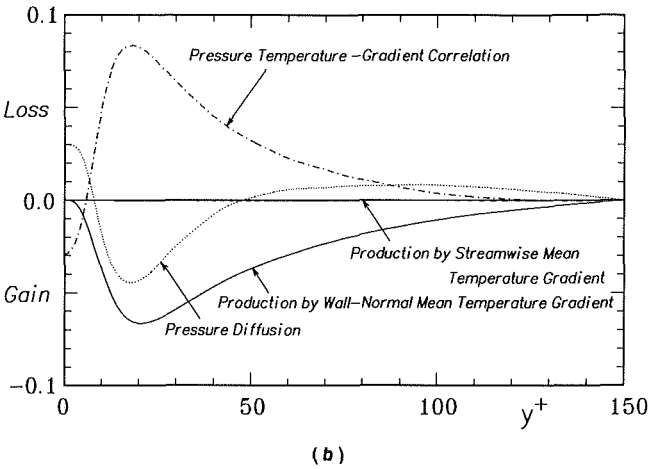

(b)

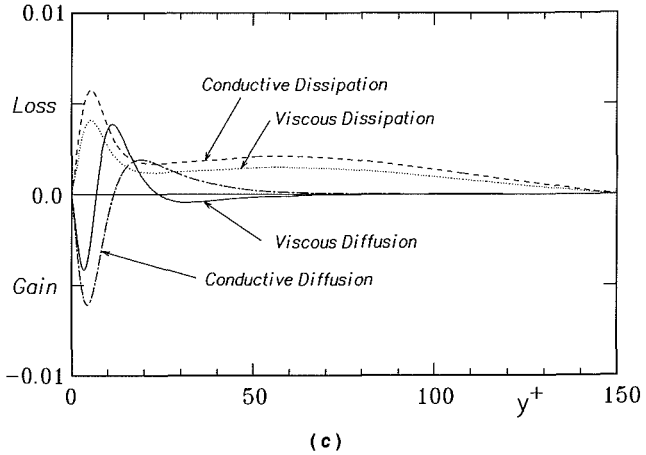

(c)

Fig. 16 Budget of the wall-normal turbulent heat flux $\overline{v'\theta'}$: (a) comparison with the data of Kim (1987), (b) decomposition of the production and pressure correlation terms, (c) decomposition of the dissipation and diffusion terms

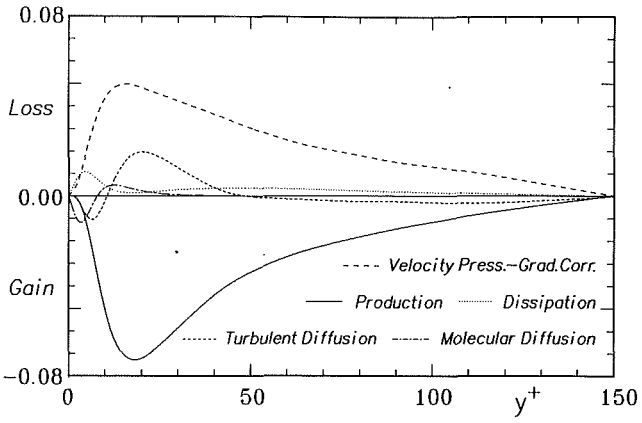

Fig. 17 Budget of the Reynolds stress $\overline{u'v'}$ (Kuroda, 1990)

Conclusions

A direct numerical simulation of the fully developed two-dimensional turbulent channel flow between two isoflux walls at a low Reynolds number and Pr = 0.71 was carried out, and various thermal turbulence statistics calculated were extensively compared with the previous experimental and numerical results. The following conclusions are derived:

1 The Nusslet number obtained is in good agreement with that recommended by Kays and Crawford (1980).

2 Despite the differences in the thermal boundary condition and the Reynolds number, the thermal turbulence statistics and their budgets presently obtained agree fairly well with those of Kim (1988) and of Kim and Moin (1989).

3 The temperature fluctuation is confirmed to be highly correlated with the streamwise velocity fluctuation, particularly near the wall. The correlation coefficient between them reaches as high as 0.96 at $y^+ = 8$. The streamwise and spanwise two-point correlations of θ' and u' show similar behavior near the wall. The cross correlation coefficient between v' and θ' closely agrees with that between u' and v'. In addition, the skewness and flatness factors of $v'\theta'$ and $u'v'$ also coincide well. These facts represent strong similarities between the turbulent transport mechanisms for momentum and heat.

4 In contrast to the empirical correlations, the turbulent Prandtl number calculated remains almost constant toward the wall. It reaches a mild maximum of about 1.1 at $y^+ \simeq 50$ and decreases gradually away from the wall. Both velocity and temperature dissipation time scales increase monotonically with the wall distance, but the former is always larger than the latter. The change in the time-scale ratio across the channel is modest, although it has a local maximum of about 0.8 at $y^+ \simeq 20$.

5 The detailed budgets for the temperature variance, its dissipation rate, and the turbulent heat fluxes are calculated. There are close similarities between them and those for the turbulent kinetic energy, its dissipation rate, and the Reynolds stresses. In the budget for k_θ, only the production and dissipation are dominant far from the wall. There are the three major production mechanisms that maintain ϵ_θ and balance with the dissipation. In the $\overline{u'\theta'}$ budget, the temperature pressure-gradient correlation and the dissipation act as major sink terms, but the former is predominantly effective in the $\overline{v'\theta'}$ budget. In general, the molecular diffusive terms are negligible except in the viscous sublayer. Among the molecular diffusion and dissipation terms of $\overline{u'\theta'}$ and $\overline{v'\theta'}$, the conductive ones are larger than the viscous ones for Pr < 1.

Acknowledgments

The authors acknowledge the financial support through the Grant-in-Aids for Cooperative Research (No. 02302043) by the Ministry of Education, Science, and Culture.

References

Béguier, C., Dekeyser, I., and Launder, B. E., 1978, "Ratio of Scalar and Velocity Dissipation Time Scales in Shear Flow Turbulence," *Physics of Fluids*, Vol. 21, pp. 307–310.

Blackwell, B. F., Kays, W. M., and Moffat, R. J., 1972, "The Turbulent Boundary Layer on a Porous Plate: An Experimental Study of the Heat Transfer Behavior With Adverse Pressure Gradients," Report HMT-16, Mech. Eng. Dept, Stanford University, Stanford, CA.

Bremhorst, K., and Bullock, K. J., 1973, "Spectral Measurements of Turbulent Heat and Momentum Transfer in Fully Developed Pipe Flow," *International Journal of Heat and Mass Transfer*, Vol. 16, pp. 2141–2154.

Cebeci, T., 1973, "A Model for Eddy Conductivity and Turbulent Prandtl Number," ASME JOURNAL OF HEAT TRANSFER, Vol. 95, pp. 227–234.

Hishida, M., Nagano, Y., and Tagawa, M., 1986, "Transport Process of Heat and Momentum in the Wall Region of Turbulent Pipe Flow," *Proceedings of the 8th International Heat Transfer Conference*, C. L. Tien et al., eds., Hemisphere Publishing Corp., Washington, DC, Vol. 3, pp. 925–930.

Iritani, Y., Kasagi, N., and Hirata, M., 1984, "Heat Transfer Mechanism and Associated Turbulence Structure in a Near-Wall Region of a Turbulent Boundary Layer," in: *Turbulent Shear Flows IV*, L. J. S. Bradbury et al., eds., Springer-Verlag, Berlin, pp. 223–234.

Isshiki, S., 1990, Private Communication.

Kader, B. A., 1981, "Temperature and Concentration Profiles in Fully Turbulent Boundary Layers," *International Journal of Heat and Mass Transfer*, Vol. 24, pp. 1541–1544.

Kasagi, N., Kuroda, A., and Hirata, M., 1989, "Numerical Investigation of Near-Wall Turbulent Heat Transfer Taking Into Account the Unsteady Heat Conduction in the Solid Wall," ASME JOURNAL OF HEAT TRANSFER, Vol. 111, pp. 385–392.

Kays, W. M., and Crawford, M. E., 1980, *Convective Heat and Mass Transfer*, 2nd ed, McGraw-Hill, New York.

Kim, J., Moin, P., and Moser, R., 1987, "Turbulence Statistics in Fully Developed Turbulent Channel Flow at Low Reynolds Number," *Journal of Fluid Mechanics*, Vol. 177, pp. 133–166.

Kim, J., 1988, "Investigation of Heat and Mass Transport in Turbulent Flows via Numerical Simulation," in: *Transport Phenomena in Turbulent Flows: Theory, Experiment and Numerical Simulation*, M. Hirata and N. Kasagi, eds., Hemisphere Publishing Corp., Washington, DC, pp. 157–170.

Kim, J., and Moin, P., 1989, "Transport of Passive Scalars in a Turbulent Channel Flow," in: *Turbulent Shear Flows VI*, J.-C. André et al., eds., Springer-Verlag, Berlin, pp. 85–96.

Kline, S. J., and Afgan, N. H., eds., 1990, *Near-Wall Turbulent: 1988 Z. Zarić Memorial Conference*, Hemisphere Publishing Corp., Washington, DC.

Krishnamoothy, L. V., and Antonia, R. A., 1987, "Temperature-Dissipation Measurements in a Turbulent Boundary Layer," *Journal of Fluid Mechanics*, Vol. 176, pp. 265–281.

Kuroda, A., 1990, "Direct Numerical Simulation of Turbulent Couette-Poiseuille Flows" (in Japanese), Dr. Eng. Thesis, Department of Mechanical Engineering, The University of Tokyo, Tokyo, Japan.

Launder, B. E., 1976, "Heat and Mass Transport," in: *Topics in Applied Physics*, Vol. 12, P. Bradshaw, ed., Springer-Verlag, Berlin, pp. 231–287.

Launder, B. E., 1988, "On the Computation of Convective Heat Transfer in Complex Turbulent Flows," ASME JOURNAL OF HEAT TRANSFER, Vol. 110, pp. 1112–1128.

Mansour, N. N., Kim, J., and Moin, P., 1988, "Reynolds-Stress and Dissipation-Rate Budgets in a Turbulent Channel Flow," *Journal of Fluid Mechanics*, Vol. 194, pp. 15–44.

Moin, P., and Kim, J., 1982, "Numerical Investigation of Turbulent Channel Flow," *Journal of Fluid Mechanics*, Vol. 118, pp. 341–377.

Moin, P., and Spalart, P. R., 1989, "Contributions of Numerical Simulation Data Bases to the Physics, Modeling, and Measurement of Turbulence," in: *Advances in Turbulence*, W. K. George and R. Arndt, eds., Hemisphere Publishing Corp., Washington, DC, pp. 11–38.

Nagano, Y., and Kim, C., 1988, "A Two-Equation Model for Heat Transport in Wall Turbulent Shear Flows," ASME JOURNAL OF HEAT TRANSFER, Vol. 110, pp. 583–589.

Perry, A. E., and Hoffmann, P. H., 1976, "An Experimental Study of Turbulent Convective Heat Transfer From a Flat Plate," *Journal of Fluid Mechanics*, Vol. 77, pp. 355–368.

Subramanian, C. S., and Antonia, R. A., 1981, "Effect of Reynolds Number on a Slightly Heated Turbulent Boundary Layer," *International Journal of Heat and Mass Transfer*, Vol. 24, pp. 1833–1846.

Tennekes, H., and Lumley, J. L., 1972, *A First Course in Turbulence*, MIT Press, Cambridge, MA.

Wassel, A. T., and Catton, I., 1973, "Calculation of Turbulent Boundary Layers Over Flat Plates With Different Phenomenological Theories of Turbulence and Variable Turbulent Prandtl Number," *International Journal of Heat and Mass Transfer*, Vol. 16, pp. 1547–1563.

Yoshizawa, A., 1988, "Statistical Modelling of Passive-Scalar Diffusion in Turbulent Channel Flow," *Journal of Fluid Mechanics*, Vol. 195, pp. 541–555.

Impingement Cooling of Electronics

B. R. Hollworth
Associate Professor,
Division of Mechanical Engineering,
Alfred University,
Alfred, NY 14802

M. Durbin
Undergraduate Research Associate,
Mechanical Engineering Department,
Gonzaga University,
Spokane, WA 98124

Experiments were conducted to determine the performance of a system of low-velocity air jets used to cool a simulated electronics package. The test model consisted of a uniform array of rectangular elements mounted to a circuit board. Each element was cooled by a cluster of four jets, and the spent fluid was vented at one end of the channel formed between the circuit board and the plate from which the jets were discharged. Reported are measurements of system pressure drop and convective heat transfer coefficients for elements at various sites within the array. Results indicate that (for the geometry tested) the largest portion of the total pressure drop occurs across the jet orifices. Further, the crossflow of spent air appears to enhance heat transfer for those elements near the exit end of the channel.

Introduction

The miniaturization of electronics circuits has led to continually increasing levels of heat dissipation per unit of component surface area. This trend has provided motivation, during the past several years, for a significant volume of research related to electronics cooling. Objectives have been to generate more reliable and comprehensible data for existing cooling systems and to develop systems that offer superior cooling performance.

In a typical package, heat dissipating elements are mounted to circuit boards, which are stacked within an enclosure. Cooling is accomplished using a fan or blower to move a low-velocity airflow through the passages between adjacent boards. A number of investigators have made heat transfer measurements for such systems. Papers by Arvizu and Moffat (1982), Sparrow et al. (1982), and Wirtz et al. (1985) are representative. This type of direct air cooling offers the advantages of being simple, reliable, and relatively inexpensive. However, it is suitable only for low to moderate heat loads.

The need to explore thermal management techniques that offer higher cooling rates, while retaining air as the working fluid, is apparent. One such technique is impingement cooling, in which a solid surface is cooled by an array of fluid jets. It is well established that this scheme produces very high rates of convective heat transfer with minimal expenditure of flow.

Impingement has been, for a number of years, an accepted technique for cooling hot section components in gas turbine engines. In fact, this particular application has historically driven most of the research related to impingement heat transfer. Past experiments have dealt mainly with jets impinging on flat or smooth curved surfaces, such as would be encountered in these engines. Papers by Kercher and Tabakoff (1970), Metzger and co-workers (1969, 1979), and Hollworth and co-workers (1978, 1987) are typical. In addition, the high supply pressures (several bars) available in gas turbine engines usually result in cooling system designs with widely spaced jets having very high (i.e., near sonic) velocities.

In a typical electronics package, the surface geometry is characterized by large (relative to the jets themselves) blocklike elements attached to an otherwise flat surface. The elements are heated while the surface is essentially adiabatic. It is apparent that heat transfer data from earlier (i.e., gas turbine oriented) studies cannot be applied directly to the design of electronics cooling systems, because of such major differences in target surface geometry and thermal boundary conditions.

Thus, the objective of our work was to investigate impingement specifically as a strategy for cooling of electronics. Experiments were conducted to measure system pressure drop and element heat transfer. In addition, tests were conducted to characterize the so-called "thermal wakes" generated by heat dissipation elements within the array. Results were correlated in terms of airflow and system geometry.

Experimental Apparatus and Methods

Figure 1 shows the test surface for which measurements were made. It is essentially a laboratory model of a regular in-line array of identical modules, mounted to a flat printed circuit board. The array has 8 rows, each containing 5 elements. Each element has a square planform with side length $L = 25$ mm and height $B = L/4$. The array is a fairly sparse one having $S = L$. This geometry had already been used for a prior study by Wirtz et al. (1985) in which the array was cooled by a uniform flow of air parallel to the P.C. board. Thus, a comparison of the cooling capabilities of the two schemes is readily made by comparing moduler heat transfer rates at the same airflow (or at the same pumping power).

Individual modules are machined from aluminum, and pol-

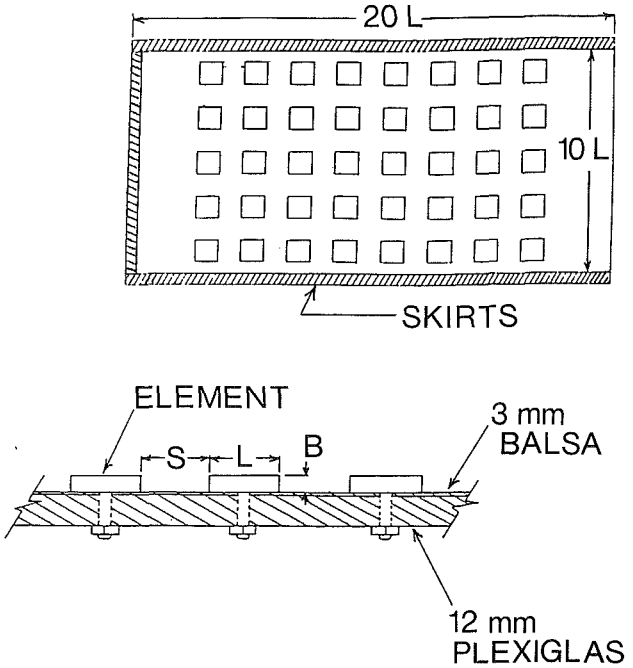

Fig. 1 Test surface

Contributed by the Heat Transfer Division for publication in the JOURNAL OF HEAT TRANSFER. Manuscript received by the Heat Transfer Division August 1991; revision received February 1992. Keywords: Electronic Equipment, Jets. Associate Technical Editor: F. P. Incropera.

ished to a mirror finish to minimize thermal radiation. Four of them are hollowed out to accommodate 60-ohm resistive heaters. The cavity size is such that the wall thickness of the module is 2 mm. Each such module is also instrumented with two 36 gage thermocouples to measure its surface temperature. These are soldered to its inner surface, one near the center of its leading edge relative to the channel flow and one near its trailing edge. Heated elements are essentially isothermal. During testing, the maximum observed difference between their readings was 1.8°C. The module heat transfer coefficient is easily deduced from the heat input (obtained by measuring current and voltage from the d-c power supply that drives the element heaters) and the measured element temperature and air temperature. The heater voltage is measured with a DVM connected across the power leads to the active element. The heater current is determined by measuring (with the same DVM) the voltage drop across a precision 1.0 ohm resistor in series with the heater. These heated elements can be moved to any location within the array at which local heat transfer is to be measured. Each of the remaining modules is instrumented with a single thermocouple near its centroid. All thermocouples are calibrated against a standard traceable to NBS: We can measure element and gas temperatures to about ±0.2°C.

The test surface itself is a laminated assembly of 3 mm balsa wood on 12 mm plexiglass, with the balsa being located on the side adjacent to the heated elements. The plexiglass provided rigidity, while the balsa (which has a low thermal conductivity) minimizes conduction losses form the back faces of the elements and lateral spreading of heat in the plane of the test surface. While the test surface itself was not instrumented with thermocouples, a simple on-dimensional analysis indicated that conduction losses through this surface never exceeded 4 percent of the heat input to a module. Furthermore, the same test surface was used for the earlier study by Wirtz et al. (1985) in which an infrared scanning system was used to map thermal wakes. The resulting thermal images showed very little spreading of heat into the balsa surface adjacent to heat-dissipating elements. Modules are held to the surface with threaded nylon fasteners, and electrical leads are routed out via small holes drilled through the wall behind each element.

Figure 2 shows the entire test facility. Impingement air is supplied by a compressor and dried and filtered upstream of the test rig. The flow rate is controlled using a pressure regulator and hand-operated valves, and measured with a laminar flow element accurate to ±2 percent of instantaneous reading. This device is essentially a constant area tube containing a porous medium. The hydraulic diameter of the flow passage is small enough so that flow is laminar, and the resulting drop in static pressure across the element (which we measured with an inclined manometer) is directly proportional to mass flow rate. For the particular unit we used, the pressure drop is about

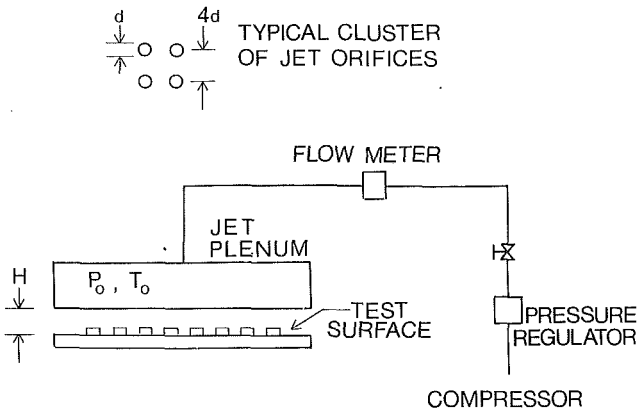

Fig. 2 Test system

16 mm of water at our minimum flow (4.0×10^{-3} kg/s) and 153 mm at our maximum flow (4.0×10^{-2} kg/s).

The jet plenum is an airtight box made from 12 mm plexiglass with outside dimensions 28 cm × 56 cm × 9 cm. One face of the plenum is the orifice plate from which air jets are discharged toward the array of modules. Air enters the plenum at room temperature and is then distributed among the jet orifices. A baffle within the plenum prevents a "ram effect" at those jet orifices opposite the air inlet tube, which would result in locally increased jet flow. The plenum has two taps for measurement of the total pressure (P_o) and two probes for measurement of the plenum temperature (T_o). The temperature is measured with thermocouples of the type described above, and the plenum pressure is measured relative to atmospheric pressure with an inclined manometer. Plenum conditions (P_o, T_o) are measured between the baffle and the orifice plate. Jets issuing from the orifice plate impinge upon the test surface described in the previous paragraph. The clearance H (see Fig. 2) is set by the side skirts shown in Fig. 1. These skirts serve as spacers between the orifice plate and the modules, and they contain the spent coolant to exhaust only at the ends of the array.

Each module is cooled by a cluster of air jets (see Fig. 2). Because the modules are square in planform, the natural choice is to adopt clusters that are square arrays of jets. For our study the clusters were all identical, and had the following geometries:

Number of jets per cluster = 4
Jet orifice diameter (d) = 3.18 mm
Center-to-center spacing between jet orifices = $4d$
Jet orifice design: square-edged with length/diameter = 4

The geometric center of each cluster is aligned with the geometric center of the corresponding heated element, so that

Nomenclature

A = element surface area, m^2
B = element height, mm
d = jet orifice diameter, mm
E = voltage drop across element heater, V
h = element heat transfer coefficient, W/m^2-°C
H = channel height, mm
I = current to element heater, A
L = side length of element, mm
m = coolant mass flow rate, kg/s
n = number of coolant jets
N = row number
P_a = atmospheric pressure, N/m^2
q = rate of convective heat transfer from heated element, W
Q = volume flow rate of coolant, m^3/s
Re = jet Reynolds number, defined by Eq. (7)
S = spacing between elements, mm
T_a = air temperature, °C
T_H = surface temperature of active element, °C
T_O = plenum temperature, °C
T_s = element surface temperature, °C
V = mean jet exit velocity, m/s
V_e = mean velocity at channel exit, m/s
W = width of channel, mm
Z = jet standoff, mm
ΔP = pressure difference, N/m^2
ΔP_o = loss in total pressure, N/m^2
ΔT = difference between element surface temperature and air temperature, °C
θ = dimensionless temperature rise defined by Eq. (10)
μ = dynamic viscosity of air, N-S/m^2
ρ = density of test air, kg/m^3
ρ_{sl} = sea level density of air, kg/m^3

each jet is (nominally) responsible for cooling one fourth of the element's surface.

The test fluid used for these experiments was air near S.T.P. (S.T.P. denotes standard sea level conditions: pressure = 1.01×10^5 Pa, temperature = 15°C) so that the Prandtl number of the fluid was held essentially constant at 0.71. Jet velocities were low enough, for all of the tests run, so that the air could be assumed incompressible.

Procedures for running the various tests were straightforward. Measurements of system pressure drop were conducted with all of the elements in place, but with none of them activated. Appropriate side skirts were chosen to determine H/B, and the rig (plenum, skirts, test surface) clamped tightly together. The air flow rate (m) was set using the manually operated valves (see Fig. 2) in the air supply line, and its value was deduced from the pressure drop measured across the laminar element with a manometer. The constant pressure provided by the regulator and the constant back pressure (i.e., ambient) ensured that the flow did not change measurably during the test run. System pressure loss was measured for both the "weak channel flow" case and the "strong channel flow" case. For the former, spent fluid was discharged at both ends of the channel formed between the plenum and the test surface. For the latter, a third skirt was installed at one end of the channel, so that spent air was discharged entirely at the other end.

For measuring element heat transfer, the rig was assembled as above; one of the elements containing a heater was installed at the site (row, column) where a measurement was required. The flow rate was set as above, and the heater power supply adjusted until the element temperature reached the desired value: usually 40°C above the jet plenum temperature. All other elements remained inactive. After the operating conditions had stabilized, the heater power, element and plenum temperatures, flow rate, etc., were recorded.

The region in the vicinity of an active (i.e., electrically heated) element in which the air temperature is measurably influenced by its heat input is termed the element's thermal wake. Any passive (i.e., not electrically heated) element that lies in such a wake assumes a so-called adiabatic element temperature, at which it is in thermal equilibrium with the heated wake fluid. Tests were conducted to characterize these wakes for an impingement cooled array. A single active element was installed in the center column of the array. The desired airflow was set and the active element's power input was adjusted until its temperature exceeded T_o by nominally 40°C. When conditions had stabilized, temperatures of passive elements in the center column and the two flanking columns were measured.

Tests to determine pressure drop, element heat transfer, and thermal wake effects were run over ranges of the test variable that the authors felt appropriate for electronics cooling. These were:

Channel height (H/B): 1.5, 2, 3
Coolant flow (m): 4.0×10^{-3} to 4.0×10^{-2} kg/s

Measurements of heat transfer were made on elements in each of the 8 rows of the array. Wake measurements were performed with the active element in rows $N = 1$, 2, 5, and 6 of the array. Rows are numbered consecutively with row 1 at the closed end of the channel. Heat transfer and wake measurements were made only for the "strong channel flow" case.

Results

It is necessary to have the pressure versus flow characteristics of a cooling system in order to specify an appropriate fan or blower to deliver air. Moreover, the product of volumetric flow rate and corresponding pressure drop represents the pumping power required to overcome losses in the cooling system. To this must be added any additional losses that occur in ductwork upstream and downstream of the cooling system proper.

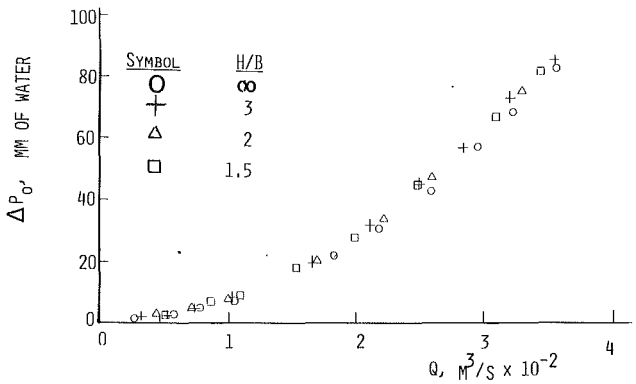

Fig. 3 Pressure drop versus airflow, channel open at both ends

Strictly speaking, it is the drop in *total* or stagnation pressure that one needs for determining the specification of an appropriate air mover/motor combination. For each volume flow rate (Q), an inclined manometer was used to measure the jet plenum pressure (P_o) relative to atmospheric pressure (P_a). Thus it indicated a reading given by

$$\Delta P = P_o - P_a. \tag{1}$$

While the term P_o is a legitimate total pressure, P_a is essentially the static pressure of the air stream that exits the test section. Equation (1) must be corrected by adding the so-called dynamic pressure term to the exit static pressure. Furthermore, these tests were run in the M.E. lab at Gonzaga University (Spokane, WA), which is about 600 m above sea level. Thus, the density (ρ) of the test air was significantly less than sea level density (ρ_{sl}), and a second correction was applied to our data to refer them to sea level conditions. The resulting expression for the total pressure loss is

$$\Delta P_o = \frac{\rho_{sl}}{\rho} (\Delta P - 1/2\ V_e^2), \tag{2}$$

where V_e is the (mean) velocity of air discharged from the channel. It was calculated for each flow (Q) using

$$V_e = \frac{Q}{MWH} \tag{3}$$

where $M = 1$ when air is vented at only one end of the channel and $M = 2$ when it is vented at both ends. The quantity ΔP_o is the desired total pressure loss that would occur at sea level; it was found never to differ from ΔP by more than 7 percent.

Figure 3 shows the variation of pressure drop (expressed as ΔP_o) with volume flow rate, based on our experimental data. For all the test runs of this figure, air was allowed to vent at both ends of the channel. Results are shown for several values of the dimensionless channel height, H/B. Data for $H/B = \infty$ were obtained by removing the test surface altogether and discharging the air jets directly into the room; as such, this represents a useful reference case in which the pressure loss is attributable entirely to the jet orifices themselves. As H/B is decreased, the channel flow velocity increases (at fixed Q), and losses in the channel contribute increasingly to ΔP_o. However, Fig. 3 indicates that orifice losses are predominant for all of the geometries considered. Even for the narrowest channel tested ($H/B = 1.5$), about 90 percent (averaged over our range of Q) of the loss occurs in the orifices.

Figure 4 shows corresponding pressure drop data for the case in which all spent air is discharged at one end of the channel. This serves to increase channel flow velocities (exit plane velocities are twice those of Fig. 3 at the same Q) so that losses in the channel contribute more significantly to the total effect than was the case in Fig. 3. For example, channel losses

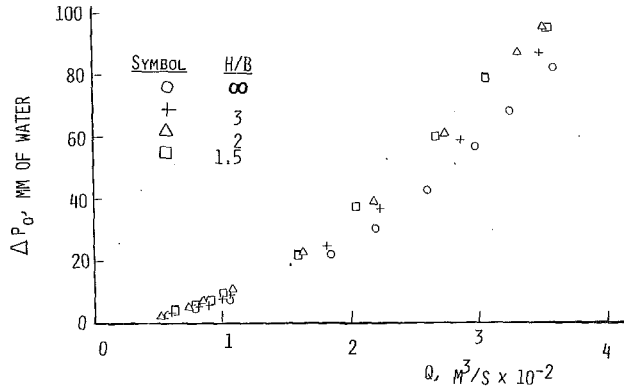

Fig. 4 Pressure drop versus airflow, channel open at one end

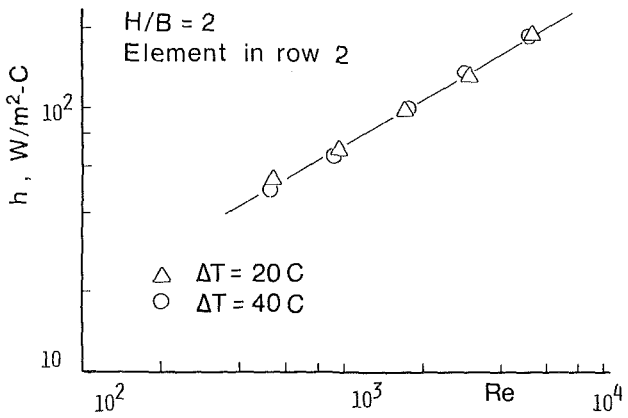

Fig. 5 Typical variation of heat transfer with jet flow

represent about 24 percent of the total (averaged over our range of Q) when $H/B=1.5$. From the measurements of Q versus ΔP at $H/B=\infty$, it was possible also to calculate the discharge coefficient (C) for the jet orifices. It was found that C depended upon the jet Reynolds number (Re) for $\mathrm{Re}<2000$ and that $C=0.77$ for the upper half of our flow range, $2000<\mathrm{Re}<5000$.

The cooling capability of a convective system is ordinarily expressed in terms of a heat transfer coefficient defined by

$$h=\frac{q}{A(T_s-T_a)} \tag{4}$$

The air temperature in Eq. (4) was taken to be equal to the jet plenum temperature and T_s was determined as the arithmetic mean of the readings from the element's two embedded thermocouples. The high thermal conductivity of the element material (aluminum) ensured that they would be essentially isothermal. We were measuring element-averaged heat transfer, so that the area A was determined by

$$A=L^2+4BL=0.00129\ \mathrm{m}^2. \tag{5}$$

It includes the total surface area of the component that is exposed to the coolant: the "top" of element (on which the jets impinge) as well as the four "sides" of the element. Finally, the rate of convective heat transfer (q) was determined from the electrical power input (EI) to the element using

$$q=EI-\Delta q. \tag{6}$$

In Eq. (6) the term Δq is a small correction for conduction and radiation losses from the element. The former was calculated assuming one-dimensional conduction through the plate to which the components were attached, and the latter was calculated assuming an emissivity of 0.06 for the element's surface. The correction never exceeded 5 percent of EI.

Figure 5 shows typical variations of the convection coefficient with cooling flow. Data shown are for an element in the center column of row 2. For pure forced convection, it is ordinarily assumed that q is proportional to the surface-to-fluid temperature difference (ΔT). Measurements of q were made at nominal ΔT's of 20°C and 40°C. As the figure shows, virtually identical h values were obtained for the two ΔT's. Thus there are no significant radiation or free convection effects, and all other tests were run using $\Delta T=40$°C.

Table 1 Variation of h within a typical row (No. 2) of the array

		Values of h, W/m²−°C		
H/B	Re	column	One column off center	Two columns off center
2	510	48	49	48
2	920	65	64	66
2	1640	94	94	92
2	2870	132	122	127
2	5040	189	183	192
3	510	48	46	48
3	930	*	64	65
3	1650	93	88	91
3	2890	*	123	129
3	5080	186	180	184

The test section was designed so that the flow would behave as if the array were infinite in the transverse direction. Under such conditions, h should not vary appreciably between elements within the same row. The heat transfer coefficient was measured for three elements in row No. 2, and the results appear in Table 1. Asterisks in the table indicate tests that were not run.

The cooling flow has been expressed as a (mean) jet Reynolds number defined by

$$\mathrm{Re}=\frac{4}{\pi}\frac{m}{n\mu d}, \tag{7}$$

where m is the total mass flow rate of air and n is the total number (160) of cooling jets. The column-to-column variation in h was found to be less than our experimental uncertainty (±5 percent), and all further tests were performed with active elements only in the center column.

Figure 6 shows the row-to-row variation in h for 3 jet Reynolds numbers, which span the range of flows for which we have data. The table below indicates the mass flow rate and mean jet exit velocity (V) that correspond to each Re:

Airflow level	Re	m, kg/s × 10⁻³	V, m/s
Low	510	4	2.7
Intermediate	1640	13	9.0
High	5040	40	27.6

The velocity V is deduced from measurements of m using

$$V=\frac{m}{\pi/4\rho nd^2}. \tag{8}$$

For $H/B=3$, h is nearly constant from one row to another. However, for the smaller spacing ($H/B=2$) there is a consistent tendency for h to increase as one approaches the open end of the channel. Typically both H/B yield nearly the same heat transfer near the closed end. However, at the open end (in row 8 for example) the h values for $H/B=2$ exceed those for $H/B=3$ by about 22 percent (average for the three flows of Fig. 6).

In the literature of impingement heat transfer, the flow of spent fluid in the channel is usually termed a crossflow; and these studies indicate that the behavior of Fig. 6 is due to two effects associated with the crossflow. First, there is a static pressure gradient in the channel, with the lowest pressure occurring at the open end. Because the plenum pressure is the same for all jets, the pressure differential is largest for those

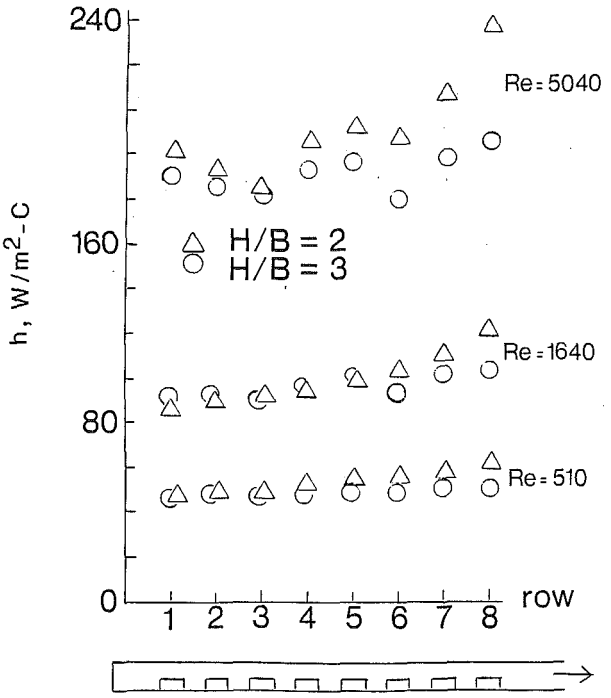

Fig. 6 Row by row variation in heat transfer

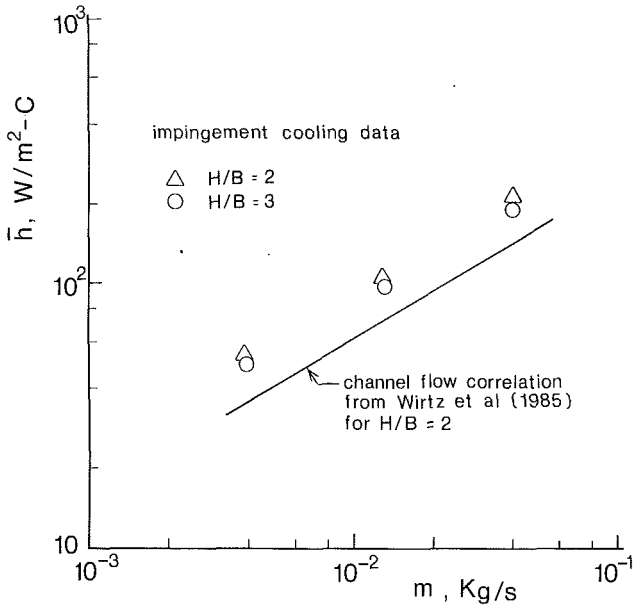

Fig. 7 Array-averaged heat transfer

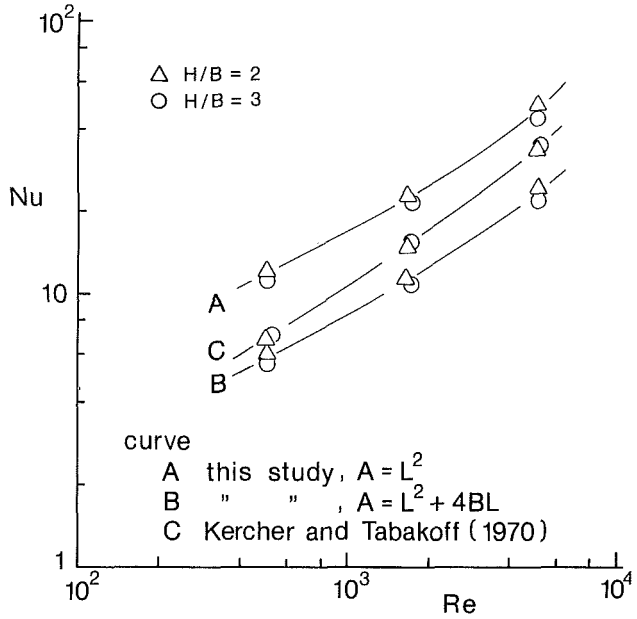

Fig. 8 Correlation of average heat transfer

near the exit. Hence the local flow per jet and the corresponding local impingement h are largest. Second, the h values reported for each element are averaged over its entire air-cooled surface. The jets impinge primarily on the top surface which, for our elements, represents 50 percent of A. The four sides (the remaining 50 percent of A) are cooled mainly by the channel flow. This crossflow is cumulative in the sense that it is the sum of all coolant introduced (as jets) farther upstream. Hence elements near the channel exit experience larger crossflow velocities and therefore increased heat transfer on their side surfaces.

It is possible that the difference in row by row variation in h for Re = 1640 and Re = 5040 in Fig. 6 is related to the characteristics of channel flows. The local pipe flow Reynolds number increases along the channel as jet flow is introduced. However, we can reasonably determine a nominal value based on the wetted perimeter of the channel (accounting for the presence of the elements) and the flow halfway along the channel (whose value is $m/2$). The resulting channel flow Reynolds numbers corresponding to the three jet Reynolds numbers of Fig. 6 (i.e., 510, 1640, and 5040) are roughly 700, 2100, and 6600, respectively. If one assumes that transition begins to occur at a channel flow Reynolds number around 2000, then this may provide an explanation of the observed behavior. Figure 6 also indicates that there is some periodicity superimposed upon the streamwise variations in h already discussed. This behavior is apparent for Re = 5040 and still observable at Re = 1640. The flow in a system such as this is extremely complex, and further work (flow visualization, etc.) is needed before either phenomenon can be explained with confidence.

Figure 7 shows the variation of array-averaged heat transfer with coolant mass flow rate. The data are shown compared to results obtained earlier (Wirtz et al., 1985) when the same matrix of elements was cooled by a channel flow of air. The impingement system yields heat transfer coefficients that exceed those of the conventional system by 50 percent (averaged over our test range of m). Strictly speaking, the h's reported by Wirtz et al. are based on so-called adiabatic element temperatures, to be discussed later in this paper as well. In the work reported here, heat transfer coefficients are based on the air plenum temperature T_o. However, heat transfer is measured for individual elements within the array with all other ones unheated. Under these conditions, the plenum temperature and the adiabatic element temperature are essentially identical. It was not possible to make such a comparison at equal pumping power as no pressure drop data was taken in the channel flow study.

Figure 8 shows our (average) heat transfer data replotted in the dimensionless variables generally used to correlate impingement data. The mean Nusselt number is defined as

$$\mathrm{Nu} = hd/K, \tag{9}$$

and the standoff ($Z = H - B$) is the distance between the orifice plate and the top surface of a typical element. It is difficult to make a direct comparison between our data and that of other investigators. To date, there are no published experiments dealing with impingement cooling of surface geometries such as found in electronics packages. Trabold and Obot (1987) measured heat transfer for jets impinging on a surface with

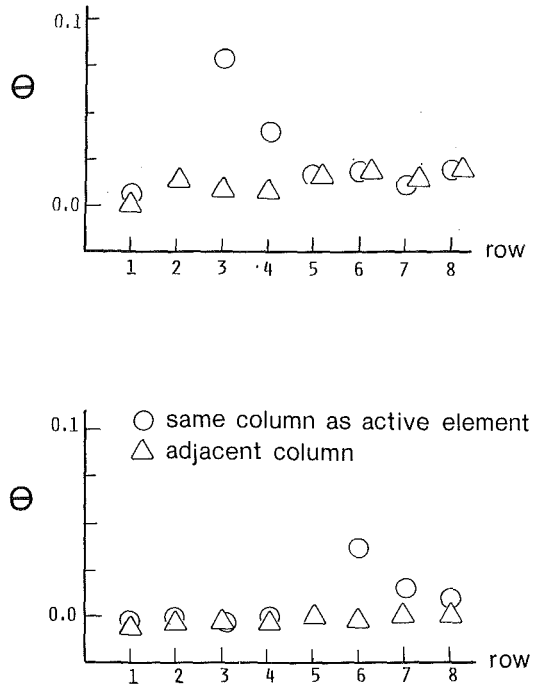

Fig. 9 Propagation of thermal wakes: (*a*) *H/B* = 3, Re = 510, active element in row 2; (*b*) *H/B* = 2, Re = 4950, active element in row 5

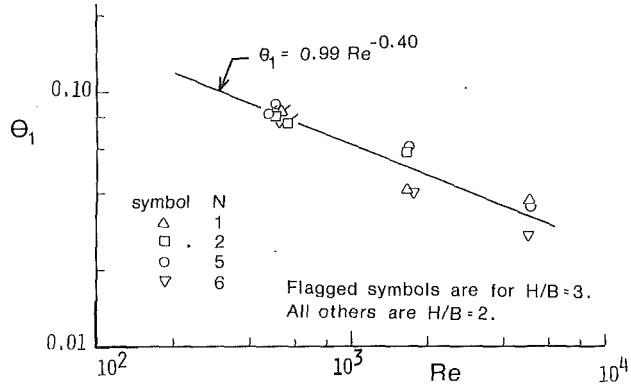

Fig. 10 Dependence of wake function on jet Reynolds number

roughness elements. However, the elements were transverse ribs whose size was small compared to the jet diameter. Furthermore, the entire surface, including the ribs, was isothermal.

Because our heated elements are large compared to the jets themselves, it seems more appropriate to compare our data to results obtained by others for jet arrays impinging on large, flat, isothermal surfaces. Figure 8 includes the correlation obtained by Kercher and Tabakoff (1970) for jet spacing/diameter = 4. Our heat transfer coefficient has been based on the total surface area of an element even though the jets impinge directly on only 50 percent of A; the remaining 50 percent is cooled (probably at a much lower rate) by the crossflow. Thus our Nu values are significantly lower (at each Re) than those of Kercher and Tabakoff, for whose experiment the *entire* heated surface was washed by jets. If one bases our h values on only the top surface area of the elements and further assumes that the remaining surfaces contribute no significant heat transfer (not entirely true of course) then our Nu values are exactly doubled at each Re. This results in the upper set of curves shown on Fig. 8. The fact that our heat transfer coefficients (defined these two ways) bracket those obtained by Kercher and Tabakoff implies a reasonable degree of agreement.

Each active element generates a so-called thermal wake. A typical passive element that resides in such a wake will be heated by the wake so that its adiabatic temperature (T_{ai}) will exceed that of the unheated fluid (T_o). Figure 9 shows distributions of passive element temperatures that result from heat input from a single active element, which will hereafter be referred to as element H. The temperature rise at a typical passive element is expressed in nondimensional form as

$$\theta \equiv \frac{T_{ai} - T_o}{T_H - T_o}, \tag{10}$$

where θ is zero for those that reside outside of the wake.

Figure 9(*a*) shows a typical row-by-row variation of θ produced when element H is in the center column (hereafter identified as column C) of row 2. Behavior is somewhat similar to that which has been observed by Arvizu and Moffat (1982) and Wirtz et al. (1985) for module arrays in conventional channel flows; for elements in the same column as element H, the temperature rise is largest for the passive element immediately downstream from the active one. The effect diminishes for elements farther downstream. The jet fluid that impinges on (and is heated by) element H is eventually turned downstream by the crossflow. For Fig. 9(*a*), the active element is near the upstream end of the channel where the crossflow is relatively weak. Apparently the heated fluid from element H is able to penetrate sufficiently in the traverse direction to produce a small but detectable temperature rise in flanking columns. This tendency was observed for all tests in which element H was in rows $N = 1$ and $N = 2$.

Figure 9(*b*) shows corresponding results produced when element H is in row 5. The behavior of passive elements in column C differs little (at the same Re) from that of Fig. 9(*a*). Row 5 is near the exit end of the channel, so that the crossflow is relatively strong. There is less lateral penetration of warm fluid from element H, so that the temperature rise in flanking columns is close to negligible.

It needs to be pointed out that the measured temperature rise ($T_{ai} - T_o$) terms were small. Those in column C never exceeded 4.0°C, while those in flanking columns were never greater than 1.0°C. Our uncertainty in measured temperature differences was estimated to be ±0.3°C. These results must be viewed with this in mind.

For a heated element in row N of column C, the largest temperature rise occurred always at the element in row $(N+1)$ of the same column. Its magnitude did not vary appreciably when the active element was moved from one row to another, nor was it affected strongly by H/B. However, there was a fairly pronounced Reynolds number effect. It is interesting to note that in an experiment dealing with channel flow cooling of electronics, Arvizu and Moffat (1982) found that $\theta_1 \propto \mathrm{Re}_L^{-0.3}$ where Re_L is a Reynolds number based on the velocity in the channel and the side length of a component. Figure 10 shows the nondimensional temperature rise (θ_1) for the element in row $(N+1)$ as a function of the (jet) Reynolds number. At each Re, θ_1 is the average of the values measured at the various H/B and N (i.e., active element row) for which we had data.

It is generally accepted that the convective heat transfer for element i in a package can be calculated using

$$q_i = h_i A (T_{si} - T_{ai}), \tag{11}$$

where the local adiabatic element temperature (T_{ai}) acts as the effective fluid temperature. Heat inputs from other modules in the array affect T_{ai}, but h_i is determined only by airflow, geometry, and the location of i in the array. In a typical situation, element i may lie in the thermal wakes of several other active elements. For channel flow cooling, Arvizu and Moffat (1982) have suggested a linear superposition technique in which the air temperature rise ($T_{ai} - T_o$) at element i is deduced simply

by adding the contributions that each other element would produce at i if only that element were active. While it is plausible that such a superposition method is applicable to impingement cooled packages, we have not as yet conducted experiments to test its validity. In spite of the discussion related to Eq. (11), we have chosen to define element heat transfer coefficients in this paper using Eq. (4), in which the plenum temperature T_o replaces T_{ai}. Use of the heat transfer data presented here is made simpler as the same effective fluid temperature is applied to all elements in the array. Furthermore, the value of T_o is readily available to the practitioner in a typical design situation.

The quantities reported in this paper are typically determined from the results of several lab measurements. As such, the uncertainty in each depends upon the errors in the measurements from which it was derived. These were estimated using the method suggested by Holman (1989).

Flow-related variables include the Reynolds number and the cooling system pressure loss. The uncertainty in Re depends upon the accuracy (± 2 percent of instantaneous reading) of the flowmeter and the tolerance (± 0.05 mm) on the jet orifice diameter. It was estimated to be ± 4.5 percent. The uncertainty in ΔP_o depends upon the accuracy with which the inclined manometer could be read (± 1 mm) and, to a lesser degree, upon uncertainties in the air density and the small correction (see Eq. (2)) for the dynamic pressure of the vented coolant. The maximum manometer deflection, 101 mm of water, was observed at the high end of our flow range. Under these conditions, the uncertainty in ΔP_o was estimated to be ± 2.5 percent. At the low end, the deflection was barely detectable to the eye, and the uncertainty could exceed 100 percent. A more realistic figure is the uncertainty in ΔP_o at the middle of our range of flows; this value is ± 5.5 percent.

Thermal variables include the module convection coefficient and the wake function. The uncertainty in h depends upon uncertainties in measuring voltages across the element heaters and across the calibrated resistor (± 1 percent), resistance of the calibrated resistor (± 1 percent), and the element-to-fluid temperature difference (± 0.4°C). Furthermore, the tolerance on each dimension of an element (± 0.13 mm) gives an uncertainty of ± 1.3 percent on its surface area. Finally, the small correction calculated for conduction and radiation losses was assumed (very conservatively) to have an uncertainty of ± 50 percent. These all contribute to an uncertainty in h of somewhat less than ± 5 percent.

The wake function θ was determined from Eq. (10) using measured values of the three temperatures indicated. For all the tests reported, the denominator $(T_H - T_o)$ had a nominal value of 40°C, and the uncertainty in measuring individual temperatures was ± 0.3°C. The largest observed value of the numerator $(T_{ai} - T_o)$ was about 4°C. Under these conditions, the uncertainty in θ is ± 11 percent. For very small θ, the uncertainty can exceed 100 percent. However, under such conditions the thermal wake effect is of no consequence anyway.

Conclusions

Experiments were conducted to characterize the performance of an impinging air jet system used for electronics cooling. The test surface was a model of a regular array (eight rows, five elements per row) of identical rectangular elements mounted on a P.C. board. Each element was cooled by a cluster of four jets impinging on its top surface. Jets issued from a plenum, and the spent fluid was vented at one or both ends of the channel formed between the plenum and the test surface. Significant findings were the following:

1 System total pressure drop (ΔP_o) occurred, for the most part, across the jet orifices for the (fairly spaced) element arrays tested. Even for the narrowest channel tested ($H/B = 1.5$) the orifices were responsible for about 90 percent of ΔP_o when air was vented at both ends of the channel, and for about 75 percent of ΔP_o when it was vented at only one end.

2 The element heat transfer coefficient (h) was measured for the case in which air was discharged at only one end of the channel. The row-to-row variation in h was found to be small for our larger channel height $H/B = 3$. For $H/B = 2$, however, h increased significantly toward the open end of the channel. This was attributed to the locally stronger crossflow, which gives increased cooling on the sides of the elements on which the jets do not directly impinge.

3 Jet arrays yield, in general, significantly higher levels of heat transfer than conventional fluid cooling methods; this was undoubtedly the case for the top surfaces of elements on which jets directly impinged. However, the sides of the elements (which represent 50 percent of their surface area for our system) must rely mainly on crossflow cooling. The net effect is that the impingement system gave array-averaged heat transfer exceeding that of conventional channel flow cooling (applied to the same package) by about 50 percent at the same airflow. We expect a greater performance increment for designs in which jets are deployed over a larger fraction of the available surface.

4 The thermal wake effect was most pronounced in the column containing the active element, with the element immediately downstream from it experiencing the greatest rise in adiabatic temperature. However, when the heated element was near the closed end of the channel, the locally weak crossflow allowed some penetration of warm fluid into adjacent columns.

Acknowledgments

The authors are grateful to the Gonzaga University Research Council, who supported this work during the summer of 1988.

References

Arvizu, D. E., and Moffat, R. J., 1982, "The Use of Superposition in Calculating Cooling Requirements for Circuit Board Mounted Electronic Componenets." IEEE Paper No. CH1781-4/82-0133.

Hollworth, B. R., and Berry, R. D., 1978, "Heat Transfer From Arrays of Jets With Large Jet-to-Jet Spacing," ASME JOURNAL OF HEAT TRANSFER, Vol. 100, pp. 352–357.

Hollworth, B. R., and Cole, G., 1987, "Heat Transfer to Arrays of Impinging Jets in a Crossflow," ASME *Journal of Turbomachinery*, Vol. 109, pp. 564–571.

Holman, J. P., 1989, *Experimental Methods for Engineers*, 5th ed., McGraw-Hill, New York, pp. 41–47.

Kercher, D. M., and Tabakoff, W., 1970, "Heat Transfer by a Square Array of Round Air Jets Impinging Perpendicular to a Flat Surface Including the Effect of Spent Air," ASME *Journal of Engineering for Power*, Vol. 92, No. 1, pp. 73–82.

Metzger, D. E., Yamashita, T., and Jenkins, G. W., 1969, "Impingement Cooling of Concave Surfaces With Lines of Circular Air Jets," ASME *Journal of Engineering for Power*, Vol. 91, p. 149.

Metzger, D. E., Florschuetz, L. W., Takeuchi, D. I., Behee, R. D., and Berry, R. A., 1979, "Heat Transfer Characteristics for Inline and Staggered Arrays of Circular Jets With Crossflow of Spent Air," ASME JOURNAL OF HEAT TRANSFER, Vol. 101, pp. 526–531.

Sparrow, E. M., Neithammer, J. E., and Chaboki, A., 1982, "Heat Transfer and Pressure Drop Characteristics of Arrays of Rectangular Modules Encountered in Electronic Equipment," *International Journal of Heat and Mass Transfer*, Vol. 25, No. 7, pp. 961–973.

Trabold, T. A., and Obot, N. T., 1987, "Impingement Heat Transfer Within Arrays of Circular Jets: Part II—Effects of Crossflow in the Presence of Roughness Elements," ASME *Journal of Turbomachinery*, Vol. 109, pp. 594–601.

Wirtz, R. A., Holloworth, B. R., and Fuller, H. A., 1985, "An Infrared Thermographic Study of Convection in an Array of Surface Mounted Components," *Proceedings, Fifth Annual International Electronics Packaging Conference*, pp. 497–507.

Effects of Wall Conduction and Darcy Number on Laminar Mixed Convection in a Horizontal Square Porous Channel

G. J. Hwang
Professor.
Mem. ASME

C. H. Chao
Ph.D. Candidate.

Department of Power Mechanical Engineering,
National Tsing Hua University,
Hsinchu, Taiwan, 30043

This paper investigates the effects of peripheral wall conduction and Darcy number on laminar mixed convection in the fully developed region of a horizontal square porous channel with a uniform heat input. Because of the combined effects on nonaxisymmetric channel configuration, buoyancy-induced secondary flow, and noninfinite wall conduction parameter, the flow and heat transfer characteristics are greatly affected by the peripherally nonuniform wall temperature distribution. A modified Darcy-Forchheimer-Ergun flow model in the porous medium and a finite-difference method are applied. Secondary flow patterns, isotherms, wall temperature distributions, the friction factor, and the Nusselt number are presented for a flow in the Darcian porous medium ($Da \to 0$) to a pure fluid flow ($Da \to \infty$) with $Kp = 10^{-4}$–10^{4}, $Gr = 0$–10^{10}, and $Pr = 0.1$, 0.73, 7.2, and 100. Wall temperature distributions and the Nusselt numbers are compared with existing experimental data.

Introduction

Transport of momentum and thermal energy in fluid-saturated porous media with low permeability is commonly described by using Darcy's model for the conservation of momentum and by an energy equation based on the velocity field found from this model. Non-Darcian effects, which are usually neglected in low-permeability media, have been shown to be very significant in media with high permeabilities (Vafai and Tien, 1981). To account for the effect of a solid boundary, Kaviany (1985) studied the forced convection heat transfer in a porous channel bounded by isothermal parallel plates based on the Brinkman-extended Darcy model, and Nakayama et al. (1988) treated the wall by a constant heat flux and a peripherally uniform wall temperature. Poulikakos and Renken (1987) investigated the effects of flow inertia, variable porosity, and solid boundary on forced convective flow through porous media between parallel plates or in circular pipes. They found that the boundary and inertia effects decrease the Nusselt number, whereas the effect of flow channelling increases the Nusselt number. Furthermore, Prasad et al. (1985) have suggested that the effective thermal conductivity should not be the one based on stagnant fluid conditions, but should include a contribution from convective motion. Similar concepts in forced convective heat transfer in a channel have been used by Cheng et al. (1988).

Laminar mixed convection in ducts is encountered in a wide variety of engineering situations, including heat exchanger without or with a porous medium for viscous fluids in chemical reactors, solar collectors, heat pipes, devices for electronic cooling, and other industrial applications. In the formal case, analyses have been performed via finite-difference schemes in the fully developed region of horizontal channels (Cheng and Hwang, 1969; Chou and Hwang, 1984). Numerous experiments (Morcos and Bergles, 1975; Chou and Hwang, 1987) were carried out for the approximate thermal boundary conditions of uniform heat flux or circumferentially uniform wall temperature. The latter case, numerical calculation (Islam and Nandakumar, 1986, 1988), examined the multiplicity of solutions on laminar mixed convection in horizontal porous channel by using the Darcy and Brinkman models with Boussinesq approximation, and the experimental studies in horizontal packed-sphere channels reported by Combarnous and Bia (1971) and Lin (1990).

In many engineering applications, the boundary conditions in mixed convection cannot be considered either uniform wall temperature or uniform heat flux. Because of the combined effects on nonaxisymmetric channel configuration, buoyancy-induced secondary flow, and noninfinite wall conduction parameter Kp, flow and heat transfer characteristics are greatly affected by the peripherally nonuniform wall temperature distribution (Hwang and Chou, 1987). Morcos and Bergles (1975) and Chou and Hwang (1987) studied the combined free and forced laminar convection in horizontal ducts with wall conduction as a correlation parameter.

When the channel is filled with a porous medium, the effective thermal conductivity and the wall conduction parameter $Kp = k_w t/(k_e^0 D_e)$ are usually greatly affected. Consequently, the flow and heat transfer characteristic are varied. According to

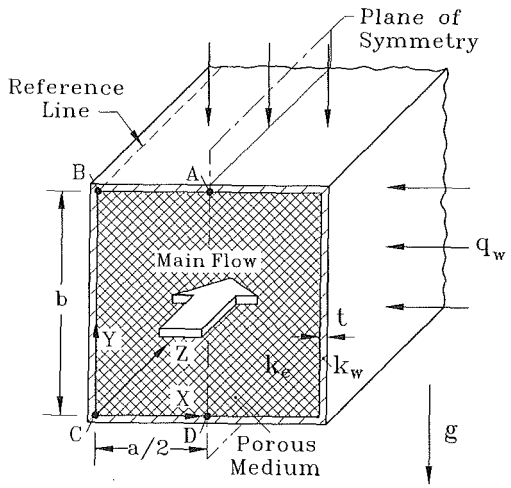

Fig. 1 Physical configuration and coordinate system

Contributed by the Heat Transfer Division for publication in the JOURNAL OF HEAT TRANSFER. Manuscript received by the Heat Transfer Division February 1991; revision received October 1991. Keywords: Augmentation and Enhancement, Mixed Convection, Porous Media.

the authors' best knowledge, the effect of wall conduction on convective heat transfer in a porous channel has not been reported in the literature yet. The main objective of this study is to examine the effects of wall conduction and Darcy number on the combined free and forced convection in the hydrodynamically and thermally fully developed region of a horizontal square porous channel.

Theoretical Analysis

Consider a steady flow in the hydrodynamically and thermally fully developed region of a horizontal square porous channel under an axially and peripherally uniform heat flux q_w on the outer surface of the channel wall with a finite wall thermal conductivity and wall thickness. The physical configuration is shown in Fig. 1. The thermal boundary condition can be achieved by electrically heating the channel wall from the outer surface. It is assumed that the fluid and the solid matrix are in local thermal equilibrium and that the magnitudes of the thermophysical properties are constant. Under these asumptions and by treating the solid matrix and the fluid as a continuum, the local volume averages of the mass, momentum, and energy equation were established by Vafai and Tien (1981) for steady, homogeneous porous media:

Continuity equation:

$$\nabla \cdot U_l = 0 \tag{1}$$

Momentum equation:

$$\frac{\rho_f}{\epsilon}(U_l \cdot \nabla)U_l = -\frac{1}{\epsilon}\nabla P + \frac{1}{\epsilon}\mu_f \nabla^2 U_l + \frac{1}{\epsilon}\rho_f \mathbf{g} - \frac{\mu_f}{K}U_l - \frac{\rho_f F \epsilon}{\sqrt{K}}(U_l \cdot U_l)J \tag{2}$$

Energy equation:

$$(\rho c)_f (U_l \cdot \nabla)T = \frac{1}{\epsilon} k_e \nabla^2 T \tag{3}$$

where J is the pore velocity unit vector. For a porous medium of uniform porosity, the Darcy–Brinkman–Forchheimer model is similar to those of Catton (1985), Hsu and Cheng (1990), and Kladias and Prasad (1989, 1990). In these studies, the conservation equations were obtained by integrating over a small volume element containing both solid and fluid regions. In Eq. (2) of the present study, U_l represents the local average velocity in fluid region only and is defined as $U_l = U_d/\epsilon$, where ϵ is the porosity and U_d is the global average velocity including both the solid and fluid regions. The averaging process is described in detail by Vafai and Tien (1981).

The present approach using Eq. (2) can be used from $\mathrm{Da} \to 0$ (Darcian flow) to $\mathrm{Da} \to \infty$ (pure fluid flow). It is seen that the second, fourth, and fifth terms on the right-hand side of Eq. (2) are expressions for channel boundary viscous drag, Darcy frictional drag, and inertia drag. Note that by keeping the first, third, and fourth terms on the right-hand-side of Eq. (2) and neglecting the rest of them, the momentum equation reduces to that for the familiar Darcian flow. On the other hand, when the porosity $\epsilon = 1$ and the permeability $K \to \infty$, Eq. (2) reduces to the convectional momentum equation for pure fluid flow. The value of permeability K and Forchheimer's constant F can be calculated from the Ergun model (Ergun, 1952) for random packed spheres as follows:

$$K = \frac{\epsilon^3 d^2}{150(1-\epsilon)^2}, \text{ and } F = \frac{1.75}{\sqrt{150}}\epsilon^{-1.5} \tag{4}$$

where d is the mean particle size (i.e., the diameter of the beads). For a two-dimensional flow and the Boussinesq fluid, the following dimensionless variables are introduced:

$$x = X/D_e, \quad y = Y/D_e, \quad u = UD_e/\nu_f, \quad v = VD_e/\nu_f, \quad w = W/\overline{W},$$
$$P = P_z(Z) + \mu_f^2/(\rho_f D_e^2)\cdot p, \text{ and } T = T_r + (q_w D_e/k_e)\cdot\theta \tag{5}$$

The axial conduction term in the energy Eq. (3) is neglected because the thermal boundary condition is axially constant heat flux for fully developed flow, i.e., $\partial T/\partial Z = dT/dZ = 4q_w/(\rho_f c_f \epsilon \overline{W} D_e) = \text{const}$. By using stream function, $u = \partial\psi/\partial y$ and $v = -\partial\psi/\partial x$, and the vorticity, $\nabla^2\psi = -\xi$, the dimensionless equations expressing the transport of vorticity, axial momentum, and energy become:

$$\mathrm{Da}\left(u\frac{\partial \xi}{\partial x} + v\frac{\partial \xi}{\partial y}\right) = \mathrm{Da}\left(\frac{\partial^2 \xi}{\partial x^2} + \frac{\partial^2 \xi}{\partial y^2}\right) + \mathrm{DaGr}\frac{\partial \theta}{\partial x} - \xi - 0.143\cdot\mathrm{Da}^{0.5}\left\{|\underline{v}|\xi + \left(v\frac{\partial}{\partial x}|\underline{v}| - u\frac{\partial}{\partial y}|\underline{v}|\right)\right\} \tag{6}$$

$$\mathrm{Da}\left(u\frac{\partial w}{\partial x} + v\frac{\partial w}{\partial y}\right) = C + \mathrm{Da}\left(\frac{\partial^2 w}{\partial x^2} + \frac{\partial^2 w}{\partial y^2}\right) - w - 0.143\mathrm{Da}^{0.5}|\underline{v}|w \tag{7}$$

$$\mathrm{Pr}\left(u\frac{\partial \theta}{\partial x} + v\frac{\partial \theta}{\partial y}\right) + 4w = \left(\frac{\partial^2 \theta}{\partial x^2} + \frac{\partial^2 \theta}{\partial y^2}\right) \tag{8}$$

where $\mathrm{Da} = K/(\epsilon D_e^2) = \mathrm{Da}'/\epsilon$, $\mathrm{Gr} = \beta g q_w D_e^4/(\nu_f^2 k_e) = \mathrm{Gr}_f(k_f/k_e)$, $|\underline{v}| = [u^2 + v^2 + (\mathrm{Re}w)^2]^{0.5}$, $\mathrm{Re} = \overline{W}D_e/\nu_f$,

Nomenclature

a = channel width or height, m
C = a constant defined in Eq. (7)
c = isobaric specific heat, J/kgK
d = characteristic particle dimension, m
Da, Da′ = modified Darcy number and Darcy number, $\mathrm{Da} = \mathrm{Da}'/\epsilon = K/\epsilon D_e^2$
D_e = hydraulic diameter, a, m
D_t = empirical constant defined in Eq. (20)
F = a constant defined in Eq. (4)
f = friction factor $= 2\bar{\tau}_w/(\rho\overline{W}^2)$
g = gravitational acceleration, m/s^2
Gr = modified Grashof number $= \beta g q_w D_e^4/(\nu_f^2 k_e)$
$\bar{h}$ = average heat transfer coefficient, W/m^{2}K
J = pore velocity unit vector $= U_l/|U_l|$, or integer
K = permeability of saturated porous medium, m^2
Kp = wall heat conduction parameter $= k_W t/(k_e^0 D_e)$
k_e = effective thermal conductivity of porous medium $= k_e^0 + k_t$, W/mK
k_e^0 = stagnant thermal conductivity of porous medium, W/mK
k_f = fluid thermal conductivity
k_t = thermal dispersion conductivity of porous medium, W/mK
m = empirical constant defined in Eq. (20)
Nu = Nusselt number $= \bar{h}D_e/k_e$
n = dimensionless inward-drawn normal, or integer
P, p = pressure and dimensionless pressure, N/m^2
Pe = particle Peclet number $= \epsilon\overline{W}d/(\alpha_f(1-\epsilon))$
Pr = modified Prandtl number $= \nu_f/\alpha_e$
q_w = wall heat flux per unit area, W/m^2
Ra_D = Darcy–Rayleigh number $= Kg\beta q_W D_e^2/(\epsilon\nu_f\alpha_e k_e)$

$C = -(dP_z/dZ)K/(\epsilon\mu_f\overline{W})$, and $\mathrm{Pr} = \nu_f/\alpha_e = \mathrm{Pr}_f\epsilon(k_f/k_e)$. It is noted that only four parameters, Da, Gr, Re, and Pr, appear in Eqs. (6) to (8) by using the modified parameters. Otherwise, two more parameters, ϵ and (k_f/k_e), will also be presented.

Because of symmetry, it is necessary to consider only half the region, and the associated boundary conditions are

$$\frac{\partial\psi}{\partial x}=\frac{\partial\psi}{\partial y}=w=0 \qquad \text{on the channel wall}$$

$$\frac{\partial\psi}{\partial y}=\frac{\partial^2\psi}{\partial x^2}=\frac{\partial w}{\partial x}=\frac{\partial\theta}{\partial x}=\xi=0 \qquad \text{along the center plane} \tag{9}$$

In the present study, the values of the stream function on the channel walls and along the center line are taken as zero for simplicity. The derivation of thermal boundary condition along the channel wall can be found from Shan and London (1978) and Hwang and Chou (1987). The dimensionless thermal boundary condition is:

$$1+\left(\frac{\partial\theta}{\partial n}\right)_\Gamma + Kp\left(\frac{\partial^2\theta}{\partial s^2}\right)_\Gamma = 0 \tag{10}$$

where the subscript Γ denotes the inside surface of the channel wall, n is inward normal, s is the circumference of cross section, and $Kp = k_w t/(k_e^0 D_e)$ is a parameter indicating the relative importance of wall heat conduction and convection in the porous channel. A noteworthy result is observed in Eq. (8) that the axial conduction term can be neglected under the assumptions of axially uniform heat input and thermally fully developed condition. Two limiting cases, $Kp = 0$ and ∞, yield the boundary conditions of uniform heat flux and uniform wall temperature, respectively. The value of Kp in a channel flow can be changed by filling the channel with a porous medium. For instance, for the case of gas flows in a thick metal channel with a relatively small D_e, Kp is high and the thermal boundary condition can be approximated as a uniform wall temperature. If the channel is filled with a metal porous medium, then k_e^0 increases drastically and the thermal boundary condition is changed. A reversed situation can be found in the case of molten metal flows in a nonmetal channel filled with a nonmetal porous medium.

Flow and Heat Transfer Characteristics

The important overall flow and heat transfer characteristics in a channel flow are indicated by the friction factor and the Nusselt number, respectively. Following the convectional definitions, the boundary viscous friction factor and the Nusselt number are written as

$$f_V = (\bar{\tau}_w)/\left(\frac{1}{2}\rho_f\overline{W}^2\right)$$
$$\mathrm{Nu} = \frac{\bar{h}D_e}{k_e} = \frac{q_w D_e}{(T_w - T_b)k_e} \tag{11}$$

where $\bar{\tau}_w$ is the mean wall shear stress and q_w is the mean wall heat flux. Deriving both the $\bar{\tau}_w$ and q_w from the averages of local derivatives, then the product of boundary viscous friction factor and the Reynolds number, and the Nusselt number become

$$f_V\mathrm{Re} = 2\overline{\left(\frac{\partial w}{\partial n}\right)\Big|_w}$$

$$\mathrm{Nu} = -\overline{\left(\frac{\partial\theta}{\partial n}\right)\Big|_w}/\overline{[w(\bar{\theta}_w-\theta)]} \tag{12}$$

On the other hand, the friction factor and the Nusselt number can be also derived from the overall force and energy balances, and the results are

$$f_V\mathrm{Re} = \frac{1}{2}\mathrm{Da}^{-1}[C-(1+0.143\cdot\mathrm{Da}^{0.5}|\underline{\bar{v}}|)]$$

$$\mathrm{Nu} = 1/\overline{[w(\bar{\theta}_w-\theta)]} \text{ where } |\underline{\bar{v}}| = \overline{[u^2+v^2+(\mathrm{Re}w)^2]}^{0.5} \tag{13}$$

In addition to the boundary frictional drag, the fully developed flow through a porous duct experiences also a bulk frictional drag induced by the solid matrix (designated as Darcy's pressure drop) and a flow inertia drag induced by the solid matrix at high flow rate (designated as Forchheimer's form drag). The bulk friction (Darcy) and the inertia (Forchheimer) drag coefficient are defined as follows:

$$f_D = (\mu_f K^{-1}\epsilon\overline{W})\left(\frac{a}{4}\right)\Big/\left(\frac{1}{2}\rho_f\overline{W}^2\right) = \frac{1}{2}\mathrm{Da}^{-1}/\mathrm{Re}$$

$$f_I = (0.143\rho_f K^{-0.5}\epsilon^{0.5}|\overline{U_l}|\overline{W})\left(\frac{a}{4}\right)\Big/\left(\frac{1}{2}\rho_f\overline{W}^2\right)$$
$$= \frac{1}{2}0.143\mathrm{Da}^{-.5}|\underline{\bar{v}}|/\mathrm{Re} \tag{14}$$

Nomenclature (cont.)

Re = Reynolds number = $\overline{W}D_e/\nu_f$
T = temperature, K
t = thickness of channel wall, m
U_d = global average velocity including both the solid and fluid regions
U_l = local average velocity vector in void volume $= v_f^{-1}\int_{v_f} U dv$
U, V, W = local average velocity components in X, Y, and Z directions, m/s
u, v, w = dimensionless velocity components in x, y, and z directions
$|\underline{v}|$ = magnitude of dimensionless velocity $= [u^2+v^2+(\mathrm{Re}\cdot w)^2]^{0.5}$
X, Y, Z = Cartesian coordinate system
x, y = dimensionless Cartesian coordinates
α_e = thermal diffusivity of porous medium $= k_e/(\epsilon\rho_f c_f)$
β = isobaric coefficient of thermal expansion of fluid, K^{-1}
ϵ = porosity of porous medium
θ = dimensionless temperature difference $= (T-T_r)/(q_w D_e/k_e)$
μ_f = viscosity of fluid, kg/ms
ν_f = kinematic viscosity of fluid, m^2/s
ξ = vorticity
ρ_f = density of fluid, kg/m^3
τ_w = wall shear stress, N/m^2
ψ = dimensionless stream function

Superscripts

$\overline{\ }$ = average value
k = number of iteration

Subscripts

b = bulk quantity
f = quantity based on fluid
i, j = nodal point
o = condition for pure forced convection
r = along reference line B in the channel direction
w = condition at wall
z = in z direction
Δ = difference

Table 1 Numerical experiment for grid size

Case \ Nu fRe	Gr	Da	Pr	Kp	Re	10×20	30×60§	50×100	
1	0	10^4	—	10^4	10	3.640 14.10	3.612 14.20	3.611 14.22	3.608 † 14.23
2	0	10^4	—	10^{-4}	10	3.120 14.10	3.101 14.20	3.100 14.22	3.08 † 14.23
3	25750	10^4	0.73	10^4	10	4.640 16.48	4.553 16.51	4.546 16.51	4.556 ‡ 16.58

§ : Grid size for present numerical study
† : Shah and London, 1978
‡ : Chou and Hwang, 1984

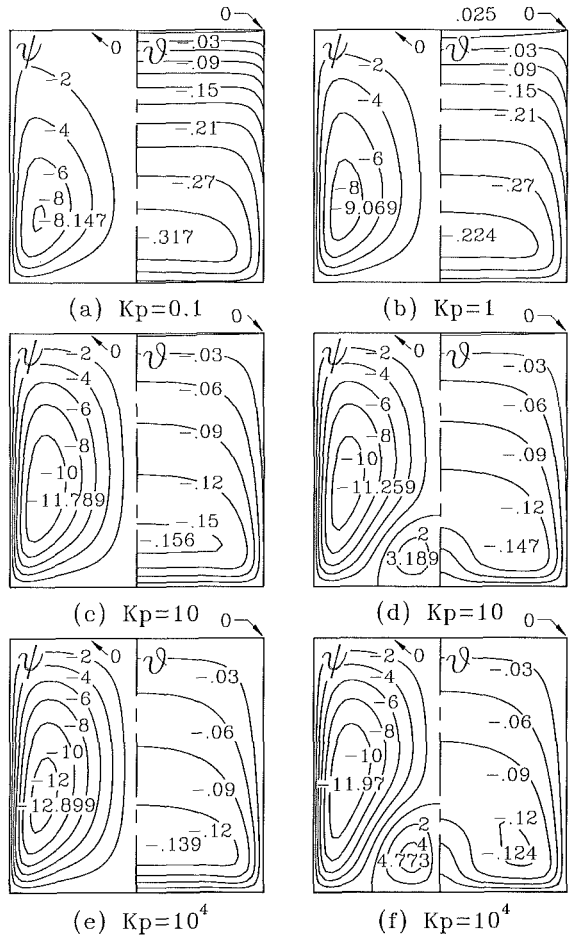

Fig. 2 Isotherms and streamlines for Pr = 0.73, Gr = 3×10^9, Da = 10^{-6}, and Re = 0-10^3 with (*a*) *Kp* = 0.1, (*b*) *Kp* = 1, (*c*)-(*d*) *Kp* = 10, and (*e*)-(*f*) *Kp* = 10^4

The summation of f_V, f_D, and f_I is

$$f_T = f_V + f_D + f_I = -(dP_z/dZ)\left(\frac{a}{4}\right)\Big/\left(\frac{1}{2}\rho_f \overline{W}^2\right) = \frac{1}{2} C\mathrm{Da}^{-1}/\mathrm{Re} \tag{15}$$

In the present study, Eqs. (13)-(15) are used.

Method of Solution

In order to predict the flow and temperature fields accurately, particularly for low Darcy numbers, a large number of nodes are required near the walls. Hence, a coordinate stretching transformation has been introduced to distribute a reasonably large number of grid points near the walls. Accordingly, the x and y coordinates are transformed by using a simple algebraic relationship $\overline{P_1P_J} = \overline{P_1P_N}(J-1/N-1)^n$, for $1 \le J \le N$ and $1 \le n \le 2$ (e.g., $n = 1$, for the case of uniform grid), where P_1 and P_N are the positions of the end points and P_J is the position of an intermediate point. The details regarding the formulation of finite difference Eqs. (6)-(8) and (10) and the related boundary condition (9) are omitted here for simplicity. In order to have a convergent solution in a higher Gr regime, the power-law scheme of Patankar (1980) and a strongly implicit scheme of Lee (1989) were employed. The procedure for solving the finite-difference equations is:

1 Assign values of Da, Pr, Gr, Re, and Kp, and initial values for ψ, ξ, w, and θ in Eqs. (6)-(8) and (10).
2 New values of the stream function ψ can be found from the assigned value of ξ at each node.
3 The velocity components u and v are then computed.
4 Values of the vorticity on the boundary are calculated from the associated boundary conditions for ψ.
5 With the assigned Da, Gr, and Re, and the values of u and v from step (4), Eq. (6) can be solved for ξ.
6 Give an initial value for the constant C and solve Eq. (7) for w. The new value of C is adjusted by considering the relation:

$$C_{\mathrm{new}} = C_{\mathrm{old}}/(\iint w dX dY/a^2) \tag{16}$$

It is noted that the value of C will be unchanged if the global continuity equation $\iint w dX dY/a^2 = 1$ is satisfied.
7 Equations (8) and (10) are solved for θ at interior points and along the wall.
8 Repeat steps (2) to (7) until the criterion of convergence for ψ, ξ, w, and θ is satisfied:

$$\mathrm{Max}|F_{i,j}^{k+1} - F_{i,j}^{k}|/\mathrm{Max}|F_{i,j}^{k+1}| \le 10^{-5} \tag{17}$$

9 Compute the friction factors and the Nusselt number.

As shown in Table 1, a numerical experiment was conducted to establish the mesh sizes for different parameters. A convergence study of the numerical solution can be also made by comparing the data with the known values for pure forced convection (Shah and London, 1978) and mixed convection (Hwang and Chou, 1987) for the limiting case of pure fluid flow Da→∞. It is seen that for grid size = 50 × 100, Gr = 0, Da = 10^4, and $Kp = 10^{-4}$ the Nusselt number and the product of friction factor and the Reynolds number, fRe, are 3.100 and 14.22, respectively. These values are within 0.65 and 0.07 percent of the known values Nu = 3.08 and fRe = 14.23 of Shah and London (1978) for pure forced convection and peripherally uniform wall heat flux. Similarly, for $Kp = 10^4$, the Nusselt number is 3.611, which also shows a small difference of 0.08 percent from the known value of 3.608 of Shah and London (1978) for the case of uniform wall temperature. For mixed convection, Nu and fRe are 4.546 and 16.51, respectively, which are within 0.2 and 0.4 percent of the known values of 4.556 and 16.58 of Chou and Hwang (1984) for Gr = 25750 and peripherally uniform wall temperature. This observation confirms the accuracy and convergence properties of the present numerical solution.

Results and Discussion

Effect of Wall Heat Conduction Parameter Kp. To illustrate the effect of wall heat conduction parameter, Kp, on the secondary flow and temperature fields, streamlines and isotherms for the cases of Kp = 0.1, 1, 10, and 10^4 with Pr = 0.73, Gr = 3×10^9, Da = 10^{-6}, and Re = 0-10^3 are shown in Figs. 2(*a-f*). The value of the stream function is set to zero along the channel wall and the center symmetry line. The maximum absolute value of the stream function may be regarded as the intensity of secondary flow. The maximum absolute value of the stream function is 8.147 for Kp = 0.1 and is 12.899 in Fig. 2(*e*) for $Kp = 10^4$ for two-vortex patterns. A 58 percent increase in the maximum value of the stream function is observed from the latter case to the former case. This indicates that the intensity of secondary flow is stronger in the case of uniform wall temperature ($Kp = 10^4$) than in the case of uniform heat flux (Kp = 0.1). Consequently, the temperature difference indicated by $-\theta$ is larger for Kp = 0.1 than

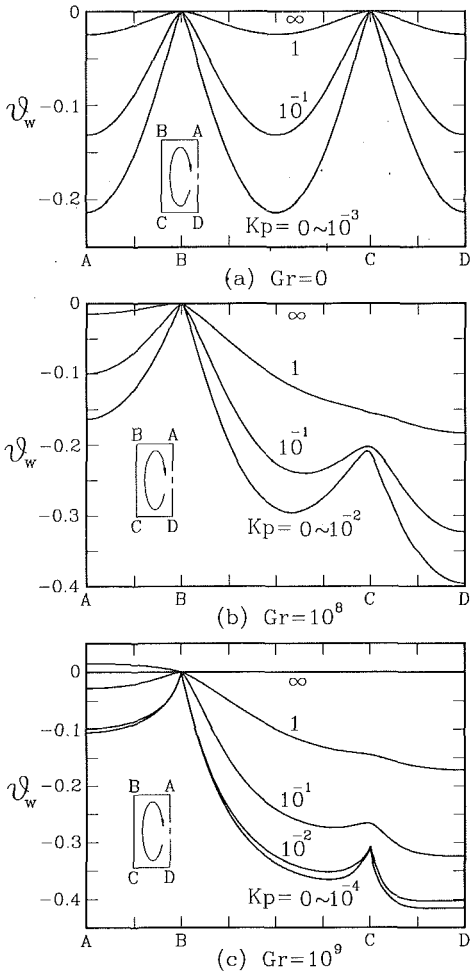

Fig. 3 Wall temperature distributions for Pr = 0.73, Da = 10^{-6}, and Re = 0-10^3 with (*a*) Gr = 0, (*b*) Gr = 10^8, and (*c*) Gr = 10^9

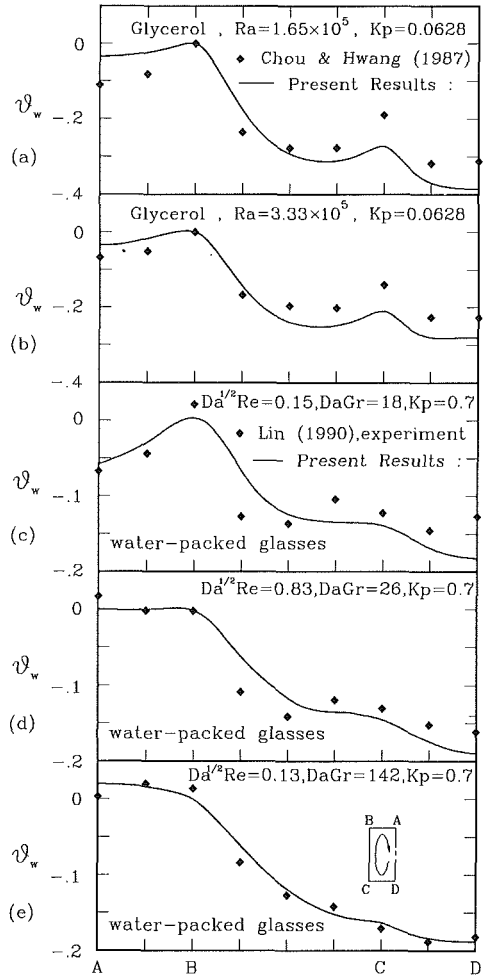

Fig. 4 Wall temperature distributions for glycerol (Pr = 5500, Da→∞) and for water (Pr = 7.2, Da = 2×10^{-5})

for $Kp = 10^4$. It is seen from Figs. 2(*c-f*) that the dual solutions of two- and four-vortex flow patterns for Kp are 10 and 10^4. Due to the additional vortex pair formed near the center-bottom wall in Figs. 2(*d*) and 2(*f*), the maximum of $-\theta$ is larger for the two-vortex than for the four-vortex case. This means that the fluid is well mixed by the stronger secondary flow motion for the case of four-vortex flow pattern.

In electronic cooling, the devices can be damaged by the highest temperature of the heat sink instead of the average one; therefore the temperature distribution along the channel wall is of practical interest for a varying wall conduction parameter Kp. Figures 3 (*a*, *b*, *c*) show the wall temperature distributions along the channel wall for the case of Pr = 0.73, Da = 10^{-6}, and Re = 0-10^3 with Gr = 0, 10^8, and 10^9, respectively. It is seen that for the case of purely forced convection Gr = 0, the temperature distribution is symmetric with respect to the horizontal center line $Y = b/2$. As the conduction parameter Kp increases, the wall temperature distributions become more and more uniform. For the cases of Gr = 10^8 and 10^9, the secondary flow cools off the lower horizontal wall *CD*, and is heated up the vertical side wall *BC* and the upper horizontal wall *AB*. The location of the highest wall temperature appears at the upper corner *B* for the case of Gr = 10^8 and on the upper horizontal wall for the case of Gr = 10^9. This phenomenon in Figs. 3(*a-c*) is quite similar to that of Hwang and Chou (1987) in the fluid flow through a channel without porous materials. In fully developed flows for pure flow Da→∞ and Darcian flow Da→0, the effect of secondary flow introduced by buoyancy force on the wall temperature distribution is similar.

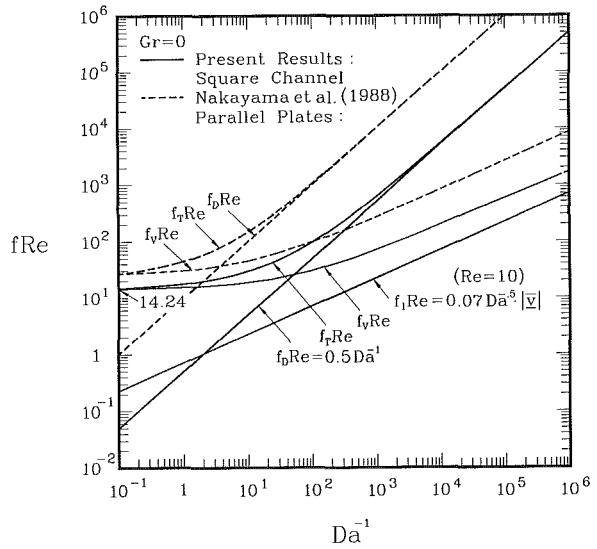

Fig. 5 *f* Re versus Da^{-1} for Gr = 0 with the effect of Re

In Figs. 4(*a*) and 4(*b*), computation for glycerol fluid flow was carried out to compare with the experimental data of Chou and Hwang (1987) for the same values of Pr, Ra, and Kp. In general, the computated data follow those of Chou and Hwang (1987) by setting $\theta_w = 0$ at point *B* and using the same dimensionless temperature. A percentage rms difference of only 14 percent is found in both Figs. 4(*a*) and 4(*b*) based on the

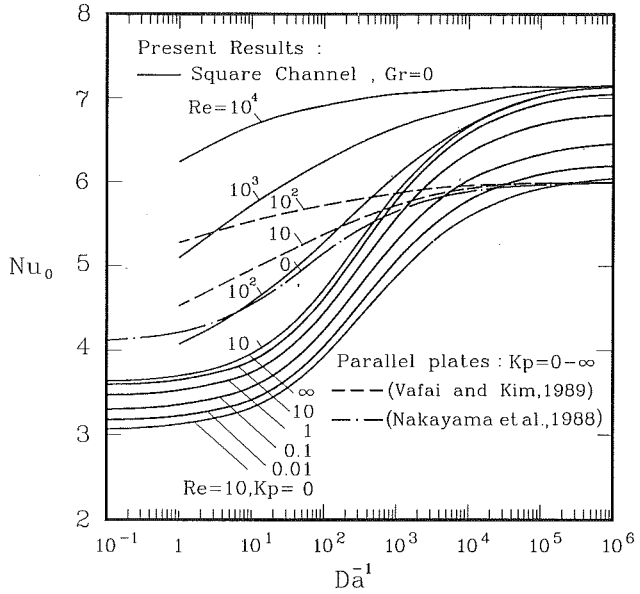

Fig. 6 Nu_0 versus Da^{-1} for Gr = 0 with the effects of *Kp* and Re

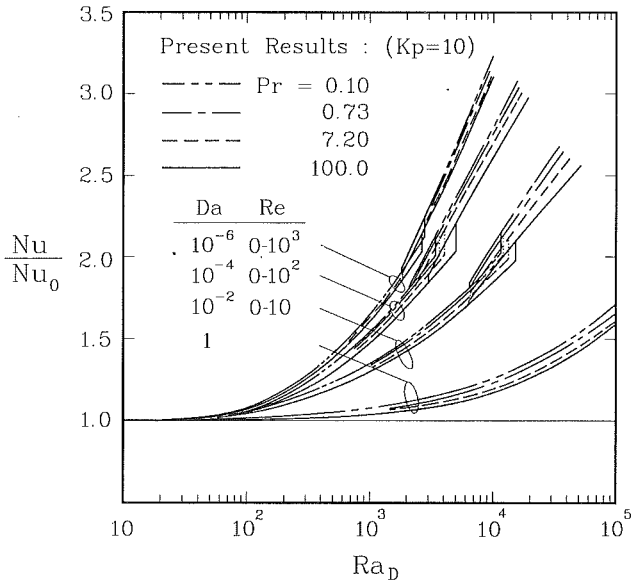

Fig. 7 Nu/Nu_0 versus Ra_D for *Kp* = 10 with the effects of Pr and Da

Table 2 Nu_0 for pure forced convection

Nu0 \ Kp / Da	0	10^{-3}	10^{-2}	10^{-1}	1	10^{1}	10^{4}
10^{-6}	6.024	6.028	6.461	6.801	7.052	7.111	7.146
10^{-5}	5.981	6.101	6.349	6.708	6.957	7.015	7.022
10^{-4}	5.649	5.808	6.057	6.374	6.606	6.661	6.668
10^{-3}	4.945	5.073	5.316	5.595	5.801	5.851	5.858
10^{-2}	3.932	4.030	4.215	4.432	4.594	4.634	4.639
10^{-1}	3.315	3.392	3.540	3.717	3.850	3.882	3.886
1	3.146	3.218	3.355	3.521	3.644	3.675	3.679
10	3.106	3.178	3.312	3.475	3.598	3.626	3.631
10^{4}	3.101	3.163	3.296	3.458	3.579	3.608	3.612
Fluid*	3.098	——	3.138	3.324	3.548	3.599	3.608

* numerical data of Hwang and Chou (1987).

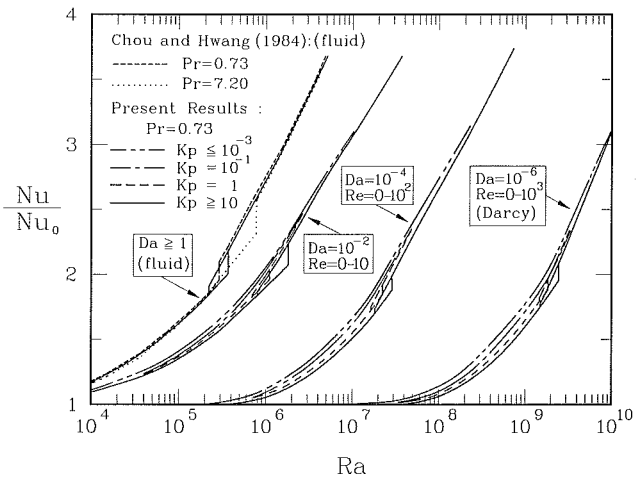

Fig. 8 Nu/Nu_0 versus Ra for Pr = 0.73 with the effects of *Kp* and Da

maximum theoretical wall dimensionless temperature difference of $(\Delta\theta_m)_{max} = 0.39$ in Fig. 4 (*a*) and 0.28 in Fig. 4(*b*). In Figs. 4(*c–e*), the computation for water flow in the packed glass bead channel was also carried out for comparison with the experiment data of Lin (1990) for the same parameters. In his report, the test sections were made of 4.75×4.75 cm stainless and 9.5×9.5 cm aluminum square channels with 2 mm wall thickness. The size of the packed glass beads is 5 mm in diameter and the stagnant conductivity k_e^0 is 0.78 W/m°C. The natural convection and flow inertia will promote the flow mixing in the channel cross section. The case in Fig. 4(*d*) with a strong flow inertia $Da^{0.5}$ Re = 0.83 and the case in Fig. 4(*e*) with a strong natural convection DaGr = 142 show more uniform wall temperature distributions along *BA* in Figs. 4(*d*) and 4(*e*) than that for the case shown in Fig. 4(*c*) with $Da^{0.5}$Re = 0.15 and DaGr = 18. These figures are plotted by setting the same mean value of θ_w and minimizing the rms wall temperature difference between the computed and the experimental data. Percentage differences are about 20, 13, and 5.9 percent for Figs. 4(*c*), 4(*d*), and 4(*e*), respectively, based on the computed maximum wall temperature difference. The agreement is reasonable and the comparison shows the validity of the present study.

Effect of Darcy Number. Figure 5 illustrates the effect of Darcy number on the product of friction factor and Reynolds number for forced convection in the square porous channel. The total friction factor, f_TRe, boundary friction factor, f_VRe, Darcy's friction factor, f_DRe, and Forchheimer's friction factor, f_IRe, are plotted over the range $10^{-1} \le Da^{-1} \le 10^6$. For $Da^{-1} \le 1$ Darcy's friction factor, f_DRe, and Forchheimer's inertia drag factor, f_IRe, are almost negligible, and the flow behaves just like the Poiseuille flow. It is seen that the value of f_DRe exceeds f_IRe when $Da^{-1} > 2$ and exceeds f_VRe when $Da^{-1} > 50$. As a result, the curve of f_TRe overlaps with the lines of f_DRe for $Da^{-1} > 10^4$. The results of parallel plates (Nakayama et al., 1988) are also plotted for comparison. A similar trend is observed between the data of parallel plates and square channel. It is also noted that the curve indicating the flow inertia drag f_IRe was not plotted for the case of parallel plates by Nakayama et al. (1988). It is noted that the importance of buoyancy effect on the flow characteristic is indicated by the product of Da and Gr. In the present study, the value of DaGr is less than 10^4, and f_TRe is only 3 percent greater than $(f_T\text{Re})_0$ for pure forced convection. Therefore, the effect of buoyancy on the friction factor will not be discussed further here.

Heat Transfer. Figure 6 shows the effects of *Kp* and Da on the Nusselt number for pure forced convection Gr = 0. The Nusselt numbers for Re = 10 increase with Da^{-1} and are bounded by the curves of constant wall temperature $Kp \to \infty$ and constant wall heat flux $Kp \to 0$. The difference in the Nusselt numbers between $Kp \to \infty$ and $Kp \to 0$ is about 0.5 for Da^{-1} = 0.1 and increases to about 1.1 for $Da^{-1} = 10^6$. When Re increases, the increment of Nu decreases as Da^{-1}approach 10^6.

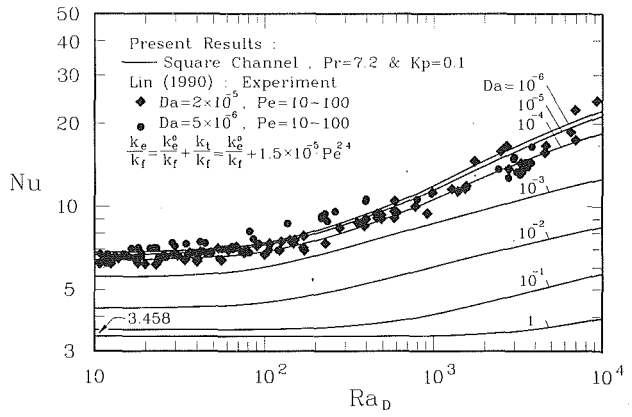

Fig. 9 Nu versus Ra_D

A similar trend is also observed for data of parallel plates (Vafai and Kim, 1989; Nakayama et al., 1988). Due to the physical configuration of parallel plate channel, these curves are valid for $Kp = 0 - \infty$. Table 2 lists the Nu_0 of pure forced convection for $Kp = 0$–10^4 and $Da = 10^{-6} - 10^4$. The fluid data are also tabled for comparison.

The variation of Nu/Nu_0 versus Ra_D with the effect of Prandtl number for Da = 1, 10^{-2}, 10^{-4}, and 10^{-6}, is shown in Fig. 7. It is pointed out by Cheng et al. (1972) that the Prandtl number effect on the fully developed laminar forced convection with secondary flow for Pr = 0.7–∞ can be correlated simply by using the parameter Ra = PrGr. By considering the small Darcy number, Eq. (6) can be reduced to

$$\mathrm{DaGr}\frac{\partial\theta}{\partial x} - \xi = 0 \tag{18}$$

Furthermore, by using the transformations $u = \mathrm{DaGr}u'$ and $v = \mathrm{DaGr}v'$, the parameter $Ra_D = \mathrm{PrDaGr}$ can be obtained readily in energy Eq. (8). It is expected that the solutions for small Da with a wide range of Pr will be well correlated by employing the parameter Ra_D. It is seen that Nu/Nu_0 will be decreased with the increase in Pr. By using the correlation parameter Ra_D, a maximum difference of only 9 percent is observed between the curves of Pr = 0.1 and 100, and 18 percent is observed between the curves for Da = 10^{-6} and 10^{-4}. It is expected that the curves obtained with the Darcy law will be the same as that for Da = 10^{-6}.

Figure 8 shows Nu/Nu_0 variation with the Rayleigh number for Da = 10^{-6}, 10^{-4}, 10^{-2}, and ≥ 1 and $Kp = 10^{-3}$, 10^{-1}, 1, and ≥ 10 for Pr = 0.73. By also considering large Da for pure fluid flow, Eq. (6) can be reduced to

$$u\frac{\partial\xi}{\partial x} + v\frac{\partial\xi}{\partial y} = \frac{\partial^2\xi}{\partial x^2} + \frac{\partial^2\xi}{\partial y^2} + \mathrm{Gr}\frac{\partial\theta}{\partial x} \tag{19}$$

Furthermore, by using the transformations $u = \mathrm{Gr}u'$ and $v = \mathrm{Gr}v'$, the parameter Ra = PrGr can be obtained readily in energy Eq. (8). It is expected that the solution for large Da and Pr will be well correlated by employing the parameter Ra. The numerical results of Chou and Hwang (1984) for Pr = 0.73 and 7.2 with uniform heat flux and circumferential uniform wall temperature are also plotted, and they are confirmed well with the curves of $Da \geq 1$. This figure also shows that dual solutions exist when $Kp \geq 1$, and the Nusselt number ratios of this region are all located near the value of 2.

Due to an adverse temperature gradient in the center region near the bottom channel wall, the bifurcation phenomenon has been found in either pure fluid flow (Fung et al., 1987; Law et al., 1987) or porous medium flow (Islam and Nandakumar, 1986, 1988). In the present study, dual solutions have been also obtained for a certain range of Ra regardless of the value of Da. The dual solutions of the two-vortex and four-vortex flow patterns in a certain range of Ra are due to the dependence of initially input flow patterns. When the computation is carried out from lower (higher) value of Ra with an initial two-vortex (four-vortex) flow pattern, a two-vortex (four-vortex) flow pattern will be obtained in the range of Ra. The detailed phenomena of dual solution in porous medium were discussed by Islam and Nandakumar (1986, 1988), and they pointed out that the Prandtl number does not appear to have an influence on the range of Ra for the dual solutions existence. This can be also observed in Fig. 7. It is seen from Fig. 8 that the curves for $KP \leq 10^{-3}$, the solution for circumferential uniform heat flux, lie above the curves for $Kp \geq 10$, the solution for uniform wall temperature. A maximum difference of 13 percent is observed at Ra = 10^9 for Da = 10^{-6}.

In order to confirm the validty of the present non-Darcy solution, Fig. 9 shows the comparison between the numerical results and the experimental data of Lin (1990) on mixed convection for packed glass beads saturated with water flowing through a square duct. In this figure the values of Nu versus Ra_D are plotted. An asymptotic behavior for small Da is observed. All the curves are bounded between the curve for small Da and the value of Nu = 3.458 for Kp = 0.1. The experimental data are correlated by using an effective thermal conductivity $k_e = k_e^0 + k_t$. The stagnant effective thermal conductivity k_e^0 of glass beads and water is calculated from the empirical formula of Prasad et al. (1989). The dynamic or dispersion conductivity k_t considers the additional thermal transport due to the radial mixing between the solid particles (Han et al., 1985; Levec and Carbonell, 1985). The k_t can be expressed as

$$k_t = D_t \mathrm{Pe}^m k_f \tag{20}$$

where $\mathrm{Pe} = \{\epsilon \overline{W}_d / [\alpha_f (1-\epsilon)]\}$ is the Peclet number; D_t and m are empirical constants. The experimental data collapse to a single line with a maximum difference of 12 percent by using dispersion constants $D_t = 1.5 \times 10^{-5}$ and m = 2.4. A good agreement with the present analysis is observed.The global thermal dispersion modeling had been successfully correlated with experimental data by Han et al. (1985) and Levec and Carbonell (1985). The present study employs the same approach and covers a wide range of Da from 10^{-6} to 1. If the local transverse thermal dispersion model (Hsu and Cheng, 1990) is used, the solution cannot cover the range of Da from 10^{-6} to 1 easily due to additional parameters involved.

Conclusions

1 The present results have shown the importance of the effects of peripheral wall conduction and Darcy number on laminar mixed convection in the hydrodynamically and thermally fully developed region of a horizontal square porous channel with a uniform external heat input. Because of the combined effects of nonaxisymmetric channel configuration, buoyancy-induced secondary flow, and noninfinite wall conduction parameter, $Kp = k_w t/(k_e^0 D_e)$, the flow and heat transfer characteristics are greatly affected by the peripherally nonuniform wall temperature distribution.

2 The intensity of secondary flow increases with an increase in Kp when the values of Pr, Gr, Da, and Re are fixed. For instance, a 58 percent increase in the maximum value of the stream function is observed from the case of Kp = 0.1 to the case of $Kp = 10^4$ for Pr = 0.73, Gr = 3×10^9, Da = 10^{-6}, and Re = 0–10^3.

3 In electronic cooling, the devices can be damaged by the highest temperature of heat sink instead of the average one; therefore the temperature distribution along the channel wall is of practical interest for a varying wall conduction parameter Kp. The temperature distributions along the channel wall agree reasonably well with the experimental data for glycerol fluid (Chou and Hwang, 1987) and water-porous medium (Lin, 1990).

4 With the empirical formula of Prasad et al. (1989) for stagnant effective thermal conductivity and the thermal dispersion model of Han et al. (1985) and Levec and Carbonell (1985), the Nu of experimental data (Lin, 1990) collapse to a single line with a maximum difference of 12 percent by using dispersion constants $D_t = 1.5 \times 10^{-5}$ and $m = 2.4$. A good agreement with the present analysis is observed.

Acknowledgments

The authors would like thank the National Science Council, Taiwan, for financial support through Grant No. NSC-80-0404-E007-01. One of the authors, C. H. Chao, is also indebted to the NSC, for a scholarship.

References

Catton, I., 1985, "Natural Convection in Porous Media," in: *Natural Convection: Fundamentals and Applications*, S. Kakac et al., eds., Hemisphere Publishing Corp., Washington, DC, pp. 514–547.

Cheng, K. C., and Hwang, G. J., 1969, "Numerical Solution for Combined Free and Forced Laminar Convection in Horizontal Rectangular Channels," ASME JOURNAL OF HEAT TRANSFER, Vol. 91, pp. 59–61.

Cheng, K. C., Hwang, G. J., and Akiyama, A., 1972, "On a Simple Correlation for Prandtl Number Effect on Forced Convection Heat Transfer With Secondary Flow," *International Journal of Heat and Mass Transfer*, Vol. 15, pp. 172–175.

Cheng, P., Hsu, C. T., and Chowdhury, A., 1988, "Forced Convection in the Entrance Region of a Packed Channel With Asymmetric Heating," ASME JOURNAL OF HEAT TRANSFER, Vol. 110, pp. 946–954.

Chou, F. C., and Hwang, G. J., 1984, "Combined Free and Forced Laminar Convection in Horizontal Channels for High ReRa," *Canadian Journal of Chemical Engineering*, Vol. 62, pp. 830–836.

Chou, F. C., and Hwang, G. J., 1987, "Experiments on Combined Free and Forced Laminar Convection in Horizontal Square Channels," *ASME-JSME Thermal Engineering Joint Conference*, Honolulu, HI, pp. 135–141.

Combarnous, M. A., and Bia, P., 1971, "Combined Free and Forced Convection in Porous Media," *Society of Petroleum Engineers Journal*, Vol. 11, pp. 399–405.

Ergun, S., 1952, "Fluid Flow Through Packed Columns," *Chemical Engineering Progress*, Vol. 48, pp. 89–94.

Fung, L., Nandakumar, K., and Masliyah, J. H., 1987, "Bifurcation Phenomena and Cellular-Pattern Evolution in Mixed-Convection Heat Transfer," *Journal of Fluid Mechanics*, Vol. 177, pp. 339–357.

Han, N. W., Bhakta, J., and Carbonell, R. G., 1985, "Longitudinal and Lateral Dispersion in Packed Beds: Effect of Column Length and Particle Size Distribution," *AIChE Journal*, Vol. 31, pp. 277–288.

Hsu, C. T., and Cheng, P., 1990, "Thermal Dispersion in a Porous Medium," *International Journal Heat and Mass Transfer*, Vol. 33, pp. 1587–1597.

Hwang, G. J., and Chou, F. C., 1987, "Effect of Wall Conduction on Combined Free and Forced Laminar Convection in Horizontal Rectangular Channels," ASME JOURNAL OF HEAT TRANSFER, Vol. 109, pp. 936–942.

Islam, R. M., and Nandakumar, K., 1986, "Multiple Solutions for Buoyancy Induced Flow in Saturated Porous Media for Large Peclet Numbers," ASME JOURNAL OF HEAT TRANSFER, Vol. 108, pp. 866–871.

Islam, R. M., and Nandakumar, K., 1988, "Mixed Convection Heat Transfer in Porous Media in the Non-Darcy Regime," *Canadian Journal of Chemical Engineering*, Vol. 66, pp. 68–74.

Kaviany, M., 1985, "Laminar Flow Through a Porous Channel Bounded by Isothermal Parallel Plates," *International Journal of Heat and Mass Transfer*, Vol. 28, pp. 851–858.

Kladias, N., and Prasad, V., 1989, "Natural Convection in Horizontal Porous Layers: Effects of Darcy and Prandtl Numbers," ASME JOURNAL OF HEAT TRANSFER, Vol. 111, pp. 926–935.

Kladias, N., and Prasad, V., 1990, "Flow Transitions in Buoyancy-Induced Non-Darcy Convection in a Porous Medium Heat From Below," ASME JOURNAL OF HEAT TRANSFER, Vol. 112, pp. 675–684.

Law, H. S., Masliyah, J. H., and Nandakumar, K., 1987, "Effect of Non-uniform Heating on Laminar Mixed Convection in Ducts," ASME JOURNAL OF HEAT TRANSFER, Vol. 109, pp. 131–137.

Lee, S. L., 1989, "A Strongly Implicit Solver for Two-Dimensional Elliptic Differential Equations," *Numerical Heat Transfer*, Vol. 16, pp. 161–178.

Levec, J., and Carbonell, R. G., 1985, "Longitudinal and Lateral Thermal Dispersion in Packed Beds," *AIChE Journal*, Vol. 31, pp. 591–602.

Lin, S. H., 1990, "An Experimental Investigation of Forced and Mixed Convection in a Horizontal Rectangular Channel Filled With Packed Spheres," Master's Thesis, National Central University, Taiwan.

Morcos, S. M., and Bergles, A. E., 1975, "Experimental Investigation of Combined Forced and Free Laminar Convection in Horizontal Tubes," ASME JOURNAL OF HEAT TRANSFER, Vol. 97, pp. 212–219.

Nakayama, A., Koyama, H., and Kuwaha, F., 1988, "An Analysis on Forced Convection in a Channel Filled With a Brinkman–Darcy Porous Medium: Exact and Approximation Solutions," *Wärme- und Stoffübertragung*, Vol. 23, pp. 291–295.

Patankar, S. V., 1980, *Numerical Heat Transfer and Fluid Flow*, McGraw-Hill–Hemisphere Corp., New York.

Poulikakos, D., and Renken, K., 1987, "Forced Convection in a Channel Filled With Porous Medium, Including the Effects of Flow Inertia, Variable Porosity, and Brinkman Friction," ASME JOURNAL OF HEAT TRANSFER, Vol. 109, pp. 880–888.

Prasad, V., Kulacki, F. A., and Keyhani, M., 1985, "Natural Convection in Porous Media," *Journal of Fluid Mechanics*, Vol. 150, pp. 89–119.

Prasad, V., Kladias, N., Bandyopadhyay, A., and Tian, Q., 1989, "Evaluation of Correlations for Stagnant Thermal Conductivity of Liquid-Saturated Porous Beds of Spheres," *International Journal of Heat and Mass Transfer*, Vol. 32, pp. 1793–1796.

Shah, R. K., and London, A. L., 1978, *Laminar Flow Forced Convection in Ducts*, Academic Press, New York.

Vafai, K., and Tien, C. L., 1981, "Boundary and Inertia Effects on Flow and Heat Transfer in Porous Media," *International Journal of Heat and Mass Transfer*, Vol. 24, pp. 195–203.

Vafai, K., and Kim, S. J., 1989, "Forced Convection in a Channel Filled With a Porous Medium: An Exact Solution," ASME JOURNAL OF HEAT TRANSFER, Vol. 111, pp. 1103–1106.

Three-Dimensional Mach-Zehnder Interferometric Tomography of the Rayleigh-Bénard Problem

Y. C. Michael

K. T. Yang

Department of Aerospace and Mechanical Engineering,
University of Notre Dame,
Notre Dame, IN 46556

A three-dimensional experimental technique based on axial tomography is demonstrated in this study for the Rayleigh-Bénard convection problem. The technique can perform under severe blockage conditions and with a small number of projections. The major requirement of the technique is an adequate initial guess of the field and the use of an iterative inversion algorithm. In this study, five views are used to study the steady-state natural convection inside a three-dimensional rectangular cavity filled with water at Ra = 5470 ± 100 and Ra = 6140 ± 100. The reconstructed results are estimated to be accurate with a standard deviation of about 0.01°C. The temperature measurements show strong three-dimensional features in the flow.

Introduction

Recent advances in computer technology have made three-dimensional numerical solutions of complicated problems in heat transfer quite common. The only three-dimensional experimental nonintrusive temperature field measurement technique that is available, however, is axial tomography. A recent review by Michael and Yang (1991a) discusses most of the applications of this technique in heat transfer and fluid flow problems. Axial tomography recovers the local field from multiple integral measurements obtained along different directions, called views or projections. The technique works very well when projections can be obtained along the whole viewing range ±90 deg. In cases, however, when, due to physical considerations, it is impossible to obtain measurements within a large viewing range, standard tomographic techniques do not perform as well due to the ill-posedness of the problem. A comparison of several techniques under such conditions is given by Sweeney and Vest (1973) and recently discussed by Bahl and Liburdy (1991). Axial tomography can also be used in conjugate heat conduction and convection problems as was done by Tolpadi and Kuehn (1991). Michael and Yang (1991b) recently suggested the use of an initial guess, a numerical solution for example, to start an iterative reconstruction algorithm in cases where the available viewing range is extremely limited. They applied this technique successfully to both a numerical phantom and a simple experimental case.

In this study, as well as in that of Michael and Yang (1991c), the same technique is applied to a typical problem for which the technique was intended. Steady-state Rayleigh-Bénard convection inside a rectangular enclosure is studied at two Rayleigh numbers. This problem was chosen because although it is very well studied numerically in three dimensions (Mukutmoni and Yang, 1991a, 1991b), there are no three-dimensional noninvasive temperature experimental field measurements except those of Oertel (1980). The problem also poses severe view blockage due to the opaque side walls of the test section.

Axial Tomographic Interferometry

The purpose of axial tomography is to reconstruct, as it was mentioned before, the local field from integral measurements. In interferometry the local field is the index of refraction $n(x, y, z)$ and the integral measurement is the fringe shift $\epsilon(r, \theta)$, which is related to the refraction index by

$$\epsilon = \frac{1}{\lambda_s} \int (n - n_{\text{ref}}) ds \tag{1}$$

where n_{ref} is the index of refraction in the reference beam and s is the path along the measuring beam. In axial tomography the reconstruction is performed at one plane at a time (constant z) by using as many integral measurements as possible, obtained along different views as shown in Fig. 1. A discussion of reconstruction methods based on Fourier transforms is given by Lewitt (1983). Methods based on the image domain have been discussed by Gordon (1974), Herman et al. (1978), Gilbert (1972), and Tan and Modarress (1985). If a sufficient number of views can be obtained over the full viewing range ±90 deg, then most inversion algorithms perform satisfactorily. If, however, the viewing range is limited due to physical considerations, or some of the views are partially blocked, or both, then some methods perform better than others (Sweeney and Vest, 1973; Bahl and Liburdy, 1991). In this study, an initial guess of the field is used as was suggested by Michael and Yang (1991b). The initial guess is obtained by numerically solving the problem in three dimensions using the code developed by Mukutmoni and Yang (1991a, 1991b). Then, the guess and successive iterations are modified using

$$f^{k+1} = f^k + \frac{\epsilon_i - \epsilon_i^k}{S_i} \tag{2}$$

where f is the function to be reconstructed, in this case $(n - n_{\text{ref}})/\lambda$, and i refers to the ith beam (measurement) and k to the kth iteration. S_i is the length of the ith beam within the

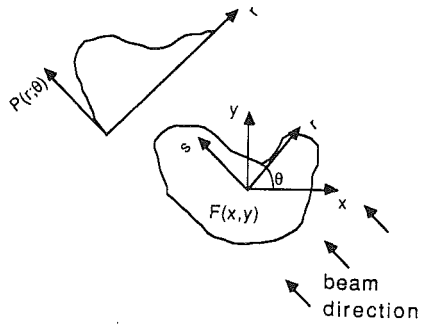

Fig. 1 Projections and coordinate system used in axial tomography

Contributed by the Heat Transfer Division for publication in the JOURNAL OF HEAT TRANSFER. Manuscript received by the Heat Transfer Division July 1991; revision received January 1992. Keywords: Enclosure Flows, Measurement Techniques.

test section. The quantity $(\epsilon_i - \epsilon_i^k)$ is the difference in fringe shift between the experimental (exact) measurement, ϵ_i, and the fringe shift corresponding to the field at the kth iteration for the ith beam, ϵ_i^k. This difference is equally distributed along the length of the beam so that the two fringe shifts become equal. This reconstruction scheme is a version of the Algebraic Reconstruction Technique (ART). The original ART is discussed by Gordon (1974). In general, the reconstruction is performed on a set of points, in this study the same as the numerical grid, that do not necessarily lie on the path of any beam (Fig. 2). For this reason, the correction for a point is obtained by interpolation between the adjacent beams on each side of the point. More details of the method are given in Michael and Yang (1991a, 1991b) and Michael (1991).

The iterations are repeated for all beams in all directions until the average fringe shift difference from the experimental measurements is less than the experimental uncertainty. Once the local values of the index of refraction are obtained, the temperature is calculated based on the refractive index measurements (Tilton and Taylor, 1938).

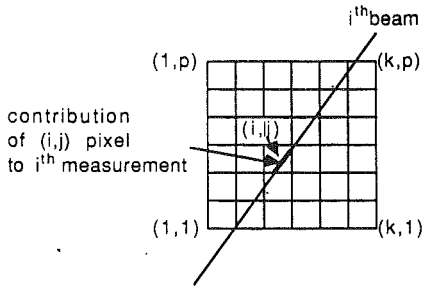

Fig. 2 Notation of reconstruction algorithm

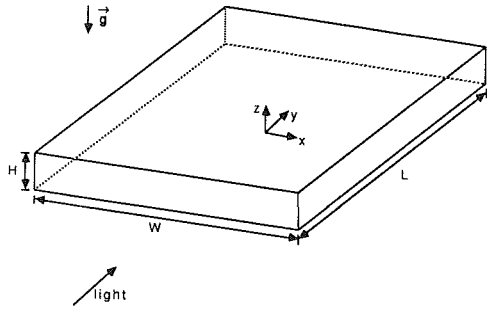

Fig. 3 Schematic of test section cavity

Experimental Apparatus

A schematic of the test section cavity is shown in Fig. 3. Using the height (8.2 mm) of the cavity as the characteristic length scale, the aspect ratios of the cavity are $A_x = 8.7$ and $A_y = 9.0$. Aluminum was used for the top and bottom surfaces of the test section to ensure isothermal conditions. The bottom surface was heated using three electric foil heaters connected in series. The top plate was cooled with cold water from a constant-temperature bath. Two sets of water channels were used flowing in opposite directions again to ensure uniform temperature. Two of the side walls were made out of delrin, which was grooved to have minimum contact with the aluminum plates. The other two side walls were formed by 25.4-mm-thick optical flats. Refraction at the air–glass and glass–water surfaces at the different view angles was taken into account in the reconstruction procedure. The top, bottom, and delrin side walls were also insulated to minimize heat losses in those directions. No insulation was used for the optically flat side walls to promote three-dimensional features in the real flow along the main direction of the light beam, so as to accentuate the difference between the experimental data and the initial guess as given by the numerical solution.

Three thermistors were used in each aluminum plate to measure the temperature variation of each plate. The thermistors were placed in holes drilled from the back side of each plate with the thermistor beads being only 3.0 mm from the plate surfaces. The thermistors were calibrated to measure temperatures with an uncertainty of $\pm 0.01°C$. The side walls were instrumented each with two copper-constantan thermocouples placed at different distances from the side wall surfaces in order to show any temperature gradients in the side walls. The thermocouples could measure temperatures within $\pm 0.05°C$. All holes were filled with conductive epoxy to provide better thermal contact.

During the experiments the surface temperature measurements of the heated and cooled plates indicated uniform temperatures within $\pm 0.01°C$. The thermocouples in the side walls showed temperature gradients corresponding to heat flux at least five orders of magnitude smaller than the output of the electric heaters. Also, no measurable temperature difference was obtained at the inlet and outlet of the water passing through the cooling channels.

The top aluminum plate had two 1.3-mm-dia holes, which were used to fill the cavity with water and allow air out. Both holes were left open during the experiment so that the pressure inside the test section remained equal to atmospheric. The water used was distilled and degassed. The test section was placed on a base that could be adjusted finely to the horizontal position. This base was mounted on a rotating base which could be rotated at any angle within $\pm 1/60$ deg.

The Mach–Zehnder interferometer used has 200-mm-dia optics and a He–Ne laser light source ($\lambda = 632.8$ nm, 10 mW). The fringe patterns were recorded on a video tape, which was later used with a frame grabber board and a Macintosh computer for further analysis.

Nomenclature

A = cavity aspect ratio
f = reconstructed function, m^{-1}
g = gravitational acceleration, m s^{-2}
L, W, H = cavity dimensions, m
n = refraction index
r, s = spatial coordinates, m
Pr = Prandtl number
Ra = Rayleigh number
S = length of beam within test section, m
T = temperature, °C
x, y, z = spatial coordinates, m
α = thermal diffusivity, m^2 s^{-1}
β = coefficient of expansion, K^{-1}
ϵ = fringe shift
θ = view angle, deg
Θ = temperature
λ = wavelength, m
ν = kinematic viscosity, m^2 s^{-1}

Subscripts

c = cold plate
h = hot plate
i = ith beam
x, y = x, y directions

Superscripts

k = kth iteration

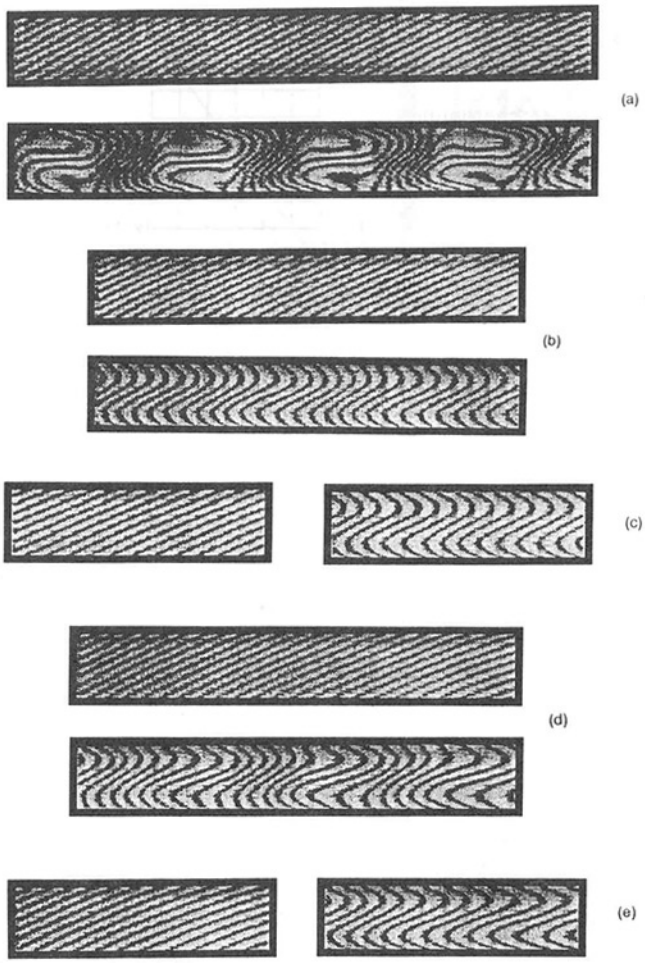

Fig. 4 Undisturbed and disturbed wedge fringes at Ra = 5470 ± 100: (*a*) θ = 0 deg, (*b*) θ = 13.3 deg, (*c*) θ = 26.9 deg, (*d*) θ = −13.3 deg, and (*e*) θ = −26.7 deg

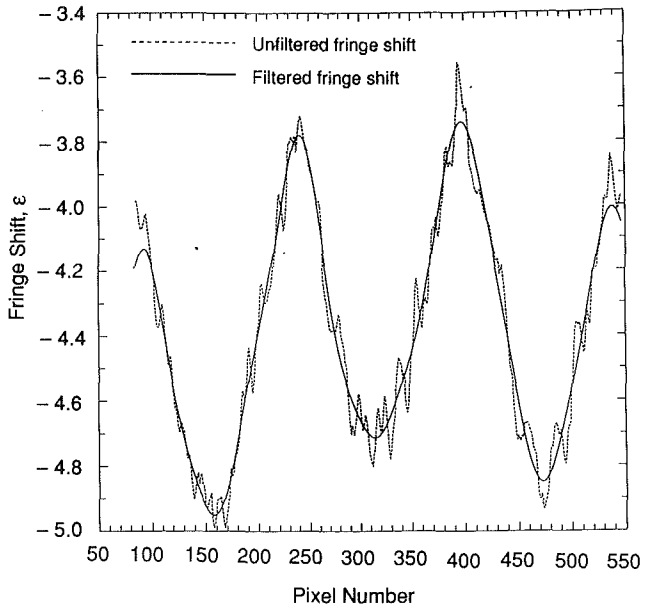

Fig. 5 Filtered and unfiltered fringe shift measurements along $z = 3H/4$ at Ra = 6140 ± 100 and θ = 0 deg

Experimental Procedure

Wedge fringes were obtained and analyzed for both the disturbed and undisturbed fringe patterns for each view that was used. The disturbed patterns at all views were recorded first and then the heating and cooling of the test section were terminated. After this, the test section was allowed to reach room temperature before the undisturbed patterns were recorded. A total of five view angles were used for each Rayleigh number studied.

Rayleigh–Bénard convection was initiated by first turning on the heaters at a low power output, which was enough to initiate convection rolls. The convection rolls were allowed to stabilize for about an hour and then the cooled water was allowed to pass through the channels of the upper plate. The water flow was increased slowly, reaching maximum capacity at about 15–30 minutes. After this, the heater output was adjusted to the desired value and the test section was allowed at least 24 hours to reach steady state before any interferograms were recorded. Sometimes the roll formations broke down, most often during the first hour after the initiation of convection, or did not form symmetrically. About half the times they formed with their axis perpendicular to the main direction of the light. In any case, if any of these happened, the experiment was terminated and a new attempt was made later. When the rolls were aligned with their axis along the main direction of the light, they were aligned parallel to the long side of the cavity, although this side was only slightly longer than the (A_x = 8.7, A_y = 9.0). This phenomenon was also observed numerically by Mukutmoni and Yang (1991a). It was chosen to study the field only when the rolls were aligned in this direction for two reasons. Firstly, the number of rolls could be obtained from the experiments and thus make sure the numerical results matched. Secondly, the direction with the least amount of three-dimensional effects was along the main direction of the light being consistent with the traditional two-dimensional use of the Mach–Zehnder interferometer. Sweeney and Vest (1973) and others mention that the resulting reconstruction error in limited view problems is smaller when this happens.

Data Reduction

A frame grabber board with a resolution of 480 × 640 pixels was used to analyze the fringe patterns. The fringe order at a given height in the disturbed and undisturbed patterns was obtained numerically for all views. The fringe shift was then obtained by finding the difference in fringe order between the disturbed and undisturbed patterns. The fringe shifts obtained with this procedure contained noise due to the board limited resolution. The noise was removed by removing the high-frequency components of the spatial Fourier transform of the fringe shifts. The five pairs of fringe patterns corresponding to the five views used for Ra = 5470 ± 100 (Ra = $g\beta(\Delta t)H^3/\nu\alpha$) are shown in Fig. 4. An example of the fringe shift measurements before and after they are filtered is shown in Fig. 5.

Results

Temperature distributions for two cases are presented in this study. The experimental conditions and water properties are shown in Table 1. The Rayleigh and Prandtl numbers are the only important physical parameters in this problem. For each case, the temperature distributions are shown at three z planes, namely $z = H/4$, $z = H/2$, and $z = 3H/4$. The isotherms shown are defined as

$$\Theta = \frac{T - T_c}{T_h - T_c}\,100 \tag{3}$$

indicating the percent of maximum temperature difference above the cold temperature. All figures show isotherms in intervals of 5.0 based on linear interepolations. In the first case, Ra = 5470 ± 100 and Pr = 6.40, eight rolls were observed with the water adjacent to the delrin side walls moving downward.

Table 1 Experimental conditions and fluid properties*

Rayleigh Number Ra (±100)	5470	6140
Prandtl Number Pr	6.40	6.18
Cold Surface T_{cold} (±0.01 °C)	22.94	24.32
Hot Surface T_{hot} (±0.01 °C)	23.51	24.91
Average Temperature T_{av} (±0.007°C)	23.23	24.62
Expansion Coefficient β (K^{-1})	2.409 E-8	2.544 E-8
Kinematic Viscosity ν ($m^2\ s^{-1}$)	9.321 E-7	9.034 E-7
Thermal Diffusivity α ($m^2\ s^{-1}$)	1.458 E-7	1.463 E-7

* Water properties adapted from Incropera and DeWitt (1985).

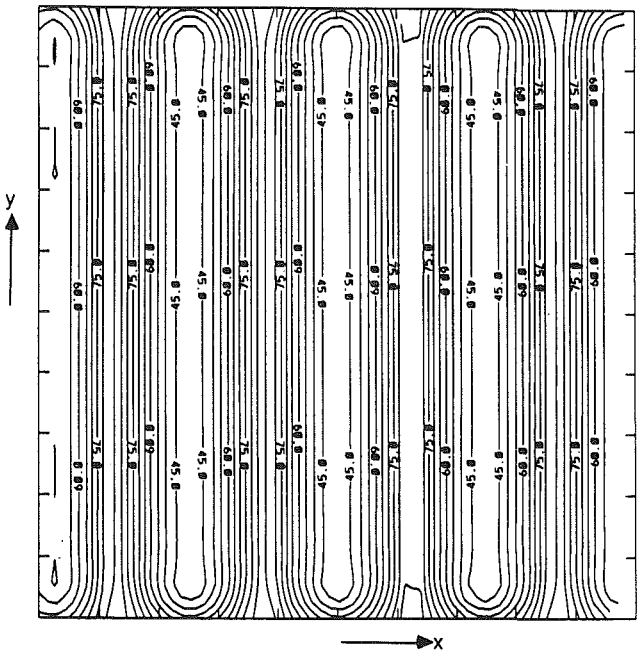

Fig. 6 Numerical temperature field used as initial guess at Ra = 5470 ± 100 and $z = H/4$

The numerical solution that was used as an initial guess in the reconstruction algorithm is shown in Fig. 6 for $z = H/4$. It was obtained using a numerical grid of 80 × 80 × 14. The reconstruction results are shown in Figs. 7, 8, and 9 for $z = H/4$, $z = H/2$, and $z = 3H/4$, respectively. The results were obtained on the same grid as the numerical solution, namely 80 × 80. The five views used in the reconstruction were obtained at $\theta = -26.7$, -13.3, 0, 13.3, and 26.9 deg. The view angle $\theta = 0$ deg corresponds to the case where the light beam is perpendicular to the optical plates and thus parallel to the long side of the cavity. The most important difference between the numerical and experimental results is the existence of three-dimensional end effects and three-dimensional features within the rolls in the reconstructed results. It seems that there are a few hot and cold regions that show a logical progression in the z direction. For example, in Fig. 7 one can see one such a region close to the upper right corner of the figure. The hottest isotherm in this region is $\Theta = 95$. In the middle cross section (Fig. 8), the size of the hot region

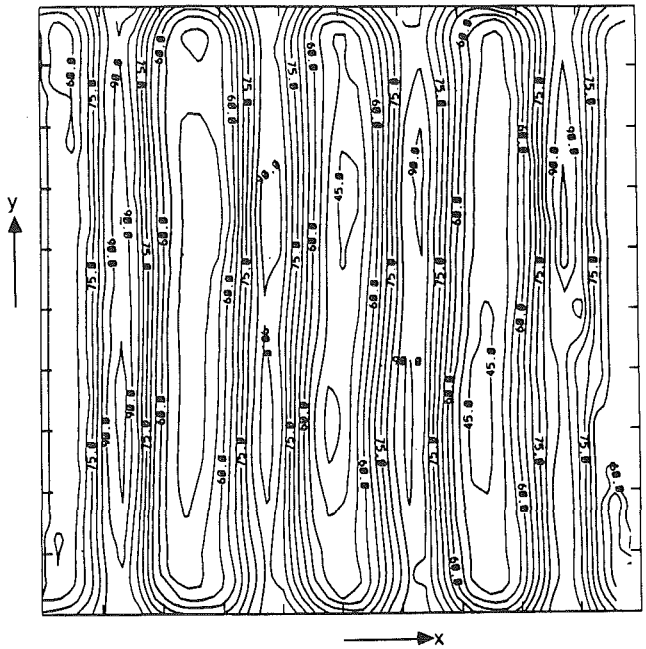

Fig. 7 Reconstructed temperature field at Ra = 5470 ± 100 and $z = H/4$

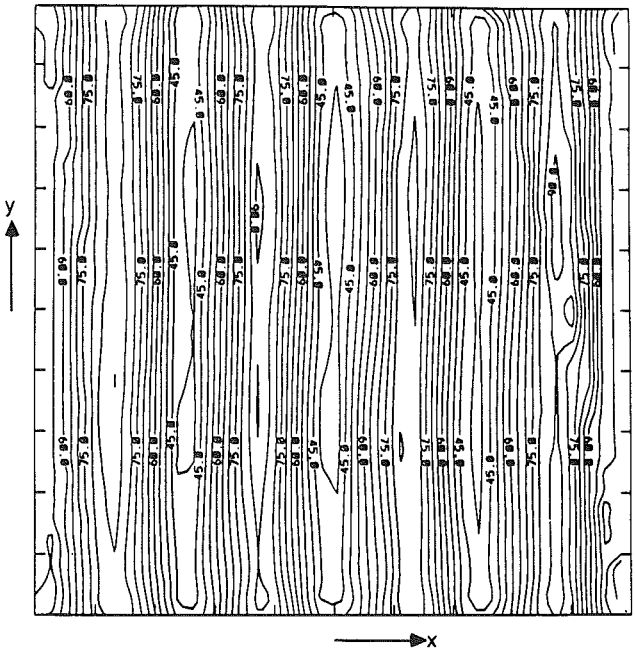

Fig. 8 Reconstructed temperature field at Ra = 5470 ± 100 and $z = H/2$

is reduced and the hottest isotherm is $\Theta = 90$. At $z = 3H/4$ (Fig. 9), the weakening of this hot region is even more pronounced and the hottest isotherm is $\Theta = 85$. Similar observations can be made for the other hot regions as well. The difference between the numerical and experimentally reconstructed fields is essentially due to the fact that the numerical solution does not fully represent the experimental conditions that were present during the experiments. For example, the numerical solution assumed that all four side walls were insulated, while during the experiments two of them (optical flats) were not completely insulated.

The strengthening of the cold spots as one moves upward can also be observed. For example, the cold region located at about three quarters from the left and about one quarter from

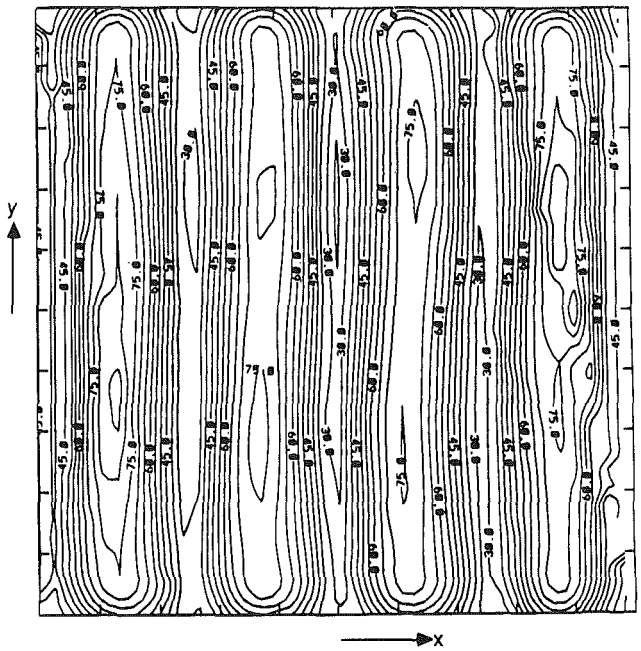

Fig. 9 Reconstructed temperature field at Ra = 5470 ± 100 and $z = 3H/4$

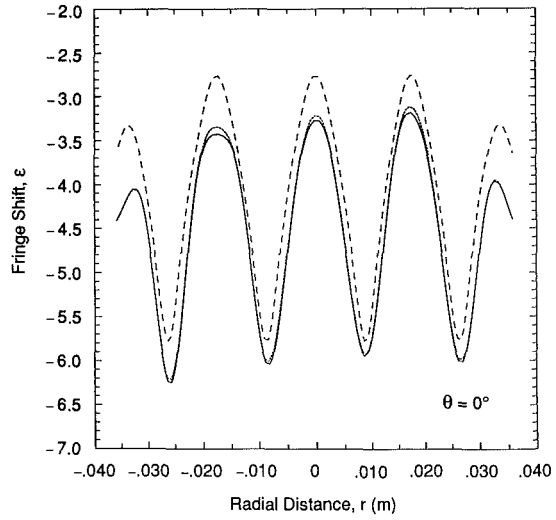

(a)

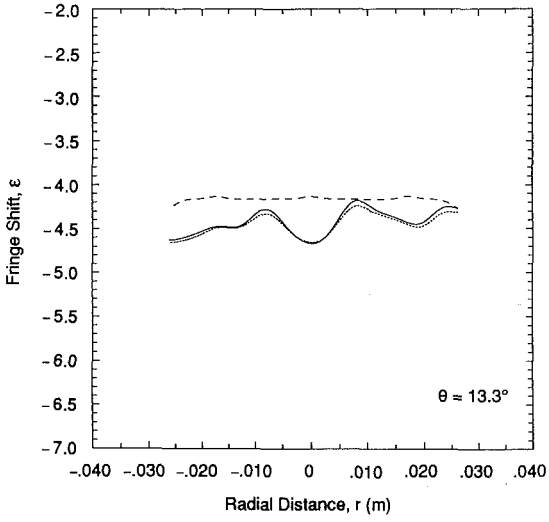

(b)

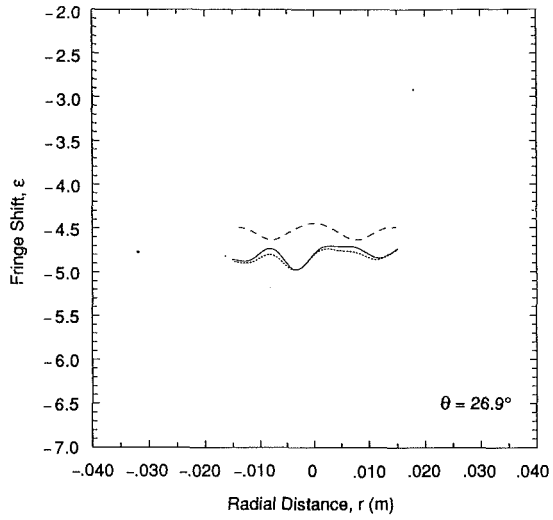

(c)

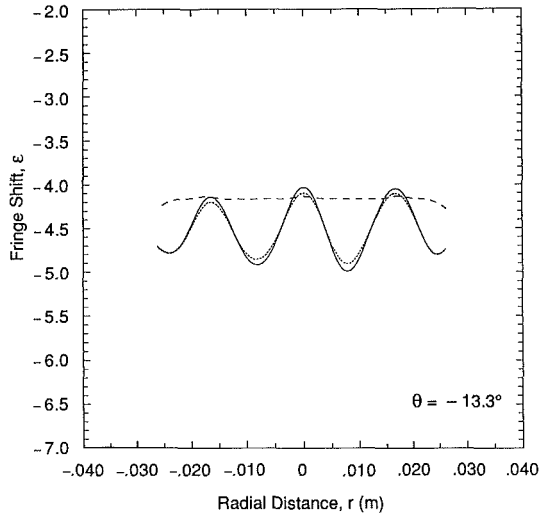

(d)

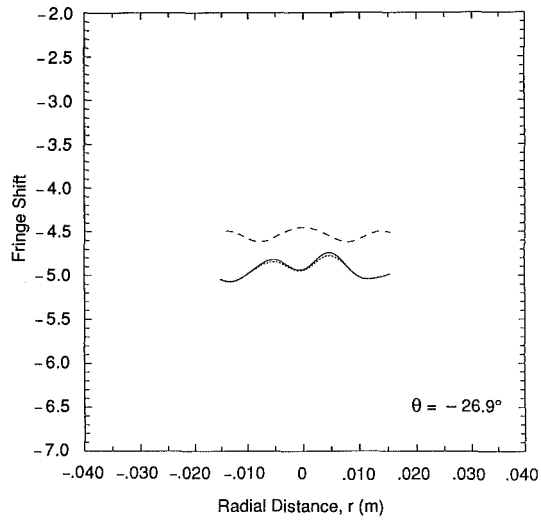

(e)

Fig. 10 Fringe shifts corresponding to the five views used in reconstruction at Ra = 5470 ± 100 and $z = H/4$: ——— exact fringe shift, ····· reconstructed fringe shift, and ····· numerical fringe shift

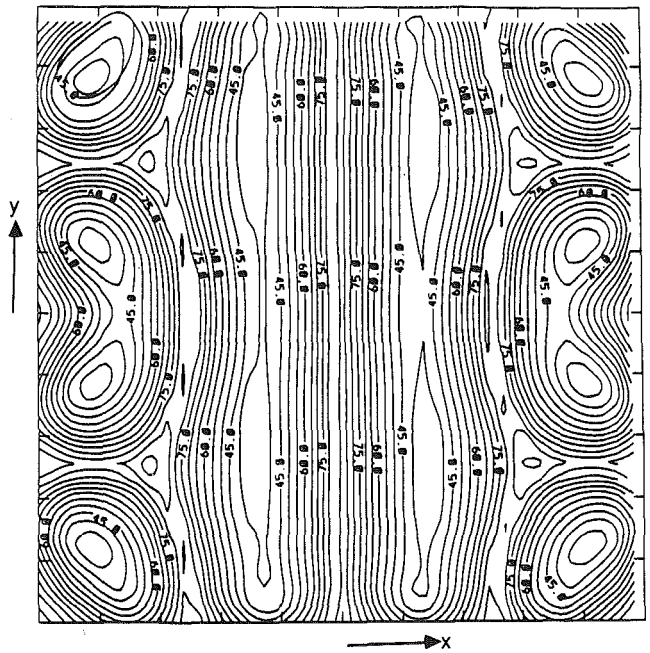

Fig. 11 Numerical temperature field used as initial guess at Ra = 6140 ± 100 and $z = H/4$

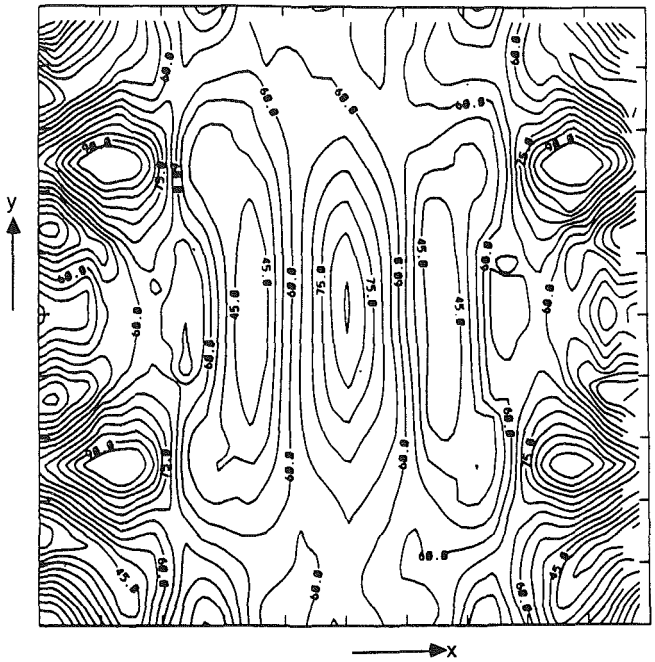

Fig. 13 Reconstructed temperature field at Ra = 6140 ± 100 and $z = H/2$

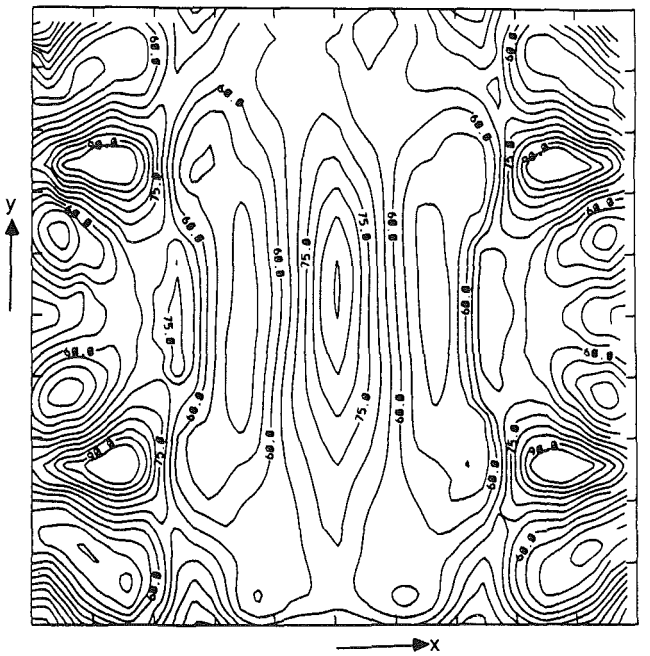

Fig. 12 Reconstructed temperature field at Ra = 6140 ± 100 and $z = H/4$

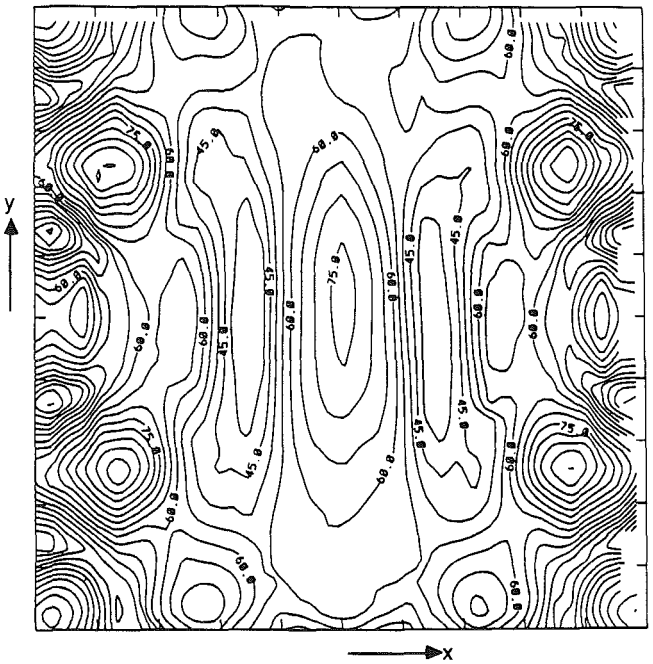

Fig. 14 Reconstructed temperature field at Ra = 6140 ± 100 and $z = 3H/4$

the bottom of Fig. 7 ($z = H/4$) shows this clearly. The coldest isotherm in this region is $\Theta = 45$ while at $z = H/2$ (Fig. 8) the coldest isotherm is $\Theta = 40$ and the $\Theta = 45$ isotherm covers the whole length of the roll. In Fig. 9 ($z = 3H/4$) the coldest isotherm is $\Theta = 30$ indicating further cooling.

The fringe shifts corresponding to this case, at $z = H/4$, are shown in Fig. 10 for the five views. In this figure, the fringe shifts shown correspond to the initial temperature distribution (numerical fringe shift), the reconstructed field (reconstructed fringe shifts), and the experimental measurements (exact fringe shifts). The average agreement between the reconstructed and experimental fringe shifts is less than 0.1 fringe shift, corresponding to an experimental uncertainty of less than 0.1 deg.

The numerical solution for Ra = 6140 ± 100 and Pr = 6.2 at $z = 3H/4$ is shown in Fig. 11. The numerical grid used was $60 \times 60 \times 14$ and the reconstruction grid 60×60. In this case only the four inner rolls are longitudinal rolls, while the two rolls at the edges broke down into three-dimensional structures. The reconstructed field obtained from five views (θ = 21.3, −10.2, 0, 11.0, and 21.9 deg) is shown in Figs. 12, 13, and 14 for $z = H/4$, $z = H/2$, and $z = 3H/4$, respectively. Again the continuity of hot and cold regions can be observed in the z direction. In this case, the center roll on one side,

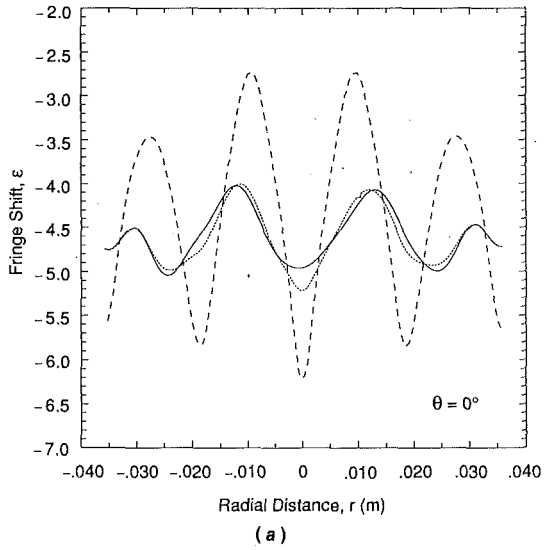

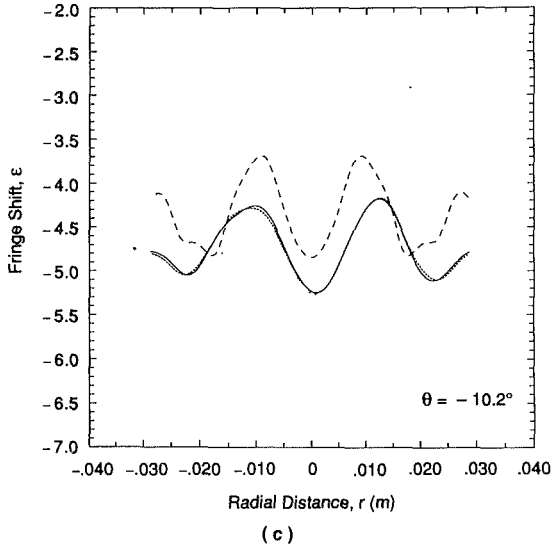

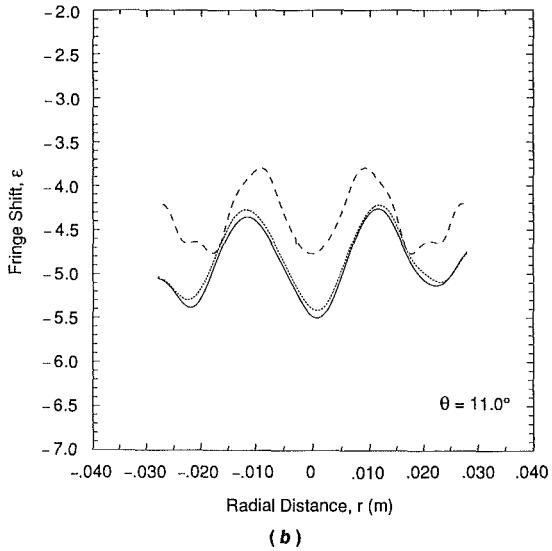

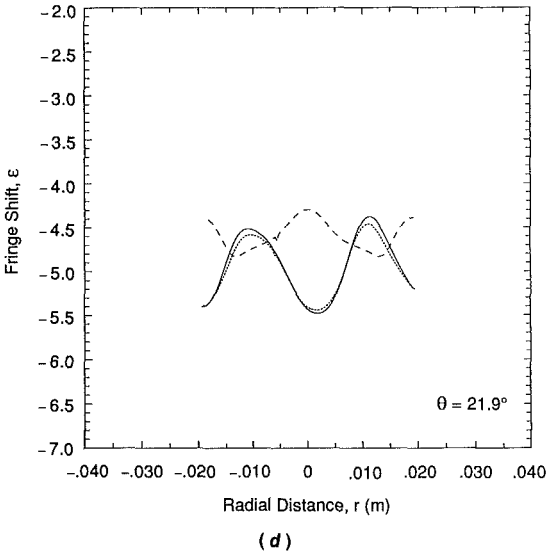

upper part of figures, bends to the left. This feature is consistent in all three cross sections studied. The fringe shifts corresponding to this case, at $z = H/4$, are shown in Fig. 15.

Error Estimate

A sensitivity analysis was performed on a number of parameters in order to get a better estimate of the error involved in the reconstruction. As is expected, there are a number of factors contributing to the final error. There are numerical/analytical sources of error as well as experimental ones. The experimental errors involve errors like the heating of part of the path of the light beam outside the test section (like the optical flats) and refraction errors due to refraction index gradients perpendicular to the direction of the beam. These errors are also present in two-dimensional studies. They were compensated by applying a correction to the fringe shift based on the hot and cold surfaces. The view angles during the experiments, needed for the reconstruction, were obtained with an uncertainty smaller than 1/60 deg. The fringe shift error corresponding to this angle uncertainty is of the order of 0.0004 fringes, which is negligible. The most important source of error is the fringe shift measurement itself which was 0.1 fringe.

The numerical/analytical sources of error include the error in inverting the data. The analytical error is present because the inversion is not exact as it is in the two-dimensional or

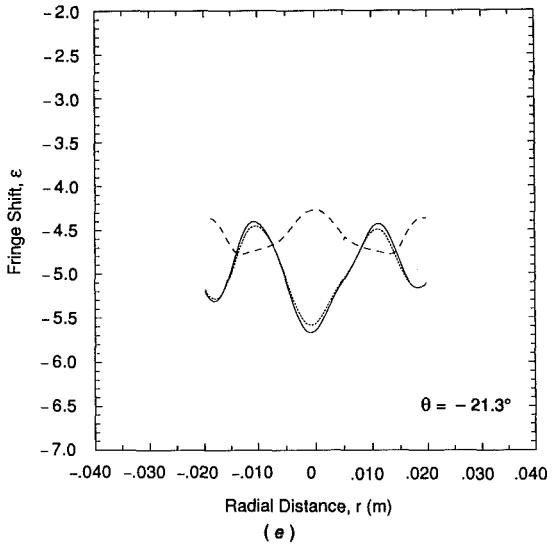

Fig. 15 Fringe shifts corresponding to the five views used in reconstruction at Ra = 6140 ± 100 and $z = H/4$; ——— exact fringe shift, ····· reconstructed fringe shift, and ····· numerical fringe shift

axisymmetric cases. There is also numerical error that occurs in applying the inversion formula. Most of this error will be due to the large number of integrations that are present in the algorithm. For this reason, the sensitivity of the results to the accuracy of the integrations was studied. It was found that if the integration was accurate within 0.1 percent of the integral value, the standard deviation of the results from the results obtained when the integration was accurate within 0.01 percent was only 0.00035°C. If the integration accuracy was relaxed to 1.0 percent, the standard deviation became 0.0019°C. At 10.0 percent integration accuracy the standard deviation was 0.0076°C. If one wants results of a certain accuracy, the integration should be such that the error due to it is at least one order of magnitude smaller than the desired accuracy. So, if results accurate within 0.01°C are desired, this restriction implies using an integration accuracy of at least 0.1 percent so that the quantity twice the standard deviation (95 percent of samples) is smaller than 0.001°C.

The effect of the number of nodes was also studied for the case of Ra = 5470 ± 100. The original grid used to obtain the results was 80 × 80. When a rougher grid of 60 × 20 was used both to generate the numerical solution and for the reconstruction, the results deviated from the original ones with a standard deviation of 0.0071°C, which should be considered small, considering the roughness of the grid.

It was also found that if only three views are used instead of five, it is better to use the three views with the largest number of data, namely $\theta = -13.3$, 0, and 13.3 deg. These views give better results than the three views with the largest viewing range ($\theta = -26.7$, 0, and 26.9 deg) or other view combinations. It seems, at least for this case, that the negative effect of side blockage is more important than the positive effect of the extra viewing range.

Moreover, an error estimate was obtained by reconstructing a "test field" similar to the one in the experiments under similar conditions using the same technique and amount of data as was done in the experiments. To do this, the "test field" must have a known solution so that the reconstructed field can be compared to it. It was chosen to use the reconstructed fields discussed in the previous section as the "test fields." The fringe shifts corresponding to these fields were calculated numerically and the same initial guess was used as was done in the actual reconstruction. The reconstruction algorithm was again terminated when the average fringe shift difference between the "test field" and the "reconstructed field" was smaller than 0.1 fringe. This procedure yielded a standard deviation of 0.010°C for Ra = 5470 ± 100 and 0.012°C for Ra = 6140 ± 100. This error estimate includes both numerical/analytical and experimental errors because all the numerical errors are generated by default, and experimental error is accounted for because the fringe shifts of the reconstructed results are only equal to the exact ones within the experimental uncertainty. For comparison, the temperature error that corresponds to a two-dimensional case under similar conditions is 0.008°C, which is smaller than the three-dimensional error, as expected.

Finally, it should be mentioned that the reconstruction error will also depend on the quality of the initial guess. A previous study by Michael and Yang (1991b) examined the effect of the initial guess in detail.

Conclusions

Axial tomography in combination with a numerical solution proved to be a valuable tool in obtaining three-dimensional temperatures of a problem that otherwise would be impossible with current means. The technique requires a relatively small amount of data, only five views in the cases studied here, and performed very well even for limited view ranges such as ±21 deg.

The three-dimensional results of the Rayleigh–Bénard convection showed considerable three-dimensional structures indicating three-dimensional flows also. This should serve as a warning to people performing two-dimensional experiments to take all the necessary steps to ensure a two-dimensional field.

Acknowledgments

The authors wish to acknowledge Dr. Devadatta Mukutmoni for his assistance in obtaining the numerical solutions used in the reconstructions. The algorithm used to obtain the numerical solutions was developed under NSF Grant No. ATM890007N to the University of Notre Dame.

References

Bahl, S., and Liburdy, J. A., 1991, "Measurement of Local Convective Heat Transfer Coefficients Using Three-Dimensional Interferometry," *International Journal of Heat and Mass Transfer*, Vol. 34, No. 4/5, pp. 949–960.

Gilbert, P. F. C., 1972, "Iterative Methods for the Three-Dimensional Reconstruction of an Object From Projections," *Journal of Theoretical Biology*, Vol. 36, No. 1, pp. 105–117.

Gordon, R., 1974, "A Tutorial on ART," *Institute of Electrical and Electronic Engineers Transactions on Nuclear Science*, Vol. NS-21, No. 3, pp. 78–93.

Herman, G. T., Lent, A., and Lutz, P. H., 1978, "Relaxation Methods for Image Reconstruction," *Communications of the Association of Computing Machinists*, Vol. 21, No. 2, pp. 152–158.

Incropera, F. P., and DeWitt, D. P., 1985, *Fundamentals of Heat and Mass Transfer*, 2nd ed., Wiley, New York.

Lewitt, R. M., 1983, "Reconstruction Algorithms: Transform Methods," *Proceedings of the Institute of Electrical and Electronic Engineers*, Vol. 71, No. 3, pp. 390–408.

Michael, Y. C., 1991, "Three-Dimensional Temperature Reconstruction Using Mach–Zehnder Interferometric Tomography," PhD Thesis, Department of Aerospace and Mechanical Engineering, University of Notre Dame, Notre Dame, IN.

Michael, Y. C., and Yang, K. T., 1991a, "Recent Developments in Axial Tomography for Heat Transfer and Fluid Flow Studies," *Experimental Thermal and Fluid Science*, Vol. 4, No. 6, pp. 637–647.

Michael, Y. C., and Yang, K. T., 1991b, "Three-Dimensional Temperature Reconstruction Using Mach–Zehnder Interferometric Tomography," *Experimental Heat Transfer, Fluid Mechanics, and Thermodynamics 1991*, J. F. Keffer, R. K. Shah, and E. N. Ganic, eds., Elsevier Science Publishing, New York, pp. 514–521.

Michael, Y. C., and Yang, K. T., 1991c, "Three-Dimensional Mach–Zehnder Interferometric Tomography of the Bénard Problem," presented at the Fourth Annual Inverse Problems Seminar, Michigan State University, East Lansing, MI.

Mukutmoni, D., and Yang, K. T., 1991a, "Flow Transitions in a Three-Dimensional Rectangular Enclosure Heated From Below," *Proceedings of the Third ASME–JSME Thermal Engineering Joint Conference*, Reno, NV, Vol. 1, pp. 77–82.

Mukutmoni, D., and Yang, K. T., 1991b, "Transition and Oscillatory Flow in Rayleigh–Bénard Convection in a Three-Dimensional Box," ASME Paper No. 91-HT-10.

Oertel, H., Jr., 1980, "Three-Dimensional Convection Within Rectangular Boxes," in: *Natural Convection in Enclosures*, 19th National Heat Transfer Conference, ASME HTD-Vol. 8, pp. 11–16.

Sweeney, D. W., and Vest, C. M., 1973, "Reconstruction of Three-Dimensional Refractive Index Fields From Multidimensional Interferometric Data," *Applied Optics*, Vol. 12, No. 11, pp. 2649–2663.

Tan, H., and Modarress, D., 1985, "Algebraic Reconstruction Technique Code for Tomographic Interferometry," *Optical Engineering*, Vol. 24, No. 3, pp. 435–440.

Tilton, L., and Taylor, J., 1938, "Refractive Index and Dispersion of Distilled Water for Visible Radiation of Temperatures 0 to 60°C," *Journal of Research of the National Bureau of Standards (U.S.)*, Vol. 20, pp. 419–477.

Tolpadi, A. K., and Kuehn, T. H., 1991, "Interferometric Reconstruction of Three-Dimensional Temperature Fields in Conjugate Conduction-Convection Flows," presented at the Third ASME–JSME Thermal Engineering Joint Conference, Reno, NV.

Flame Temperature Measurement by Monitoring an Alkali Emission Doublet Exposed to a Selectively Filtered Background Source

H. A. Pattee
Assistant Professor.
Mem. ASME

R. B. Peterson
Associate Professor.
Mem. ASME

Department of Mechanical Engineering,
Oregon State University,
Corvallis, OR 97331

The traditional line reversal method for measuring flame temperatures has been modified to eliminate balancing of the background radiation source and facilitate real-time measurement. Two closely spaced emission lines of a Group IA element are simultaneously monitored and compared to the emission of a known source. The new technique uses optical filtering to reduce the apparent temperature of the source at the wavelength corresponding to one of the transitions. The ratio of the absorption/emission intensities of the two lines is directly related to the flame temperature. Flames as hot as 2800 K can readily be probed using the new technique. Experimental data for cool flat flames compare well with thermocouple measurements.

1 Introduction

Combustion researchers often need a quick, reliable, inexpensive means of measuring flame temperatures. Pt/Pt-Rh thermocouples are frequently used for temperature probing of cool flames. Thermocouples disturb the flame somewhat and must be corrected for radiative and conductive losses as well as for catalytic effects, but they provide a simple and consistent means of determining flame temperature profiles. At temperatures above about 2000 K, however, thermocouple probing is less practical. It becomes necessary to use tungsten thermocouples, which are incompatible with an oxidizing environment. Sheathing for an inert gas purge severely reduces spatial resolution.

Optical, laser-based methods have the advantage of probing a flame without disturbing it and have been used extensively in optically clean environments. One accurate laser technique, CARS (Coherent Anti-Stokes Raman Spectroscopy), has been useful in soot-laden environments and in highly luminous flames. However, the specialized equipment required is not readily available in many research labs. There are several simpler optical techniques that can be implemented with common laboratory equipment. The most popular of these, the line reversal method, measures a flame's temperature by equating its emission to that of a radiation source whose temperature is adjustable and calibrated. Implementing the method is straightforward, but the comparison process introduces subjectivity into the measurements and requires the investigator to interact continually with the system.

An adaptation of the conventional line reversal technique has been developed that eliminates the need to adjust the reference source. The method, which provides a more direct measurement of flame temperature, can readily be used to probe flames up to 2800 K. It was primarily developed for temperature characterization of highly luminous, seeded H_2/O_2 diffusion flames that are being subjected to electric and magnetic fields. The technique is well suited for this purpose since the flames already contain atoms of a Group IA element, a necessary condition for implementing line reversal.

Contributed by the Heat Transfer Division for publication in the JOURNAL OF HEAT TRANSFER. Manuscript received by the Heat Transfer Division June 1991; revision received January 1992. Keywords: Combustion, Fire/Flames, Measurement Techniques.

2 Background

Kurlbaum (1902a, 1902b) described a simple method of measuring a flame's temperature by comparing its spectral brightness to that of a known radiation source. The techniques he developed were then applied to specific resonance lines of sodium, and the name "line reversal" was adopted. The method, described in detail in many places (Gaydon and Wolfhard, 1970; Penner, 1949; Reif et al., 1973), became popular during the middle of this century.

To implement line reversal, a bright background source is viewed through a flame into which sodium (or another element) has been introduced. If the flame temperature is higher than the brightness temperature of the source, the element's characteristic transition lines will appear in emission. Conversely, a flame temperature below the brightness temperature of the source results in absorption at the same wavelengths. When the background source and flame are at the same temperature, neither emission nor absorption is seen; this condition is known as the reversal point.

Line reversal has been used in many laboratory flame studies on both premixed and diffusion flames (Wolfhard and Parker, 1949). It is useful for fundamental studies and has frequently been implemented for practical temperature measurements in a variety of applications including, for example, an MHD generator (Daily and Kruger, 1976) and rifle muzzle flash (Klingenberg and Mach, 1976). Thomas (1968a) has shown that the technique can be adjusted for use in flames containing particles and in cases where boundary layer effects are present. Due to its simplicity, versatility, and low cost, the method has become widely used and well accepted (Gaydon and Wolfhard, 1970).

3 Development

Traditional Line Reversal. The emissive power of a blackbody is a function of both temperature and wavelength, as described by Planck and approximated by Wien's law (Siegel and Howell, 1981):

$$I \propto \lambda^{-5} e^{-\frac{c}{\lambda T}} \tag{1}$$

For a specific wavelength, the emissive power of a source at a given temperature can be equated to that of a blackbody radiator at a somewhat lower temperature (known as the "brightness temperature" of the source). When radiation is

passed through a gas or flame, some of it will be absorbed at specific wavelengths corresponding to ground state transitions of species present. Additionally, the gas emits radiation at these wavelengths based on its own temperature. Application of Kirchhoff's law (Siegel and Howell, 1981) yields a differential equation describing the resultant radiation intensity:

$$dI = (I_f - I)\alpha dx \tag{2}$$

In general, both α and I_f can vary with position. If only emission in a very narrow wavelength band (e.g., that corresponding to a spectral line) is considered, and if the gas composition and temperature are constant, the value of α can be taken as constant in a gaseous element. The solution of Eq. (2) is then:

$$Ie^{\alpha x} = \int I_f \alpha e^{\alpha x} dx \tag{3}$$

Equation (3) can now be solved for the flame geometry. Integrating across the flame (from $x=0$ to $x=l$) and applying the boundary condition $I_{x=0} = I_b$:

$$I = I_f(1 - e^{-\alpha l}) + I_b e^{-\alpha l} \tag{4}$$

The difference between intensity at the spectral line wavelength and that at a nearby wavelength can now be determined. For the latter, $\alpha = 0$ and the intensity is simply I_b. The difference ΔI, which represents the height of an emission or absorption peak above the background, is:

$$\Delta I = (I_f - I_b)(1 - e^{-\alpha l}) \tag{5}$$

In traditional line reversal, the temperature of the background radiation source is adjusted until $\Delta I = 0$. Solving Eq. (5), $I_b = I_f$ for this condition, meaning that the background temperature equals the flame temperature ($T_b = T_f$). Since the temperature of the background source has been calibrated, the flame temperature is thus determined.

Two-Temperature Modification. Line reversal can be modified to eliminate the need to balance a background source. Thomas (1968b) developed a method that instead used two different background temperatures and compared the intensity difference ΔI obtained for each. He derived an expression that directly relates the ratio of the two values to flame temperature:

$$R = \frac{\Delta I_1}{\Delta I_2} = \frac{I_f - I_{b1}}{I_f - I_{b2}} \tag{6}$$

Expressing the intensities as in Eq. (1):

$$R = \frac{e^{-\left(\frac{c}{\lambda T_f}\right)} - e^{-\left(\frac{c}{\lambda T_{b1}}\right)}}{e^{-\left(\frac{c}{\lambda T_f}\right)} - e^{-\left(\frac{c}{\lambda T_{b2}}\right)}} \tag{7}$$

From Eq. (7), measurement of the peak height at each of two background temperatures can be used to deduce flame temperature. The peak is not "reversed" at all during the process. Since the source need not be adjusted to match the flame, temperatures several hundred degrees Kelvin above the maximum attainable background temperature can also be measured.

The disadvantage of this two-temperature method is that the source must continually be switched between T_{b1} and T_{b2}. Because of the time lag, there is no assurance that the same flame temperature is being measured with each source.

Two-Wavelength Modification. Group IA elements such as sodium, potassium, and cesium share the characteristic of having two strong, closely spaced emission lines. Both lines can be monitored simultaneously, and will reverse at the same background brightness temperature. It is also possible to expose the two transitions to different effective source brightness temperatures. If a filter with a cut-on wavelength between the two transitions is placed in front of the source, the background intensity at the lower wavelength will be reduced more than that at the higher wavelength. This effectively causes the two emission peaks to respond as if each were being measured against a different comparison source. For sodium, the emission doublet is too closely spaced for practical implementation of this technique. Potassium, rubidium, and cesium, however, are all potential candidates for this method. The two-temperature ratio equation is modified to reflect the difference in wavelength, with the wavelength dependent terms no longer canceling as they did in Eq. (7):

$$R = \left(\frac{\lambda_2}{\lambda_1}\right)^5 \left[\frac{e^{-\left(\frac{c}{\lambda_1 T_f}\right)} - e^{-\left(\frac{c}{\lambda_1 T_{b1}}\right)}}{e^{-\left(\frac{c}{\lambda_2 T_f}\right)} - e^{-\left(\frac{c}{\lambda_2 T_{b2}}\right)}}\right] \left[\frac{(1 - e^{-\alpha_1 l})}{(1 - e^{-\alpha_2 l})}\right] \tag{8}$$

The absorption coefficient α is different for the two transitions and is temperature dependent. If the (αl) product for the weaker line is maintained at a value on the order of 10 or greater, the final term of Eq. (8) reduces to one and a simpler expression for the peak height ratio can be written:

$$R = \left(\frac{\lambda_2}{\lambda_1}\right)^5 \left[\frac{e^{-\left(\frac{c}{\lambda_1 T_f}\right)} - e^{-\left(\frac{c}{\lambda_1 T_{b1}}\right)}}{e^{-\left(\frac{c}{\lambda_2 T_f}\right)} - e^{-\left(\frac{c}{\lambda_2 T_{b2}}\right)}}\right] \tag{9}$$

By monitoring two peaks simultaneously, the benefits of the two-temperature method are realized without sacrificing time resolution. The resulting method does not require adjustment of the background source. Temperatures above the maximum attainable source temperature can be measured, and no operator interaction with the system is required.

Nomenclature

C = second radiation constant = 0.014388 m-K
dx = thickness of gas element
I = radiation intensity
I_b = radiation intensity at background brightness temperature
I_f = radiation intensity at flame temperature
l = flame thickness
R = ratio of peak heights at λ_1 and λ_2
T = temperature
T_b = brightness temperature of background source
T_f = flame temperature
T_{fil} = lamp filament temperature
$t_{\lambda 1}$ = net transmission through color filter and first lens at lower transition wavelength
w_{T_b} = uncertainty in brightness temperature
$w_{T_{fil}}$ = uncertainty in filament temperature
α = absorption coefficient of gas
ΔI = peak height above background spectrum
$\epsilon_{\lambda, T_{fil}}$ = emissivity of filament at a given wavelength and temperature
λ = wavelength
ϕ = stoichiometric equivalence ratio of flame

Subscripts

1 = lower transition wavelength of alkali doublet
2 = upper transition wavelength of alkali doublet

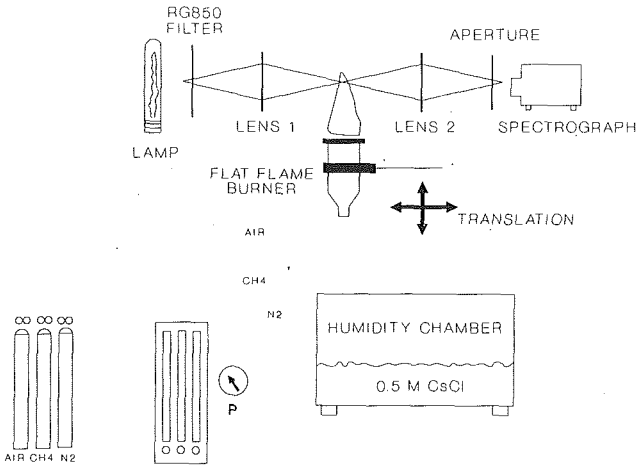

Fig. 1 Experimental apparatus

4 Experimental

Burner and Gas Delivery System. To conduct line reversal, atoms of the element being monitored must be introduced into the flame. The measurement technique discussed here was developed primarily for use with seeded flames being subjected to electric and magnetic fields. These flames already contain sufficient concentrations of cesium to perform line reversal.

Figure 1 details the present system, which consists of a burner sitting directly above an ultrasonic humidifier modified for this experiment. Before entering the burner, gaseous fuel is fed through the humidifier chamber, where a fine mist of salt solution is introduced into the flow. This provides an easily controlled means of introducing various elements into the reactant stream.

Bottled gas pressures are controlled with two-stage pressure regulators. Gas flow rates are monitored using rotameters equipped with high-accuracy needle valves. Pressures are measured with a dial gage at the rotameter exit. The fuel (CH_4 or H_2) is sent into the mist chamber for seeding with a 0.5 M CsCl solution. An ultrasonic transducer beneath the liquid surface generates a fine mist, which is carried along toward the burner. At the gas flow rates being used, the CsCl solution is introduced at a rate of approximately 0.3 ml/min. Premixed O_2/N_2 is combined with the fuel below the burner entrance. Combustible mixtures are never allowed into the mist chamber, which is equipped with an N_2 purge for use before and after lighting each flame. The mist chamber can be fitted with two different burners, one for examining premixed flames and the other for diffusion flames.

For premixed flat flames a stainless steel screen burner similar to that described by Altenkirch et al. (1979) is used. The spacing and mesh sizes of the smoothing screens can be changed to optimize flow characteristics for different conditions. The top screen, above which the flame is stabilized, can be cooled by flowing water through 0.3 mm hypodermic tubing, which is woven through the screen. The burner diameter of 43 mm can be reduced to 20 mm for exploring high-speed flames without increasing the working range of gas flow rates. A 30 mesh stainless steel screen can be positioned about 17 mm above the burner to help stabilize the flames.

The entire mist chamber/burner assembly is mounted on an x-z stage. Temperature profiles are obtained by vertical translation of the burner relative to the fixed optical system, with spatial repeatability of 0.1 mm.

Optical System. The optical system is also shown in Fig. 1. Its primary components are the background radiation source with temperature-reducing color filter, focusing lenses and apertures, and a spectrograph equipped with a photodiode array detector. The detector interfaces with a computerized data acquisition system.

A 500 W double coil tungsten/halogen lamp with a quartz envelope serves as the background radiation source. It is powered with output from a 0–140 V Variac. Normal operating voltages for the lamp range from 60 to 120 V. The operating temperature of the lamp is calibrated against voltage, as described in the following section. Radiation from the lamp passes through a RG850 color filter with a nominal cut-on wavelength of 850 nm and a transmittance of 0.91 above 900 nm. At the transition wavelengths of cesium, 852 and 894 nm, the filter transmittances are 0.55 and 0.88, respectively.

Radiation from the lamp is focused into the flame, then refocused onto the slit of a spectrograph, using a pair of 25-mm-dia double convex lenses. A 0.3-mm-dia aperture serves as a field stop and limits the intensity reaching the spectrograph. The spectrograph slit is oriented vertically and has a width of 0.05 mm. A holographically ruled diffraction grating with 600 grooves/mm gives a spectral resolution of 0.125 nm/element. A 512 element photodiode array detector is used, giving a scan range of 64 nm; this is compatible with the 42 nm wavelength spacing of the peaks being monitored. Detector sensitivity decreases at higher wavelengths, an effect that must be considered in calculating peak ratios. The background source, optical components, and spectrograph are all mounted on an optical bench to maintain consistent alignment.

Background Source Calibration. The tungsten lamp was calibrated to determine filament temperature versus applied voltage. This was accomplished by performing a series of power measurements using various known filters placed between the lamp and a calorimeter. By considering the emissive properties of the tungsten filament (De Vos, 1954) and the transmission characteristics of the lamp's quartz envelope, the filters, and the measuring device, filament temperatures were inferred as follows.

For a specific lamp voltage setting, an absorbing disk calorimeter was used to measure transmitted power through each of three color filters. For each filter, a ratio of the filtered power to the unfiltered value was calculated. Because the geometry remained constant, the power ratio was independent of the solid angle being measured.

The expected power ratio for a given filament temperature can also be determined analytically. Assuming a true filament temperature, and knowing the filament's emissivity characteristics at that temperature, the total power emitted over all wavelengths can be calculated from theory. If the intensity at each wavelength is multiplied by the known transmittance of a color filter, a somewhat lower power emission results. Both values can be corrected to account for the transmission characteristics of the quartz lamp envelope and the absorber disk. The ratio of these two values is characteristic of the temperature and the filter. This procedure was applied repeatedly for a series of temperatures and three different color filters, and a plot of power ratio versus temperature was prepared for each filter. These curves are shown in Fig. 2. For each filter, the power ratio reaches a flat maximum; in general, these maxima occur at lower temperatures as the filter cut-on wavelength increases.

To calibrate the lamp, data were taken at seven lamp voltages. For each, the power ratios for the three filters were converted to temperature using the theoretical curves described above. If the experimentally obtained ratio fell in the flat region of the curve for one filter, only the data from the other two filters were used to estimate temperature. Good agreement among the three filters was achieved. Figure 3 shows a calibration curve of filament temperature as a function of lamp voltage. Error bars are shown to represent 95 percent confi-

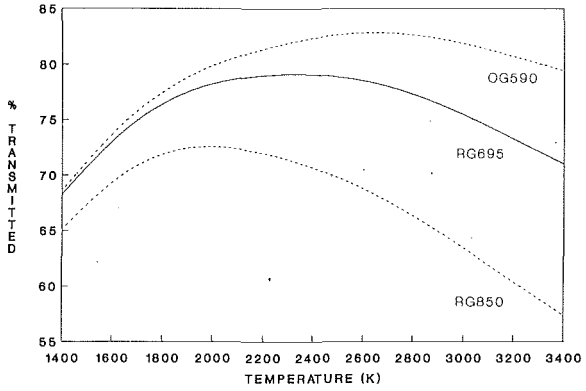

Fig. 2 Power ratio versus temperature for color filters

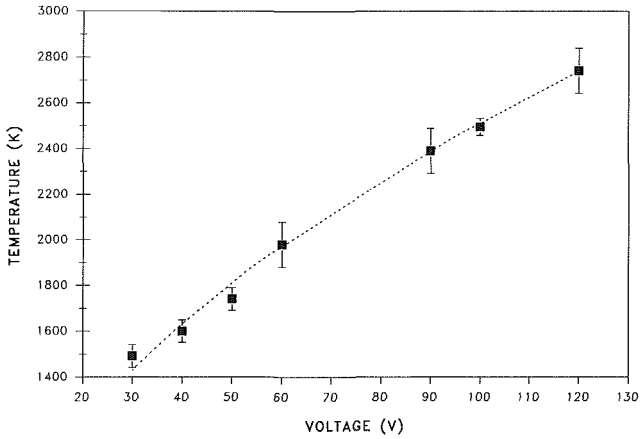

Fig. 3 Tungsten lamp calibration curve

dence intervals, based on the spread in experimentally obtained temperature values at each voltage. From theoretical considerations, the equilibrium filament temperature would be expected to vary approximately as the square root of voltage. The rate of energy input is proportional to voltage squared, while the primary mode of energy loss is by radiation and is proportional to T_{fil}^4. The dotted line in Fig. 3 is a regression line of T against $V^{1/2}$, and the experimentally obtained data follow the predicted relationship with a correlation coefficient of 0.992.

5 Results

Peak Height Ratio Versus Temperature. For a known lamp voltage, lamp filament temperature is determined from the calibration curve. Knowing this and the emissivity characteristics of tungsten, the filament brightness temperature at wavelength λ is:

$$T_b = \left\{ \frac{1}{T_{fil}} - \frac{\lambda}{C} \ln(\epsilon_{\lambda, T_{fil}}) \right\}^{-1} \tag{10}$$

When the lamp radiation is passed through the RG850 color filter, the apparent source temperatures at 852 and 894 nm will be lower than the temperature calculated in Eq. (10). The equation for T_{b1}, for example, is:

$$T_{b1} = \left\{ \frac{1}{T_{fil}} - \frac{\lambda_1}{C} \ln(t_{\lambda 1} \epsilon_{\lambda 1, T_{fil}}) \right\}^{-1} \tag{11}$$

When the lamp is operated at 100 V, for example, the resulting values are:

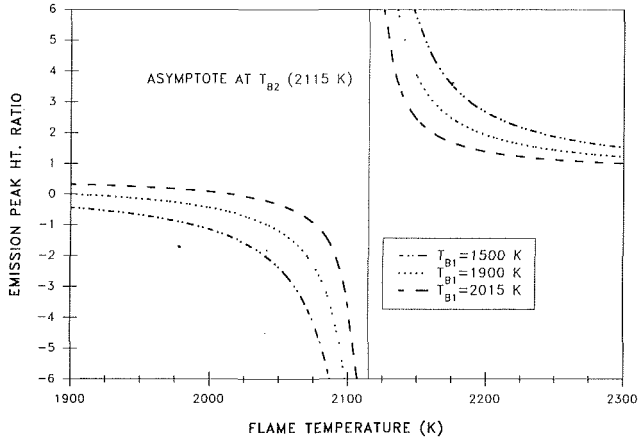

Fig. 4 Peak height ratio as a function of flame temperature

$$T_{fil} = 2492 \text{ K}$$

$$T_{b1} = 2015 \text{ K}$$

$$T_{b2} = 2115 \text{ K}$$

Once T_{b1} and T_{b2} are known, a plot of R versus T_f is prepared. Three plots of this type, corresponding to three different T_{b1} values, are shown in Fig. 4. The curve representing a set of actual conditions is shown (lamp voltage of 100 V with an RG850 filter), along with two curves representing theoretical conditions for lower T_{b1} values (i.e., filters with lower transmissions at 852 nm). Ideally, the method should be operated in the steepest region of the curve, where small temperature differences give rapidly changing peak height ratios. This means that the method is most accurate when T_f is in the region near T_{b1} and T_{b2}. At flame temperatures far below T_{b1} or far above T_{b2} the curve is too flat to use the method effectively. At higher lamp temperatures, and with the equipment used here, the usable range extends about 200 K above T_{b2}. The usable temperature range widens for larger differences between T_{b1} and T_{b2}, although spreads of more than about 600 K no longer change the curves appreciably. During actual temperature measurement, T_f can be determined numerically rather than graphically.

Flame Profiles. Data have been collected for two premixed flat flames. Cool (<2200 K) flames were chosen so that verification using a Pt/Pt-Rh thermocouple would be possible. Both were rich CH_4/air flames, flame I at stoichiometric equivalence ratio ϕ of 1.7 and flame II at ϕ of 1.2.

At each flame position, 100 scans were made at a rate of one every 15 ms; the 100 scans were averaged to yield the reversal spectrum. A typical time-averaged scan is shown in Fig. 5. This scan, taken with effective background temperatures of 1686 K and 1755 K, represents a flame temperature of 1707 K. Accordingly, the 852 nm peak is seen in emission ($T_f > T_{b1}$) while the 894 nm transition is in absorption relative to the background ($T_f < T_{b2}$).

Optically measured temperature profiles as a function of height above the burner surface are shown in Fig. 6 for flames I and II. Corresponding thermocouple measurements for each flame are included in the same figure; these have been corrected to account for radiation losses to the surroundings and losses due to conduction to the lead wires. Vertical error bars represent the uncertainty in the thermocouple data, most of which is due to the inability to determine precisely the emissivity of the thermocouple bead. The size of the symbols in Fig. 6 has been chosen to correspond to the uncertainty in the optical measurement of ±22 K. Calculation of the error associated with the optical measurements is discussed in the next section.

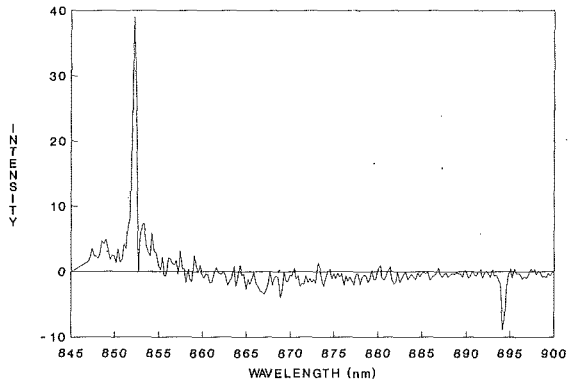

Fig. 5 Typical spectrum

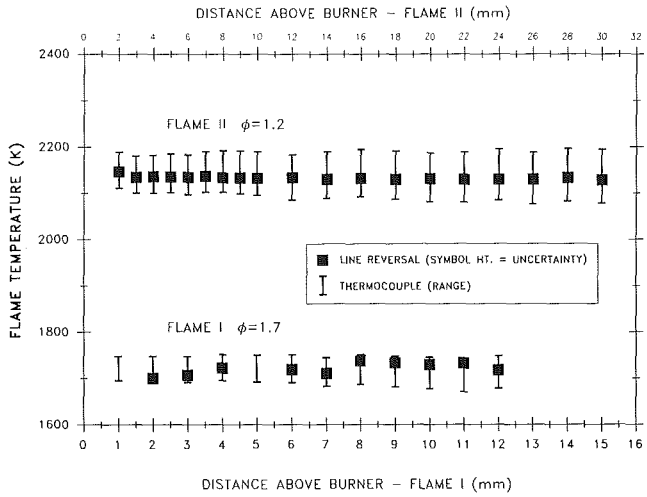

Fig. 6 Temperature profiles for flames I and II

Flame I represents temperatures near the lower limit of this method's useful range, for two reasons. First, below about 1700 K the number density of cesium atoms quickly falls to levels too low to provide an adequate signal. Second, lower temperature flames require using a lower source temperature for a given filter. At lower source temperatures the difference between T_{b1} and T_{b2} decreases, limiting the useful range of the method. This technique is therefore best suited to measuring temperatures around 2000 to 2800 K with a tungsten lamp as the background source.

One possible way to spread T_{b1} and T_{b2} and increase the working range would be to replace the color filter with an interference filter having about a 50 nm bandwidth. The interference filter could be tuned by rotation to give a variety of background temperature pairs.

Limitations and Sources of Error. As previously stated, an assumed condition of applying Eq. (9) is that the (αl) product for the weaker transition must be maintained above about 10. For a flame diameter of 1 cm this corresponds to $\alpha \geq 10$ cm^{-1}. The absorption coefficient depends on oscillator strength and the number density of absorbing atoms, and for the limiting case it yields a required number density on the order of 3×10^{12} cm^{-3}. For cesium at 2500 K, approximately 1 percent of the cesium exists as free Cs atoms, the remainder being tied up primarily in CsCl and CsOH. The total cesium concentration for the limiting case is therefore approximately 3×10^{14} cm^{-3}, which corresponds to a minimum mole fraction of about 10^{-5} in the inlet gas stream. This is about two orders of magnitude below the number density obtained when a cesium solution is atomized into the inlet gas. As such, minimum seed density is not likely to be an issue in application of this method, except in the case of very thin flames. The sufficiently large (αl) product also eliminates any effect of temperature on excited state populations. Although temperature-dependent population differences would affect the relative absorption coefficients at the two transition wavelengths, both values are always large enough that their effect on the ratio calculation in Eq. (9) is negligible.

In the experiments reported here, the filament temperature calibration represents the greatest uncertainty. The calibration is sensitive to accurate knowledge of tungsten emissivity for the actual filament, correct filter transmittance values over all wavelengths, and the transmission characteristics of the quartz envelope. There is also uncertainty in the peak heights, which affects the ratio used to calculate flame temperature. Using the method of Kline and McClintock (1953), these errors can be traced to determine their effect on the final temperature calculation. In the worst case, lamp voltages between 60 and 90 V have errors in the filament temperature of ± 30 K. This affects the two background brightness temperatures T_{b1} and T_{b2} through Eq. (11). The uncertainty in the brightness temperature can be found from

$$\frac{w_{Tb}}{T_b} = \left\{1 - \frac{\lambda T_{fil}}{C} \ln(t_\lambda \epsilon_{\lambda, T_{fil}})\right\}^{-1} \left(\frac{w_{T_{fil}}}{T_{fil}}\right) \tag{12}$$

In the range of values being used here, the resulting uncertainty in the two brightness temperatures is ± 24 K. Both temperatures will be in error in the same direction, however, and this lessens the ultimate effect on the final flame temperature. The result will also depend to a great extent on the region of operation on the R versus T curve. Because Eq. (9) cannot be solved analytically for T_f as a function of R, conventional methods cannot be used to estimate the uncertainty in T_f due to that in the two brightness temperatures. For the values reported here, the numerical solution of R was repeated for several measurements with T_{b1} and T_{b2} varying over the range of their uncertainty. The resultant uncertainty in the final flame temperature is estimated at ± 15 K when the lamp is operated in the region corresponding to the flame I and II measurements.

The error in R caused by the uncertainty in measurement of the peak heights will also vary depending on the region of operation on the curve. The peak at 894 nm has the greater uncertainty due to decreased detector sensitivity at higher wavelengths. For the measurements reported here the 894 nm peak height uncertainty is estimated at ± 10 percent. The resulting effect on reported flame temperature is approximately ± 7 K.

The accuracy of the final results depends on the steepness of the R versus T_f curve in the area of operation. If the flame temperature is far below T_{b1} or far above T_{b2}, accuracy is sacrificed. Ways to improve the operating range by increasing the spread between T_{b1} and T_{b2} have been discussed in a previous section. As long as care is taken to operate within the prescribed region, the relative change in R for a given temperature change will be large enough to make this a negligible source of error.

Thomas (1968a) and others (Daily and Kruger, 1976) have discussed the effects of a cool boundary layer on the final results of line reversal temperature measurements. Where thick boundary layers exist, corrections are possible to account for the increased absorption (Strong and Bundy, 1954). The effect of a cool boundary layer is to reabsorb the radiation emitted at the center of the line. However, cooler gases have a much lower cesium atom concentration and this weakens the effect. Because both peaks are affected to the same extent, the peak ratio is not substantially changed. This is an advantage over traditional line reversal, where self-absorption caused by a boundary layer affects the source balance point. For the ex-

perimental data reported here, flat flames were used with temperatures that vary little in the transverse direction. The contribution of boundary layer effects was negligible compared to the overall error.

6 Conclusions

Using a filtered reference source and monitoring two closely spaced transition lines, flame temperatures can be determined by line reversal without balancing the source. Flame temperatures as much as 200 K higher than the source brightness temperature can be measured, and the system can be fully automated without sacrificing temporal resolution. Errors can be minimized by using an accurately calibrated reference source and selecting filters carefully. The method is well suited for measuring cesium-seeded flames. Other Group IA elements can also be used with appropriate choice of filter, spectrograph grating density, and detector sensitivity.

References

Altenkirch, R. A., Peck, R. E., and Chen, S. L., 1979, "The Appearance of Nitric Oxide and Cyanide in One-Dimensional Coal Dust/Oxidizer Flames," *Combustion Science and Technology*, Vol. 20, pp. 49–58.

Daily, J. W., and Kruger, C. H., 1976, "Boundary Layer Measurements of Temperature and Electron Number Density Profiles in a Combustion MHD Generator," *Combustion Measurements*, Academic Press, pp. 119–126.

De Vos, J. C., 1954, "A New Determination of the Emissivity of Tungsten Ribbon," *Physica*, Vol. 20, pp. 690–714.

Gaydon, A. G., and Wolfhard, H. G., 1970, *Flames—Their Structure, Radiation, and Temperature*, 3rd ed., Chapman and Hall Ltd., London, United Kingdom.

Kline, S. J., and McClintock, F. A., 1953, "Describing Uncertainties in Single-Sample Experiments," *Mechanical Engineering*, Jan., pp. 3–8.

Klingenberg, G., and Mach, H., 1976, "Investigation of Combustion Phenomena Associated With the Flow of Hot Propellant Gases—Spectroscopic Temperature Measurements Inside the Muzzle Flash of a Rifle," *Combustion and Flame*, Vol. 27, pp. 163–176.

Kurlbaum, F., 1902a, "Über Eine Einfache Methode, die Temperatur Leuchtender Flammen zu Bestimmen," *Physikalische Zeitschrift*, Vol. 3, pp. 187–188.

Kurlbaum, F., 1902b, "Über das Reflexionsvermögen von Flammen," *Physikalische Zeitschrift*, Vol. 3, pp. 332–334.

Penner, S. S., 1949, "Optical Methods for the Determination of Flame Temperatures. I. Two-Color and Line-Reversal Techniques," *American Journal of Physics*, Vol. 17, pp. 422–429.

Reif, I., Fassel, V. A., and Kniseley, R. N., 1973, "Spectroscopic Flame Temperature Measurements and Their Physical Significance—I. Theoretical Concepts—A Critical Review," *Spectrochimica Acta*, Vol. 28B, pp. 105–123.

Siegel, R., and Howell, J. R., 1981, *Thermal Radiation Heat Transfer*, 2nd ed., McGraw-Hill, New York.

Strong, H. M., and Bundy, F. P., 1954, "Measurement of Temperatures in Flames of Complex Structure by Resonance Line Radiation. I. General Theory and Application to Sodium Line Reversal Methods," *Journal of Applied Physics*, Vol. 25, pp. 1521–1526.

Thomas, D. L., 1968a, "Problems in Applying the Line Reversal Method of Temperature Measurement to Flames," *Combustion and Flame*, Vol. 12, pp. 541–549.

Thomas, D. L., 1968b, "An Automatic Remotely Operated Sodium D-Line Reversal Temperature Measuring Technique," *Combustion and Flame*, Vol. 12, pp. 569–574.

Wolfhard, H. G., and Parker, W. G., 1949, "A New Technique for the Spectroscopic Examination of Flames at Normal Pressures," *Proceedings of the Physics Society*, Vol. A62, pp. 772–730.

G. Chen
Graduate Student Researcher.

C. L. Tien
A. Martin Berlin Professor.
Fellow ASME

Department of Mechanical Engineering,
University of California,
Berkeley, CA 94720

Partial Coherence Theory of Thin Film Radiative Properties

A new approach based on the partial coherent theory of light is introduced to predict the radiative properties of a thin film. General expressions obtained for the normal reflectance and transmittance of a thin film not only degenerate into the limiting results of the wave and the geometric optics in the coherent and incoherent cases, but also apply for all partial coherent states between the limits. The key element in the formulation is the complex degree of coherence, for which a general integral expression is obtained and further approximated algebraically for nearly monochromatic radiation. Limiting criteria and regime maps are established to demonstrate the range of applications for the various methods.

Introduction

There exist two different methods for calculating radiative properties of a thin film: the wave optics formulation and the geometric optics formulation. The two approaches yield very different results because wave optics, based on superposition of the amplitudes of the electromagnetic fields, includes interference phenomena (Heavens, 1965) while geometric optics, based on intensity superposition, excludes interference (Siegel and Howell, 1981). Bohren and Huffman (1983) pointed out that the intensity superposition expressions, with certain restrictions, can be obtained from averaging the amplitude superposition formulation over a frequency interval. They also discussed qualitatively the applicability of the two extremes by analyzing the interference structure of film transmittance. Harris et al. (1951) compared the two methods for a metal film on a nonabsorbing substrate and concluded that intensity superposition is applicable for a sufficiently thick substrate when its thickness or the wavelength of the incident radiation (or both) has a large range of probable values.

No quantitative criterion has been presented to characterize the range of applications for the two methods. When measuring the spectral reflectance and/or transmittance of films to obtain the optical constants or film thickness, the vague terms "thin film" and "thick film" are often used to help choose the appropriate formulation. It is not difficult to understand that the detected interference signals depend not only on the thickness of the film, but also on the coherent state of the radiation source and, for the spectral measurement, on the bandwidth or the resolution of the instruments. Moreover, an intermediate range—films with thickness falling between the two extremes—is easily perceived. Bohren and Huffman (1983) warned of the potential error of using the two extreme formulations to deduce the optical constants from measured spectra, and pointed out the lack of a general approach for the intermediate range. It is shown here, however, that this gap can be bridged under the *partial coherence theory of light* (Born and Wolf, 1975; Marathay, 1982).

Nearly all real radiation sources and fields are partially coherent. As Metha (1963) pointed out, even the *most* chaotic source—blackbody radiation—is coherent in a small region. The partial coherence theory of light deals with correlations among the radiation fields at different points in space and/or at different time intervals. The key elements in the theory are the normalized correlation functions namely, the *complex degree of coherence* for space-temporal coherent properties, and the *complex degree of spectral coherence* for space-spectral coherent properties (Mandel and Wolf, 1976). Although the theory of partial coherence of light has found wide applications in many fields, it has not been introduced to predict the radiative properties of thin films.

The new model presented in this paper takes into account the partial coherent states of actual radiation fields. Developed from this model are general expressions for the radiative properties of a thin film, i.e., reflectance, transmittance, and local absorptance, which include the wave optics and geometric optics as two limiting cases. An integral expression for the complex degree of coherence is obtained and further approximated by a simpler algebraic expression for nearly monochromatic radiation. Sample calculations show the difference between the three approaches, namely, geometric optics, wave optics, and the partial coherence formulation. Criteria are established to show when and which of the methods should be chosen. Regime maps are also constructed on the basis of these criteria.

Model and Formulation

The present model originates from a detailed re-examination of the wave and geometric optics models. For simplicity, only the case of normal incidence is considered. The incidence is from a remote point source. The film is assumed smooth during the derivation of the new formulation. The effects of surface roughness will be discussed later.

In the geometric optics approach, as shown in Fig. 1(*a*), the incident radiation ray splits into many forward and backward ones through multireflections at the two film interfaces. Each

Contributed by the Heat Transfer Division and presented at the ASME Winter Annual Meeting, Atlanta, Georgia, December 1-6, 1991. Manuscript received by the Heat Transfer Division August 1991; revision received January 1992. Keywords: Radiation, Thermophysical Properties. Associate Technical Editor: R. O. Buckius.

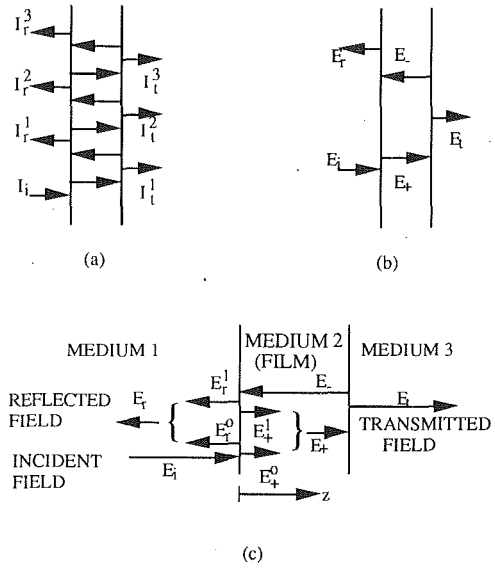

Fig. 1 Model for the radiative properties of a thin film: (*a*) geometric optics, (*b*) wave optics, (*c*) partial coherence approach

backward ray is partially reflected at interface 1. The reflected part then becomes a forward ray. Actually, only one forward ray does not evolve from these reflected backward rays; that is, the one that is directly refracted from the incidence. Superposition of intensity gives the reflectance of the film as

$$R_g = R_{12} + \frac{R_{23}T_{12}T_{21}e^{-2\alpha L}}{1 - R_{21}R_{23}e^{-2\alpha L}} \tag{1}$$

where $\alpha(=4\pi k_2\nu/c_o)$ is the absorption coefficient of the film. It is implicit in Eq. (1) that a Beer's law type of attenuation has been assumed inside the film.

In the resultant wave approach (Heavens, 1965; Bohren and Huffman, 1983), as shown in Fig. 1(*b*), the incident electromagnetic field is divided into two parts inside the film. One is the forward propagating wave and the other is the backward one. Boundary conditions that require continuity of the tangential components of the electric and magnetic fields are applied to obtain relations between E_+, E_-, E_t, and E_i. Superposition of the amplitudes of the electromagnetic fields yields the reflectance of a film as

$$R_w = \frac{R_{12} + 2\mathrm{Re}[r_{12}^* r_{23}\exp(i4\pi N_2 L/\lambda)] + R_{23}e^{-2\alpha L}}{1 + 2\mathrm{Re}[r_{12}r_{23}\exp(i4\pi N_2 L/\lambda)] + R_{12}R_{23}e^{-2\alpha L}} \tag{2}$$

where r_{12} and r_{23} are Fresnel coefficients giving by

$$r_{12} = (N_1 - N_2)/(N_1 + N_2), \quad r_{23} = (N_2 - N_3)/(N_2 + N_3)$$

and $R_{12} = r_{12}r_{12}^*$, $R_{23} = r_{23}r_{23}^*$.

Comparing with the geometric optics model, one can see that in the resultant wave model, all the forward propagating fields, including the part refracted directly from the incident field and the part reflected from the backward one, are compounded into a single forward propagating field. It will become clear later that this failure to distinguish between the refracted field and the reflected one in the forward propagating field covers the true mechanism of the interaction between the forward and the backward electromagnetic fields inside the film.

The new model distinguishes the above-mentioned two constituents of the forward field inside the film, and similarly, the two constituents of the reflected field outside the film. As shown in Fig. 1(*c*), now the forward propagating field consists of two parts: one, E_+^o, is directly refracted from the incident field, and the other, E_+^1, evolves from the reflection of the backward propagating field at interface 1. An important observation to be made here is that the backward electric field at interface 1, E_-, originates from the refracted electric field, E_+^o, at the same point but has a time delay:

$$\tau = 2L/c = 2n_2L/c_o \tag{3}$$

where n_2 is the real part of the complex refractive index of the film.

So the forward electric field inside the film at $z=0$ and time t is given by

$$E_+(0, t) = E_+^o(0, t) + E_+^1(0, t-\tau) \tag{4}$$

where $E_+^o(0, t)$ is the part refracted from the incident electric field at interface 1 and time t, $E_+^1(0, t-\tau)$ represents the part reflected from the backward propagating electric field $E_-(0, t-\tau)$, and the argument $t-\tau$ denotes the temporal retardation of the backward field relative to the incident radiation at in-

Nomenclature

A = absorptance
B = time limit of the integration in Eq. (9)
c = speed of light
E = electric field
f = resolution parameter $= \Delta\nu/\nu_o$
G = mutual spectral density
I = incident radiation intensity
i = $\sqrt{-1}$
k = imaginary part of complex refractive index
L = film thickness
N = complex refractive index $= n + ik$
n = real part of complex refractive index
R = reflectance
r = reflection function, Fresnel coefficient
$\mathbf{r}$ = position vector
T = transmittance
t = time, with subscript representing transmission function or Fresnel coefficient
x = thickness parameter $= 4\pi n_2 L\nu_o/c_o$
z = coordinate
α = absorption coefficient $= 4\pi k_2 L\nu/c_o$
β = transmittance inside the film
γ = complex degree of coherence
λ = wavelength in vacuum
ν = frequency
τ = time retardation
ΔL = mean square root deviation of film thickness
$\Delta\nu$ = half bandwidth

Subscripts

g = geometric optics
i = incident field or intensity
r = reflected field or intensity
t = transmitted field or intensity
w = wave optics
z = at location z
$+$ = forward propagating field
$-$ = backward propagating field
o = vacuum, at frequency ν_o
0 = at $z=0$
1 = medium 1, the interface between medium 1 and the film
12 = from medium 1 to the film at interface 1
21 = from the film to medium 1 at interface 1
2 = the film, the interface between the film and medium 3
3 = medium 3
23 = from the film to medium 3 at interface 2

Superscripts

o = directly from the incidence
1 = evolved from the backward field
$*$ = complex conjugate
$'$ = backward direction

terface 1. Notice that $E_-(o, t-\tau)$ is a resultant field—the sum of all the backward fields through multiple reflections inside the film. So the time lag τ is not exactly as defined in Eq. (3) but represents the multiple reflection effect. Such a difference, however, does not affect the formulation below and is taken into account later in obtaining the general expression for the complex degree of coherence. Similar remarks hold for τ_1 introduced later.

Similarly, the reflected electric field $E_r(0, t)$ at $z=0$ is composed of two parts:

$$E_r(0, t)=E_r^o(0, t)+E_r^1(0, t-\tau) \tag{5}$$

where $E_r^o(0, t)$ is the direct reflection of the incident electric field while $E_r^1(0, t-\tau)$ is refracted from $E_-(0, t-\tau)$.

The fields, $E_+^o(0, t)$ and $E_r^o(0, t)$, in Eqs. (4) and (5) are related to the incident field $E_i(0, t)$ through the transmission function, t_{12}, and the reflection function, r_{12}, from medium 1 to medium 2 by

$$E_+^o(0, t)=t_{12}E_i(0, t) \tag{6a}$$

$$E_r^o(0, t)=r_{12}E_i(0, t) \tag{6b}$$

For monochromatic or nearly monochromatic radiation, t_{12} and r_{12} are given by the Fresnel coefficients. For wide spectrum incidence, an integral average of the Fresnel coefficients should be used because of the dispersion of the optical constant. Similar remarks apply for all the reflection and transmission properties used in the following treatment and will not be repeated.

The retarded fields, $E_+^1(0, t-\tau)$ and $E_r^1(0, t-\tau)$, in Eqs. (4) and (5) evolve from the backward field and are given by

$$E_+^1(0, t-\tau)=r_{21}E_-(0, t-\tau) \tag{7a}$$

$$E_r^1(0, t-\tau)=t_{21}E_-(0, t-\tau) \tag{7b}$$

At $z=L$, there is no time retardation between the forward, backward, and transmitted fields. Although there is a time delay between the fields at this interface and those at interface $z=0$, it will not affect the formulation. Again, relations among the fields at $z=L$ can be expressed by

$$E_t(L, t)=t_{23}E_+(L, t) \tag{8a}$$

$$E_-(L, t)=r_{23}E_+(L, t) \tag{8b}$$

Note that all the above quantities are defined in the space-time domain; the field at each point is composed of many frequency components determined by the source. These real time signals are fluctuating in nature. Detectable quantities, i.e., the intensity, are the various quadratic forms of them averaged over time, defined by (Mandel and Wolf, 1965)

$$\langle f(\mathbf{r}, t)\rangle=\lim_{2B\to\infty}\frac{1}{2B}\int_{-B}^{B}f(\mathbf{r}, t)dt \tag{9}$$

When $f(\mathbf{r}, t)=E_i(0, t)E_i^*(0, t)$, the above average yields the incident radiation intensity at $z=0$ (except for a numeric factor).

Inside the film, both the forward and the backward field intensities are attenuated due to absorption,

$$\langle E_+(L, t)E_+^*(L, t)\rangle=\beta\langle E_+(0, t)E_+^*(0, t)\rangle \tag{10a}$$

$$\langle E_-(0, t)E_-^*(0, t)\rangle=\beta'\langle E_-(L, t)E_-^*(L, t)\rangle \tag{10b}$$

where β and β' are transmittance of the forward and backward intensities inside the film. In the case of monochromatic or nearly monochromatic incidence, they are given by, according to Beer's law, $\beta=\beta'=\exp(-\alpha L)$.

Combining Eqs. (8) and (10) gives

$$\langle E_-(0, t)E_-^*(0, t)\rangle=R_{23}\beta\beta'\langle E_+(0, t)E_+^*(0, t)\rangle \tag{11}$$

To obtain the reflectance and transmittance of the film, which are defined as

$$R=\frac{\langle E_r(0, t)E_r^*(0, t)\rangle}{\langle E_i(0, t)E_i^*(0, t)\rangle} \tag{12a}$$

$$T=\frac{n_3}{n_1}\frac{\langle E_t(L, t)E_t^*(L, t)\rangle}{\langle E_i(0, t)E_i^*(0, t)\rangle} \tag{12b}$$

requires finding the ratio $\langle E_+(0, t)E_+^*(0, t)\rangle/\langle E_i(0, t)E_i^*(0, t)\rangle$.

By substituting Eqs. (6*a*) and (7*a*) into Eq. (4) and recasting it as

$$E_+(0, t)-r_{21}E_-(0, t-\tau)=t_{12}E_i(0, t)$$

then multiplying the above equation with its complex conjugate, and taking the time average, there follows

$$\langle E_+(0, t)E_+^*(0, t)\rangle-2\mathrm{Re}[r_{21}^*\langle E_+(0, t)E_-^*(0, t-\tau)\rangle]+R_{21}\langle E_-(0, t-\tau)E_-^*(0, t-\tau)\rangle=T_{12}\langle E_i(0, t)E_i^*(0, t)\rangle \tag{13}$$

where $R_{21}=r_{21}r_{21}^*$ and $T_{12}=t_{12}t_{12}^*$.

In the above equation, the terms $\langle E_+(0, t)E_+^*(0, t)\rangle$, $\langle E_-(0, t-\tau)E_-^*(0, t-\tau)\rangle$, and $\langle E_i(0, t)E_i^*(0, t)\rangle$ represent the forward, backward, and incident radiation intensities, respectively, at interface 1. Even though there is a numerical factor in the real intensity expression (Heavens, 1965), it will not affect the reflectance and transmittance defined by Eqs. (12*a*, *b*) due to cancellation. Notice that the term $\langle E_+(0, t)E_-^*(0, t-\tau)\rangle$ in Eq. (13) is of particular interest here. It is the correlation function of the electric field at $z=0$ between the forward and backward propagating electric fields, thus the main concern of the theory of *partial coherence of light*. Such a correlation, called the *mutual coherence function*, is often normalized, resulting in the *complex degree of coherence* defined as (Born and Wolf, 1975)

$$\gamma(\mathbf{r}_1, \mathbf{r}_2, \tau)=\frac{\langle E_+(\mathbf{r}_1, t)E_-^*(\mathbf{r}_2, t-\tau)\rangle}{(\langle E_+(\mathbf{r}_1, t)E_+^*(\mathbf{r}_1, t)\rangle\langle E_-(\mathbf{r}_2, t-\tau)E_-^*(\mathbf{r}_2, t-\tau)\rangle)^{1/2}} \tag{14}$$

where $\mathbf{r}_1$ and $\mathbf{r}_2$ are different points in space. For normal incidence, the corresponding complex degree of coherence at $z=0$ is

$$\gamma_0(\tau)=\gamma(0, 0, \tau)=\frac{\langle E_+(0, t)E_-^*(0, t-\tau)\rangle}{(\langle E_+(0, t)E_+^*(0, t)\rangle\langle E_-(0, t-\tau)E_-^*(0, t-\tau)\rangle)^{1/2}} \tag{15}$$

Substitution of Eqs. (11) and (15) into Eq. (13) yields

$$\frac{\langle E_+(0, t)E_+^*(0, t)\rangle}{\langle E_i(0, t)E_i^*(0, t)\rangle}=\frac{T_{12}}{1-2\mathrm{Re}(r_{21}^*\gamma_0(\tau))(R_{23}\beta\beta')^{1/2}+R_{21}R_{23}\beta\beta'} \tag{16}$$

In deriving the above equation and the following Eqs. (19), (27), and (29), the relation

$$\langle E_-(0, t-\tau)E_+^*(0, t-\tau)\rangle=\langle E_+(0, t)E_+^*(0, t)\rangle$$

has been used. This is true because the temporally averaged quantities, defined in Eq. (9), are invariant under the transformation of time origin.

From Eqs. (8*a*), (10*a*), (12*b*), and (16), the transmittance of the film becomes

$$T=\frac{n_3}{n_1}\frac{T_{12}T_{23}\beta}{1-2\mathrm{Re}(r_{21}^*\gamma_0(\tau))(R_{23}\beta\beta')^{1/2}+R_{21}R_{23}\beta\beta'} \tag{17}$$

To derive the reflectance, multiplying Eq. (5) with its complex conjugate, substituting in Eqs. (6*b*) and (7*b*), and taking the time average yields

$$\langle E_r(0, t)E_r^*(0, t)\rangle=R_{12}\langle E_i(0, t)E_i^*(0, t)\rangle+T_{21}\langle E_-(0, t-\tau)E_-^*(0, t-\tau)\rangle+2\mathrm{Re}[r_{12}t_{21}^*\langle E_i(0, t)E_-^*(0, t-\tau)\rangle] \tag{18}$$

where $T_{21}=t_{21}t_{21}^*$.

Substituting Eqs. (4), (6*a*), (7*a*), and (11) into Eq. (15) and solving for $\langle E_i(0, t)E^*_-(0, t-\tau)\rangle$ gives

$$\langle E_i(0, t)E^*_-(0, t-\tau)\rangle = [\gamma_0(\tau)/(R_{23}\beta\beta')^{1/2} - r_{21}] \times \langle E_-(0, t-\tau)E^*_-(0, t-\tau)\rangle / t_{12} \quad (19)$$

From Eqs. (11), (12*a*), (16), (18), and (19), the reflectance of the film can be obtained as

$$R = R_{12} + \left(T_{21} + 2\mathrm{Re}\left\{\frac{r_{12}t^*_{21}}{t_{12}}\left[\frac{\gamma_0(\tau)}{(R_{23}\beta\beta')^{1/2}} - r_{21}\right]\right\}\right) \times \frac{T_{12}R_{23}\beta\beta'}{1 - 2\mathrm{Re}(r^*_{21}\gamma_0(\tau))(R_{23}\beta\beta')^{1/2} + R_{21}R_{23}\beta\beta'} \quad (20)$$

Equations (17) and (20) for transmittance and reflectance would look more familiar if Beer's law holds for β and β'. In this case, they can be rewritten as

$$T = \frac{n_3}{n_1}\frac{T_{12}T_{23}e^{-\alpha L}}{1 - 2\mathrm{Re}(r^*_{21}\gamma_0(\tau))e^{-\alpha L}(R_{23})^{1/2} + R_{21}R_{23}e^{-2\alpha L}} \quad (21)$$

$$R = R_{12} + \left(T_{21} + 2\mathrm{Re}\left\{\frac{r_{12}t^*_{21}}{t_{12}}\left[\frac{\gamma_0(\tau)e^{\alpha L}}{(R_{23})^{1/2}} - r_{21}\right]\right\}\right) \times \frac{T_{12}R_{23}e^{-2\alpha L}}{1 - 2\mathrm{Re}(r^*_{21}\gamma_0(\tau))e^{-\alpha L}(R_{23})^{1/2} + R_{21}R_{23}e^{-2\alpha L}} \quad (22)$$

Similar procedures are applied to get local absorptance inside the film. The local dimensionless field intensity can be expressed as

$$\frac{\langle E(z, t)E^*(z, t)\rangle}{\langle E_i(0, t)E^*_i(0, t)\rangle} = T_{12}e^{-\alpha z} \times \frac{1 + 2e^{-\alpha(L-z)}(R_{23})^{1/2}\mathrm{Re}(\gamma_z(\tau_1)) + R_{23}e^{-2\alpha(L-z)}}{1 - 2\mathrm{Re}(r^*_{21}\gamma_0(\tau))e^{-\alpha L}(R_{23})^{1/2} + R_{21}R_{23}e^{-2\alpha L}} \quad (23)$$

and the local absorptance is

$$A(z) = \frac{n_2}{n_1}\frac{d}{dz}\left(\frac{\langle E(z, t)E^*(z, t)\rangle}{\langle E_i(0, t)E^*_i(0, t)\rangle}\right) \quad (24)$$

where $E(z, t)$ is the electric field inside the film, $\gamma_z(\tau_1) = \gamma(z, z, \tau_1)$ is the complex degree of coherence, and $\tau_1 = 2n_2(L-z)/c_o$ represents time retardation of the backward field relative to the forward field at point z.

Equations (17) and (20) are general expressions for the transmittance, reflectance of an ideal film, while Eqs. (21), (22), and (24) are applicable when the Beer's law type of attenuation is assumed. The key element in the expressions is the complex degree of coherence. As will be shown in the following section, these expressions will degenerate respectively into wave optics and geometric optics results in two extreme cases, namely the completely coherent and the completely incoherent limits. The present theory, however, is not restricted to these extremes. It applies to the intermediate case—the partially coherent state—as well. The next section will therefore concentrate on the complex degree of coherence.

Complex Degree of Coherence

Incoherent Limit. Consider an arbitrary point z inside the film. The forward electric field at this point and at time t is composed of two parts: One, $E^o_+(z, t)$, is from the incident field, and the other, $E^1_+(z, t-\tau)$, is from the backward field, where τ is used because $E^1_+(z, t-\tau)$ originates from $E^o_+(z, t)$, but travels an extra distance $2L$. The backward electric field at z is $E_-(z, t-\tau_1)$, where τ_1 is used because $E_-(z, t-\tau_1)$ travels a longer distance by $2(L-z)$ than $E_+(z, t)$. Note that the following statements are valid:

$$\tau = \tau_1,\ \tau_1 \neq 0 \quad \text{when } z = 0 \quad (25a)$$

$$\tau \neq \tau_1,\ \tau_1 \neq 0 \quad \text{when } 0 < z < L \quad (25b)$$

$$\tau \neq \tau_1,\ \tau_1 = 0 \quad \text{when } z = L \quad (25c)$$

So, when $0 < z < L$, neither $E^o_+(z, t)$ nor $E^1_+(z, t-\tau)$ is in phase with $E_-(z, t-\tau_1)$. In this case, incoherence implies that $\langle E_+(z, t)E^*_-(z, t-\tau_1)\rangle$ equals zero. Thus, the complex degree of coherence is

$$\gamma_z(\tau_1) = 0 \quad \text{when } 0 < z < L \quad (26)$$

The situation is different at $z = 0$, because, as indicated by Eq. (25*a*), at that point there is no time retardation between $E^1_+(z, t-\tau)$ and $E_-(z, t-\tau_1)$. Substitution of Eqs. (4), (6*a*), (7*a*), and (11) into Eq. (15) gives

$$\gamma_0(\tau) = r_{21}(R_{23}\beta\beta')^{1/2} + \frac{\langle t_{12}E_i(0, t)E^*_-(0, t-\tau)\rangle}{(\langle E_+(0, t)E^*_+(0, t)\rangle\langle E_-(0, t-\tau)E^*_-(0, t-\tau)\rangle)^{1/2}} \quad (27)$$

Due to the time retardation between $E^o_+(z, t)$ and $E_-(z, t-\tau_1)$ at $z = 0$, incoherence implies that $\langle t_{12}E_i(0, t)E^*_-(0, t-\tau)\rangle$ equals zero. Assuming Beer's law is valid, the complex degree of coherence of the forward and backward fields inside the film at interface 1 is

$$\gamma_0(\tau) = r_{21}e^{-\alpha L}(R_{23})^{1/2} \quad \text{when } z = 0 \quad (28)$$

At $z = L$, τ_1 equals zero, indicating that $E_+(z, t)$ and $E_-(z, t-\tau_1)$ are in phase. Actually, Eqs. (8*b*) and (14) give

$$\gamma_L(\tau) = \gamma(L, L, \tau) = r^*_{23}/(R_{23})^{1/2} \quad \text{when } z/L \quad (29)$$

Substituting Eq. (28) into Eq. (22) results in exactly Eq. (1)—the reflectance of a film from the geometric optics approach. It can be readily shown that the transmittance, Eq. (21), and the dimensionless radiation intensity inside the film, Eq. (23), also degenerate into the geometric optics expressions.

Unlike what one might have expected, Eq. (28) shows that the complex degree of coherence between the forward and backward fields inside the film at surface 1 is not zero, but rather is a definite value decided by the film thickness, the refractive indices of the film, and the surrounding media. This means that the forward and backward fields are partially coherent at this point, even though they are incoherent inside the film. This partial coherence behavior is explicit in the current model, but is rather implicit and undetermined in the geometric optics approach where ray tracing and intensity superposition is used.

Coherent Limit. Absolutely coherent radiation exists only possibly in a monochromatic field (Born and Wolf, 1975). For a coherent monochromatic field, the wave equation can be solved, giving exact relations between the forward and backward fields as (Bohren and Huffman, 1983; Heavens, 1965)

$$E_-(0, t-\tau) = E_+(0, t)r_{23}e^{i2\pi\nu\tau} \quad (30a)$$

$$E_-(z, t-\tau_1) = E_+(z, t)r_{23}e^{i2\pi\nu\tau_1} \quad (30b)$$

Substitution of the above equations respectively into Eqs. (15) and (14), yields

$$\gamma_0(\tau) = r^*_{23}e^{-i2\pi\nu\tau}/(R_{23})^{1/2} \quad (31a)$$

$$\gamma_z(\tau_1) = r^*_{23}e^{-i2\pi\nu\tau_1}/(R_{23})^{1/2} \quad (31b)$$

Now substituting the complex degree of coherence [Eq. (31*a*)] into the reflectance expression (22), one obtains exactly Eq. (2), the formula from wave optics (Appendix). It can be proven that the transmittance given by Eq. (21) and the dimensionless radiation intensity inside the film given by Eq. (23) also degenerate to the corresponding wave optics expressions.

It is interesting to notice that the moduli of the complex degree of spectral coherence $\gamma_0(\tau)$ and $\gamma_z(\tau_1)$ given by Eqs. (31*a*, *b*) are exactly one, which verifies from another aspect that the case under examination is indeed absolutely coherent.

Partial Coherence. Having shown the two limiting cases, a general expression for the complex degree of coherence is in order. Following Born and Wolf (1975), the mutual coherence function in Eq. (27) can be written as

$$\langle E_i(0,\ t)E_-^*(0,\ t-\tau)\rangle = 4\int_0^\infty G_{12}(\nu)e^{-2\pi i\nu\tau}d\nu \tag{32}$$

In the above expression, $G_{12}(\nu)$ is called the *mutual spectral density*, given by

$$G_{12}(\nu) = \lim_{t\to\infty}\overline{(t_{12}E_i(0,\ \nu)E_-^*(0,\ \nu)/2t)} \tag{33}$$

where the bar denotes ensemble average, and the argument ν indicates that the field is in frequency domain.

For the spectral components; results from solving the electromagnetic wave equations still hold (Heavens, 1965; Bohren and Huffman, 1983):

$$E_+^o(0,\ \nu) = t_{12}E_i(0,\ \nu) \tag{34}$$

$$E_-(0,\ \nu) = [1 - N_1/N_2 + (1 + N_1/N_2)r]E_i(0,\ \nu)/2 \tag{35}$$

$$E_+(0,\ \nu) = [1 + N_1/N_2 + (1 - N_1/N_2)r]E_i(0,\ \nu)/2 \tag{36}$$

where

$$r = \frac{r_{12} + r_{23}\exp(i4\pi N_2 L\nu/c)}{1 + r_{12}r_{23}\exp(i4\pi N_2 L\nu/c)} \tag{37}$$

An important observation can be made here that the time retardation factor $\exp(-2\pi i\nu\tau)$ in Eq. (32) is already taken into consideration during the derivation of Eqs. (35) and (36). So, when Eq. (35) is used for calculating $G_{12}(\nu)$, the factor $\exp(-2\pi i\nu\tau)$ in Eq. (32) should be dropped. This will become clear when one substitutes Eqs. (33)–(35) and (37) into Eq. (32), giving

$$\langle t_{12}E_i(0,\ t)E_-^*(0,\ t-\tau)\rangle = 4\int_0^\infty [t_{12}(-r_{12}+r)^*/t_{21}^*]I(\nu)d\nu$$

$$= 4\int_0^\infty \left(\frac{t_{12}^*}{t_{21}}\frac{r_{23}(1-r_{12}^2)\exp(i4\pi N_2\nu L/c)}{1 + r_{12}r_{23}\exp(i4\pi N_2\nu L/c)}\right)^* I(\nu)d\nu \tag{38}$$

where $I(\nu)$ denotes the incidence spectral intensity given by

$$I(\nu) = \lim_{t\to\infty}\overline{(E_i(0,\ \nu)E_i^*(0,\ \nu)/2t)}$$

Examining the numerator of the integrand in Eq. (38) shows that the exponential term contains the factor $\exp(-2\pi i\nu\tau)$, which proves the argument made above.

Similarly, the forward and backward field intensities can be expressed in terms of $I(\nu)$. Substituting these relations into Eq. (27) gives

$$\gamma_0(\tau) = r_{21}(R_{23}\beta\beta')^{1/2}$$

$$+ \frac{\displaystyle\int_0^\infty [t_{12}(-r_{12}+r)^*/t_{21}^*]I(\nu)d\nu}{\left(\displaystyle\int_0^\infty |(1-r_{12}r)/t_{21}|^2 I(\nu)d\nu \int_0^\infty |(-r_{12}+r)/t_{21}|^2 I(\nu)d\nu\right)^{1/2}} \tag{39}$$

Equation (39) is the general expression for the complex degree of coherence of a thin film. Its evaluation generally requires numerical integration. However, it will be shown in the next section that when the incidence or the detected signal is in a narrow spectral range, the formula can be well approximated by an algebraic one.

Calculation and Discussion

In many applications, such as the FTIR measurement of optical properties (Phelan et al., 1991), and the determination of thin film thickness (Musilova and Ohlidal, 1990), spectral quantities are measured. Although the ideal case is to distinguish every single frequency, due to the finite resolution of instruments, the measured results have actually been averaged over a finite bandwidth—the detected signal is a partially coherent one. For the FTIR measurement, such a bandwidth is decided by the resolution of the instrument, while in other applications using filters, it is controlled by filter bandwidth. In these cases, the incident spectral intensity around the frequency of the band center, ν_o, can be approximated as

$$I_i(\nu) = \begin{cases} 1 & \nu_o - \Delta\nu < \nu < \nu_o + \Delta\nu \\ 0 & \text{other} \end{cases} \tag{40}$$

If $\Delta\nu$ is small compared with ν, it is reasonable to neglect the dispersion effect and use Beer's law. Under these assumptions, Eq. (39) becomes

$$\gamma_0(\tau) = r_{21}e^{-\alpha L}(R_{23})^{1/2}$$

$$+ \frac{\displaystyle\int_{\nu_o-\Delta\nu}^{\nu_o+\Delta\nu} t_{12}(-r_{12}+r)^*/t_{21}^*d\nu}{\left(\displaystyle\int_{\nu_o-\Delta\nu}^{\nu_o+\Delta\nu} |(1-r_{12}r)/t_{21}|^2 d\nu \int_{\nu_o-\Delta\nu}^{\nu_o+\Delta\nu} |(-r_{12}+r)/t_{21}|^2 d\nu\right)^{1/2}} \tag{41}$$

Although the above formula still looks formidable, numerical calculation shows that for most of the refractive indices used in the calculation it can be well approximated by neglecting the change of the denominator of r in Eq. (37) and integrated as

$$\gamma_0(\tau) = r_{21}e^{-\alpha L}(R_{23})^{1/2} + \{1 + r_{12}r_{23}\exp[ix(1 + ik_2/n_2)]\}$$

$$\times \frac{(r_{23}e^{ix}\sinh[ifx(1 + ik_2/n_2)]/[ifx(1 + ik_2/n_2)])^*}{(R_{23}\sinh[2fxk_2/n_2]/[2fxk_2/n_2])^{1/2}} \tag{42}$$

where the thickness parameter x and the resolution parameter f are defined as

$$x = 4\pi n_2 L\nu_o/c_o, \tag{43a}$$

$$f = \Delta\nu/\nu_o \tag{43b}$$

A typical value of x ranges from 10 to 1000 for films of the micron range. For FTIR, the resolution parameter f may change from 10^{-5} to 10^{-1}, depending on the wavelength measured and the resolution. For interference filters, f may vary from 10^{-3} to 10^{-1}.

It can be shown that Eq. (42) degenerates into Eqs. (28) and (31*a*) as $f\to\infty$ and $f\to 0$, respectively, corresponding to absolutely incoherent and absolutely coherent incidence.

If absorption inside the film can be neglected, Eq. (42) can be further simplified as

$$\gamma_0(\tau) = \frac{r_{23}^*}{(R_{23})^{-1/2}}(r_{12}r_{23} + e^{-ix})\mathrm{sinc}(xf) + r_{21}(R_{23})^{1/2} \tag{44}$$

where the sinc function is defined as $\sin(x)/x$ (Marathay, 1982). All the refractive indices in Eqs. (42) and (44) are evaluated at ν_o.

The accuracy of the approximate Eqs. (42) and (44) is affected mainly by the refractive indices. Increasing film absorption will decrease the sinuous term in the denominator of r [Eq. (37)], thus enhancing the accuracy of the approximation. For the worst case, transparent films, calculation shows that the approximations are satisfactory if

$$R_{12}R_{23} < 0.25 \tag{45}$$

Examining Eqs. (41)–(44), one can see that the complex degree of coherence depends on x, f, α, r_{12}, and r_{23}. Among them, x and f are the most important. In the following sample calculation, refractive indices are taken close to those used by Born and Wolf (1975, p. 631). Results of calculation are shown in Figs. 2–7.

Figure 2 compares the amplitude of the complex degree of coherence calculated from numerical integration of Eq. (41) (solid lines) and from the approximate expressions (42) and (44) (dotted lines). Since no absorption is included, the curves represent the maximum error between numerical integration and approximation for the given real part of refractive indices.

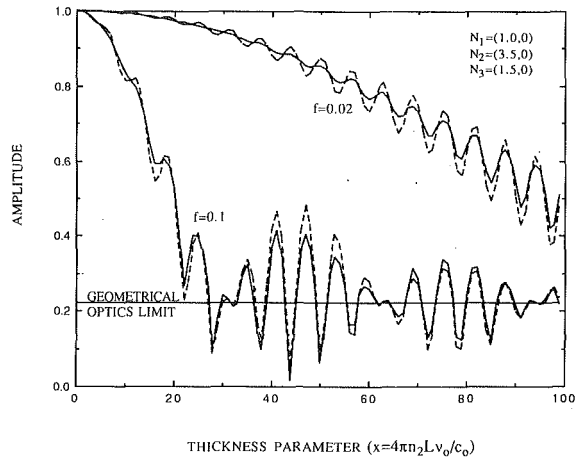

Fig. 2 Amplitude of the complex degree of coherence as a function of thickness parameter

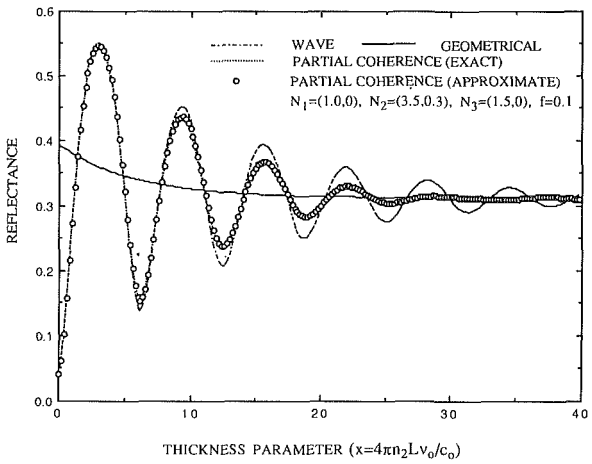

Fig. 5 Comparison of reflectance among wave, geometric, and partial coherence approaches

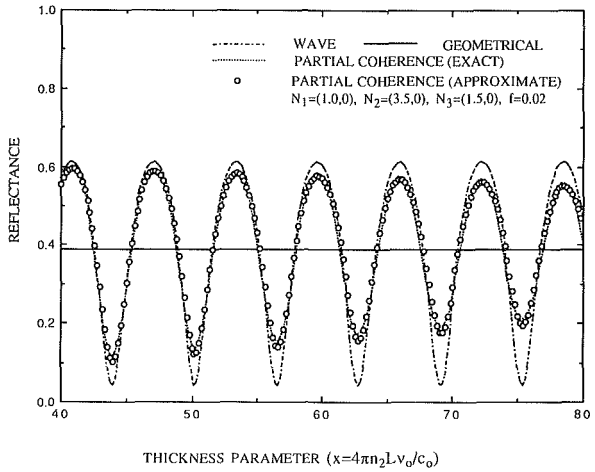

Fig. 3 Comparison of reflectance among wave, geometric, and partial coherence approaches

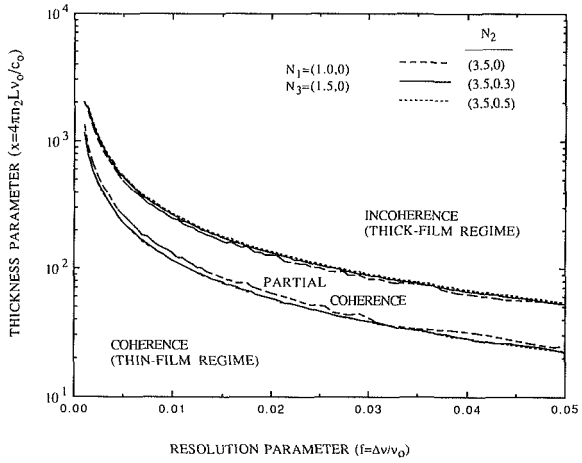

Fig. 6 Effects of absorption on the coherence, partial coherence, and incoherence regimes

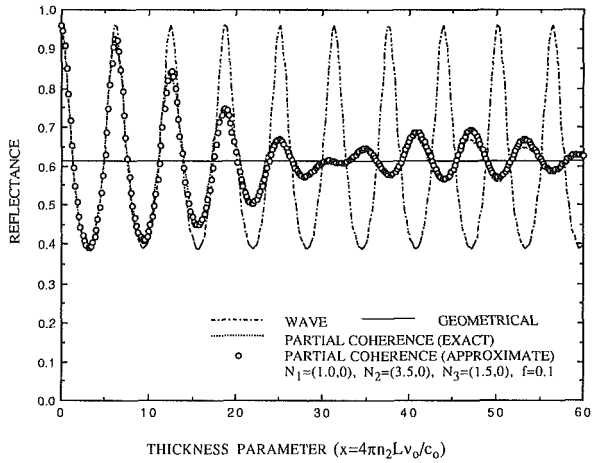

Fig. 4 Comparison of transmittance among wave, geometric, and partial coherence approaches

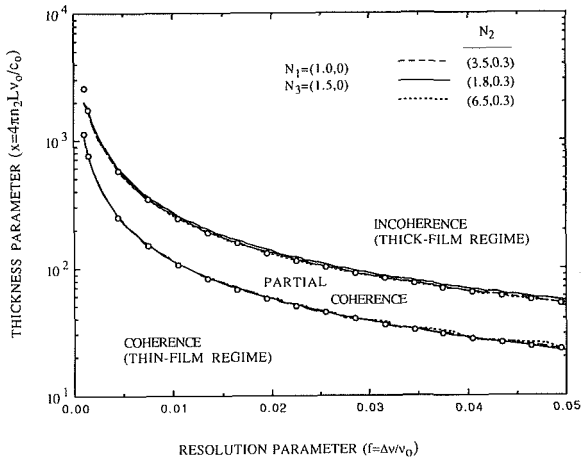

Fig. 7 Effects of the real part of complex refractive index on the coherence, partial coherence, and incoherence regimes

Adding absorption inside the film tends to decrease such discrepancy and damp the oscillation in the presented curves. Also shown in the figure is the amplitude of the complex degree of coherence calculated from the geometric optics limit, Eq. (28). This figure shows that the approximate expressions (42) and (44) give good results. The oscillation in the curves is typical of the complex degree of coherence (Metha and Wolf, 1967), and is essentially due to interference. The slight overshoot of the approximate expression is understandable by examining the approximations made—the sinuous denominator in the integrand is replaced by its value at frequency ν_o.

Figures 3 and 4 compare reflectance and transmittance of a

nonabsorbing thin film calculated from the three different approaches. Also shown in the figures are comparisons between reflectance and transmittance calculated from using the integral and the approximate expressions for the complex degree of coherence, although the results using the integral expression are almost entirely covered by those using the approximate one. In Fig. 3, the resolution parameter is taken as 0.02, while in Fig. 4 and later Fig. 5, it is taken as 0.1 to get an overview of the variation of the reflectance and transmittance with x. The behavior of reflectance and transmittance calculated from the partial coherence formulation is well expected: When x is small, the reflectance and transmittance match the wave optics results, and when x is large, they approach the geometric optics limit. But similar to the amplitude of the complex degree of coherence shown in Fig. 2, their envelopes also show some long-range periodicity. Clearly, there is an interval in which neither wave optics nor geometric optics is correct. It is also seen from the figures that increasing the resolution parameter will accelerate the reflectance/transmittance to the geometric optics limit, and that the small discrepancies between the numerical integration of the complex degree of coherence and its approximation (Fig. 2) are further decreased in reflectance and transmittance calculation. In Fig. 5, the effect of film absorption on the reflectance calculation is shown. Due to the damping of the oscillation of reflectance when absorption is present, the absolute errors between the three approaches are smaller than those of nonabsorbing films. Direct integral averaging of the wave optics formula, Eq. (2), over frequency interval $(\nu_o - \Delta\nu, \nu_o + \Delta\nu)$ is also performed but not shown in the figures, because the results are identical with those calculated from the partial coherence formulation with numerically integrated complex degree of coherence. This is not surprising because the complex degree of coherence is a concept in the space–time domain, and the spectral formulation is in the frequency domain. They are interconnected through Fourier transformation. Even from the quantum theory (Loudon, 1983), the second-order coherence, which is applied here, will not differ from the classical theory. Theoretically, the partial coherence formulation is a more natural approach since instruments are always limited by their resolution and detectors measure only the averaged temporal signal. The practical advantage of the new approach is clear: Integration is avoided through very good approximation. Furthermore, this work assumes normal incidence and remote point sources, which in essence, are only for the temporal coherence properties. When these idealizations are relaxed, the complex degree of coherence will include the spatial as well as the temporal coherence properties, and will also depend on the dimension of the source, the incident angle, and the distance between the film and the source. For these cases, the partial coherence approach will possess greater advantage over doing many integrations from the spectral formulation (Born and Wolf, 1975).

It is convenient in practice to have some criteria for selecting which formulation to use. Apparently, for the coherence limit, the amplitude of the complex degree of coherence is the best candidate. For the incoherence limit the same quantity is not appropriate because it approaches the geometric optics limit, which is variable according to Eq. (28). So, for the incoherence limit, the amplitude of the difference between the complex degree of coherence and that of geometric optics is used to characterize the geometric optics regime. The coherence regime is then characterized as

$$|\gamma_0(\tau)| \geq 0.8 \tag{46}$$

and the incoherence regime as

$$|\gamma_0(\tau) - \gamma_{0g}(\tau)| \leq 0.2 \tag{47}$$

where the subscript $0g$ represents the complex degree of coherence in the geometric optics limit.

In Eq. (46), the constant is chosen based on the relative error between the reflectance calculated from the partial coherence approach and that from the wave approach. Actually, the error, if plotted, is also oscillating with x due to the nature of interference. The constant, 0.8, is taken when the relative error in reflectance reaches about 10 percent during its first oscillation period (Fig. 3). The constant in Eq. (47) is selected with some degree of fuzziness because the relative error between the geometric and the partial coherence results also shows some long-range periodicity (Fig. 4). The chosen constant, 0.2, corresponds to the last peak in the relative error between the geometric optics and the partial coherence data just before the first long-range period ends and the second one commences. Such relative error is about 10 to 20 percent for the calculated cases.

Figures 6 and 7 show regime maps for different refractive indices based on the above definitions. In Fig. 6, the effects of absorption inside the thin film on the regime map are examined. For nonabsorbing films, the demarcation lines between the three regions are not smooth. In fact, there were some irregular peaks in the calculated results. Such irregularities again can be understood from examining the fluctuating behavior of the amplitude of the complex degree of coherence (Fig. 2). When absorption is increased, the kinks disappear because, as mentioned before, absorption damps the oscillation of the complex degree of coherence. Other calculations performed show that further increase of k_2 has little effect on the position of the line delineating the coherence and the partial coherence regimes, but will push the line dividing the partial coherence and the incoherence regimes further into the incoherence region, thus enlarging the partial coherence regime. But such effect on the partial coherence regime is not important because when absorption is increased, both the wave and the partial coherence formulations will approach the geometric limit for small x, as can be seen from Fig. 5. Therefore, the regime map shown can be used for both small and large absorption. Figure 7 shows that the real part of the refractive index, n_2, has very little effect on the regime map. Since both Figs. 6 and 7 contain the case $n_2 = (3.5, 0.3)$, the two figures are actually nearly identical.

Substituting Eq. (42) into the left-hand sides of Eqs. (46) and (47), it is found that for the calculation performed, one term, $\mathrm{sinc}(xf)$, is dominant. This explains the near independence of the regime map on the refractive indices (except in the thickness parameter x). Such near independence agrees with the qualitative discussion by Bohren and Huffman (1983). Keeping only the sinc term, the inequalities (46) and (47) can be solved and give

$$xf \leq 1.13 \qquad \text{coherence regime} \tag{48}$$

$$xf \geq 2.59 \qquad \text{incoherence regime} \tag{49}$$

The dots in Fig. 7 are obtained from the above relations. They match the calculated curves very well. Numerical analysis shows that the inequalities (48) and (49) are valid when Eq. (45) is satisfied.

The above discussions assume that the film is smooth. The regime map, however, can also be applied to rough surface under certain situations. This is based on the observation that the film thickness and frequency always appear in product form, νL. Although they represent different physical quantity, mathematically, they are equivalent. For thermal radiation wavelength, it is reasonable to assume that the surface roughness does not cause significant change of the direction of the reflected fields but only their path length. Under such an assumption, the regime map can be applied to include the surface roughness by replacing the resolution parameter with

$$f = \Delta\nu/\nu_o + \Delta L/L_o \tag{50}$$

where L_o is the average film thickness and ΔL is the mean

square root deviation of the film thickness. It is cautioned, however, that to use Eq. (50) in the partial coherence formulation, the film thickness variation has to be assumed uniformly distributed around the mean value.

Conclusions

This work presents a general partial coherent theory of the radiative properties of a thin film for normal radiation incidence. The new model is based on a detailed analysis of the wave optics and the geometric optics models. It is noted that the forward propagating field in the wave optics model is actually composed of two parts. One is refracted directly from the incident field, and the other evolves from the reflection of the backward field. The important difference between these two components is that the latter has a time retardation relative to the former. A statistical average method is applied to obtain general expressions for radiative properties, namely, reflectance, transmittance, and local absorptance of the thin film.

The key element in these expression is the complex degree of coherence. In the geometric optics limit, the complex degree of coherence inside the film is zero, but is finite on the two surfaces. Such partial coherent properties are rather implicit and undetermined in geometric optics where ray tracing and intensity superposition is applied. In the wave optics limit, the modulus of the complex degree of spectral coherence is one but the phase depends on the refractive indices of the film and its surrounding media. The general formulation degenerates into the wave optics and geometric optics expressions, respectively, when the corresponding complex degree of coherence is used.

The current relations not only include the wave and geometric optics expressions, but more importantly, they apply to the general case—the partially coherent case—as well. A general integral expression for the complex degree of coherence is established. For nearly monochromatic incidence or resolution limited spectral measurements, the general expression for complex degree of coherence can be well approximated by an algebraic one. Comparisons of the current formulation with the wave and geometric optics approaches are performed through sample calculation. The results show clearly the existence of a region in which neither the wave nor the geometric formulation yields accurate results. Such a partial coherence regime is quantitatively characterized through the amplitude of the complex degree of coherence. Regime maps are constructed and simple expressions delineating the various regimes are given.

Acknowledgments

The authors gratefully acknowledge the financial support of the U.S. Department of Energy, and the K. C. Wong Education Foundation.

References

Born, M., and Wolf, E., 1975, *Principles of Optics*, 5th ed., Pergamon Press, Oxford, United Kingdom.

Bohren, C. F., and Huffman, D. R., 1983, *Absorption and Scattering of Light by Small Particles*, Wiley, New York.

Harris, L., Beasley, J. K., and Loeb, A. L., 1951, "Reflection and Transmission of Radiation by Metal Films and the Influence of Nonabsorbing Backing," *Journal of the Optical Society of America*, Vol. 41, pp. 604–614.

Heavens, O. S., 1965, *Optical Properties of Thin Solid Films*, Dover Publications, Inc., New York.

Loudon, R., 1983, *The Quantum Theory of Light*, 2nd ed., Clarendon Press, Oxford, United Kingdom.

Mandel, L., and Wolf, E., 1965, "Coherence Properties of Optical Fields," *Reviews of Modern Physics*, Vol. 37, pp. 231–287.

Mandel, L., and Wolf, E., 1976, "Spectral Coherence and the Concept of Cross-Spectral Purity," *Journal of the Optical Society of America*, Vol. 66, pp. 529–535.

Marathay, A. S., 1982, *Elements of Optical Coherence Theory*, Wiley, New York.

Metha, C. L., 1963, "Coherence-Time and Effective Bandwidth of Blackbody Radiation," *Nuovo Cimento*, Vol. 21, pp. 401–408.

Metha, C. L., and Wolf, E., 1967, "Coherence Properties of Blackbody Radiation. III. Cross-Spectral Tensors," *Physical Review*, Vol. 161, pp. 1328–1334.

Musilova, J., and Ohlidal, I., 1990, "Possibilities and Limitations of the Film Thickness Determination Method Based on White Light Interference," *Journal of Physics D: Applied Physics*, Vol. 23, pp. 1227–1238.

Phelan, P. E., Chen, G., and Tien, C. L., 1992, "Thickness-Dependent Radiative Properties of Y-Ba-Cu-O Thin Films," ASME JOURNAL OF HEAT TRANSFER, Vol. 114, pp. 227–233.

Siegel, R., and Howell, J. R., 1981, *Thermal Radiation Heat Transfer*, McGraw-Hill, New York.

APPENDIX

Using Eq. (31*a*) and Beer's law, Eq. (20) becomes

$$R = R_{12} + \left(T_{21} + 2\mathrm{Re}\left\{ \frac{r_{12} t_{21}^*}{t_{12}} \left[\frac{r_{23}^* e^{-i2\pi\nu\tau}}{R_{23} e^{-\alpha L}} - r_{21} \right] \right\} \right) \times \frac{T_{12} R_{23} e^{-2\alpha L}}{1 + 2\mathrm{Re}[r_{12} r_{23} \exp(i4\pi N_2 L/\lambda)] + R_{12} R_{23} e^{-2\alpha L}} \quad \text{(A1)}$$

Re-writing the above expression into a single fraction, and grouping the numerator into the sum of three terms:

$$\text{Term 1} = 2R_{12}\mathrm{Re}[r_{12} r_{23} \exp(i4\pi N_2 L/\lambda)] + 2T_{12} R_{23} e^{-2\alpha L} \mathrm{Re}\left\{ \frac{r_{12} t_{21}^*}{t_{12}} \left[\frac{r_{23}^* e^{-i2\pi\nu\tau}}{R_{23} e^{-\alpha L}} \right] \right\}$$

$$= 2\mathrm{Re}[R_{12} r_{12} r_{23} \exp(i4\pi N_2 L/\lambda)] + 2\mathrm{Re}[r_{12} t_{12}^* t_{21}^* r_{23}^* \exp(-i4\pi N_2^* L/\lambda)]$$

$$= 2\mathrm{Re}\{ r_{23} \exp(i4\pi N_2 L/\lambda)[R_{12} r_{12} + r_{12}^* t_{12} t_{21}] \} = 2\mathrm{Re}[r_{12}^* r_{23} \exp(i4\pi N_2 L/\lambda)] \quad \text{(A2)}$$

$$\text{Term 2} = T_{21} T_{12} R_{23} e^{-2\alpha L} + 2\mathrm{Re}\left\{ \frac{r_{12} t_{21}^*}{t_{12}} r_{21} \right\} T_{12} R_{23} e^{-2\alpha L}$$

$$= e^{-2\alpha L} R_{23}[(1 + r_{12})(1 + r_{12})^*(1 - r_{12})(1 - r_{12})^* + 2\mathrm{Re}(r_{12} t_{21}^* t_{12}^* r_{21})] = e^{-2\alpha L} R_{23}(1 - R_{12}^2) \quad \text{(A3)}$$

$$\text{Term 3} = R_{12}(1 + R_{12} R_{23} e^{-2\alpha L}) \quad \text{(A4)}$$

Substitution of Eqs. (A2)–(A4) into Eq. (A1) gives exactly Eq. (2).

Z. M. Zhang

B. I. Choi

T. A. Le

M. I. Flik

Department of Mechanical Engineering,
Massachusetts Institute of Technology,
Cambridge, MA 02139

M. P. Siegal

J. M. Phillips

AT&T Bell Laboratories,
Murray Hill, NJ 07974

Infrared Refractive Index of Thin $YBa_2Cu_3O_7$ Superconducting Films

This work investigates whether thin-film optics with a constant refractive index can be applied to high-T_c superconducting thin films. The reflectance and transmittance of $YBa_2Cu_3O_7$ films on $LaAlO_3$ substrates are measured using a Fourier-transform infrared spectrometer at wavelengths from 1 to 100 μm at room temperature. The reflectance of these superconducting films at 10 K in the wavelength region from 2.5 to 25 μm is measured using a cryogenic reflectance accessory. The film thickness varies from 10 to 200 nm. By modeling the frequency-dependent complex conductivity in the normal and superconducting states and applying electromagnetic-wave theory, the complex refractive index of $YBa_2Cu_3O_7$ films is obtained with a fitting technique. It is found that a thickness-independent refractive index can be applied even to a 25 nm film, and average values of the spectral refractive index for film thicknesses between 25 and 200 nm are recommended for engineering applications.

Introduction

The design of promising high-T_c superconductor infrared detectors requires the determination of the radiative properties of very thin films. Phelan et al. (1992) studied the influence of film thickness on the absorptance of either the film or the film–substrate composite due to absorption and interference effects. The radiative properties of very thin films are also crucial for the thermal design of deposition processes for high-T_c superconducting films. Flik et al. (1992a) performed a thermal radiation analysis of the substrate-temperature evolution in the sputtering deposition of high-T_c superconducting films. They applied thin-film optics and used the complex refractive index of a single crystal to determine the optical properties of very thin films. But in addition to absorption and interference effects, the microstructure can affect the optical properties of thin films through crystalline misorientation (Sengupta et al., 1991). As the temperature decreases, the electron mean free path becomes large. When the electron mean free path is comparable with the thickness, boundary scattering will reduce the electrical conductivity (Olsen, 1962). Boundary scattering can also occur at grain boundaries. At present, it is not known whether the radiative properties of the thinnest films can be predicted using thin-film optics and a thickness-independent refractive index, or whether there is a size effect on the refractive index of very thin films.

The optical properties of high-quality $YBa_2Cu_3O_7$ superconducting films and crystals have been investigated by several groups (Schützmann et al., 1989; Kamaras et al., 1990; Orenstein et al., 1990; Cooper et al., 1989; Schlesinger et al., 1990; Collins et al., 1989; Timusk et al., 1988). Phelan et al. (1992) measured the radiative properties of 35 and 75 nm $YBa_2Cu_3O_7$ films on MgO substrates at room temperature. Gao et al. (1991) measured the transmittance and reflectance of 48, 156, and 180 nm $YBa_2Cu_3O_7$ films on MgO substrates for wavelengths between 30 and 500 μm at temperatures from 20 to 300 K. They used a two-fluid model along with a mid-infrared band for the superconducting state and obtained a BCS-like temperature dependence for the superfluid density. Bozovic et al. (1987) studied the reflectance and transmittance spectra of 90 to 1000-nm-thick $YBa_2Cu_3O_7$ films on $SrTiO_3$ substrates. The influence of film thickness on the refractive index of very thin films has not been investigated. In contrast to the previous studies, this work determines for the first time the refractive index of $YBa_2Cu_3O_7$ films as thin as 10 nm on $LaAlO_3$ substrates at room temperature and at 10 K.

The samples are *c*-axis oriented and fabricated by co-evaporation of Y, Cu, and BaF_2 on $LaAlO_3$ substrates, followed by an optimized *ex situ* anneal. The thickness of the films used in this study varies from 10 to 200 nm. The substrate thicknesses are between 518 and 543 μm. A Fourier-transform infrared spectrometer is employed to measure the nearly normal reflectance and transmittance from 1 to 100 μm wavelengths. The reflectance at 10 K from 2.5 to 25 μm wavelengths is measured with a cryogenic reflectance accessory. The incident radiation is reflected, transmitted, or absorbed by the film–substrate composite as shown in Fig. 1. The reflectance and transmittance are functions of the complex refractive indices and thicknesses of the film and substrate. The complex refractive index in the *a–b* plane of $YBa_2Cu_3O_7$ is obtained for

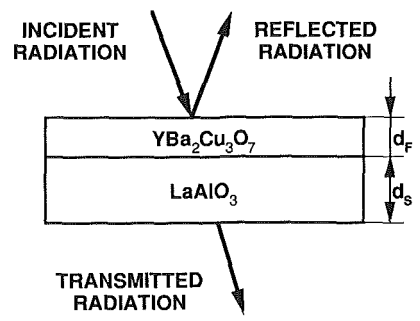

Fig. 1 Schematic of the incident, reflected, and transmitted radiation for a film-substrate composite

Contributed by the Heat Transfer Division and presented at the ASME Winter Annual Meeting, Atlanta, Georgia, December 1-6, 1991. Manuscript received by the Heat Transfer Division July 1991; revision received January 1992. Keywords: Cryogenics, Radiation, Thermophysical Properties.

Table 1 Sample characteristics and fitting parameters

MEASURED				FITTED				
				ROOM TEMPERATURE			T = 10 K	
d_F (nm)	d_s (μm)	T_c (K)	ρ_{dc} (300 K) (μΩ cm)	ρ_{dc} (μΩ cm)	$1/\tau$ (cm^{-1})	n_e (m^{-3})	ρ_{dc} (μΩ cm)	Y
10	521	85	840±80	880±220	300±90	1.1×10^{27}	160	0.60±0.20
25	518	90	360±40	420±40	400±60	3.0×10^{27}	80	0.42±0.05
50	533	89	295±30	340±30	520±50	4.8×10^{27}	60	0.44±0.04
100	540	91	330±30	340±30	480±50	4.5×10^{27}	65	0.42±0.04
200	543	91	520±50	510±30	500±50	3.1×10^{27}	90	0.46±0.04

films with different thicknesses by fitting the measured data to a model dielectric function and applying thin-film optics. The Drude model is used to calculate the frequency-dependent electrical conductivity at room temperature. The electrical conductivity in the superconducting state is calculated using the computational method developed by Zimmermann et al. (1991), which yields the frequency-dependent complex conductivity of weak coupling superconductors with any given electron scattering rate.

Based on the comparison of the refractive indices for films with different thicknesses, averaged values of the refractive indices obtained for film thicknesses between 25 and 200 nm are recommended for use in radiative transfer calculations.

Thin-Film Specimens

Table 1 lists the thickness of the $YBa_2Cu_3O_7$ film, d_F, the thickness of a $LaAlO_3$ (100) substrate, d_s, the critical temperature, T_c, and the room-temperature d-c resistivity in the a–b plane of $YBa_2Cu_3O_7$ films, ρ_{dc} (300 K), for each sample. The samples are approximately 12 × 12 mm^2. The 50, 100, and 200-nm-thick films are grown by an optimized annealing process using flowing wet and dry oxygen gas in a tube furnace. Special care is taken to use only films with Y:Ba:Cu stoichiometry of 1:2:3 within 1 percent. These films are annealed at a maximum temperature of 900°C for 30 minutes in wet O_2. This procedure results in c-axis oriented $YBa_2Cu_3O_7$ films of high structural and morphological quality, which is determined from Rutherford backscattering/ion channeling, x-ray diffraction, and scanning electron microscopy. Detailed descriptions of the deposition and characterization of these samples are given by Siegal et al. (1990a, 1990b) and Carlson et al. (1990).

The film quality for thicknesses less than 50 nm or larger than 200 nm suffers from this annealing process. Recent reports indicate that thicker films can be grown with a smooth morphology and a high T_c using a reduced O_2 ambient partial pressure to simulate the thermodynamic environment of *in situ* growth (Mogro-Campero and Tumer, 1991; Feenstra et al., 1991). Using these ideas, the 10 and 25 nm films used in this study are grown for the first time with T_c = 85 K and T_c = 90 K, respectively. The first stage of the *ex situ* anneal is at 750°C for 30 minutes using a N_2:O_2 gas mixture (1 percent O_2) bubbled through deionized water. The annealing conditions for the second stage are the same as those of the 50, 100, and 200 nm films: 30 minutes at 525°C in flowing dry O_2. Rutherford back-scattering spectrometry, scanning electron microscopy, and x-ray diffraction measurements showed that the crystalline structure of the 25 nm films is close to that of the thick films, while the crystalline structure of the 10 nm film is not as good as that of the others. The surface roughness of the films used in this study is approximately 10 nm. The electrical resistivities in the normal state are measured using different samples with the same deposition and annealing conditions. Figure 2 shows the temperature dependence of the electrical resistivity in the a–b plane of the $YBa_2Cu_3O_7$ films used in this study. The electrical resistivity changes almost linearly with temperature above T_c and decreases abruptly to zero at T_c. The c-axis lattice constant for $YBa_2Cu_3O_7$ is about 1.2 nm (Zhang et al., 1988), yielding an average of eight unit cells on top of each other for the 10 nm film. Recently, ultrathin $YBa_2Cu_3O_7$ superconducting films of one to two unit cells have been deposited by several groups (Gao et al., 1990; Xi et al., 1990; Terashima et al., 1991).

Measurement Technique and Results

Room Temperature. A Biorad FTS-60A Fourier-transform infrared spectrometer is employed for the measurement of the reflectance and transmittance of the film–substrate com-

Nomenclature

A = energy gap parameter $= 2\Delta_0/kT_c$
c = speed of light in vacuum $= 2.998\times10^8$ m s^{-1}
d_F = thickness of film, m
d_s = thickness of substrate, m
e = electron charge $= -1.602\times10^{-19}$ C
h = Planck's constant $= 6.626\times10^{-34}$ J s
i = $(-1)^{1/2}$
k = Boltzmann constant $= 1.381\times10^{-23}$ J K^{-1}
m_e = electron effective mass, kg
n_e = electron number density, m^{-3}
n_F = real part of the film refractive index
T = film temperature, K
T_c = critical temperature, K
v_F = Fermi velocity
Y = normalized scattering rate $= h/(4\pi\tau\Delta)$
γ_e = oscillator width for midinfrared band, rad s^{-1}
Δ = energy gap, J
Δ_0 = energy gap at 0 K, J
ϵ = dielectric function
ϵ_0 = electrical permittivity of free space $= 8.854\times10^{-12}$ C V^{-1} m^{-1}
ϵ_∞ = high-frequency dielectric constant
θ = Debye temperature, K
κ_F = imaginary part of film refractive index
λ = wavelength in vacuum, m
Λ_0 = electron mean free path at 0 K, m
ξ_0 = superconductor coherence length at 0 K $= hv_F/(2\pi^2\Delta_0)$, m
ρ_{dc} = d-c electrical resistivity, Ω m
ρ_d = electrical resistivity resulting from defects, Ω m
ρ_L = electrical resistivity due to scattering on phonons, Ω m
ρ_θ = constant, Eq. (7), Ω m
σ = frequency-dependent electrical conductivity, $\Omega^{-1}m^{-1}$
σ_{dc} = d-c electrical conductivity, $\Omega^{-1}m^{-1}$
$1/\tau$ = electron scattering rate, rad s^{-1}
ω = angular frequency, rad s^{-1}
ω_e = center frequency of midinfrared band, rad s^{-1}
ω_p = plasma frequency, rad s^{-1}
ω_{pe} = plasma frequency of midinfrared band, rad s^{-1}

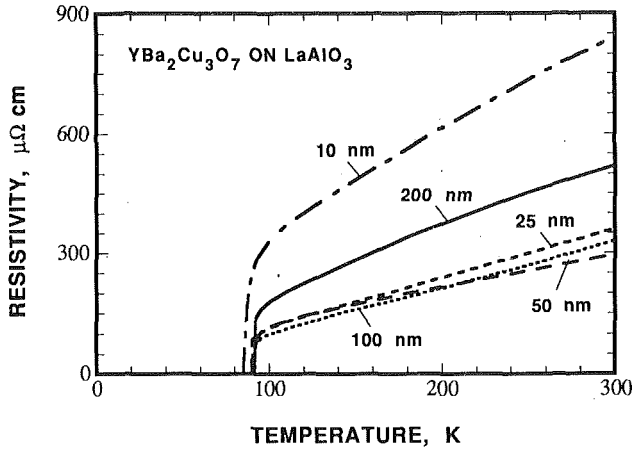

Fig. 2 Temperature dependence of the electrical resistivity in the *a–b* plane of $YBa_2Cu_3O_7$ films

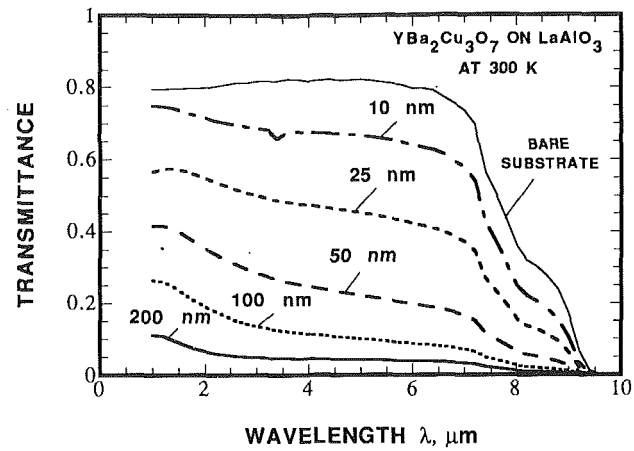

Fig. 3 Room-temperature transmittance of film-substrate composites and a bare substrate

posites and a substrate without a film. Different sources, beam splitters, and detectors are used to obtain data for wavelengths from 1 to 100 μm. A tungsten halogen source, a quartz beam splitter, and a PbSe photoconductive detector are used in the near-infrared region from 1 to 3 μm. A Globar ceramic source, a KBr beamsplitter, and a DTGS pyroelectric detector with a CsI window are used in the mid-infrared from 2.5 to 25 μm. The Globar source is also used in the far-infrared region from 20 to 100 μm with a Mylar beam splitter and a DTGS detector with a polyethylene window. The resolutions used in the measurements are 8 cm^{-1} in the near- and mid-infrared regions and 2 cm^{-1} in the far-infrared. To achieve high photometric accuracy, special filters are used to remove radiation of undesired wavelengths and attenuate the incident radiation power (Flik and Zhang, 1992). The agreement of the data within the overlapping spectral regions is better than 2 percent. Calibrations for the transmittance measurements have been performed using silicon, calcium fluoride, and strontium titanate crystals of optical quality. The results show that a photometric accuracy better than 1 percent is achieved in the near- and mid-infrared regions and 2 percent in the far-infrared.

A gold mirror is used as the reference for the reflectance measurement. The spectral reflectance is obtained by dividing the spectral response with the sample by the spectral response with the mirror. The reflectance of the gold mirror is estimated to be 0.99 for all wavelengths (Toscano and Cravalho, 1976), which is used as a correction factor for the raw data. Reflections from the sample holder to the sample are avoided by placing a piece of black tape with a reflectance of less than 0.01 beneath the sample. The photometric accuracy in the reflectance measurements is estimated to be better than 3 percent considering the uncertainty in the estimated reflectance of the mirror.

Figure 3 shows the room-temperature transmittance for the five samples listed in Table 1 and a bare $LaAlO_3$ substrate. The thickness of the bare substrate is 446 μm. The transmittance decreases monotonically as the film thickness increases. At wavelengths greater than 10 μm, the substrate is opaque. Figure 4 shows the room-temperature reflectance for these samples and the bare substrate. The three reflectance peaks around 15, 23, and 53 μm are due to the influence of the substrate. As the film thickness decreases, the reflectance of the film-substrate composite approaches the substrate reflectance. As a result of absorption and interference inside the film-substrate composite, the reflectance increases with film thickness except in the regions 13 $\mu m < \lambda < 15$ μm, 17 $\mu m < \lambda < 23$ μm, and 36 $\mu m < \lambda < 53$ μm, where the reflectance of a bare substrate can be higher than that of the film-substrate composites. The real part of the substrate refractive index in these regions is close to zero, which implies that very little

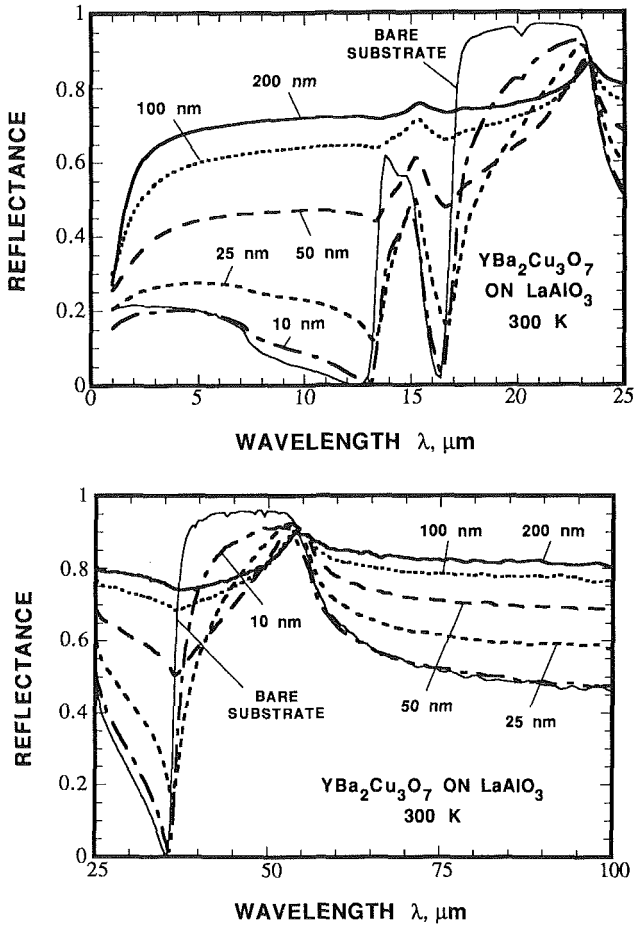

Fig. 4 Room-temperature reflectance of film-substrate composites and a bare substrate

radiation power can penetrate into the substrate. With the addition of an $YBa_2Cu_3O_7$ film, the total absorptance of the film-substrate composite increases, causing a decrease in the reflectance.

Since the substrate is opaque for $\lambda > 10$ μm, Fig. 4 provides information on the absorptance of the film-substrate composite, which equals one minus the reflectance. This parameter is of paramount importance for the design of infrared detectors because it determines how effectively the detector captures the incident radiation power. A high-T_c superconducting infrared detector using the film-substrate composite as an absorber

is not a broad-band detector because the absorptance is a strong function of the wavelength. The absorptance in the bands $10\ \mu m < \lambda < 13\ \mu m$, $25\ \mu m < \lambda < 34\ \mu m$, and $\lambda > 60\ \mu m$ strongly increases with decreasing film thickness. If the film thickness is reduced from 200 to 10 nm, then the absorptance at 12 and 30 μm increases by a factor of 3, and at 80 μm by a factor of 2.5. This implies that the responsitivity of an infrared detector can be increased by a factor of two to three by reducing the film thickness. Carr et al. (1990) tested the bolometric response of high-T_c superconducting detectors with subnanosecond synchrotron radiation pulses using $YBa_2Cu_3O_7$ films of different thickness on MgO substrates. They observed that the detector responsitivity increased by a factor of 2 to 3 for $10\ \mu m < \lambda < 100\ \mu m$ if a 48-nm-thick film was used instead of a 156 nm film. Their observation can be explained by the change in the absorptance of the film–substrate composite. The operating temperature of a high-T_c superconducting detector is close to $T_c \sim 90$ K. Since the radiative properties of $YBa_2Cu_3O_7$ at T_c are not very different from those at 300 K, the foregoing conclusions obtained from room-temperature measurements are valid in principle for 90 K. Similar observations over a more limited range of film thicknesses were made by Phelan et al. (1992).

Cryogenic Temperatures. A schematic of the reflectance accessory made by Harrick Scientific Corporation is shown in Fig. 5. Incoming radiation from the source is guided by a set of mirrors to the sample and then to the detector. The incident angle can be adjusted by rotating the two flat mirrors, which in this study is fixed at 10 deg. At low temperatures, a detachable-tail liquid-helium dewar made by Janis Research Company is employed, which has an inner liquid helium chamber and an outer liquid nitrogen chamber. Between the two chambers and on the outside of the liquid nitrogen chamber, there are two interconnected vacuum jackets for thermal insulation. A mechanical pump is used to achieve a vacuum of approximately 10^{-5} bar. The sample is mounted on a cold finger inside the vacuum space at the bottom of the dewar and is sealed by a KRS-5 hemispherical window for the low-temperature reflectance measurements from 2.5 to 25 μm wavelengths. The sample temperature is monitored by a silicon diode, which is mounted inside the cold finger close to the sample, as depicted in Fig. 5. A Lakeshore 805 temperature controller is used for the temperature reading. The temperature difference between sample and cold finger could be several degrees Kelvin due to the contact resistance (Mikic, 1974). To obtain the actual sample temperature, calibration is performed by mounting another silicon diode on the front surface of a $LaAlO_3$ substrate. The temperature of the sample is between 9 and 10 K while the temperature of the cold finger is between 5 and 6 K. The accuracy of the temperature sensor is 0.5 K at $T < 100$ K.

The reflectance at 10 K is obtained relative to the room-temperature reflectance, which is measured using a gold reference. For each sample, the spectral response is measured at 10 and 300 K with the same configuration as shown in Fig. 5. The spectral reflectance for a given sample at 10 K is determined by multiplying the room-temperature reflectance by the ratio of the spectral response at 10 K to the spectral response at 300 K, since the spectral response is proportional to the spectral reflectance. A gold mirror is not used as the reference for the reflectance measurements at 10 K due to the difficulties in obtaining identical alignments for the cases with gold mirror and with samples. Kamaras et al. (1990) used this method to study the temperature dependence of the reflectance of high T_c superconducting films. This method is valid only if the optical efficiency of the spectrometer does not vary with time. After the sample has achieved the steady-state temperature of 10 K, the spectral response at wavelengths from 2.5 to 10 μm

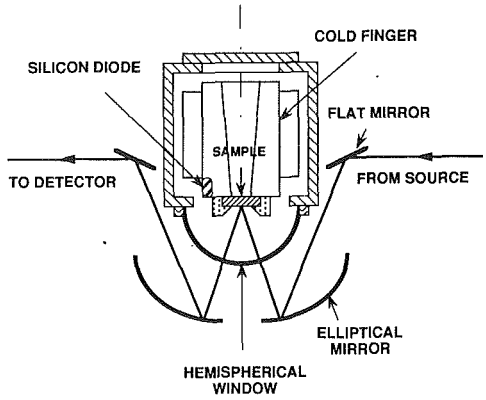

Fig. 5 Experimental apparatus for low-temperature reflectance measurement

slowly decreases with time, while the spectral response at wavelengths from 10 to 25 μm does not change. For a 50 nm film at 10 K, two spectral responses taken before and after a time interval of 100 minutes show relative differences of 5 percent at $\lambda = 5\ \mu m$ and 19 percent at $\lambda = 2.5\ \mu m$. The effect of thermal drift was also observed by van der Marel et al. (1991) in their midinfrared reflectance measurements. Although the sample is at steady-state temperature after the dewar has been charged with liquid helium, the temperature of the hemispherical window, which is close to room temperature, may vary with time due to its large thermal time constant. The optical properties of the KRS-5 window may vary with time due to the temperature variation, causing a change in the total optical efficiency. In order to investigate the photometric accuracy of low-temperature reflectance measurements, a gold mirror is mounted at the sample position. The uncertainty at low temperatures is evaluated based on the spectral responses obtained with the gold mirror, since the change of the reflectance of gold from 300 to 10 K is less than 1 percent (Toscano and Cravalho, 1976). Due to the variation of response, the maximum relative uncertainty is estimated to be 20 percent for $2.5\ \mu m < \lambda < 5\ \mu m$ and 5 percent for $5\ \mu m < \lambda < 22\ \mu m$. Since the signal-to-noise ratio is very low for wavelengths close to the cutoff wavelength of 25 μm, two spectra taken for one sample at same temperature may differ from each other by several percent. Hence, the maximum relative uncertainty is estimated to be 10 percent for $22\ \mu m < \lambda < 25\ \mu m$.

Figure 6 shows the reflectance of these samples and the bare substrate at 10 K from 2.5 to 25 μm. Compared with the room-temperature measurements (Fig. 4), the substrate reflectance increases about 30 percent between 13 and 16 μm but does not change very much for other wavelengths. The reflectance of the film–substrate composites increases as temperature decreases from room temperature to 10 K at long wavelengths. As the wavelength approaches 2.5 μm, the reflectance at 10 K is lower than the reflectance at room temperature. The crossover wavelength is between 5 and 9 μm. Note the decrease in the reflectance at short wavelengths at 10 K is within the estimated measurement uncertainty. Other reports indicated that the reflectance of high-T_c superconductors is essentially temperature-independent for short wavelengths (Timusk and Tanner, 1989; Kamaras et al., 1989). The peak in the reflectance data at 15 μm is due to the substrate, indicating that these films are not opaque at 10 K. The peak at 23.8 μm for the 200 nm film is caused by measurement error, due to the low signal-to-noise ratio. The reflectance at the peak is approximately 6 percent higher than that at the base, which is within the estimated maximum relative uncertainty of 10 percent for $22\ \mu m < \lambda < 25\ \mu m$. Similar peaks between 23 and 25 μm occur sometimes with other films and a gold mirror.

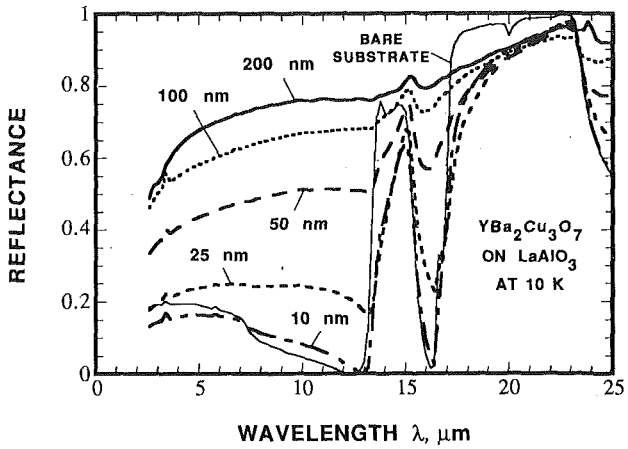

Fig. 6 Midinfrared reflectance of film-substrate composites and a bare substrate at 10 K

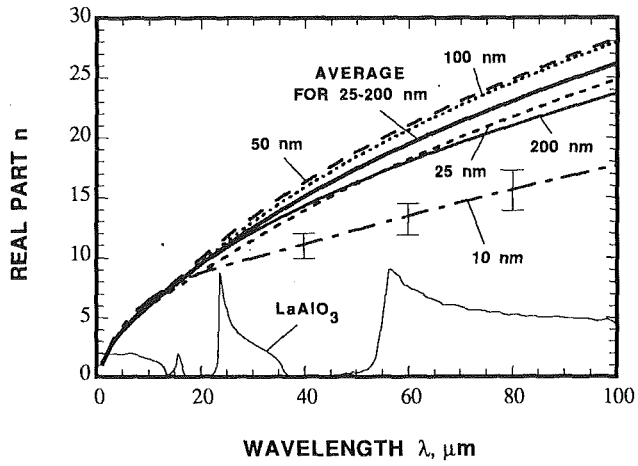

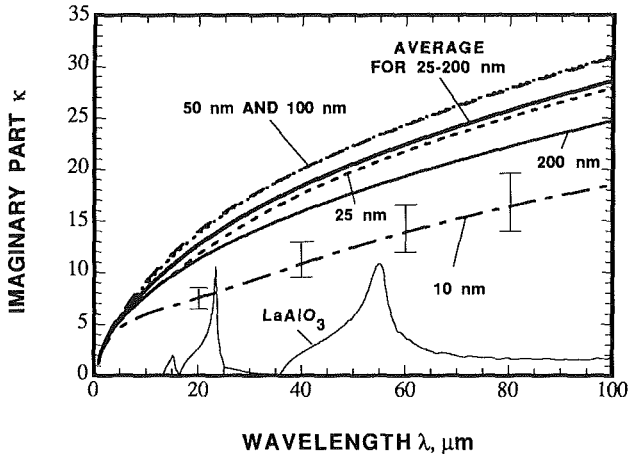

Fig. 7 Refractive index of $YBa_2Cu_3O_7$ films with different thicknesses and a $LaAlO_3$ substrate at room temperature

Refractive Index Analysis

In order to understand the radiative properties of the films, the substrate refractive index must be investigated. In the wavelength region from 1 to 10 μm where the substrate is transparent, both the reflectance and transmittance are measured. The substrate may be treated as a thin film in the transparent region, since interference fringes can be observed in the transmittance measurements by using high resolutions, 0.5 cm^{-1} for example. The resolution of 8 cm^{-1} used in the actual measurement is larger than the spacing of approximately 5 cm^{-1} between two interference extrema, yielding no interference fringes in the measured transmittance and reflectance. Choi et al. (1991) extracted the complex refractive index of a $LaAlO_3$ substrate from reflectance and transmittance measurements. The relations between the reflectance and transmittance and the complex refractive index were obtained using the ray-tracing method without considering the interference (Siegel and Howell, 1981). These results can also be derived by integrating the spectral reflectance and transmittance determined from thin-film optics (Bohren and Huffman, 1983). The Kramers-Kronig relations were applied for the opaque region (Wooten, 1972). The reflectance outside of the measured range was extrapolated by using the constant values at 1 μm for short wavelengths and 100 μm for long wavelengths. The measured reflectance of 0.46 at $\lambda = 100$ μm is close to that of 0.45 calculated from the dielectric constant at 1 MHz reported by Lee et al. (1990). The inaccuracy in the reflectivity for $\lambda < 1$ μm introduced by using the constant value at 1 μm produces an error in the calculated phase shift, which is approximately proportional to the frequency for 10 $\mu m \leq \lambda \leq$ 100 μm. A correction term is added based on the calculated n_s and κ_s at $\lambda = 9.5$ μm where both transmittance and reflectance are measured. A detailed discussion on the application of the Kramers-Kronig transformation in extrapolating the complex refractive index of $LaAlO_3$ is given by Choi et al. (1991). The substrate refractive index is shown in Fig. 7.

The reflectance of the substrate at 10 K is measured from 2.5 to 100 μm. For 2.5 $\mu m < \lambda < 10$ μm, since the measured reflectance does not vary with temperature, the room-temperature refractive index is used for the substrate at 10 K. For 10 $\mu m \leq \lambda \leq 100$ μm, the refractive index of the substrate at 10 K is obtained using the Kramers-Kronig relations. The reflectance and transmittance calculated from the extracted refractive index are identical to the measured data, which confirms the extrapolation techniques.

The frequency-dependent dielectric function of $YBa_2Cu_3O_7$ is assumed to be a linear superposition of several terms (Timusk and Tanner, 1989; Zimmermann et al., 1991).

$$\epsilon(\omega) = \epsilon_\infty + \frac{\omega_{pe}^2}{\omega_e^2 - \omega^2 - i\omega\gamma_e} + \frac{i\,\sigma(\omega)}{\omega\,\epsilon_0} \tag{1}$$

The first term on the right, ϵ_∞, is the high-frequency dielectric constant, which is approximately 4 (Zimmermann et al., 1991). The second term is a temperature-independent midinfrared band, due to the electronic absorption caused by interband electronic transitions, which has a center frequency of ω_e, a plasma frequency of ω_{pe}, and a width of γ_e. The last term is the contribution of conduction electrons, where ϵ_0 is the electrical permittivity of free space and $\sigma(\omega)$ is the frequency-dependent complex conductivity. The real part, $n_F(\omega)$, and the imaginary part, $\kappa_F(\omega)$, of the film refractive index are determined by

$$[n_F(\omega) + i\,\kappa_F(\omega)]^2 = \epsilon(\omega) \tag{2}$$

For an electric field perpendicular to the c-axis of the $YBa_2Cu_3O_7$ film, the contribution of phonons to the dielectric function is negligible due to their weak oscillator strengths (Renk et al., 1990). Therefore, the phonon contributions are not considered in Eq. (1). The midinfrared band is fixed using the data of Bauer (1990) for the electric field perpendicular to the c-axis: $\omega_e = 1800$ cm^{-1}, $\omega_{pe} = 24150$ cm^{-1}, and $\gamma_e = 7500$ cm^{-1}. Note that 1 cm^{-1} is equal to 1.88×10^{11} rad s^{-1}. The evidence for the existence of a midinfrared band has been reviewed by Timusk and Tanner (1989). In contrast, Bozovic (1990) and Bozovic et al. (1987) stated that this electronic transition is not a characteristic of the high-T_c superconducting material but rather of some structurally or

compositionally disordered regions in less homogeneous samples.

The normal-state frequency-dependent conductivity can be expressed as a function of frequency using the Drude model

$$\sigma(\omega)=\frac{\sigma_{dc}}{1-i\omega\tau} \tag{3}$$

where τ is the scattering time, whose reciprocal $1/\tau$ is the electron scattering rate, and σ_{dc} is the d-c conductivity, which is the inverse of the d-c resistivity ρ_{dc}. Kinetic theory relates the electron scattering rate to the d-c electrical conductivity by

$$\frac{1}{\tau}=\frac{n_e e^2}{m_e \sigma_{dc}} \tag{4}$$

where n_e is the electron number density, e the electron charge, and m_e the electron effective mass. Schlesinger et al. (1990) adopted a frequency-dependent electron scattering rate and effective mass in their analysis, i.e., both the scattering rate and the plasma frequency, $\omega_p = (n_e e^2/\epsilon_0 m_e)^{1/2}$, are dependent on frequency. In the present study, similar to the work of Kamaras et al. (1989), the d-c conductivity and electron scattering rate are the adjustable parameters for the fitting, and the electron number density is then calculated from Eq. (4).

For a given scattering rate and d-c conductivity, the film refractive index is calculated using Eqs. (1), (2) and (3). Based on thin-film optics, the reflectance and transmittance are obtained as functions of the refractive indices and thicknesses of the film and substrate, respectively (Choi et al., 1991). For 10 μm $< \lambda <$ 100 μm, where the substrate is opaque, the expression for the reflectance of the film–substrate composite is identical to that derived by Born and Wolf (1980) for an absorbing film adjacent to an absorbing semi-infinite medium. Thin-film optics for a two-layer system is applied for 1 μm $< \lambda <$ 10 μm. The substrate interference effect is neglected, because the interference inside the substrate is not observable experimentally with a resolution of 8 cm^{-1}. By comparing the calculated reflectance with the measured data, the best fitting parameters are obtained. The calculated transmittance is then compared with the measured transmittance to check the agreement.

An algorithm developed by Zimmermann et al. (1991) is employed to calculate the ratio of the frequency-dependent conductivity in the superconducting state to the normal-state d-c conductivity, σ_{dc}. It was adopted from the macroscopic expressions derived by Lee et al. (1988, 1989) using the quasi-classical formalism of energy-integrated Green functions. This theory applies for weak-coupling isotropic BCS superconductors with an arbitrary normal-state electron scattering rate. The energy gap parameter for a weak coupling BCS superconductor is $A = 2\Delta_0/kT_c = 3.53$, where Δ_0 is the superconductor energy gap at zero temperature and k is the Boltzmann constant. The energy gap, Δ, for $T < 0.3T_c$ is almost identical to that at zero temperature. Hence, the energy gap at 10 K is equal to that at 0 K for high-T_c materials.

The applicability condition for the theory of Zimmermann et al. (1991) is the *local* limit (Lee et al., 1988), i.e., the superconductor coherence length, ξ, which is a measure of the spatial extension of the superconducting electron pairs, is much smaller than both the wavelength of the incident radiation and the magnetic penetration depth. The superconducting coherence length at 0 K is $\xi_0 = \hbar v_F/(2\pi^2\Delta_0)$, where $\hbar$ is Planck's constant and v_F is the Fermi velocity. The Fermi velocity of $YBa_2Cu_3O_7$ is approximately 1.5×10^5 m s^{-1} (Goodson and Flik, 1991), yielding a superconductor coherence length of 2.3 nm at 0 K. The magnetic penetration depth for $\lambda > 1$ μm is close to the zero-frequency value, which is the London penetration depth. The London penetration depth is approximately 150 nm for $YBa_2Cu_3O_7$ at 0 K and increases with temperature (Harshman et al., 1989). Hence, the *local* limit is valid for $YBa_2Cu_3O_7$ at $\lambda > 1$ μm at temperatures not too close to T_c.

The input parameters are the ratio of the sample temperature to the critical temperature, T/T_c, and a normalized scattering rate, $Y = \hbar/(4\pi\tau\Delta)$. Note that at 0 K, $Y = (\pi/2)(\xi_0/\Lambda_0)$, where $\Lambda_0 = v_F\tau$ is the electron mean free path at 0 K. The electron mean free path is approximately 10 nm at 0 K (Goodson and Flik, 1991). The calculated Y from the superconductor coherence length and the electron mean free path at 0 K is about 0.36. For $Y \gg 1$, the electron mean free path is much shorter than the superconductor coherence length, and the superconductor is in the impure limit. In this limit, the theory of Zimmermann et al. (1991) gives the same results as the Mattis–Bardeen relations (Mattis and Bardeen, 1958). For a pure superconductor with $Y < 1$, which is the case for $YBa_2Cu_3O_7$, the deviation from the Mattis–Bardeen relations is large. Similar expressions considering a finite scattering rate were derived by Tinkham (1970) and Leplae (1983), and applied by Rao et al. (1990) for high-T_c materials.

The selection of σ_{dc} has a strong influence on the calculated reflectance. Since the d-c electrical resistivity is zero below T_c, the parameter σ_{dc} cannot be measured directly. It is the conductivity that the material would possess if it were in the normal state at temperatures below T_c. Phelan et al. (1991) extrapolated the resistivity to zero at 0 K using a linear temperature dependence of the d-c resistivity. Their calculated reflectivity for opaque samples showed a strong temperature dependence even at $T \ll T_c$. In the present study, similar to the approach of Goodson and Flik (1991), Matthiessen's rule is used to determine the d-c resistivity at temperatures below T_c (Ziman, 1960)

$$\rho_{dc}=\rho_d+\rho_L \tag{5}$$

where ρ_d is the electrical resistivity due to scattering on defects, which does not depend on temperature, and ρ_L is the electrical resistivity resulting from scattering on phonons, which is expressed by the Bloch formula (Ziman, 1960)

$$\rho_L = 4\,\rho_\theta (T/\theta)^5\, J_5(\theta/T) \tag{6}$$

where θ is the Debye temperature and ρ_θ is a constant. The Debye integral $J_5(x')$ is

$$J_5(x') = \int_0^{x'} \frac{x^5\, e^x}{(e^x-1)^2}\, dx \tag{7}$$

Note that ρ_L is very small for $T < \theta/10$. It is approximately a linear function of temperature for $T > \theta/3$ and approaches $\rho_\theta T/\theta$ for $T \gg \theta$. In the present study, the Debye temperature is 470 K, which was calculated by Goodson and Flik (1991) from specific-heat data. Although the Bloch formula given by Eq. (6) is not the most rigorous determination of the electrical resistivity, it is in excellent agreement with experimental data for metals. More detailed theories considering electron-phonon Umklapp scattering are far more difficult to apply and give the same trends for $T > \theta$ and $T \ll \theta$ as those given by the Bloch formula (Ziman, 1960). The d-c resistivities measured at temperatures above T_c are used to obtain ρ_θ and ρ_d with the fitting technique described by Goodson and Flik (1991) and Flik et al. (1992b). The d-c resistivity obtained at temperatures below $T_c/2$ is very close to ρ_d. The d-c resistivity at 10 K for each film is listed in Table 1, which is equal to the residual resistivity, ρ_{dc} (0 K). A linear extrapolation of the d-c resistivity would result in a value of ρ_{dc} (10 K) much smaller than the values listed in Table 1.

After the d-c conductivity is determined, the normalized scattering rate Y is the only fitting parameter for the superconducting state. Equations (1) and (2) are used to calculate the refractive index of the films in the superconducting state. By comparing the reflectance calculated from thin-film optics

with the measured data, the best fitting parameter Y is obtained for each film.

Results and Discussion

Room Temperature. The fitted d-c resistivities, the scattering rates, and the electron number densities are listed in Table 1. Note that a scattering rate of 1 cm^{-1} is equal to a scattering time of 5.3×10^{-12} s. The agreement of the reflectance calculated using the fitting parameters with the measured data is better than 3 percent for wavelengths from 60 to 100 μm for all films. Below 10 μm, the agreement in both the reflectance and transmittance is better than 10 percent. For the 50, 100, and 200 nm films, the calculated reflectance is less than the measured data with a maximum deviation of 10 percent in the wavelength regions between 20 and 25 μm and between 50 and 55 μm. This is an indication that some phonon absorption structures exist in these films. The oscillator frequencies are approximately 180 and 350 cm^{-1}, which agree with other studies (Feile, 1989; Choi et al., 1991). The 25 nm film shows broad phonon features around these frequencies and the phonon features almost disappear in the 10 nm film. The film thicknesses are determined from Rutherford backscattering. The uncertainty of the film thickness is estimated to be 5 percent, yielding a 2 percent deviation in the calculated reflectance. The sensitivity of the fitting technique is investigated by individually varying the fitting parameters. Once the best fitting parameters are obtained, the uncertainty is estimated by varying either of the fitting parameters to a value that causes approximately 3 percent deviation in the calculated reflectance. The resulting uncertainties are listed in Table 1. For the the 10 nm film, the optical properties of the film-substrate composite are very close to those of the substrate, yielding an uncertainty of as large as 30 percent in the electrical resistivity and electron scattering rate.

The critical temperature, d-c conductivity, and electron number density for the 10 nm film are the lowest, indicating the presence of more defects in the film microstructure. The d-c conductivities and the electron number densities for the 50 and 100 nm films are the largest. The scattering rates are very close for the 50, 100, and 200 nm films. The decrease in the scattering rate for the 25 and 10 nm films is due to the weak strengths of the phonon oscillators in these films. The reason for the weak phonon oscillator strengths might be due to the better orientation and/or less oxygen deficiency. The optically obtained d-c resistivity agrees with the measured data within the uncertainties of the fitting technique and transport measurements. The scattering rate of 300 to 500 cm^{-1} determined in this study at room temperature is in good agreement with that of 300 cm^{-1} obtained by Kamaras et al. (1990) for different $YBa_2Cu_3O_7$ films and that of 400 cm^{-1} obtained by Orenstein et al. (1990) for $YBa_2Cu_3O_7$ crystals.

Figure 7 shows the refractive index of $YBa_2Cu_3O_7$ films with different thicknesses. The averages for film thicknesses from 25 to 200 nm are also shown. The deviation of the refractive index from the average is less than 10 percent except for the 10 nm film. The deviation is not systematic and is attributed to variations in sample properties. The uncerainty in the fitted parameters yields a maximum error of 6 percent in the refractive indices for film thicknesses larger than or equal to 25 nm. Error bars shown in Fig. 7 indicate the large error in the calculated refractive index of the 10 nm film due to the fitting uncertainty. If the average of the refractive index for film thicknesses between 25 and 200 nm is used to calculate the reflectance, the agreement with the data is better than 10 percent. The average of the refractive index is recommended for design calculations of the thermal radiative properties of $YBa_2Cu_3O_7$ thin films with thicknesses not smaller than 25 nm.

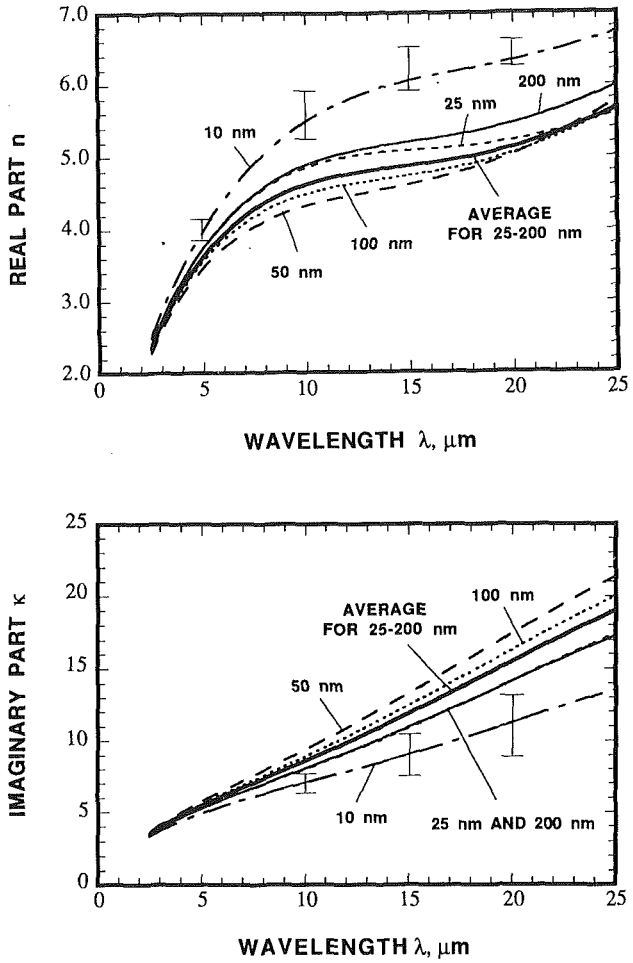

Fig. 8 Refractive index of $YBa_2Cu_3O_7$ films with different thicknesses at 10 K

Superconducting State. Figure 8 shows the fitted refractive indices for films of different thicknesses at 10 K. The average values of the refractive indices for film thicknesses from 25 to 200 nm are also shown. The deviation of the refractive index from the average is within 10 percent except for the 10 nm film. The fitted normalized scattering rate Y for each sample is listed in Table 1. Note that $Y = 1$ corresponds to a scattering rate of 217 cm^{-1} or a scattering time of 2.4×10^{-14} s. At wavelengths greater than 10 μm, the agreement between the reflectance calculated from the fitted scattering rate and the measured data is better than 5 percent for 10 $\mu m < \lambda < 23$ μm and 10 percent for 23 $\mu m < \lambda < 25$ μm. At wavelengths less than 10 μm, the deviation increases with decreasing wavelength and reaches a maximum of 12 percent for the 200 nm film at 2.5 μm. The sensitivity of the reflectance to Y is indicated by the uncertainty in Table 1. The uncertainty of the fitted parameter Y is estimated by varying it from the best fitted value to one that causes approximately 3 percent deviation in the calculated reflectance. The uncertainty of the fitted value of Y yields a maximum error of 6 percent in the refractive indices for film thicknesses larger than or equal to 25 nm. The error in the calculated refractive index of the 10 nm film is indicated by the error bars in Fig. 8. Because at high frequencies the electrical conductivity term in Eq. (1) is very small compared with the first and second terms, the dielectric function and the refractive index at $\lambda < 5$ μm is not very sensitive to the fitting parameter. The fitting is based on the reflectance at wavelengths greater than 5 μm; therefore, the large uncer-

tainty in the measurements at $\lambda < 5$ μm will not affect the fitting quality.

For the impure limit, $Y \to \infty$, the theory of Zimmermann et al. (1991) gives exactly the same results as the Mattis–Bardeen relations . For a 100 nm film at $T = 10$ K and $\lambda = 10$ μm, the reflectance predicted by the Mattis–Bardeen relations is 0.92, which is much higher than the measured value of 0.67 and that of 0.65 predicted using the fitted value of $Y = 0.44$ in the theory of Zimmermann et al. (1991). In general, both the real and imaginary parts of the refractive index predicted by the Mattis–Bardeen relations are much higher than those predicted by the theory of Zimmermann et al. (1991) with the fitted parameters. Hence, the Mattis–Bardeen relations yield an underprediction of the radiation penetration depth and an overprediction of the total reflectance.

At low temperatures, the electron scattering is dominated by defects. The electron number density does not change with temperature. The scattering rate at 10 K can be calculated from Eq.(4) using the extrapolated d-c conductivity at 10 K and the electron number density obtained at room temperature. For films of thickness from 25 to 200 nm the calculated scattering rates agree with the fitted ones within 15 percent. The calculated scattering rate for the 10 nm film is $Y = 0.25$, which is less than one half of the fitted value of $Y = 0.60$. The disagreement between the fitted and the calculated electron scattering rates at 10 K is of the same order as the uncertainty in the fitting process for the 10 nm film. Since the electron mean free path at 10 K is comparable to the thickness of the 10 nm film, boundary scattering can increase the electron scattering rate. The calculation of the scattering rate from the d-c resistivity and the electron number density does not take into account the boundary scattering. Besides boundary scattering, the deviation in the refractive index between the 10 nm film and the other films may be caused by a different microstructure, since the crystalline structure of the 10 nm film is not as good as that of the other films.

The average value of $Y = 0.42$, corresponding to a scattering rate of $1/\tau = 91$ cm^{-1}, for film thicknesses between 25 to 200 nm is an optically observed scattering rate. Its agreement with the value of $Y = (\pi/2)\,(\xi_0/\Lambda_0) = 0.36$, which was determined from independent electrical resistivity measurements and analysis for a different film, is a powerful confirmation of the applicability of the model dielectric function, Eq. (1). The $YBa_2Cu_3O_7$ is a pure superconductor but is not in the extreme pure limit.

Conclusions

1 A systematic size effect on the refractive index is not observed for film thicknesses from 25 to 200 nm. For a 10 nm film at low temperatures, since the electron mean free path is comparable to the film thickness, boundary scattering can play a role in the electron scattering processes. The difference between the refractive index of the 10 nm film and those of the other films may also be caused by the different microstructure of the 10 nm film.

2 The Drude model plus a broad midinfrared band can be used to fit the room-temperature reflectance for films as thin as 10 nm. The average values of the fitted refractive index for film thicknesses between 25 and 200 nm are recommended for design calculations of the thermal radiative properties of $YBa_2Cu_3O_7$ thin films.

3 In the superconducting state, since $YBa_2Cu_3O_7$ is a pure superconductor, the Mattis–Bardeen theory cannot be applied. A dielectric function with a variable scattering rate along with the midinfrared band is a successful approach. The optically obtained electron scattering rate at 10 K of about 91 cm^{-1} agrees well with that obtained from the superconductor coherence length and electron mean free path reported by other groups. The average values of the refractive index for film thicknesses between 25 and 200 nm are recommended for design calculations.

4 The increase of the measured absorptance of the film-substrate composite with decreasing film thickness can explain the increase of the responsivity of high-T_c superconducting infrared detectors achieved by using thinner films.

Acknowledgments

The work at M.I.T. was supported by the C. S. Draper Laboratory, Cambridge, MA, contract No. DL-H-418480, and by the National Science Foundation, contract No. CTS-9007765. The authors wish to thank Prof. J. L. Smith and R. Gertsen for their help in building the spectroscopy laboratory, K. E. Goodson and C. G. Malone for their helpful discussions, and Andrew Yablon, Andres Pieczanski, and Prajoy Kadkade for their assistance in the experiments. The official reviewers' comments are much appreciated.

References

Bauer, M., 1990, "Untersuchungen an Hochtemperatursupraleitern vom Typ $YBa_2Cu_3O_{7-\delta}$ mit Hilfe der Infrarot-Spektroskopie (Investigations of High-Temperature Superconductors of the Type $YBa_2Cu_3O_{7-\delta}$ Using Infrared Spectroscopy)," Ph.D. dissertation, Tübingen University, Germany, p. 77.

Bohren, C. F., and Huffman, D. R., 1983, *Absorption and Scattering of Light by Small Particles*, Wiley, New York, Chap. 2.

Born, M., and Wolf, E., 1980, *Principles of Optics*, Pergamon Press, Oxford, United Kingdom, pp. 627–633.

Bozovic, I., Kirillov, D. Kapitulni, A., Char, K., Hahn, M. R. Beasley, M. R., Geballe, T. H., Kim, Y. H., and Heeger, A. J., 1987, "Optical Measurements on Oriented Thin $YBa_2Cu_3O_{7-\delta}$ Films: Lack of Evidence of Excitonic Superconductivity," *Phys. Rev. Lett.*, Vol. 59, pp. 2219–2221.

Bozovic, I., 1990, "Plasmons in Cuprate Superconductors," *Phys. Rev. B*, Vol. 42, pp. 1969–1984.

Carlson, D. J., Siegal, M. P., Phillips, J. M., Tiefel, T. H., and Marshall, J. H., 1990, "Stoichiometric Effects in Epitaxial $Ba_{2-x}Y_{1-y}Cu_{3-z}O_{7-\delta}$ Thin Films on $LaAlO_3$ (100)," *J. Mater. Res.*, Vol. 5, pp. 2797–2801.

Carr, G. L., Quijada, M., Tanner, D. B., Hirschmugl, C. J., Williams, G. P., Etemad, S., Dutta, B., DeRosa, F., Inam, A., Venkatesan, T., and Xi, X., 1990, "Fast Bolometric Response by High T_c Detectors Measured With Subnanosecond Synchrotron Radiation," *Appl. Phys. Lett.*, Vol. 57, pp. 2725–2727.

Choi, B. I., Zhang, Z. M. Flik, M. I., and Siegrist, T., 1991, "Radiative Properties of Y-Ba-Cu-O Films With Variable Oxygen Content," in: *Thin-Film Heat Transfer—Properties and Processing*, M. K. Alam, et al., eds., ASME HTD-Vol. 184, pp. 73–80; to appear in ASME JOURNAL OF HEAT TRANSFER.

Collins, R. T., Schlesinger, Z., Holtzberg, F., and Feild, C., 1989, "Infrared Evidence for Gap Anisotropy in $YBa_2Cu_3O_7$," *Phys. Rev. Lett.*, Vol. 63, pp. 422–425.

Cooper, S. L., Thomas, G. A., Orenstein, J., Rapkine, D. H., Capizzi, M., Timusk, T., Millis, A. J., Schneemeyer, L. F., and Waszczak, J. V., 1989, "Properties of Optical Features in $YBa_2Cu_3O_{7-\delta}$," *Phys. Rev. B*, Vol, 40, pp. 11358–11361.

Feenstra, R., Lindemer, T. B., Budai, J. D., and Galloway, M. D., 1991, "Effect of Oxygen Pressure on the Synthesis of $YBa_2Cu_3O_{7-x}$ Thin Films by Post Deposition Annealing," *J. Appl. Phys.*, Vol. 69, pp. 6569–6585.

Feile, R., 1989, "Lattice Vibrations in High-T_c Superconductors: Optical Spectroscopy and Lattice Dynamics," *Physica C*, Vol. 159, pp. 1–32.

Flik, M. I., Choi, B. I., Anderson, A. C., and Westerheim, A. C., 1992a, "Thermal Analysis and Control for Sputtering Deposition of High-T_c Superconducting Films," ASME JOURNAL OF HEAT TRANSFER, Vol. 114, pp. 255–263.

Flik, M. I., Zhang, Z. M., Goodson, K. E., Siegal, M. P., and Phillips, J. M., 1992b, "Electron Scattering Rate in Epitaxial $YBa_2Cu_3O_7$ Superconducting Films," to appear in *Phys. Rev. B*, Sept. 1.

Flik, M. I., and Zhang, Z. M., 1992, "Influence of Nonequivalent Detector Responsivity on FT-IR Photometric Accuracy," *J. Quant. Spectrosc. Radiat. Transfer*, Vol. 47, pp. 293–303.

Gao, J., Hauser, B., and Rogalla, H., 1990, "High Critical Current Density Ultrathin $YBa_2Cu_3O_x$ Films Made by a Modified RF-Magnetron Sputtering Technique," *J. Appl. Phys.*, Vol. 67, pp. 2512–2515.

Gao, F., Carr, G. L. Porter, C. D., Tanner, D. B., Etemad, S., Venkatesan, T., Inam, A., Dutta, B., Wu, X. D., Williams, G. P., and Hirschmugl, C. J., 1991, "Far-Infrared Transmittance and Reflectance Studies of Oriented $YBa_2Cu_3O_{7-\delta}$ Thin Films," *Phys. Rev. B*, Vol. 43, pp. 10383–10389.

Goodson, K. E., and Flik, M. I., 1991, "Electron and Phonon Thermal Conduction in Epitaxial High-T_c Superconducting Films," in *Cryogenic Heat Transfer*—1991, A. Adorjan and A. Bejan, eds., ASME HTD-Vol. 167, pp. 27–35; to appear in ASME JOURNAL OF HEAT TRANSFER.

Harshman, D. R., Schneemeyer, L. F., Waszczak, J. V., Aeppli, G., Cava,

R. J., Batlogg, B., Rupp., L. W., Ansaldo, E. J., and William, D. L., 1989, "Magnetic Penetration Depth in Single-Crystal $YBa_2Cu_3O_{7-\delta}$," *Phys. Rev. B*, Vol. 39, pp. 851–854.

Kamaras, K., Herr, S. L., Porter, C. D., Tanner, D. B., Etemad, S., and Chan, S. W., 1989, "Optical Excitations in Thin Film $YBa_2Cu_3O_7$," in: *Progress in High Temperature Superconductivity*, Vol. 17, L. H. Bennet, Y. Flom, and G. C. Vezzoli, eds., World Scientific Publishing Co., Singapore.

Kamaras, K., Herr, S. L., Porter, C. D., Tache, N., Tanner, D.B., Etemad, S., Venkatesan, T., Chase, E., Inam, A., Wu, X. D., Hegde, M. S., and Dutta, B., 1990, "In a Clean High-T_c Superconductor You Do Not See the Gap," *Phys. Rev. Lett.*, Vol. 64, pp. 84–87.

Leplae, L., 1983, "Derivation of an Expression for the Conductivity of Superconductors in Terms of the Normal-State Conductivity," *Phys. Rev. B*, Vol. 27, pp. 1911–1912.

Lee, A. E., Platt, C. E., Burch, J. F., and Simon, R. W., 1990, "Epitaxially Grown Sputtered $LaAlO_3$ Films," *Appl. Phys. Lett.*, Vol. 57, pp. 2019–2021.

Lee, W., Rainer, D., and Zimmermann, W., 1988, "Quasiclassical Linear Response Theory," *Internal Report*, Theoretical Physics III, Physikalisches Institut, University of Bayreuth, D-8580 Bayreuth, Germany.

Lee, W., Rainer, D., and Zimmermann, W., 1989, "Holstein Effect in the Far-Infrared Conductivity of High-T_c Superconductors," *Physica C*, Vol. 159, pp. 535–544.

Mattis, D. C., and Bardeen, J., 1958, "Theory of the Anomalous Skin Effect in Normal and Superconducting Metals," *Phys. Rev.*, Vol. 111, pp. 412–417.

Mikic, B. B., 1974, "Thermal Contact Conductance; Theoretical Considerations," *Int. J. Heat Mass Transfer*, Vol. 17, pp. 205–214.

Mogro-Campero, A., and Tumer, L. G., 1991, "Lower Temperature Postannealing of Thin Films of $YBa_2Cu_3O_7$ at Lower Oxygen Partial Pressure," *Appl. Phys. Lett.*, Vol. 58, pp. 417–418.

Olsen, J. L., 1962, *Electron Transport in Metals*, Interscience Publishers, New York, Chap. 4.

Orenstein, J., Thomas, G. A., Millis, A. J., Cooper, S. L., Rapkine, D. H., Timusk, T., Schneemeyer, L. F., and Waszczak, J. V., 1990, "Frequency- and Temperature-Dependent Conductivity in $YBa_2Cu_3O_{6+x}$ Crystals," *Phys. Rev. B*, Vol. 42, pp. 6342–6362.

Phelan, P. E., Flik, M. I., and Tien, C. L., 1991, "Radiative Properties of Superconducting Y–Ba–Cu–O Thin Films," ASME JOURNAL OF HEAT TRANSFER, Vol. 113, pp. 487–493.

Phelan, P. E., Chen, G., and Tien, C. L., 1992, "Thickness-Dependent Radiative Properties of Y–Ba–Cu–O Thin Films," ASME JOURNAL OF HEAT TRANSFER, Vol. 114, pp. 227–233.

Rao, A. M., Eklund, P. C., Lehman, G. W., Face, D. W., Doll, G. L., Dresselhaus, G., and Dresselhaus, M. S., 1990, "Far-Infrared Optical Properties of Superconducting $Bi_2Sr_2CaCu_2O_x$ Films," *Phys. Rev. B*, Vol. 42, pp. 193–201.

Renk, K. R., Eschrig, H., Hofmann, U., Keller, J. Schützmann, J., and Ose, W., 1990, "Dynamical Conductivity of High-T_c Superconductors," *Physica C*, Vol. 165, pp. 1–7.

Schlesinger, Z., Collins, R. T., Holtzberg, F., Feild, C., Koren, G., and Gupta, A., 1990, "Infrared Studies of the Superconducting Energy Gap and Normal-State Dynamics of the High-T_c Superconducting $YBa_2Cu_3O_7$," *Phys. Rev. B*, Vol. 41, pp. 11237–11259.

Schützmann, J., Ose, W., Keller, J., Renk, K. F., Roas, B., Schultz, L., and Saemann-Ischenko, G., 1989, "Far-Infrared Reflectivity and Dynamical Conductivity of an Epitaxial $YBa_2Cu_3O_{7-\delta}$ Thin Film," *Europhys. Lett.*, Vol. 8, pp. 679–684.

Sengupta, L. C., Huang, D., Roughani, B., Aubel, J. L., and Sundaram, S., 1991, "Spectroscopic Ellipsometry Studies of $YBa_2Cu_3O_{7-\delta}$ Deposited on $SrTiO_3$," *J. Appl. Phys.*, Vol. 69, pp. 8272–8276.

Siegal, M. P., Phillips, J. M., van Dover, R. B., Tiefel, T. H., and Marshall, J. H., 1990a, "Optimization of Annealing Parameters for Growth of Epitaxial $Ba_2YCu_3O_{7-x}$ Films on $LaAlO_3$ (100)," *J. Appl. Phys.*, Vol. 68, pp. 6353–6360.

Siegal, M. P., Phillips, J. M., Hsieh, Y.-F., and Marshall, K. H., 1990b, "Growth of Epitaxial $Ba_2YCu_3O_{7-x}$ Films on $LaAlO_3$ (100)," *Physica C*, Vol. 172, pp. 282–286.

Siegel, R., and Howell, J. R., 1981, *Thermal Radiation Heat Transfer*, 2nd ed., McGraw-Hill, New York, Chap. 19.

Terashima, T., Shimura, K., Bando, Y., Matsuda, Y., Fujiyama, A., and Komiyama, S., 1991, "Superconductivity of One-Unit-Cell Thick $YBa_2Cu_3O_7$ Thin Film," *Phys. Rev. Lett.*, Vol. 67, pp. 1362–1365.

Timusk, T., Herr, S. L., Kamaras, K., Porter, C. D., Tanner, D. B., Bonn, D. A., Garrett, J. D., Stager, C. V., Greedan, J. E., and Reedyk, M., 1988, "Infrared Study of *ab*-Plane Oriented Oxide Superconductors," *Phys. Rev. B*, Vol. 38, pp. 6683–6688.

Timusk, T., and Tanner, D. B., 1989, "Infrared Properties of High-T_c Superconductors," in: *Physical Properties of High-Temperature Superconductors I*, D. M. Ginsberg, ed., World Scientific Publishing Co., Singapore, pp. 339–407.

Tinkham, M., 1970, "Far Infrared Absorption in Superconductors," in: *Far-Infrared Properties of Solids*, S. S. Mitra and S. Nudelman, eds., Plenum Press, New York, pp. 223–246.

Toscano, W. M., and Cravalho, E. G., 1976, "Thermal Radiation Properties of the Noble Metals at Cryogenic Temperatures," ASME JOURNAL OF HEAT TRANSFER, Vol. 98, pp. 438–445.

Van der Marel, D., Habermeier, H.-U., Heitmann, D., König, W., and Wittlin, A., 1991, "Infrared Study of the Superconducting Phase Transition in $YBa_2Cu_3O_{7-x}$," *Physica C*, Vol. 176, pp. 1–18.

Wooten, F., 1972, *Optical Properties of Solids*, Academic Press, New York, Chap. 6.

Xi, X. X., Geerk, J., Linker G., Li, Q., and Meyer, O., 1990, "Preparation and Superconducting Properties of Ultrathin $YBa_2Cu_3O_{7-x}$ Films," *Appl. Phys. Lett.*, Vol. 54, pp. 2367–2369.

Zhang, K., Bunker, G. B., Zhang, G., Zhao, Z. X., Chen, L. Q., and Huang, Y. Z., 1988, "Extended X-Ray Absorption Fine-Structure Experiment on the High-T_c Superconductor $YBa_2Cu_3O_{7-\delta}$," *Phys. Rev. B*, Vol. 37, pp. 3375–3380.

Ziman, J. M., 1960, *Electrons and Phonons*, Oxford University Press, Oxford, United Kingdom, Chap. 9.

Zimmermann, W., Brandt, E. H., Bauer, M., Seider, E., and Genzel, L., 1991, "Optical Conductivity of BCS Superconductors With Arbitrary Purity," *Physica C*, Vol. 183, pp. 99–104.

Evaluation of Total Emittance of an Isothermal Nongray Absorbing, Scattering Gas-Particle Mixture Based on the Concept of Absorption Mean Beam Length

W. W. Yuen

A. Ma

Department of Mechanical and Environmental Engineering, University of California, Santa Barbara, CA 93106

A general methodology to evaluate the total emittance of an isothermal, nongray, isotropically scattering particle-gas mixture is illustrated. Based on the concept of absorption mean beam length (AMBL), the methodology is demonstrated to be computationally efficient and accurate. As an illustration, the total emittance of a slab containing carbon particles and CO_2 is evaluated. The nongray extinction coefficient and scattering albedo of carbon particles are calculated based on Mie theory and the available index of refraction data. The narrow-band fixed-line-spacing model (Edwards et al., 1967) is used to characterize the nongray spectral absorption coefficient of CO_2. Numerical data show that the combined nongray and scattering effects are quite significant. For particles with moderate and large radius (say, ≥ 1 μm), ignoring the effect of scattering can lead to error in the prediction of total emittance by more than 20 percent. The no-scattering results also yield incorrect qualitative behavior of the total emittance in terms of its dependence on the mixture temperature and particle concentration. The accuracy of many of the existing predictions of total emittance of gas-particle mixtures that ignore the scattering effect is thus highly uncertain.

1 Introduction

In the assessment of performance of high-temperature engineering equipment such as industrial furnaces, the ability to predict accurately the radiative emission from a mixture of particles and gas is essential. Until now, this essential ability has been limited largely to absorbing particles and gas mixtures. With available spectroscopic absorption data for various gases and particles, together with the concept of mean beam length (MBL) originally introduced by Hottel (1927), accurate predictions of total emittance of multidimensional nongray absorbing gas-particle mixtures are now accepted as routine. Two important factors contribute to the success of these efforts. First, reasonably reliable spectral absorption data are now available for most gases. Second, MBL has been shown to be primarily a function only of geometry (i.e., independent of wavelength) and can be, to a good approximation, considered as constant in a nongray calculation. The necessary spectral integration is thus reduced to a one-dimensional form and can be readily evaluated.

The success in estimating the radiative emission from a nongray absorbing, scattering particle-gas mixture, on the other hand, has been quite limited. The primary difficulty is that even when the medium can be considered as gray, accurate numerical solution to the radiative transfer equation is difficult to obtain. Many approximation methods (see the review article by Viskanta and Menguc, 1987) have been proposed. The accuracy of such methods, however, is generally unknown. For nongray analysis, two general approaches are utilized. In one approach (Menguc and Viskanta, 1986), the computational method developed for a gray analysis is extended to the nongray case by the Hottel's MBL concept. This extension, however, is done on an ad hoc basis. Without a rigorous theoretical justification, the accuracy of this approach is highly uncertain. The second approach is to develop approximate solution techniques directly for the nongray analysis (Skocypec and Buckius, 1984). While this approach has been successful in generating numerical data for a few selected problems (say, parallel slab geometry), the applicability of the method to analysis of general enclosures is uncertain. The accuracy of all existing solution approaches is also difficult to assess because of the lack of reliable "benchmark" numerical data for direct comparison.

The objective of this work is to show that utilizing the concept of absorption mean beam length (AMBL) (Yuen, 1990, 1991), a general methodology can be developed for the evaluation of radiative emission from a nongray absorbing-scattering particle-gas mixture. The methodology is computationally efficient, accurate, and applicable to enclosures with arbitrary geometry. As an illustration, the total emittance of a carbon particles/CO_2 containing slab is calculated. In addition to generating a set of numerical data, which serves as a benchmark set of "exact" results for this class of problem, the importance of the scattering effect on the total emittance is also illustrated quantitatively.

2 Analysis

A schematic of the general methodology for the evaluation of total emittance of a nongray absorbing-scattering particle-gas mixture is shown in Fig. 1. Similar to the MBL approach, which was successful for the evaluation of total emittance of a nonscattering medium, the fundamental principle of the methodology is to separate the geometric effect and the spectral effect in the numerical integration. Except for the increased complexity in the evaluation of AMBL, the present approach

Contributed by the Heat Transfer Division for publication in the JOURNAL OF HEAT TRANSFER. Manuscript received by the Heat Transfer Division April 1991; revision received February 1992. Keywords: High-Temperature Phenomena, Modeling and Scaling, Radiation. Associate Technical Editor: R. O. Buckius.

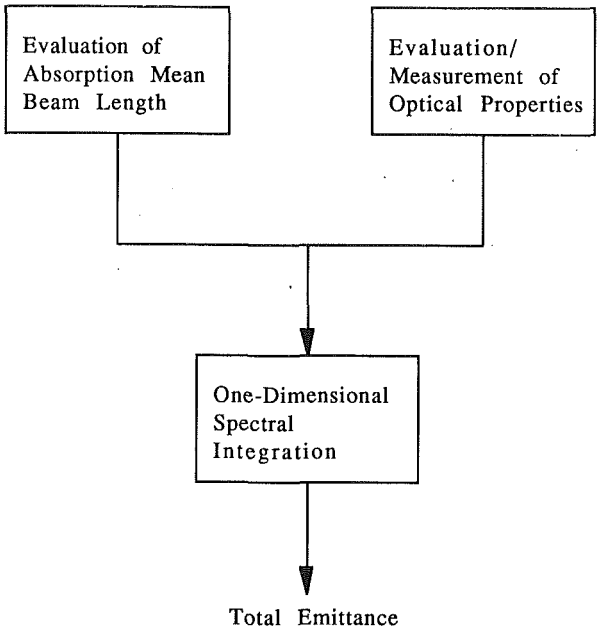

Fig. 1 Schematics of the general methodology for the evaluation of total emittance of an absorbing/scattering particle-gas mixture

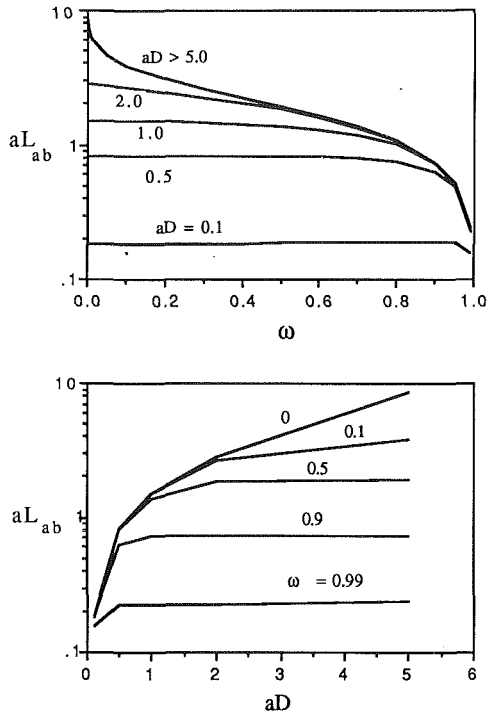

Fig. 2 Absorption mean beam length for a parallel slab with different absorption optical thickness, *aD*, and scattering albedo, ω

has the same degree of mathematical complexity as the conventional MBL approach.

2.1 Evaluation of AMBL. As shown in earlier work (Yuen, 1990, 1991), AMBL is the radius of an equivalent purely absorbing and emitting hemisphere such that the heat flux evaluated at the center of its base is identical to the actual heat flux. For an isothermal medium with a known geometry, temperature T, and optical properties (i.e., absorption coefficient a_λ, scattering albedo ω_λ and scattering phase function); the spectral heat transfer, q_λ, can be calculated by standard numerical techniques developed for a gray medium, e.g., the Monte Carlo Method (Howell and Perlmutter, 1964), the Zonal/Network Method (Hottel and Sarofim, 1967; Yuen, 1990) for isotropically scattering media and Generalized Zonal Method (Yuen and Takara, 1990) for anisotropically scattering media. The mathematical definition of AMBL, $L_{ab,\lambda}$, is given by

$$q_\lambda = e_{\lambda,b}(T)(1 - e^{-a_\lambda L_{ab,\lambda}}) \tag{1}$$

For an isothermal slab and with the assumption that the scattering is isotropic, AMBL calculated for the radiative heat transfer to one of its surfaces (Yuen, 1991) is presented in Fig. 2. Note that the mathematical behavior of AMBL is quite different from that of Hottel's MBL. In contrast to MBL, for example, AMBL varies strongly with absorption coefficient and scattering albedo. While MBL increases as the characteristic dimension of the physical system increases, AMBL approaches an asymptotic finite value in the optically thick limit for a medium with nonzero scattering albedo. Physically, MBL correlates approximately the optical "size" of the medium. AMBL, on the other hand, correlates only the optical "size" that contributes to the heat transfer. For a medium with a finite scattering albedo, increase in the physical dimension of the system will have less and less effect on AMBL since the additional medium has less and less influence on the overall heat transfer due to the effect of scattering. This explains the asymptotic behavior of AMBL in the optically thick limit. In the limit of a large scattering albedo. AMBL can be quite small even for a physically "large" system because the optical "size" that contributes to the heat transfer is small.

Fundamentally, the important function of AMBL is to account for the effect of enclosure geometry on radiation heat transfer without a simultaneous consideration of the detailed spectral properties of a specific mixture. The numerical data in Fig. 2, for example, account for the effect of the parallel slab geometry on radiation heat transfer over the entire range of radiation parameter. The same data can be used to analyze

Nomenclature

a_λ = absorption coefficient
B = gas absorption correlation parameters, Eq. (2)
C = gas absorption correlation parameters, Eqs. (2) and (3)
C_1 = gas absorption correlation parameters, Eqs. (3) and (4)
C_2 = gas absorption correlation parameters, Eq. (4)
C_3 = gas absorption correlation parameters, Eqs. (3) and (4)
d = gas absorption correlation parameters, Eqs. (2) and (5)
d_0 = gas absorption correlation parameters, Eq. (5)
$e_{\lambda,b}$ = blackbody emissive power
$L_{ab,\lambda}$ = absorption mean beam length
n = gas absorption correlation parameters, Eq. (6)
N = particle number density
P_A = partial pressure of the absorbing gas
P_B = partial pressure of the N_2 broadening gas
P_e = effective pressure parameter, Eq. (6)
P_0 = reference pressure = 1 atm
q_λ = heat flux
Q_{abs} = absorption cross section
Q_{sca} = scattering cross section
r = particle radius
T = temperature
T_0 = reference temperature = 100 K
ϵ_λ = emittance
κ = extinction coefficient
λ = wavelength
ρ = gas density, Eq. (2)
τ = transmissivity
ω = scattering albedo

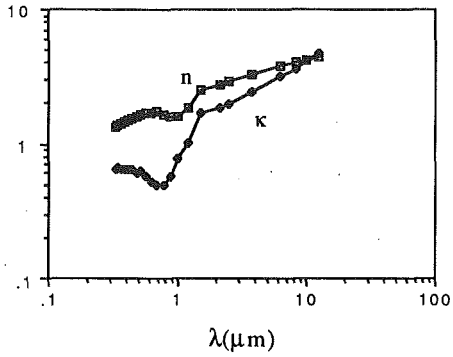

Fig. 3 Measured data on complex index of refraction ($n - i\kappa$) for carbon

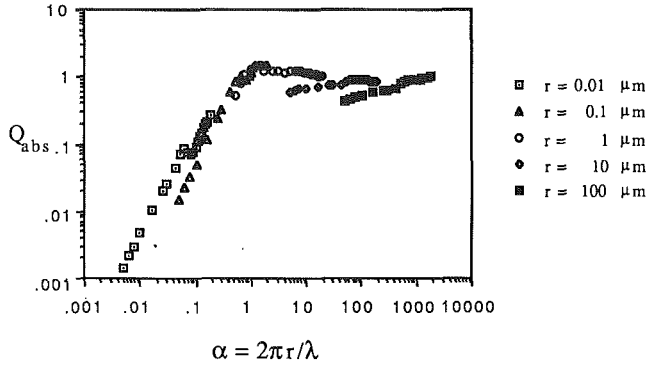

Fig. 4(*a*) Absorption efficiency for carbon particles of different radius

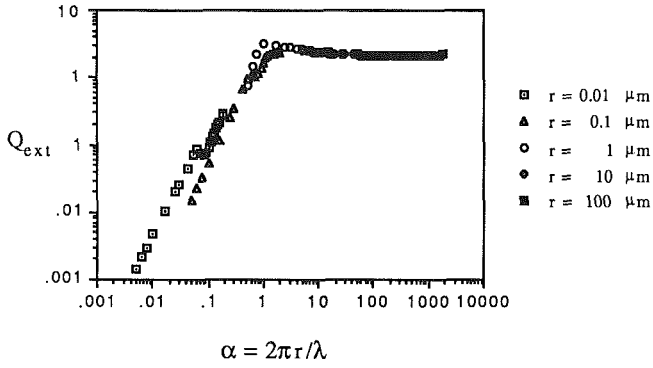

Fig. 4(*b*) Extinction efficiency for carbon particles of different radius

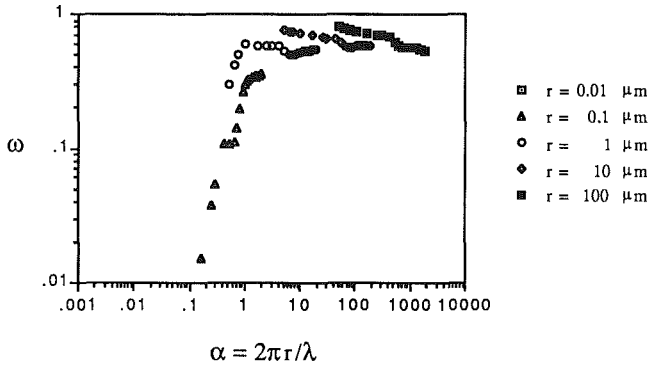

Fig. 4(*c*) Scattering albedo for carbon particles of different radius

any isothermal mixture with the same geometry. Since AMBL is readily computable with established computational methods (developed for gray analysis) and the spectral integration is one dimensional, the overall computation is straightforward and requires little effort.

2.2 Evaluation of Spectral Optical Properties. This process can be readily accomplished utilizing well-established numerical procedures and/or experimental data. For many common absorbing gaseous species, for example, the narrow-band fixed-line-spacing model (Edwards et al., 1967) is known to be an effective engineering approximation for the nongray spectral absorption behavior. The gaseous absorption coefficient (suppressing the subscript λ for simplicity) is given by

$$a = \frac{\rho C^2 \sinh(\pi B^2 P_e/2)}{\cosh(\pi B^2 P_e/2) - \cos(2\pi\nu^*/d)} \tag{2}$$

where ν^* is the wavenumber measured from the center of the band, $C^2(\nu, T)$, $B^2(\nu, T)$, d and P_e are specified in terms of isothermal gas correlation parameters as

$$C^2 = (C_1/C_3)e^{-\nu^*/C_3} \tag{3}$$

$$B^2 = C_2^2/(4C_1C_3) \tag{4}$$

$$d = d_0 C_3(T_0), \quad T_0 = 100 \text{ K} \tag{5}$$

$$P_e = [(P_B + bP_A)/P_0]^n, \quad P_0 = 1 \text{ atm} \tag{6}$$

with P_A being the partial pressure of the absorbing gas and P_B the partial pressure of the N_2 broadening gas. The gas correlation parameters, C_1, C_2, C_3, b, and n are defined for various common gaseous species (e.g., CO_2, H_2O, CO, and CH_4) in standard reference (Edwards et al., 1967).

In the present work, the absorbing gas is assumed to be a CO_2/N_2 mixture at atmospheric pressure. Over the expected mixture temperature range (500 to 3000 K), numerical experiments show that the present calculation can predict the pure CO_2 emittance data from Hottel's chart (Hottel, 1967) to within 10 percent by setting $d_0 = 30$. This assumption is therefore used in the generation of all numerical data.

If carbon particles in the mixture are assumed to be spherical, the evaluation of optical properties is also straightforward utilizing Mie theory (Van der Hulst, 1957). Specifically, for the set of index of refraction ($n - i\kappa$) data for graphite carbon (Phillips, 1977) as shown in Fig. 3, the absorption efficiency Q_{abs}, the extinction efficiency Q_{ext}, and scattering albedo $\omega = 1 - Q_{abs}/Q_{ext}$ can be readily calculated for different particle sizes utilizing computer programs provided in standard references (Bohren and Huffman, 1983). The absorption coefficient, a, and extinction coefficient, κ, can be generated from these efficiency factors by

$$a = N\pi r^2 Q_{abs} \qquad \kappa = N\pi r^2 Q_{ext} \tag{7}$$

and N being the particle's number density and r the particle radius. Numerical results are presented in Figs. 4(*a*), 4(*b*), and 4(*c*). It can be readily observed that the effect of scattering is quite significant when the particle radius is greater than 1 μm.

It is important to note that all results presented in this section are based on established information that is available from standard references. While the mixture characteristics are somewhat idealistic (pure CO_2 and spherical carbon particles) and differ from those of an actual combustion product mixture, the assumed mixture is sufficient to illustrate the effectiveness of the proposed methodology and the qualitative effect of scattering on the mixture's emittance. The adaptation of the present approach to a combustion medium with "real" properties is straightforward.

2.3 Integration to Obtain Total Emittance. Based on results generated from sections 2.1 and 2.2, the total emittance of a homogeneous gas-particle mixture can be written as

$$\epsilon = \frac{1}{\sigma T^4}\int_0^\infty e_{\lambda b}(T)(1 - e^{-a_{t,\lambda}L_{ab,\lambda}(a_{t,\lambda},\omega_{t,\lambda})})d\lambda \tag{8}$$

Table 1 Effect of temperature and number density on particle emittance, ϵ_p (values in parenthesis are generated ignoring the effect of scattering)

	T = 500 K	1000 K	1500 K	2000 K	2500 K	3000 K
particle radius = 0.1 μm						
ND = 10^{12}	0.00201 (0.00201)	0.00550 (0.00548)	0.0109 (0.0109)	0.0164 (0.0163)	0.0218 (0.0216)	0.0263 (0.0260)
10^{13}	0.0201 (0.0201)	0.0539 (0.0537)	0.102 (0.101)	0.146 (0.145)	0.182 (0.181)	0.213 (0.212)
10^{14}	0.177 (0.176)	0.334 (0.335)	0.504 (0.511)	0.618 (0.639)	0.686 (0.726)	0.724 (0.786)
particle radius = 1.0 μm						
	T = 500 K	1000 K	1500 K	2000 K	2500 K	3000 K
ND = 10^{10}	0.0342 (0.0335)	0.0354 (0.0347)	0.0343 (0.0335)	0.0337 (0.0329)	0.0336 (0.0328)	0.0338 (0.0330)
10^{11}	0.257 (0.258)	0.263 (0.266)	0.258 (0.262)	0.257 (0.260)	0.257 (0.260)	0.259 (0.262)
10^{12}	0.707 (0.838)	0.673 (0.874)	0.663 (0.887)	0.672 (0.903)	0.680 (0.913)	0.687 (0.920)
particle radius = 10 μ m						
	T = 500 K	1000 K	1500 K	2000 K	2500 K	3000 K
ND = 10^{8}	0.0325 (0.0318)	0.0341 (0.0335)	0.0362 (0.0355)	0.0386 (0.0378)	0.0406 (0.0398)	0.0422 (0.0413)
10^{9}	0.248 (0.251)	0.258 (0.261)	0.271 (0.273)	0.287 (0.289)	0.300 (0.301)	0.310 (0.310)
10^{10}	0.6583 (0.8773)	0.6759 (0.8787)	0.6999 (0.8921)	0.7295 (0.9144)	0.7511 (0.9281)	0.7666 (0.9362)

with $a_{t,\lambda}$ and $\omega_{t,\lambda}$ being the absorption coefficient and scattering albedo of the mixture given by

$$a_{t,\lambda} = a_{p,\lambda} + a_{g,\lambda} \tag{9}$$

and

$$\omega_{t,\lambda} = 1 - \frac{a_{t,\lambda}}{\kappa_{p,\lambda} + a_{g,\lambda}} \tag{10}$$

Note that the spectral AMBL, $L_{ab,\lambda}$, is evaluated based on the total absorption coefficient and total scattering albedo for the mixture. The subscript λ is inserted to emphasize the spectral dependence of all optical properties and the AMBL. For mathematical convenience, the total emittance can be separated into a particle emittance, ϵ_p, and a particle attenuated gas emittance, $\tau_p\epsilon_g$, by

$$\epsilon = \epsilon_p + \tau_p\epsilon_g \tag{11}$$

with

$$\epsilon_p = \frac{1}{\sigma T^4}\int_0^\infty e_{\lambda b}(T)(1 - e^{-a_{p,\lambda}L_{ab,\lambda}(a_{t,\lambda}\omega_{t,\lambda})})d\lambda \tag{12}$$

and

$$\tau_p\epsilon_g = \frac{1}{\sigma T^4}\int_0^\infty e_{\lambda b}(T)e^{-a_{p,\lambda}L_{ab,\lambda}(a_{t,\lambda}\omega_{t,\lambda})} (1 - e^{-a_{g,\lambda}L_{ab,\lambda}(a_{t,\lambda}\omega_{t,\lambda})})d\lambda \tag{13}$$

As in the utilization of conventional mean beam length for nonscattering media, AMBL reduces the spectral integration to an equivalent one-dimensional integral.

3 Results and Discussion

All numerical computations as outlined in sections 2.1, 2.2, and 2.3 are straightforward and can be carried out accurately and efficiently with little effort. Indeed, all numerical results presented in this work are generated either by a personal computer or a workstation and they are accurate to within a relative error of less than 1 percent. The present approach is thus particularly convenient for practical industrial applications.

Table 2 Particle emittance (in the optically thick limit), $\epsilon_{p,\infty,\lambda}$, for a particle-$N_2$ mixture and a particle-CO_2 mixture at different temperatures and particle sizes

	particle-CO_2 mixture			particle-N_2 mixture
particle radius = 0.1 μm				
λ (μm)	T = 1000K	2000K	3000K	
2.7	0.466	0.682	0.775	0.971
4.3	0.104	0.130	0.166	0.991
9.4	0.591	0.683	0.780	0.997
10.4	0.516	0.640	0.752	0.997
15.0	0.00360	0.0141	0.0311	0.997
particle radius = 1 μm				
	particle-CO_2 mixture			particle-N_2 mixture
λ (μm)	T = 1000K	2000K	3000K	
2.7	0.158	0.264	0.330	0.708
4.3	0.0781	0.0953	0.116	0.730
9.4	0.539	0.611	0.664	0.842
10.4	0.525	0.606	0.674	0.877
15.0	0.00489	0.0190	0.0410	0.942
particle radius = 10 μm				
	particle-CO_2 mixture			particle-N_2 mixture
λ (μm)	T = 1000K	2000K	3000K	
2.7	0.181	0.300	0.372	0.760
4.3	0.0748	0.0904	0.111	0.747
9.4	0.423	0.468	0.517	0.708
10.4	0.377	0.437	0.492	0.700
15.0	0.00665	0.0233	0.0458	0.691

3.1 Particle Emittance. The effect of temperature, particle radius, and particle number density on the particle emittance, ϵ_p, is illustrated by numerical data presented in Table 1. Results generated without consideration of the scattering effect are presented with the "exact" numerical results to illustrate the importance of the scattering effect.

For particles with small radius ($r = 0.1$ μm) for which the scattering albedo is small ($\omega < 0.1$), scattering has no effect on the particle emittance. ϵ_p increases with temperature because the absorption coefficient increases with increasing size parameter ($\alpha = 2\pi r/\lambda$) in the small particle size range. As the particle size increases, the scattering albedo increases ($\omega > 0$ 5 for particle with radius greater than 1 μm) and the "no-scattering" results are in significant error when the particle concentration is large. Except for the lower temperature range, scattering also reduces the effect of temperature on ϵ_p because the variation of the scattering albedo with the size parameter is, in general, less than that of the absorption coefficient.

In the optically thick limit ($D \to \infty$ with optical properties kept constant), the spectral AMBL approaches a finite optically thick ($aD > 5.0$) distribution as shown in Fig. 2. Physically, scattering reduces the contribution of the particle emission to a layer of thickness AMBL. At a given wavelength λ, a scattering optically thick particle/gas layer thus behaves as a nongray emitter with

$$\epsilon_{p,\infty,\lambda} = 1 - e^{-aL_{ab}(\omega\lambda)} \tag{14}$$

and the particle emittance is reduced to less than unity. Since the scattering albedo is based on the optical properties of the mixture, the presence of an absorbing gas has an important effect on the particle emittance. The emittance can also be a function of temperature because of the temperature dependence of the gas absorption coefficient. As an illustration, $\epsilon_{p,\infty,\lambda}$ for a particle-N_2 mixture and that for a particle-CO_2 mixture (with total gas pressure of 1 atm) at the center of the five CO_2 absorption bands are tabulated in Table 2.

3.2 Particle Attenuated Gas Emittance. The effect of temperature, particle radius, and particle number density on the particle attenuated gas emittance, $\tau_p\epsilon_g$, is illustrated by numerical data presented in Table 3. In contrast to its effect on the particle emittance, scattering increases the particle attenuated gas emittance. Mathematically, the increase in $\tau_p\epsilon_g$ is

Table 3 Effect of temperature and number density on particle attenuated gas emittance, $\tau_p \epsilon_g$ (values in parentheses are generated ignoring the effect of scattering)

particle radius = 0.1 μm						
	T = 500 K	1000 K	1500 K	2000 K	2500 K	3000 K
ND = 0	0.164	0.189	0.156	0.114	0.0826	0.0605
10^{12}	0.164 (0.164)	0.189 (0.189)	0.155 (0.155)	0.114 (0.114)	0.0824 (0.0823)	0.0603 (0.0603)
10^{13}	0.162 (0.162)	0.185 (0.185)	0.151 (0.151)	0.111 (0.110)	0.0797 (0.0796)	0.0582 (0.0582)
10^{14}	0.147 (0.147)	0.155 (0.155)	0.120 (0.120)	0.0849 (0.0847	0.0598 (0.0595)	0.0429 (0.0427)
particle radius = 1 μm						
	500 K	1000 K	1500 K	2000 K	2500 K	3000 K
ND = 0	0.164	0.189	0.156	0.114	0.0826	0.0605
10^{10}	0.161 (0.161)	0.186 (0.186)	0.153 (0.152)	0.112 (0.112)	0.0809 (0.0808)	0.0592 (0.0591)
10^{11}	0.141 (0.141)	0.159 (0.158)	0.129 (0.128)	0.0940 (0.0931)	0.0674 (0.0667)	0.0490 (0.0484)
10^{12}	0.0818 (0.0717)	0.0910 (0.0718)	0.0705 (0.0518)	0.0487 (0.0336)	0.0335 (0.0219)	0.0235 (0.0147)
particle radius = 10 μm						
	500 K	1000 K	1500 K	2000 K	2500 K	3000 K
ND = 0	0.1637	0.1893	0.1555	0.1143	0.0826	0.0605
10^{8}	0.161 (0.161)	0.186 (0.186)	0.153 (0.152)	0.112 (0.112)	0.0809 (0.0807)	0.0591 (0.0591)
10^{9}	0.140 (0.139)	0.160 (0.159)	0.129 (0.128)	0.0939 (0.0930)	0.0674 (0.0666)	0.0489 (0.0483)
10^{10}	0.0847 (0.0678)	0.0927 (0.0715)	0.0709 (0.0516)	0.0485 (0.0334)	0.0332 (0.0216)	0.0232 (0.0145)

Table 4 Effect of temperature and number density on total emittance, ϵ_t (values in parentheses are generated ignoring the effect of scattering)

particle radius = 0.1 μm						
	500 K	1000 K	1500 K	2000 K	2500 K	3000 K
ND = 0	0.164	0.189	0.156	0.114	0.0826	0.0605
10^{12}	0.166 (0.166)	0.194 (0.194)	0.166 (0.166)	0.130 (0.130)	0.104 (0.104)	0.0867 (0.0862)
10^{13}	0.182 (0.182)	0.239 (0.239)	0.253 (0.252)	0.256 (0.255)	0.262 (0.261)	0.271 (0.270)
10^{14}	0.324 (0.324)	0.489 (0.490)	0.624 (0.631)	0.703 (0.723)	0.746 (0.785)	0.767 (0.829)
particle radius = 1 μm						
	500 K	1000 K	1500 K	2000 K	2500 K	3000 K
ND = 0	0.164	0.189	0.156	0.114	0.0826	0.0605
10^{10}	0.196 (0.195)	0.221 (0.221)	0.187 (0.186)	0.146 (0.145)	0.115 (0.114)	0.0930 (0.0921)
10^{11}	0.398 (0.398)	0.422 (0.424)	0.387 (0.390)	0.351 (0.353)	0.325 (0.327)	0.308 (0.310)
10^{12}	0.788 (0.910)	0.764 (0.946)	0.734 (0.939)	0.720 (0.937)	0.713 (0.935)	0.711 (0.934)
particle radius = 10 μm						
	500 K	1000 K	1500 K	2000 K	2500 K	3000 K
ND = 0	0.164	0.189	0.156	0.114	0.0826	0.0605
10^{8}	0.194 (0.193)	0.220 (0.219)	0.189 (0.188)	0.151 (0.150)	0.122 (0.121)	0.101 (0.100)
10^{9}	0.388 (0.390)	0.418 (0.420)	0.400 (0.402)	0.381 (0.382)	0.368 (0.368)	0.359 (0.358)
10^{10}	0.743 (0.945)	0.769 (0.950)	0.771 (0.944)	0.778 (0.948)	0.784 (0.950)	0.790 (0.951)

due to the reduction of AMBL caused by the scattering effect. The particle transmissivity, $e^{-a_{p,\lambda} i^{L_{ab,\lambda}(a_{t,\lambda},\omega_{t,\lambda})}}$, is increased by scattering while the gas emission effect, $1-e^{-a_{g,\lambda} L_{ab,\lambda}(a_{t,\lambda},\omega_{t,\lambda})}$, is reduced by scattering. Since the gas emission effect is essentially optically thin except near the center of an absorption band, the increase in the particle transmissivity dominates and leads to a larger value for the particle attenuated gas emittance.

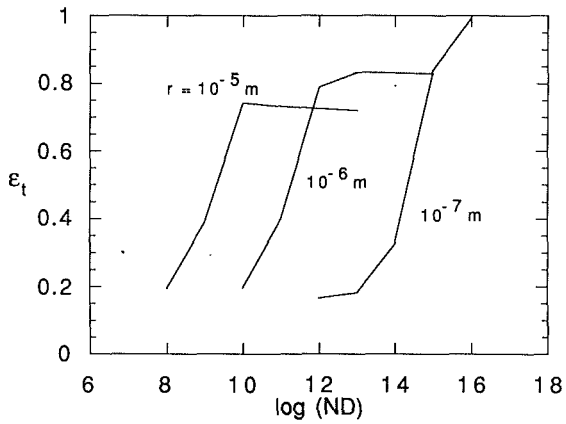

Fig. 5 Total emittance of a particle/CO_2 mixture at 500 K

Physically, this increase in the particle attenuated gas emittance can be attributed to the fact that scattering limits the mixture's contribution to the total heat transfer to within a layer of finite absorption optical thickness. Since particle absorption is the dominant effect, the particle attenuated gas emittance increases even though the region of particle emission decreases.

3.3 Total Emittance. Numerical data for the total emittance are presented in Table 4. Since the scattering effect simultaneously increases the particle attenuated gas emittance and decreases the particle emittance, its effect on the total emittance varies strongly with the particle size and temperature. For moderate and large particle sizes (1 and 10 μm), scattering reduces the optically thick limiting value of the total emittance to less than unity. Since the limiting value can be as low as 0.711 ($ND = 10^{12}$ 1/m^2, particle radius = 1.0 μm, $T = 1000$ K), this effect is quite appreciable and should not be ignored in practical engineering applications. At the low temperature limit (500 K) and high particle concentration (beyond the range shown in Table 4), the effect of scattering leads to the unusual behavior that the total emittance does not increase monotonically with increasing particle concentration. This behavior is illustrated graphically in Fig. 5.

4 Conclusion

The absorption mean beam length (AMBL) is demonstrated to be an effective concept in generating accurate prediction of the emittance of an absorbing, emitting, and scattering particle-gas mixtures. Numerical data for a carbon particle/CO_2 slab is presented to provide benchmark solution for this class of problem and to demonstrate the effect of scattering on the mixture's emittance.

The effect of scattering is shown to be very important and leads to qualitative behavior which differs significantly from the traditional no-scattering results. Specifically, the traditional concept that an optically thick particle-gas mixture is effectively black is shown to be incorrect. A mixture of large carbon particles ($r = 1$, 10 μm) has an emittance of less than unity in the optically thick limit (large particle number concentration). At low and moderate temperature, the mixture's emittance can become a nonmonotonic function of the particle concentration due to the scattering effect. The mixture's emittance first increases with particle concentration, becomes a maximum at a finite particle number concentration, and then decreases toward a lower limiting value.

Acknowledgments

This paper is based upon work supported by the National Science Foundation under Grant No. CTS-8915042.

References

Bohren, C. F., and Huffman, D. R., 1983, *Absorption and Scattering of Light by Small Particles*, Wiley, New York.

Edwards, D. K., Glassen, L. K., Hauser, W. C., and Tuchscher, J. S., 1967, "Radiative Heat Transfer in Nonisothermal Nongray Gases," ASME JOURNAL OF HEAT TRANSFER, Vol. 89, pp. 219–229.

Felske, J. D., and Tien, C. L., 1973, "Calculation of the Emissivity of Luminous Flames," *Combustion, Science and Technology*, Vol. 7, pp. 25–31.

Hottel, H. C., 1927, *Transaction American Institute of Chemical Engineers*, Vol. 19, p. 173.

Hoteel, H. C., and Sarofim, A. F., 1967, *Radiative Transfer*, McGraw Hill, New York.

Howell, J. R., and Perlmutter, M., 1964, "Monte Carlo Solution of Radiative Heat Transfer in a Nongray Nonisothermal Gas With Temperature Dependent Properties," *AIChE Journal*, Vol. 10, No. 4, pp. 562–567.

Menguc, M. P., and Viskanta, R., 1986, "An Assessment of Spectral Radiative Heat Transfer Prediction for a Pulverized Coal-Fired Furnace," *Heat Transfer—1986*, Vol. 2, pp. 815–820.

Phillips, H. R., 1977, "Infrared Optical Properties of Graphite," *Physical Review B*, Vol. 16, No. 6, p. 2896.

Skocypec, R. D., and Buckius, R. O., 1984, "Total Hemispherical Emissivity for CO_2 or H_2O Including Particulate Scattering," *International Journal of Heat and Mass Transfer*, Vol. 27, No. 1, pp. 1–13.

Van der Hulst, H. C., 1957, *Light Scattering by Small Particles*, Wiley, New York.

Viskanta, R., and Menguc, M. P., 1987, "Radiation Heat Transfer in Combustion Systems," *Progress in Energy and Combustion Science*, Vol. 13, pp. 97–160.

Yuen, W. W., 1990, "Development of a Network Analogy and Evaluation of Mean Beam Lengths for Multi-dimensional Absorbing/Isotropically-Scattering Media," ASME JOURNAL OF HEAT TRANSFER, Vol. 112, pp. 408–414.

Yuen, W. W., and Takara, E., 1990, "Development of a Generalized Zonal Method for the Analysis of Radiative Heat Transfer in Absorbing and Anisotropically-Scattering Media," *Numerical Heat Transfer*, K. Vafai and J. L. S. Chen, eds., ASME HTD-Vol. 130, pp. 123–132.

Yuen, W. W., 1991, "Scaling of Radiative Heat Transfer Effect in High Temperature Absorbing, Isotropically-Scattering Systems (Concepts of Absorption and Extinction Mean Beam Length," *Proceedings of the 4th International Symposium of Transport Phenomena in Heat and Mass Transfer*, Sydney, Australia, Vol. 3, pp. 1188–1198.

Transient Structure and Radiation Properties of Strongly Radiating Buoyant Flames

Y. R. Sivathanu

J. P. Gore

Thermal Sciences and Propulsion Center,
School of Mechanical Engineering,
Purdue University,
West Lafayette, IN 47907

Measurements of instantaneous temperature and soot volume fractions based on absorption and emission in highly buoyant turbulent acetylene/air and propylene/air flames are reported. These measurements are used to predict mean, rms, probability density functions, and power spectral densities of spectral radiation intensities along a representative horizontal chord in the flame. The results show the presence of large quantities of relatively cold soot in the vicinity of smaller amounts of hot soot particles. The resulting inhomogeneity in the temperature of soot in the flame leads to negative cross correlations between temperature and soot volume fractions. The treatment of such correlations was found necessary for predicting the observed probability density functions and the power spectral densities of spectral radiation intensities.

Introduction

Radiation properties of turbulent pool flames burning acetylene and propylene in air have been studied in the past (Sivathanu, 1990; Sivathanu et al., 1991a). These studies used measurements of soot statistics obtained from laser absorption in conjunction with a two-level model for soot temperatures to predict mean radiation intensities. The approach provided reasonable results for propylene/air flames. However, predictions of mean radiation intensity for acetylene/air flames required the use of very low temperatures (Sivathanu, 1990). The predictions for both acetylene/air and propylene/air flames were very sensitive to the choice of the upper temperature level. The discrepancies between measurements and predictions were between 15 and 100 percent.

Sivathanu et al. (1991b) measured soot volume fractions in acetylene/air jet flames using simultaneous two-line emission data (f_{ve}) and one-line absorption data (f_{va}). A two-line emission temperature (T) was also obtained during the process. The f_{ve} measurements represent Planck-function weighted averages of soot volume fractions over the probe volume. Based on the large differences between measurements of f_{ve} and f_{va}, Sivathanu et al. (1991b) concluded that the bulk of soot particles seen by the absorption probe were at relatively low temperatures. The measured emission temperatures (T) yielded reasonable predictions of spectral intensities leaving the flames when used in conjunction with local emissivities based on f_{ve}. Use of emissivities based on f_{va} led to a substantial overprediction of radiation intensities. Furthermore, the cross correlations between f_{ve} and T were found to be important in the determination of the radiation intensity.

Turbulence radiation interactions (the effect of fluctuations in scalar properties on mean radiation intensities recognized in several publications: Kabashnikov and Kmit, 1979; Grosshandler and Joulain, 1986; Gore and Faeth, 1988) were treated differently in the work reported by Sivathanu et al. (1991a, 1991b). In the earlier work (Sivathanu et al., 1991a) the turbulence properties of soot volume fractions were treated by using simultaneous two-point transient absorption measurements to account for temporal and spatial correlations. The turbulent fluctuations in temperature were not measured simultaneously. A temperature–soot volume fraction state relationship model involving two temperature levels was used. The level of temperature associated with each soot volume fraction measurement was based on an underfire-overfire intermittency inferred from a single-line emission intensity. Recently, Sivathanu et al. (1991b) have used simultaneous single point measurements of emission temperatures (T) and soot volume fractions (f_{ve}) to obtain improved predictions of radiation intensities for diametric paths in acetylene/air jet flames. The treatment of turbulence-radiation interactions included temporal autocorrelations and single point cross-correlations between f_{ve} and T.

The objective of the present work was to apply the experimental and theoretical methods developed by Sivathanu et al. (1991b) to highly buoyant turbulent acetylene/air and propylene/air flames. This application is interesting since these flames represent a longer residence time limit for radiative heat loss compared to the jet flames studied by Sivathanu et al. (1991b). It is also of interest to determine whether the findings regarding the large quantities of cold soot and the negative cross-correlations between temperatures and soot volume fractions apply to pool flames. Finally, Sivathanu et al. (1991b) reported measurements and predictions of mean and rms spectral radiation intensities, while the present paper includes Probability Density Functions (PDF) and Power Spectral Density (PSD), providing a relatively complete description of the turbulent fluctuations.

Single point transient measurements of T, f_{va}, and f_{ve} resolved to approximately 10 mm length were obtained for several radial positions at a representative axial station above the burner. These data were used in conjunction with a bivariate simulation to predict the intensity leaving a horizontal diametric path at the axial station. Comparison between measurements of radiation intensity and the results of the bivariate simulation were used to verify the length and time scale resolution necessary for effective treatment of turbulence/radiation interactions.

Experimental Methods

The experimental apparatus consisted of a 50-mm-dia gas-fired burner similar to the one studied by Sivathanu (1990). The burner consisted of a 600 mm straight steel pipe with a 100-mm-long honeycomb section and a 50 mm layer of glass

Contributed by the Heat Transfer Division for publication in the JOURNAL OF HEAT TRANSFER. Manuscript received by the Heat Transfer Division October 1991; revision received January 1992. Keywords: Combustion, Fire/Flames, Radiation Interactions.

Table 1 Experimental conditions

Burner diameter = 50 mm

Fuel	$\dot{m}$ (mg/s)	Re[a]	Fr[b]	X_R[c]	L_f[d] (mm)
Acetylene	398	840	1.16	59	550
Acetylene	223	470	0.48	58	421
Propylene	460	1370	0.62	45	600
Propylene	251	750	0.34	46	504

[a] Reynolds number = $U_o d_o / \nu_o$, based on fuel properties at exit.

[b] Froude Number = $\sqrt{gd} / U_o$

[c] Radiative loss fraction obtained using radial and axial traverses of a wide angle radiometer.

[d] Flame length obtained from a high speed photographs (1000 Hz).

beads to eliminate swirl and provide uniform velocity profile of the fuel stream at the exit. The burner was cooled by circulating tap water through copper tubes wrapped on the outside of the flame attachment region. The flow conditions are summarized in Table 1 and are similar to those of Sivathanu (1990). The Froude numbers for the four flames vary between 0.34 and 1.16, indicating that the flames are buoyancy dominated. However, the Froude numbers are an order of magnitude higher than typical liquid pool fires.

Local measurements were completed using the three-line absorption-emission probe (absorption at 632 nm and emission at 900 nm and 1000 nm) identical to previous studies (Sivathanu et al., 199b; Sivathanu and Gore, 1991). The details of the measurement system were described earlier so the following description is brief. The intensity leaving the probe volume (6 mm in diameter and 10 mm in length) was collected by a nitrogen-purged probe and divided into three parts by two beam splitters. The intensities at 900 nm and 1000 nm were measured by two calibrated photomultiplier tubes with narrow band optical filters (10 nm half band width) in front of them. The absorption data were obtained from measurement of the intensity of a He–Ne (632.8 nm) laser before and after passing through the probe. The data were sampled at 1000 Hz with a low pass anti-aliasing analog filter applied at 500 Hz. All measurements were performed at an axial location corresponding to $x/d = 6.73$ (random selection as a representative location). The path integrated measurements were also completed at 2300 nm to test the effectiveness of the simulation at longer wavelengths.

The emission intensity at a wavelength λ is given by:

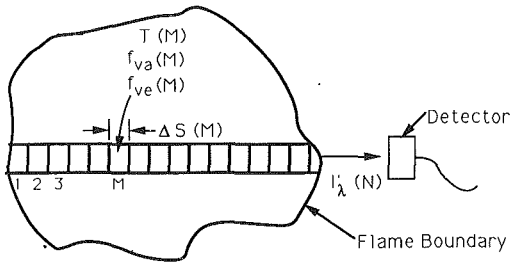

Fig. 1 Horizontal radiation path through flame

$$I_{\lambda e} = \frac{(1 - \exp(-K_\lambda f_{ve} L/\lambda))2hc^2}{\lambda^5(\exp(hc/\lambda kT) - 1)} \quad (1)$$

where L is the probe length, T is the emission temperature, and f_{ve} is the soot volume fraction based on emission. K_λ is a constant dependent on the refractive indices of soot and taken to be 5.33 for $\lambda = 900$ nm and 5.59 for $\lambda = 1000$ nm (Dalzell and Sarofim, 1969). The above values were chosen to be consistent with past work, and the use of those given by Tien and Lee (1982) did not change the evaluation of temperature because the wavelengths are close together. The above expression yields two equations (for the 900 nm and 1000 nm wavelengths), which were solved for temperature and emission soot volume fractions, f_{ve} (Sivathanu et al., 1991b).

The soot volume fractions based on laser absorption, f_{va}, were obtained from measurement of the laser intensity before and after the probe volume at 632 nm, with $K_\lambda = 4.93$:

$$f_{va} = -\ln(I_\lambda / I_\lambda^o)\lambda / K_\lambda L \quad (2)$$

For homogeneous material in the probe volume, the soot volume fractions measured using absorption and emission (Eqs. (2) and (1)) would be identical. For probe volumes with temperature inhomogeneity, the emission data (f_{ve}) are a measure of the relatively hot particles while the absorption data (f_{va}) are a measure of all (hot and cold) soot particles.

Radiation Analysis

In order to obtain total radiation heat flux incident on any point such as the detector shown in Fig. 1, the intensity leaving individual radiation paths through the flame must be calculated. To illustrate the present technique a diametric radiation path is considered as shown in Fig. 1.

The radiation path is modeled to consist of N discrete participating (absorbing and emitting) segments of different individual lengths (ΔS_i, $i = 1, N$). The calculation of average spectral radiation intensity leaving the path requires information concerning the instantaneous soot volume fractions

Nomenclature

c = velocity of light
d = burner diameter
Fr = Froude number
f_{va} = soot volume fraction based on extinction data
f_{ve} = soot volume fraction based on emission data
$\overline{f_{ve}' T'}$ = cross correlation between f_{ve} and T
h = Planck's constant
I_λ = spectral radiation intensity
I_λ^o = laser intensity before entering probe volume
$I_{\lambda e}$ = spectral intensity emitted by a local flame segment
$I_{\lambda M}$ = contribution from intensity emitted by segment M to the intensity leaving the flame
$\overline{I_\lambda'}$ = rms of spectral radiation intensity
K = extinction coefficient
k = Boltzmann's constant
L = probe length
L_f = flame length
$\dot{m}$ = mass flow rate
Re = Reynolds number
S = distance along radiation path
T = temperature
x = distance above burner exit
X_R = radiative loss fraction
ΔS = length of radiation segment
λ = wavelength
τ = transmission coefficient

Subscripts

a = based on an absorption measurement
e = based on an emission measurement
λ = wavelength

Superscripts

$'$ = rms value with an overbar

(following the Rayleigh approximation, Tien and Lee, 1982) and temperatures. Although the present measurements provide time series records of the quantities for the individual segments, simultaneous measurements are not available. To utilize the individual time series in lieu of the simultaneous information, the lengths of the individual segments should be about the size of the local integral scales (Kounalakis et al., 1989). The choice of appropriate scales for luminous flames is known only for absorption soot volume fractions (Sivathanu, 1990).

The intensity leaving the Nth segment of the diametric path shown in Fig. 1 can be calculated using a discretized form of equation of radiative transfer neglecting scattering.

$$I_\lambda(N) = I_{\lambda e}(1) \prod_{J=2}^{N} \tau_{\lambda a}(J) + I_{\lambda e}(2) \prod_{J=3}^{N} \tau_{\lambda a}(J) + \ldots + I_{\lambda e}(M) \prod_{J=M+1}^{N} \tau_{\lambda a}(J) + \ldots + I_{\lambda e}(N) \quad (3)$$

Each term in Eq. (3) represents the contribution of an individual segment to the intensity leaving the flame after accounting for absorption by the interceding segments. The emission intensity of a typical segment M is defined as:

$$I_{\lambda e}(M) = (1 - \tau_{\lambda e}(M)) \frac{2hc^2}{\lambda^5(\exp(hc/\lambda kT) - 1)} = (1 - \tau_{\lambda e}(M)) I_{\lambda b}(M) \quad (4)$$

where $\tau_{\lambda e}(M)$ is the transmittance of segment M defined as:

$$\tau_{\lambda e}(M) = \exp(-K_\lambda f_{ve} \Delta S(M)/\lambda) \quad (5)$$

where f_{ve} is the soot volume fraction based on emission data.

Simultaneous measurements of $I_{\lambda b}$ and $\tau_{\lambda e}$ are available for each segment, allowing exact treatment of the turbulence radiation interactions resulting from T and f_{ve} fluctuations in Eqs. (4) and (5). The effective radial resolution of the local data is 5 mm at the centerline and linearly improves to 0.5 mm at the edge. The gradients near the center at most locations are low, allowing sufficient spatial resolution for the transient simulations. In Eq. (3), $\tau_{\lambda a}(J)$ represents the transmittance of the segments along the path between the segment M and the detector. The contributions to the radiation intensity $I_{\lambda M}(N)$ at the detector location due to emission from the individual segments are represented by individual terms of Eq. (3):

$$I_{\lambda M}(N) = I_{\lambda e}(M) \prod_{J=M+1}^{N} \tau_{\lambda a}(J) \quad (6)$$

In order to account for the spatial cross correlation between the emission intensity for segment M and the absorption transmittance of the remaining segments, simultaneous multipoint data are required. Since such measurements are not presently available and the techniques to obtain these are not well developed, the present calculations relied on fully uncorrelated statistics between $I_{\lambda e}(M)$ and $\tau_{\lambda a}(J)$ for $J = M+1$ to N. This resulted in substantial underprediction of the radiation intensity. It was found that the use of negative spatial correlations between $I_{\lambda e}(M)$ and $\tau_{\lambda a}(J)$ was necessary for predicting the average path-integrated radiation intensity. This finding suggests that the instantaneous flame structure involves presence of unobstructed emission from hot soot particles.

The instantaneous radial measurements of T and f_{ve} were used in conjunction with Eqs. (3), (4), and (5) to calculate the instantaneous intensity. The $\tau_{\lambda a}(J)$ in Eq. (3) were replaced by $\tau_{\lambda e}(J)$ in order to account for the apparent highly negative spatial correlations between $I_{\lambda e}(M)$ and $\lambda_{\lambda a}(J)$. This choice, as discussed in the following, provides an effective method of treating the effects of turbulence/radiation interactions in lieu of complete knowledge of the transient behavior of T, f_{ve}, and f_{va} along the radiation path.

The resulting time series of the spectral radiation intensity incident on the detector was treated as numerical data to obtain mean, rms, Probability Density Functions, and Power Spectral Densities of spectral radiation intensities. The time series were sampled at 1000 Hz and results passed through a fourth-order Butterworth digital filter set at 500 Hz similar to the analog filter used in the experiments.

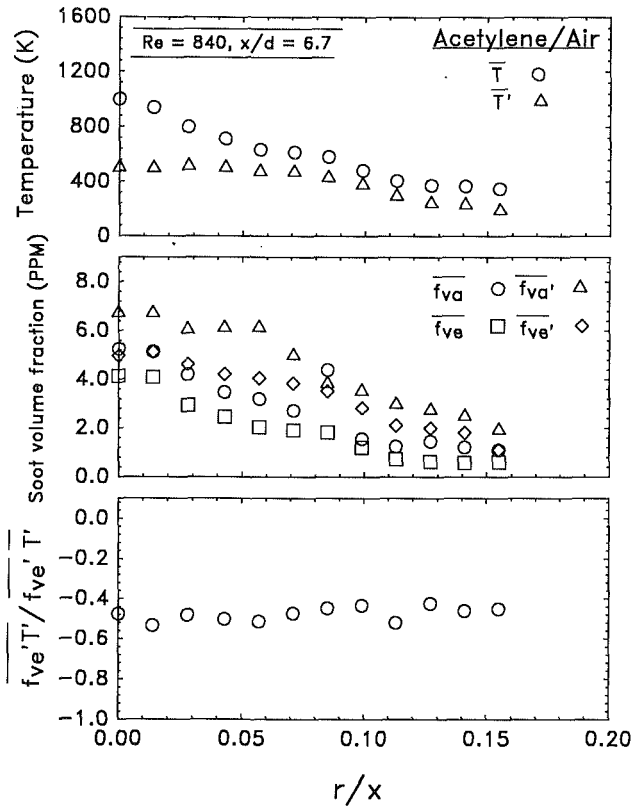

Fig. 2 Radial profiles of mean and fluctuating temperatures and soot volume fractions for Re = 840 acetylene/air flame at $x/d = 6.7$

The absolute uncertainties in the soot volume fractions depend on the different estimates of refractive indices available in the literature. The uncertainties in temperature are dominated by discretization errors at low values of measured intensity. The uncertainties in temperature were less than 40 K for $f_{ve} > 0.1$ ppm and temperatures greater than 1200 K. The uncertainties in absorption soot volume fractions are less than 10 percent at 10 ppm, increasing approximately to 40 percent at 0.01 ppm due to digitization error. The uncertainties in emission soot volume fractions are dominated by the uncertainties in the measurement of temperatures using Eq. (1). The uncertainties in emission soot volume fractions were less than 25 percent at a temperature of 1400 K and f_{ve} of 1 ppm.

Results and Discussion

Temperatures and Soot Volume Fractions. Figure 2 shows the measurements of mean and rms T, f_{ve}, f_{va} as well as the cross correlation between f_{ve} and T as a function of radial distance at $x/d = 6.7$ for the Re = 840 (also implies high Froude No. for present conditions) acetylene/air flame. The flame height is approximately 10 diameters (Table 1) and the underfire/overfire intermittency at $x/d = 6.7$ is quite low at the centerline (approximately 8 percent, Sivathanu, 1990).

The mean temperature is approximately 1100 K at the centerline and decreases toward the edge. The rms value of temperature is also highest at the center, typical of positions fairly high up in the flame. The intensity of temperature fluctuations is significantly higher than in the jet flames. The mean f_{ve} and f_{va} are lower than those found in the jet flames (Sivathanu et

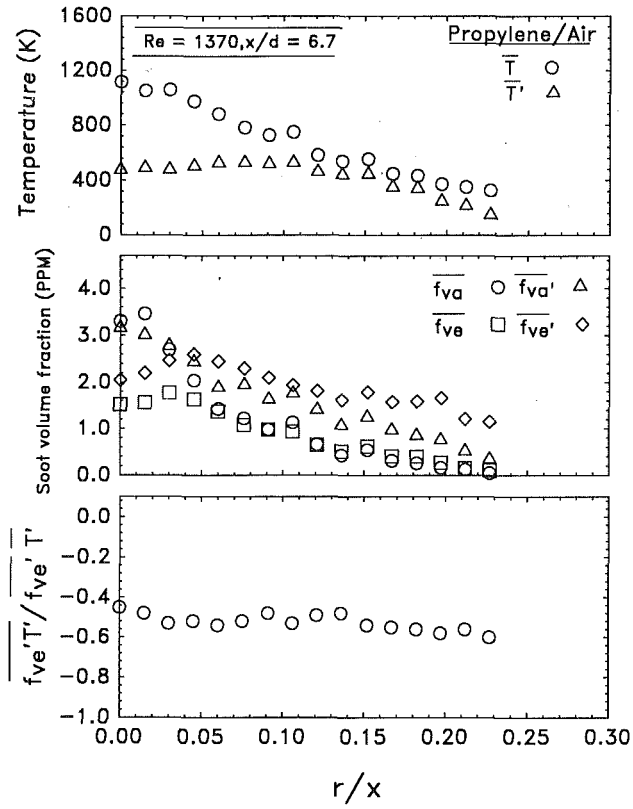

Fig. 3 Radial profiles of mean and fluctuating temperatures and soot volume fractions for Re = 1370 propylene/air flame at $x/d = 6.7$

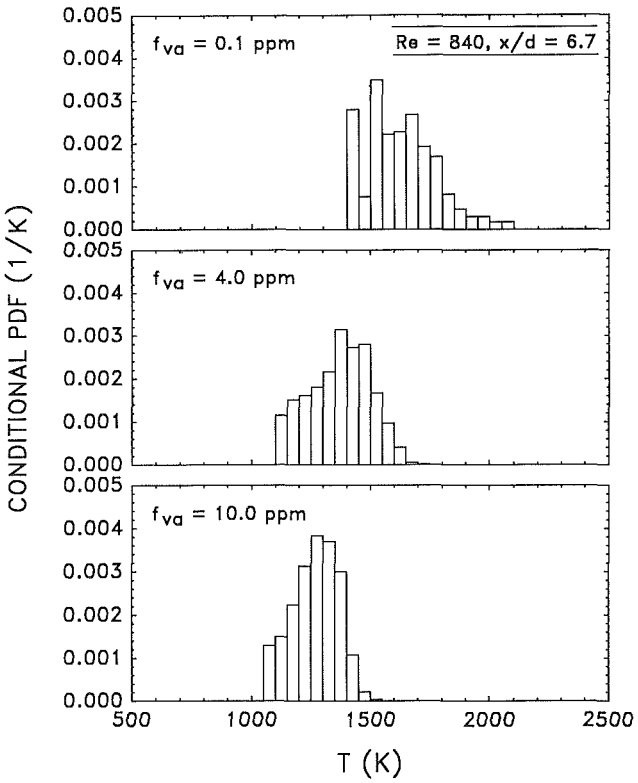

Fig. 4 Conditional Probability Density Functions of temperature conditioned on absorption soot volume fractions for Re = 840 acetylene/air flames

al., 1991b). The mean f_{ve} are lower by up to a factor of 3 compared to the mean f_{va}. As discussed before, f_{ve} are Planck-function weighted values of f_{va}. The difference between these two indicates that some of the soot particles seen by the absorption probe are relatively cold and do not contribute to the emission intensities. The differences between the f_{va} and f_{ve} are smaller than those observed in jet flames (Sivathanu et al., 1991b). The reduced differences are partly due to the longer residence times of radiative cooling for all soot particles and partly due to greater homogeneity of flame structure. The lower (than jet) Reynolds number flames are expected to have larger local integral scales, which results in greater probe volume homogeneity. Similar to the findings in jet flames, the cross correlations between the emission soot volume fractions and temperature have a relatively constant negative value of around 0.5. Sivathanu et al. (1991b) have demonstrated the importance of T-f_{ve} cross correlations in the prediction of mean intensity. The negative sign of the T-f_{ve} cross correlations is consistent with the analysis of subgrid scale flame structure reported by Gore and Jang (1991).

Figure 3 shows the measurements of mean and rms T, f_{ve}, f_{va} as well as the cross correlation between f_{ve} and T as a function of radial distance at $x/d = 6.7$ for the Re = 1370 propylene/air flame. The results are similar to the acetylene/air flames; however, close to the edge of the flame the differences between the f_{ve} and f_{va} are much lower. This is due to the lower absolute values of soot volume fraction in these flames. It is interesting to note that the negative cross correlation is constant and has the same value for the propylene/air and acetylene/air flames. This suggests that the negative cross correlation is independent of fuel, and whenever the soot volume fraction is high, the local temperature is low for all fuels. The results for the Re = 470 acetylene/air and Re = 750 propylene/air flames leads to similar conclusions and are not shown for brevity.

To highlight further the negative cross correlation between soot volume fractions and temperature, the conditional PDF of temperature, conditioned on soot volume fraction for the Re = 840 acetylene/air flame, is studied. Figure 4 shows the PDFs of temperature conditioned on absorption soot volume fraction at $r/x = 0.0$ for three different soot volume fractions. These PDFs are in reasonable agreement with measurements reported by Sivathanu and Faeth (1990). A wide range of temperatures are observed from 1100 K (the lower limit of the instrument sensitivity) to approximately 2100 K. The higher temperatures are associated with the lower soot volume fractions. It is interesting to note that even in the long residence time limit, a significant difference in the temperatures of regions with high soot loading and those with low soot loading exists. This observation supports the flame structure predictions of Gore and Jang (1991). PDFs from other radial positions are not very different from those at the centerline since the residence times are long for all positions.

The PDFs of temperature conditioned on emission soot volume fraction are shown in Fig. 5. Similar to the results shown in Fig. 4, the lower soot volume fractions are associated with the higher temperatures. This is expected since the emission data are Planck-function weighted soot volume fractions, and the temperature has a negative correlation with soot volume fractions as seen in Figs. 2 and 3.

Radiation Intensities. Five different realizations of the radiation terms in Eq. (3) for the Re = 840 acetylene/air flame are shown in Fig. 6. These realizations are taken from the instantaneous emission intensity data at different radial positions. The path is divided into 25 segments covering a distance of 100 mm across the local flame diameter. The detector is located beyond $S = 100$ mm at which point the path is essentially transparent. The length of each segment (ΔS_M) is chosen to be 4 mm. The solid lines show the emission intensity ($I_{\lambda e}(M)$) leaving each of the 25 ($N = 25$) segments. The dashed lines show the portion of $I_{\lambda e}(M)$ that reaches the detector $I_{\lambda M}(N)$.

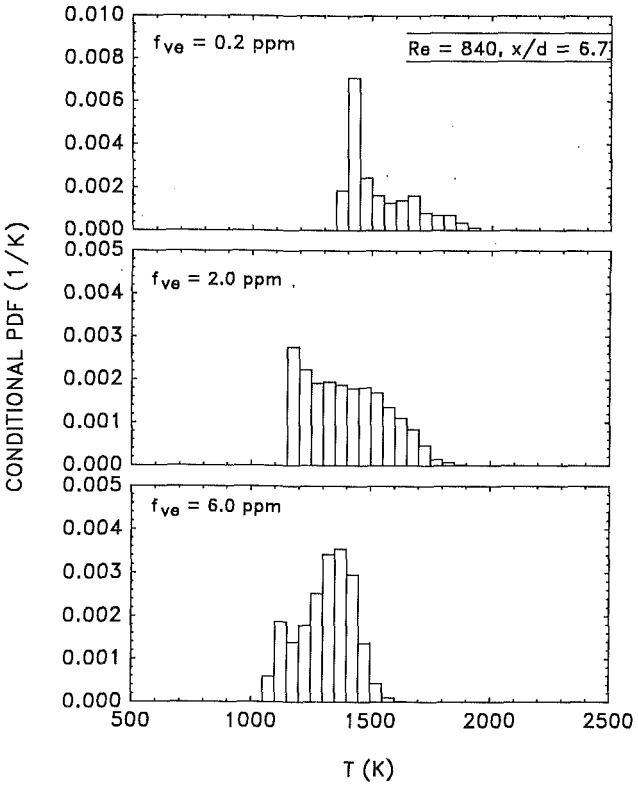

Fig. 5 Conditional Probability Density Functions of temperature conditioned on emission soot volume fractions for Re = 840 acetylene/air flames

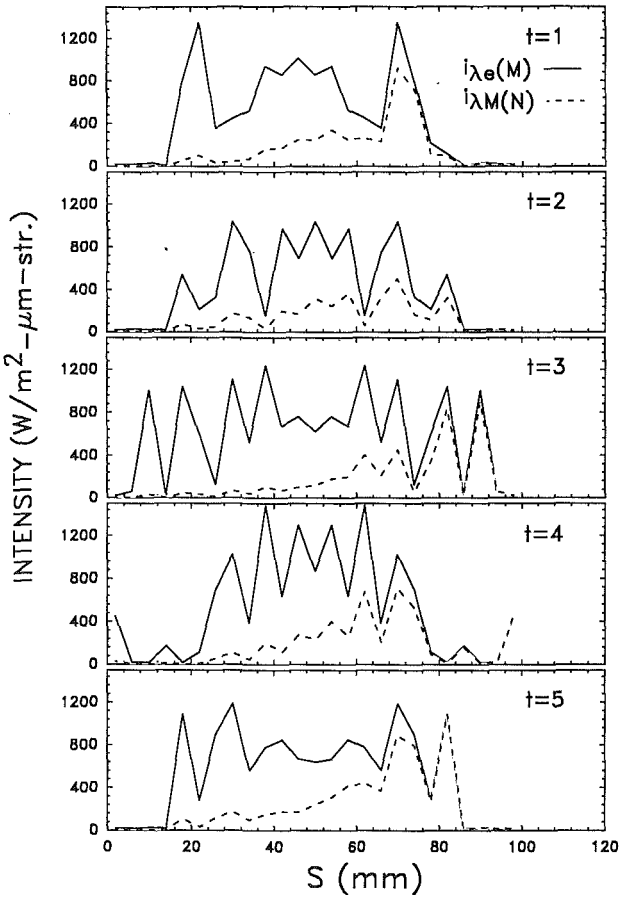

Fig. 6 Typical realizations of spectral radiation intensities along a horizontal path at $x/d = 6.7$ in the Re = 840 acetylene/air flame

Figure 6 shows that the variations in the properties of the radiating path are treated automatically in the present analysis due to the use of discrete data from the relevant locations. For example, the path at $t = 3$ appears to be approximately 20 percent longer than those at $t = 1$, 2, and 5. Since the flames are axisymmetric in the mean and spatial cross correlations are not treated in the present simulation, the realizations shown in Fig. 6 are axisymmetric. The $I_{\lambda M}(N)$ calculations (dashed lines) show that a large fraction of the radiation intensity observed by the detector originates from flame segments located between 70–100 mm. This is a result of the location of the high-temperature flame front and the relatively large optical thickness of the flame segments due to large volume fractions of soot particles. The differences between $I_{\lambda e}(M)$ and $I_{\lambda M}(N)$ for locations away from the detector ($S < 50$ mm) show that a large fraction of the energy emitted by these segments in the direction of the detector is absorbed by other flame segments. In fact, approximately 95 percent of the intensity emitted by the flame sheet farther from the detector is self-absorbed by the flame. However, the intensity reaching the detector consists of at least 30 percent contribution from locations between $S = 50$ mm and $S = 70$ mm. Therefore, the flame sheet located between $S = 70$ mm and $S = 100$ mm may not be treated as an optically thick layer. Based on a study of typical realizations from the other flames and different radiation paths, it was found that the observations apply to different conditions. The flame sheet of propylene/air flame is even less optically thick.

Table 2 shows a comparison between measurements and predictions of mean and rms spectral radiation intensities at 1000 nm and 2300 nm for the different flame conditions. The mean intensities at both the wavelengths are predicted reasonably well for the various flame conditions showing that the essential physics of the problem is captured quite well by the simulation. For the Re = 470 acetylene/air, Re = 750 propylene/air, and Re = 1370 propylene/air flames, the rms intensities are predicted quite well. However, the rms intensities are underpredicted by approximately 30 percent for the Re = 840 acetylene/air flames, which could be due to the uncertainties in the temperature and soot volume fraction measurements.

Table 2 Measurements and predictions of $\overline{I_\lambda}$ and $\overline{I_\lambda'}$

Fuel	λ	Re	$\overline{I_\lambda}$ (kW/m^2-μm-str)		$\overline{I_\lambda'}/\overline{I_\lambda}$ %	
			Data	Pred	Data	Pred
C_2H_2	1000	840	1.76	1.72	66	45
C_2H_2	2300	840	5.11	5.46	64	54
C_2H_2	1000	470	1.32	1.46	55	57
C_3H_6	1000	1370	1.86	1.56	54	49
C_3H_6	2300	1370	4.00	3.94	47	40
C_3H_6	1000	750	1.51	1.32	65	61
C_3H_6	2300	750	3.11	2.95	55	58

The probability density functions of the spectral radiation intensity for the acetylene/air flames are shown in Fig. 7. The simulation reproduces the experimental PDF very well with the exception of the spike at very low intensities. This spike is probably caused by the spatially correlated radiation blockage and large-scale flame flapping phenomena. Sivathanu (1990) observed similar spikes in the PDFs at the lowest intensities. However, the spatially correlated model based on time series of f_{va} does not predict these spikes well. The spikes at the lowest end are smaller than those observed by Sivathanu (1990). This could be due to the different levels of flame flap-

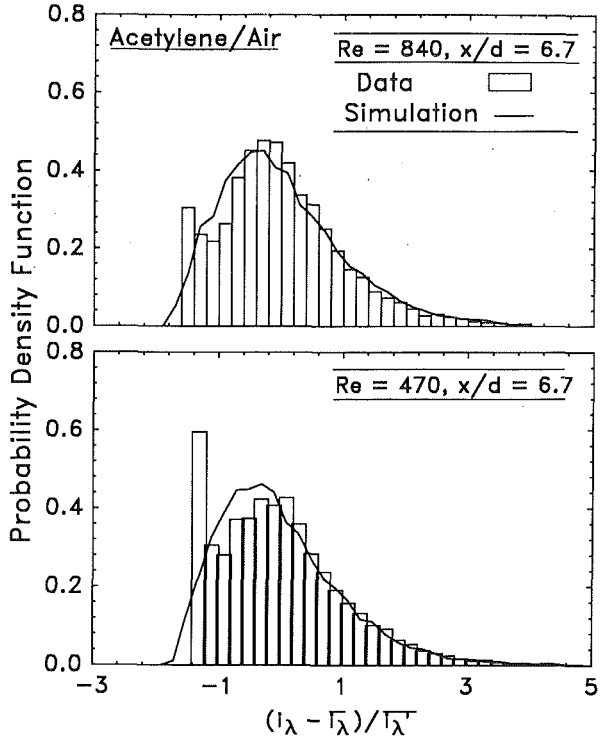

Fig. 7 Probability Density Function of spectral radiation intensity at 1000 nm for acetylene/air flames at $x/d = 6.7$

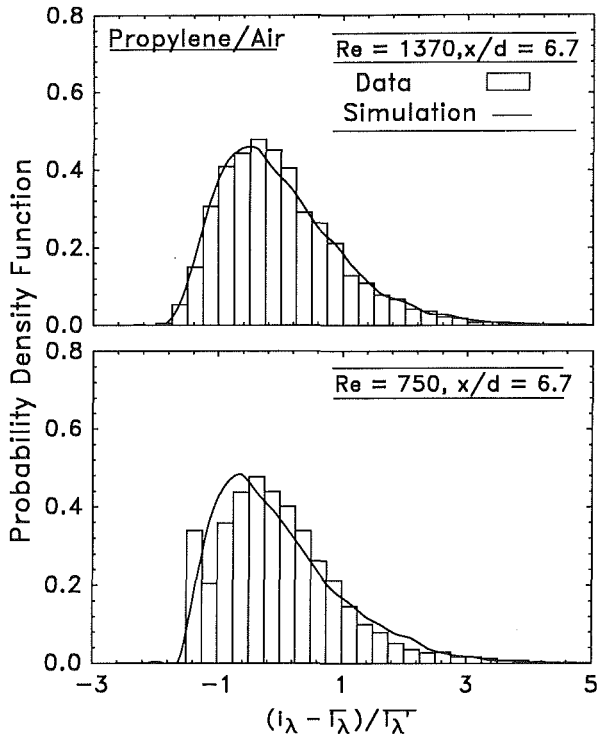

Fig. 8 Probability Density Function of spectral radiation intensity at 1000 nm for propylene/air flames at $x/d = 6.7$

ping in the two laboratories. Highly buoyant flames are hard to duplicate exactly and flame flapping is more an effect of the local environment (exhaust fan, room size, etc.) than of the burner.

The probability density functions of the spectral radiation intensity for the propylene/air flames are shown in Fig. 8. Again with the exception of the low-intensity spike, the simulation reproduces the data quite well.

The Power Spectral Densities of spectral radiation intensity for the Re = 840 acetylene/air and Re = 1370 propylene/air flames are shown in Fig. 9. Similar to previous simulations (Sivathanu et al., 1990; Kounalakis et al., 1991), a temporally correlated time series reproduces the observed power spectral density at low frequencies quite well. The application of the digital filter to the simulation results in good agreement with the experiment at high frequencies as well. These results show that the power spectral densities can be predicted well with a temporally correlated and digitally filtered stochastic simulation. The simulation for the low Reynolds No. flames shows similar agreement with measurements and is not shown for brevity.

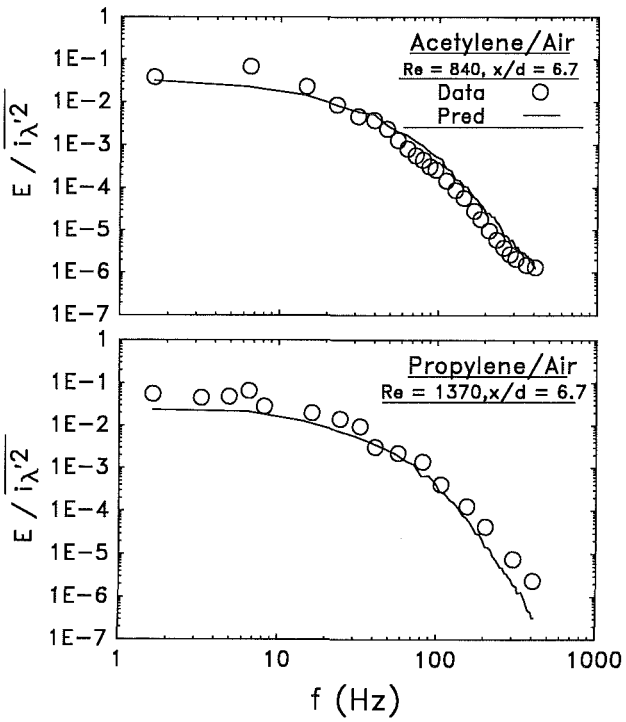

Fig. 9 Power Spectral Densities of spectral radiation intensity at 1000 nm for Re = 840 acetylene/air and Re = 1370 propylene/air flames

Conclusions

The present work involved an extension of a previous jet flame study to highly buoyant turbulent flames including detailed statistical properties (PDFs and PSDs) of spectral radiation intensities. Specific conclusions that can be drawn from the study are:

1 The large amounts of relatively cold soot observed in turbulent jet flames are also found in the highly buoyant flames. However, the differences in mean soot volume fractions measured by absorption and emission probes are smaller than those in the jet flames. This is due to the longer residence times available for the soot particle temperatures to equilibrate and the larger spatial scales leading to lower probe volume inhomogeneities.

2 The highly buoyant flames, which are in the long residence time limit, also exhibit a high negative cross correlation between soot volume fractions and temperatures. Remarkably, the value of this cross correlation has been found to be independent of level of buoyancy and type of fuel.

3 The bivariate stochastic radiation analysis with a digital filter applied to the output time series is effective in reproducing the mean, rms, probability density function as well as the power spectral density of spectral radiation intensity. Spatial corre-

lation effects require the use of $\tau_{\lambda e}$ in Eqs. (3) and (6) instead of the instantaneous $\tau_{\lambda a}$.

Based on these findings, it is clear that methods of calculating radiation from flames in a large range of operating conditions must consider the fluctuations in temperature and soot volume fractions and their cross correlations. The presence of relatively cold and hot soot particles in the highly buoyant flames strengthens the earlier discovery of a unique flame structure for strongly radiation flames.

Acknowledgments

This study was completed while the authors were members of the Mechanical Engineering Department at the University of Maryland. This study is partially supported by the National Science Foundation under Grant No. CTS-8914520 with Drs. Charles Garris, Joan Gosink, and William Grosshandler serving as NSF Scientific Officers. Partial support of this work by the National Institute of Standards and Technology under Grant No. 60NANB9D0944 with Dr. T. Kashiwagi serving as NIST Technical Officer is also acknowledged.

References

Dalzell, W. H., and Sarofim, A. F., 1969, "Optical Constants of Soot and Their Application to Heat Flux Calculations," ASME JOURNAL OF HEAT TRANSFER, Vol. 91, pp. 100–104.

Gore, J. P., and Faeth, G. M., 1988, "Structure and Radiation Properties of Turbulent Acetylene/Air Diffusion Flames," ASME JOURNAL OF HEAT TRANSFER, Vol. 110, pp. 173–181.

Gore, J. P., and Jang, J. H., 1991, "Transient Radiation Properties of a Subgrid Scale Eddy," ASME JOURNAL OF HEAT TRANSFER, in press.

Grosshandler, W. L., and Joulain, P., 1986, "The Effect of Large Scale Fluctuations on Flame Radiation," *Prog. Astro. and Aero.*, Vol. 105, Part II, AIAA, Washington, pp. 123–152.

Kabashnikov, V. P., and Kmit, G. I., 1979, "Influence of Turbulent Fluctuations on Thermal Radiation," *Appl. Spect.*, Vol. 31, pp. 963–967.

Kounalakis, M. E., Gore, J. P., and Faeth, G. M., 1989, "Mean and Fluctuating Radiation Properties of Nonpremixed Turbulent Carbon Monoxide/Air Flames," ASME JOURNAL OF HEAT TRANSFER, Vol. 111, pp. 1021–1030.

Kounalakis, M. E., Sivathanu, Y. R., and Faeth, G. M., 1991, "Infrared Radiation Statistics of Nonluminous Turbulent Diffusion Flames," ASME JOURNAL OF HEAT TRANSFER, Vol. 113, pp. 437–445.

Sivathanu, Y. R., 1990, "Soot and Radiation Properties of Buoyant Turbulent Diffusion Flames," Ph. D. Thesis, The University of Michigan, Ann Arbor, MI.

Sivathanu, Y. R., and Faeth, G. M., 1990, "Temperature/Soot Volume Fractions Correlations in the Fuel-Rich Region of Buoyant Turbulent Diffusion Flames," *Comb. Flame*, Vol. 81, pp. 141–150.

Sivathanu, Y. R., Kounalakis, M. E., and Faeth, G. M., 1991a, "Soot and Continuum Radiation Statistics of Luminous Turbulent Diffusion Flames," *Twenty-Third Symposium (International) on Combustion*, The Combustion Institute, Pittsburgh, PA, pp. 1543–1550.

Sivathanu, Y. R., Gore, J. P., and Dolinar, J., 1991b, "Transient Scalar Properties of Strongly Radiating Jet Flames," *Combust. Sci. and Tech.*, Vol. 76, pp. 45–66.

Sivathanu, Y. R., and Gore, J. P., 1991, "Simultaneous Multiline Emission Absorption Measurements in Optically Thick Turbulent Flames," *Combust. Sci. and Tech.*, Vol. 80, pp. 1–21.

Tien, C. L., and Lee, S. C., 1982, "Flame Radiation," *Prog. Energy Combust. Sci.*, Vol. 8, pp. 41–59.

Heat Transfer Regimes in Microstructures

M. I. Flik
Assistant Professor.

B. I. Choi
Research Assistant.

K. E. Goodson
Research Assistant.

Department of Mechanical Engineering,
Massachusetts Institute of Technology,
Cambridge, MA 02139

Submicron dimensions are the hallmark of integrated electronic circuits, photovoltaic cells, sensors, and actuators. The design of these devices requires heat transfer analysis. Often it is not known to the designer whether a given microstructure can be analyzed using macroscale heat transfer theory, i.e., a method not considering the size dependence of a transport property such as thermal conductivity. This study develops regime maps showing the boundary between the macroscale and microscale heat transfer regimes. The maps relate the geometric dimension separating the two regimes to temperature for conduction in solids, to temperature, pressure, and Reynolds number for convection in gases, and to the temperature of the emitting medium for radiative transfer. The material purity and defect structure strongly influence the regime boundaries. Microstructures pertaining to a given technology are marked on these maps to determine whether macroscale heat transfer theory is applicable. By marking regions on the maps for the expected future development of microtechnologies, research needs in microscale heat transfer can be anticipated.

1 Introduction

Structures with dimensions between 100 μm and 50 Å can be fabricated with modern film deposition and patterning techniques. These microstructures are the basis of integrated electronic circuits, photovoltaic cells, sensors, and actuators. The analysis of heat transfer in these devices is essential for their successful design and fabrication. Often it is not known whether heat transfer in microstructures can be analyzed with *macroscale* theories, i.e., methods that do not consider the size dependence of a transport property such as thermal conductivity or thermal radiation reflectance.

If macroscale heat transfer theory is applied to a microstructure in a situation for which it is inappropriate, then a significant error in the calculated heat transfer rate or temperature distribution can result. Such an error can cause the device to be designed to perform in a suboptimal manner or prevent it from being able to function. In electronic devices, microscale effects in a thin layer can inhibit the flow of heat from hotspots within the layer, such as the channel of a MOSFET in silicon-on-insulator electronics, resulting in peaks of temperature of a magnitude greater than those predicted by macroscale analysis (Goodson and Flik, 1992). These temperature peaks can affect the performance of the device and reduce the mean time to failure of an electronic circuit. If the influence of the film thickness on the absorptance of an infrared radiation detector element is not considered, then the detector sensitivity is different from the design value. A pyrometric measurement of the substrate temperature during film deposition is in error if the emissivity variation with the film thickness is neglected, resulting in poor temperature control (Flik et al., 1992). The designer of microstructures must have a criterion with which to decide whether macroscale heat transfer theory can be applied to a given device or whether *microscale* theory must be used. Microscale theory determines the effect of the structure dimensions on a transport property by considering the physical mechanism of transport, e.g., electron conduction or electromagnetic wave propagation.

Fundamentals and applications were presented for microscale thermal conduction by Ziman (1960), Devienne (1965), and Tien et al. (1969), and for microscale thermal radiation by Yeh (1988), Cravalho et al. (1967), Armaly and Tien (1970), and Chen and Tien (1991). Recently, microscale heat transfer phenomena have received intensive interest due to the emergence of thermal microsensors (Udell et al., 1990) and high-T_c superconducting films (Flik and Tien, 1990; Goodson and Flik, 1991). None of these studies presented the boundary of the microscale heat transfer regime for a given transport mechanism in terms of parameters available to the microstructure designer, i.e., the structure dimensions and the operating temperature. Hence, based on these works it is not immediately possible to decide whether macroscale theory is applicable for a microstructure or not.

The present study develops heat transfer *regime maps* for microstructures relating a geometric length scale to temperature. The boundary between the microscale and macroscale regimes is determined as a function of temperature by the requirement that the application of macroscale theory yields an error in the transport property not exceeding 5 percent. Through the mechanistic length scale governing the transport process, this functional relation depends on the material properties, i.e., the scattering mechanisms for electron and phonon heat conduction in solids, and the electromagnetic dispersion relations for thermal radiation absorption. The geometric lengthscale is the smallest structure dimension, except for conduction in rapidly moving gases, where it is given by the boundary-layer thickness. Previous regime maps delineating boundaries between applicable theories of transport phenomena were published for rarified gas dynamics by Tsien (1946) and for thermal radiation in packed beds by Tien (1988). Recently, Majumdar (1991) illustrated the analogy between microscale conduction in dielectrics and radiative transfer, and presented a regime map for diamond films similar to the one in the present study.

The impact of these regime maps is twofold. First, specific microdevices can be represented with a region in a regime map, showing immediately whether or not a certain transport process in a given device can be analyzed with macroscale theory. Second, demands for future research in microscale heat transfer can be anticipated by marking regions in the regime maps that correspond to the expected development of a given microtechnology. This work does not present new physics information. It relies on known physical foundations of transport phenomena. But this knowledge has not been applied to date in thermal analysis and design. By providing regime maps, this work attempts to aid in the development of microscale thermal analysis and experimentation.

Contributed by the Heat Transfer Division for publication in the JOURNAL OF HEAT TRANSFER. Manuscript received by the Heat Transfer Division August 1991; revision received February 1992. Keywords: Conduction, Cryogenics, Radiation. Associate Technical Editor: L. S. Fletcher.

2 Mechanistic Length Scales

2.1 Thermal Conduction. *Mean Free Path.* In solids, heat is carried by electrons and lattice waves, whose quanta are phonons. In pure metals, the electron contribution is dominant. In dielectrics and semiconductors, the phonon contribution is dominant. In gases, heat is carried by molecules.

Kinetic theory yields the thermal conductivity (Rohsenow and Choi, 1961):

$$k=\frac{1}{3}C v \Lambda. \tag{1}$$

For gas conduction, the specific heat $C=C_m$ is that of the gas at constant volume per unit volume, $v=v_m$ is the average molecular velocity, and $\Lambda=\Lambda_m$ is the molecular mean free path. For thermal conduction in metals, $C=C_e$ is the electron specific heat, $v=v_e$ is the electron Fermi velocity (Kittel, 1986), and $\Lambda=\Lambda_e$ is the electron mean free path. For conduction in dielectrics and semiconductors, $C=C_s$ is the phonon specific heat, $v=v_s$ is the average speed of sound, and $\Lambda=\Lambda_s$ is the phonon mean free path. The specific heat C to be used in Eq. (1) is only that portion of the total specific heat which is due to the energy carrier.

Solids. Figure 1 illustrates that for a thin layer, the importance of boundary scattering increases with the ratio Λ/d, where Λ is the bulk value of the mean free path of the dominant carriers of heat, and d is the layer thickness. Scattering on the boundaries of the layer reduces the carrier mean free path from its bulk value, reducing the thermal conductivity according to Eq. (1). For $\Lambda \ll d$, this reduction may be neglected, but for $\Lambda \sim d$ and $\Lambda > d$, the effect of boundary scattering must be considered. For this case, the effective thermal conductivity even in an isotropic film depends on the direction of energy flow. In what follows, the effective thermal conductivity along the layer is the absolute value of the ratio of the heat flux to the temperature gradient along the layer. The effective thermal conductivity normal to the layer is the product of the heat flux normal to the layer and the layer thickness divided by the temperature difference between the top and bottom surfaces of the layer.

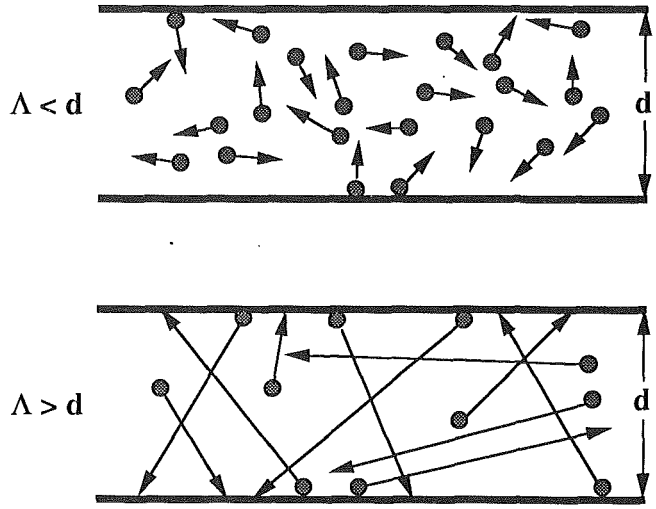

Fig. 1 Thermal conduction in a thin layer

Fuchs (1938) and Sondheimer (1952) determined the effect of the boundary scattering of electrons on the effective electrical conductivity along thin metal films by solving the Boltzmann equation. Tien et al. (1969) and Kumar and Vradis (1991) showed that this result may be used with little error up to room temperature to determine the effective thermal conductivity along thin metal films. Majumdar (1991) developed the equation of phonon radiative transfer from the Boltzmann equation to determine microscale phonon conduction in dielectrics. This equation considers the variation of the phonon free paths about the mean free path and the dependence of the phonon mean

Nomenclature

C = specific heat at constant volume per unit volume, J m^{-3} K^{-1}
D = molecular diameter, m
d = smallest dimension, m
e = electron charge = -1.60×10^{-19} C
h = heat transfer coefficient, W m^{-2} K^{-1}
i = $(-1)^{1/2}$
i'_λ = directional spectral intensity, W m$^{-2}\mu$m^{-1}sr^{-1}
k = thermal conductivity, W m^{-1}K^{-1}
k_B = Boltzmann constant = 1.38×10^{-23} J K^{-1}
L = smallest streamwise dimension, m
M = Mach number
m_e = electron mass = 9.11×10^{-31} kg
m_e^* = effective electron mass, kg
Nu = Nusselt number = hL/k
$\bar{n}$ = complex refractive index = $n + i\kappa$
n = real part of complex refractive index = refractive index
n_e = electron number density, m^{-3}
n_m = molecule number density, m^{-3}
Pr = Prandtl number = ν/α
p = pressure, N m^{-2}
R = reflectance
Re = Reynolds number = LV_∞/ν
R_I = reflectance calculated considering interference
R_N = reflectance calculated not considering interference
T = temperature, K
T_r = reference temperature, K, Eqs. (11), (13), and (14)
t = time, s
V_∞ = free-stream velocity, m s^{-1}
v = average carrier velocity, m s^{-1}
α = thermal diffusivity, m^2 s^{-1}
γ = Sommerfeld parameter, J m^{-3} K^{-2}
δ = boundary layer thickness, m; oxygen content parameter of $YBa_2Cu_3O_{7-\delta}$
ϵ = dielectric function
ϵ_0 = electric permittivity of vacuum = 8.85×10^{-12} C^{2}N^{-1}m^{-2}
ϵ_∞ = high-frequency dielectric constant
θ = Debye temperature, K
κ = imaginary part of complex refractive index = extinction coefficient
Λ = carrier mean free path, m
λ = wavelength in vacuum, m
ν = kinematic viscosity, m^2 s^{-1}
ρ = electrical resistivity, Ωm
σ = Stefan–Boltzmann constant = 5.67×10^{-8} W m^{-2} K^{-4}
τ = relaxation time = Λ/v, s
ϕ = phase difference = $4\pi nd/\lambda$
ω = frequency, rad s^{-1}
ω_p = plasma frequency, rad s^{-1}

Subscripts

A = I or N, Eq. (5)
e = electron property
e,i = electron property limited by scattering on imperfections
e,s = electron property limited by scattering on phonons
m = molecular property
p = photon property
s = phonon property
s,e = phonon property limited by scattering on electrons
s,i = phonon property limited by scattering on imperfections
s,s = phonon property limited by scattering on phonons
tot = total property

free path on the phonon frequency. Chen and Tien (1992) solved the equation of radiative transfer considering the transmission of carriers through the film boundaries to determine the effective thermal conductivity normal to and along GaAs films in a GaAs–AlGaAs multilayer structure. Because of the complexity of solutions to this equation and the uncertainty in the frequency dependence of the mean free path, the equation of phonon radiative transfer is not used to determine regime boundaries in the present work.

Flik and Tien (1990), by assuming that all carrier free paths are equal to the mean free path in the absence of boundary scattering, obtained approximate closed-form solutions for the effective electron or phonon conductivity along or normal to a film. The result for conduction along a film agrees within 20 percent with that of Fuchs (1938) and Sondheimer (1952). For $d > \Lambda$, the analysis of Flik and Tien (1990) yielded $k_{\text{eff}}/k = 1 - \Lambda/(3d)$ for the effective conductivity normal to the layer, and $k_{\text{eff}}/k = 1 - 2\Lambda/(3\pi d)$ for the effective conductivity along the layer, where k and Λ are the isotropic bulk values of the conductivity and the mean free path. The use of the bulk value of k rather than k_{eff} results in an error greater than 5 percent for $d < 7\ \Lambda$ for conduction normal to the layer, and for $d < 4.5\ \Lambda$ for conduction along the layer. These inequalities determine the microscale regimes in the present analysis.

These criteria determine whether the microscale effect increases the volume resistance of the film. They do not consider the thermal boundary resistance, which can cause the effective conductivity normal to multilayer structures to vary with the layer thicknesses. If the temperature difference across the interface is small and the temperature is below about 30 K, the thermal boundary resistance at a dielectric–dielectric or metal–dielectric interface is governed by the acoustic mismatch between the materials and is inversely proportional to the third power of the lower temperature (Swartz and Pohl, 1989). At temperatures above 100 K, the boundary resistance is between 10^{-7} and 10^{-8} m^2 K W^{-1} (Swartz and Pohl, 1989). The partial transmission of carriers through the boundaries, which is limited by the boundary resistance, is not considered in the present analysis. Partial transmission increases the free path of some carriers, and can reduce the dimension separating the microscale and macroscale regimes for conduction normal to a film. Chen and Tien (1992) showed that if the conduction in the bounding media is neglected and carrier transmission through the boundaries is diffuse, the effective phonon conductivity along a dielectric layer does not depend on the phonon transmission coefficients at the boundaries.

The hyberbolic heat conduction equation considers the finite propagation speed of energy and was proposed for use when the duration of a thermal disturbance is very small (Joseph and Preziosi, 1989, 1990), i.e., in a temporal microscale situation. For conduction in the absence of a heat source, the hyperbolic conduction equation is

$$\frac{\tau}{\alpha}\frac{\partial^2 T}{\partial t^2} + \frac{1}{\alpha}\frac{\partial T}{\partial t} = \nabla^2 T, \tag{2}$$

where α is the thermal diffusivity and τ is the relaxation time. The relaxation time is the average time a carrier travels between collisions and is given by $\tau = \Lambda/v$. Majumdar (1991) showed that Eq. (2) can be derived from the Boltzmann equation for dielectric films only if the film thickness is much larger than the phonon mean free path. Equation (2) reduces to the macroscale heat conduction equation if the second term on the left is much larger than the first term. Order-of-magnitude analysis yields the criterion $(\tau/\alpha)(\Delta T/\Delta t^2) \ll (1/\alpha)(\Delta T/\Delta t)$ for the macroscale regime, where Δt is the characteristic time scale of the heat transfer process and ΔT is the characteristic temperature difference. If for a thin layer of thickness d the characteristic time scale Δt is given by diffusion across the layer, then it satisfies $d \sim (\alpha \Delta t)^{1/2}$, and the macroscale criterion is $d^2 \gg \alpha\tau$. Using Eq. (1), the thermal diffusivity can be expressed as $\alpha = k/C \sim v\Lambda$. Since $\tau = \Lambda/v$, the final criterion for macroscale conduction is $d^2 \gg \Lambda^2$. If no time scales shorter than d^2/α are present, then the Fourier equation is valid for conduction across a thin film as long as carrier boundary scattering is not important. For shorter time scales, or if d is of the order of or smaller than Λ, the Fourier equation is not valid. Vedavarz et al. (1991) prepared a regime map for hyperbolic heat conduction, but their use of Eq. (2) in the regime of $d^2 \sim \Lambda^2$ requires further examination.

Moving Gases. The case of laminar gas convection from a surface with a large radius of curvature and $\text{Re}_L > 1$, where L is the streamwise dimension, is considered in the present analysis. For this case, the microscale regime is governed by the ratio of the molecular mean free path to the boundary layer thickness, Λ_m/δ. Tsien (1946) derived a regime map for this case, separating the macroscale regime from the slip-flow regime by the criterion $\Lambda_m/\delta = 0.01$. To obtain a more precise criterion in the present analysis, the result of Rohsenow and Choi (1961) is used for the average Nusselt number for slip-flow convection from a flat plate of length L in terms of the Mach number, M, the Reynolds number, Re_L, and the Prandtl number, Pr. In the macroscale limit, this solution approaches $\text{Nu} = 1.13\ (\text{Re}_L \text{Pr})^{1/2}$. For air convection with $\text{Pr} = 0.72$, this macroscale approximation exceeds the exact result by more than 5 percent for $\text{Re}_L^{1/2}/\text{M} < 55$. Tsien (1946) derived the relationship $L \sim (\text{Re}_L/\text{M})\Lambda_m$, yielding the microscale criterion $L < 55\ \text{Re}_L^{1/2}\Lambda_m$, which is used in the present analysis.

In a gas and a solid, heat transfer is modeled using carriers that move independently of one another between scattering events. Their interactions are characterized simply by the mean free path. In a liquid, transport phenomena cannot be explained by such ideal carriers. Cohesive forces between liquid molecules, such as van der Waals forces and those due to hydrogen bonds, are sufficiently strong to prevent random motion (Moore, 1972). Thus, a mechanistic length scale delineating the regime boundary for liquids may not be defined in the same way as for gases and solids, and further study is necessary for understanding microscale convection in liquids. Bankoff (1990) stated that the behavior of thin liquid films thinner than 100 nm is influenced by van der Waals forces. The flow of liquid in small channels has been studied by several groups. Experimental work provided conflicting results. Israelachvili (1986) measured the apparent viscosity of tetradecane, $CH_3(CH_2)_{12}CH_3$, and water flowing through a very thin gap. The apparent viscosities of the liquids did not depend on the gap size and were within 10 percent of their bulk values even for a gap thinner than 5 nm. This result is made plausible by classical theories for the viscosity and thermal conductivity of liquids (Bird et al., 1960), which are based on nearest-neighbor interactions between molecules, resulting in a mechanistic lengthscale of the order of the molecular size. Pfahler et al. (1991) measured the friction coefficients of silicon oil flowing in microchannels. In contrast to the observations of Israelachvili (1986), the apparent viscosities were smaller than the bulk viscosity and decreased with decreasing channel dimension. The study of liquid convection in microchannels is a fruitful field with technical impact.

2.2 Thermal Radiation. For thermal radiation, there are two mechanistic lengthscales, the photon mean free path and the wavelength within the medium of propagation. The two lengthscales are illustrated in Fig. 2 for a free-standing film. For normal incidence, the interference of light in a film is governed by the phase difference acquired upon traversing the film, $4\pi nd/\lambda$. The attenuation of the intensity of radiation in an absorbing medium is governed by the ratio of the film thickness to the photon mean free path, $\Lambda_p = \lambda/(4\pi\kappa)$.

The present discussion is limited to thin films. Microscale criteria for small particles and their agglomerates were reviewed by Tien (1988). The regime boundary was represented in terms of the particle size and the particle volume fraction. Chen and

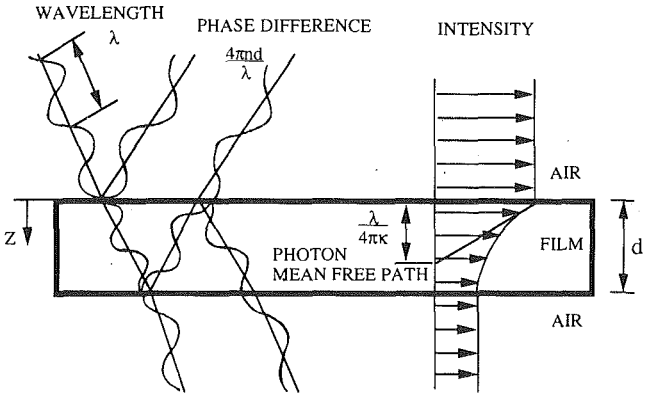

Fig. 2 Wave interference and attenuation in a thin layer

Tien (1991) discussed the regimes for thin-film optics and for geometric optics using the partial coherence theory. They obtained regime boundaries for a nearly monochromatic wave without considering dispersion. The finite bandwidth of the monochromatic wave produces incoherence and the regime boundary was expressed in terms of the product of the phase difference and the relative bandwidth of the wave. In the present study, the microscale regime boundary is determined considering radiation having the Planck energy distribution, and the frequency dependence of optical constants is considered. The regime maps for thin layers presented here are different from those of Chen and Tien (1991) because the current maps concern thermal radiation with a large bandwidth. Chen and Tien (1991) applied the partial coherence theory only to nearly monochromatic fields. However, the partial coherence formulation can be applied to thermal radiation with a large bandwidth if the film refractive index is independent of wavelength within the bandwidth.

Nonabsorbing Materials. If the film thickness is much larger than the wavelength, the reflectance can be predicted correctly by ray tracing. If the film thickness is less than or comparable to the wavelength in the film, the interference of waves has a measurable influence on the reflectance. The radiative transfer of nonabsorbing layers is defined to be microscale if the reflectance predicted by ray tracing differs by more than 5 percent from that predicted by accounting for interference. The light source is assumed to emit polychromatic thermal radiation. The microscale criterion is applied to the total normal reflectance for radiation having the spectral distribution of blackbody radiation.

The normal spectral reflectance of a single nonabsorbing layer considering interference, R_I, is given by thin-film optics (Yeh, 1988),

$$R_I = \frac{(n^2-1)^2\left[1-\cos\left(\frac{4\pi nd}{\lambda}\right)\right]}{n^4+6n^2+1-(n^2-1)^2\cos\left(\frac{4\pi nd}{\lambda}\right)}, \tag{3}$$

where n is the refractive index. The normal spectral reflectance without interference, R_N, is (Siegel and Howell, 1981)

$$R_N = \frac{(n-1)^2}{n^2+1}. \tag{4}$$

The total normal reflectance for radiation having the spectral distribution of blackbody radiation at temperature T is

$$R_{A,tot} = \frac{\int_{\lambda_1}^{\lambda_2} R_A\, e_b(\lambda, T)\, d\lambda}{\sigma T^4}, \qquad A = I \text{ or } N \tag{5}$$

where e_b is the blackbody emissive power. The numerical integration covers the spectral range from $\lambda_1 = 1666.7/T$ to $\lambda_2 = 16666.7/T$, which includes 95 percent of the total blackbody energy. As the film thickness is increased, the spacing of interference fringes decreases and the difference between $R_{N,tot}$ and $R_{I,tot}$ becomes smaller. The boundary between the microscale and the macroscale regimes is the film thickness for which the relative difference between $R_{N,tot}$ and $R_{I,tot}$ is equal to 5 percent. Equation (4) shows that in the macroscale regime, the reflectance does not depend on the film thickness. For a given nonabsorbing material, the regime boundary thickness is expressed in terms of the temperature of the emitting blackbody.

Absorbing Materials. Absorbing thin-film materials are technically important for application in radiation detectors. The radiative properties depend on the film thickness if it is smaller than the photon mean free path, Λ_p. The intensity of radiation at a depth z normal to the film surface is (Siegel and Howell, 1981)

$$i'_\lambda(z) = i'_\lambda(0)\exp\left(\frac{-z}{\Lambda_p}\right) = i'_\lambda(0)\exp\left(\frac{-4\pi\kappa z}{\lambda}\right) \tag{6}$$

where i'_λ is the directional spectral intensity and κ is the extinction coefficient. If the film thickness is greater than the photon mean free path, the absorption strongly reduces the intensity of the wave reflected at the second interface. If the film thickness is much greater than the photon mean free path, $d \gg \Lambda_p$, radiative properties can be obtained considering only the air–film interface and do not depend the film thickness, i.e., the film acts as a semi-infinite medium.

The boundary between the microscale and macroscale regimes is defined based on the total normal reflectance. The normal spectral reflectance, R_I, considering interference is given by Yeh (1988),

$$R_I = \left| \frac{1-\exp\left(i\frac{4\pi\bar{n}d}{\lambda}\right)}{\frac{1+\bar{n}}{1-\bar{n}} - \frac{1-\bar{n}}{1+\bar{n}}\exp\left(i\frac{4\pi\bar{n}d}{\lambda}\right)} \right|^2, \tag{7}$$

where $\bar{n}$ is the complex refractive index of the film material. The normal spectral reflectance of a semi-infinite medium, R_N, is

$$R_N = \frac{(n-1)^2+\kappa^2}{(n+1)^2+\kappa^2}. \tag{8}$$

The total normal reflectances, $R_{N,tot}$ and $R_{I,tot}$, are calculated from Eq. (5). The boundary between the microscale and the macroscale regimes is the film thickness for which the relative difference between $R_{N,tot}$ and $R_{I,tot}$ is equal to 5 percent.

3 Material Properties

3.1 Thermal Conduction. *Metals.* The theory of thermal conduction in metals was summarized by Wilson (1953) and Ziman (1960). The electron mean free path may be obtained from experimental values of the thermal conductivity using Eq. (1), the electron specific heat, C_e, and the Fermi velocity, v_e. The thermal conductivity of metals was given by Touloukian et al. (1970). The Fermi velocities of electrons in metals are of the order of 10^6 m s^{-1} and were tabulated by Kittel (1986). The volumetric specific heat of electrons, C_e, is proportional to temperature,

$$C_e = \gamma T, \tag{9}$$

The Sommerfeld parameter, γ, was tabulated for metals by Kittel (1986) and is of the order of 100 J m^{-3} K^{-2}.

The mean free path of electrons in metals is limited by scattering on imperfections and phonons. Imperfections include impurity atoms and lattice defects. Matthiessen's rule

breaks the inverse electron mean free path, $1/\Lambda_e$, into components due to imperfection scattering, $1/\Lambda_{e,i}$, and phonon scattering, $1/\Lambda_{e,s}$,

$$\frac{1}{\Lambda_e}=\frac{1}{\Lambda_{e,i}}+\frac{1}{\Lambda_{e,s}}. \tag{10}$$

The imperfection-limited mean free path $\Lambda_{e,i}$ is independent of temperature, while the phonon-limited mean free path $\Lambda_{e,s}$ decreases with increasing temperature. At very low temperatures, $T \ll \theta$, where θ is the Debye temperature, the absence of phonon scattering allows $\Lambda_{e,i}$ to be determined.

The scattering of electrons on phonons dominates over the scattering of electrons on imperfections above a temperature near 50 K. When phonon scattering dominates, $\Lambda_{e,s}$ can be determined from thermal conductivity data using Eq. (1). The value of $\Lambda_{e,s}$ may be extrapolated to lower temperatures using the formula of Wilson (1953) for electron thermal conduction limited by scattering on phonons. At temperatures below a low reference temperature, $T<T_r<\theta/10$, this formula may be simplified with less than 10 percent error in metals to $k_{e,s}(T)/k_{e,s}(T_r)=(T_r/T)^2$. This result and Eqs. (1) and (9) yield the mean free path for $T<T_r$,

$$\frac{\Lambda_{e,s}(T)}{\Lambda_{e,s}(T_r)}=\left(\frac{T_r}{T}\right)^3,\quad T_r<\theta/10. \tag{11}$$

Dielectrics and Semiconductors. Phonon conduction in dielectrics and semiconductors was reviewed by Ziman (1960). The phonon mean free path in dielectrics is calculated from experimental conductivity data using Eq. (1), the phonon specific heat, C_s, and the average speed of sound in the material, v_s. The specific heats of dielectrics and semiconductors were given by Touloukian and Buyco (1970a, 1970b).

Phonon conduction in dielectrics is limited by scattering on other phonons and on imperfections, which include lattice defects and isotopes. In doped semiconductors, the free carriers also scatter phonons. Matthiessen's rule yields (Ziman, 1960)

$$\frac{1}{\Lambda_s}=\frac{1}{\Lambda_{s,i}}+\frac{1}{\Lambda_{s,s}}+\frac{1}{\Lambda_{s,e}}, \tag{12}$$

where Λ_s is the phonon mean free path, $\Lambda_{s,i}$ is the phonon mean free path limited by scattering on imperfections, $\Lambda_{s,s}$ is the phonon mean free path limited by scattering on phonons, and $\Lambda_{s,e}$ is the phonon mean free path limited by scattering on free carriers in semiconductors. The third term on the right of Eq. (12) is zero for dielectrics.

Below a reference temperature, $T<T_r\ll\theta$, the phonon mean free path limited by scattering on phonons is approximately

$$\frac{\Lambda_{s,s}(T)}{\Lambda_{s,s}(T_r)}=\exp\left[\frac{\theta}{2}\left(\frac{1}{T}-\frac{1}{T_r}\right)\right]. \tag{13}$$

At low temperatures, the phonon mean free path in undoped crystals is limited by scattering on isotopes and point imperfections. When this mechanism is dominant and $T<T_r\ll\theta$, the phonon mean free path is well approximated by (Berman et al., 1956)

$$\frac{\Lambda_s(T)}{\Lambda_s(T_r)}=\left(\frac{T_r}{T}\right)^4. \tag{14}$$

Gases. Rohsenow and Choi (1961) derived an approximate expression for the mean free path of a gas molecule,

$$\Lambda_m=\frac{1}{n_m \pi D^2}, \tag{15}$$

where n_m is the number density of molecules. The molecular diameter D was tabulated for technically important gases by Hirschfelder et al. (1954). Values of D include 0.2789 nm for neon, 0.3617 nm for air, and 0.4055 nm for xenon. The values of D for xenon and neon bound those for the most important gases.

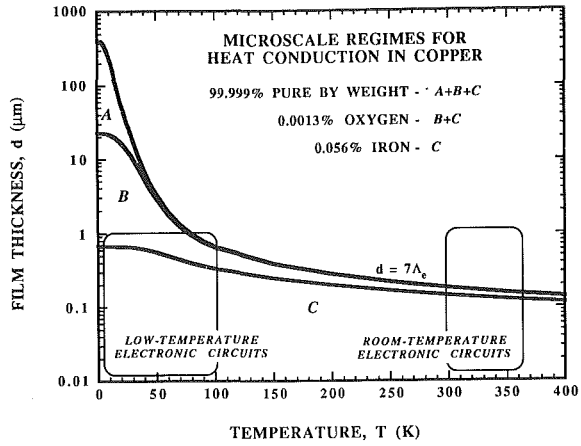

Fig. 3 Regime map for thermal conduction normal to copper films

If the gas is ideal, the molecular number density is related to the pressure, p, and temperature, T, by $p=n_m k_B T$, where $k_B=1.38\times10^{-23}$ J K^{-1} is the Boltzmann constant. Using Eq. (15), the mean free path is

$$\Lambda_m=\frac{k_B T}{\pi D^2 p}. \tag{16}$$

3.2 Thermal Radiation. The optical behavior of materials is governed by the complex refractive index, $n+i\kappa$. In doped semiconductors, the imaginary part increases with the carrier number density. The optical properties of doped semiconductors are described by the Drude model (Senitzky and Weeks, 1981). The dielectric function is

$$\epsilon=\epsilon_\infty+\frac{i\omega_p^2}{\omega(1/\tau-i\omega)}, \tag{17}$$

where ω is the frequency, ω_p is the plasma frequency, and ϵ_∞ is the high-frequency dielectric constant. The plasma frequency is $\omega_p=(n_e e^2/m_e^*\epsilon_0)^{1/2}$, where m_e^* is the electron effective mass and ϵ_0 is the vacuum electrical permittivity.

The optical properties of the high-temperature superconductor $YBa_2Cu_3O_{7-\delta}$ vary dramatically with varying oxygen content ($6.0<7-\delta\le7.0$) (Kamaras et al., 1989; Bozovic, 1990). The optical properties of $YBa_2Cu_3O_6$ are important for the thermal analysis of the film deposition process (Flik et al., 1992). Choi et al. (1991) obtained the optical constants of $YBa_2Cu_3O_{7-\delta}$ films with varying oxygen content by fitting the measured reflectance to the Drude-Lorentz model. An $YBa_2Cu_3O_7$ film has a highly metallic behavior. As the oxygen content of the film decreases, the film becomes more transparent.

The optical constants are assumed to be independent of the film thickness. When the electron mean free path or the radius of an electron-hole pair is comparable to the film thickness, then the optical constants depend on the film thickness. The present study does not account for the influence of the film thickness on n and κ.

4 Regime Maps

4.1 Thermal Conduction. Figure 3 shows the regimes for thermal conduction in annealed, polycrystalline copper. The mean free path is given by Eq. (10). Above 30 K, $\Lambda_{e,s}$ is obtained using Eqs. (1) and (9) and values of the thermal conductivity recommended by Touloukian et al. (1970). Below 30 K, $\Lambda_{e,s}$ is obtained using Eq. (11) with $T_r=30$ K. Based on Eqs. (1) and (9) and low-temperature thermal conductivity data from the following sources, the imperfection-limited mean free path for copper at least 99.999 percent pure by weight is $\Lambda_{e,i}=57$ μm

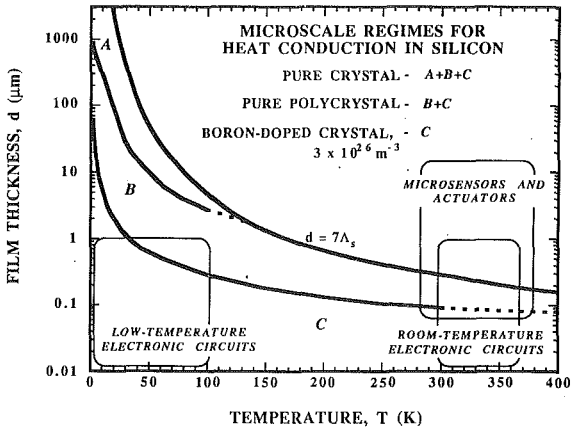

Fig. 4 Regime map for thermal conduction normal to silicon films

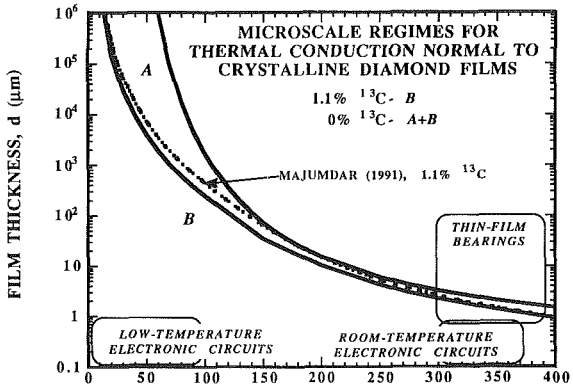

Fig. 5 Regime map for thermal conduction normal to diamond films

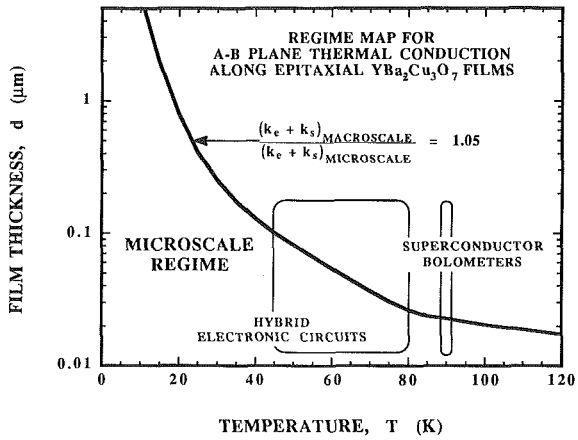

Fig. 6 Regime map for thermal conduction along epitaxial films of the high-T_c superconductor $YBa_2Cu_3O_7$

(White and Tainsh, 1960), for copper containing 0.0013 percent oxygen it is $\Lambda_{e,i} = 3.2$ μm (Powell et al., 1957), and for copper containing 0.056 percent iron it is $\Lambda_{e,i} = 0.096$ μm (White and Woods, 1954). Below 30 K, the film thickness denoting the microscale regime boundary varies by three orders of magnitude depending on the purity. In cryogenic electronics applications, the effective thermal conductivity of almost all copper films is size dependent, while at room temperature films of thickness greater than about 0.1 μm belong to the macroscale regime.

Figure 4 is a regime map for thermal conduction normal to silicon layers. The average speed of sound is $v_s = 6500$ m s^{-1} (McSkimin, 1953) and the values of the pure crystalline thermal conductivity are those recommended by Touloukian et al. (1970). The mean free path is extrapolated to low temperatures for an infinite crystal using Eq. (14) with $T_r = 25$ K. The data of Rosenberg (1954) are employed for the thermal conductivity of polycrystalline silicon below 100 K. The dashed curve section in the left of Fig. 4 indicates that the mean free paths for the crystal and polycrystal must approach one another with increasing temperature and is not supported by experimental data. Slack (1964) gave the thermal conductivity of a boron-doped silicon crystal from which the dashed curve section on the right of Fig. 4 is extrapolated. The dimension bounding the microscale regime is highly dependent on the carrier concentration, and at low temperatures it is reduced by grain boundary scattering in a polycrystalline specimen compared to a crystal. Silicon microstructures used in the majority of room-temperature sensors and actuators do not exhibit a size-dependent thermal conductivity, in contrast to films in low-temperature electronic circuits. The doping level determines whether a silicon film is in the microscale conduction regime at room temperature.

Regimes for conduction normal to type IIa diamond films are shown in Fig. 5. The thermal conductivity was given by Berman et al. (1956) and the average speed of sound, $v_s = 13{,}500$ m s^{-1}, by McSkimm and Andreatch (1972). Equation (14) determines the imperfection-limited mean free path at temperatures where boundary scattering was important. The reference temperature is $T_r = 100$ K, which satisfies $T_r \ll \theta$ because the Debye temperature of diamond is $\theta = 1880$ K. Although the primary constituent of diamond is the ^{12}C atom, naturally occurring diamond contains 1.1 percent of the isotope ^{13}C. At low temperatures, scattering on this isotope limits the thermal conductivity of natural diamond. Majumdar (1991) presented an algorithm to determine the regime boundary for diamond as a function of the fraction of ^{13}C. In Fig. 5, the regime boundary for diamond with a ^{13}C content of 1.1 percent calculated using his algorithm is shown to be in agreement with the regime boundary of the present analysis.

Anthony et al. (1990) achieved a ^{13}C content of 0.07 percent in a synthetic diamond crystal and showed that its thermal conductivity at room temperature was 50 percent greater than that measured previously for diamond. Based on this result, the mean free path of a hypothetical crystal containing no isotopes or lattice defects is estimated using Eq. (13) with $T_r = 300$ K. The microscale regime for this case is shown in Fig. 5 and indicates the largest value of d for a given temperature at which microscale conduction may ever occur in diamond. The regime map shows that it is not possible to achieve in thin diamond films in electronic circuits the same high thermal conductivities measured in bulk crystals. Because of the low coefficient of friction between diamond surfaces, diamond films possess great potential for application as bearing materials (Guyer and Koshland, 1990). Figure 5 shows that for room-temperature applications, the thermal conductivity of bearing films thinner than 3 μm is size dependent. This fact can strongly affect the temperature fields existing in such bearings due to dissipation.

Figure 6 concerns thermal conduction *along* epitaxial films of the high-temperature superconductor $YBa_2Cu_3O_7$. The orthorhombic, nearly tetragonal crystal structure of this material results in similar thermal conductivities in the a and b crystal axis directions, but a different thermal conductivity in the c direction. The films with the best superconducting properties are deposited epitaxially with the c axis normal to the film surface, such that conduction along the films occurs in the a-b plane. Goodson and Flik (1991) determined the contribution of each carrier to energy transport and its mean free path as functions of temperature. The thinnest high-T_c superconductor films will exhibit microscale conduction in detectors and electronic circuits. Flik and Hijikata (1990) demonstrated that thermal conduction in hybrid superconducting-semiconducting electronic circuits results in a packing limit.

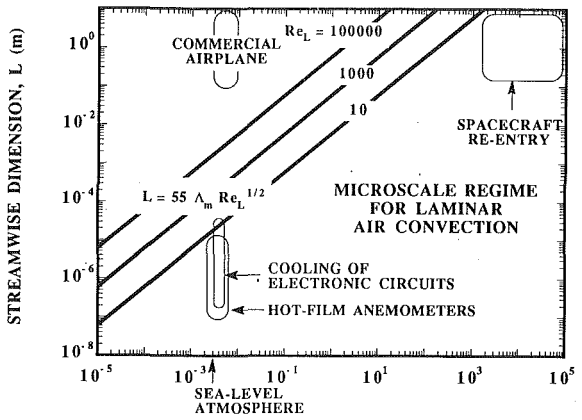

Fig. 7 Approximate regime map for air convection

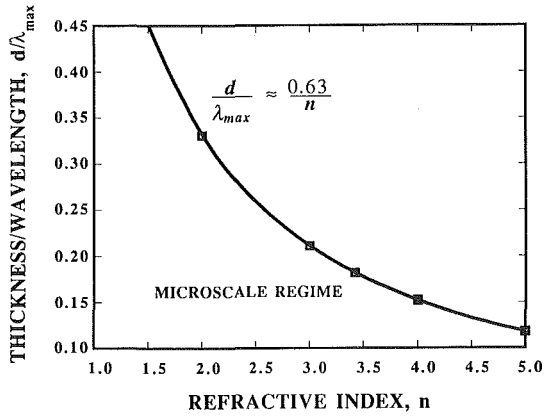

Fig. 8 General regime map for reflection from nonabsorbing films

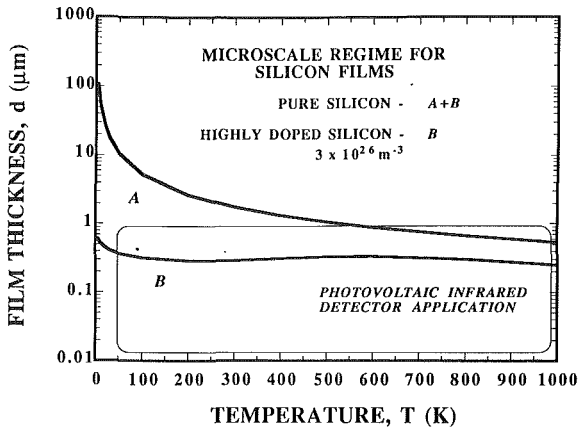

Fig. 9 Regime map for reflection from silicon films

Air convection regimes are shown in Fig. 7. The regime maps for other gases can be constructed from the air regime map by substituting the mean free path of the particular gas, which depends on the molecular diameter. Convective heat transfer from individual electronic devices and from hot-film mass-flow sensors does not follow the continuum theory. Commercial airplanes fall well within the continuum regime, in contrast to convection from spacecraft re-entering the atmosphere of the earth.

4.2 Thermal Radiation. Figure 8 displays the microscale regime for reflection from nonabsorbing materials. The film thickness is normalized by the wavelength where blackbody radiation has the maximum spectral energy for a given temperature, λ_{max}, which is given by Wien's displacement law, $\lambda_{max}T = 2897.8\ \mu m$ K. The refractive index is assumed to be constant over the total spectral range. For materials used for windows and filters, generally the refractive index does not change strongly within the transparent spectral range. Pure silicon has a refractive index close to 3.42 for the whole infrared range (Edwards, 1985). ZnS has $2.1 \le n \le 2.4$ for $0.5\ \mu m \le \lambda \le 14\ \mu m$ and ZnSe has $2.3 \le n \le 2.7$ for $0.55\ \mu m \le \lambda \le 18\ \mu m$ (Li, 1984). For all materials whose refractive indices vary little with wavelength, the generalized regime map of Fig. 8 can be used.

The boundary between the microscale and macroscale regimes can be approximated as $d/\lambda_{max} \approx 0.63/n$. Since the mechanistic lengthscale associated with the wave interference is $\lambda/4\pi n$, the film thickness denoting the regime boundary decreases as the refractive index increases. As the refractive index approaches unity, the reflectance of the film approaches zero. In this limit, even a small difference between $R_{N,tot}$ and $R_{I,tot}$ produces a large relative error and the film thickness that separates the regimes increases dramatically. In contrast, for large n the reflectance is close to unity, and the film must be very thin to exhibit a size-dependent reflectance. If the partial coherence theory presented by Chen and Tien (1991) is used, the regime boundary between partial coherence and incoherence is $d/\lambda_{max} = 0.40/n$. The regime boundary is based on the mutual coherence function and the relative error between $R_{N,tot}$ and $R_{I,tot}$ is between 10 and 20 percent. This error is larger than 5 percent, which is used to determine the regime boundary of the present study. The present regime boundary is more stringent.

In pure silicon, the imaginary part of the complex refractive index is extremely small in the whole infrared range (Edwards, 1985). For highly doped silicon, the optical constants are calculated from Eq. (17). The high-frequency dielectric constant and effective mass were given as $\epsilon_\infty = 11.7$ and $m_e^* = 0.26\ m_e$ by Spitzer and Fan (1957). The plasma frequency and relaxation time are (Senitzky and Weeks, 1981),

$$(\omega_p/\omega) = (5.87 \times 10^{-14}\ \mu m^{-1}\ m^{3/2})\ \lambda (n_e)^{1/2}, \qquad (18)$$

$$(1/\tau\omega) = [5.74 \times 10^{-23}\ \mu m^{-1}\ m^3\ (\Omega m)^{-1}]\lambda\ n_e \rho, \qquad (19)$$

where λ is the wavelength in a vacuum and ρ is the d-c electrical resistivity. The dependence of the d-c resistivity of doped silicon on the carrier density was given by Irvin (1962). The refractive index is obtained from the relation $n + i\kappa = \epsilon^{1/2}$.

The regime map for pure and highly doped silicon films is shown in Fig. 9. The region below each curve is the microscale regime. The temperature denotes that of the blackbody emitting the radiation, which is reflected by the room-temperature film. When the film temperature differs from room temperature, a new regime map must be constructed using the optical properties at that temperature. The regime boundary for pure silicon is derived from the results of Fig. 8 using $n = 3.42$. Since the highly doped silicon film has a high density of free carriers, it shows metallic optical behavior. For highly doped silicon films, the boundary of the microscale regime is determined by the attenuation criterion. The photon mean free path of doped silicon is found to be nearly wavelength independent for wavelengths up to 30 μm because the extinction coefficient increases proportional to the wavelength. The regime boundary of the doped silicon film is independent of temperature above 100 K. In photovoltaic infrared detector applications, doped silicon films with thicknesses less than 0.3 μm are in the microscale regime.

Figure 10 shows the regime map for $YBa_2Cu_3O_{7-\delta}$ films with three different oxygen contents. The oxygen content has a similar influence on the reflectance as the doping level of a semiconductor. The films with oxygen contents of 7.0 and 6.6 are highly absorbing and the boundary between the microscale and macroscale regimes is determined by the attenuation cri-

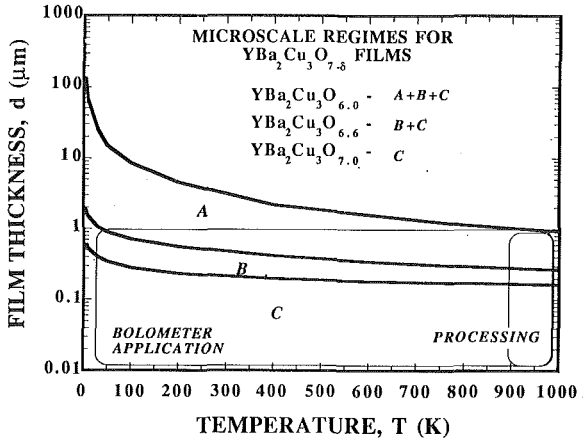

Fig. 10 Regime map for reflection from superconducting $YBa_2Cu_3O_{7-\delta}$ films

terion. The $YBa_2Cu_3O_6$ film has the optical properties of a dielectric material and the boundary of the microscale regime is determined by the interference criterion. It is shown in Fig. 10 that in bolometer applications of $YBa_2Cu_3O_7$ and during the film deposition process ($YBa_2Cu_3O_6$), thin films of this superconductor exhibit strong microscale behavior. The emittance change with the growth of the film is a major process control problem (Flik et al., 1992).

5 Concluding Remarks

The criteria developed for microscale conduction, convection, and radiation are summarized in Table 1.

5.1 Thermal Conduction. For thermal conduction in solids, the dimension that separates the microscale and macroscale regimes is related to the carrier mean free path and depends strongly on the purity and microstructure of the solid. The present regime maps do not consider the effect of the transmission of carriers through interfaces, which was accounted for by Chen and Tien (1992) in an analysis of the thermal conductivity of multiple quantum wells.

For gas convection, the streamwise length denoting the microscale regime boundary is linearly related to $Re^{1/2}T/p$. No simple regime maps may be constructed for liquid convection, due to the complexity of the intermolecular and surface forces. Investigations of the microscale regime boundary for liquid convection are particularly warranted in view of the results of Pfahler et al. (1991).

5.2 Thermal Radiation. Regime maps for thermal radiation must consider the entire spectral region of the Planck energy distribution and account for the spectral variation of optical constants. The microscale regime boundary is determined by two mechanistic length scales: the wavelength in the medium for nonabsorbing materials and, in addition, the photon mean free path for absorbing materials. For nonabsorbing materials, the regime boundary is $d=0.63\ \lambda_{max}/n$ if n is independent of wavelength.

The optical constants n and κ of the microstructures are assumed to be the same as those of the bulk materials. They may change, however, if the size of the microstructures approaches the electron mean free path or the exciton radius. Further study is required to determine size effects on optical constants.

5.3 Property Measurements. The present state of research in microscale heat transfer displays an imbalance between theoretical and experimental achievements. In the area of thermal conduction in solids, several excellent computational studies were presented recently (Majumdar, 1991; Kumar and Vradis, 1991). But it was not possible to verify these predictions experimentally. More experiments on microscale heat conduction must be performed. In the area of microscale radiation, experiments are needed on the size dependence of the optical constants of microstructures, such as multiple quantum wells, quantum wires, and quantum dots.

Table 1. Summary of microscale regime criteria

	MICROSCALE CRITERION	REFER TO THESE EQUATIONS
Thermal Conduction: Metal Films	$d < 7\Lambda_e$	(1), (9), (10), (11)
Thermal Conduction: Semiconducting and Dielectric Films	$d < 7\Lambda_s$	(1), (12), (13), (14)
Thermal Convection: Air	$L < 55\ Re_L^{1/2}\Lambda_m$	(1), (15), (16)
Thermal Radiation: Reflection From Non-absorbing Films	$d < 0.63\lambda_{max}/n$	(3), (4), (5)
Thermal Radiation: Reflection From Absorbing Films	No explicit form	(6), (7), (8), (17), (18), (19)

Acknowledgments

This work owes its basic ideas to a seminar held by Professor C. L. Tien at the University of California, Berkeley, in the spring term of 1988. Discussions with Professors M. Kaviany and A. Bar-Cohen contributed to this study. K. E. G. acknowledges the support of the Office of Naval Research through an academic fellowship. B. I. C. is grateful to the Consortium for Superconducting Electronics for DARPA support under contract number MDA 972-90-C-0021.

References

Anthony, T. R., Banholzer, W. F., Fleischer, J. F., Wei, L., Kuo, P. K., Thomas, R. L., and Pryor, R. W., 1990, "Thermal Diffusivity of Isotopically Enriched ^{12}C Diamond," *Phys. Rev. B*, Vol. 42, pp. 1104-1111.

Armaly, B. F., and Tien, C. L., 1970, "Emissivities of Thin Metallic Films at Cryogenic Temperatures," *Proc. 4th International Heat Transfer Conference*, Vol. 3, pp. R1.1-R1.9, Elsevier, Amsterdam, The Netherlands.

Bankoff, S. G., 1990, "Dynamics and Stability of Thin Heated Liquid Films," ASME JOURNAL OF HEAT TRANSFER, Vol. 112, pp. 538-546.

Berman, R., Foster, E. L., and Ziman, J. M., 1956, "The Thermal Conductivity of Dielectric Crystals: The Effect of Isotopes," *Proc. R. Soc. London, Ser. A*, Vol. 237, pp. 344-354.

Bird, R. B., Stewart, W. E., and Lightfoot, E. N., 1960, *Transport Phenomena*, Wiley, New York, pp. 26-29, 260-261.

Bozovic, I., 1990, "Plasmons in Cuprate Superconductors," *Phys. Rev. B*, Vol. 42, pp. 1969-1984.

Chen, G., and Tien, C. L., 1991, "Partial Coherence Theory of Thin Film Radiative Properties," *Thin-Film Heat Transfer—Properties and Processing*, M. K. Alam et al., eds., ASME HTD-Vol. 184, pp. 9-20.

Chen, G., and Tien, C. L., 1992, "Thermal Conductivity of Quantum Well Structures," *AIAA 30th Aerospace Science Meeting*, Reno, NV, Jan. 6-9, Paper No. 92-0707.

Choi, B. I., Zhang, Z. M., Flik, M. I., and Siegrist, T., 1991, "Radiative Properties of Y-Ba-Cu-O Films With Variable Oxygen Content," *Thin-Film Heat Transfer—Properties and Processing*, M. K. Alam et al., eds., ASME HTD-Vol. 184, pp. 73-80; to appear in ASME JOURNAL OF HEAT TRANSFER.

Cravalho, E. G., Tien, C. L., and Caren, R. P., 1967, "Effect of Small Spacings on Radiative Transfer Between Two Dielectrics," ASME JOURNAL OF HEAT TRANSFER, Vol. 89, pp. 351-358.

Devienne, F. M., 1965, "Low Density Heat Transfer," *Advances in Heat Transfer*, Vol. 2, J. P. Hartnett and T. F. Irvine, Jr., eds., Academic Press, New York, pp. 271-356.

Edwards, D. F., 1985, "Silicon," in: *Handbook of Optical Constants of Solids*, E. D. Palik, ed., Academic Press, Orlando, FL, pp. 547-569.

Flik, M. I., and Hijikata, K., 1990, "Approximate Thermal Packaging Limit for Hybrid Superconductor-Semiconductor Electronic Circuits," *Heat Transfer 1990*, G. Hetsroni, ed., Vol. 2, pp. 319-324, Hemisphere, New York.

Flik, M. I., and Tien, C. L., 1990, "Size Effect on the Thermal Conductivity of High-T_c Thin-Film Superconductors," ASME JOURNAL OF HEAT TRANSFER, Vol. 112, pp. 872-881.

Flik, M. I., Choi, B. I., Anderson, A. C., and Westerheim, A. C., 1992, "Thermal Analysis and Control for Sputtering Deposition of High-T_c Superconducting Films," ASME JOURNAL OF HEAT TRANSFER, Vol. 114, pp. 255-263.

Fuchs, K., 1938, "The Conductivity of Thin Metallic Films According to the Electron Theory of Metals," *Proc. Cambridge Phil. Soc.*, Vol. 34, pp. 100-108.

Goodson, K. E., and Flik, M. I., 1991, "Electron and Phonon Thermal Conduction in Epitaxial High-T_c Superconducting Films," in: *Cryogenic Heat Transfer*, A. Adorjan and A. Bejan, eds., ASME HTD-Vol. 16, pp. 27-35; to appear in ASME JOURNAL OF HEAT TRANSFER.

Goodson, K. E., and Flik, M. I., 1992, "Effect of Microscale Heat Conduction on the Packing Limit of Silicon-on-Insulator Electronics," Proceedings of the *Third Intersociety Conference on Thermal Phenomena in Electronic Systems*, Feb. 5-7, Austin, TX, A. Ortega and S. Oktay, eds., pp. 122-126, IEEE Catalog No. 92CH3096-5, New York; to appear in *IEEE Trans. on Components, Hybrids, and Manufacturing Technology*.

Guyer, R. L., and Koshland, D. E., Jr., 1990, "Diamond: Glittering Prize for Materials Science," *Science*, Vol. 250, pp. 1640-1643.

Hirschfelder, J. O., Curtiss, C. F., and Bird, R. B., 1954, *Molecular Theory of Gases and Liquids*, Wiley, New York, pp. 1110-1111.

Irvin, J. C., 1962, "Resistivity of Bulk Silicon and of Diffused Layers in Silicon," *Bell System Tech.*, Vol. 41, pp. 387-410.

Israelachvili, J. N., 1986, "Measurement of the Viscosity of Liquids in Very Thin Films," *J. Colloid and Interface Science*, Vol. 110, pp. 263-271.

Joseph, D. D., and Preziosi, L., 1989, "Heat Waves," *Rev. Mod. Phys.*, Vol. 61, pp. 41-73.

Joseph, D. D., and Preziosi, L., 1990, "Addendum to the Paper Heat Waves," *Rev. Mod. Phys.*, Vol. 62, pp. 375-391.

Kamaras, K., Herr, S. L., Porter, C. D., Tanner, D. B., Etemad, S., and Chan, S. W., 1989, "Optical Excitations in Thin Film $YBa_2Cu_3O_7$," in: *Progress in High Temperature Superconductivity*, Vol. 17, L. H. Bennet, Y. Flom, and G. C. Vezzoli, eds., World Scientific Publishing Co., Singapore.

Kennard, E. H., 1938, *Kinetic Theory of Gases*, McGraw-Hill, New York, pp. 311-327.

Kittel, C., 1986, *Introduction to Solid State Physics*, Wiley, New York, pp. 134, 141.

Kumar, S., and Vradis, G. C., 1991, "Thermal Conduction by Electrons Along Thin Films: Effects of Thickness According to Boltzmann Transport Theory," *Micromechanical Sensors, Actuators, and Systems*, D. Cho et al., eds., ASME DSC-Vol. 32, pp. 89-101.

Li, H. H., 1984, "Refractive Index of ZnS, ZnSe, and ZnTe and Its Wavelength and Temperature Derivatives," *J. Phys. Chem. Ref. Data*, Vol. 13, pp. 103-150.

Majumdar, A., 1991, "Microscale Heat Conduction in Dielectric Thin Films," *Thin-Film Heat Transfer—Properties and Processing*, M. K. Alam et al., eds., ASME HTD-Vol. 184, pp. 33-42.

McSkimin, H. J., 1953, "Measurement of Elastic Constants at Low Temperatures by Means of Ultrasonic Waves—Data for Silicon and Germanium Single Crystals, and for Fused Silica," *J. Appl. Phys.*, Vol. 24, pp. 988-997.

McSkimin, H. J., and Andreatch, P., Jr., 1972, "Elastic Moduli of Diamond as a Function of Pressure and Temperature," *J. Appl. Phys.*, Vol. 43, pp. 2944-2948.

Moore, W. J., 1972, *Physical Chemistry*, 4th ed., Prentice-Hall, Englewood Cliffs, NJ, Chap. 19.

Pfahler, J., Harley, J., Bau, H., and Zemel, J. N., 1991, "Gas and Liquid Flow in Small Channels," *Micromechanical Sensors, Actuators, and Systems*, D. Cho et al., eds., ASME DSC-Vol. 32, pp. 49-60.

Powell, R. L., Rogers, W. M., and Coffin, D. O., 1957, "An Apparatus for Measurement of Thermal Conductivity of Solids at Low Temperatures," *J. Res. N. Bur. Stand.*, Vol. 59, pp. 349-355.

Rohsenow, W. M., and Choi, H. Y., 1961, *Heat, Mass, and Momentum Transfer*, Prentice-Hall, Englewood Cliffs, NJ, Chaps. 11 and 20.

Rosenberg, H. M., 1954, "The Thermal Conductivity of Germanium and Silicon at Low Temperatures," *Proc. Phys. Soc., London*, Vol. A67, pp. 837-840.

Senitzky, B., and Weeks, S. P., 1981, "Infrared Reflectance Spectra of Thin Expitaxial Silicon Layers," *J. Appl. Phys.*, Vol. 52, pp. 5308-5314.

Siegel, R., and Howell, J. R., 1981, *Thermal Radiation Heat Transfer*, 2nd ed., McGraw-Hill, New York, Chap. 19.

Slack, G. A., 1964, "Thermal Conductivity of Pure and Impure Silicon, Silicon Carbide, and Diamond," *J. Appl. Phys.*, Vol. 35, pp. 3460-3466.

Sondheimer, E. H., 1952, "The Mean Free Path of Electrons in Metals," *Advances in Physics*, Vol. 1, pp. 1-42.

Spitzer, W. G., and Fan, H. Y., 1957, "Determination of Optical Constants and Carrier Effective Mass of Semiconductors," *Phys. Rev.*, Vol. 106, pp. 882-890.

Swartz, E. T., and Pohl, R. O., 1989, "Thermal Boundary Resistance," *Rev. Mod. Phys.*, Vol. 61, pp. 605-668.

Tien, C. L., 1988, "Thermal Radiation in Packed and Fluidized Beds," ASME JOURNAL OF HEAT TRANSFER, Vol. 110, pp. 1230-1242.

Tien, C. L., Armaly, B. F., and Jagannathan, P. S., 1969, "Thermal Conductivity of Thin Metallic Films and Wires at Cryogenic Temperatures," *Proc. 8th Thermal Conductivity Conference*, Plenum Press, New York, pp. 13-19.

Touloukian, Y. S., Powell, R. W., Ho, C. Y., and Klemens, P. G., 1970, "Thermal Conductivity: Metallic Elements and Alloys," *Thermophysical Properties of Matter*, Vol. 1, IFI/Plenum, New York.

Touloukian, Y. S., and Buyco, E. H., 1970a, "Specific Heat: Metallic Elements and Alloys," *Thermophysical Properties of Matter*, Vol. 4, IFI/Plenum, New York.

Touloukian, Y. S., and Buyco, E. H., 1970b, "Specific Heat: Nonmetallic Solids," *Thermophysical Properties of Matter*, Vol. 5, IFI/Plenum, New York.

Tsien, H. S., 1946, "Superaerodynamics," *J. Aero Sci.*, Vol. 13, pp. 653-664.

Udell, K. S., Pisano, A. P., Howe, R. T., Muller, R. S., and White, R. M., 1990, "Microsensors for Heat Transfer and Fluid Flow Measurements," *Experimental Thermal and Fluid Science*, Vol. 3, pp. 52-59.

Vedavarz, A., Kumar, S., and Moallemi, M. K., 1991, "Significance of Non-Fourier Heat Waves in Microscale Conduction," *Micromechanical Sensors, Actuators, and Systems*, D. Cho et al., eds., ASME DSC-Vol. 32, pp. 109-122.

White, G. K., and Woods, S. B., 1954, "The Lattice Conductivity of Dilute Copper Alloys at Low Temperatures," *Philos. Mag.*, Vol. 45, pp. 1343-1345.

White, G. K., and Tainsh, R. J., 1960, "Lorenz Number for High-Purity Copper," *Phys. Rev.*, Vol. 119, pp. 1869-1871.

Wilson, A. H., 1953, *The Theory of Metals*, Cambridge University Press, Cambridge, United Kingdom, pp. 286-296.

Yeh, P., 1988, *Optical Waves in Layered Media*, Wiley, New York, Chap. 4.

Ziman, J. M., 1960, *Electrons and Phonons*, Oxford University Press, Oxford, United Kingdom, Chaps. 8 and 9.

T. Banerjee

C. Chang

W. Wu

U. Narusawa
Mem. ASME

Department of Mechanical Engineering,
Northeastern University,
Boston, MA 02115

Solidification With a Throughflow in a Porous Medium

A steady throughflow in a porous medium is studied in the presence of a solidified layer due to cooling of the walls. Under the assumption of a moderately sloped melt-solid interface, analytical solutions are obtained for both a flow between parallel plates and a circular pipe. Differences and similarities are examined between the Darcian and the Brinkman porous media, as well as the effects of various parameters, such as the Peclet number, the ratio of diffusivities in the longitudinal and the lateral directions, and a parameter indicating the degree of wall cooling and flow heating, on thermofluid structure of a flow in porous media accompanied by solidification.

Introduction

Flow through a porous medium accompanied by solidification is studied. There exists a fair amount of literature on freezing of liquids in flow between parallel plates or in a tube (Zerkle and Sunderland, 1968; Ozisik and Mulligan, 1969; Shibani and Ozisik, 1977, and papers cited therein), based on a parallel flow assumption. In the present analysis a similar method of solution is employed. The most notable difference between the present study and the previous studies is the presence of porous matrices as well as a low filter (or superficial) velocity in a porous medium. A direct application of solidification in a flow through a porous medium may be found in the formation of metal matrix composites by infiltration of molten metals into fibrous preforms (Masur et al., 1987; Mortensen et al., 1988). In contrast to the actual metal infiltration process, which involves a transient flow of molten metal through porous matrices, the present analysis focuses on a steady flow of molten metal through a porous medium accompanied by a solidified layer. At present, both Darcian and Brinkman equations are commonly used for the study of porous media. A more basic objective of this study is to examine quantitatively Darcian and Brinkman approaches to the problem as well as the effects of various thermofluid parameters, such as the Peclet number, the Darcy number, and the conductivity ratio, on the flow and thermal structures in porous media, for the case in which the melt-solid interface must be determined as part of the solution.

Formulation and Method of Solution

Figure 1(*a*) shows a schematic diagram of a flow between parallel plates with an accompanying solidified layer. The space between two flat plates with distance $2L$ is filled with a fluid-saturated porous medium. The region $z' \le 0$ consists of a fully developed flow and is at uniform temperature T_0 and velocity u_0. The region $z' \ge 0$ is characterized by the presence of a solidified layer. Under a steady-state condition, temperatures of both the liquid-filled porous medium, $T_l(0 < y' \le s, z')$, and the solidified porous medium, $T_s(s \le y' \le L, z')$ are established as the solidification front, located at $y' = s(z')$, develops downstream. The development of the solidification front takes place in the downstream region due to the fact that the temperature of the plates is maintained at T_w ($T_w \le T_l$). It may be noted that the flow and temperature field develop in both y' and z' directions with the plates being extended to infinity in the x' direction.

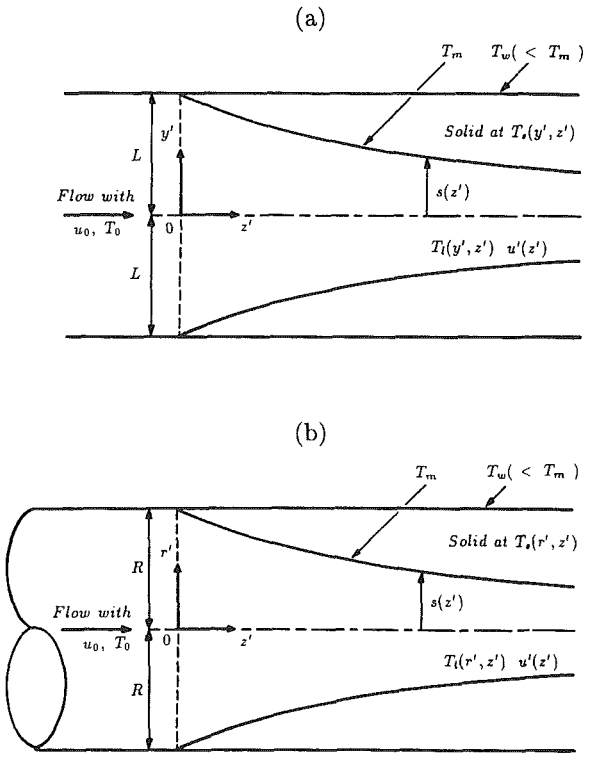

Fig. 1 Schematic diagram of (*a*) flow between parallel plates with solidification, (*b*) flow through a pipe with solidification

It may be shown from conservation of mass that a slope of streamlines in the region $z' \ge 0$ has the same order of magnitude as the slope of the liquid–solid interface, ds/dz'; hence, as $ds/dz' \to 0$, v' (velocity component in y' direction) $\to 0$.

From the argument above, it follows that the assumption of a moderately sloped interface implies that streamlines are nearly parallel. Furthermore, in the energy equation for the solid phase, the diffusion in the z direction may be neglected compared to diffusion in the y direction when the assumption of a moderately sloped interface is combined with the assumption of a thin solid layer at the entrance region relative to the distance between the two plates. Other major assumptions employed for the present analysis are as follows:

1 The flow is steady and incompressible.
2 The flow through the porous medium is described either by Darcy's equation or by the Brinkman equation, excluding such non-Darcian effects as Forchheimer's acceleration effect and thermal dispersion.
3 The fluid is composed of one component and as a result the solidification takes place at a single specific temperature, T_m.

Contributed by the Heat Transfer Division for publication in the JOURNAL OF HEAT TRANSFER. Manuscript received by the Heat Transfer Division November 1990; revision received February 1992. Keywords: Materials Processing and Manufacturing Processes, Phase-Change Phenomena, Porous Media. Technical Editor: R. Viskanta.

4 Thermal properties are constant and thermal equilibrium exists between fluid and porous solid.

For the Brinkman flow between two plates with a half-depth, L, the velocity profile may be given as,

$$u' = \left(-\frac{K}{\mu}\right)\left(\frac{dp}{dz'}\right)\left(\frac{1-\cosh(y'\sqrt{K\mu_0})}{\cosh(L\sqrt{K\mu_0})}\right)$$

where $\mu_0 = \hat{\mu}/\mu$ with $\hat{\mu}$ = effective viscosity of the porous medium (Rudraiah, 1985; Ping Cheng, 1978).

For the rectangular geometry of Fig. 1(*a*), nondimensional variables are defined as

$$z = z'/L,\ y = y'/\sqrt{sL},\ \Delta = s/L,\ u = u'/u_0,$$

$$\theta_s = \frac{T_s(y', z') - T_w}{T_m - T_w},\ \theta_l = \frac{T_l(y', z') - T_m}{T_0 - T_m}$$

where the reference velocity, u_0, is an average filter velocity in a Brinkman porous medium between two parallel plates with distance $2L$. Then the governing equations may be written as

$$u = \frac{1 - \dfrac{\cosh(\sigma\sqrt{\Delta}y)}{\cosh(\sigma\Delta)}}{\Delta\left(1 - \dfrac{1}{\sigma\Delta}\tanh(\sigma\Delta)\right)} \tag{1}$$

$$\mathrm{Pe}\Phi\left(1 - \frac{\cosh(\sigma\sqrt{\Delta}y)}{\cosh(\sigma\Delta)}\right)\frac{\partial\theta_l}{\partial z} = \frac{\partial^2\theta_l}{\partial y^2} + \hat{D}\Delta\frac{\partial^2\theta_l}{\partial z^2} \tag{2}$$

$$\theta_s = \frac{1 - \sqrt{\Delta}y}{1 - \Delta} \tag{3}$$

$$\frac{\partial\theta_l}{\theta y}(y = \sqrt{\Delta}) = -\frac{\sqrt{\Delta}}{(1-\Delta)\omega} \tag{4}$$

where

$$\Phi = \frac{1}{1 - \dfrac{1}{\sigma\Delta}\tanh(\sigma\Delta)},\quad \sigma = \frac{1}{\sqrt{\mu_0 Da}},$$

Equation (1) is continuity. Equation (2) is the energy equation in the fluid-saturated porous medium, while Eq. (3) is a solution to the energy equation in the solidified layer (i.e., a one-dimensional conduction equation) with Eq. (4) as the equation of the melt–solid interface, $\Delta = \Delta(z)$, describing the heat flux continuity. The boundary conditions are

$$\theta_l(z = 0) = 1, \tag{5}$$

$$\theta_l(z \to \infty) = \text{finite} \tag{6}$$

$$\theta_l(y = \sqrt{\Delta}) = 0, \tag{7}$$

$$\frac{\partial\theta_l}{\partial y}(y = 0) = 0 \tag{8}$$

A nondimensional interfacial heat flux, Q, may be given as,

$$Q\left(= \frac{q}{k_y\left(\dfrac{T_0 - T_m}{L}\right)}\right) = \frac{1}{(1-\Delta)\omega} \tag{9}$$

Also, a nondimensional pressure gradient, P_z, defined as the ratio of the pressure gradient with solidification to that of a flow between two flat plates, becomes,

$$P_z = \frac{1}{\Delta}\left(\frac{1 - \dfrac{1}{\sigma}\tanh(\sigma)}{1 - \dfrac{1}{\sigma\Delta}\tanh(\sigma\Delta)}\right) \tag{10}$$

We now attempt to find a solution to the equations above (Chang, 1991). A solution to Eq. (2) is assumed to be

Nomenclature

Da = K/L^2 (case I: a flow between two flat plates); K/R^2 (case II: a flow in a pipe); Darcy number
D_r = thermal diffusivity in r direction
D_y = thermal diffusivity in y direction
D_z = thermal diffusivity in z direction
$\hat{D}$ = D_z/D_y (case I); D_z/D_r (case II) = diffusivity ratio
H = $\beta R\Delta$
I_0 = modified Bessel function of the zeroth order
I_1 = modified Bessel function of the first order
k_r = thermal conductivity in r direction
k_s = thermal conductivity of solidified layer
k_y = thermal conductivity in y direction
$\hat{k}$ = k_y/k_s (case I); k_r/k_s (case II)
K = permeability of porous medium
L = half depth between two parallel plates
Pe = u_0L/D_y (case I); u_0R/D_r (case II) = Peclet number
P_z = nondimensional pressure gradient
Q = nondimensional heat flux at liquid–solid interface
r' = dimensional coordinate
r = r'/s = nondimensional coordinate
R = radius of pipe
s = half-depth of solidification front for region $z' > 0$
T_l = temperature of fluid-saturated porous medium
T_m = solidification temperature of porous medium at interfacial location, $\Delta = \Delta(z')$
T_0 = uniform temperature of porous medium for region $z' \le 0$
T_s = temperature of solidified porous medium for region $z' > 0$
T_w = temperature of top and bottom plates
$\widehat{\Delta T}$ = $T_0 - T_m/T_m - T_w$
u_0 = characteristic velocity
u' = $u'(z')$: horizontal dimensional velocity in z' direction
u = u'/u_0: horizontal nondimensional velocity in z direction
y' = dimensional coordinate
y = $y'/\sqrt{sL}$: nondimensional coordinate
z' = dimensional coordinate
z = z'/L (case I); z'/R (case II) = nondimensional coordinate
Δ = $\Delta(z) = s/L$ (case I), s/R (case II) = interfacial location for region $z' > 0$
β = $1/\sqrt{\mu_0 K}$
βR = $1/\sqrt{\mu_0 \mathrm{Da}}$
θ_l = $T_l - T_m/T_0 - T_m$: nondimensional temperature for flow in porous medium
θ_s = $T_s - T_w/T_m - T_w$: nondimensional temperature for solidified region
μ = fluid viscosity
$\hat{\mu}$ = effective viscosity of porous medium
μ_0 = $\hat{\mu}/\mu$
σ = $1/\sqrt{\mu_0 \mathrm{Da}}$
Φ = $1/(1 - 1/\sigma\delta \cdot \tanh(\sigma\delta))$ (case I); $I_0(H)/I_2(H)$ (case II)
ω = $\hat{k}\widehat{\Delta T}$

$$\theta_l = \sum_{n=1}^{N} A_n f_n(y) \exp(-\lambda_n z) \tag{11}$$

$$f_n(y) = \sum_{j=0}^{M-1} a_{nj} \cos\left(\left(\frac{1}{2}+j\right)\frac{\pi y}{\sqrt{\Delta}}\right) \tag{12}$$

The eigenvalues, λ_n, and the corresponding eigenvectors, a_{nj}, will be determined by the Galerkin method. It should be mentioned here that this form of trial function, based on the Darcian (uniform flow) solution, satisfies the boundary conditions, Eqs. (6), (7), and (8). Weighted residuals of Eq. (2), upon an application of the Galerkin method, are set to zero to yield,

$$\sum_{j=0}^{M-1} a_{nj}\left[\left(\hat{D}\Delta\lambda_n^2 - \left(\frac{1}{2}+j\right)^2\frac{\pi^2}{\Delta}\right)\frac{\sqrt{\Delta}}{2}\delta_{ij} + \mathrm{Pe}\Phi\lambda_n\left(\frac{\sqrt{\Delta}}{2}\delta_{ij} - \frac{\bar{a}\cdot\tanh(\sigma\Delta)}{2}RI\right)\right] = 0$$
$$\text{for } i = 0, 1, 2, \cdots, M-1 \tag{13}$$

where

$$\delta_{ij} = \begin{cases} 1, & \text{if } i=j \\ 0, & \text{if } i\neq j \end{cases}, \quad RI = (-1)^{i+j+1}\left(\frac{1}{\bar{a}^2+\bar{b}^2} - \frac{1}{\bar{a}^2+\bar{c}^2}\right),$$
$$\bar{a} = \sigma\sqrt{\Delta},\ \bar{b} = (i+j+1)\pi/\sqrt{\Delta},\ \bar{c} = (i-j)\pi/\sqrt{\Delta}.$$

An $(M\times M)$ determinant, constructed from the coefficients of a_{nj} in Eq. (13), is set to zero to find the eigenvalues, λ_n $(n=1, 2, \cdots, N)$ as well as the corresponding eigenvectors, a_{nj} $(j=1, 2, \cdots, M)$. As may be seen from Eq. (13), the elements of the determinant are either quadratic or linear with respect to λ_n; hence, the eigenvalues and the eigenvectors must be obtained one by one numerically.

As a next step, the coefficients, A_n, in Eq. (11) are sought. It was confirmed numerically that the same number of (positive real) eigenvalues, N, exists as the size of the determinant, M. Therefore, the coefficients, A_n, may be obtained from the boundary condition, Eq. (5), which yields,

$$\sum_{n=1}^{N} A_n a_{ni} = (-1)^i \frac{4}{(1+2i)\pi} \quad \text{for } i=0, 1, 2, \cdots, M-1. \tag{14}$$

It should be noted that a_{ni} in the equation above should be those evaluated at $\Delta = 1$. Finally, the location of the interface is determined from the equation of the interface, Eq. (4).

The formulation and the solution outline are described briefly for the corresponding problem in the cylindrical geometry depicted in Fig. 1(*b*) (Banerjee, 1991). For the Brinkman flow in a pipe of radius R, an average filter velocity, u_0, is;

$$u_0 = \left(-\frac{K}{\mu}\right)\left(\frac{dp}{dz'}\right)_R\left(1 - \frac{2I_1(\beta R)}{\beta R I_0(\beta R)}\right),$$

where I_1 and I_0 are the modified Bessel functions of the first and zeroth order, respectively.

Governing equations and boundary conditions, corresponding to Eqs. (1)–(8) of the rectangular geometry, are

$$-\frac{K}{\mu}\left(\frac{dp}{dz'}\right)_R\left(\frac{1}{2} - \frac{I_1(\beta R)}{\beta R I_0(\beta R)}\right) = -\frac{K}{\mu}\left(\frac{dp}{dz'}\right)_S \Delta^2\left(\frac{1}{2} - \frac{I_1(\beta R\Delta)}{\beta R\Delta I_0(\beta R\Delta)}\right) \tag{1A}$$

$$\mathrm{Pe}\Phi\left(1 - \frac{I_0(\beta R\Delta r)}{I_0(\beta R\Delta)}\right)\frac{\partial\theta_l}{\partial z} = \frac{1}{r}\frac{\partial}{\partial r}\left(r\frac{\partial\theta_l}{\partial r}\right) + \hat{D}\Delta^2\frac{\partial^2\theta_l}{\partial z^2} \tag{2A}$$

$$\theta_s = 1 + \frac{\ln r}{ln\Delta}, \tag{3A}$$

$$\left.\frac{\partial\theta_l}{\partial r}\right|_{r=1} = \frac{1}{\omega\ln\Delta} \tag{4A}$$

$$\theta_l(z=0) = 1, \tag{5A}$$

$$\theta_l(z\to\infty) = \text{finite} \tag{6A}$$

$$\theta_l(r=1) = 0, \tag{7A}$$

$$\frac{\partial\theta_l}{\partial r}(r=0) = 0. \tag{8A}$$

It should be mentioned here that the nondimensional radial coordinate, r, is defined with the radius of solidification front, s, as the reference length. The interfacial heat flux, Q, and the pressure gradient, P_z, in nondimensional form may also be defined in a manner similar to the case of the rectangular geometry as shown below:

$$Q = -\frac{1}{\omega\Delta\ln\Delta}, \tag{9A}$$

$$P_z = \frac{1 - \dfrac{2I_1(\beta R)}{\beta R I_0(\beta R)}}{\Delta^2\left(1 - \dfrac{2I_1(H)}{HI_0(H)}\right)}. \tag{10A}$$

A solution for the temperature, Q_l, is assumed to have the following form:

$$\theta_l = \sum_{j=1}^{k} A_j\left[\sum_{n=1}^{N} a_{nj}(1-r^{2n})\right]\exp(-\lambda_j z)$$

Eigenvalues, $\lambda_n(>0)$ as well as the corresponding eigenvectors, a_{nj} $(n=1, \cdots, N)$, are sought by applying the Galerkin method to the eigenvalue problem obtained from the energy equation, Eq. (2A); while the coefficients, A_j $(j=1, \cdots, k)$, are determined from the boundary condition, Eq. (5A), through the application of the least-square collocation method (Forsythe et al., 1977). (See Banerjee, 1991, for details of the method of solution.)

Finally, for the case of Darcian porous media, a uniform cross-sectional velocity profile permits us to obtain exact solutions for both the rectangular and the cylindrical geometries. A summary of the solutions are provided in the appendix for comparison.

Results and Discussion

A solution for the Darcian (Brinkman) flow depends on the following nondimensional parameters:

$$\mathrm{Pe} = u_0 L/D_y,\ \hat{D} = D_z/D_y,\ \omega = (k_y/k_s)(T_0 - T_m)/(T_m - T_w),$$

and σ for the Cartesian case (or βR for the cylindrical case). Using $u_0 \sim 10^{-3}$ to 10^{-2} [m/s], $L \sim 10^{-2}$ to 10^{-1} [m], $D_y \sim 10^{-4}$ to 10^{-6} [m^2/s] as typical values for infiltration of molten metals into porous matrices, the range of the Peclet number is estimated to be $1 \le \mathrm{Pe} \le 100$. The magnitude of the diffusivity ratio, $\hat{D}$, indicates the diffusivity difference due to a heterogeneous porous structure; while the value of ω indicates the degree to which either the incoming flow temperature T_0 is raised above T_m or the wall temperature is lowered below T_m. The effective viscosity, $\hat{\mu}$, is associated with the diffusion term in conservation of momentum, originally proposed by Brinkman to account for the viscous effect in high-porosity porous media. Although the value of $\hat{\mu}$ varies with porosity, $\mu_0 = \hat{\mu}/\mu$ is of the order of unity (Durlofsky and Brady, 1987; Ping Cheng, 1978; Lundgren, 1972). Therefore, roughly speaking, the parameter, σ (or βR), is inversely proportional to $\sqrt{\mathrm{Da}}$, with σ (or βR) = 10 corresponding to a highly permeable porous medium.

As may be seen from Fig. 1 as well as from the formulation,

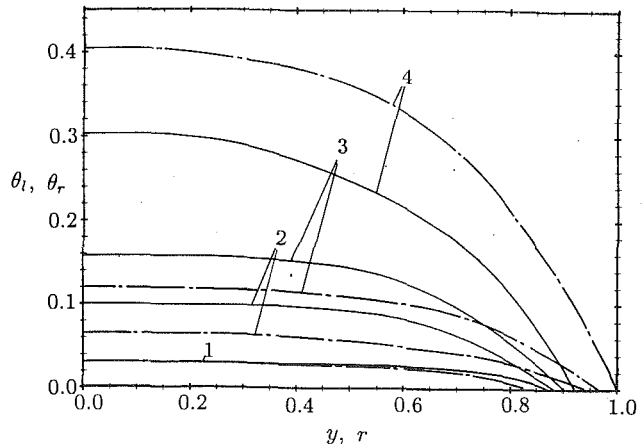

Fig. 2 Typical temperature profiles, θ_l (solid curves) for the Cartesian case and θ_r (broken curves) for the cylindrical case, across a half depth (Brinkman flow): Pe = 100, $\hat{D} = 1$, $\omega = 100$, $\sigma = 10$ for $\Delta = 0.98$ (curve 4), 0.94, 0.90, and 0.70 (curve 1); note that each curve ends at $y = \sqrt{\Delta}$, where θ_l (or θ_r) = 0

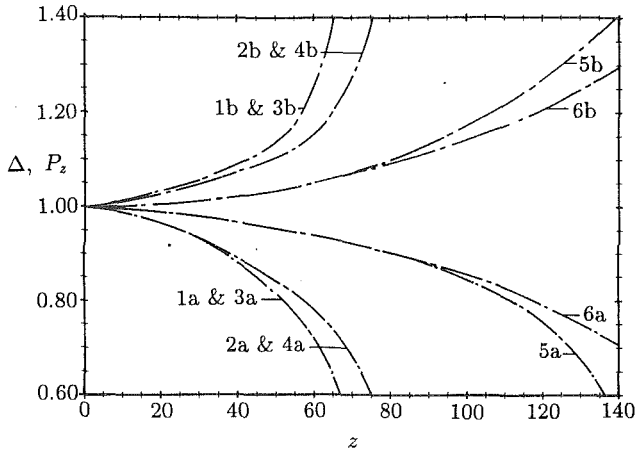

Fig. 3 Δ and P_z profiles for Brinkman flow with Pe = 1 (Cartesian case) showing a comparison between the cases, $\sigma = 100$ (~ Darcian flow) and $\sigma = 10$: (*a*) Δ profiles, (*b*) P_z profiles; curves 1-6 for ($\hat{D}$, ω, σ) = (1, 100, 100), (1, 100, 10), (1, 1000, 100), (1, 1000, 10), (10, 100, 100), (10, 100, 10), respectively

the point ($y = 1$, $z = 0$) is a singular point. The velocity is very low as the Peclet number ranges from ~1 to ~100. Also, the computation is performed for the range of Δ in which the interfacial slope, $d\Delta/dz$, is smaller than 0.1 to satisfy the assumption of a moderately sloped interface.

Based on these considerations, the results to be discussed cover the following range for various parameters:

$$\mathrm{Pe} = 1,\ 10,\ 100$$

$$\hat{D} = 0.1,\ 1,\ 10$$

$$\omega = 10,\ 100,\ 1000$$

$$10 \le \sigma \le 100$$

$$\sim 0.6 \le \Delta \le 1.0 \text{ for } \mathrm{Pe} = 10 \text{ and } 100$$

$$\sim 0.8 \le \Delta \le 1.0 \text{ for } \mathrm{Pe} = 1$$

Because of the double series expansion of the solution, the convergence of series solution was achieved at a relatively low order of approximation. We found that solutions with N (the number of terms in the series expansion) $= 7$ in the Galerkin approximation yielded results with a sufficient accuracy for both the rectangular and the cylindrical cases. (Although N is increased to as high as 10 in selected cases to check convergence, the difference from the corresponding solution with $N = 7$ is found to be much less than 0.5 percent in terms of the interfacial location, $\Delta = \Delta(z)$.) The eigenvalues, starting from the lowest mode, converge to their limiting values as the order of approximation is increased. It should also be mentioned here that the eigenvalues take quite different values, depending on the magnitude of nondimensional parameters as well as the solidified layer thickness. In Fig. 2, typical solutions to the Brinkman flow are plotted, showing a gradual decrease of the temperature of the flow ($\theta_l(y, z)$ for the rectangular geometry and $\theta_r(r, z)$ for the cylindrical geometry) downstream as well as their cross-sectional variations.

Figures 3, 4, and 5 represent the solutions to the Brinkman flow for Pe = 1, 10, and 100, respectively. Common to both the Darcian and the Brinkman flows, the following observations may be made: (1) As the Peclet number increases, the growth rate of the solidified layer decreases downstream. (2) The nondimensional parameter, ω, is the second influential factor, the magnitude of which significantly affects the flow with a solidified layer. (3) For a low Peclet number flow (Pe = 1), shown in Fig. 3, the magnitude of $\hat{D}$ has a significant effect on the thermo-fluid structure, implying the importance of a difference in conductivity in the axial and the cross-sectional directions, caused by a heterogeneous structure of a porous

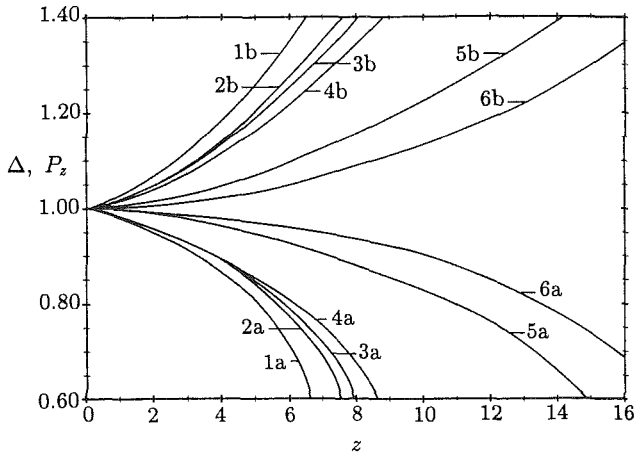

Fig. 4 Δ and P_z profiles for Brinkman flow with Pe = 10 (Cartesian case): (*a*) Δ profiles, (*b*) profiles; curves 1-6 for ($\hat{D}$, ω, σ) = (1, 10, 100), (1, 10, 10), (10, 10, 100), (10, 10, 10), (1, 100, 100), (1, 100, 10), respectively

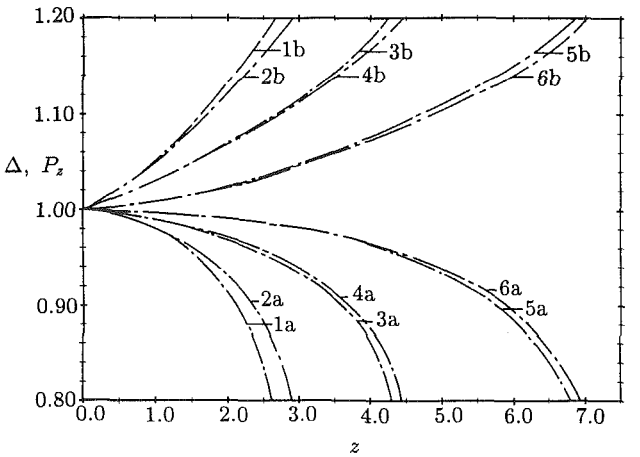

Fig. 5 Δ and P_z profiles for Brinkman flow with Pe = 100 (Cartesian case): (*a*) Δ profiles, (*b*) profiles; curves 1-6 for ($\hat{D}$, ω, σ) = (1, 10, 100), (1, 10, 10), (10, 10, 100), (10, 10, 10), (1, 100, 100), (1, 100, 10), respectively

medium. However, when the Peclet number is increased to 100 (shown in Fig. 5), a change in $\hat{D}$ from 1 to 10 shows very little effect on the flow in the presence of a solidified layer, indicating that the convective effect dominates over that of $\hat{D}$.

A solution to the Brinkman equation is expected to converge to a solution to the corresponding Darcy's law as the porosity of the porous medium (or permeability) is reduced. For a study of natural convection in porous media, there are theoretical and numerical results that support the convergence (Ping Cheng, 1978). When comparisons are made between the Brinkman solution and the Darcian solution of the present problem, it is confirmed that the Brinkman solution converges to the corresponding Darcian solution as $Da \to 0$. The difference is less than 1.5 percent for the Cartesian case (and less than 3.5 percent for the cylindrical case) when the location of the melt-solid interface, $\Delta(z)$, is compared between the Darcian solution and the Brinkman solution with $\sigma = 100$ for the Cartesian case ($\beta R = 100$ for the cylindrical case).

It should be noted that, in discussing differences and similarities between the Darcian and the Brinkman cases, the characteristic velocity, u_0, is defined as the average filter velocity of the flow for both the Darcian and the Brinkman cases. This means that for a fixed value of Pe, comparisons are made between the two cases under the condition of an identical flow rate. As σ decrease below 100 with $\sigma = 10$ representing a highly permeable porous structure, the Brinkman solution starts to deviate from the corresponding Darcian solution; however, roughly speaking, σ has a secondary influence, compared to Pe and ω, over the thermofluid structure of a flow through porous medium with a solidified layer (see Figs. 3, 4, and 5). A more careful examination of results shows that for a low Peclet number flow, a decrease of σ from 100 may cause small corrections to the corresponding Darcian solution for a given set of values for $\hat{D}$ and ω, and that as the Peclet number increases above 1, the effects of σ on flow and thermal structures become increasingly important.

Figure 6 shows the profile of Δ and P_z for the Brinkman flow in the cylindrical case with $Pe = 1$. Compared to the corresponding Cartesian case depicted in Fig. 3, the solidified layer develops much earlier due to the geometry in the cylindrical case being completely bounded by the cold wall, which results in a temperature profile variation quite different from that of the Cartesian case, as shown in Fig. 2. Qualitative conclusions, similar to those observed from the Cartesian case may be drawn for the cylindrical case as well (see Banerjee, 1991 for details).

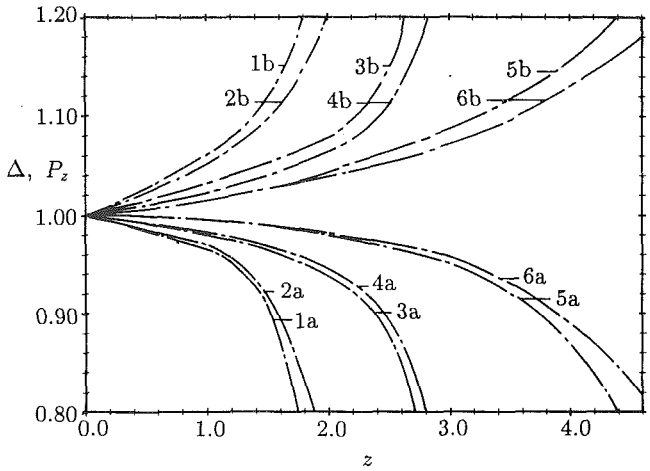

Fig. 6 Δ and P_z profiles for Brinkman flow with Pe = 1 (cylindrical case) showing a comparison between the cases, $\beta R = 100$ (~ Darcian flow) and $\beta R = 10$: *a*) Δ profiles, (*b*) profiles; curves 1-6 for ($\hat{D}$, ω, βR) = (1, 100, 100), (1, 100, 10), (1, 1000, 100), (1, 1000, 10), (10, 100, 100), (10, 100, 10), respectively

Conclusions

A steady flow through a porous medium with solidification is analyzed for both flow between parallel plates (Cartesian case) and flow through a pipe (cylindrical case). Although the assumptions of steady state and of a moderately sloped interface limit the range of study, the results will provide a useful set of criteria to understand the effects of various thermal and hydrodynamic parameters on the flow through porous media accompanied by solidifed layer. Specific conclusions are:

1 Generally, if $\sigma(\beta R) \geq 100$, the Darcian solution may be used to predict interactions between the flow and the solidified layer, since the Brinkman solution in this range is practically identical to the corresponding Darcian solution.

2 For $Pe \sim 1$, ω and $\hat{D}$, both being related to the conduction mode of heat transfer, are the dominant parameters. The magnitude of $\hat{D}$ has a particularly significant effect on thermofluid structure.

3 For $Pe \sim 10$, ω remains an important parameter with $\hat{D}$ and $\sigma(\beta R)$ providing small corrections to the Darcian solution.

4 For $Pe \sim 100$, the effect of $\hat{D}$ diminishes considerably while magnitudes of both ω and $\sigma(\beta R)$ must be taken into consideration for an accurate description of the solidification problem under the presence of a throughflow.

5 The quantitative differences between solutions in the Cartesian and the cylindrical case, such as the earlier development of solidified layer for the cylindrical case, are due primarily to its geometry being completely bounded by the cold wall, resulting in a temperature profile quite different from that of the Cartesian case.

References

Banerjee, T., 1991, "Solidification With a Through-Flow in a Porous Medium in a Pipe," M.S. thesis, Northeastern University, Boston, MA.

Chang, C., 1991, "Solidification With a Through-Flow in a Porous Medium Between Two Parallel Plates," M.S. thesis, Northeastern University, Boston, MA.

Durlofsky, L., and Brady, J. F., 1987, "Analysis of the Brinkman Equation as a Model for Flow in Porous Media," *Phys. Fluids*, Vol. 30, pp. 3329-3341.

Forsythe, G. E., Malcom, A., and Moler, C. B., 1977, *Computer Methods for Mathematical Computations*, Prentice-Hall, Englewood Cliffs, NJ, p. 229.

Lundgren, T. S., 1972, "Slow Flow Through Stationary Random Beds and Suspensions of Spheres," *J. Fluid Mechanics*, Vol. 51, pp. 273-299.

Masur, L. J., Mortensen, A., Cornie, J. A., and Flemings, M. C., 1987, "Pressure Casting of Fiber-Reinforced Metals," ICCM6, London, United Kingdom, pp. 2320-2329.

Mortensen, A., Michaud, V. J., Cornie, J. A., Flemings, M. C., and Masur, L., 1988, "Kinetics of Fiber Perform Infiltration," *Proceedings of the Int. Symp. on Adv. in Cast Reinforced Metal Composites*, ASM International Paper No. 8816-006.

Ozisik, M. N., and Mulligan, J. C., 1969, "Transient Freezing of Liquids in Forced Flow Inside Circular Tubes," ASME JOURNAL OF HEAT TRANSFER, Vol. 91, pp. 385-390.

Ping Cheng, 1978, *Advances in Heat Transfer*, J. P. Hartnett and T. F. Irvine, Jr., eds., Vol. 14, pp. 1-105.

Rudraiah, N., 1985, "Coupled Parallel Flows in a Channel and a Boundary Porous Medium of Finite Thickness," ASME *Journal of Fluids Engineering*, Vol. 107, pp. 327-341.

Shibani, A. A., and Ozisik, M. N., 1977, "A Solution of Freezing of Liquids of Low Prandtl Number in Turbulent Flow Between Parallel Plates," ASME JOURNAL OF HEAT TRANSFER, Vol. 99, pp. 20-24.

Zerkle, R. D., and Sunderland, J. E., 1968, "The Effect of Liquid Solidification in a Tube Upon Laminar-Flow Heat Transfer and Pressure Drop," ASME JOURNAL OF HEAT TRANSFER, Vol. 90, pp. 183-190.

APPENDIX

A Summary of Solutions for the Case of Darcian Porous Media

I Flow Between Two Flat Plates

(Temperature profile in a fluid-saturated porous medium)

$$\theta_l = \sum_{n=0}^{\infty} (-1)^n \frac{4}{(1+2n)\pi} \cos(\sqrt{\beta_n} y) \exp(-\alpha_n z)$$

$$\beta_n = \frac{(1+2n)^2}{4} \frac{\pi^2}{\Delta}, \quad \alpha_n = \frac{\mathrm{Pe}}{2\hat{D}\Delta}\left(-1 + \sqrt{1 + \frac{4\hat{D}\Delta}{\mathrm{Pe}^2}\beta_n}\right)$$

(Location of the interface)

$$\sum_{n=0}^{\infty}\exp(-\alpha_n z)=\frac{\Delta}{2(1-\Delta)\omega}$$

(Pressure gradient)

$$P_z=\frac{1}{\Delta}$$

The Peclet number is defined in terms of $u_0=(K/\mu)(-dp/dz')_L$, as the Darcian uniform flow velocity in a porous medium with permeability, K, between two flat plates.

II Flow in a Pipe

(Temperature profile in a fluid-saturated porous medium)

$$\theta_l=\sum_{n=1}^{\infty}C_n J_0(\beta_n r)\exp(-\alpha_n z)$$

$$J_0(\beta_n)=0,\ \alpha_n=\frac{\mathrm{Pe}}{2\hat{D}\Delta^2}\left[-1+\left(1+\frac{4\hat{D}\Delta^2\beta_n^2}{\mathrm{Pe}^2}\right)^{1/2}\right]$$

$$C_n=\frac{2}{\beta_n J_1(\beta_n)}$$

(Location of the interface)

$$\sum_{n=1}^{\infty}\exp(-\alpha_n z)=-\frac{1}{2\omega\ln\Delta}$$

(Pressure gradient)

$$P_z=\frac{1}{\Delta^2}$$

It should also be noted that the equations for the nondimensional heat flux, Q, are the same for both case I and II as the corresponding cases of the Brinkman porous media.

Freezing and Thawing Heat Transfer With Water Flow Around Isothermally Cooled Cylinders in Staggered and Aligned Arrangements

T. Hirata
Associate Professor,
Department of Mechanical Systems Engineering,
Faculty of Engineering,
Shinshu University,
Nagano 380, Japan

H. Matsui
Mitsubishi Electric Co.,
2-2-3 Marunouchi Chiyoda-ku,
Tokyo 100, Japan

Ice formation and melting phenomena with water flow around isothermally cooled cylinders arranged in staggered and aligned manners, respectively, are examined. Experiments are performed for transient freezing and melting processes as well as for steady-state conditions. Analytical models are also introduced to examine heat transfer characteristics of the transient processes. It is found that the melting is twice as fast as the freezing for both the staggered and aligned arrangements. Experimental correlations for ice storage efficiency as well as for the ice filling-up rate are proposed. It is shown that the ice filling-up rate is strongly affected by the Reynolds number, cooling temperature, and cylinder pitch perpendicular to water flow.

1 Introduction

Ice formation or melting around cooled cylinders in a water flow is a basic engineering problem. It introduces many practical applications such as water-cooled heat exchangers in refrigeration systems and low-temperature storage systems utilizing the latent heat of phase change of ice. In these cases, the transient and steady-state heat transfer characteristics are important, and the problems must be examined as ice formation or melting process around tube bundles in a convective water flow. However, very few such studies have been reported so far (Torikoshi et al., 1990).

In the previous studies by Hirata and Matsui (1989, 1990), the ice formation phenomena and heat transfer with water flow around isothermally cooled cylinders arranged in a single line were studied. It was found that under certain conditions the cylinders are linked by ice layers and the heat transfer characteristics on the surface of the linked ice layers are completely different from those of the ice layer around a single cylinder. The parameters that describe the onset conditions for the linked ice layers, the ice storage efficiency, and the volume of ice growth in a steady-state condition, respectively, were also proposed in the previous studies.

On the other hand for the ice-formation process around a bundle of cooled cylinders in a water flow, few studies have been reported. Okada et al. (1987) examined the heat transfer on the ice layers around staggered cooled cylinders. They suggested that the heat transfer coefficients on the ice layers are almost the same as those for staggered cylinders without ice.

In the present study, the ice formation and melting phenomena in a transient process are examined experimentally for staggered as well as for aligned arrangements. The heat transfer characteristics in the transient process are studied by introducing simple analytical models for the ice formation and melting processes, respectively. The ice storage efficiency and the volume of ice growth in a steady-state condition are also discussed, where the steady-state condition is defined as stoppage of ice formation or melting process resulting from heat flow balance at the ice-water interface.

2 Experiment Apparatus and Procedure

Figure 1 shows the experimental apparatus consisted of a calming section, a test section, a flow meter, a refrigeration unit, and two circulation systems of water and a coolant. The flow conditions at the inlet of the test section were assumed to be a laminar and a uniform velocity profile based on the result of visual observations by a dye-injection method. Figure 2 shows a schematic illustration of the test section. The test section had a 150 mm × 40 mm cross-sectional area and was 1000 mm in length. The walls were made of transparent acrylic resin plates in order to observe the growth of the ice layer. They were installed in the vertical position to minimize the effect of the natural convection of water. Isothermally cooled cylinders 41 mm in o.d. and 40 mm in length were arranged in a staggered or aligned manner and installed in the test section. For the staggered arrangement, the cylinder pitches perpendicular and parallel to flow direction were chosen as $a = 150$ mm and $b = 37.5$ mm, respectively. The cylinders were arranged in three rows with seven cylinders for each row, as shown in Fig. 2. All measurements were done for the cylinders of the middle row. The aligned arrangement was provided by relocating the middle row cylinders by as much as 37.5 mm in the upstream direction. To produce a uniform wall temperature, copper was used to fabricate the cylinders. The coolant was led directly from a constant temperature bath to each cylinder and was circulated at a high velocity inside the cylinders. The flow of water in the test section was in the upward vertical direction.

The wall temperatures of the cooled cylinders, T_w, were measured by four thermocouples located at the top and 90 deg from the top of the third and fifth cylinders, respectively. Although a small temperature difference between the two cylinders was detected during the initial stage of ice formation, the difference became negligible with ice growth. An isothermal wall condition was satisfied within an error of 3 percent in $(T_f - T_w)$. The free-stream water temperature, T_∞, was estimated from the mean value of the inlet and outlet of the test section. The variation of the inlet water temperature due to

Contributed by the Heat Transfer Division and presented at the Third International Symposium on Cold Regions Heat Transfer, Fairbanks, Alaska, June 12–14, 1991. Manuscript received by the Heat Transfer Division July 29, 1991; revision received October 21, 1991. Keywords: Forced Convection, Phase-Change Phenomena, Thermal Energy Storage.

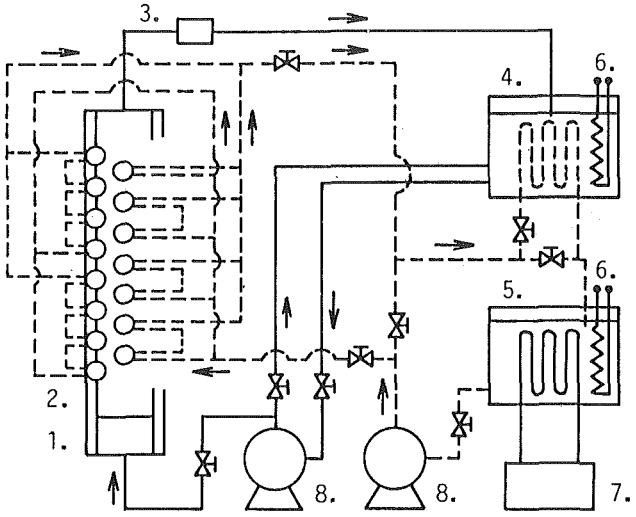

1. Calming section
2. Test section
3. Flow meter
4. Water bath
5. Coolant bath
6. Thermostatically controlled heater
7. Refrigeration unit
8. Pump

Fig. 1 Schematic illustration of experimental apparatus

the dynamics of the refrigeration system yielded a maximum error of 2 percent in $(T_\infty - T_f)$. After a steady-state condition was reached, a small amount of dye was injected into the water stream to enhance the ice-water interface. To measure the thickness of the ice layer, the ice around the cylinders was photographed and the coordinates of the ice-water interface were measured. An anastigmatic lens (Nikon Micro Nikkor 200 mm F4S) was used to avoid distortion of the object.

The flow condition around the rear surface of the seventh cylinder was different from the others; therefore, an effective length L of the row of cylinders was defined, as shown in Fig. 2, as $L = 470.5$ mm. All measurements of ice thickness were done in this region. The two dimensionality of heat flow from the water to the cylinders was confirmed by the fact that a

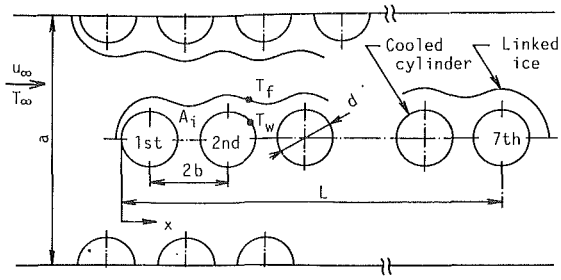

Fig. 2 Schematic illustration of test section

two-dimensional ice layer was produced around the cylinders. Although the effect of heat conduction through the acrylic resin plates of the test section wall was observed at both ends of each cylinder, the region with this effect was considered to be negligible as compared to the cylinder length. The effect of side walls of the test section on the heat transfer coefficient on the ice surface was considered to be negligible, judging from the experimental result that the change of local heat transfer coefficient along the cylinder row was consistent over its length.

The ice formation test was started by circulating the water and the coolant from the constant temperature baths, respectively, through the test section. To avoid a supercooling of water, small physical impact was given by a hammer to the test section for the aid of ice nucleation. The melting test was started as follows: After a steady-state ice layer was obtained, the circulation of water and coolant was shut off. As soon as the temperatures of the constant temperature baths were at their predetermined values, the circulation was started again for the melting test. Measurements were done both in a transient process and in a steady-state condition. The steady-state condition was confirmed by measuring the growth rate of ice thickness with slide calipers from the outside of the test section. Experimental ranges covered in the present experiment were:

for the staggered arrangement:

$$u_\infty = 0.014\text{–}0.056 \text{ m/s},\ T_\infty = 0.9\text{–}1.4^\circ\text{C}$$

$$\text{Re}_d = 700\text{–}2810,\ \theta = 3.00\text{–}5.20$$

Nomenclature

a = cylinder pitch perpendicular to flow direction
a^* = dimensionless parameter = a/d
A_i = volume of ice around a row of cylinders, m^3/m
A^* = ice filling-up rate defined in Eq. (20)
b = cylinder pitch parallel to flow direction
b^* = dimensionless parameter = b/d
Cp_i, Cp_w = specific heats of ice and water
d = diameter of cylinder
h_x, h_m = local and mean heat transfer coefficients
H = dimensionless parameter defined in Eq. (18)
L = effective length of row of cylinders shown in Fig. 1
L^* = dimensionless parameter = L/d
L_f = latent heat of fusion
Nu_m = mean Nusselt number = $h_m d/\lambda_w$
$\text{Nu}_{m,L}$ = mean Nusselt number = $h_m L/\lambda_w$
Pr = Prandtl number
q_i = amount of heat rate stored by ice, J/m
q_w = amount of heat rate transferred from water to ice, W/m
q^* = ice storage efficiency defined in Eq. (17), s
Q^* = dimensionless parameter defined in Eq. (4)
r = radius of ice surface shown in Fig. 8
r^* = dimensionless parameter = r/d
Re_d = cylinder Reynolds number = ud/ν_w
$\text{Re}_{\max}$ = Reynolds number = $u_{\max} d/\nu_w$
Re_∞ = Reynolds number = $u_\infty a/\nu_w$
Ste = Stefan number = $Cp_i(T_f - T_w)/L_f$
t = time
T_f, T_w, T_∞ = temperatures of freezing, cylinder wall, and water
u = velocity of water around cylinders without ice = $u_\infty a/(a-2d)$
$u_{\max}$ = maximum velocity around cylinders with ice shown in Fig. 8
u_∞ = free-stream velocity of water upstream of cylinders
δ_m = mean ice thickness = $A_i/(2L)$
δ_m^* = dimensionless parameter = δ_m/d
θ = dimensionless cooling temperature ratio = $(T_f - T_w)/(T_\infty - T_f)$
κ_i = thermal diffusivity of ice
λ^* = thermal conductivity ratio of ice to water = λ_i/λ_w
ρ_i = density of ice
τ = dimensionless time defined in Eq. (2)

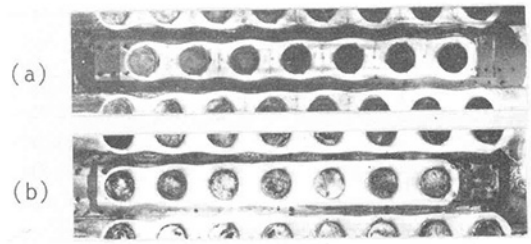

Fig. 3 Ice formation pattern in a steady-state condition (note: flow direction is from left to right and the actual experiments were done with the test section vertical): (*a*) $Re_d = 702$, $\theta = 4.25$, (*b*) $Re_d = 304$, $\theta = 2.74$

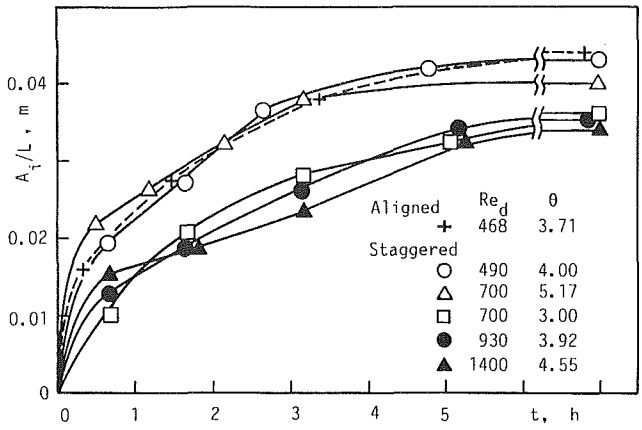

Fig. 4 Change of ice volume in a freezing process

for the aligned arrangement:

$$u_\infty = 0.006\text{–}0.052 \text{ m/s}, \quad T_\infty = 0.6\text{–}1.9°\text{C}$$

$$Re_d = 304\text{–}2630, \quad \theta = 2.06\text{–}7.71$$

where Re_d is a Reynolds number and θ is a cooling temperature ratio defined by $\theta = (T_f - T_w)/(T_\infty - T_f)$. In the present experiment, the case in which the water flow of the test section is shut off by ice blockage is not the subject.

The uncertainty in θ is approximately 6 percent for $\theta = 4.00$, and that in the Reynolds number is approximately 5 percent for $Re_d = 2000$. The uncertainty in the volume of ice, A_i, is 3 percent, and those in the mean ice thickness, δ_m, and the mean Nusselt numbers, Nu_m and $Nu_{m,L}$, which are calculated from A_i, are the same as that in A_i.

The local heat transfer coefficient on the ice surface in the transient process was estimated by using the boundary element method (Brebbia, 1978) on the assumption of a quasi-steady-state condition. The detailed procedure was explained in the literature by Hirata and Matsui (1990).

3 Experimental Results

3.1 Ice Formation Phenomena for Staggered and Aligned Arrangements. Figure 3 shows typical results of linked ice shapes formed in a steady-state condition. The flow direction is from left to right, and the ice layer is shown by gray-color areas around the cylinders. Figure 3(*a*) is the result for the staggered arrangement. In this case the ice-water interface clearly shows the sinuous shape of a wavelength corresponding with the cylinder pitch, since the flow between the linked ice layers meanders due to the staggered arrangement. Figure 3(*b*) is the result for the aligned arrangement. In this case the ice-water interface is comparatively flat when compared with that of Fig. 3(*a*), since the local ice growth between adjacent rows of cylinders is suppressed due to the increase of heat transfer coefficient with increasing water velocity resulting from flow blockage by ice growth.

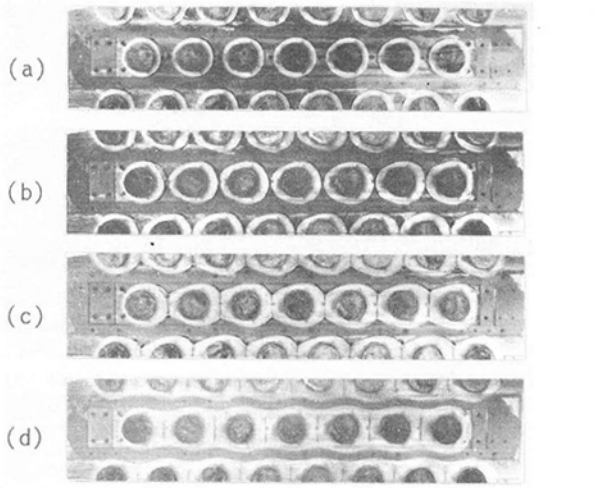

Fig. 5 Ice formation pattern in a transient freezing process, $Re_d = 490$, $\theta = 4.00$: (*a*) $t = 40$ min, (*b*) $t = 100$ min, (*c*) $t = 160$ min, (*d*) steady-state condition

Although there is the abovementioned difference in the ice shapes between staggered and aligned arrangements, the volumes of ice are not significantly different from one another. Figure 4 shows the mean ice-layer thickness for a row of cylinders, A_i/L, in a transient freezing process, where A_i is the volume of ice around a row of cylinder (m^3/m). For instance, in Fig. 4, the experimental data indicated by the symbols (o) and (+) show the changes of ice volume in a transient freezing process for the staggered and aligned arrangements, respectively. At the beginning of ice formation, the volume of ice for the aligned arrangement shows a slightly larger value than that for the staggered one, since the heat transfer around the cylinders is controlled by that around a bundle of cylinders without ice. However, for steady state, the volumes of ice for the both arrangements almost coincide with each other, as shown in Fig. 4. This implies that the total volume of ice is not largely affected by the ice-water interface shape, since a large amount of ice exists between the upstream and downstream sides of each cylinder. In the following section, therefore, the discussions will be focused mainly on the staggered arrangement.

3.2 Ice Formation Phenomena in a Transient Process. Figure 5 shows the transient freezing process for a smaller Reynolds number. At $t = 40$ min, the ice shape is concentric with the cylinder. At $t = 100$ min, the ice changes to an elliptic shape, since the heat transfer coefficient over the ice surface between the upstream and downstream cylinders decreases due to stagnation of the flow. At $t = 160$ min, the cylinders are linked by the ice layer and the flow pattern between the ice layers becomes completely different from those of Figs. 5(*a*) and 5(*b*).

Figure 6 shows the result for a larger Reynolds number. At $t = 40$ min, the ice has a triangular shape. A similar result was observed in the previous study of Hirata and Matsui (1990) for the ice formation around cooled cylinders arranged in a single line. This means that the triangular shape of the ice layer is not the typical result for staggered arrangement but is due to mutual interactions among the ice shape, the flow field, and the heat transfer around the cylinders. In a steady-state condition, a significant change in the ice shape with Reynolds number was not observed, as can be seen in Figs. 5(*d*) and 6(*d*).

In Fig. 4, at the beginning of ice formation, the ice thickness increases rapidly with time, since the ice formation occurs around the cylinders independently; after that, a moderate increase of the ice thickness is observed, which is the typical

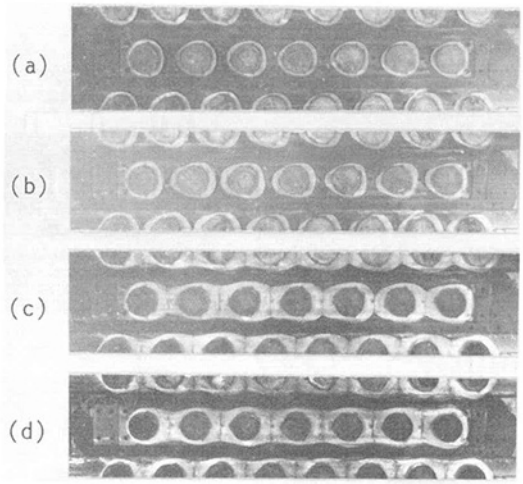

Fig. 6 Ice formation pattern in a transient freezing process, $Re_d = 1400$, $\theta = 4.55$: (*a*) $t = 40$ min, (*b*) $t = 100$ min, (*c*) $t = 310$ min, (*d*) steady-state condition

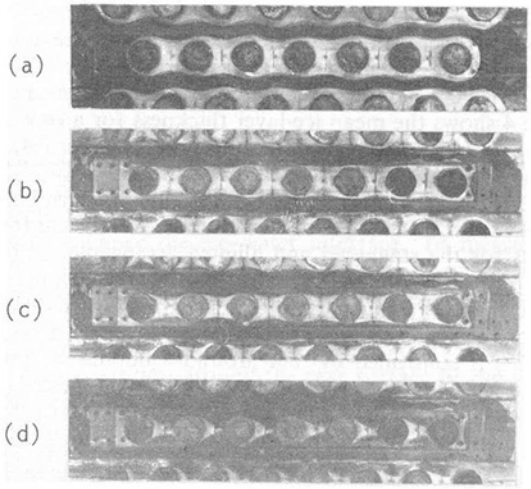

Fig. 7 Melting pattern in a transient process, $Re_d = 700$, $\theta = 3.00 \rightarrow 0.37$: (*a*) $t = 0$ min, (*b*) $t = 10$ min, (*c*) $t = 60$ min, (*d*) $t = 140$ min

freezing process controlled by the heat transfer in the separated and reattached flows around the cylinders. As can be seen in Fig. 4, this typical freezing process is maintained for a longer period of time with increasing Re_d. It suggests that the ice growth rate in the freezing process decreases due to larger heat transfer by the separated and reattached flows. As a result, 9–17 hours were required to obtain a steady-state condition in the present experiment ranges.

3.3 Melting Phenomena in a Transient Process. Figure 7 shows the typical result of the melting process, where the initial ice layer was at steady state for $Re_d = 700$, $\theta = 3.00$, and the melting was started by changing the temperature of $\theta = 3.00$ to a smaller value of $\theta = 0.37$. At $t = 10$ min, the ice-water interface shows almost a flat shape, which suggests that the melting proceeds uniformly at early stages. At $t = 60$ min, the ice layer at the flow passage becomes very thin, and the melting proceeds to the ice layer at the upstream and downstream sides of each cylinder. At $t = 140$ min, the linked ice layer shows a triangular shape due to separated and reattached flows around the ice layer. At steady state, a very thin ice layer was formed around each of the cylinders.

Figure 8 shows the change of mean ice thickness in the melting process. It is shown that for smaller Re_d the melting rate decreases rapidly for about $t > 1$ hour. This phenomenon

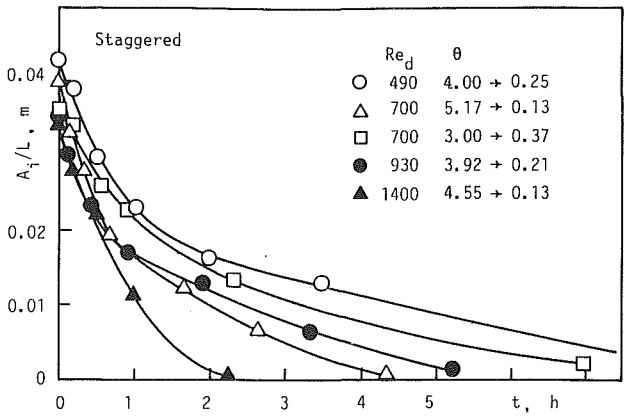

Fig. 8 Change of ice volume in a melting process

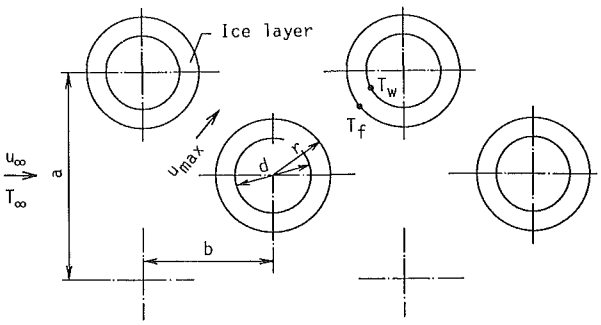

Fig. 9 Cylindrical ice model

coincides with the melting characteristic in Fig. 7(*d*). That is, when the Reynolds number is small, the flow at the upstream and downstream sides of each cylinder is rather stagnant and the melting rate of the triangular-shape ice layer decreases. On the other hand, when the Reynolds number is large, the heat transfer is augmented by the separated and reattached flows and the melting rate does not decrease significantly. In the present melting experiments, 2–8 hours were required to reach a steady-state condition, which is less than half that needed for the ice formation experiments. It is recognized that the ice formation process is controlled mainly by conduction heat transfer through the ice layer, and the thermal resistance of the ice layer increases with ice growth, whereas the melting process is controlled mainly by convective heat transfer over the ice surface.

In the present melting experiment, the effect of sensible heat on the melting process was negligible, since the difference of Stefan numbers before and after the melting was small, e.g., $0.017 < \Delta Ste < 0.033$.

4 Discussions for Transient Process

The ice formation and melting phenomena in the transient process are closely related to flow conditions around the cylinders as described above. The flow conditions depend on whether or not the cooled cylinders are linked by ice layer. It is, therefore, difficult to predict the heat transfer coefficient on the ice surface in the transient process. In the following discussions, to give better understanding for the transient characteristics, two simple analytical models will be considered for the early stage of ice formation and for steady state, respectively. The former will be referred to as a cylindrical ice model and the latter, as a flat ice model.

4.1 Cylindrical Ice Model. Okada et al. (1987) reported that the volume of ice for an individually formed ice layer for the staggered arrangement could be estimated from the Nusselt

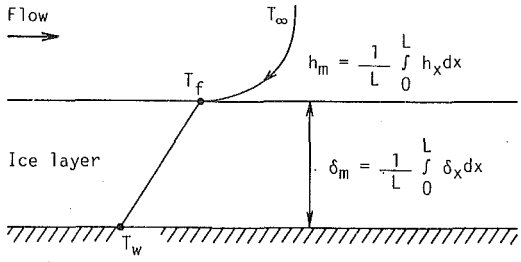

Fig. 10 Flat ice model

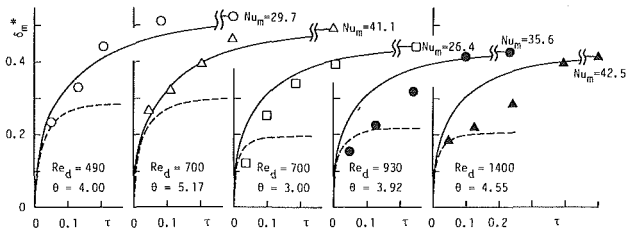

Fig. 11 Mean ice thickness in a freezing process

number for staggered tubes without ice (Özişik, 1985). Figure 9 shows the analytical model for the individually formed ice layer. It is assumed that (1) the ice layer is concentric with the cylinder, (2) the ice formation process is in a quasi-steady-state condition, (3) the heat transfer coefficient on the ice surface is the same for the all cylinders, and (4) the density of water does not change with phase change. Then, the heat balance equation at the ice–water interface is given by

$$\rho_i L_f \frac{dr}{dt} = \lambda_i \frac{(T_f - T_w)}{r\ln(2r/d)} - h_m(T_\infty - T_f) \tag{1}$$

Dimensionless parameters are defined as

$$r^* = \frac{r}{d}, \quad \lambda^* = \frac{\lambda_i}{\lambda_w}, \quad \mathrm{Ste} = \frac{Cp_i(T_f - T_w)}{L_f}$$
$$\mathrm{Fo} = \frac{\kappa_i t}{d^2}, \quad \tau = \mathrm{SteFo}, \quad \mathrm{Nu}_m = \frac{h_m d}{\lambda_w} \tag{2}$$

Integration of Eq. (1) yields

$$\tau = \int_0^{r^*} \frac{r^* \ln 2r^*}{1 - Q^* r^* \ln 2r^*} dr^* \tag{3}$$

where Q^* represents the ratio of convective heat transfer rate from the water to the ice surface to conduction heat rate through the ice layer, and is given by

$$Q^* = h_m(T_\infty - T_f) \Big/ \left[\lambda_i \frac{T_f - T_w}{d}\right] = \frac{\mathrm{Nu}_m}{\lambda^* \theta} \tag{4}$$

where the mean Nusselt number for staggered tubes, Nu_m, is given by Zukauskas as follows (see Özişik, 1985):

$10^2 < \mathrm{Re}_{max} < 10^3$:

$$\mathrm{Nu}_m = 1.2\left\{0.3 + \frac{0.62\mathrm{Re}_{max}^{1/2}\,\mathrm{Pr}^{1/3}}{[1 + (0.4/\mathrm{Pr}^{2/3})]^{1/4}} \times \left[1 + \left(\frac{\mathrm{Re}_{max}}{282{,}000}\right)^{5/8}\right]^{4/5}\right\} \tag{5}$$

$10^3 < \mathrm{Re}_{max} < 2 \times 10^5$:

$$\mathrm{Nu}_m = 0.35\left(\frac{a^*}{b^*}\right)^{0.2} \mathrm{Pr}^{0.36}\left(\frac{\mathrm{Pr}}{\mathrm{Pr}_w}\right)^{0.25} \mathrm{Re}_{max}^{0.6} \tag{6}$$

where a^* and b^* are dimensionless cylinder pitches and Re_{max} is a Reynolds number defined by the maximum water velocity between the neighboring cylinders, u_{max}. Equation (7) or (8) is used to evaluate the value of u_{max}, depending on which equation gives a larger value.

$$u_{max} = u_\infty \frac{2a^*}{(a^{*2} + 4b^{*2})^{0.5} - 4r^*} \tag{7}$$

$$u_{max} = u_\infty \frac{a^*}{a^* - 2r^*} \tag{8}$$

The analytical results can be obtained by substituting Eqs. (4)–(8) into Eq. (3) and by integrating Eq. (3) numerically.

4.2 Flat Ice Model. In the previous paper by the authors (Hirata and Matsui, 1990), it was reported that the average value of the local Nusselt number for the linked ice layer in a steady-state condition showed that same tendency as that for a flat plate in a turbulent flow. If it is assumed that the cylinder pitch in the flow direction, b^*, decreased to its limits, the linked cylinders can be considered, from a macroscopic viewpoint, as cooled flat plates arranged in lines. Then, the simple analytical model shown in Fig. 10 can be drawn. The ice layer thickness and the heat transfer coefficient on the ice surface will be defined by mean values in the region of effective length of cylinder row, $x = 0 - L$. If it is assumed that (*a*) the density of water does not change with phase change and (*b*) the ice formation process is in a quasi-steady-state condition, the heat balance equation at the ice–water interface is given by

$$\rho_i L_f \frac{d\delta_m}{dt} = \lambda_i \frac{T_f - T_w}{\delta_m} - h_m(T_\infty - T_f) \tag{9}$$

Substitution of $\delta_m^* = \delta_m/d$ into Eq. (9) and integration of the resulting equation with the boundary condition of $\delta_m^* = 0$ at $\tau = 0$ yields

$$\tau = -\frac{[Q^*\delta_m^* + \ln(1 - Q^*\delta_m^*)]}{Q^{*2}} \tag{10}$$

where $Q^* = \mathrm{Nu}_m/\lambda^*\theta$. To calculate the analytical values of the mean ice thickness, δ_m^*, the experimental values of Nu_m in a steady-state condition are used. They are $\mathrm{Nu}_m = 29.7$ for $\mathrm{Re}_d = 490$, $\theta = 4.00$; $\mathrm{Nu}_m = 41.1$ for $\mathrm{Re}_d = 700$, $\theta = 5.17$; $\mathrm{Nu}_m = 26.4$ for $\mathrm{Re}_d = 700$, $\theta = 3.00$; $\mathrm{Nu}_m = 35.6$ for $\mathrm{Re}_d = 930$, $\theta = 3.92$ and $\mathrm{Nu}_m = 42.5$ for $\mathrm{Re}_d = 1400$, $\theta = 4.55$, as shown in Fig. 11.

The flat ice model can also be applicable for the initial stage of melting process. Integration of Eq. (9) with the boundary condition of $\delta_m^* = \delta_o^*$ at $\tau = 0$ yields

$$\tau = \frac{Q^*(\delta_o^* - \delta_m^*) - \ln[(1 - Q^*\delta_m^*)/(1 - Q^*\delta_o^*)]}{Q^{*2}} \tag{11}$$

The values of Nu_m for the melting process are estimated from the experimental values shown in Fig. 11 and are assumed constant during melting. The sensible heat of ice can be neglected as compared to the latent heat of melting.

4.3 Discussions. Figure 11 shows the experimental and analytical results of dimensionless mean ice thickness, δ_m^*, for the ice formation process. The dashed lines show the results for the cylindrical ice model and the solid lines, the results for the flat ice model. It is shown that the increasing rate of δ_m^* is affected by the Reynolds number. For the smaller Reynolds numbers, the experimental data are close to the results obtained by the flat ice model. On the other hand, for the larger Reynolds numbers, the experimental data lie between the analytical values of the two models at the initial stage of ice formation, and approach the values by the flat ice model as ice is developed. The difference in these ice formation processes with Reynolds number results from change in the heat transfer characteristics on the ice surface.

In Fig. 12, the change of average Nusselt number with ice growth is shown, where the arrows show the time when the

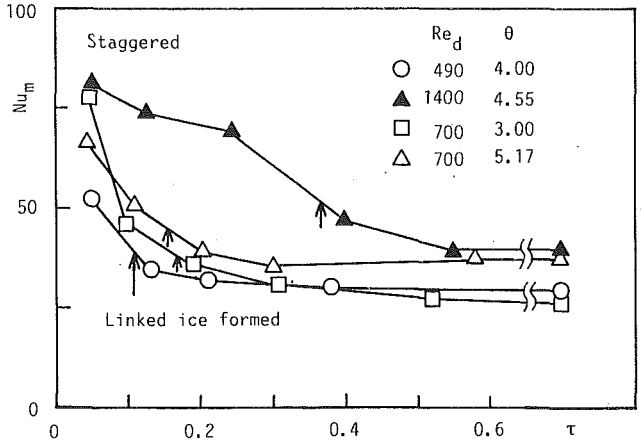

Fig. 12 Mean Nusselt number around ice layer in a freezing process

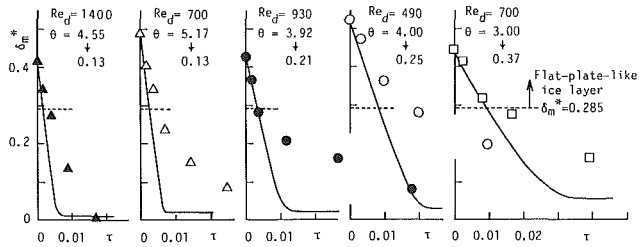

Fig. 13 Mean ice thickness in a melting process

linked ice layer was formed. The values of Nu_m were calculated under the assumption of quasi-steady-state. To calculate Nu_m, the values of r or δ_m were measured and then steady forms of Eq. (1) or (9) were used, respectively. The errors caused by neglecting the amount of latent heat is approximately 34 percent at $\tau=0.1$ and 7 percent at $\tau=0.4$ for both $Re_d=490$ and 700, and is 9 percent at $\tau=0.1$–0.4 for $Re_d=1400$. For the smaller Reynolds numbers, it is shown that the values of Nu_m are almost constant for $\tau>0.1$. On the other hand, for $Re_d=1400$, Nu_m is not constant and decreases with time for $0<\tau<0.4$. The decrease coincides with the ice formation process from individually formed ice layers to a linked ice layer. That is, for larger Re_d, a high heat transfer rate is maintained due to strength of turbulence around the cylinders and, therefore, the ice growth rate decreases gradually. On the other hand, for smaller Re_d, the heat transfer rate becomes small due to stagnation of flow around the cylinders, and the ice growth rate is maintained at a higher value, as shown in Fig. 11. From these results, it is noted that the simple flat ice model is useful for an ice storage system with a comparatively low water-flow velocity.

Figure 13 shows the experimental data and the analytical results of the flat ice model in the melting process. The dashed lines in Fig. 13 indicate the dimensionless mean ice thickness at which the local ice thickness just coincides with the height of the cylinder radius, $\delta_m^*=(2bd-\pi d^2/4)/(4bd)=0.285$. It is shown that the melting for $\delta_m^*>0.285$ proceeds along with the results of the flat ice model, while for $\delta_m^*<0.285$, the analytical results deviate from the experimental data. This results from the evaluation of Nu_m values. In the analysis, the value of Nu_m was estimated from a steady-state condition and was assumed to be constant. In the experiment, however, under the condition of thinner ice layers for $\delta_m^*<0.285$, the water at the rear side of the cylinders becomes stagnant; therefore, the heat transfer coefficient decreases with proceeding of the melting.

It is difficult to estimate the Nu_m values in a transient process experimentally, because the local ice thickness around the cylinder is very thin, as shown in Figs. 7(*c*) and 7(*d*), and it causes a large number of errors in calculating Nu_m from the ice thickness. It is, therefore, difficult to predict the value of δ_m^* for $\delta_m^*<0.285$.

5 Discussions for Steady-State Condition

5.1 Ice Storage Efficiency. To analyze the efficiency of ice storage system, the ice storage efficiency, q_i/q_w, defined as the ratio of stored heat around the cylinder, q_i, to removed heat from the cylinder, q_w, was proposed in the previous report (Hirata and Matsui, 1990).

Neglecting the sensible heat as compared with the latent heat, the stored heat, q_i, for a unit of time is given by

$$q_i=\rho_i L_f A_i \tag{12}$$

where ρ_i is the density of ice; L_f is the latent heat. The heat removed from the cylinder for a unit of time, q_w, which is equal to the heat transferred from the water to the ice surface under the steady-state condition, is given by

$$q_w=2\int_0^L h_x(T_\infty-T_f)dx \tag{13}$$

where L is the effective length of the row of cylinders. Because the value of h_x on the right-hand side of Eq. (13) showed the same tendency as that of turbulent heat transfer on a flat plate, the ice storage efficiency on a cooled flat plate was first derived to examine what parameters govern the efficiency of the cooled cylinders. The volume of ice on both sides of a cooled flat plate in a turbulent flow is given by

$$A_i=2\int_0^L \delta(x)dx \tag{14}$$

where $\delta(x)$ is given by Hirata et al. (1979) as

$$\delta(x)=\lambda^*\theta x/Nu_x \tag{15}$$

The local Nusselt number Nu_x of turbulent heat transfer on a flat plate is given by Eq. (16) for $5\times10^5<Re_x<10^7$ (Holman, 1976).

$$Nu_x=0.0296\ Re_x^{0.8}\ Pr^{1/3} \tag{16}$$

The ice storage efficiency on a cooled flat plate in a turbulent flow is then obtained from Eqs. (12)–(16) as

$$q^*=q_i/q_w=3.32\ L^{*2}H \tag{17}$$

where L^* is a dimensionless parameter of the effective length, L, and H is defined by

$$H=\frac{\lambda^*\theta}{Nu_{m,L}^2}\frac{L_f}{Cp_w(T_\infty-T_f)} \tag{18}$$

where λ^* is the thermal conductivity ratio of ice to water; $Nu_{m,L}$ is the mean Nusselt number for $x=0-L$. H is the dimensionless parameter representing the stored heat in ice. The physical properties of water were estimated at 0°C.

Figure 14 shows the ice storage efficiency against the dimensionless parameter, $L^{*2}H$, where the results obtained for the single-lined cylinders in the previous report are also shown. The uncertainty in q^* is approximately 9 percent. The estimate accounts for uncertainties associate with A_i, $(T_\infty-T_f)$ and the local heat transfer coefficient, h_x, determined by using the boundary element method (see Hirata and Matsui, 1990). In Fig. 14, the result for a cooled flat plate given by Eq. (17) is also shown for comparison. It is seen that the ice storage efficiency for a cooled flat plate gives smaller values than that for cooled cylinders. This implies that cooled cylinders are preferable for storing ice to a cooled flat plate. In Fig. 14, it is shown that the ice storage efficiency for the linked ice layer (shown by the solid symbols) is well correlated by $L^{*2}H$ for all three kinds of cylinder arrangements and that q^* increases

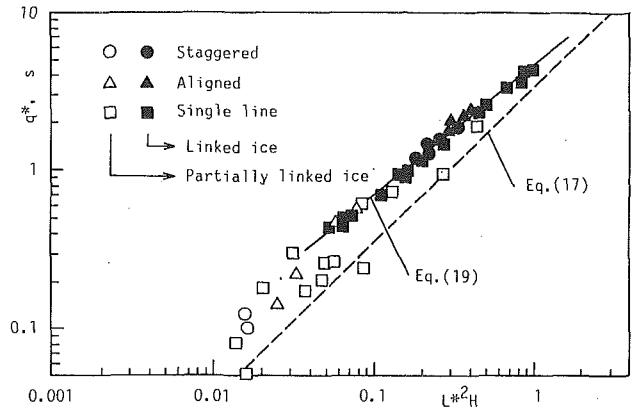

Fig. 14 Ice storage efficiency in a steady-state condition

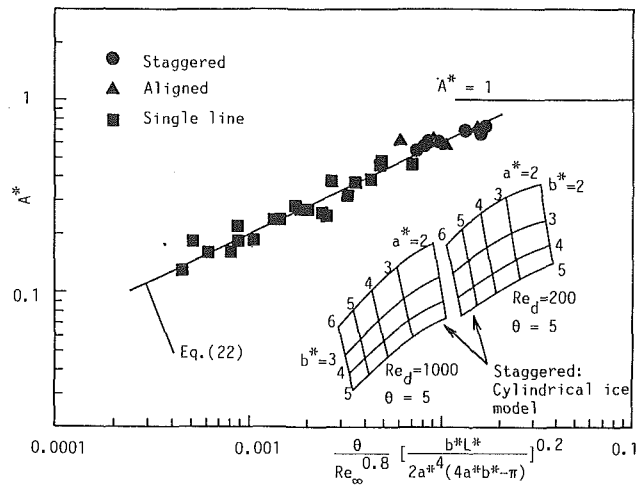

Fig. 15 Ice filling-up rate in a steady-state condition

with $L^{*2}H$. These results imply that as far as the ice storage efficiency is concerned the value of $L^{*2}H$ should be made large for any cylinder arrangements. On the other hand, for a partially linked ice layer (shown by the open symbols), q^* shows smaller values, which suggests that the linked ice layer is preferable for storing low-temperature heat by ice. The value of ice storage efficiency given in Fig. 14 is well correlated by the following expression:

$$q^* = 4.50\ (L^{*2}H)^{0.822} \tag{19}$$

where the standard error of estimate (SEE) of Eq. (19) is 0.138 and the applicable range is $0.054 < L^{*2}H < 1.04$.

5.2 Ice Filling-Up Rate. In the present paper, the ice filling-up rate, A^*, is defined by the ratio of the ice volume to the flow passage volume, which describes how much of the flow passage is filled by ice.

$$A^* = A_i \Big/ \left[\frac{aL}{2} - \pi \left(\frac{d}{2}\right)^2 \frac{L}{2b} \right] \tag{20}$$

where $0 < A^* < 1$. Assuming that the local Nusselt number on the linked ice surface is controlled by that of a turbulent flat plate, one can obtain the following equation by substitution of Eqs. (12)–(16) into Eq. (20).

$$A^* = f\left(\frac{\theta}{\mathrm{Re}_\infty^{0.8}} \left[\frac{b^* L^*}{2a^{*4}(4a^* b^* - \pi)} \right]^{0.2} \right) \tag{21}$$

where $\mathrm{Re}_\infty = u_\infty a/\nu_w$. The right-hand side of Eq. (21), which involves the temperature and flow conditions, the cylinder pitches a^* and b^*, and the effective cylinder length, L^*, is considered to be a parameter that governs the ice filling-up rate.

In Fig. 15, the values of ice filling-up rate are plotted on the coordinate system obtained by Eq. (21). The values for the cylindrical ice model given by Eqs. (3)–(8) are also shown for comparison for $\mathrm{Re}_d = 200$–1000, $\theta = 5$, $a^* = 2$–6 and $b^* = 2$–5. It is shown that the ice filling-up rate can be correlated well with the parameter in the right-hand side of Eq. (21) for all the cylinder arrangements. It is also shown that the results from the cylindrical ice model show significantly smaller ice filling-up rate than those for the linked ice layer. Because the ice layer for the cylindrical ice model forms individually around each cylinder, the ice amount is less than that for the linked ice layer. From Fig. 14, it is realized that the value of the right-hand side in Eq. (21) should be made large to increase the ice filling-up rate. The experimental values for the linked ice layer shown in Fig. 15 can be correlated by

$$A^* = 5.54 \left(\frac{\theta}{\mathrm{Re}_\infty^{0.8}} \right)^{0.48} \left[\frac{b^* L^*}{2a^{*4}(4a^* b^* - \pi)} \right]^{0.096} \tag{22}$$

where the standard error of estimate (SEE) is 0.042 and the applicable range is for $0.12 < A^* < 0.8$. The values of exponent in Eq. (22) suggests that the ice filling-up rate is a strong function of the parameters concerned with temperature and flow conditions, θ, Re_∞, and a^*, and a weak function of the parameters concerned with cylinder arrangement, b^* and L^*.

It should be noted that the onset conditions for the linked ice layer for the staggered and aligned arrangements have been confirmed to coincide with the results reported for a single-line arrangement (Hirata and Matsui, 1990).

6 Conclusions

The ice formation and melting phenomena around the cooled cylinders in staggered and aligned arrangements in water flow were examined experimentally. The ice storage efficiency and the ice filling-up rate in a steady-state condition were also discussed. The following conclusions may be drawn:

1 The ice growth rate in a transient freezing process can be approximated by the flat ice model for smaller Reynolds numbers. However, for larger Reynolds numbers, the ice growth rate changes gradually from the values obtained by the cylindrical ice model to those from the flat ice model. On the other hand, for the melting process, the melting rate can be approximated by the flat ice model only for an early stage of melting.

2 The ice storage efficiency in a steady-state condition was defined by the parameter in Eq. (18) and represented by Eq. (19) for both staggered and aligned arrangements.

3 The ice filling-up rate is given by Eq. (22) and is a strong function of Reynolds number, the cooling temperature ratio, and the cylinder pitch perpendicular to flow condition.

References

Brebbia, C. A., 1978, *The Boundary Element Method for Engineers*, Pentech Press.

Hirata, T., Gilpin, R. R., and Cheng, K. C., 1979, "The Steady State Ice Layer Profile on a Constant Temperature Plate in a Forced Convection Flow: II, The Transition and Turbulent Regimes," *Int. J. Heat Mass Transfer*, Vol. 22, pp. 1435–1443.

Hirata, T., and Matsui, H., 1989, "Ice Formation Phenomena With Water Flow Around Isothermally Cooled Cylinders Arranged in a Line," *Proc. 2nd Int. Symp. Cold Regions Heat Transfer*, Seki et al., eds., pp. 33–38.

Hirata, T., and Matsui, H., 1990, "Ice Formation and Heat Transfer With Water Flow Around Isothermally Cooled Cylinders Arranged in a Line," ASME JOURNAL OF HEAT TRANSFER, Vol. 112, pp. 707–713.

Holman, J. P., 1976, *Heat Transfer*, McGraw-Hill, New York, p. 180.

Okada, M., Goto, K., and Nakamura, S., 1987, *Proc. 65th National Conf. of JSME* [in Japanese], No. 870-4, pp. 304–305.

Özişik, M. N., 1985, *Heat Transfer*, McGraw-Hill, New York, p. 387.

Torikoshi, K., Nakazawa, Y., and Yamashita, H., 1990, "An Experimental Study of Formation and Melting of Ice About Horizontal Tubes," ASME HTD-Vol. 143, p. 57.

Heat Transfer Analysis of Local Evaporative Turbulent Falling Liquid Films

N. M. Al-Najem

K. Y. Ezuddin

M. A. Darwish

Mechanical Engineering Dept.,
Kuwait University,
Safat, 13060, Kuwait

A theoretical study has been conducted for evaporative heating of turbulent free-falling liquid films inside long vertical tubes. The methodology of the present work is based on splitting the energy equation into homogeneous and nonhomogeneous problems. Solving these simple problems yields a rapidly converging solution, which is convenient for computational purposes. The eigenvalues associated with the homogeneous problem can be computed efficiently, without missing any one of them, by the sign-count algorithm. A new correlation for the local evaporative heat transfer coefficient along the tube length is developed over wide ranges of Reynolds and Prandtl numbers. Furthermore, the average heat transfer coefficient is correlated as a function of Reynolds and Prandtl numbers as well as the interfacial shear stress. A correlation for the heat transfer coefficient in the fully developed region is also presented in terms of Reynolds and Prandtl numbers. Typical numerical results showed excellent agreement of the present approach with the available data in the literature. Moreover, a parametric study is made to illustrate the general effects of various variables on the velocity and temperature profiles.

Introduction

Falling films in long tube evaporators are characterized by their high heat transfer rates, low feed rates, and high heat transfer coefficients at low temperature differences. Falling liquid films have numerous industrial applications, which involve mass and heat transfer by condensation or evaporation. Such applications can be found in chemical distillation and desalination plants, wetted-wall absorption columns, two-phase heat exchangers, cooling systems for nuclear fuel elements, and electronic packages.

Several studies have been reported in the literature for the evaporative heat transfer coefficient in fully developed region. Chun and Seban (1971) obtained experimental correlations for average evaporative heat transfer coefficients in laminar and turbulent flows outside an electrically heated tube for $320 \le \mathrm{Re} \le 21{,}000$ and $1.7 \le \mathrm{Pr} \le 5.7$. Hubbard et al. (1976) suggested an eddy diffusivity model that incorporates the effect of interfacial shear due to cocurrent vapor flow. Their model was comprised of a modified van Driest model (1956) for the region close to the solid wall and the gas absorption data of Chung (1974) for the region near the interface where turbulence damping is considered. They indicated good agreement with the nonshear data of Chun and Seban, especially at Prandtl numbers greater than 1.75. The optimum turbulent Prandtl number was shown to be in the range $0.9 \le \mathrm{Pr}_t \le 1.0$. Fujita and Ueda (1978) performed some experiments on saturated water films flowing outside an electrically heated tube. They correlated the average heat transfer coefficients in terms of Reynolds number only. Their data are about 10 percent higher than those of Chun and Seban. Saibabu et al. (1986) developed a theoretical correlation for the average heat transfer coefficient as a function of Reynolds, Prandtl, and Kapitza numbers. The indicated maximum deviation is ± 13 percent from Chun and Seban's data. A new model for the eddy diffusivity function was proposed by Madawwar and El-Masri (1986). The model consists of a single and continuous profile that extends over the entire film thickness. They indicated satisfactory agreement between their numerical results and the experimental data of Chun and Seban, and Fujita and Ueda. They correlated their results for the average fully developed heat transfer coefficients in terms of Reynolds and Prandtl numbers. Shmerler and Mudawwar (1988) investigated numerically and experimentally the case of turbulent falling and evaporating films flowing outside an electrically heated vertical tube. Their experimental data on the average heat transfer coefficients for fully developed flow are fitted in terms of Re and Pr numbers over the ranges $5000 \le \mathrm{Re} \le 37500$ and $1.75 \le \mathrm{Pr} \le 5.4$. Comparing their correlation with Chun and Seban's reveals good agreement at high Prandtl numbers and large differences at lower Pr numbers. Faghri and Seban (1988) treated the case of combined heat and mass transfer for turbulent film flow of a binary solution down a wall, with the free surface contacting the solvent vapor. They obtained an algebraic solution for the mean temperature distribution as well as for the distribution of the mean concentration for the case of constant wall temperature and constant wall heat flux. They used the assumption that the transfer coefficients at the wall and at the interface are relatively independent.

Only limited works are available for local evaporative heat transfer coefficients in turbulent falling films. In the evaporative falling films, it is well known that the thermal development length extends over a long portion of the tube length due to the formation of a boundary layer at the film interface (Shmerler and Mudawwar, 1988). Furthermore, a literature survey reveals a lack of correlations for the local evaporative heat transfer coefficients. The present work provides a new correlation for the local evaporative heat transfer coefficient in turbulent falling films. In addition, for the case of long vertical falling film evaporators, the effect of vapor shear stress at the film interface upon the heat transfer coefficients becomes more significant as compared with that of short tubes. The effect of the interfacial shear stress is neglected in most of the available studies. In the present work the effect of interfacial shear stress is considered in the development of a new correlation of the average heat transfer coefficient.

In our analysis, a general analytical solution is developed for turbulent falling films. This solution is expressed in a rapidly converging form by utilizing the splitting procedure explained by Mikhailov and Ozisik (1984). Such a solution is very convenient for computational purposes. Here it should

Contributed by the Heat Transfer Division for publication in the JOURNAL OF HEAT TRANSFER. Manuscript received by the Heat Transfer Division May 20, 1990; revision received October 8, 1991. Keywords: Evaporation, Multiphase Flows, Turbulence.

be pointed out that all previous results for turbulent cases are obtained either experimentally or numerically.

Mathematical Formulation

Consider the case of a steady turbulent falling liquid film with incompressible fluid having constant properties flowing along a vertical plane surface or inside a vertical circular tube. The flow is assumed two dimensional and hydrodynamically fully developed.

The momentum equation and the boundary conditions in dimensionless form are given, respectively, as:

$$\frac{d}{dR}\left[(S-R)^n E_m(R)\frac{dW(R)}{dR}\right]+[\beta+\varphi](S-R)^n=0 \quad (1a)$$

$$W(R)=0 \text{ at } R=0 \quad (1b)$$

$$\frac{dW(R)}{dR}=\bar{\tau}_i \text{ at } R=1 \quad (1c)$$

$$\theta=0 \text{ at } R=1 \quad (2c)$$

$$\theta=0 \text{ at } Z=0 \quad (2d)$$

where:

$$n=\begin{cases}0 & \text{for plane wall}\\ 1 & \text{for circular tube}\end{cases}$$

$$E_h(R)=\frac{L\alpha}{\delta^2 u_m}\left(1+\frac{\epsilon_m}{\nu}\frac{\mathrm{Pr}}{\mathrm{Pr}_t}\right) \quad (2e)$$

$$E_m(R)=1+\frac{\epsilon_m}{\nu} \quad (2f)$$

The studies of Singh (1958) showed that for Peclet number $\mathrm{Pe}>100$, the axial conduction is negligible. Further, the viscous energy dissipation is generally negligible for low Prandtl number such as water.

Integrating the momentum Eq. (1*a*) subjected to boundary condition Eqs. (1*b*) and (1*c*) gives the dimensionless velocity profile across the film thickness as:

$$W(R)=\frac{\gamma_1\int_0^R \frac{(S-1)^{n+1}-(S-R)^{n+1}}{E_m(R)(S-R)^n}dR+\gamma_2\int_0^R\frac{1}{E_m(R)(S-R)^n}dR}{\gamma_1\int_0^1 \frac{(S-1)^{n+1}-(S-R)^{n+1}}{E_m(R)(S-R)^n}dR+\gamma_2\int_0^1\frac{1}{E_m(R)(S-R)^n}dR} \quad (3a)$$

The energy equation for evaporation of turbulent falling films with negligible axial heat conduction and viscous energy dissipation in dimensionless form is:

$$\frac{\partial}{\partial R}\left[(S-R)^n E_h(R)\frac{\partial\theta}{\partial R}\right]=(S-R)^n W(R)\frac{\partial\theta}{\partial Z} \quad (2a)$$

$$\frac{\partial\theta}{\partial R}=-Q_0 \text{ at } R=0 \quad (2b)$$

where

$$\gamma_1=\frac{-\delta^2}{n+1}\left(\frac{g}{\nu}+\frac{1}{\mu}\frac{dp}{dz}\right) \quad (3b)$$

$$\gamma_2=\frac{\tau_i\delta(S-1)^n}{\mu} \quad (3c)$$

In this work, the turbulent eddy diffusivity function is adopted from the model suggested by Mudawwar and El-Masri (1986) as:

Nomenclature

$C1....C6$ = correlation constants in Table 1
C_p = specific heat of liquid film
$\frac{dp}{dz}$ = pressure gradient in the flow direction
$E_h(R)$ = dimensionless eddy diffusivity for heat, Eq. (2*e*)
$E_m(R)$ = dimensionless eddy diffusivity for momentum, Eq. (2*f*)
g = gravitational acceleration
h^* = dimensionless local heat transfer coefficient, Eq. (12)
h^*_{avg} = average dimensionless heat transfer coefficient over the tube length, Eq. (14)
h^*_{ful} = dimensionless fully developed heat transfer coefficient, Eq. (16)
h_{fg} = latent heat, J/kg
k = thermal conductivity of the liquid film
Ka = Kapitza number $=g\mu^4/\rho\delta^3$
L = tube length
N_i = normalization integral, Eq. (9*c*)
Pr_t = turbulent Prandtl number $=\epsilon_m/\epsilon_h$
q_0 = wall heat flux
Q_0 = dimensionless heat flux $=q_0\delta/k\Delta T$
Q_1, Q_2 = dimensionless constants defined in Eqs. (9*b*) and (11), respectively
r_0 = tube radius
R = dimensionless normal position $=y/\delta$
S = r_0/δ
T_s, T_w = saturation and wall temperature, respectively
u_m = velocity at liquid film surface
$W(R)$ = dimensionless velocity function $=u/u_m$
y = position measured from solid wall $=r_0-r$
Z = dimensionless axial position $=z/L$
α = thermal diffusivity of liquid film
β = $gs^2/\nu u_m$
ΔT = temperature difference $=T_w-T_s$
δ = film thickness
$\bar{\delta}$ = dimensionless film thickness, Eq. (3*e*)
ϵ_m = momentum eddy diffusivity
ϕ_1 = δ^2/L^2
ϕ_2 = $\nu L u_m/\delta^2 C_p\Delta T$
ψ = $\delta^2/\mu u_m dp/dz$
θ = dimensionless temperature $=(T-T_s)/\Delta T$
θ_1, θ_2 = solutions of the homogeneous and nonhomogeneous problems, Eqs. (7), (8), respectively
γ_1, γ_2 = constants in the velocity function, Eqs. (3*b*), (3*c*)
μ, ν = dynamic and kinematic viscosity of liquid film, respectively
μ_i = eigenvalues
ρ, ρ_v = liquid and vapor density, respectively
σ = surface tension
ψ_i = eigenfunctions
τ_i = interfacial shear stress
$\bar{\tau}_i$ = $\tau_i\delta/\mu u_m$
$\bar{\tau}^*_i$ = dimensionless interfacial shear stress, Eq. (15)
τ_w = wall shear stress
$\bar{\tau}_w$ = dimensionless quantity in the model Eq. (3*h*)
τ^o_w = wall shear stress with no interfacial shear, Eq. (3*i*)

$$E_m(R)=\frac{1}{2}+\frac{1}{2}\sqrt{1+0.64\bar{\delta}^2R^2(1-R)^2\left[1-\exp\left\{(1-R)^{1/2}\left(\frac{6.65\times10^{-3}R}{\mathrm{Ka}^{0.185}}-\frac{\bar{\delta}R}{26}\right)\right\}\right]^2} \quad (3d)$$

where

$$\bar{\delta}=\frac{\delta}{\nu}\sqrt{\frac{\tau_w}{\rho}} \quad (3e)$$

The above turbulence model represents a continuous and smooth profile across the entire film thickness. It originated from a combination of the van Driest function (1956) and the experimental data of Ueda et al. (1977). However, for studying the effects of interfacial shear stress on the flow and heat transfer, the model presented by Hubbard et al. (1976) is also applied, and a comparison is made between the results obtained from both models. The model of Hubbard consists of two parts: One is applicable for the region near the solid wall, which is the conventional van Driest model of diffusivity, and the other applies for the region near the liquid–vapor interface, which is based on the results of Chung (1974) for gas absorption into turbulent liquid films. The model is given by:

$$E_m(R)=\frac{1}{2}+\frac{1}{2}\sqrt{1+0.64\bar{\delta}^2R^2\left(1+\frac{R}{\bar{\tau}_w}\right)\left[1-\exp\left(\frac{-R\bar{\delta}}{2.6}\right)\right]^2}, \quad 0\le R<R_1 \quad (3f)$$

$$E_m(R)=1+\frac{8.13\times10^{-17}(\nu g)^{2/3}}{\mathrm{Ka}(\bar{\tau}_w/\rho)}\times\mathrm{Re}^{1390\nu^{1/2}}\left[1+(0.9+1.73\times10^{12}\nu^2)\left(\frac{\tau_i}{\tau_w^o}\right)\right]^2\times\bar{\delta}^2(1-R)^2, \quad R_1\le R\le1 \quad (3g)$$

where R_1 is the intersection point of both equations.

$$\bar{\tau}_w=\frac{\tau_w}{(\rho-\rho_v)g\delta} \quad (3h)$$

$$\tau_w^o=\rho\left(\frac{\mathrm{Re}\nu}{57.2\delta}\right)^2 \quad (3i)$$

Wave effects are neglected, hence an average constant film thickness is assumed in the analysis. The correlation of Gimbutis (1974) is utilized for calculating the film thickness as a function of Reynolds number. The expression is given by:

$$\delta=(0.0318\mathrm{Re}^{0.92}+8)^{2/3}\frac{\nu^{2/3}}{g^{1/2}} \quad (3j)$$

Once the turbulent eddy diffusivity is known, then the velocity profile across the film is obtained by integrating Eq. (3*a*) numerically.

The temperature distribution across the film, and consequently, the heat transfer coefficients at any location (Z) along the tube length, are obtained by solving energy Eq. (2) using the splitting procedure as now described. Assume the solution of energy Eq. (2) is of the form:

$$\theta(R,Z)=\theta_1(R)+\theta_2(R,Z) \quad (4)$$

Such a solution has to satisfy Eq. (2) and its associated boundary conditions. The splitting of the energy problem gives two simple problems: homogeneous $\theta_2(R,Z)$ and nonhomogeneous $\theta_1(R)$ as follows:

The nonhomogeneous problem $\theta_1(R)$ is given by:

$$\frac{d}{dR}\left[(S-R)^nE_h(R)\frac{d\theta_1(R)}{dR}\right]=0 \quad (5a)$$

$$\frac{d\theta_1(R)}{dR}=-Q_0 \text{ at } R=0 \quad (5b)$$

$$\theta_1(R)=0 \text{ at } R=1 \quad (5c)$$

The homogeneous problem $\theta_2(R,Z)$ is:

$$(S-R)^nW(R)\frac{\partial\theta_2(R,Z)}{\partial Z}=\frac{\partial}{\partial R}\left[(S-R)^nE_h(R)\frac{\partial\theta_2(R,Z)}{\partial R}\right] \quad (6a)$$

$$\frac{\partial\theta_2(R,Z)}{\partial R}=0 \text{ at } R=0 \quad (6b)$$

$$\theta_2(R,Z)=0 \text{ at } R=1 \quad (6c)$$

$$\theta_2(R,Z)=-\theta_1(R) \text{ at } Z=0 \quad (6d)$$

The nonhomogeneous system (5) is solved by direct integration to yield:

$$\theta_1(R)=Q_1\int_R^1\frac{1}{(S-R)^nE_h(R)}\,dR \quad (7)$$

The solution of the homogeneous problem (6) is obtained by application of integral transform method, which results in:

$$\theta_2(R,Z)=-Q_1\sum_{i=1}^{\infty}\frac{1}{N_i}\psi_i(\mu_i,R)\frac{1}{\mu_i^2}e^{-\mu_i^2Z} \quad (8)$$

Hence the complete solution of energy problem (2) becomes:

$$\theta(R,Z)=Q_1\left[\int_R^1\frac{1}{(S-R)^nE_h(R)}\,dR-\sum_{i=1}^{\infty}\frac{1}{N_i}\psi_i(\mu_i,R)\frac{1}{\mu_i^2}e^{-\mu_i^2Z}\right] \quad (9a)$$

where:

$$Q_1=\frac{Q_0L\alpha S^n}{\delta^2u_m} \quad (9b)$$

$$N_i=\int_0^1(S-R)^nW(R)\psi_i^2(\mu_i,R)dR \quad (9c)$$

Having established the former analytical solution for the energy problem, it is necessary to solve the relevant eigenvalue problem, which is defined as a special case of the Sturm-Liouville system:

$$\frac{d}{dR}\left[(S-R)^nE_h(R)\frac{d\psi(R)}{dR}\right]+[(S-R)^nW(R)\psi(R)\mu^2]=0 \quad (10a)$$

with the homogeneous boundary conditions:

$$\frac{d\psi(R,\mu)}{dR}=0 \text{ at } R=0 \quad (10b)$$

$$\psi(R,\mu)=0 \text{ at } R=1 \quad (10c)$$

The solution of the eigenvalue problem involves the determination of the permissible eigenvalues μ_i so that the trivial solution $\psi(R,\mu)=0$ is excluded. The exact solution of the above eigenvalue problem is too difficult to obtain analytically. Thus it becomes necessary to treat the problem by numerical means. One of the methods that have been developed for evaluating the eigenvalues is the Runge-Kutta technique, which uses Newton's iterative method. This technique is useful for determining lower eigenvalues. However, for higher order ones, the technique becomes unreliable and requires extreme care to account

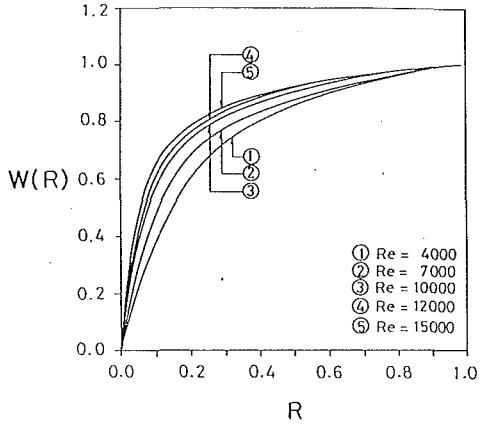

Fig. 1 Effect of Reynolds number on the dimensionless velocity function at different normal positions from the wall

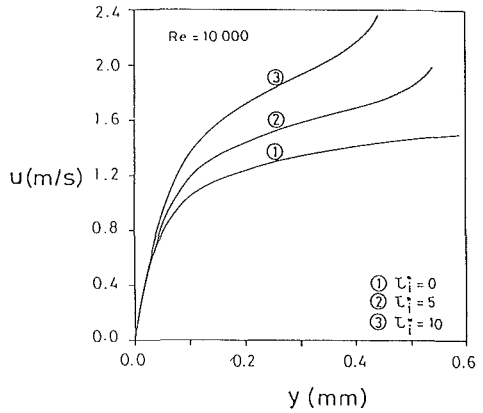

Fig. 2 Velocity distribution measured from the solid wall for different τ_l^+

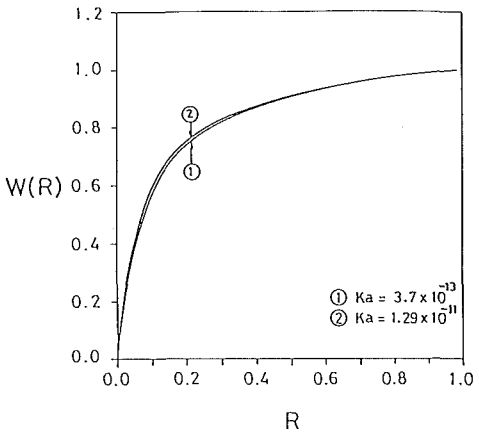

Fig. 3 Effect of Ka on the dimensionless velocity along the dimensionless normal distance measured from the wall

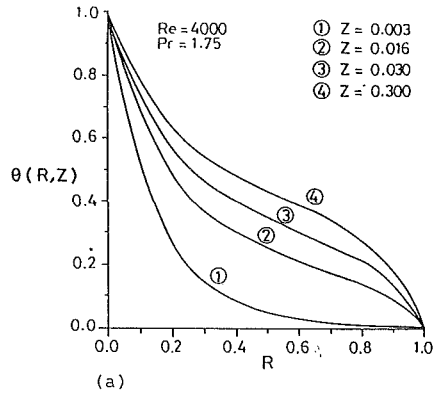

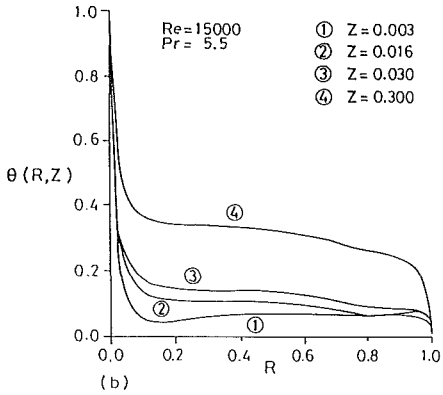

Fig. 4 Dimensionless temperature distribution at different axial distances of the tube

for the possibility of missing some of those high-order eigenvalues.

In order to overcome these difficulties, another more efficient technique, called the sign-count method (Mikhailov and Ozisik, 1984) is adopted for our calculations. The sign-count method for evaluating the eigenvalues, eigenfunctions, and the norm of the Sturm–Liouville system is a reliable approach that provides safe and automatic computation of the eigenvalues and eigenfunctions, with the main advantage that as many eigenvalues as desired can be calculated without missing any one of them. (A detailed description of the sign-count method is available upon request.)

The splitting procedure presented here is more convenient for computational purposes than the conventional methods. The integral term that appears in Eq. (9*a*) is a closed form, whereas this term is expressed in a slow converging series when solving the energy equation by the conventional methods. Here it should be pointed out that for laminar falling films a closed-form solution can be obtained for the velocity and temperature distributions as special cases from Eqs. (3*a*) and (9*a*), respectively. Once the temperature profile is determined, then the dimensionless local evaporative heat transfer coefficient is obtained from its definition as:

$$h^* = h\nu^{2/3}/kg^{1/3} \tag{10}$$

which results in:

$$h^* = Q_2\left[\int_0^1 \frac{1}{(S-R)^n E_h(R)}\,dR - \sum_{i=1}^{\infty}\frac{1}{N_i}\frac{1}{\mu_i^2}e^{-\mu_i^2 z}\right]^{-1} \tag{11}$$

where

$$Q_2 = \frac{\delta u_m \nu^{2/3}}{L\alpha S^n g^{1/3}} \tag{12}$$

Results and Discussion

Parametric and sensitivity analyses have been conducted to illustrate the influence of various parameters in the evaporative falling film inside a vertical tube heated by condensing steam outside the tube. In these results, the fluid properties are evaluated at the saturation temperature, and the turbulent Prandtl number is taken as 0.9. Axial position is normalized with respect to a tube length of 3.0 m.

The dimensionless velocity profiles for several Reynolds numbers are depicted in Fig. 1. It is noticed that the velocity profile becomes more flat as the Reynolds number increases. The effects of interfacial shear on the velocity profile and the film thickness are shown in Fig. 2. The average velocity in-

Table 1 Correlation constants

	6000≤Re≤14000		14000< Re ≤ 19000	
	0.03 ≤ Z ≤ 0.27	0.27 < Z ≤ 1.0	0.03 ≤ Z ≤ 0.13	0.13 < Z ≤ 1.0
C1	0.00264	0.00527	0.00211	0.0043
C2	0.4415	0.371	0.443	0.3902
C3	0.5427	0.547	0.7107	0.526
C4	501.83	25701	144.68	480.8
C5	1	1	0	1
C6	0.85	2	0.85	0.85

Table 2 Percentage mean deviation

Pr \ Re	6000	7000	9000	11000	13000	15000	17000	19000
1.75	5.91	3.33	1.02	0.47	0.60	0.86	1.34	2.47
2.25	4.04	1.89	0.36	0.91	0.89	0.89	0.93	2.01
2.75	2.86	1.01	0.79	1.29	1.04	1.05	0.94	1.93
3.25	2.10	0.62	1.10	1.44	0.98	1.03	1.07	2.02
3.75	1.53	0.52	1.19	1.39	0.87	0.89	1.24	2.17
4.25	1.60	0.64	1.16	1.21	1.06	0.77	1.47	2.44
4.75	2.04	0.83	1.06	1.03	1.29	0.84	1.79	2.81
5.50	3.04	1.16	1.20	1.39	1.77	1.26	2.45	3.45

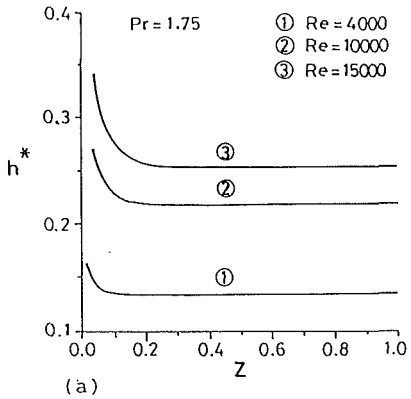

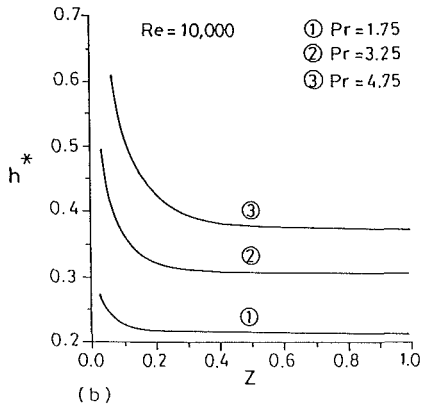

Fig. 5 Local dimensionless heat transfer coefficient

creases by increasing the interfacial shear and obviously the film thickness decreases for fixed Reynolds number. Kapitza number has little effect on the velocity distribution, as shown in Fig. 3.

Figure 4(*a*) shows some typical dimensionless temperature profiles across the film thickness for different axial distance along the wall and Re = 4000 and Pr = 1.75. The temperature distribution becomes more flat and uniform across the film thickness by increasing Pr or Re or both, as shown in Fig. 4(*b*), as compared with the results of Fig. 4(*a*). Furthermore, as is seen from Fig. 4(*a*), the effect of energy loss at the film interface becomes more noticeable at $Z > 0.003$ at which an interfacial temperature gradient starts to develop due to the

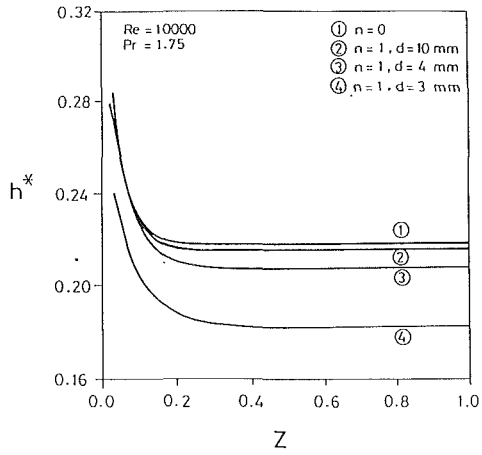

Fig. 6 Effect of surface curvature on the dimensionless heat transfer coefficient h^*

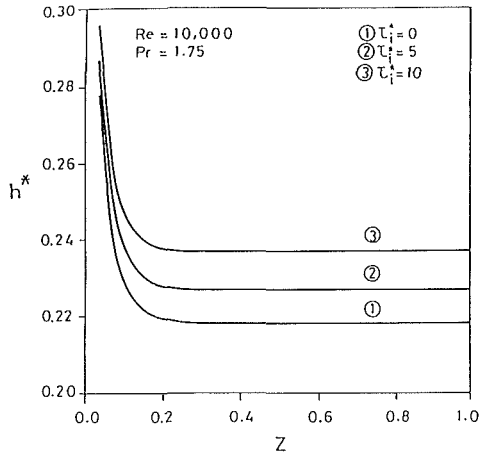

Fig. 7 Effect of the interfacial shear stress on the dimensionless heat transfer coefficient

formation and the growing of a secondary thermal boundary layer at the film surface. Such an interfacial thermal resistance acts to delay the formation of a fully established temperature profile, resulting in an extended thermal development length, which characterizes the evaporative condition.

The dimensionless local heat transfer coefficients for different Reynolds and Prandtl numbers are given in Figs. 5(*a*,*b*). The reduction of the heat transfer coefficient along the tube is caused by an increase of the wall temperature in that direction for constant wall heat flux. The results show that at high Reynolds and Prandtl numbers, the fully developed condition is reached at about $Z \approx 0.4$. In our study, the local heat transfer coefficient is correlated in terms of Reynolds and Prandtl numbers along the tube length and a new formula has been developed as follows:

$$h^* = C1\,\mathrm{Re}^{C2}\mathrm{Pr}^{C3} + \frac{\mathrm{Pr}^{C5}}{C4(Z^{C6})} \quad \text{for } 1.75 \le \mathrm{Pr} \le 5.5 \qquad (13)$$

where the constants C at different locations and Reynolds number are given in Table 1. The maximum percentage mean deviation for this correlation is 5.91 percent occurring at Re = 6000 and Pr = 1.75 as shown in Table 2.

The effect of surface curvature on the local heat transfer coefficient is presented in Fig. 6. It is found that the curvature effect is insignificant for tube diameters larger than 10 mm.

The effect of vapor shear stress becomes more important for long tube evaporators. The film thickness is decreased and the average velocity is increased as the interfacial shear stress is increased. Figure 7 depicts the effect of interfacial shear stress on the heat transfer coefficient.

In the present work, the effect of interfacial shear is studied

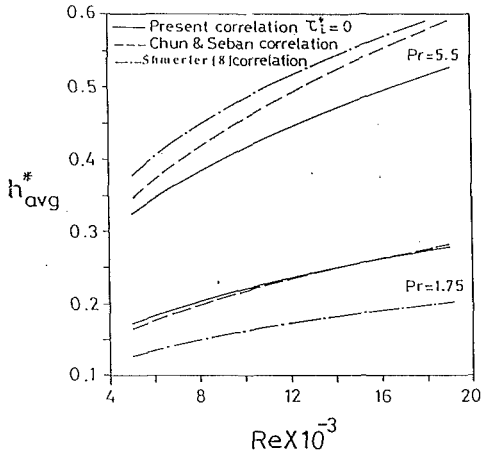

Fig. 8 Comparison between the average heat transfer coefficient obtained by Chun and Seban (1971) and Shmerler and Mudawwar (1988) and the present work

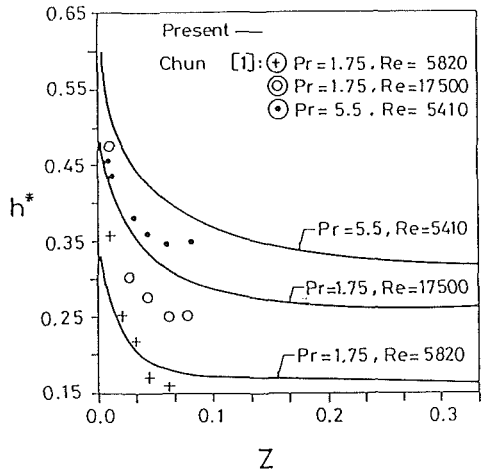

Fig. 9 Comparison with the experimental data of Chun and Seban (1971)

by employing the eddy diffusivity model of Mudawwar and El-Masri (1986) and the model of Hubbard et al. (1976). The results obtained from both models showed that the percentage increase in the heat transfer coefficient is almost in the range of 10.5 to 16 percent for increasing the interfacial shear from $\tau_i^*=0$ to $\tau_i^*=10$.

A new correlation of the average heat transfer coefficient is developed to accommodate the effect of vapor shear stress as:

$$h^*_{avg}=\mathrm{Re}^{0.363}\mathrm{Pr}^{0.555}(0.00572+0.0002234\tau_i^{*0.439}) \quad \text{for } 5000\le \mathrm{Re}\le 20000,\ 1.75\le \mathrm{Pr}\le 5.5,\ \text{and } 0\le \tau^*\le 10 \tag{14}$$

where

$$\tau_i^*=\frac{\tau_i}{(g^2\rho\mu^2)^{1/3}} \tag{15}$$

The correlation uses the model of Mudawwar et al. for calculating the heat transfer coefficient against the variation of interfacial shear stress. This correlation has a mean percent relative difference of 2.9 percent and standard deviation of 2.0.

Figure 8 shows a comparison between the present correlation with $\tau_i^*=0$ and the correlation obtained by Chun and Seban (1971) for the average evaporative heat transfer coefficient. Here the deviation between the two correlations is increased by increasing Pr number, and the maximum deviation is 12.2 percent occurring at Re = 19,000 and Pr = 5.5. Shmerler and Mudawwar (1988) presented an experimental correlation for the average heat transfer coefficient over a heated length of 0.781 m. The correlation is given by: $h^*_{avg}=0.0038\ \mathrm{Re}^{0.35}\mathrm{Pr}^{0.95}$. The mean percentage relative difference was shown to be 6 percent with a standard deviation of 0.023. A comparison of our correlation with $\tau_i^*=0$ and the correlation of Shmerler and Mudawwar is again shown in Fig. 8, where our correlation gives higher values for h^* than their correlation at Pr = 1.75 and lower values at Pr = 5.5. This is also seen in Fig. 9, showing lower experimental data of Chun and Seban as compared with the present calculated values of h^*. The difference between theoretical and experimental results can be attributed to the eddy diffusivity function, which does not consider the wave activity at the film interface.

A fully developed heat transfer coefficient for $Z>0.4$ is also correlated in terms of Re and Pr numbers but without interfacial shear stress as follows:

$$h^*_{ful}=0.006362\mathrm{Re}^{0.351}\mathrm{Pr}^{0.528} \quad \text{for } 6000\le \mathrm{Re}\le 19000 \text{ and } 1.75\le \mathrm{Pr}\le 5.5 \tag{16}$$

This relation has a mean present relative difference of 1.54 percent and maximum of 3.6 percent. The standard deviation is 1.19.

Only the convective type of flow boiling is studied in the present work, in which heat is transferred by conduction and convection through the thin liquid film, and evaporation takes place at the liquid–vapor interface. On the other hand, nucleate boiling is characterized by the formation of bubbles that nucleate at the solid surface. Davis and Anderson (1966) have shown that nucleate flow boiling occurs if

$$\Delta T>\sqrt{\frac{8\sigma T_s q_0}{h_{fg}\rho_v k}} \tag{17}$$

where ΔT is the difference between the wall and saturation temperatures. The expression relates the maximum wall temperature to the heat flux to avoid nucleate boiling. For Re = 10,000 and Pr = 1.75, it is found that according to Eq. (17), ΔT is greater than 0.899°C. However, in this study the maximum $\Delta T=0.617$°C, which ensures convective boiling.

Conclusions

A successful general semi-analytical methodology is presented for the velocity and temperature profiles in rectangular and cylindrical coordinates for evaporative heating of free turbulent falling liquid films inside long vertical tubes. New correlations have been developed for the local as well as the fully developed and average turbulent heat transfer coefficients.

The splitting procedure utilized in the present work provides an efficient solution for computational purposes. Moreover, the eigenvalues, eigenfunctions, and the norm associated with the resulting homogeneous problem are efficiently computed by the sign-count algorithm. The reliability and accuracy of the method are demonstrated by several numerical results, which showed excellent agreement with the available data in literature.

The sensitivity study showed that the Reynolds and Prandtl numbers with the interfacial shear have significant effects on the heat transfer coefficient. Furthermore, the Kapitza number and surface curvature have little effect upon the turbulent heat transfer coefficient. The present analysis can be extended, with modifications, to handle local sensible heating cases as well as condensation on vertical and horizontal surfaces.

Acknowledgments

The authors appreciate the support of Kuwait University, Office of the Vice Rector for Research, through research project grant No. EM051.

References

Chun, K. R., and Seban, R. A., 1971, "Heat Transfer to Evaporating Liquid Films," ASME JOURNAL OF HEAT TRANSFER, Vol. 93, pp. 391–396.

Chung, D. K., 1974, "An Experimental Investigation of Gas Absorption Into a Turbulent Liquid Film With Interfacial Shear," PhD dissertation, University of California, Los Angeles, CA.

Davis, E. J., and Anderson, G. H., 1966, "The Incipience of Nucleate Boiling in Forced Convection Flow," *AIChE J.*, Vol. 12, pp. 774–780.

Driest, E. van, 1956, "On Turbulent Flow Near a Wall," *J. Aero. Science*, Vol. 23, pp. 1007–1011.

Faghri, A., and Seban, R. A., 1988, "Heat and Mass Transfer to a Turbulent Falling Film," *Int. J. Heat Mass Transfer*, Vol. 31, pp. 891–894.

Faghri, A., and Seban, R. A., 1989, "Heat and Mass Transfer to a Turbulent Falling Film—II," *Int. J. Heat Mass Transfer*, Vol. 32, pp. 1796–1798.

Fujita, T., and Ueda, T., 1978, "Heat Tarnsfer to Falling Liquid Films and Film Breakdown—II," *Int. J. Heat Mass Transfer*, Vol. 21, pp. 109–118.

Gimbutis, G., 1974, "Heat Transfer of a Turbulent Falling Film," *Proc. 5th Int. Heat Transfer Conf.*, Tokyo, Japan, Vol. 2, pp. 85–89.

Hubbard, G. L., Mills, A. F., and Chung, D. K., 1976, "Heat Transfer Across a Turbulent Falling Film With Cocurrent Vapor Flow," ASME JOURNAL OF HEAT TRANSFER, Vol. 98, pp. 319–320.

Mikhailov, M. D., and Özişik, M. N., 1984, *Unified Analysis and Solutions of Heat and Mass Diffusion*, Wiley, New York.

Mudawwar, I., and El-Masri, M. A., 1986, "Momentum and Heat Transfer Across Freely Falling Turbulent Liquid Films," *Int. J. Multiphase Flow*, Vol. 12, pp. 771–790.

Saibabu, J., Sarma, P. K., Rao, V., and Raju, G. J., 1986, "Experimental and Theoretical Investigation on Dynamics and Heating of Turbulent Falling Films," *Proc. 8th Int. Heat Transfer Conf.*, San Francisco, CA, Vol. 4.

Singh, S. N., 1958, "Heat Transfer by Laminar Flow in Cylindrical Tubes," *Appl. Sci. Res. Sec. A*, Vol. 7, No. 5, pp. 325–340.

Shmerler, J. A., and Mudawwar, I., 1988, "Local Evaporative Heat Transfer Coefficient in Turbulent Free-Falling Liquid Films," *Int. J. Heat Mass Transfer*, Vol. 31, No. 4, pp. 731–742.

Ueda, H., Moller, R., Komori, S., and Mizushima, T., 1977, "Eddy Diffusivity Near the Free Surface of Open Channel Flow," *Int. J. Heat Mass Transfer*, Vol. 20, pp. 1127–1136.

J. Orozco
Associate Professor.
Mem. ASME

H. Francisco
Graduate Student.

Florida International University,
Department of Mechanical Engineering,
University Park Campus,
Miami, FL 33199

Free Convection Film Boiling Heat Transfer From a Rotating Surface

A boundary layer model of laminar, subcooled, free convection film boiling from a rotating sphere has been developed. The conservation equations for the vapor and liquid were simplified, transformed into ordinary differential equations using an integral approach, and solved numerically. The theoretical variation of vapor film thickness with heater temperature and the resulting boiling fluxes were investigated. An experimental facility was built for the purpose of verifying the validity of the theoretical model and good agreement was found between the model and the experimental data at low rpm. The instability of the vapor film near the minimum heat flux for a rotating surface flux was also investigated.

Introduction

A review of the boiling heat transfer literature over the past four decades reveals that a great deal has been accomplished in developing an understanding of film boiling. Nevertheless, there are still issues that have not been resolved. The first theoretical and experimental study of saturated film boiling heat transfer from a horizontal cylinder in a pool of liquid was made by Bromley (1950). His analysis, as demonstrated by the work of Breen and Westwater (1962), was applicable only to a limited range of heater diameters. The effect of heater diameter for spheres has also been examined. The theoretical models of Hendricks and Baumeister (1969), and Gunnerson and Cronenberg (1980) have indicated a large enhancement of heat flux for small spheres compared to large ones. Manson (1966), Ungar and Eichorn (1982), as well as Sankaran and Witte (1986) have shown that there is an azimuthal angular variation in film boiling fluxes over the surface of a spherical heater. Merte and Clark (1964) studied the boiling of nitrogen on copper spheres, 12.7 and 25.4 mm in diameter, under standard and fractional gravity conditions. The film boiling heat transfer coefficient at $0.1 < g_c/g < 1$, was proportional to $(g_c/g)_{1/3}$, whereas the sphere diameter was not found to affect the heat transfer rates. Frederking and Clark (1962) performed an analytical study of heat transfer in pool building on a sphere with the assumption of a laminar vapor flow and a smooth vapor interface. Their final result, written in nondimensional form, differs from Bromley's analysis of a horizontal cylinder only by a numerical constant. Forced convection film boiling from a sphere in subcooled water was studied by Jacobson and Shair (1970) using a 5-kW, high-frequency induction heater to heat a 6.35-cm copper sphere continuously. They determined that the resulting heat transfer rates were higher than those theoretically predicted by Witte (1968) for saturated liquid. Witte and Orozco (1984) improved Witte's theoretical formulation of film boiling from spheres submerged in a flowing liquid by incorporating the effects of liquid pressure on the vapor film. Later, Orozco and Witte (1986) obtained the boiling curves for flow film boiling of Freon-113 from a fluid heater copper sphere. The theory developed by Witte and Orozco predicted heat fluxes very well for the heat transfer regime where stable film boiling existed over the entire heated area. For the case where a large vapor wake occurred behind the spherical heater, the measured film boiling fluxes were found to be higher, approximately by a factor of two, than the theoretically predicted fluxes. Heat transfer rates from nickel plated copper spheres moving in water were measured by Aziz et al. (1986). They were also able to identify a new boiling regime. In this regime, small bubbles similar to those observed in nucleate boiling at low temperature were emitted from the interfacial region. The underprediction of the experimental data by the various theoretical models has been addressed by Witte et al. (1983). They attributed part of the underprediction to the contribution of liquid–solid contact to the heat transfer process. This effect was incorporated by Witte et al. into the theoretical formulation previously developed by them. Recently, Dix and Orozco (1990) measured the heat transfer rates in the wake region of a sphere in forced convection film boiling. Heat transfer rates comparable to those obtained in the stable film boiling region were measured in the wake region. These measurements have made obsolete the commonly held notion that film boiling fluxes in the wake region were negligible. Another interesting aspect of film boiling research has been the determination of the stability criteria leading to the termination of the film boiling regime. The work of Henry et al. (1974) is of special significance in this field. Using Berenson's approach (1961) for film boiling stability over a flat plate, they added the effect of liquid–solid contact. Bradfield (1966), Stevens and Witte (1973), Yao and Henry (1978), Orozco and Witte (1986), and Sakurai et al. (1990) have provided evidence suggesting that the wavy nature of the film boiling liquid–vapor interface and the condition of the heated surface are the main causes for the occurrence of liquid–solid contacts and the driving forces behind the destabilization of the vapor film. Recently, Tanaka (1988) presented a model for film boiling destabilization; however, his model does not match the theoretical findings very well.

This brief literature review indicates that a good understanding of the heat transfer mechanisms of film boiling has been obtained in the last few years. With the purpose of further advancing our knowledge of the film boiling regime, this article reports on research designed to determine the influence of angular velocity on film boiling from a rotating sphere in a pool of liquid. A theoretical model based on boundary layer approximations has been developed. Experiments were conducted to verify the validity of the model on film boiling of Freon-113 from a 2.54-cm-dia rotating copper sphere. The behavior of the vapor film in the vicinity of the minimum flux was investigated.

Experimental Apparatus

The experimental apparatus used in this study employed a transient quenching technique and involved submerging a rotating 2.54-cm-o.d. heated copper sphere in a pool of Freon-113. An overview of the apparatus is shown in Fig. 1. The essential component of the experiment, a hollow copper sphere, was made from two hollow hemispheres machined from a 4.00-cm copper bar. The two hemispheres were press fitted along

Contributed by the Heat Transfer Division for publication in the JOURNAL OF HEAT TRANSFER. Manuscript received by the Heat Transfer Division August 1990; revision received November 1991. Keywords: Boiling, Multiphase Flows, Rotating Flows.

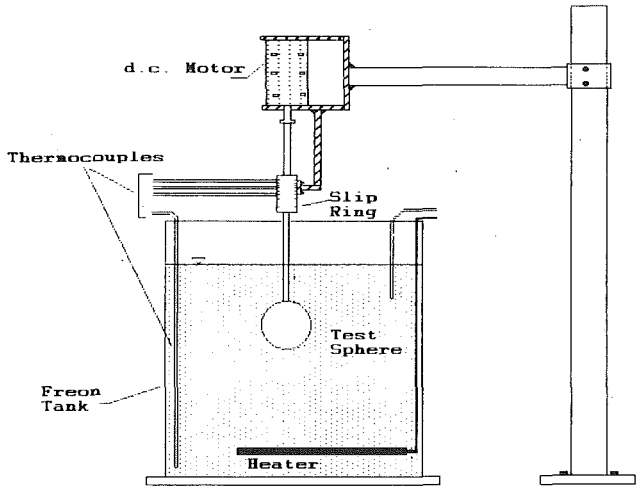

Fig. 1 Experimental apparatus

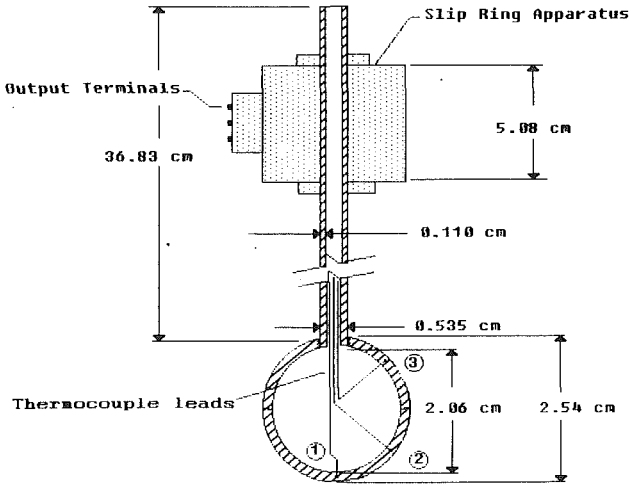

Fig. 2 Schematic of test sphere and slip ring apparatus

the equator after having three, 30-gage, copper-constantan thermocouples mechanically peened to the inner surface of the hemispheres. The peening of the thermocouples was accomplished by machining three 0.120-cm-deep cavities in the sphere inner surface. The thermocouples were then placed in the cavities and peened in place. The softness of the copper mass allowed for excellent thermal contact between the thermocouple beads and the copper mass. The hollow copper sphere including the location of the three thermocouples is shown in Fig. 2. An effort was made to minimize the fin effect of the sphere support rod on the heat transfer process. The rod was constructed out of stainless steel and its diameter was the smallest possible diameter that would accommodate all the thermocouple lead wires. Errors in thermocouples measurements were estimated to be on the order of 1 percent. The sphere was heated to a temperature adequate to achieve film boiling with the aid of an electric furnace. The electric furnace consisted of two semicircular ceramic shell heaters rated at 1000 W maximum power output. Thermocouple measurements were made with a six-ring instrumentation slip ring mounted on the stem of the sphere. The slip ring was designed to handle a maximum of three thermocouples, as shown in Fig. 2. The device, although relatively simple in nature, allows the sphere to be set in motion while monitoring its temperature without any lead breakage. The instrumentation slip ring consisted of a fixed outer cylinder and a rotating inner cylinder with a set of six input and output terminals. The sphere thermocouples wires were connected to the inner cylinder input terminals by means of solderless connectors. The signals from the output leads were then sent to a Hewlett-Packard 3852 data acquisition/control unit. Thermocouple measurements were made at the rate of 50 samples per second. A 50.80-cm-tall rectangular tank with a 40.64 cm by 20.32 cm cross section was used for the experiments. The tank was constructed of 0.160-cm-thick glass plate and had a capacity of 41.60 liters. The tank joints were cemented with high strength silicon adhesive and then reinforced with silicon rubber cement to prevent leakage. An immersion heater maintained the working fluid at the desired temperature level. The Freon-113 temperature was monitored with two copper-constantan, 304 stainless steel sheathed thermocouples connected to a digital thermometer with an accuracy of $\pm$ 0.1°C. An effort was made to provide, as nearly as possible, a constant sphere angular rotation while the sphere was submerged in the liquid pool. The sphere was set in motion by means of a 0.25-hp, 90-V, electric motor and a d-c motor speed controller.

Video recordings of the experiments were obtained with aid of a Sony TV Zoom Camera equipped with a 12.5–75 mm, f1.8, zoom lens. In addition to the Sony camera, a large-format, Crown Graphic Special view camera was used to record the boiling phenomena in detail. Photographs were taken at 1/500 second on Polaroid type-55 Land film.

Data Acquisition and Reduction

Significant temperature variations occurred on the surface

Nomenclature

a_0, a_1, a_2 = polynomial coefficients, see Eq. (5)
c_p = specific heat
g = gravitational constant
g_c = reduced gravity
h_{fg} = modified heat of vaporization
k = thermal conductivity
$\dot{m}$ = mass flux
R = sphere radius
q = heat rate
q'' = heat flux
T = temperature
$\Delta T_v = T_w - T_{sat}$
$\Delta T_b = T_{sat} - T_\infty$
t = time
Δt = time step
V = volume
u, v, w = velocity components in the x, y, and z directions
x, y, z = coordinate system differentiation with respect to θ

Subscripts

α = thermal diffusivity
δ_v = vapor layer
δ_l = liquid layer thickness
δ = ratio of vapor to liquid layer thickness
η = dimensionless thickness
θ = angular position measured from the sphere forward stagnation point
μ = absolute viscosity
ν = kinematic viscosity
ρ = density
ϕ = azimuthal angle
ω = angular velocity
b = boiling
c = conduction
i = inner
int = interface
l = liquid
max = maximum
min = minimum
o = outer
s = sphere
sat = saturation
v = vapor
w = wall
∞ = liquid region unaffected by and far away from liquid–vapor interface

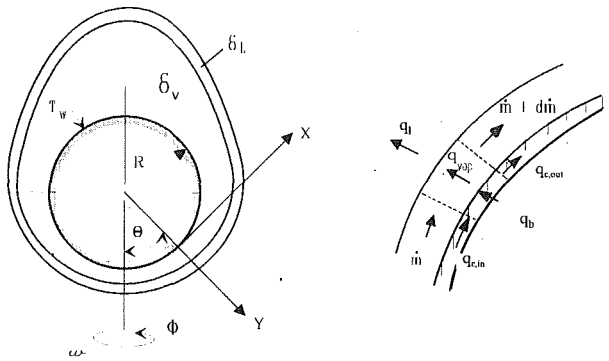

Fig. 3 Theoretical model

of the sphere during the boiling process. These variations in surface temperature brought about a dependence of the system boiling flux on both time and angular position. To solve for the sphere local boiling flux, a differential energy balance was conducted on the control volume shown in Fig. 3. Neglecting the effects of thermal radiation and convection between the air inside the sphere and the sphere's inside surface, the energy balance yields

$$(\rho c_p)_s \frac{\partial T_s}{\partial t} dV = q_{c(\text{in})} - q_{c(\text{out})} - q_b \tag{1}$$

where

$$q_{c(\text{out})} - q_{c(\text{in})} = \frac{\partial}{\partial \theta}\left(kR \sin\theta \frac{\partial T}{\partial \theta}\right) d\theta\, dy\, d\phi \tag{2}$$

and

$$q_b = R^2 \sin\theta\, d\theta\, d\phi\, q_b'' \tag{3}$$

Substituting Eqs. (2) and (3) into Eqs. (1) and completing some algebraic steps (Dix and Orozco, 1990) yields the following expression for the local boiling flux:

$$q_b'' = \frac{k_s(R_o - R_i)}{R_o R_i}\left[\cos\theta \frac{\partial T}{\partial \theta} + \frac{\partial^2 T}{\partial \theta^2}\right] - (\rho c_p)_s (R_o - R_i)\frac{\partial T}{\partial t}$$

In order to compute the boiling flux as given by Eq. (4), the first and second derivatives of temperature with respect to angular position were evaluated as follows:

A polynomial in θ of the form

$$T(\theta) = a_o + a_1 \cos\left(\frac{\theta}{2}\right) + a_2 \cos\left(\frac{\theta}{2}\right) \tag{5}$$

subject to the following boundary conditions

$$T(\theta = 0) = T_1$$
$$T(\theta = \pi/4) = T_2 \tag{6}$$
$$T(\theta = 3\pi/4) = T_3$$

and

$$\left.\frac{\partial T}{\partial \theta}\right|_{\theta=0} = \left.\frac{\partial T}{\partial \theta}\right|_{\theta=\pi} = 0$$

was assumed for the temperature distribution along the θ direction. T_1, T_2, and T_3 are the temperature measurements at the 0, 45, and 135 deg angular positions, respectively. Once the time-dependent polynomial coefficients a_0, a_1, and a_2 for Eq. (5) were determined, expressions for the first and second derivatives of temperatures with respect to θ were computed. The partial derivative of temperature with respect to time in Eq. (4) was next evaluated using the thermocouple measurements as follows:

$$\left.\frac{\partial T}{\partial t}\right|_{\text{time}=t} = \frac{T(t+\Delta t) - T(t-\Delta t)}{2\,\Delta t} \tag{7}$$

where Δt is the time interval between consecutive thermocouple measurements. The process of computing the coefficients of Eq. (5) and the partial derivatives of temperature with respect to time and angular position was repeated at each time step.

Theoretical Analysis

It has been demonstrated by Rao and Prasad (1983) that film boiling problems are successfully approached using an integral solution. An integral method was, therefore, utilized in the formulation of film boiling from a rotating sphere to a subcooled liquid.

Consider a rotating sphere in a subcooled liquid with film boiling occurring at the sphere surface. The sphere is maintained at a uniform constant temperature T_w and heat is transferred from the sphere mainly by conduction and radiation. The vapor and liquid boundary layers are assumed to be symmetric about the vertical axis. In addition to the standard film boiling boundary layer assumptions, we assumed that the flow was laminar, with eventual transition to turbulent flow. The physical model and coordinate system are shown in Fig. 4. The velocity component u is in the x direction, v is in the y direction, w is the transverse velocity due to the body spin, and the angle θ, measured from the forward stagnation point, denotes angular position. Neglecting any wake effects and assuming constant physical properties, the describing equations are presented below.

Vapor Region. The velocity and temperature profiles in the vapor film are subject to the following boundary conditions:

Heated surface ($y = -\delta_v$)

$$u_v = v_v = 0 \tag{8a}$$
$$T_v = T_w \tag{8b}$$
$$\frac{\partial^2 u_v}{\partial y^2} = \frac{g \sin\theta(\rho_v - \rho_l)}{\mu_v} - \frac{\omega^2 R^2 \sin^2\theta}{x \nu_v} \tag{8c}$$

where the last boundary condition evolves from the use of the momentum equation at the heated surface.

Liquid–vapor interface ($y = 0$)

$$u_v = u_{\text{int}} = u_l \tag{9a}$$
$$T_v = T_{\text{sat}} \tag{9b}$$
$$\mu_l \frac{u_l}{\partial y} = \mu_v \frac{\partial u_v}{\partial y} \tag{9c}$$
$$\rho_l\left(v_l - u_l \frac{\partial \delta_v}{\partial x}\right) = \rho_v\left(v_v - u_v \frac{\partial \delta_v}{\partial x}\right) = \dot{m} \tag{9d}$$

The vapor boundary conditions on the x component of velocity and on temperature, Eqs. (8) and (9), are satisfied by the following two polynomials:

$$u_v = u_{\text{int}}(1 + \eta_v) + \frac{\delta_v^2}{2}\eta_v(1 + \eta_v)\left[\frac{g \sin\theta(\rho_v - \rho_l)}{\mu_v} - \frac{\omega^2 R^2 \sin^2\theta}{x\, \nu_v}\right] \tag{10}$$

and

$$T_v = T_{\text{sat}} - \Delta T_v\, \eta_v \tag{11}$$

where u_{int} is the liquid interface velocity, which is determined from the equality of velocity and shear stress at the liquid–vapor interface, and η_v the dimensionless vapor thickness.

Liquid Region. The temperature and velocity boundary conditions in the liquid region are as follows:

$$u_l = 0$$
$$T_l = T_\infty \qquad \text{at } y = \delta_l \tag{12}$$
$$\frac{\partial u_l}{\partial y} = 0$$

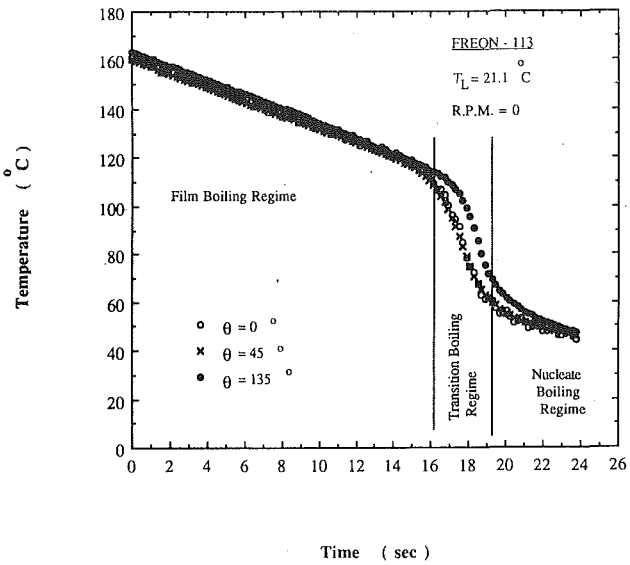

Fig. 4 Typical temperature versus time curve and various stages of pool boiling during quenching of a sphere in subcooled Freon-113

Second and third degree polynomials are prescribed for the temperature and velocity profiles in the liquid subject to the conditions given by Eq. (9) and (12)

$$u_l = u_{\text{int}}\,(1-\eta_l)^3 + \frac{\delta_l\, g\, \sin\theta(\rho_l-\rho_\infty)(1-\eta_l)^3\,\eta_l}{2\,\mu_l} \tag{13}$$

$$T_l = T_\infty + \Delta T_b(1-\eta_l)^2 \tag{14}$$

From the equality of shear stresses at the liquid-vapor interface, we obtain the interface velocity, which is given by

$$u_{\text{int}} = \frac{\delta_l^2}{2}\left[\frac{B_1 - \delta\mu C_1}{3+\mu/\delta}\right] \tag{15}$$

where

$$B_1 = g\,\sin\theta(\rho_l-\rho_\infty)/\mu_l \tag{16}$$

and

$$C_1 = \frac{g\,\sin\theta(\rho_v-\rho_l)}{\mu_v} - \frac{\omega^2 R^2\,\sin^2\theta}{x\,\nu_v} \tag{17}$$

Mass-Energy Balance. The heat balance on a differential film element as shown in Fig. 4

$$dq = dq_{\text{vap}} + dq_l \tag{18}$$

where dq_{vap} is the energy required to form vapor, and dq_l is the energy conducted into the subcooled liquid when $T_l < T_{\text{sat}}$. Equation (18) can be expanded as

$$k_v \left.\frac{\partial T_v}{\partial y}\right|_0 R\,\sin\theta - k_l \left.\frac{\partial \Gamma}{\partial y}\right|_0 R\,\sin\theta = h_{fg}\frac{d}{dx}\left[\int_0^{-\delta_v} \rho_v\, u_v\, R\,\sin\theta\, dy\right] \tag{19}$$

The use of the liquid and vapor velocity and temperature profiles in the energy-mass balance yields the following ordinary differential equation:

$$\frac{d\delta_l}{d\theta}\,X_1\,(\theta,\,\delta_v,\,\delta_l) + \frac{d\delta_l}{d\theta}\,X_2(\theta,\,\delta_v,\,\delta_1) = X_3\,(\theta,\,\delta,\,\delta_1) \tag{20}$$

The coefficients of Eq. (20) are complex functions involving fluid properties, angular position, and the liquid and vapor thicknesses.

We next focus our attention on the liquid region. In this region, the energy equation may be rearranged into the conservation form

$$\frac{\partial(u_l T_l)}{\partial x} + \frac{\partial(u_\rho T_l)}{\partial y} = \alpha_l \frac{\partial^2 T_l}{\partial y^2} \tag{21}$$

The integration of Eq. (21) across the liquid boundary layer, see Fig. 4, yields

$$\frac{d}{dx}\int_0^{\delta_l} u_l(T_l - T_\infty)\,dy - \Delta T_b\, u_{\text{int}}(1-\rho)\frac{d\delta_v}{dx} + \Delta T_b \rho \int_{-\delta_v}^{0}\left(\frac{\partial u_v}{\partial x} + \frac{u_v}{x}\right)dy = -\alpha_l \left.\frac{\partial T_l}{\partial y}\right|_0 + \int_0^{\delta_l}\frac{u_\rho}{x}(T_\infty - T_l) \tag{22}$$

The integration is finally completed when the velocity and temperature profiles in the two boundary layers are substituted into Eq. (22). The substitution results in the following first-order nonlinear ordinary differential equation:

$$\frac{d\delta_v}{d\theta}\,Y_2\,(\theta,\,\delta_v,\,\delta_l) + \frac{d\delta_l}{d\theta}\,Y_1(\theta,\,\delta_v,\,\delta_l) = Y_3(\theta,\,\delta_v,\,\delta_l) \tag{23}$$

where Y_1, Y_2, and Y_3 are functions similar to those found in Eq. (20). Expressions for the coefficients of Eqs. (20) and (23) are given in the appendix. Equations (20) and (23) allow us to solve for the thicknesses of the vapor and liquid layers as functions of angular position. A numerical solution to these two equations is now possible if the condition of symmetry at the forward stagnation point is used. This condition reads as follows:

$$\frac{\partial\delta_v}{\partial\theta} = \frac{\partial\delta_l}{\partial\theta} = 0 \text{ at } \theta = 0 \tag{24}$$

Once the thicknesses of the two boundary layers are determined, heat transfer results are obtained pertaining to both the local and overall heat transfer rates from the rotating sphere to the liquid region. The local heat transfer is given by

$$q'' = k_v\frac{(T_w - T_{\text{sat}})}{\delta_v} \tag{25}$$

since the temperature profile inside the vapor film is linear. Based on the above equation, it is easy to show that the local heat transfer coefficient and the local Nusselt number are

$$h = \frac{k_v}{\delta_v} \tag{26}$$

$$\text{Nu} = \frac{hD}{k_v} = \frac{D}{\delta_v}$$

The numerical integration of Eqs. (20) and (23) was performed using a fourth-order Runge-Kutta scheme after having determined the initial values of δ_v and δ_l from condition (24). Details on the numerical scheme have been discussed by Orozco et al. (1988).

Discussion of Results

Experimental Results. Figure 4 shows the temperature versus time history for thermocouples T_1(deg), T_2 (45 deg), and T_3 (135 deg) and Fig. 5 presents the calculated heat fluxes at the 45 deg and 135 deg locations for a nonrotating sphere in Freon-113 at 21°C. The curves in Fig. 4 are representative of those temperature curves where the combination of initial sphere and liquid temperatures was such that the three boiling regimes that characterize pool boiling were achieved. In Fig. 4 T_{min} marks the end of the film boiling regime and the heat flux at this point is commonly known as the minimum heat flux or q''_{min}. This minimum film boiling temperature exhibited a dependency on liquid temperature and sphere rotation. Beyond T_{min} the heated surface experienced a sharp drop in temperature caused by the collapse of the vapor film. As liquid came into contact with the heated surface, the sphere entered the transition boiling regime and the slope of temperature

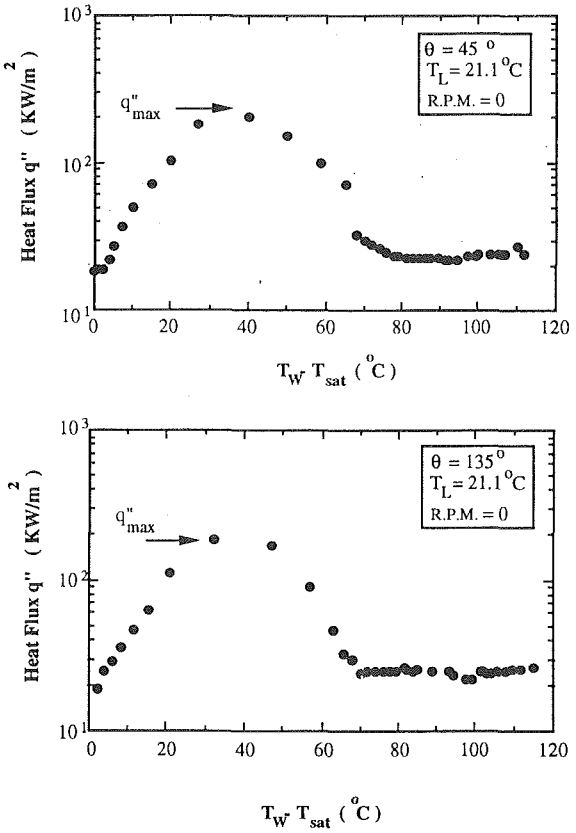

Fig. 5 Heat fluxes for Freon-113 at 21°C at the 45 deg and 135 deg angular locations

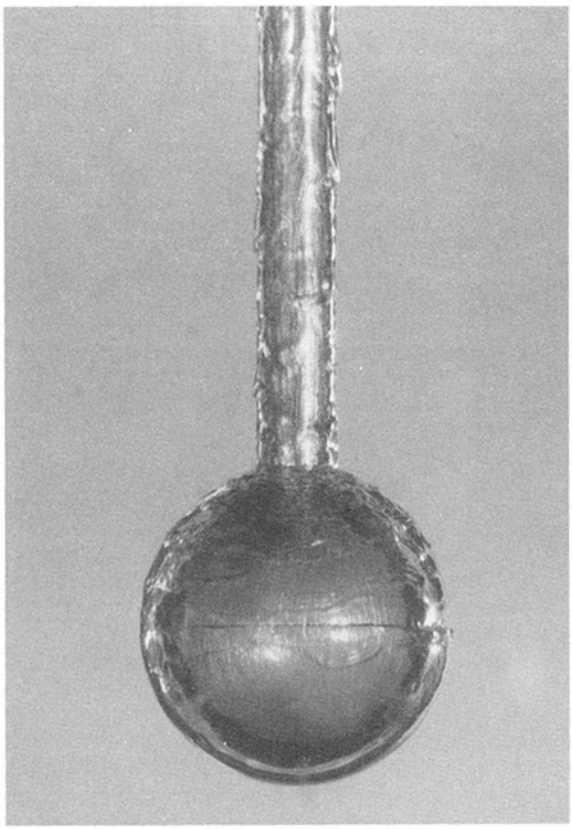

Fig. 6 Still photograph of stable film boiling for Freon-113 at 21°C, zero rotation, and $T_w = 150$°C

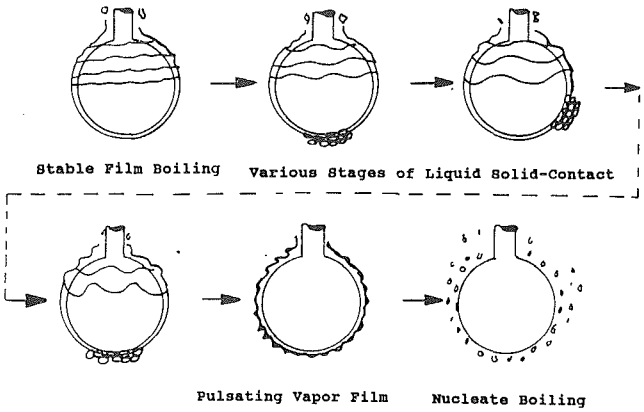

Fig. 7 Sequence of vapor film destabilization for zero surface rotation

versus time curve reached a maximum, which indicated that the surface of the sphere was releasing a maximum amount of energy per unit area. Thus, the upper limit in Fig. 5 is denoted as q''_{max}, the peak heat flux. Beyond q''_{max} the sphere entered the nucleate boiling regime. In the film boiling regime, the sphere surface was virtually at a uniform temperature and with a vapor blanket surrounding the heated surface. The photograph in Fig. 6 illustrates the nature of the stable film boiling regime observed in Freon-113 for zero sphere rotation. It is also worth mentioning at this point that an effort was made to eliminate the influence of surface condition on the boiling process. The sphere was not only polished to a mirrorlike finish before every experimental run, but it was also heated in an argon atmosphere within the electric heater to prevent oxidation of the heated surface.

Effect of Surface Rotation for a Fixed Liquid Temperature. The effect of rotation of the heated surface on the film boiling process was examined for five different angular velocities at a constant liquid temperature. For the case of no rotation, waves in the vapor film originated at the sphere forward stagnation point and traveled toward the sphere back while increasing in amplitude and wavelength. Temperature measurements and video recordings of the process shown by sketches in Fig. 7 indicated that due to the oscillatory behavior of the liquid-vapor interface, liquid-solid contact occurred on the upper half of the sphere during stable film boiling. The destabilization of the vapor film was observed to occur first on the bottom half of the sphere preceded by frequent instances of liquid-solid contact and followed by the occurrence of the same phenomenon on the sphere upper half. However, once the sphere was rotated, the destabilization of the vapor film occurred in reversed order. The upper half of the sphere was observed to enter the transition regime before the sphere lower half. The photograph in Fig. 8 depicts the collapse of the vapor film for a sphere rotation of 500 rpm. For high surface rotation the vapor film became very unorganized in contrast to that observed at low rpm. Figure 9 shows the temperature behavior of the heated surface for sphere rotations of 500 and 1020 rpm, and Fig. 10 illustrates the computed fluxes. The dramatic increase in film boiling fluxes shown in Fig. 10 was due to the occurrence of two hydrodynamic effects as the rotation of the sphere was increased. First, an increase in both amplitude and frequency of oscillation of the waves emanating from the forward stagnation point was observed. Second, a wave pattern in the azimuthal direction was also observed. The additive effect of these two wave patterns gave the liquid-vapor interface a pulsating appearance and also resulted in a dramatic increase in the frequency of liquid-solid contact. The photograph in Fig. 11 shows the two wave patterns observed for a rotation of 1020 rpm in liquid Freon-113 at 21°C. Multiple

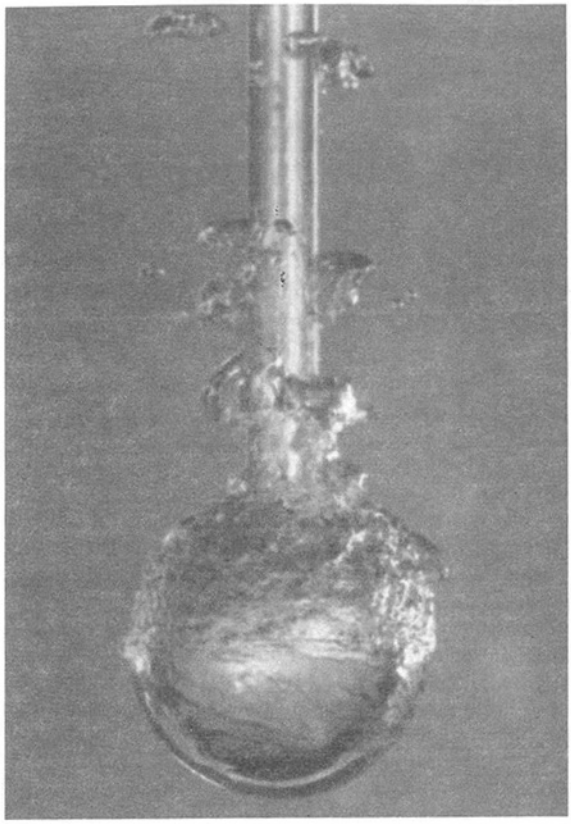

Fig. 8 Still photograph of vapor film destabilization for a 500 rpm rotation and T_w = 110°C

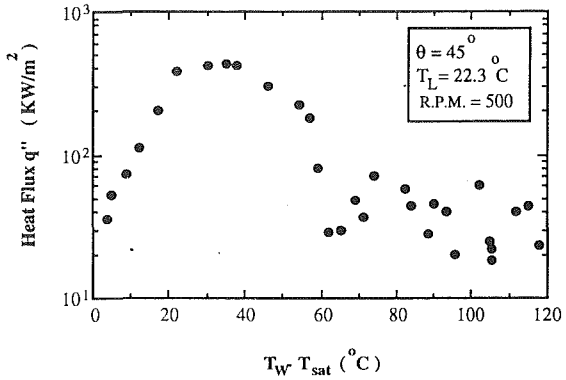

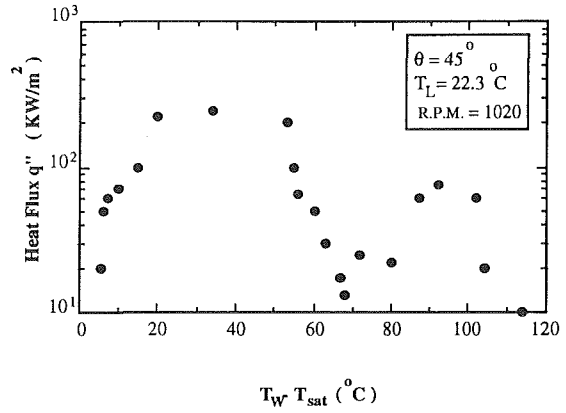

Fig. 10 Boiling heat fluxes for Freon-113 at 22.3°C

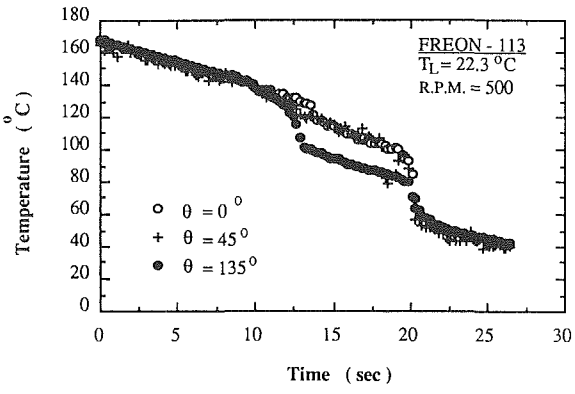

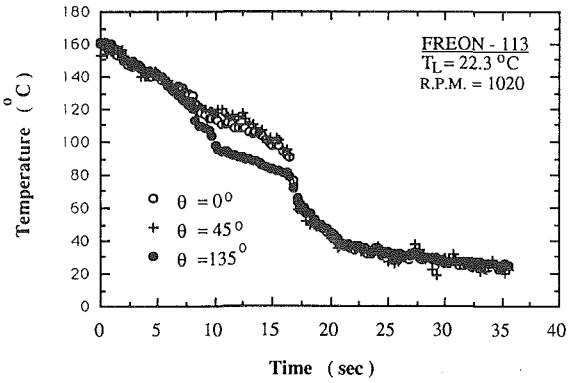

Fig. 9 Temperature versus time behavior of the heated surface for sphere rotations of 500 and 1020 rpm

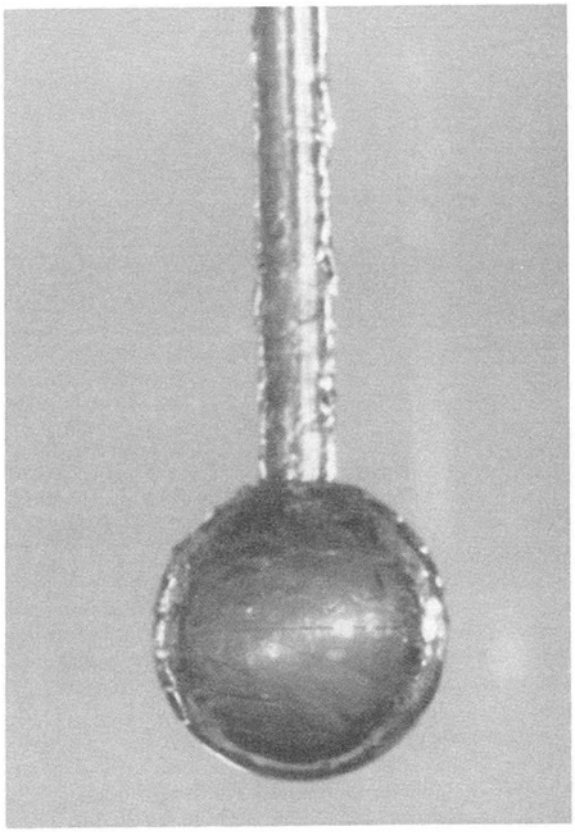

Fig. 11 Photograph illustrating the wave pattern observed for a sphere rotation of 1020 rpm and T_w = 130°C

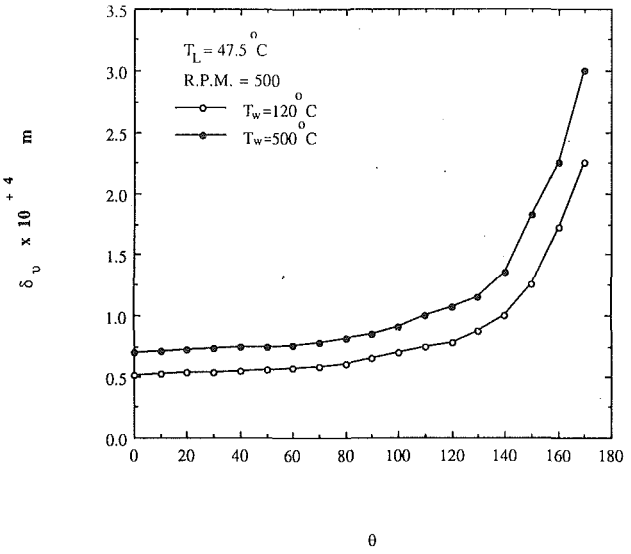

Fig. 12 Dependence of vapor film thickness on angular location for two different degrees of superheat

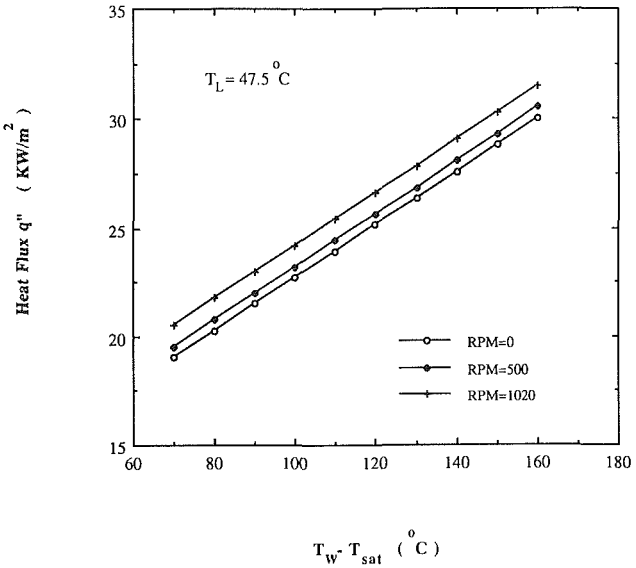

Fig. 13 Effect of sphere rotation on theoretical film boiling fluxes

"humps" (more than one maximum) in the system boiling curves were observed once the sphere was set in motion. These multiple "humps" are a direct consequence of the frequent instances of liquid–solid contact registered during the quenching process.

Numerical Results and Comparison With Experimental Data. All of the fluid properties used in the theoretical calculation were for Freon-113. This facilitated the comparison between theory and experiments at this end of the study. The dependence of the vapor layer thickness on angular position for a 500 rpm rate of rotation is illustrated in Fig. 12. The effect of surface rotation on the film boiling process is relatively weak when compared to the effect of liquid temperature. Figure 13 shows the computed theoretical heat fluxes for different rotation rates for a liquid temperature of 21°C. In order to facilitate the comparison between the theoretical model and the experimental data, the computer model was corrected to allow the surface temperature to vary in accordance with our measurements. The surface temperature, as prescribed by Eq. (5), was assumed constant and uniform at each angular position. A comparison between theory and experiment for various liquid temperature, see Fig. 14, indicates that the theoretical solution predicts the film boiling fluxes very well for low rpm. However, the large fluctuations in film boiling fluxes observed at high rpm are not predicted by the model. The theoretical model basically addressed stable film boiling and therefore cannot predict the film boiling fluxes resulting from the hydrodynamic instability caused by the rotation of the surface. The model should be adequate for predicting the average film boiling fluxes for high surface rotation. Figures 14(*a*, *b*, and *c*) illustrate the comparison between the theoretical model and the experimental data for three different rotational speeds.

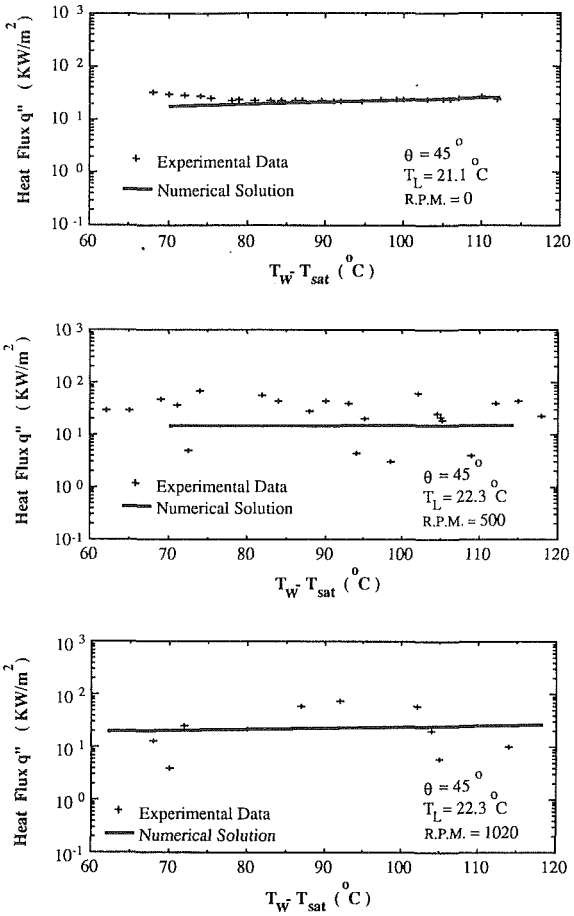

Fig. 14 Comparison between theory and experiment

Conclusions

A theoretical model of film boiling from a rotating sphere in a pool of liquid has been presented. The model is able to predict the experimental data for low rpm. The model does not account for the instability of the vapor film at high rpm, and thus fails to predict the experimental data. The model, however, can be used to predict the average film boiling fluxes at high surface rotation. The high film boiling fluxes at high rpm are the result of liquid wetting the heated surface while the system is in the film boiling regime. This phenomenon is caused by the development of interfacial instability in the vapor film brought about by the rotation of the heated surface.

Acknowledgments

The authors are grateful for support from the National Science Foundation under grant No. CBT-880898.

References

Aziz, S., Hewitt, G. F., and Kenning, D. B. R., 1986, "Heat Transfer in Forced Convection Film Boiling From Spheres," *Proc. Eighth Int. Heat Transf. Conf.*, San Francisco, Vol. 5, pp. 2149–2154.

Berenson, P. J., 1961, "Film Boiling Heat Transfer From a Horizontal Surface," ASME JOURNAL OF HEAT TRANSFER, Vol. 83, pp. 351–358.

Bradfield, W. S., 1966, "Liquid-Solid Contacts in Stable Film Boiling," *I. & E.C. Fundamentals*, Vol. 5, No. 202, pp. 200–204.

Breen, B. P., and Westwater, J. W., 1962, "Effect of Diameter of Horizontal Tubes on Film Boiling Heat Transfer," *Chem. Eng. Progress*, Vol. 58, No. 7, pp. 67–72.

Bromley, L. A., 1950, "Heat Transfer in Stable Film Boiling," *Chem. Eng. Progress*, Vol. 46, pp. 221–227.

Dix, D., and Orozco, J., 1990, "Boiling Heat Transfer From a Sphere in Forced Convection of Subcooled Freon-113," *J. of Experimental Heat Transfer*, Vol. 3, No. 2, pp. 129–148.

Frederking, T. K. H., and Clark, J. A., 1962, "Natural Convection Film Boiling on a Sphere," *Adv. Cyro. Eng.*, Vol. 8, pp. 501–506.

Gunnerson, F. S., and Cronenberg, A. W., 1980, "On the Minimum Film Boiling Conditions for Spherical Geometries," ASME JOURNAL OF HEAT TRANSFER, Vol. 102, pp. 335–341.

Hendricks, R. C., and Baumeister, K. J., 1969, "Film Boiling From Submerged Spheres," NASA TN D-5124, Washington, DC.

Henry, R. E., 1974, "A Correlation for the Minimum Film Boiling Temperature," *AIChE Symp. Series*, No. 138, Vol. 70, pp. 81–90.

Jacobson, R. N., and Shair, F. M., 1970, "Film Boiling From a Sphere During Forced Convection of Subcooled Water," *I. & E. C. Fundamentals*, Vol. 9, pp. 183–185.

Manson, L., 1966, "Cooldown of Shrouded Spherical Vessels in Liquid Nitrogen," *Advc. Cryogenic Eng.*, Vol 112, pp. 373–380.

Merte, H., and Clark, J. A., 1964, "Boiling Heat Transfer With Cryogenic Fluids at Standard, Fractional, Near-Zero Gravity," ASME *Journal of Heat Transfer*, Vol. 86, pp. 251–359.

Orozco, J. A., and Witte, L. C., 1986, "Flow Boiling From a Sphere to a Subcooled Freon-113," ASME JOURNAL OF HEAT TRANSFER, Vol. 108, pp. 934–938.

Orozco, J. A., Poulikakos, D., and Gutjahr, 1988, "Flow Film Boiling From a Sphere and From a Cylinder Embedded in a Porous Medium," *AIAA J. Thermophysics and Heat Transfer*, Vol. 2, No. 4, pp. 359–364.

Rao, J. R., and Prasad, K. K., 1983, "Integral Method Solutions for Forced Convection Film Boiling," in: *Proceedings of Seventh National Heat and Mass Transfer Conference*, Oxford and IBH Publishing Co., New Delhi, India, Vol. F3, pp. 335–339.

Sakurai, A., Shiotsu, M., and Hata, K., 1990, "A General Correlation for Pool Film Boiling Heat Transfer From a Horizontal Cylinder to Subcooled Liquid: Part 2—Experimental Data for Various Liquids and Its Correlation," ASME JOURNAL OF HEAT TRANSFER, Vol. 112, pp. 441–450.

Sankaran, S., and Witte, L. C., 1985, "Quenching of a Hollow Sphere in Methanol," ASME JOURNAL OF HEAT TRANSFER, Vol. 109, pp. 262–264.

Stevens, J. W., and Witte, L. C., 1973, "Destabilizing of Vapor Film Boiling Around Spheres," *Int. J. Heat Mass Transfer*, Vol. 13, pp. 669–678.

Tanaka, H., 1988, "On the Stability of Vapor Film in Pool Film Boiling," *Int. J. Heat Mass Transfer*, Vol. 31, No. 1, pp. 129–134.

Ungar, E., and Eichhorn, R., 1982, "Local Surface Boiling Heat Transfer From a Quenched Sphere," ASME Paper No. 82-HT-27.

Witte, L. C., 1968, "Film Boiling From a Sphere," *I. & E.C. Fundamentals*, Vol. 7, pp. 517–518.

Witte, L. C., Orozco, J., and Chang, K.-H., 1983, "On the Role of Liquid-Solid Contact in Subcooled Flow Film Boiling From Submerged Bodies," *Interfacial Transport Phenomena*, ASME HTD-Vol. 23, pp. 67–74.

Witte, L. C., and Orozco, J. A., 1984, "Vapor Velocity Effects on Subcooled Flow Film Boiling From Submerged Bodies," ASME JOURNAL OF HEAT TRANSFER, Vol. 106, pp. 191–197.

Yao, S. C., and Henry, R. E., 1978, "An Investigation of the Minimum Film Boiling Temperature on Horizontal Surfaces," ASME JOURNAL OF HEAT TRANSFER, Vol. 100, pp. 260–267.

APPENDIX

In the development of Eqs. (20) and (23), the following expressions were obtained for the coefficients of these two equations:

$$X_1(\theta, \delta_v, \delta_1) = \frac{\delta_v^2 C_1}{4} - \frac{u_{\text{int}}}{2} + \frac{\delta_v \delta_l \mu C_1}{4E} - \frac{\delta_v \delta_l C_2}{4} \tag{A1}$$

$$X_2(\theta, \delta_v, \delta_2) = -u_{\text{int}}\,\delta - \frac{\mu C_1 \delta_v^2}{4E} + \frac{\delta_v^2 C_2}{4} \tag{A2}$$

$$X_3(\theta, \delta_v, \delta_1) = \left(\frac{Z_1}{\delta_l} - \frac{Z_2}{\delta_v}\right) - \cot\theta\left[\frac{\delta_v C_1}{12} - \frac{u_{\text{int}}\delta_v}{2}\right] - \frac{\delta_v^3 \dot{C}_1}{12} + \frac{\delta_v \delta_l^2 \dot{B}_1}{4E} - \frac{\delta_v \delta_l^2 \mu \dot{C}_1 \delta}{4E} \tag{A3}$$

$$Y_1(\theta, \delta_v, \delta_1) = \left[\frac{u_{\text{int}}}{6} + 3\,\delta_l^2\, g \sin\theta\, B_0\right] \tag{A4}$$

$$Y_2(\theta, \delta_v, \delta_2) = \left[u_{\text{int}}\left(\frac{3}{2}\rho - 1\right) - \frac{\rho\delta_v^2}{4}\left(g\sin\theta\, B_2 - \frac{\sin\theta\, B_3}{\theta}\right)\right] \tag{A5}$$

$$Y_3(\theta, \delta_v, \delta_1) = \dot{u}_{\text{int}}\left(\frac{\delta_l}{6} + \frac{\delta_v \rho}{2}\right) + \frac{2\alpha_l R}{\delta_l} + \frac{R\,\delta_l}{x}\left(\frac{u_{\text{int}}}{6} + \delta_l^2\, g \sin\theta\, B_0\right) + \frac{R\rho\,\delta_v\, u_{\text{int}}}{2x} - \rho\,\frac{\delta_v^3}{12}\left[g\cos\theta B_2 - B_3\left(\frac{2\sin\theta\cos\theta}{\theta} - \frac{\sin^2\theta}{\theta^2}\right)\left(\frac{g\sin\theta\, B_2}{\theta} - \frac{\sin^2\theta\, B_3}{\theta^2}\right)\right] \tag{A6}$$

where

$$B_1 = \frac{\rho_l - \rho_\infty}{60\,\mu} \qquad C_2 = \frac{B_l - \delta\mu\, C_1}{(3+\mu/\delta)^2}\,\frac{\mu}{\delta}$$

$$B_2 = \frac{\rho_v - \rho_l}{\mu_v} \qquad E = (3 + \mu/\delta) \tag{A7}$$

$$B_3 = \omega^2 R/\nu_v \qquad Z_2 = \frac{k_v\,\Delta T_v\, R}{h_{fg}\,\rho_v}$$

$$Z_1 = \frac{2\,k_l\,\Delta T_l\, R}{h_{fg}\,\rho_v}$$

Analysis of Rewetting for Surface Tension Induced Flow

X. F. Peng
Research Associate.

G. P. Peterson
Tenneco Professor of Mechanical Engineering. Mem. ASME

Department of Mechanical Engineering, Texas A&M University, College Station, TX 77843-3123

An analytical investigation was conducted to determine the rewetting characteristics of thin, surface tension driven liquid films over heated plates as a function of the fluid properties, the film thickness, and the applied heat flux. Analytical expressions for the maximum sustainable heat flux and the rewetting velocity were developed for both flat and grooved plates and were compared with data from previous investigations. The results indicated good agreement for low film velocities; however, at high velocities the experimental data deviated significantly from the theoretical predictions. It was hypothesized that this deviation was due to the presence of liquid sputtering near the liquid front. To compensate for this liquid sputtering, the expressions for maximum sustainable heat flux and rewetting velocity were modified using an empirical correction factor developed from the data of previous thin film thickness investigations. The resulting modified expressions were found to compare very favorably with available experimental data over a large range of flow conditions and velocities.

Introduction

The evaporation of thin liquid films provides an excellent method for cooling hot surfaces and can result in extremely high heat transfer rates. Applications that utilize this technique are numerous and are playing an increasingly important role in such fields as heat pipe thermal control systems, evaporative coolers, heat transfer augmentation devices, and other more general applications in the chemical and petrochemical industries. Because of the importance of thin film cooling, several recent experimental investigations have been undertaken to determine the parameters that govern this phenomenon. Specifically, recent developments in the thermal control of high-density electronic components (Peterson and Ortega, 1990) and two-phase heat rejection systems for spacecraft thermal control (Ellis, 1990) have served to focus attention on the problems associated with the heat transfer in the thin film region. Of particular interest in both of these situations are the rewetting characteristics of heated plates, determination of the maximum heat flux a plate with a given film thickness can sustain, and the rate at which a liquid will rewet a surface once all of the liquid has been evaporated.

Several experimental investigations (Shires et al., 1964; Elliot and Rose, 1970; Kanlinin, 1969; Iloeje et al., 1982; Stroes et al., 1990) have attempted to determine experimentally the rewetting characteristics of thin liquid films on the outer surface of heated rods, the inner and outer surfaces of heated tubes, and the horizontal surface of flat plates. Several other researchers including Orell and Bankoff (1971), Bankoff (1971, 1990), and Ueda et al. (1983a, 1983b), have investigated the fundamental mechanisms involved in dryout and the flow rewetting of thin liquid film flow. As noted by Bankoff (1990), these investigations provided substantial experimental data and considerable insight into the behavior of thin films on both circular tubes and flat plates; however, some of the conclusions reached have been contradictory. In general, it is apparent from reviewing the literature that no physical model exists that is capable of describing the governing physical phenomena or the effects of surface tension on the rewetting behavior of the thin liquid film region.

Recently, Stroes et al. (1990) experimentally investigated heat flux induced dryout and rewetting in thin films. The results of this work indicate that the film thickness, mass flow rate, surface tension, and inclination angle all significantly affect the minimum heat flux required for dryout and the maximum heat flux under which rewetting can occur. In addition, Peng and Peterson (1991) have developed an exact analytical solution for determining the rewetting velocity of thin liquid films as a function of the mass flux, i.e., pressure-driven flow where surface tension is neglected. Although this type of situation is important, it does not consider the transition behavior of surface tension induced flow. The inclusion of surface tension into these flow models is of critical importance in micro or zero gravity applications where these large body forces are not present, such as the design of high-capacity heat pipes for spacecraft thermal control (Alario et al., 1983; Ambrose and Holmes, 1991).

In the high-capacity heat pipes currently under consideration for Space Station Freedom, the working fluid is distributed over the evaporator by a series of parallel circumferential grooves machined into the inner surface of the vapor channel. During orbital adjustments and/or docking maneuvers, local gravitational accelerations may result in depriming of these grooves and hence dryout. In order better to understand the rewetting characteristics of these types of thin, surface tension driven flows over heated surfaces, an analytical investigation was conducted to develop an expression for the rewetting velocity as a function of the fluid properties (including surface tension), the film thickness, and the applied heat flux.

Theoretical Analysis

Once dryout has occurred and the liquid begins to rewet a heated surface, the advancing liquid film is subjected to a wall shear stress and a capillary driving force. To simplify the problem, assume initially that the liquid film is flowing on a flat horizontal plate, the liquid wets the surface of the plate, and a capillary force is induced by the surface tension and some characteristic capillary radius, R. Also assume that the flow is laminar and that the thermophysical properties are constant.

With these assumptions, an integral technique can be used to analyze the liquid film flow. If the entire liquid layer is taken as the control volume and the liquid mass is assumed to increase as the length of the liquid layer increases, the physical model can be represented as shown in Fig. 1. For a given

Contributed by the Heat Transfer Division for publication in the JOURNAL OF HEAT TRANSFER. Manuscript received by the Heat Transfer Division February 1991; revision received January 1992. Keywords: Boiling, Multiphase Flows, Porous Media. Associate Technical Editor: H. R. Jacobs.

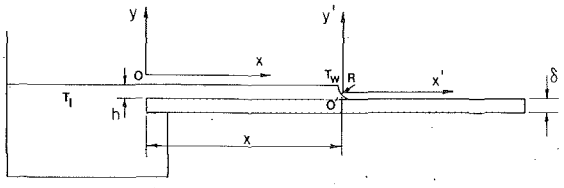

Fig. 1 Physical model

time, t, the length of the liquid layer, x, is fixed and the liquid velocity would be the same for any point in the control volume (by continuity). This liquid velocity can be approximated by the mean liquid velocity, U, based on the layer thickness. Clearly, because the driving force (i.e., capillary pressure) is constant but the liquid mass and frictional force vary, the mean liquid velocity, U, will vary with respect to time and hence also with respect to the length of the liquid layer, x.

Based on the above considerations, Newton's law for a liquid film that fully wets the surface can be written as:

$$\frac{2\sigma}{R}h-\tau_w x=\rho_l xh\frac{dU}{dt} \tag{1}$$

where U is the average velocity of the liquid film, x is the length of the liquid layer, and τ_w is the wall shear stress. The time can be found from the relationship for velocity as,

$$dt=\frac{dx}{U} \tag{2}$$

For Newtonian fluids in laminar flow, the shear stress at the wall can be expressed as

$$\tau_w=\mu_l\frac{\partial u}{\partial y}\bigg|_{y=0} \tag{3}$$

For the case of interest here, the film thickness, h, and the average velocity, U, are both very small, hence it is reasonable to express the wall shear stress as

$$\tau_w=\mu_l\frac{\partial u}{\partial y}\bigg|_{y=0}=\mu_l\frac{U}{h/2}=\frac{2\mu_l U}{h} \tag{4}$$

Substituting Eqs. (2) and (4) into Eq. (1) and rearranging yields

$$\frac{dU}{dx}=\frac{2\sigma}{\rho_l xRu}-\frac{2\mu_l}{\rho_l h^2} \tag{5}$$

with boundary conditions,

$$x=0,\quad U=0 \tag{6}$$

The rewetting velocity, U, should theoretically be determined by Eq. (5) with Eq. (6). However, a direct analytical solution for Eq. (5) is not available. Hence, a numerical technique was employed. Figure 2 illustrates the results obtained for several

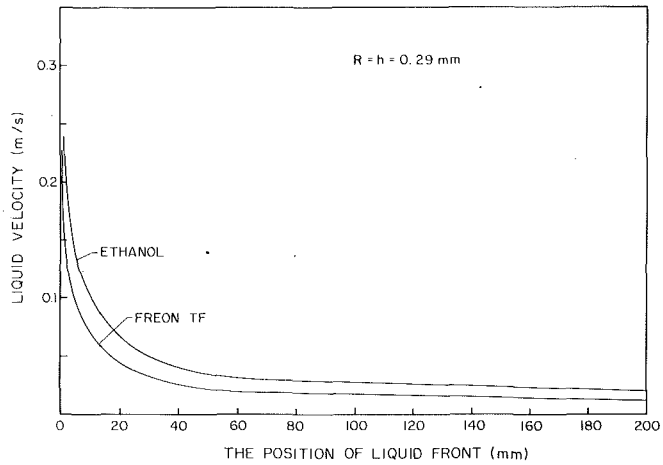

Fig. 2 Liquid velocity as a function of position

different cases in which the capillary radius was assumed to be equal to the film thickness, h. It should be noted that for very small changes in the liquid layer length (i.e., small values of x) the change in momentum due to the increase in the mass of liquid in the control volume is comparable to the acceleration term in Eqs. (1) and (5) and cannot be neglected. However, for most practical applications, the question of greatest interest is whether the plate will rewet for large values of x. For these conditions, Fig. 2 illustrates that the results given by Eq. (5), in which the momentum change due to the mass increase is neglected, are reasonable.

For the case of rewetting of the surface once dryout has occurred, the liquid film front was assumed to be driven by surface tension, and to advance along the surface of a plate on which a uniform heat flux, q, was applied. At the leading edge of the advancing liquid front, some of the liquid that is flowing due to surface tension is vaporized and the remaining liquid advances with a velocity U_w, known as the wetting front velocity. The heat required to vaporize the liquid is supplied by conduction from the dry hot zone of the plate. Two things are intuitively apparent: First, the wetting velocity for an unheated plate is higher than for a heated plate, since in the latter case, some of the liquid is vaporized, reducing the liquid mass flow rate and second, when dryout occurs not all of the heat supplied to the plate is absorbed by the vaporization of the liquid.

To solve this problem, the conduction equations for the plate were transformed to a coordinate system moving with the wetting front at a velocity U_w, as shown in Fig. 1. In addition, several other fundamental assumptions were made. These can be summarized as follows:

1 Conduction heat transfer through the plate is one-dimensional.

Nomenclature

c = specific heat of the plate
h = thickness of liquid films
h_f = liquid latent heat
k = conductivity of the plate
$\dot{m}_v$ = vaporization rate of liquid
Pr = Prandtl number
q = heat flux
Q = total heat input
R = capillary radius
Re = Reynolds number
T = temperature
t = time
T_s = liquid saturation temperature
T_w = surface temperature at the rewetting front
U = average velocity of the liquid
U_w = rewetting velocity
u = liquid velocity
x = length of liquid film layer
α = thermal diffusivity of the plate
δ = thickness of the plate
δ_t = thermal boundary layer thickness
δ_t' = the superheated liquid thermal boundary layer thickness
μ = absolute viscosity
ρ = density
σ = surface tension
τ_w = shear stress

Subscripts

$'$ = moving coordinate frame
l = liquid
max = maximum
w = wetting

2 The thermophysical properties are constant.

3 The liquid temperature at the rewetting front, T_l, is different from the rewetting temperature, T_w, which is assumed to be constant and equal to saturation temperature, T_s.

4 The convective heat transfer between the plate (dry hot zone) and air (or vapor) along with the radiation between the hot surface and the surroundings is neglected.

Utilizing these assumptions, the one-dimensional conduction equation for the plate yields

$$k\frac{\partial^2 T}{\partial x'^2}-\rho c\frac{q}{\delta}=-\rho c\frac{\partial T}{\partial t} \tag{7}$$

and for a moving coordinate system,

$$dt=-\frac{dx'}{U_w} \tag{8}$$

Hence, Eq. (7) simplifies to:

$$k\frac{d^2T}{\partial x'^2}-\frac{q}{\delta}=\rho cU_w\frac{dT}{dx'} \tag{9}$$

with boundary conditions,

$$x'=0,\quad T(x')=T_w$$

$$x'\to\infty,\quad \frac{\partial T}{\partial x'}\to\text{finite value} \tag{10}$$

The solution for the resulting one-dimensional, homogeneous equation

$$k\frac{d^2T}{dx'^2}-\rho cU_w\frac{dT}{dx'}=0 \tag{11}$$

is

$$T=c_1+c_2\exp\left[\frac{\rho cU_w}{k}x'\right] \tag{12}$$

where c_1 and c_2 are integral constants. Further, the nonhomogeneous equation, Eq. (9), with the conditions given by Eq. (10) can be solved, and yields

$$T=T_w+\frac{q}{\rho cU_w\delta}x' \tag{13}$$

From this, the total heat conduction at $x' = 0$ can be found as,

$$Q=\delta k\left.\frac{dT}{dx'}\right|_{x'=0}=\frac{qk}{\rho cU_w}=\frac{q\alpha}{U_w} \tag{14}$$

Utilizing an energy balance, the total heat conduction in the region of the wetting front is equal to the energy absorbed by the liquid vaporization, or

$$Q=\dot{m}_v h_f=(U-U_w)\rho_l h h_f \tag{15}$$

where U is determined by Eq. (5). Combining Eqs. (4) and (15) yields

$$(U-U_w)\rho_l h h_f=\frac{q\alpha}{U_w} \tag{16}$$

or

$$U_w^2-UU_w+\frac{q\alpha}{\rho_l h h_f}=0 \tag{17}$$

Solving this expression for the rewetting velocity yields

$$U_w=\frac{1}{2}\left[U\pm\sqrt{U^2-\frac{4q\alpha}{\rho_l h h_f}}\right] \tag{18}$$

If the second term of the right-hand side of Eq. (18) is negative, the rewetting velocity must increase with increases in the applied heat flux, because the second term becomes smaller with increases in the applied heat flux. This is obviously not possible; therefore, the second term must be positive. Hence, the rewetting velocity can be expressed as,

$$U_w=\frac{1}{2}\left[U+\sqrt{U^2-\frac{4q\alpha}{\rho_l h h_f}}\right] \tag{19}$$

When the surface temperature of a plate is higher than the rewetting temperature, T_w, and the heat flux is below the rewetting value, the plate will rewet and the rewetting velocity can be found by Eq. (19). It is clear from this expression that the rewetting velocity is closely related to the heat flux, the liquid film thickness, the thermal properties of both the liquid and the plate, and the velocity of the liquid film. Practically, however, the velocity of the liquid film depends only on the thermophysical properties of the liquid, the film thickness, the capillary radius, and the position of the film front. As a result, the rewetting velocity depends strongly upon the thermal properties of the liquid and the plate, the applied heat flux, the film thickness, the capillary radius, and finally, on the position of the film front. This expression, Eq. (19), provides theoretical evidence to support the explanations proposed by several previous experimental investigations. Furthermore, because the wetting conditions of the heated plate, the existing real roots of Eq. (17) or Eq. (18) should be

$$U^2-\frac{4q\alpha}{\rho_l h h_f}\geq 0 \tag{20}$$

the limiting condition is,

$$U^2-\frac{4q\alpha}{\rho_l h h_f}=0 \tag{21}$$

Therefore, for a given film flow driven by surface tension, the maximum heat flux under which rewetting can occur is

$$q_{\max}=\frac{\rho_l h h_f U^2}{4\alpha} \tag{22}$$

The maximum heat flux, $q_{\max}$, is related to the thermophysical properties, the film thickness, the capillary radius, and the position. The analysis shows that the applied heat flux cannot exceed the value predicted by Eq. (22), otherwise the liquid film will be unable to provide sufficient cooling to allow the surface to rewet. What is also apparent, and perhaps more significant, is that the maximum sustainable heat flux, $q_{\max}$, depends on the position of the liquid film front. This indicates that some dry hot regions may never rewet or that the rewetting length of a flat plate is limited and dependent upon a given heat flux.

The relationship between the maximum heat flux and the position of the film front is illustrated in Fig. 3 and corresponds to the case in Fig. 2 for a Freon TF/copper combination. As illustrated, the maximum heat flux varies with respect to changes in the position. To verify and determine reliability and accuracy of the analytical solution, experimental data from the investigation of Stroes et al. (1990) are also illustrated. It is important to note that the experimental data points plotted in Fig. 3 are for velocities that correspond with the theoretical solution but not necessarily the liquid position. As illustrated, the experimentally obtained rewetting heat flux values for Freon TF on a copper plate are in reasonably good agreement with the theoretical values obtained using Eq. (22), at low velocities. However, as the film velocity increases, the difference between the measured and predicted values diverge significantly.

Effect of Sputtering

In the previous analysis, all of the liquid was assumed either to be vaporized or to remain on the plate with the advancing front. In the actual case, however, some of the liquid may leave the plate as droplets, due to the explosive forces resulting from boiling, and may be deposited a short distance ahead or

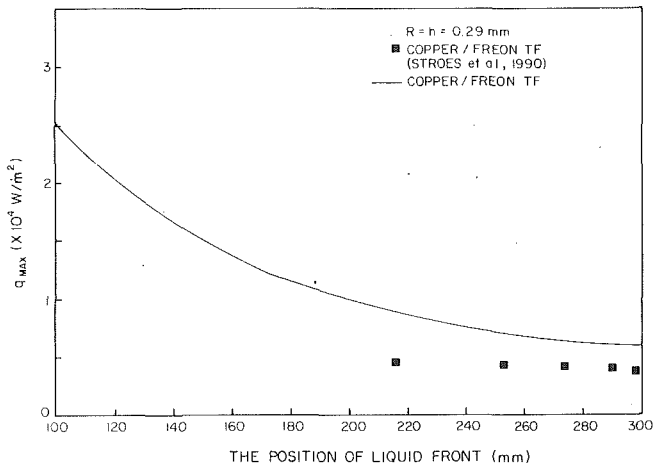

Fig. 3 Maximum heat flux as a function of position

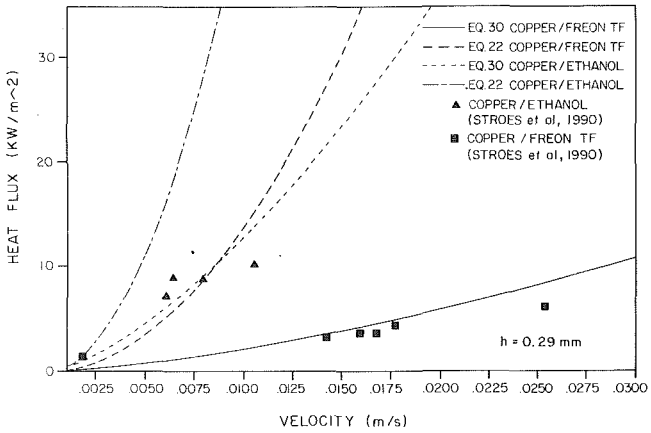

Fig. 4 Comparison of the analytical model and the experimental data of Stroes et al. (1990)

behind the advancing front. This phenomenon is referred to as sputtering and may account for the variation between the theoretical values predicted by Eq. (22) and the values measured by Stroes et al. (1990).

Clearly, evaporation of the liquid will occur only after the liquid has been heated to some level of superheat. At the wetting front, the film is heated by the hot plate to a temperature that approaches the Leidenfrost temperature. In actuality, only a thin layer of the liquid immediately adjacent to the plate will reach a sufficiently high temperature to be vaporized. Because of the rapid boiling that occurs in this thin layer, the liquid above it may be carried off by sputtering. To compensate for the liquid carried off by sputtering, an expression for the thermal boundary layer thickness for laminar flow presented by Kays and Crawford (1980)

$$\frac{\delta_t}{x'} = 4.64\ \mathrm{Re}_{x'}^{-\frac{1}{2}}\mathrm{Pr}_l^{-\frac{1}{3}} \tag{23}$$

was modified as

$$\frac{\delta_t}{h} = 4.64\left(\frac{x'}{h}\right)^{\frac{1}{2}}\mathrm{Re}_h^{-\frac{1}{2}}\mathrm{Pr}_l^{-\frac{1}{3}} \tag{24}$$

where δ_t replaces h as the thickness of the evaporated liquid film. The exact shape and length of the liquid film at the wetting front where vaporization occurs is difficult to determine analytically. As a result, the term x'/h can be determined experimentally and used as a correction factor to compensate for the liquid lost through sputtering.

Trial and error indicated that letting this correction factor equal one-eighth, i.e.,

$$\frac{x'}{h} = \frac{1}{8} \tag{25}$$

would result in significant improvement in the agreement between the theoretical predictions from Eq. (22) and the experimental data of Stroes et al. (1990). Substitution results in the following expression:

$$\frac{\delta_t}{h} = 0.58\mathrm{Re}_h^{-\frac{1}{2}}\mathrm{Pr}_l^{-\frac{1}{3}} \tag{26}$$

In the thin liquid region near the advancing front, the liquid may be superheated and hence vaporized. For this case, an energy balance yields

$$(U-U_w)\rho_l h_f \delta_t = -\delta k \left.\frac{dT}{dx'}\right|_{x'=0} \tag{27}$$

Combining Eqs. (26) and (27) yields

$$(U-U_w)\ \rho_l h_f \left[0.58\mathrm{Re}_h^{-\frac{1}{2}}\mathrm{Pr}_l^{-\frac{1}{3}}\right] h = \frac{q\alpha}{U_w} \tag{28}$$

Rearranging and simplifying yields a modified expression for the rewetting velocity, U_w, of

$$U_w = \frac{1}{2}\left[U + \sqrt{U^2 - \frac{4q\alpha}{0.58\mathrm{Re}_h^{-\frac{1}{2}}\mathrm{Pr}_l^{-\frac{1}{3}}\rho_l h_f h}}\right] \tag{29}$$

in terms of the Reynolds and Prandtl numbers. Likewise, a modified expression for the maximum heat flux, $q_{\max}$, can be found as

$$q_{\max} = 0.145\ \frac{(\mu_l\rho_l)^{\frac{1}{2}} h_f h^{\frac{1}{2}}}{\alpha \mathrm{Pr}_l^{\frac{1}{3}}}\ U^{\frac{3}{2}} \tag{30}$$

Figure 4 compares the maximum heat flux as predicted by Eqs. (22) and (30) with the experimental data of Stroes et al. (1990). As illustrated, Eq. (22) significantly overpredicts the maximum heat flux at large mass fluxes, while the modified correlation, Eq. (29), compares quite favorably for a wide range of mass flux values.

Regardless of whether sputtering occurs, provisions must be made for the sensible heating of the liquid in the thermal boundary region. This can be done by applying an energy balance in the region of the wetting front or

$$0.58\mathrm{Re}_h^{-\frac{1}{2}}\mathrm{Pr}_l^{-\frac{1}{3}}\ (U-U_w)\ \rho_l h_f h\left[c_p\left(\frac{T_w+T_l}{2}-T_l\right)+ch_f\right] = \frac{q\alpha}{U_w} \tag{31}$$

Letting

$$h_f' = c_p\left(\frac{T_w-T_l}{2}+ch_f\right) \tag{32}$$

and the coefficient c be used to represent the amount of subcooling of the liquid (i.e., when $\delta_t' \le c\delta_t$ the liquid temperature is higher than the saturation temperature and liquid can be evaporated) the rewetting velocity and maximum heat flux can be written as

$$U = \frac{1}{2}\left[U + \sqrt{U^2 - \frac{4q\alpha}{\rho_l h_f' h\left[0.58\mathrm{Re}_h^{-\frac{1}{2}}\mathrm{Pr}_l^{-\frac{1}{3}}\right]}}\right] \tag{33}$$

and

$$q_{\max} = 0.145 \frac{(\mu_l \rho_l)^{-\frac{1}{2}} h_f'^{\frac{1}{2}} h^{\frac{1}{2}}}{2\,\mathrm{Pr}_l^{\frac{1}{3}}} U^{\frac{3}{2}} \tag{34}$$

respectively. It should be noted that although the correction used for sputtering here results in a favorable comparison of the experimental and theoretical values, the correction factor proposed must be verified through other experimental investigations prior to general use.

Conclusions

An analytical investigation was conducted to determine the rewetting characteristics of thin, surface tension driven liquid films over heated plates as a function of the fluid properties, the film thickness, and the applied heat flux. Analytical expressions for the maximum sustainable heat flux and the rewetting velocity were developed for both flat and grooved plates and were compared with data from previous investigations. The results indicated good agreement for low film velocities; however, at high velocities the experimental data deviated significantly from the theoretical predictions. It is believed that this deviation is due to the presence of liquid sputtering near the liquid front. To compensate for this liquid sputtering, the expressions for maximum sustainable heat flux and rewetting velocity were modified using an empirical correction factor developed from the data of previous thin film thickness investigations. The resulting modified expressions were found to compare very favorably with available experimental data over a large range of flow conditions and velocities.

Through the use of this analytical model, the rewetting characteristics of high-capacity heat pipes in reduced gravity environments can be predicted and the heat reduction required for rewetting to occur can be determined.

References

Alario, J., Brown, R., and Kossan, R., 1983, "Monogroove Heat Pipe Development for the Space Constructible Radiator," AIAA Paper No. AIAA-83-1431, June.

Ambrose, J., and Holmes, S. R., 1991, "Development of the Graded Groove High Performance Heat Pipe," AIAA Paper No. AIAA-91-0366, Jan.

Bankoff, S. G., 1971, "Stability of Liquid Flow Down a Heated Inclined Plane," *Int. J. Heat Mass Transfer*, Vol. 14, pp. 377–385.

Bankoff, S. G., 1990, "Dynamics and Stability of Thin Heated Liquid Films," ASME JOURNAL OF HEAT TRANSFER, Vol. 112, pp. 538–546.

Elliott, D. F., and Rose, P. W., 1970, "The Quenching of a Heated Surface by a Film of Water in a Steam Environment at Pressures up to 53 Bar," Report No. AEEW-M976, Atomic Energy Establishment, Winfrith, United Kingdom.

Ellis, W., 1990, "The Space Station Active Thermal Control Technical Challenge," presented at the 27th Aerospace Sciences Meeting, Paper No. AIAA-89-0073, Reno, NV, Jan.

Iloeje, O. C., Plummer, D. N., Rohsenow, W. N., and Griffith, P., 1982, "Effects of Mass Flux, Flow Quality, Thermal and Surface Properties of Materials on Rewet of Dispersed Flow Film Boiling," ASME JOURNAL OF HEAT TRANSFER, Vol. 104, pp. 304–308.

Kalinin, E. K., 1969, "Investigation of the Crisis of Film Boiling in Channels," *Proc. Two Phase Flow and Heat Transfer in Rod Bundles Symp.*, ASME Winter Annual Meeting, Los Angeles, CA.

Kays, W. M., and Crawford, M. E., 1980, *Convective Heat and Mass Transfer*, McGraw-Hill, New York.

Orell, A., and Bankoff, S. G., 1971, "Formation of a Dry Spot in a Liquid Film Heated From Below," *Int. J. Heat Mass Transfer*, Vol. 14, pp. 1838–1842.

Peng, X. F., and Peterson, G. P., 1991, "Analytical Investigation of the Rewetting Characteristics of Heated Plates With Grooved Surfaces," 1991 National Heat Transfer Conference, Paper No. AIAA 91-4004, Minneapolis, MN.

Peterson, G. P., and Ortega, A., 1990, "Thermal Control of Electronic Equipment and Devices," *Advances in Heat Transfer*, Pergamon Press, pp. 181–314.

Shires, G. L., Pickering, A. R., and Blacker, P. T., 1964, "Film Cooling of Vertical Fuel Rods," Report No. AEEW-R343, Atomic Energy Establishment, Winfrith, United Kingdom.

Stroes, S., Fricker, D., Issacci, F., and Catton, I., 1990, "Heat Flux Induced Dryout and Rewet in Thin Films," *Proc. 9th Int. Heat Trans. Conf.*, Vol. 6, pp. 359–364.

Ueda, T., Inoue, M., Iwata, Y., and Sogawa, Y., 1983a, "Rewetting of a Hot Surface by a Falling Liquid Film," *Int. J. Heat Mass Transfer*, Vol. 14, pp. 401–410.

Ueda, T., Tsunenori, S., and Koyanagi, M., 1983b, "An Investigation of Critical Heat Flux and Surface Rewet in Flow Boiling Systems," *Int. J. Heat Mass Transfer*, Vol. 26, No. 8, pp. 1189–1198.

Forced Convection Condensation of Steam on a Small Bank of Horizontal Tubes

A. G. Michael
Rein Haus (Cyprus) Ltd.,
Larnaca, Cyprus

W. C. Lee
Polytechnic of Central London,
Faculty of Engineering and Science,
London, United Kingdom

J. W. Rose
Department of Mechanical Engineering,
Queen Mary and Westfield College,
University of London,
London, United Kingdom

Heat transfer measurements are reported for condensation of steam flowing vertically downward over a small bank of staggered horizontal tubes having 10 rows with 4 and 3 tubes per row. The tubes in each row were connected in series and separately supplied with cooling water. The cooling water flow rate and temperature rise were measured individually for each row and tube-wall temperatures were measured on selected tubes. Data were obtained at slightly above atmospheric pressure and the range of steam approach velocity (based on the cross-sectional area of the duct) was 6 to 23 m/s. A general trend of decreasing heat transfer coefficient with depth in the bank was found. However, superimposed on this was a "saw-tooth" effect with the three-tube rows having higher coefficients than the rows with four tubes. The amplitude of the coefficient variation decreased down the bank and was also less pronounced at lower vapor velocities. When compared with other experimental data for condensation of steam on small staggered banks, the present data exhibit somewhat higher vapor-side, heat transfer coefficients.

Introduction

Many of the condensers used in the chemical, process, and power industries employ banks of horizontal tubes with vapor condensing on the outside of the tubes. It is usual to use baffles to direct the vapor in crossflow over the tube banks. In practice, all directions of vapor flow in relation to the tubes are possible. However, vertical vapor downflow, where mean shear stress effects and gravity are in the same direction, lends itself most readily to the study of the complex phenomena involved.

For vertical vapor downflow, observations have shown that the vapor-side, heat transfer coefficient decreases with penetration down the bank. This can be attributed to:

(*i*) The drop-off in the vapor shear effect due to the removal of vapor by condensation and the consequent decrease in vapor velocity,
(*ii*) inundation, and
(*iii*) the build-up of the noncondensing gas concentration as vapor is removed by condensation.

The interaction between these effects and their relative importance has resulted in much scatter of experimental data obtained in earlier investigations (Fuks, 1957; Grant and Osment, 1968; Eissenberg, 1972; Fujii et al., 1972b; Nobbs, 1975; Nobbs and Mayhew, 1976).

The combined effect of vapor shear stress and condensate inundation is often evaluated by multiplying an "inundation-correction factor" and a heat transfer coefficient given by a single-tube equation. For the case of the single tube, Shekriladze and Gomelauri (1966) used the asymptotic (infinite condensation rate) expression for the shear stress at the condensate surface to obtain an approximate interpolation formula, which may be expressed as:

$$\mathrm{Nu}\,\tilde{\mathrm{R}}\mathrm{e}^{-1/2} = 0.64[1+(1+1.69F)^{1/2}]^{1/2} \qquad (1)$$

Equation (1) satisfies both gravity and vapor-shear controlled extremes, and gives values of Nu within 2 percent of numerical solutions. Rose (1984) resolved the Shekriladze-Gomelauri problem and obtained an improved equation

$$\mathrm{Nu}\,\tilde{\mathrm{R}}\mathrm{e}^{-1/2} = \frac{0.9+0.728F^{1/2}}{(1+3.44F^{1/2}+F)^{1/4}} \qquad (2)$$

which agreed with numerical solutions to within 0.4 percent.

Fujii et al. (1972a) attempted a more accurate representation of the surface shear stress by considering both the condensate film and the vapor boundary layer and matching the shear stress on either side of the interface. An approximate integral method was used for the vapor boundary layer. Numerical results were summarized by an approximate equation, which may be written

$$\mathrm{Nu}\,\tilde{\mathrm{R}}\mathrm{e}^{-1/2} = 0.9(1+G^{-1})^{1/3}\left[1+\frac{0.421F}{(1+G^{-1})^{4/3}}\right]^{1/4} \qquad (3)$$

For most of the practical range for which $G>1$, the Nusselt numbers given by Eqs. (1), (2), and (3) are very close to one another and they virtually coincide for values of G greater than about 5.

The use of an inundation correction factor together with a single-tube, vapor-shear equation, in the calculation of the heat transfer coefficient for tube banks, neglects the interaction between vapor and condensate flows. For example, Nobbs (1975) suggested that, as the vapor velocity increases, liquid entrainment into the vapor flow also increases. Brickell (1981) suggested a two-phase flow approach whereby pressure-drop considerations could indicate the nature of the flow from which its effects on heat transfer might be deduced.

It is clear that the physical processes associated with condensation on tube banks are not well understood. The effects of vapor shear stress and condensate inundation still remain to be accurately evaluated. Toward this end, the present paper provides new, reliable experimental data for steam at slightly above atmospheric pressure flowing vertically downward over a staggered tube bank. The data are compared with earlier single-tube steam results of Michael et al. (1989) and Michael (1988) and with the tube-bank results of Fujii et al. (1972b) and Nobbs (1975) also for steam.

Apparatus and Procedure

Site steam was supplied at an absolute pressure of approx-

Contributed by the Heat Transfer Division for publication in the JOURNAL OF HEAT TRANSFER. Manuscript received by the Heat Transfer Division April 1991; revision received February 1992. Keywords: Condensation, Heat Exchangers, Phase-Change Phenomena. Associate Technical Editor: L. C. Witte.

imately 8 bar and a temperature of about 175°C. After passing through a separator, where any liquid water was removed, the steam flow was metered using an orifice plate of diameter 30 mm. Steady conditions were maintained by means of pneumatically actuated flow and pressure controllers, which were set to automatic mode at the desired conditions. This gave, at approach to the test section, a steam pressure slightly above atmospheric with superheat in the range 20 K to 50 K depending on the flow rate. The steam was then passed, via flow straighteners, into a calming section (3.6 m long) before entering the test section where the experimental tube bank was located. Downstream of the test section, condensate was removed by a second separator and passed through a cooler prior to discharging into a drain. The excess vapor was led to a "dump" condenser operating at near-atmospheric pressure. A "vent" condenser could also be operated at high steam flow rates for additional condensing duty. The condensate from the dump and vent condensers was collected in a tank, fitted with a glass level-indicating tube, before finally returning to the boiler via a condensate manifold.

Figure 1 shows a schematic diagram of the test section. This was a 330-mm-high rectangular cross-section (180 mm active tube length by 80 mm width) duct fitted with observation windows on both sides to enable viewing of the condensation process and the two-phase flow within the tube bank. The tube bank was 10 rows deep and preceded by three dummy, i.e., uncooled, rows. Alternate rows of four and three tubes were used with dummy half-tubes on the test-section walls for the three-tube rows. The condenser tubes (outside and inside diameters of 14 mm and 9.88 mm, respectively) were nickel plated to minimize the possibility of dropwise condensation and were arranged in a staggered configuration with an equilateral triangular pitch of 20 mm. The tubes were insulated from the walls of the test section with nylon bushes.

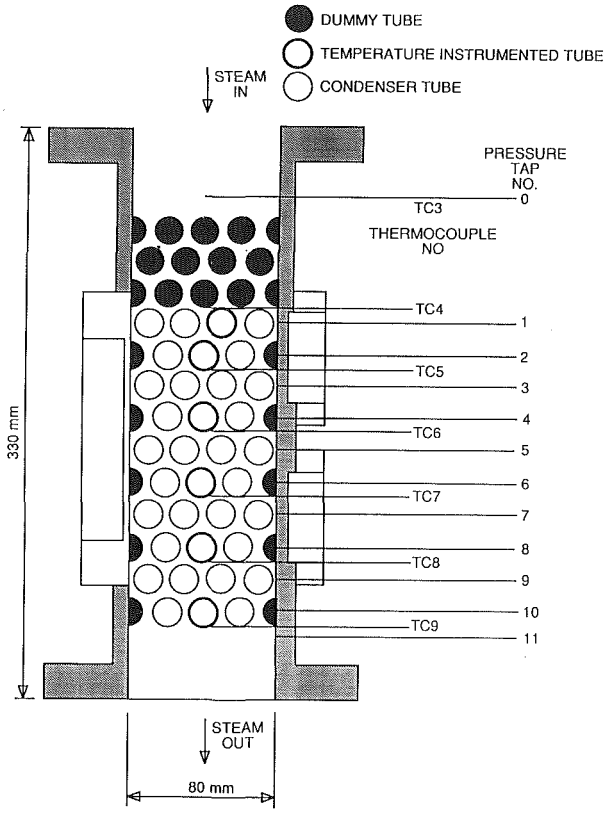

Fig. 1 Schematic view of test section

Nomenclature

A = flow area, see also Eq. (5)
A_i = tube row inside surface area
$A_{\min}$ = minimum flow area in vapor space
A_{mv} = "mean void" flow area in vapor space, defined in Eq. (9)
A_o = tube row outside surface area
A_{ts} = cross-sectional area of vapor duct
C_i = constant in Eq. (8)
D_i = tube inside diameter
D_o = tube outside diameter
F = $\mu g D_o h_{fg}/(kU_\infty^2 \Delta T_v)$
F_{ts} = value of F when U_∞ is based on A_{ts}
G = $k\Delta T_v(\rho\mu/(\rho_v\mu_v))^{1/2}/(\mu h_{fg})$
g = gravitational acceleration
h_{fg} = specific enthalpy of evaporation
k = condensate thermal conductivity
k_c = coolant thermal conductivity (calculated at mean coolant temperature)
k_w = tube wall thermal conductivity
L = tube length
$\dot{M}_{cd,i}$ = mass condensation rate on the ith row of tubes
$\dot{M}_v$ = vapor mass flow rate upstream of test section
N = tube row number
Nu = Nusselt number = $\alpha_o D_o/k$
Nu_c = coolant Nusselt number = $QD_i/(k_c\Delta T_{wc})$ (properties at mean coolant temperature)
P = steam pressure
P_t = pitch
Pr_c = Prandtl number of the coolant (properties at mean coolant temperature)
Q = heat transfer rate
R_w = tube wall thermal resistance = $D_o \ln(D_o/D_i)/2k_w$
$\tilde{\mathrm{Re}}$ = two-phase Reynolds number = $U_\infty D_o \rho/\mu$
Re_c = Reynolds number of the coolant (properties at mean coolant temperature)
$\tilde{\mathrm{Re}}_{ts}$ = value of $\tilde{\mathrm{Re}}$ when U_∞ is based on A_{ts}
$T_{\mathrm{sat}}(P)$ = saturation temperature at P
T_w = mean outside tube wall temperature
U_o = overall heat transfer coefficient
U_∞ = vapor approach velocity
$U_{\infty,N+1}$ = vapor velocity at approach to $(N+1)$th row, see Eq. (5)
U_c = coolant velocity
α_i = coolant-side, heat transfer coefficient
α_o = vapor-side, heat transfer coefficient
ΔT_{lm} = log-mean temperature difference
ΔT_v = temperature drop across the condensate film
ΔT_{wc} = inside wall to mean coolant temperature difference
μ = condensate dynamic viscosity
μ_c = coolant dynamic viscosity (calculated at mean coolant temperature)
μ_{cw} = coolant dynamic viscosity calculated at the tube wall inside temperature
μ_v = vapor dynamic viscosity
ρ = condensate density
ρ_v = vapor density

Cooling water was pumped through the condenser tubes via ten turbine flowmeters. Each row of tubes was individually cooled and nylon header plates at each end of the test section were used to series-connect the tubes in each row. A mixing chamber was located at each row outlet to ensure that a good mixed bulk temperature was measured. In each test the coolant flow rate was set as nearly as possible to be the same for all tube rows. Three coolant velocities in the range 1.75–3.25 m/s were used for each steam flow rate. The inlet and outlet temperatures for each row were measured using accurately calibrated thermocouples and having regard to adequate isothermal immersion of the leads near the junctions. In earlier single-tube tests (see Michael, 1988), using the same apparatus, the coolant temperature rise, measured as in the present work, agreed with measurements using platinum-resistance thermometers to within ±0.1 K; this represents about 1 percent of the lowest cooling water temperature rise measured across any row. The observed coolant temperature rise in the present work was in the range 14–20 K for the top row and 10–15 K for the bottom row. On this basis, and allowing for uncertainty in the coolant flow rate measurement, the mean heat flux for each tube row was determined to within 2 to 3 percent.

The vapor velocity was found from the steam flow rate calculated from the measured pressure drop across the orifice plate. In earlier single-tube tests using the same apparatus (see Michael, 1988) the measured steam flow rate was compared with that obtained from condensate collection measurements and the agreement was found to be better than ±3 percent. The steam pressure and temperature variations through the tube bank were measured with a differential-pressure transducer (accuracy of ±0.25 percent of calibrated span) and seven mineral-insulated copper-constantan thermocouples, respectively, at the locations indicated in Fig. 1.

Tube-wall temperatures were measured by copper-constantan thermocouples embedded in the walls of selected tubes in the first, second, fourth, sixth, eighth, and tenth condensing row. Four thermocouples, circumferentially equispaced and with junctions midway along the tube, were located in slots in each instrumented tube. Two instrumented tubes were placed in the tenth condensing row to provide data on the variation of the wall temperature in the direction of the coolant flow. The measured vapor-side temperature differences were in the approximate range 10 to 20 K.

For steady conditions, pressures, temperatures, and flow rates were measured at several cooling water flow rates and for several steam approach velocities. A total of 25 runs (steam and coolant flow rate combinations) was carried out.

The steam approach velocity U_∞ was obtained from

$$U_\infty = \frac{M_v}{\rho_v A_{ts}} \tag{4}$$

and the steam velocity just upstream of the $(N+1)$th row, $U_{\infty,N+1}$, from

$$U_{\infty,N+1} = \frac{\dot{M}_v - \sum_{i=1}^{N} \dot{M}_{cd,i}}{A \rho_v} \tag{5}$$

where $\dot{M}_{cd,i}$ is the mass condensation rate on the ith row of tubes and was obtained from the observed heat transfer rates, and A is the appropriate flow area defined later.

For rows with thermocouple-instrumented tubes, the steam-side heat transfer coefficient was obtained from the observed heat flux and the difference between the vapor temperature and the arithmetic mean of the measured tube-wall temperatures. A small correction was made for the temperature drop in the tube wall between the surface and the position of the thermocouple. For the other rows (third, fifth, seventh, and ninth), the condensing heat transfer coefficient was inferred by subtracting coolant-side and wall thermal resistances from the measured overall thermal resistance. The latter was given by

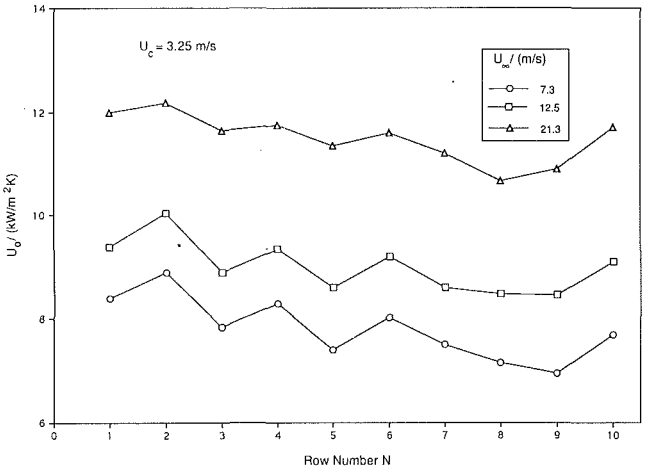

Fig. 2 Variation of overall heat transfer coefficient with tube row number for three steam velocities

$$\frac{1}{U_o A_o} = \frac{\Delta T_{lm}}{Q} \tag{6}$$

and, assuming uniform radial conduction within the tube wall so that

$$\frac{1}{U_o A_o} = \frac{1}{\alpha_i A_i} + \frac{R_w}{A_o} + \frac{1}{\alpha_o A_o} \tag{7}$$

The areas in Eqs. (6) and (7) relate to a *row* of tubes.

An equation of the form

$$\alpha_i = C_i \frac{k_c}{D_i} \mathrm{Re}_c^{0.8} \mathrm{Pr}_c^{1/3} \left(\frac{\mu_c}{\mu_{cw}}\right)^{0.14} \tag{8}$$

was used for the coolant-side heat transfer coefficient. A value of 0.0285 was used for C_i in Eq. (8). C_i was determined by fitting the measured coolant-side coefficient for the top condensing row which has the same number of tubes (i.e., four) as the uninstrumented rows (see Fig. 3). The value of C_i adopted is very close to that obtained using the expression given in Bird et al. (1960) for the present length-to-diameter ratio and range of coolant Reynolds number.

Results and Discussion

In contrast to the observations of Eissenberg (1972), Nobbs (1975), and Nobbs and Mayhew (1976) the present investigators did not observe "side drainage" of the condensate toward the walls of the test section. The condensate appeared to drain vertically in droplets from one tube to the next.

After the first condensing row, the observed steam temperatures were close to saturation values and were essentially uniform through the bank owing to the small pressure drop. Saturation temperatures corresponding to the observed pressures were used in the calculation of the vapor-side temperature drops and heat transfer coefficients.

Figure 2 shows the variation of the overall heat transfer coefficient with row number for a coolant velocity of 3.25 m/s (all tube rows) and three steam approach velocities. The general trend, in all three cases, shows that the heat transfer coefficient decreases slightly with penetration down the bank. However, an unexpected row-to-row "saw-tooth" variation of coefficient is revealed, with the three-tube rows apparently more effective than the four-tube rows. It may be noted that the variations in overall heat transfer coefficient were the result of variations in the heat flux from row to row. For instance, for the case where U_∞ = 12.5 m/s, the heat fluxes for the first three rows were 483 kW/m^2, 531 kW/m^2, and 462 kW/m^2.

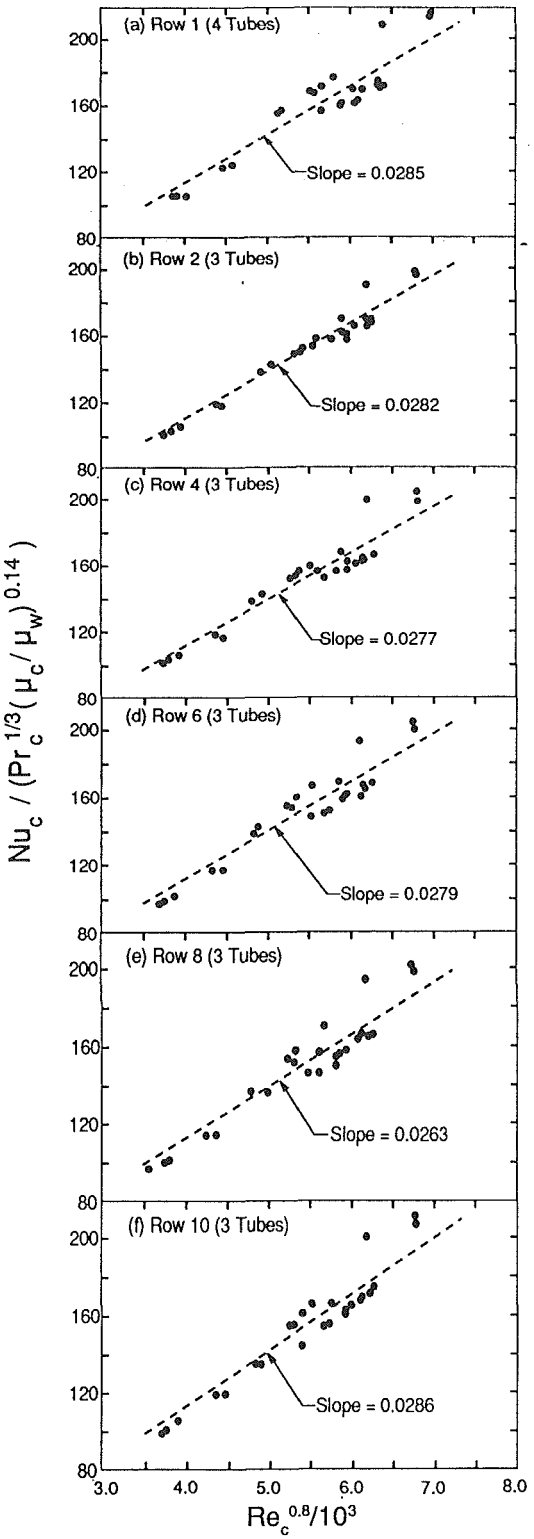

Fig. 3 Observed coolant-side heat transfer results for the first, second, fourth, sixth, eighth, and tenth rows

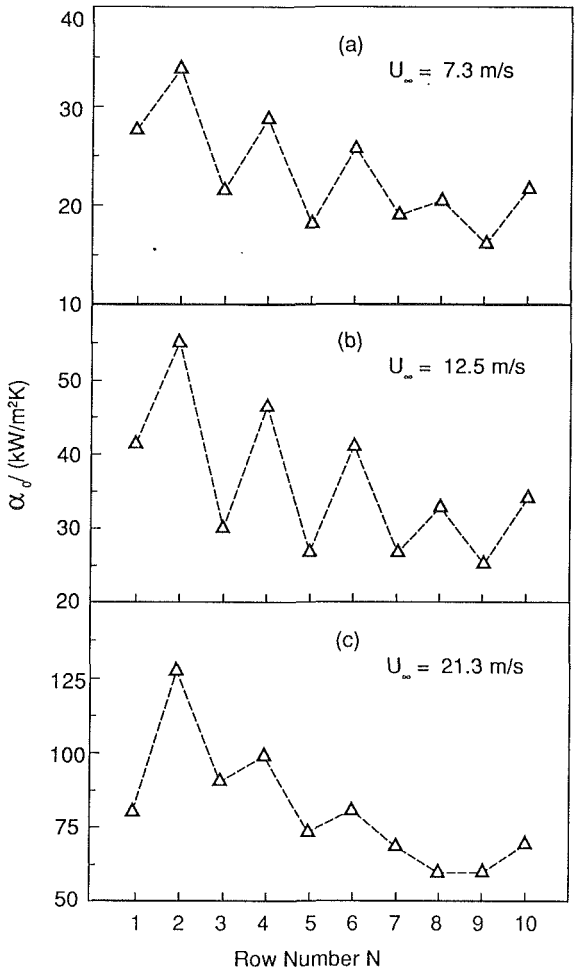

Fig. 4 Variation of steam-side heat transfer coefficient with row number for three steam approach velocities (U_i = 3.25 m/s)

For all rows, the logarithmic mean overall temperature difference varied by less than 3 percent about a mean value near to 53 K. The behavior shown in Fig. 2 is typical of that found at all vapor and coolant velocities.

As the tube-wall temperature were measured only for the first, second, fourth, sixth, eighth, and tenth condensing rows, it was necessary to obtain a coolant-side heat transfer correlation to determine the vapor-side heat transfer coefficients for the other rows. The coolant-side heat transfer results for each of the six temperature-instrumented tube rows are shown in Fig. 3. It can be seen that similar results are obtained for all rows. The range of values of the leading coefficient C_i in Eq. (3) (slope of the "least-squares" line) is 0.0263 to 0.0286.

The fact that the amplitude of the row-to-row variation in overall coefficient decreases with increasing vapor velocity (increasing vapor-side coefficient) suggests that the saw-tooth is a vapor-side phenomenon. Figure 4 shows the variation of the steam-side, heat transfer coefficient with row number for the same runs as those shown in Fig. 2. The vapor-side, heat transfer coefficients for rows with thermocouple-instrumented tubes were determined from the observed heat fluxes and measured vapor-to-wall temperature differences. For the rows without wall thermocouples, the vapor-side heat transfer coefficients were calculated from Eqs. (6)–(8), using a value of 0.0285 for C_i. This was the value found for the top condensing row, which has the same number of tubes (i.e., four) as the uninstrumented rows. Note that closely similar results would have been obtained when using any values of C_i in the range 0.0263–0.0286.

It is clearly seen from Fig. 4 that the row-to-row saw-tooth variation of the overall heat transfer coefficient (shown in Fig. 2) is due to corresponding variation of the steam-side coefficient. The three-tube rows are apparently more effective than the four-tube rows. Similar behavior has also been found by Shah (1978) for condensation of isopropanol at pressures in the approximate range 1 to 1.5 atm, on a nine-row, staggered tube bank with alternate rows of six and five tubes (see Fig. 5). As in the present case, Shah found that the higher coef-

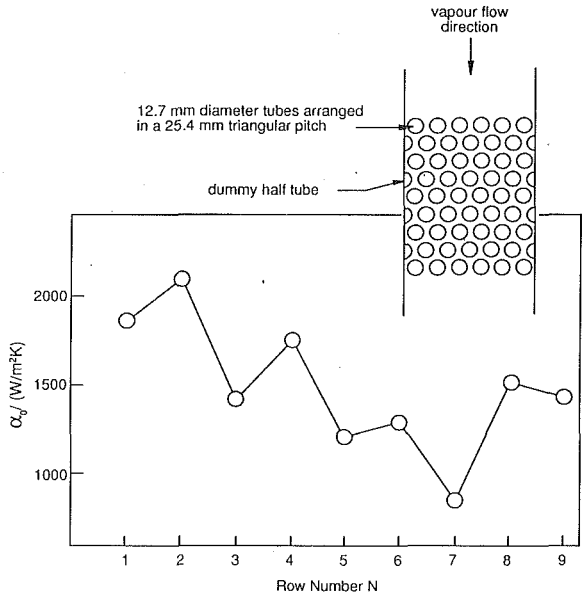

Fig. 5 Heat transfer coefficient for isopropanol condensing on a staggered tube bank (Shah, 1978)

ficients occurred on the rows with fewer condensing tubes and incorporating dummy half-tubes on the walls of the test section.

For a particular vapor approach velocity, the amplitude of the variation of the heat transfer coefficient appears to decrease with tube-row number. This behavior is observed for all three vapor approach velocities considered and is most clearly shown at the two lower values of U_∞ (7.3 m/s and 12.5 m/s). For these cases, the magnitudes of the thermal resistances on the vapor and coolant sides are closer to each other and the calculated vapor-side coefficients for the rows without an instrumented tube are therefore more accurate. At the highest vapor velocity (21.3 m/s), there are larger uncertainties in the calculated values of α_o for the uninstrumented rows as the process becomes coolant-side dominated.

The general trend of the present data shows the condensing heat transfer coefficient decreasing with penetration down the bank, as expected. This may be attributable both to the drop-off in the vapor-shear effect as condensation occurs and also to increased inundation.

Comparisons between the present tube-bank data and the single-tube theoretical result (i.e., Eq. (2)) are made in Fig. 6 for three vapor approach velocities. In determining the dimensionless parameters Nu, Re, and F, h_{fg} was evaluated at $T_{sat}(P)$ and other properties at (1/3) $T_{sat}(P)$ + (2/3) T_w. For a given approach velocity, each tube row experiences a different effective vapor velocity owing to condensation on the rows above. Thus, for a given run, each tube row provides separate values of the parameters used in plotting Fig. 6. Vapor velocities for each row were found using Eq. (5) where the area A may be one of the following:

(*i*) the cross-sectional area of the steam duct, A_{ts},
(*ii*) the minimum flow area, $A_{\min}$, and
(*iii*) the "mean void area," A_{mv}, as defined by Nobbs (1975), and for the present tube bank, given by

$$A_{mv} = 4L\left(P_t - \frac{\pi D_o^2}{2\sqrt{3}\,P_t}\right) \tag{9}$$

A_{mv} is the void volume of the bank (i.e., volume of the duct less volume occupied by the tubes) divided by the height of the bank.

It is seen that the data follow the same general trend as the theoretical single-tube line with measured values of $\mathrm{Nu}\tilde{\mathrm{R}}\mathrm{e}^{-1/2}$ higher for higher vapor approach velocities. Best

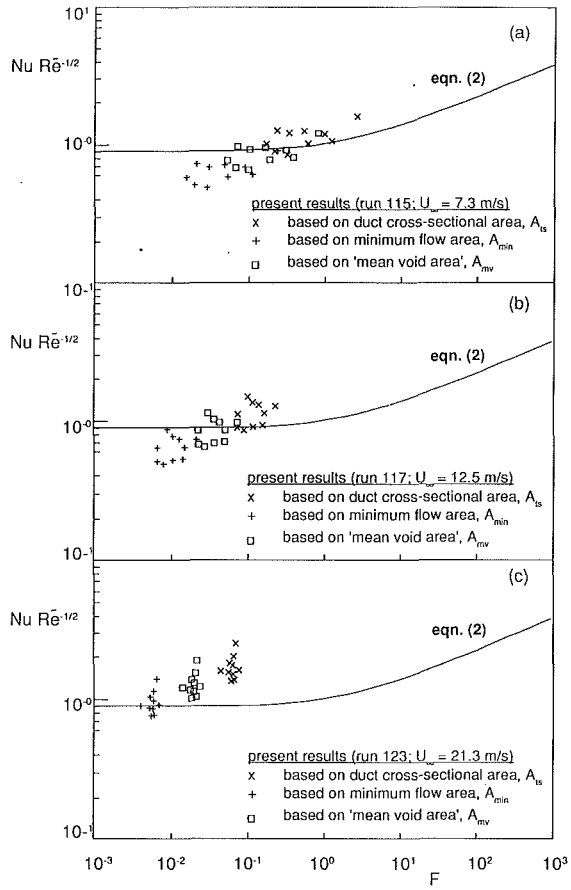

Fig. 6 Comparison of present data with Eq. (2) using three different areas for calculating vapor velocity

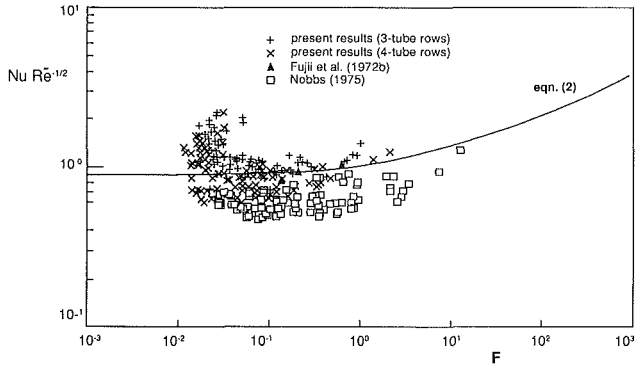

Fig. 7 Comparison of present data with those of Fujii et al. (1972b) and Nobbs (1975); all vapor velocities based on "mean void area"

overall agreement is found when the vapor velocity is based on the "mean void area" (method (*iii*) above). For this case most of the present tube-bank data are represented by the single-tube theoretical result to within about ±35 percent.

The present data are compared in Fig. 7 with earlier measurements for condensation of steam on small tube banks. The present data for the rows with three tubes and those with four tubes are distinguished. The parameters of the single-tube theoretical equation (Eq. (2)) have been used as a basis for the comparison. The mean void area has been used to calculate the vapor velocity in all cases. The following may be noted:

(*a*) The present data are in fairly good agreement with those of Fujii et al. (1972b).
(*b*) The results of Nobbs (1975) are generally lower.
(*c*) The present results are, except at the lowest values of

F (highest vapor velocities), in quite good general agreement with Eq. (2). Equation (2) is conservative with respect to the data for the highest vapor velocities.

It should be noted that the present heat transfer data were obtained for condensation of steam at near-atmospheric pressures on a staggered tube bank having ten condensing rows of alternate four and three tubes per row with three dummy (i.e., noncondensing) rows at the top of the bank. The data of Fujii et al. (1972b) and Nobbs (1975) were for condensation of steam on a staggered tube bank and on a single tube within a dummy staggered tube bank, respectively. During the experiments of Fujii et al. (1972b), low-pressure steam flowed horizontally across the tube bank and heat transfer measurements were obtained for each of five- and four-tube rows. In the case of Nobbs (1975), steam at slightly above atmospheric pressure flowed vertically downward and inundation water, simulating up to around 60 higher tubes, was provided by means of three perforated tubes situated at the top of the bank.

Conclusions

1 In general, the vapor-side heat transfer coefficient was found to decrease with penetration down the tube bank. This might be attributable to both the drop-off of the vapor-shear effect and increased condensate inundation. Comparison with theory that does not incorporate inundation suggests that inundation effects are small for these tests. A relatively small effect of inundation might be explained by the fact that, while the condensate film on lower tubes is thicker, it could be turbulent. (Note that, for a staggered bank, the vertical separation of vertically aligned tubes is relatively large. Inundation may be more important for an in-line bank where the vertical separation of tubes is small.)

2 A row-to-row saw-tooth variation of the vapor-side heat transfer coefficient was observed with the three-tube rows apparently more effective than the four-tube rows. This could be attributable to the fact that the dummy half-tubes deflect the steam toward the inner tubes and do not contribute to the reduction in vapor velocity as the vapor crosses the row. Whatever the explanation, it is considered that the effect is real and well within the accuracy of the measurements. The results for the four-tube rows (i.e., without dummy half-tubes) should probably be more representative of a large bank. Furthermore, since the heat transfer coefficients for the four-tube rows were smaller this would be conservative for design purposes. Data from small tube banks, where individual rows are not instrumented, should be treated with caution.

3 The present vapor-side Nusselt numbers for steam are generally in agreement with those of Fujii et al. (1972b) and somewhat higher than those measured by Nobbs (1975). It may be noted that the work of Fujii et al. (1972b) was for near-horizontal flow of low-pressure steam and Nobbs (1975) used a single condensing tube in a dummy tube bank.

4 Equation (2), with vapor velocity based on mean void area, is in general agreement with the present data for moderate vapor velocity. It is to be noted that Eq. (2) takes no account of inundation. The present data, therefore, suggest that for this fluid, geometry, vapor velocity range and pressure, effects of inundation are relatively small.

Acknowledgment

This work was undertaken under the HTFS research program, which receives funding from the UK Department of Trade and Industry. The authors wish to acknowledge the many helpful comments by Mr. J. M. McNaught of NEL in the course of this work. Thanks are also due to Mr. P. M. Beech for help in preparation of the figures.

References

Bird, R. B., Stewart, W. E., and Lightfoot, E. N., 1960, *Transport Phenomena*, Wiley, New York.

Brickell, G. M., 1981, "Potential Problem Areas in Simulating Condenser Performance," in: *Power Condenser Heat Technology*, P. J. Marto and R. H. Nunn, eds., Hemisphere, pp. 51–61.

Eissenberg, D. M., 1972, "An Investigation of the Variables Affecting Steam Condensation on the Outside of a Horizontal Tube Bundle," PhD Thesis, University of Tennessee, Knoxville, TN.

Fuks, S. N., 1957, "Heat Transfer With Condensation of Steam Flowing in a Horizontal Tube Bundle," *Teploenergetika*, Vol. 4, pp. 35–39.

Fujii, T., Uehara, H., and Kurata, C., 1972a, "Laminar Filmwise Condensation of Flowing Vapour on a Horizontal Cylinder," *Int. J. Heat Mass Transfer*, Vol. 15, pp. 235–246.

Fujii, T., Uehara, H., Hirata, K., and Oda, K., 1972b, "Heat Transfer and Flow Resistance in Condensation of Low Pressure Steam Flowing Through Tube Banks," *Int. J. Heat Mass Transfer*, Vol. 15, pp. 247–260.

Grant, I. D. R., and Osment, B. D. J., 1968, "The Effect of Condensate Drainage on Condenser Performance," NEL Report No. 350.

Honda, H., Nozu, S., and Fujii, T., 1982, "Vapour to Coolant Heat Transfer During Condensation of Flowing Vapour on a Horizontal Tube," *Proc. 7th Int. Heat Transfer Conf.*, Vol. 5, pp. 77–82.

Lee, W. C., Rahbar, S., and Rose, J. W., 1984, "Film Condensation of Refrigerant-113 and Ethanediol on a Horizontal Tube," ASME JOURNAL OF HEAT TRANSFER, Vol. 106, pp. 524–530.

Michael, A. G., 1988, "Condensation of Steam at High Velocity on a Horizontal Tube and a Small Tube Bank," PhD Thesis, Queen Mary College, University of London, United Kingdom.

Michael, A. G., Rose, J. W., and Daniels, L. C., 1989, "Forced Convection Condensation on a Horizontal Tube—Experiments With Vertical Downflow of Steam," ASME JOURNAL OF HEAT TRANSFER, Vol. 111, pp. 792–797.

Nobbs, D. W., 1975, "The Effect of Downward Vapour Velocity and Inundation on the Condensation Rates on Horizontal Tubes and Tube Banks," PhD Thesis, University of Bristol, United Kingdom.

Nobbs, D. W., and Mayhew, Y. R., 1976, "Effect of Downward Vapour Velocity and Inundation on Condensation Rates in Horizontal Tube Banks," *Symposium on Steam Turbine Condensers*, NEL Report No. 619, pp. 39–52.

Nusselt, W., 1916, "Die Oberflachenkondensation des Wasserdampfes," *ZVDI*, Vol. 60, pp. 541–546, pp. 569–575.

Rose, J. W., 1984, "Forced Convection Film Condensation on a Horizontal Tube—Effect of Pressure Variation in the Condensate Film," *Int. J. Heat Mass Transfer*, Vol. 27, pp. 39–47.

Shah, A. K., 1978, "Multicomponent Condensation on a Horizontal Tube Bank," MSc Thesis, University of Manchester, United Kingdom.

Shekriladze, I. G., and Gomelauri, V. I., 1966, "Theoretical Study of Laminar Film Condensation of Flowing Vapour," *Int. J. Heat Mass Transfer*, Vol. 9, pp. 581–591.

Pure Steam Condensation Experiments on Nonisothermal Vertical Plates

H. J. H. Brouwers[1]
Akzo Research Laboratories Arnhem,
Fibers Division,
Department of Mechanical Engineering,
Arnhem, The Netherlands

Pure steam condensation experiments on flat channel plates have been performed. To provide a range of values of the governing groups NTU and Ad, steam was condensed crosscurrentwise on polyvinylidene fluoride (PVDF) plates and cocurrentwise on brass plates ($8.0\times10^{-6}\leq Ad\leq 8.4\times10^{-2}$, $0\leq NTU^{-1}\leq 10$). The theoretical predictions, based on an analysis of Nusselt-type condensation on nonisothermal plates, agree excellently with the plastic-plate measurements. The brass-plate experiments, however, agree with the theoretical model only in a limited range of NTU and Ad.

Introduction

Laminar film condensation of pure saturated vapors on vertical flat plates has often been examined in the past. Several extensions and improvements have been proposed to the original analysis of Nusselt (1916). Bromley (1952) and Rohsenow (1956) included the heat capacity of the condensate, Sparrow and Gregg (1959) extended this analysis to include the inertia of the condensate, and Koh et al. (1961) additionally analyzed the effect of vapor drag. Chen (1961), Koh (1961), and Churchill (1986) derived approximate solutions accounting for the aforesaid effects. Ünsal (1988) extended the classical Nusselt model with the effect of surface waves on the condensate. Brouwers (1989) considered the Nusselt condensation on nonisothermal plates. In this paper increases in temperature of the cooling liquid in a channel plate due to liberated latent heat were included. It was furthermore demonstrated that the co-, counter-, and crosscurrent processes are governed by NTU and Ad (see the nomenclature for definitions).

In order to validate the Nusselt condensation model, numerous pure vapor condensation experiments on isothermal plates have been reported, e.g., steam condensation by Slegers and Seban (1970). These efforts, however, were limited to experiments on flat isothermal plates, thus only verifying the special case $Ad=\infty$; see Brouwers (1989). Accordingly, pure steam condensation experiments have been carried out on brass and polyvinylidene fluoride (PVDF) channel plates for a wide range of NTU and Ad values. The results of these experiments are presented in this paper.

Apparatus

The low-pressure steam used is supplied by the central boilerhouse. Since the water has been degassed before boiling, it is not expected to contain any noncondensables. The steam has an absolute pressure P_v of 2.25 bar, with a corresponding saturation temperature T_{sat} of 124°C, and is somewhat superheated; $T_{v,in}=135$°C. This degree of superheat is, however, insignificant, e.g., see Sparrow and Eckert (1961) or Minkowycz and Sparrow (1966); hence the steam can be regarded as saturated. The steam enters a cylindrical chamber with thick (20 mm) PVDF walls to condense on four parallel channel plates; see Figs. 1 and 2. The distance between the plates is such that interactions between the condensation processes on the separate plates are excluded. The entire test chamber is thermally insulated with plastic foam to avoid undesired heat

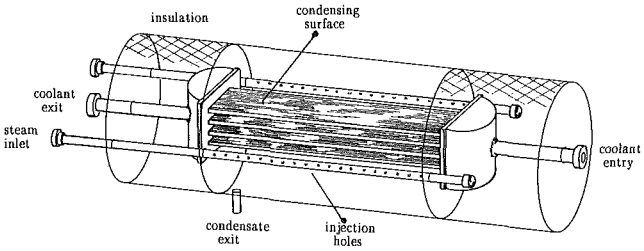

Fig. 1 Tested PVDF channel plates

	PVDF	brass
B_{tot} (mm)	40.2	40
d_1 (mm)	1.4	3.4
d_2 (mm)	1.6	3.4
d_3 (mm)	0.4	0.6
d_4 (mm)	0.3	0.3
d_5 (mm)	40	40
d_6 (mm)	2.0	4.0
k_w (W/mK)	0.19	85
$\bar{h}_w$ (W/m^{2}K)	1266.6	56.6 10^4

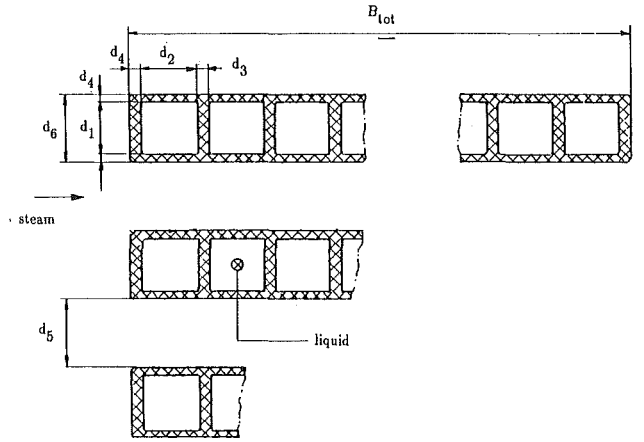

Fig. 2 Properties and dimensions of tested channel plates

[1]Present address: Twente University, Department of Civil Engineering, P.O. Box 217, 7500 AE Enschede, The Netherlands.

Contributed by the Heat Transfer Division for publication in the JOURNAL OF HEAT TRANSFER. Manuscript received by the Heat Transfer Division November 1990; revision received December 1991. Keywords: Condensation, Heat Exchangers, Mass Transfer.

loss. The entering coolant, i.e., water, has during the experiments an inlet temperature $T_{l,in}$ of about 11°C. The various temperatures of the test setup are measured with laboratory mercury thermometers, and the coolant flow with calibrated flowmeters.

At the start of the experiments, the condensate in the connecting tubes was removed by blowing through steam. By injecting steam, with zero coolant flow, the air present was driven out of the test chamber through a vent hole in the bottom.

In order to create two different McAdams numbers, both PVDF and brass (DIN Ms 63) channel plates have been tested. Because of the poor thermal conductivity of PVDF, the corresponding Ad was small. The difference with the larger Ad of the brass plate is furthermore increased by adapting the orientation of the setup with respect to the vertical: The vapor condenses cocurrentwise on the brass plates and crosscurrentwise on the PVDF plates. In Fig. 2 the dimensions of both setups are listed. The NTU is simply varied by adjusting the liquid mass flow through the plates, since NTU is inversely proportional to the liquid capacity flow through a plate.

Theory

To obtain NTU^{-1} and Ad, the physical properties of both fluids have to be determined. As these properties depend on temperature, the proper reference temperatures have to be calculated. The McAdams number is defined as:

$$\mathrm{Ad} = \frac{\bar{h}_{pl}^4 \eta_c (L \text{ or } B)(T_{\mathrm{sat}} - T_{l,in})}{16 \rho_c^2 H_{fg} k_c^3 g}. \tag{1}$$

For co- and countercurrent condensation, L should be used in this equation, while for crosscurrent condensation B should be considered, corresponding with the flow-off length of the processes concerned. The McAdams number is a measure of the ratio, to the fourth power, of the total heat transfer coefficient of the plate and the heat transfer coefficient of the condensate films. The total heat transfer coefficient of the plate $\bar{h}_{pl}$, appearing in Ad and NTU, is defined by:

$$\frac{1}{\bar{h}_{pl}} = \frac{1}{\bar{h}_w} + \frac{1}{\bar{h}_l}. \tag{2}$$

The heat transfer coefficient $\bar{h}_w$ of the walls follows from:

$$\bar{h}_w = 2\frac{k_w}{d_4}, \tag{3}$$

and is listed in Fig. 2. The heat transfer coefficient from channel plate to coolant follows from:

$$\bar{h}_l = \frac{2\overline{\mathrm{Nu}}_l k_l}{D_{h,l}} \left(\frac{\mathrm{Pr}_l}{\mathrm{Pr}_{l,w}} \right)^{0.11} \cong \frac{4\overline{\mathrm{Nu}}_l k_l}{(d_1 + d_2)} \left(\frac{\mathrm{Pr}_l}{\mathrm{Pr}_{l,w}} \right)^{0.11}. \tag{4}$$

In this paper the correlation of Dennis et al. (1959) ($\mathrm{Nu}_{l,\infty} = 2.98$) is employed for the average laminar convective flow Nusselt number because in both plates the flow remains in the laminar flow regime. This correlation only accounts for the effect of the thermal entry length, not the hydrodynamic. Neti and Eichhorn (1983) demonstrated numerically that the hydrodynamic development region has little effect for $\mathrm{Pr}_l > 6$ and $\mathrm{Re}_l \mathrm{Pr}_l D_{h,l}/L < 120$. As these conditions are satisfied in the tested channel plates, the correlation of Dennis et al. (1959) can be used. The factor of two in Eqs. (3) and (4) accounts for the heat transfer on both sides of the plate.

For the brass channel plates (unlike the plastic plates) the Nusselt number in Eq. (4) is furthermore multiplied by a factor of two to account for the heat transfer through the intermediate walls in the plate, which act as extra heat transfer surfaces. In Eq. (4) also the Sieder and Tate correction appears; see V.D.I. (1988). This correction is of minor importance for plastic plates since the temperature (and related dynamic viscosity) variation across the channels will be small; $\bar{h}_{pl}$ is dominated by $\bar{h}_w$ rather than by $\bar{h}_l$.

The physical properties of the coolant are evaluated at:

$$T_l^* = \frac{T_{l,in} + T_{l,\mathrm{out}}}{2}, \tag{5}$$

as suggested by V.D.I. (1988).

To calculate the coolant Prandtl number at the brass wall, $\mathrm{Pr}_{l,w}$, the temperature at the wall needs to be known; see Eq. (4). This temperature follows from the energy balance:

$$\bar{h}_w (T_{c,w}^* - T_{l,w}^*) = \bar{h}_l (T_{l,w}^* - T_l^*), \tag{6}$$

see Fig. 3. The mean wall reference temperature is derived from Eq. (6) as:

$$T_{l,w}^* = \frac{T_{c,w}^* \bar{h}_w + T_l^* \bar{h}_l}{\bar{h}_w + \bar{h}_l}. \tag{7}$$

The mean reference interface temperature $T_{c,w}^*$ at condensate-plate surface follows from the energy balance:

$$\bar{h}_{pl} (T_{c,w}^* - T_l^*) = \bar{h}_c (T_{\mathrm{sat}} - T_{c,w}^*). \tag{8}$$

This equation is rewritten to obtain the reference temperature:

Nomenclature

Ad = McAdams number $= \bar{h}_{pl}^4 \eta_c (L \text{ or } B)(T_{\mathrm{sat}} - T_{l,in})/16\rho_c^2 H_{fg} k_c^3 g$
B = net plate width, m
c_p = specific heat, $\mathrm{Jkg^{-1}K^{-1}}$
D_h = hydraulic diameter = four times the cross-sectional/the perimeter, m
d_i = geometric property of heat exchanger, see Fig. 2, m
g = acceleration due to gravity, $\mathrm{ms^{-2}}$
H_{fg} = latent heat of condensation, $\mathrm{Jkg^{-1}}$
h = heat transfer coefficient, $\mathrm{Wm^{-2}K^{-1}}$
Ku = Kutateladze number $= c_{p,c}(T_{\mathrm{sat}} - T_{c,w})/H_{fg}$
k = thermal conductivity, $\mathrm{Wm^{-1}K^{-1}}$
L = net plate length, m
M = Morton number $= g\eta_c^4/\sigma_c^3\rho_c$
$\dot{m}$ = local mass flux into condensate, $\mathrm{kgm^{-2}s^{-1}}$
NTU = number of transfer units $= \bar{h}_{pl} BL/w_l c_{p,l}$
Nu = Nusselt number $= hD_h/k$
P = pressure, bar
Pr = Prandtl number $= \eta c_p/k$
Q = dimensionless condensate formation $= (1 - \Theta_{\mathrm{out}})/\mathrm{NTU}$
Re_c = condensate flow Reynolds number $= w_c/2\eta_c(L \text{ or } B)$
Re_l = coolant flow Reynolds number $= w_l/\eta_l B$
T = temperature, K
w = mass flow, $\mathrm{kgs^{-1}}$
η = dynamic viscosity, Pas
Θ = dimensionless temperature $= (T_{\mathrm{sat}} - T_l)/(T_{\mathrm{sat}} - T_{l,in})$
ρ = density, $\mathrm{kgm^{-3}}$
σ = surface tension, $\mathrm{Nm^{-1}}$

Subscripts

c = condensate
in = entry
l = liquid in channel plate
out = exit
pl = channel plate
sat = saturation
tot = total
v = vapor
w = channel plate/coolant or channel plate/condensate interface
∞ = fully developed flow

Superscripts

$\bar{}$ = mean
* = reference

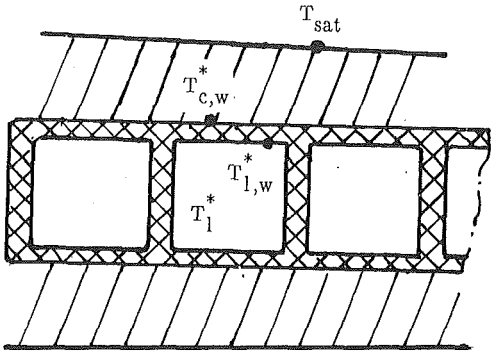

Fig. 3 Heat transfer from vapor-condensate surface to coolant

$$T^*_{c,w} = \frac{\bar{h}_c T_{sat} + \bar{h}_{pl} T^*_l}{\bar{h}_c + \bar{h}_{pl}}. \tag{9}$$

The mean heat transfer coefficient of the Nusselt condensation model reads:

$$\bar{h}_c = \frac{8}{3}\left[\frac{\rho_c^2 H_{fg} k_c^3 g}{4\eta_c (L \text{ or } B)(T_{sat} - T^*_{c,w})}\right]^{1/4}, \tag{10}$$

(which can, for instance, be found from Bird et al., 1960). For co- and countercurrent condensation, L should be employed in Eq. (10), while for crosscurrent condensation B should be used. Following Minkowycz and Sparrow (1966), the properties of the condensate are evaluated at reference temperature:

$$T^*_c = \frac{T_{sat} + 2T^*_{c,w}}{3}, \tag{11}$$

except for H_{fg}, which is evaluated at T_{sat}. To determine $\bar{h}_l$ and $\bar{h}_c$, the reference temperatures $T^*_{l,w}$ and $T^*_{c,w}$ have to be known to determine the physical properties of both fluids. These heat transfer coefficients, however, depend on the physical properties. A successive substitution method is used to determine the matching $\bar{h}_l$, $\bar{h}_c$, $T^*_{l,w}$, and $T^*_{c,w}$. The $T^*_{c,w}$ thus determined is furthermore used to evaluate the physical properties of the condensate contained in Ad; see Eq. (11).

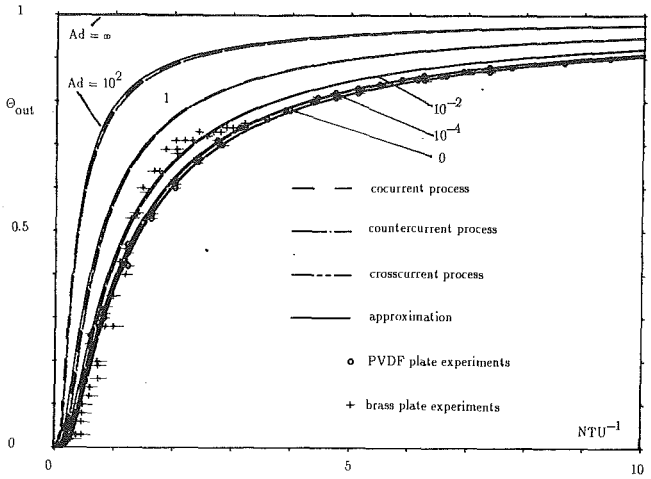

Fig. 4 Theoretical (Brouwers, 1989) and experimental variation of Θ_{out} with NTU^{-1}

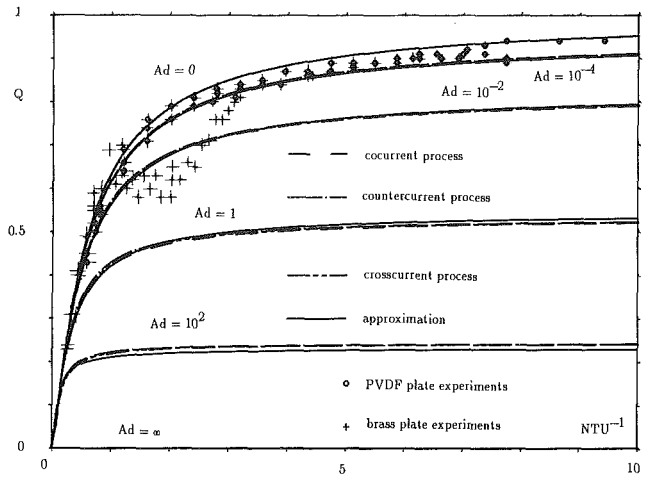

Fig. 5 Theoretical (Brouwers, 1989) and experimental variation of Q with NTU^{-1}

Results

In Figs. 4 and 5 the results of the experiments on brass and PVDF plate are depicted as a function of NTU^{-1}. In these figures also the theoretical Q and Θ_{out} predictions of Brouwers (1989) are plotted. The thin horizontal and vertical bars in both figures are the ranges of experimental uncertainty. The primary measurements of temperature and liquid flow introduce uncertainties in NTU, Θ_{out}, and Q, which are derived in the appendix.

The largest NTU^{-1} of the PVDF plates corresponds to $Re_l = 993$ and $Re_c Pr_c^{0.95} = 13$; consequently, both fluids are in the laminar flow regime (V.D.I., 1988). The maximum condensate Reynolds number follows from an overall mass balance of vapor entering the condensate films on both sides of the plate, w_c (by Brouwers, 1989, referred to as: M), and condensate flowing off the plate:

$$Re_c = \frac{w_c}{2\eta_c (L \text{ or } B)}, \tag{12}$$

where L should be used for crosscurrent condensation and B for co- and countercurrent condensation. For crosscurrent condensation, however, the produced condensate and Re_c varies with the distance from the entry of the coolant; the maximum condensate mass flux is found where the coolant enters the plate. The local mass flux times latent heat of condensation equals the heat flux from vapor–condensate surfaces to coolant. The local mass flux into the films is highest if the heat resistance of the film is neglected. Hence, an overestimation of Re_c is obtained when

$$w_c = LB\dot{m} < LB\,\frac{\bar{h}_{pl}(T_{sat} - T_{l,in})}{H_{fg}} \tag{13}$$

is substituted into Eq. (12). Combining Eqs. (12) and (13) results in said maximum value $Re_c Pr_c^{0.95} = 13$ for the PVDF experiments.

The Ad of the PVDF experiments increased with rising NTU^{-1} from 0.8×10^{-5} to 1.1×10^{-5}. This minor variation is due to the poor heat transfer coefficient of the plastic walls; $\bar{h}_w = 1266.6$ W/m^{2}K (see Fig. 2). Although the heat transfer from coolant to wall is enhanced by larger mass flows, entry effects cause a $\bar{h}_l$ range from 2600 W/m^{2}K to 3800 W/m^{2}K, and $\bar{h}_{pl}$ and Ad remain dominated by $\bar{h}_w$. Figures 4 and 5 illustrate the excellent agreement between experiment and theory, which predicts hardly any influence of the formed condensate on heat transfer for small values of Ad. Note that Ad $\simeq 0$ represents a limiting case of the analysis of Brouwers (1989) (the other one is: Ad $= \infty$), which has never been examined experimentally.

In both figures the experimental results of the condensation on the brass plate are also presented as a function of NTU^{-1}. The largest NTU^{-1} in these plots, NTU$^{-1} = 3.2$, corresponds to maximum $Re_l = 2218$ and $Re_c Pr_c^{0.95} = 209$, so that laminar

coolant and condensate flow are guaranteed. The maximum Reynolds number Re_c of the condensate is obtained using Eq. (12) with B applied. The thickness of the condensate films flowing off the plates is one-dimensional for co- and countercurrent condensation. Hence w_c need not be assessed with Eq. (13), but follows readily from the overall energy balance:

$$w_c H_{fg} = w_l c_{p,l} (T_{l,\text{out}} - T_{l,in}). \quad (14)$$

The subcooling of the condensate is neglected in Eq. (14), which is allowed for small Ku.

During the experiments $\bar{h}_l$ increased from 2600 W/m^{2}K to 5600 W/m^{2}K with increasing NTU^{-1} owing to entry effects. As $\bar{h}_l$ dominates $\bar{h}_{pl}$ (see Eq. (2) and note that $\bar{h}_w = 566{,}000$ W/m^{2}K (Fig. 2)), $\bar{h}_{pl}$ and Ad rise almost to the same extent as $\bar{h}_l$: Ad increased from 0.29×10^{-2} to 8.4×10^{-2} with increasing coolant flow.

Figures 4 and 5 illustrate the departure from the theory for very small and large NTU^{-1}. The discrepancy for very small NTU^{-1} is attributed to the contribution of unavoidable leakage heat flows to the coolant in the brass headers (the PVDF plates were fitted in thermally well-insulating PVDF headers). Accordingly, unreasonably high exit temperatures are measured. Some Θ_{out} even lie below the curve pertaining to Ad = 0, which is physically impossible. Beyond $NTU^{-1} = 2$ the experimental exit temperatures lie between the curves Ad = 0 and Ad = 10^{-2}, and are thus in agreement with the theoretical prediction. However, for $NTU^{-1} > 2$, the experimental Θ_{out} intersects the curve Ad = 10^{-2} and tends to approach the curve Ad = 0, although the experimental Ad approximates 8.4×10^{-2}. This implies that the measured value of Θ_{out} is smaller than predicted, that is to say, the calculated exit temperature is too low. The heat transfer from vapor to coolant is apparently better than predicted by the model. Three possible departures from the ideal model conditions are:

- ripples on the condensate surface,
- dropwise condensation,
- forced vapor flow in the test chamber.

In the literature the appearance of ripples is often quoted as a major explanation of the Nusselt condensation model underestimating the heat transfer from condensate to wall. For all experiments the dimensionless combination Ku/Pr_c was much smaller than 0.1. This implies that the results of the model of Ünsal (1988) can be applied (Ku/Pr_c is referred to as F in this note).

In Ünsal's paper the heat transfer through a condensate film with ripples is compared with that through a film without ripples: the Nusselt solution. One of the results relevant here is that for $4Re_c = 400$, the heat transfer from condensate to plate is augmented by ripples by at most a factor of 1.5; see Fig. 6 for a comparison with Nusselt's solution. An additional requirement for this value to be attained is that the Morton number M be larger than 1.06×10^{-12}. For all condensation experiments, however, this number proved to be of the order of 0.16×10^{-12}, so the effect of surface ripples should be less pronounced.

In Fig. 6 experimental data of Ratiani and Shekriladze (1964) are also shown, as well as the heat transfer coefficient of Nusselt's model and its corrected expression for the effect of waves following Kutateladze and Gogonin (1979):

$$\bar{h}_c = \frac{8}{3}\left[\frac{\rho_c^2 H_{fg} k_c^3 g}{4\eta_c (L \text{ or } B)(T_{\text{sat}} - T_{c,w})}\right]^{1/4} \text{Re}_c^{0.04}, \quad (15)$$

where Re_c is the maximum Reynolds number of the condensate and $T_{c,w}$ the constant temperature of the isothermal plate. For condensation on isothermal plates the maximum condensate Reynolds number reads:

$$\text{Re}_c = \frac{\rho_c^2 k_c g}{3\eta_c^2}\left[\frac{\rho_c^2 H_{fg} k_c^3 g}{4\eta_c (L \text{ or } B)(T_{\text{sat}} - T_{c,w})}\right]^{-3/4}. \quad (16)$$

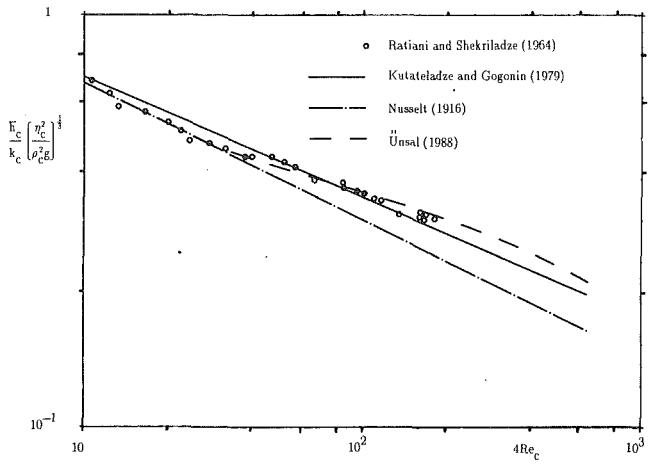

Fig. 6 Condensation heat transfer according to Nusselt (1916), Ünsal (1988), Ratiani and Shekriladze (1964), and Kutateladze and Gogonin (1979)

Ünsal (1988) refers to Re_c as "$\overline{Re}_L$" (for "$\overline{Re}_L^{1/3}$" in Eq. (13) of this paper one should read "$\overline{Re}_L^{-1/3}$"). Figure 6 illustrates the fair agreement between the result of the comprehensive analysis of Ünsal (1988), the compact correction suggested by Kutateladze and Gogonin (1979), and experiments reported by Ratiani and Shekriladze (1964). However, all experimental and theoretical results indicate that ripples alone cannot explain why the calculated heat transfer is so poor. For when Ad is divided by 5, corresponding with the suspected effect of waves to the fourth power, the calculated exit temperature is still too low.

During the experiments it was not possible to watch the plates and verify whether film condensation actually occurred. However, the experimental and theoretical results indicate that the discrepancy between the results depends on the coolant mass flow (and related condensation rate), revealing that the deviation cannot be explained by possible dropwise condensation only. Moreover, dropwise condensation is not expected because the brass plates do not have smooth and clean surfaces. They are constructed from square channels joined by soldering.

The amount of steam injected into the test chamber and condensed on the plates increases with higher coolant flow rates. For the brass plate experiments the maximum steam mass flow amounts to 44 kg/h, owing to the excellent heat transfer in this plate. Although the steam is injected by two injectors, provided with many holes turned away from the channel plates, it is suspected that the condensate films are disturbed, or even blown off the plates, by the incoming steam. In general, forced convection reduces the condensate film thickness and hence also the related heat resistance of the film. Enhanced heat transfer through the film leads to a small experimental Ad. The experimental data indeed approximate the theoretical curves for Ad = 10^{-2} and Ad = 10^{-4} (note that Ad = 0 corresponds physically to a negligible/absent film).

The effect of forced flow in the test chamber was also regarded by Slegers and Seban (1970) as the most acceptable explanation for their experimental results being 20 percent above theory. For that matter, during their experiments the maximum amount of injected steam was only about 1 kg/h.

For the PVDF plate the steam flow reaches a maximum rate of 9 kg/h. It is conceivable that here, too, film heat transfer is enhanced by forced steam flow. This cannot be observed because even for ideal Nusselt condensation the film is negligible (since Ad ≃ 0). However, good agreement between theory and experiments is also found for small coolant (and related vapor and condensate) flow rates. Accordingly, one can assume that at least for small coolant (and vapor mass) flows, where

Nusselt condensation is ensured, theory and experiment are in agreement.

Conclusions

In the past the Nusselt condensation model has only been compared with isothermal plate and tube condensation experiments ($Ad \simeq \infty$). Based on the assumption of Nusselt type condensation, which has been thoroughly verified, pure steam condensation experiments have been carried out on nonisothermal plates. Crosscurrent condensation experiments performed on PVDF channel plates ($Ad \simeq 10^{-5}$, $0 \leq NTU^{-1} \leq 10$) confirm that the predictions of Brouwers (1989) are essentially correct. The thermal conductivity of these plates is such that it entirely dominates the heat transfer (the film can be regarded as isothermal or absent).

The theoretical predictions of cocurrent condensation on brass plates correspond with experiments ($0.29 \times 10^{-2} \leq Ad \leq 8.4 \times 10^{-2}$, $0 \leq NTU^{-1} \leq 3.2$) only in a limited range of both governing dimensionless groups NTU and Ad. Complete agreement with the model might have been obtained if perfect thermal insulation and quiescent vapor conditions had been more nearly achieved.

Acknowledgments

The author thanks the management of Akzo Research Laboratories Arnhem for their permission to publish this paper and Messrs. H. P. Korstanje and G. Vegt for their support. He also expresses his gratitude to Prof. A. K. Chesters of Eindhoven University of Technology for his stimulating discussion on the subject.

References

Bird, R. B., Stewart, W. E., and Lightfoot, E. N., 1960, *Transport Phenomena*, Wiley, New York.

Bromley, L. A., 1952, "Effect of Heat Capacity of Condensate," *Ind. Eng. Chem.*, Vol. 44, pp. 2966-2969.

Brouwers, H. J. H., 1989, "Film Condensation on Non-isothermal Vertical Plates," *Int. J. Heat Mass Transfer*, Vol. 32, pp. 655-663.

Chen, M. M., 1961, "An Analytical Study of Laminar Film Condensation: Part 1—Flat Plates," ASME JOURNAL OF HEAT TRANSFER, Vol. 83, pp. 48-54.

Churchill, S. W., 1986, "Laminar Film Condensation," *Int. J. Heat Mass Transfer*, Vol. 29, pp. 1219-1226.

Dennis, S. R. C., Mercer, A. M., and Poats, G., 1959, "Forced Heat Convection in Laminar Flow Through Rectangular Ducts," *Quart. Appl. Math.*, Vol. 17, pp. 285-297.

Holman, J. P., 1978, *Experimental Methods for Engineers*, 3rd ed., McGraw-Hill, New York.

Kline, S. J., and McClintock, F. A., 1953, "Describing Uncertainties in Single-Sample Experiments," *Mech. Eng.*, Vol. 75, pp. 3-8.

Koh, J. C. Y., 1961, "On Integral Treatment of Two-Phase Boundary Layer in Film Condensation," ASME JOURNAL OF HEAT TRANSFER, Vol. 83, pp. 359-362.

Koh, J. C. Y., Sparrow, E. M., and Hartnett, J. P., 1961, "The Two Phase Boundary Layer in Laminar Film Condensation," *Int. J. Heat Mass Transfer*, Vol. 2, pp. 69-82.

Kutateladze, S. S., and Gogonin, I. I., 1979, "Heat Transfer in Film Condensation of Slowly Moving Vapor," *Int. J. Heat Mass Transfer*, Vol. 22, pp. 1593-1599.

Minkowycz, W. J., and Sparrow, E. M., 1966, "Condensation Heat Transfer in the Presence of Noncondensables, Interfacial Resistance, Superheating, Variable Properties, and Diffusion," *Int. J. Heat Mass Transfer*, Vol. 9, pp. 1125-1144.

Neti, S., and Eichhorn, R., 1983, "Combined Hydrodynamic and Thermal Development in a Square Duct," *Num. Heat Transfer*, Vol. 6, pp. 497-510.

Nusselt, W., 1916, "Die Oberflächenkondensation des Wasserdampfes," *Z. Ver. dt. Ing.*, Vol. 60, pp. 541-546, 569-575 [in German].

Ratiani, G. V., and Shekriladze, I. G., 1964, "An Experimental Study of the Heat Exchange Process on Transition From Laminar to Turbulent Flow of the Film," *Thermal Engng.*, Vol. 11, pp. 101-102.

Rohsenow, W. M., 1956, "Heat Transfer and Temperature Distribution in Laminar-Film Condensation," *Trans. ASME*, Vol. 78, pp. 1645-1648.

Slegers, L., and Seban, R. A., 1970, "Laminar Film Condensation of Steam Containing Small Concentrations of Air," *Int. J. Heat Mass Transfer*, Vol. 13, pp. 1941-1947.

Sparrow, E. M., and Gregg, J. L., 1959, "A Boundary Layer Treatment of Laminar-Film Condensation," *Trans. ASME*, Vol. 81, pp. 13-17.

Sparrow, E. M., and Eckert, E. R. G., 1961, "Effects of Superheated Vapor and Noncondensable Gases on Laminar Film Condensation," *AIChE Journal*, Vol. 7, pp. 473-477.

Ünsal, M., 1988, "Effect of Waves on Nusselt Condensation," *Int. J. Heat Mass Transfer*, Vol. 31, pp. 1944-1947.

V.D.I., 1988, *V.D.I.—Wärmeatlas*, 5. Aufl., V.D.I. Verlag GmbH [in German].

APPENDIX

Uncertainty Analysis

The uncertainty analysis presented here follows the procedures described by Kline and McClintock (1953) and Holman (1978). The primary experimental data, such as $T_{l,in}$, w_l, $T_{l,out}$, etc., are used to calculate the desired dimensionless quantities NTU, Θ_{out}, and Q. The uncertainty in these calculated results is obtained by considering the uncertainties in the primary measurements and is discussed below.

The uncertainty in a calculated result I, which is a function of the independent variables i_1, i_2, ..., i_n, reads:

$$\left(\frac{dI}{I}\right)^2 = \left(\frac{\partial I}{\partial i_1}\frac{di_1}{I}\right)^2 + \left(\frac{\partial I}{\partial i_2}\frac{di_2}{I}\right)^2 + \ldots + \left(\frac{\partial I}{\partial i_n}\frac{di_n}{I}\right)^2, \quad \text{(A1)}$$

where di_1, di_2, ..., di_n represent the uncertainties in the quantities i_1, i_2, ..., i_n. Applying Eq. (A1) to Θ_{out} gives:

$$\left(\frac{d\Theta_{out}}{\Theta_{out}}\right)^2 = \left(\frac{dT_{l,in}}{T_{sat} - T_{l,in}}\right)^2 + \left(\frac{dT_{l,out}}{T_{sat} - T_{l,out}}\right)^2 + \left[\frac{(T_{l,out} - T_{l,in})\,dT_{sat}}{(T_{sat} - T_{l,in})\,(T_{sat} - T_{l,out})}\right]^2. \quad \text{(A2)}$$

This expression constitutes the relative uncertainty in Θ_{out} as a result of the uncertainties in the measured $T_{l,in}$, $T_{l,out}$, and T_{sat}, represented by $dT_{l,in}$, $dT_{l,out}$, and dT_{sat}, respectively. These temperatures are measured with mercury thermometers with inaccuracies of 0.1°C. The maximum $d\Theta_{out}$ amounts to 0.13×10^{-2} and 0.12×10^{-2} for the brass and PVDF experiments, respectively.

The uncertainty in NTU, denoted by dNTU, depends on dw_l, $dc_{p,l}$, dk_l, dk_p, dL, dB, dd_1, dd_2, and dd_4, see Eqs. (2), (3), and (4). Neglecting uncertainties in the physical and geometric properties, which are much smaller than the uncertainty of the liquid mass flow, Eq. (A1) produces:

$$\left(\frac{d\text{NTU}}{\text{NTU}}\right) = \left(\frac{dw_{g,in}}{w_{g,in}}\right). \quad \text{(A3)}$$

The total liquid mass flow is measured with the aid of a rotameter with an inaccuracy $4dw_l$ of 0.015 kg/s (the factor of 4 is introduced because the water is divided over 4 channel plates). For the experimental data of Figs. 3 and 4, the maximum dNTU amounts to 0.122 and 0.072 for the brass and PVDF experiments, respectively.

The uncertainty in Q depends on both the uncertainties in Θ_{out} and NTU. Applying Eq. (A1) yields:

$$\left(\frac{dQ}{Q}\right)^2 = \left(\frac{d\Theta_{out}}{1 - \Theta_{out}}\right)^2 + \left(\frac{d\text{NTU}}{\text{NTU}}\right)^2, \quad \text{(A4)}$$

where both $d\Theta_{out}$ and dNTU readily follow from Eqs. (A2) and (A3), respectively. For the brass experiments the maximum dQ reads 0.120, and for the PVDF experiments the maximum dQ amounts to 0.049.

Accurate Heat Transfer Measurements for Condensation on Horizontal, Integral-Fin Tubes

A. Briggs

X.-L. Wen

J. W. Rose

Queen Mary and Westfield College,
University of London,
London, United Kingdom

In most earlier experimental investigations of condensation on low-fin tubes, vapor-side heat transfer coefficients have been found from overall (vapor-to-coolant) measurements using either predetermined coolant-side correlations or "Wilson plot" methods. When the outside resistance dominates, or is a significant proportion of the overall resistance, these procedures can give satisfactory accuracy. However, for externally enhanced tubes, and particularly with high-conductivity fluids such as water, significant uncertainties may be present. In order to provide reliable, high-accuracy data, to assist in the development of theoretical models, tests have been conducted using specially constructed plain and finned tubes fitted with thermocouples to measure the tube wall temperature, and hence the vapor-side heat transfer coefficient, directly. The paper describes the technique for manufacturing the tubes and gives results of systematic heat transfer measurements covering the effects of fin height, thickness, and spacing, tube diameter, and vapor velocity. The tests were carried out with steam, ethylene glycol, and R-113, with vertical vapor downflow. The heat flux was measured using an accurately calibrated 10-junction thermopile and paying particular attention to coolant mixing and isothermal immersion of thermocouple junctions. Care was taken to avoid errors due to the presence in the vapor of noncondensing gas and the occurrence of dropwise condensation. Smooth, consistent, and repeatable results were obtained in all cases. The data are presented in easily accessible form and are compared with the results of previous investigations, where indirect methods were used to determine the vapor-side data, and with theory.

1 Introduction

The theoretical model of Beatty and Katz (1948) has been widely used to predict condensation heat transfer coefficients for low integral-finned tubes. More recently, it has been generally appreciated that this simple model, which ignores surface tension effects, is unsatisfactory. Since surface tension has both beneficial and detrimental effects, these tend to cancel, and the Beatty and Katz model may, in certain circumstances, give acceptable heat transfer coefficients. However, owing to the neglect of condensate retention between the fins on the lower parts of the tube, this theory predicts that the heat transfer coefficient should improve continuously with increasing fin density. It therefore provides no guidance to the optimum fin density for use in a given application. Moreover, the simple model has been shown to be inadequate for fluids with higher surface tension.

In order to validate more recent and complex theories (e.g., Honda et al., 1987; Adamek and Webb, 1990), accurate experimental data are needed. Although in a few investigations (Honda et al., 1983; Webb et al., 1985; Sukhatme et al., 1990) attempts have been made to measure the tube wall temperature directly, in the past, heat transfer coefficients have generally been inferred from overall vapor-to-coolant measurements using either predetermined coolant-side correlations, or "Wilson plots" (Yau et al., 1985; Wanniarachchi et al., 1986; Marto et al., 1988). As the vapor-side coefficient is enhanced, its determination by these indirect methods becomes increasingly inaccurate. In the present work, specially constructed finned tubes, incorporating thermocouples buried in the tube walls, have been used to determine the vapor-side coefficients directly. Furthermore, care has been taken to measure the heat transfer rate to the tubes with extreme precision and to ensure that the results were not vitiated by the presence of noncondensing gas in the vapor or the occurrence of dropwise condensation. The results, for three different condensing fluids (steam, ethylene glycol, and refrigerant-113), two tube diameters, and a range of vapor velocities, fin thicknesses, fin heights, and fin spacings, are believed to be the most accurate so far available. The main purpose of the paper is to make the data available, so as to help development and refinement of theoretical models.

2 Apparatus and Procedure

Two closed-loop, stainless steel test rigs were used. Diagrams of the apparatus are shown in Fig. 1. In one rig (duct diameter 101 mm), smaller diameter (12.7 mm at the fin root) condenser tubes were tested at lower vapor velocities. The second, larger apparatus (duct diameter 152 mm), was used to test larger diameter (19.1 mm at the fin root) tubes and at higher vapor velocities. In both cases the vapor was generated in electrically heated boilers (maximum power 16 kW and 30 kW) and directed vertically downward through a calming section, before flowing over the horizontal, water-cooled, test condenser tube. Excess vapor passed to an auxiliary condenser from which the condensate returned to the boiler by gravity.

The smaller tubes had a diameter at the fin root of 12.7 mm, fin thickness 0.5 mm, fin height 1.59 mm, and fin spacings of 0.5, 1.0 and 1.5 mm. The larger tubes had a diameter at the fin root of 19.1 mm, fin thickness and height 1.0 mm, and fin spacings of 0.5, 1.0, and 1.5 mm. For comparison, instrumented plain tubes, having outside diameters of 12.7 mm and 19.1 mm, were also used. PTFE inserts were used to insulate the inside of the test tubes thermally before and after the test section so that the inside and outside surface areas available to heat transfer were of equal length.

The vapor velocity, at approach to the test section, was found

Contributed by the Heat Transfer Division for publication in the JOURNAL OF HEAT TRANSFER. Manuscript received by the Heat Transfer Division September 1991; revision received January 1992. Keywords: Condensation, Finned Surfaces, Phase-Change Phenomena.

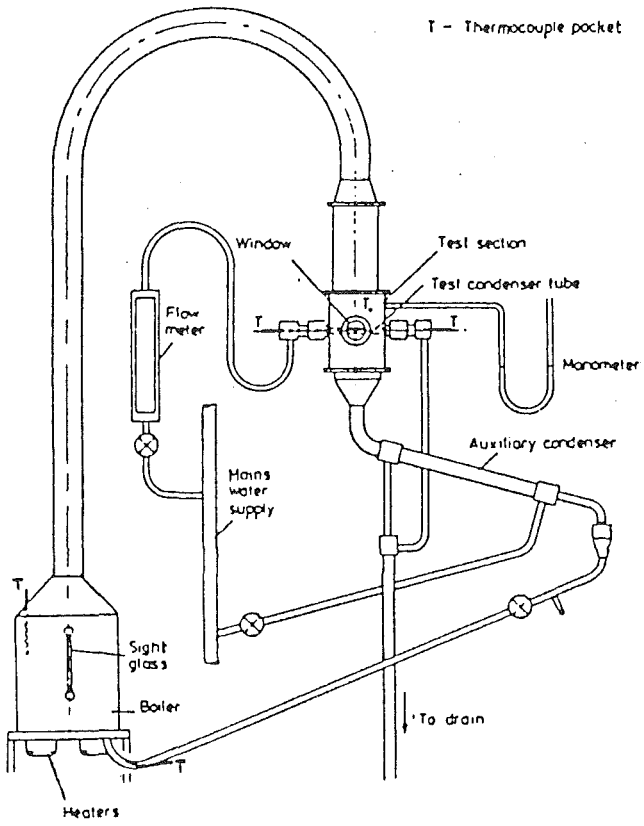

a) Smaller Apparatus

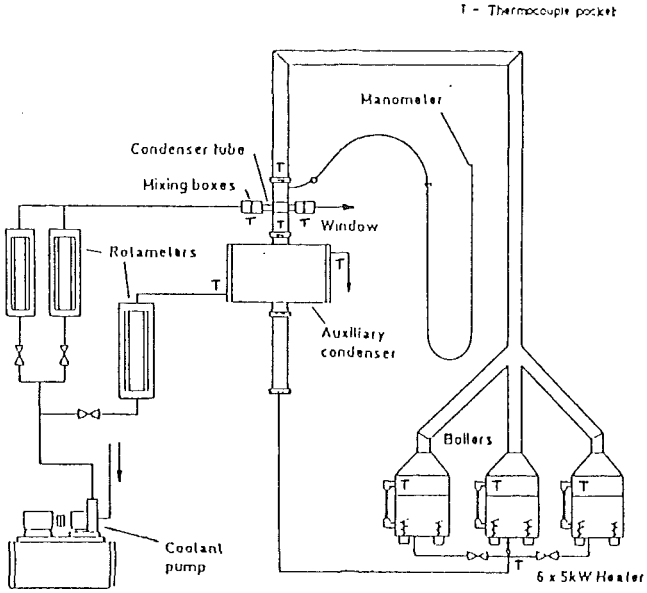

b) Larger Apparatus

Fig. 1 Diagrams of the apparatus

from the measured power input to the boiler. A small, predetermined correction, for the heat loss from the well-insulated apparatus, was included in the calculation of the vapor velocity. To extend the range of heat flux obtainable, some tests were conducted using a wire-wrapped-rod insert to enhance the coolant-side, heat transfer coefficient. The cooling water temperature rise, from which the heat transfer rate to the test tube was calculated, was measured using a 10-junction thermopile, with adequate isothermal immersion of the junctions, and special mixing arrangements. The test condenser tube was well insulated from the body of the test section. A predetermined correction for the dissipation temperature rise of the cooling water was incorporated in the calculation of the heat transfer rate. The estimated accuracy of the measurement of the coolant temperature rise was better than 0.01 K. For the smaller apparatus, the range of coolant temperature rise was 0.1 to 13.5 K and for the larger 0.2 to 24.1 K.

The tube wall temperature was measured directly using specially manufactured, instrumented tubes, each with four thermocouples embedded in the wall at 90 deg intervals around the tube. All test tubes were made from relatively thick-walled copper tube. Four equispaced slots, 1.5 mm square, were machined axially along the outer surface. Thermocouples were inserted in the slots and their junctions soldered midway along the tube. Close-fitting copper strips were soldered in the grooves over the thermocouple leads and the outer surface turned smooth. For the plain tubes, the tubes were then thinly copper plated. For the finned tubes, the tubes were next copper plated to a diameter exceeding that of the required diameter over the fins. Finally the tubes were turned down to the fin tip diameter

Nomenclature

A = constant in Eqs. (3) and (4)
b = spacing between fins
d = plain tube diameter, diameter at fin root
$e(\Delta T) = \left\{\frac{1}{j}\sum(\Delta T_{obs} - \Delta T_{calc})^2\right\}^{1/2}$
$e(q) = \left\{\frac{1}{j}\sum\left(\frac{q_{obs} - q_{calc}}{q_{obs}}\right)^2\right\}^{1/2}$
$F = \mu h_{fg} dg/U_v^2 k\Delta T$
g = specific force of gravity
h_{fg} = specific enthalpy of evaporation
i = number of runs on different days
j = number of data points used in curve fit
k = thermal conductivity of condensate
Nu = Nusselt number $= qd/k\Delta T$
n = constant in Eq. (3)
P = pressure
q = heat flux based on area of plain tube with fin root diameter
q_{calc} = calculated heat flux
q_{obs} = observed heat flux
Re = two-phase Reynolds number $= U_v \rho d/\mu$
T_v = vapor temperature
T_w = mean wall temperature
T^* = reference temperature, see Eq. (2)
U_v = vapor approach velocity
α = vapor-side, heat transfer coefficient
$\epsilon_{\Delta T}$ = vapor-side enhancement ratio at same vapor-side temperature difference, see Eq. (5)
ΔT = mean vapor-to-surface temperature difference
ΔT_{calc} = calculated mean vapor-to-surface temperature difference
ΔT_{max} = highest ΔT value for experimental data
ΔT_{min} = lowest ΔT value for experimental data
ΔT_{obs} = observed mean vapor-to-surface temperature difference
μ = viscosity of condensate
ρ = density of condensate

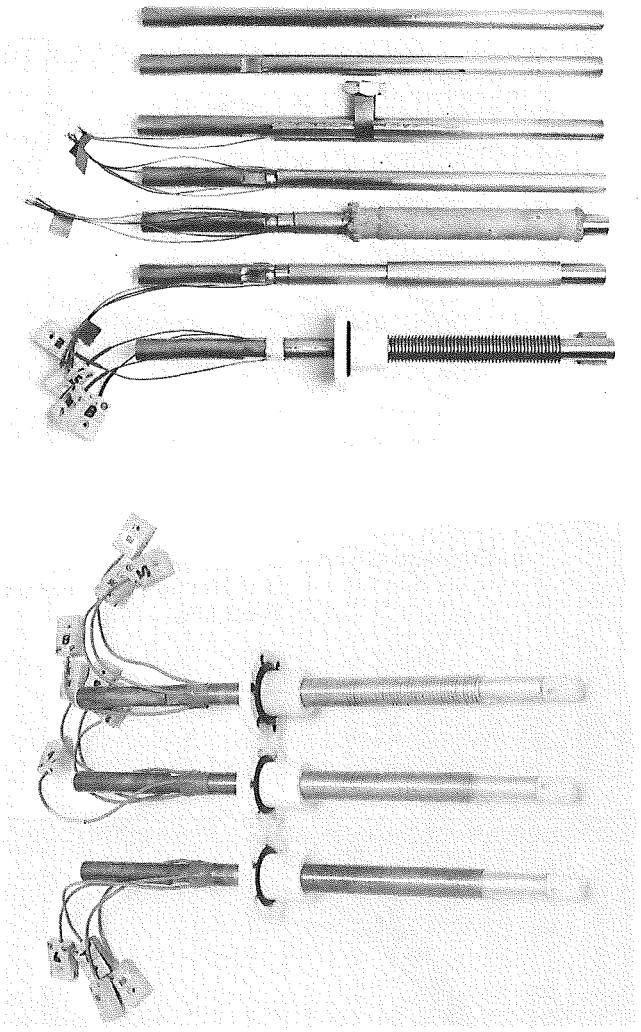

Fig. 2 Instrumented test tubes: (*a*) stages of manufacture; (*b*) finished smaller diameter tubes

and rectangular profile fins machined to the required root diameter. Figure 2 shows the various stages in the manufacture of the special instrumented test tubes, and the finished smaller diameter tubes. When inserted in the test section, the tubes were oriented so that the positions of the thermocouples were at angles of 22.5, 112.5, −67.5, and −157.5 deg from the top of the tube. In the case of the smaller diameter tubes, tests were also carried out with the tubes oriented such that the thermocouples were at angles of 0, 90, 180, and −90 deg from the top of the tube so that wall temperatures at a total of eight angular positions were obtained for these tubes. In the heat transfer data given below, the wall temperature used is the arithmetic mean of the four local wall temperatures. An approximate correction was made for the temperature drop in the tube wall between the tube surface (at the fin root diameter) and the thermocouple position. This was based on the mean heat flux and the assumption of uniform radial conduction. The magnitude of the associated error in the mean vapor-to-surface temperature difference is not immediately obvious. However, it may be noted that, for the finned tubes, the correction had maximum values of 8, 4, 22, and 20 percent of ΔT, for R-113, ethylene glycol, steam at atmospheric pressure, and steam at low pressure, respectively. For the plain tubes, where the heat fluxes were much smaller, the correction was negligible.

Steam, ethylene glycol, and R-113 were used as condensing fluids in both rigs. For the smaller apparatus, all tests were conducted at a pressure slightly above atmospheric pressure. For the larger apparatus, measurements were made at slightly above atmospheric pressure for steam and R-113, and also at lower pressures for steam and ethylene glycol. Full details of apparatus, procedure, and precautions to avoid errors due to noncondensing gases and dropwise condensation have been given by Yau et al. (1985) and Memory and Rose (1986).

3 Results and Discussion

The results for the larger diameter tubes are shown in Fig. 3. The data are shown in the form of heat flux (based on the plain tube area at fin root diameter) against mean vapor-to-surface temperature difference, i.e., the measured quantities. Traditional heat transfer coefficient plots have not been used since these exaggerate errors at low vapor-to-surface temperature difference. For each tube, fluid, and pressure, tests were performed on at least two separate occasions. In all cases the results show very good consistency and reproducibility; this was also true for the smaller tubes.

For the plain tube the results are compared to the theoretical model of Shekriladze and Gomelauri (1966), represented by the equation given by Rose (1984)

$$\mathrm{Nu}/\tilde{\mathrm{R}}\mathrm{e}^{1/2} = \frac{0.9 + 0.728F^{1/2}}{(1 + 3.44F^{1/2} + F)^{1/4}} \tag{1}$$

When plotting the lines given by Eq. (1), the condensate properties were evaluated at the reference temperature,

$$T^* = \frac{2}{3}T_w + \frac{1}{3}T_v \tag{2}$$

It is seen in Fig. 3 that for steam, the experimental data at both pressures, for the larger diameter plain tube, are in very good agreement with Eq. (1). For ethylene glycol, the measured heat fluxes for the plain tube fall below the theoretical line, while for R-113, the experimental data fall above theory. Similar results were found for the smaller diameter plain tube. These trends for plain tubes have been reported by Memory and Rose (1986), for ethylene glycol, and Lee et al. (1984), for R-113.

For both diameters, it was found that the best performing finned tubes were those with fin spacings of 1.5 mm, 1.0 mm, and 0.5 mm, for steam, ethylene glycol, and R-113 respectively. In Fig. 3 an effect of vapor velocity is evident for all three fluids. This is smaller for the finned tubes than the plain tube in all cases, and smallest of all for the best performing tube for each fluid.

The present data are believed to have superior accuracy to earlier measurements. So as to make the data readily available in compact form, for use in theoretical modeling, the heat flux-temperature difference curves have been fitted (by minimization of sums of squares of residuals in ΔT) by equations of the form:

$$\left(\frac{q}{\mathrm{W/m^2}}\right) = A\left(\frac{\Delta T}{\mathrm{K}}\right)^n \tag{3}$$

where A and n are given in Tables 1 and 2. The lines through the finned tube data in Fig. 3 are given by Eq. (3) with the constants in Table 1. It can be seen from the tables that in most cases the index n is close to 0.75, i.e., the value given by Nusselt (1916) for a quiescent vapor condensing on a plain tube. When the data are refitted to an equation of the form:

$$\left(\frac{q}{\mathrm{W/m^2}}\right) = A\left(\frac{\Delta T}{\mathrm{K}}\right)^{0.75} \tag{4}$$

i.e., when n is forced to 0.75, slightly less good, but still satisfactory, fits are obtained. In this case the "enhancement ratio," defined as the heat transfer coefficient for a finned tube, divided by that for a plain tube at the same vapor-side

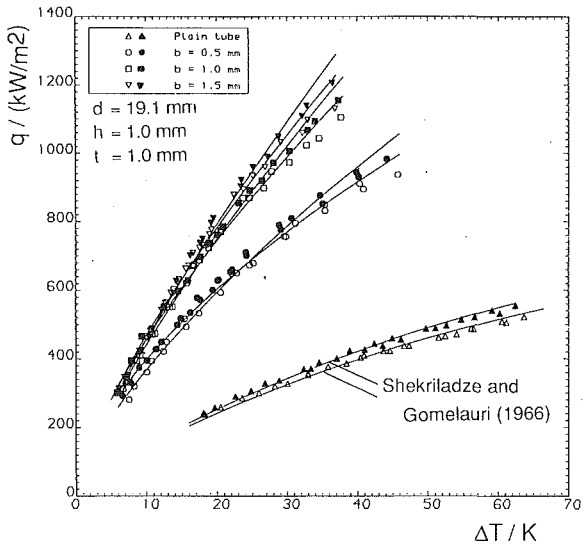

a) Steam $U_v = 0.8$ m/s (open points)
$U_v = 1.2$ m/s (solid points)
$P = 100$ kPa

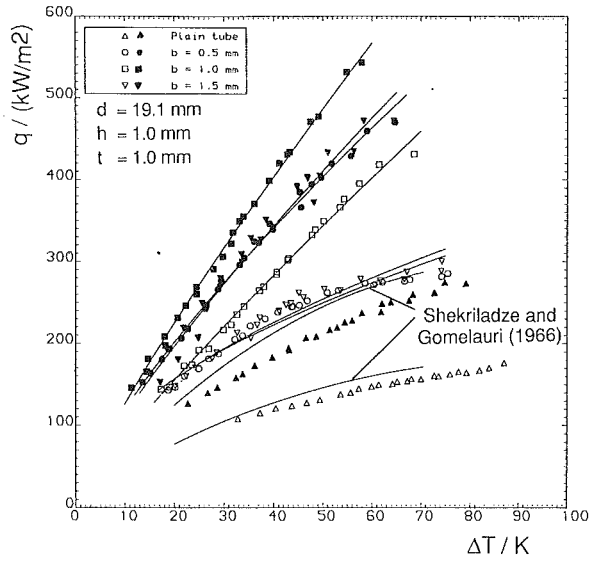

c) Ethylene Glycol $U_v = 8$ m/s (open points)
$U_v = 28$ m/s (solid points)
$P = 3$ kPa

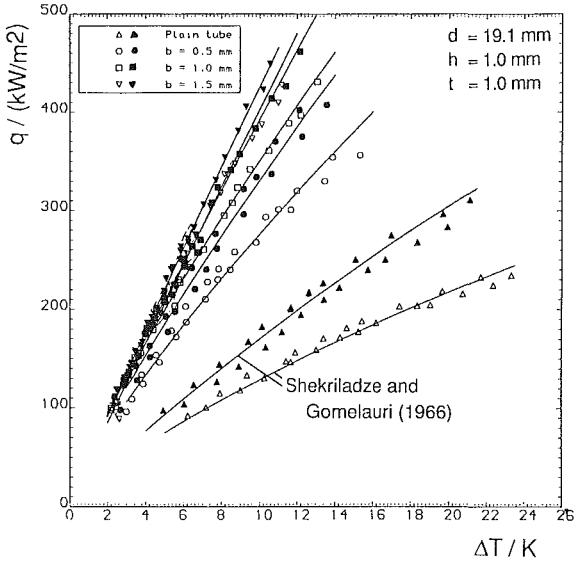

b) Steam $U_v = 2.6$ m/s (open points)
$U_v = 8.4$ m/s (solid points)
$P = 14$ kPa

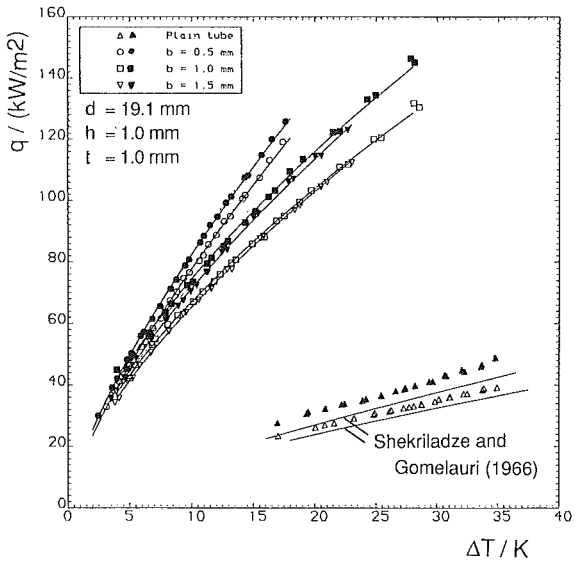

d) R-113 $U_v = 0.4$ m/s (open points)
$U_v = 1.5$ m/s (solid points)
$P = 100$ kPa

Fig. 3 Dependence of heat flux on vapor-side temperature difference (lines through finned tube data are best fits of the form $q = A\Delta T^n$

temperature difference, is conveniently independent of temperature difference, i.e.,

$$\epsilon_{\Delta T} = \left(\frac{\alpha_{\text{finned tube}}}{\alpha_{\text{plain tube}}}\right)_{\text{same } \Delta T} = \left(\frac{q_{\text{finned tube}}}{q_{\text{plain tube}}}\right)_{\text{same } \Delta T} = \left(\frac{A_{\text{finned tube}}}{A_{\text{plain tube}}}\right)_{\text{same } n\ (0.75)} \quad (5)$$

Enhancement ratios have been calculated for all the tube and fluid combinations tested in the present investigation, and are given in Tables 1 and 2.

4 Comparison With Data From Earlier Investigations

In Fig. 4, present data for the smaller diameter tubes are compared, on the basis of enhancement ratio against fin spacing, with the earlier data of Yau et al. (1985) for steam, Masuda and Rose (1985) for R-113, and Masuda and Rose (1988) for ethylene glycol. In these earlier investigations, the fin and tube dimensions and the vapor velocities were the same as those for the present, smaller diameter tubes. Yau et al. (1985) obtained the vapor-side temperature differences by subtracting the wall and coolant-side resistance, obtained from a predetermined (using an instrumented plain tube) correlation, from the measured overall resistance. Masuda and Rose (1985, 1988) obtained vapor-side results by the same method, and also by using a "modified Wilson plot." While the results are in general agreement with the present data, significant differences can be seen, even though great care was taken to obtain reliable overall data in the earlier investigations. The indirectly obtained en-

Table 1 Summary of experimental results for larger diameter tubes; $d = 19.1$ mm, $t = 1.0$ mm, $h = 1.0$ mm, (see Eq. 3))

Fluid	P/kPa	b/mm	U_V/(m/s)	i	j	ΔT_{min}	ΔT_{max}	Ax10^{-3}	n	e(ΔT)/K	e(q),%	$\varepsilon_{\Delta T}$
R-113	100	0.0*	0.4	2	24	17	35	2.94	0.728	0.28	0.70	-
"	"	"	0.6	"	"	17	35	3.32	0.704	0.39	1.05	-
"	"	"	0.8	"	"	17	35	3.03	0.739	0.40	1.11	-
"	"	"	1.1	"	"	17	35	2.95	0.761	0.48	1.35	-
"	"	"	1.3	"	"	17	35	3.27	0.739	0.49	1.38	-
"	"	"	1.5	"	"	16	35	3.24	0.754	0.54	1.46	-
"	"	0.5	0.4	"	"	3	17	14.01	0.744	0.12	0.94	5.05
"	"	"	0.6	"	"	3	17	14.21	0.746	0.13	1.12	4.95
"	"	"	0.8	"	"	3	17	14.66	0.737	0.13	0.86	4.87
"	"	"	1.1	"	"	3	17	15.09	0.729	0.13	0.84	4.70
"	"	"	1.3	"	"	3	17	15.04	0.734	0.10	0.69	4.58
"	"	"	1.5	"	"	3	17	15.26	0.733	0.09	0.78	4.46
"	"	1.0	0.4	"	"	5	27	15.67	0.632	0.31	1.27	4.06
"	"	"	0.6	"	"	5	27	16.64	0.621	0.39	1.39	4.03
"	"	"	0.8	"	"	5	27	16.69	0.627	0.29	1.20	4.01
"	"	"	1.1	"	"	5	27	17.13	0.626	0.30	1.19	3.93
"	"	"	1.3	"	"	5	27	16.97	0.637	0.23	1.58	3.88
"	"	"	1.5	"	"	5	27	17.18	0.637	0.34	2.17	3.79
"	"	1.5	0.4	"	"	5	22	14.43	0.656	0.11	0.94	4.11
"	"	"	0.6	"	"	5	22	14.96	0.655	0.15	0.79	4.10
"	"	"	0.8	"	"	5	22	14.92	0.664	0.11	0.64	4.07
"	"	"	1.1	"	"	5	22	15.39	0.659	0.11	0.51	3.98
"	"	"	1.3	"	"	5	22	15.20	0.668	0.12	0.65	3.88
"	"	"	1.5	"	"	5	22	15.34	0.668	0.13	0.77	3.77
Glycol	2.5	0.0*	8.	"	"	32	88	19.49	0.491	1.08	1.21	-
"	"	"	12.	"	"	30	87	20.78	0.511	1.30	1.52	-
"	"	"	14.	"	"	27	86	18.14	0.558	0.88	1.29	-
"	"	"	18.	"	"	25	85	17.80	0.589	0.92	1.46	-
"	"	"	22.	"	"	23	81	18.56	0.599	0.96	1.63	-
"	"	"	28.	"	"	22	78	17.07	0.643	0.86	1.17	-
"	"	0.5	8.	"	"	20	72	33.94	0.510	2.04	2.78	2.00
"	"	"	12.	"	"	18	70	29.37	0.580	2.32	3.23	1.95
"	"	"	14.	"	"	16	69	26.85	0.616	2.17	3.11	1.84
"	"	"	18.	"	"	15	68	24.39	0.671	2.10	3.11	1.95
"	"	"	22.	"	"	14	66	21.96	0.723	1.18	1.95	1.97
"	"	"	28.	"	"	13	65	20.68	0.759	0.79	1.79	1.93
"	"	1.0	8.	"	"	17	65	11.53	0.867	0.91	2.20	2.73
"	"	"	12.	"	"	16	64	15.57	0.812	0.93	2.14	2.54
"	"	"	14.	"	"	15	63	16.07	0.811	1.09	2.52	2.47
"	"	"	18.	"	"	13	62	17.22	0.816	0.96	2.41	2.39
"	"	"	22.	"	"	12	62	18.76	0.814	0.85	2.27	2.37
"	"	"	28.	"	"	10	60	19.97	0.843	0.61	2.38	2.27
"	"	1.5	8.	"	"	20	71	31.78	0.531	2.33	3.31	2.04
"	"	"	12.	"	"	18	70	25.16	0.626	1.97	3.31	2.01
"	"	"	14.	"	"	16	69	26.60	0.625	2.36	3.72	1.99
"	"	"	18.	"	"	14	67	24.27	0.679	1.73	3.25	2.01
"	"	"	22.	"	"	13	64	23.73	0.709	0.57	1.62	2.02
"	"	"	28.	"	"	13	64	17.53	0.806	1.97	6.01	1.94

Fluid	P/kPa	b/mm	U_V/(m/s)	i	j	ΔT_{min}	ΔT_{max}	Ax10^{-3}	n	e(ΔT)/K	e(q),%	$\varepsilon_{\Delta T}$
Steam	100	0.0*	0.8	2	24	17	63	39.97	0.621	0.40	0.71	-
"	"	"	1.0	"	"	17	62	38.31	0.638	0.73	1.15	-
"	"	"	1.2	"	"	17	61	37.08	0.657	0.62	1.13	-
"	"	0.5	0.8	"	"	7	48	99.36	0.602	0.82	2.07	2.48
"	"	"	1.0	"	"	6	44	87.93	0.642	0.78	2.18	2.49
"	"	"	1.2	"	"	6	45	74.75	0.692	0.90	2.93	2.36
"	"	1.0	0.8	"	"	7	37	90.53	0.703	0.82	3.37	3.19
"	"	"	1.0	"	"	7	37	77.45	0.757	0.69	2.60	3.20
"	"	"	1.2	"	"	7	37	75.62	0.765	0.57	2.29	3.04
"	"	1.5	0.8	"	"	6	36	85.92	0.737	0.90	2.71	3.36
"	"	"	1.0	"	"	6	36	76.52	0.766	0.61	2.18	3.36
"	"	"	1.2	"	"	6	35	73.43	0.794	0.66	2.28	3.22
"	14	0.0*	2.6	"	"	6	23	25.78	0.711	0.56	2.89	-
"	"	"	4.0	"	"	6	22	25.06	0.748	0.62	3.29	-
"	"	"	5.5	"	"	6	22	23.49	0.801	0.47	2.78	-
"	"	"	6.7	"	"	5	22	23.74	0.816	0.44	2.80	-
"	"	"	8.4	"	"	5	21	25.23	0.824	0.65	4.85	-
"	"	0.5	2.6	"	"	2	15	44.42	0.793	0.47	4.51	2.11
"	"	"	4.0	"	"	2	15	45.80	0.797	0.42	4.74	2.04
"	"	"	5.5	"	"	2	15	42.13	0.857	0.41	5.76	1.97
"	"	"	6.7	"	"	2	14	44.41	0.853	0.46	5.09	1.96
"	"	"	8.4	"	"	2	14	48.05	0.837	0.42	5.79	1.89
"	"	1.0	2.6	"	"	2	13	53.54	0.816	0.20	2.71	2.65
"	"	"	4.0	"	"	2	13	53.37	0.837	0.22	2.95	2.55
"	"	"	5.5	"	"	2	12	50.97	0.862	0.12	2.54	2.38
"	"	"	6.7	"	"	2	12	49.64	0.887	0.15	2.56	2.31
"	"	"	8.4	"	"	2	12	48.41	0.909	0.16	2.41	2.17
"	"	1.5	2.6	"	"	2	11	43.14	0.970	0.35	6.50	2.87
"	"	"	4.0	"	"	2	11	48.20	0.927	0.14	2.72	2.74
"	"	"	5.5	"	"	2	11	45.86	0.957	0.13	1.94	2.56
"	"	"	6.7	"	"	2	11	46.88	0.954	0.13	2.07	2.46
"	"	"	8.4	"	"	2	10	47.63	0.951	0.12	2.06	2.29

* Indicates plain tube

Table 2 Summary of experimental results for smaller diameter tubes; $d = 12.7$ mm, $t = 0.5$ mm, $h = 1.6$ mm (see Eq. (3))

Fluid	P/kPa	b/mm	U_V/(m/s)	i	j	ΔT_{min}	ΔT_{max}	Ax10^{-3}	n	e(ΔT)/K	e(q),%	$\varepsilon_{\Delta T}$
R-113	100	0.0*	0.28	4	60	11	24	1.75	0.926	0.67	3.14	-
"	"	0.5	"	"	58	2	16	21.03	0.735	0.24	2.48	6.80
"	"	1.0	"	"	58	2	18	20.76	0.657	0.36	2.35	5.47
"	"	1.5	"	"	58	2	18	17.44	0.706	0.38	3.00	5.22
Glycol	"	0.0*	0.42	"	43	122	152	28.52	0.468	1.51	1.15	-
"	"	0.5	"	"	41	58	110	146.04	0.444	0.65	1.26	4.48
"	"	1.0	"	"	41	60	120	71.60	0.613	1.18	1.13	4.77
"	"	1.5	"	"	41	80	126	65.37	0.600	1.99	1.73	4.17
Steam	"	0.0*	0.72	"	54	27	55	31.53	0.705	0.69	1.67	-
"	"	0.5	"	"	52	13	35	63.95	0.772	0.53	2.76	2.47
"	"	1.0	"	"	54	13	37	45.81	0.877	0.59	2.43	2.49
"	"	1.5	"	"	54	13	32	52.82	0.898	0.65	3.32	3.01

* Indicates plain tube

hancement ratios are higher for R-113 and lower for steam than the present values.

In Fig. 5 comparisons are made with the data of Wanniarachchi et al. (1986) for steam, and Marto et al. (1990) for R-113, for which the fin and tube dimensions, and the vapor

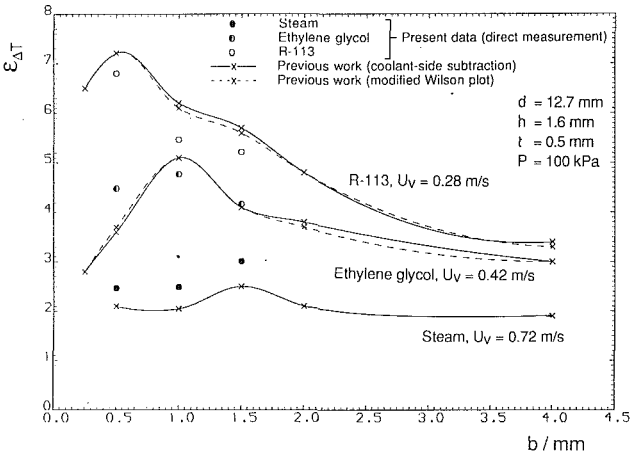

Fig. 4 Comparison of present data with those of Yau et al. (1985, steam), Masuda and Rose (1986, ethylene glycol), and Masuda and Rose (1985, R-113)

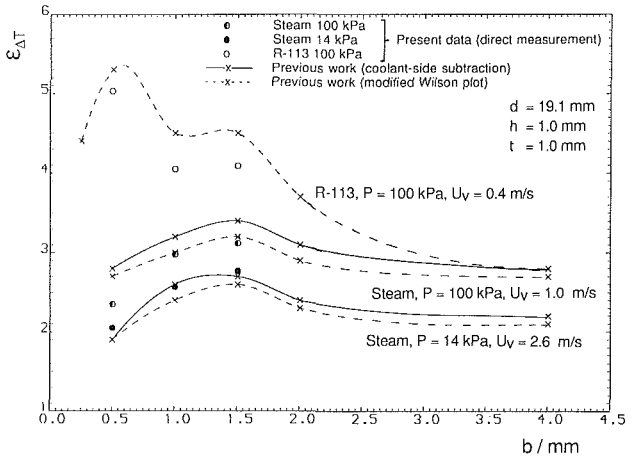

Fig. 5 Comparison of present data with those of Wanniarachchi et al. (1986, steam) and Marto et al. (1988, R-113)

velocities, were the same as those for the present larger diameter tubes. Wanniarachchi et al. (1986) obtained vapor-side results by subtracting wall and predetermined coolant-side resistances, and by modified Wilson plot, as indicated, while Marto et al. (1988) used a modified Wilson plot. Again, the indirectly obtained enhancement ratios for R-113 are higher than the present values.

It should be noted that discrepancies in enhancement ratios between the present and earlier data may be due to errors in both the finned and plain tube data. This is illustrated in Fig. 6, where the present data for steam condensing on one of the smaller diameter finned tubes (fin spacing 1.5 mm) and the smaller diameter plain tube are compared with the earlier data of Yau et al. (1985) on a heat flux-temperature difference basis. In Fig. 6, the earlier data for the finned tube fall slightly below the present data, while for the plain tube they fall slightly above. These small discrepancies combine to give larger differences in the calculated ratio shown in Fig. 4.

The generally good agreement seen in Figs. 4, 5, and 6, between the earlier indirectly obtained data and those obtained in the present investigation, demonstrates that satisfactory vapor-side results can be obtained by indirect methods. Attention is drawn, however, to the great care taken in these earlier investigations to obtain very high accuracy in the overall data measurements.

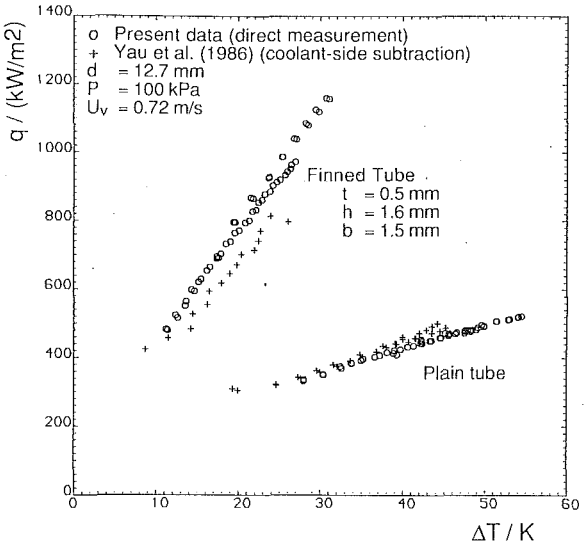

Fig. 6 Dependence of heat flux on vapor-side temperature difference for present and earlier investigations

5 Comparison With Theory

In Figs. 7 and 8, the present data are compared to the simple model of Beatty and Katz (1948), and with calculations carried out by Honda (1991), using the more complex model of Honda et al. (1987). The model of Beatty and Katz (1948) does not take account of the detrimental effect of surface tension, i.e., condensate "flooding" or "holdup" on the lower part of the tube, or the enhancing effect of surface tension on the unflooded part of the tube. With the smaller diameter tubes, and with relatively high surface tension fluids such as steam and ethylene glycol (Figs. 7*a* and 7*b*), the effect of flooding is significant, and the experimental data fall well below the theory of Beatty and Katz. For low surface tension R-113 condensing on both size tubes (Figs. 7*c* and 8*d*), the effect of flooding is small, and the Beatty and Katz model is conservative for all but one of the tubes tested in the present investigation. (The near-perfect agreement seen in Fig. 7*c* for $b = 0.5$ mm is fortuitous.) For the case of steam and ethylene glycol condensing on the larger diameter tubes (Figs. 8*a*, *b*, and *c*), the beneficial and detrimental effects of surface tension approximately cancel out, and the Beatty and Katz model gives fairly good agreement with the experimental data. However, it should be noted that the model predicts the performance of a finned tube increases continuously as fin density increases, whereas the present data for steam and ethylene glycol show maximum enhancement ratios for fin spacings of 1.5 and 1.0 mm, respectively.

The model of Honda et al. (1987) includes both condensate flooding and the enhancing effect of surface tension drainage on the unflooded part of the tube. Consequently it gives generally better agreement with the experimental data. For steam and R-113 the Honda et al. model also predicts the correct dependence of the heat flux-temperature difference relationship on fin density. For ethylene glycol, however, the theory gives the best performing tubes to be those with a fin spacing of 0.5 mm, while the experimental data show an optimum spacing of 1.0 mm.

6 Conclusion

The present results are intended to serve as an accurate data base for use in the development and improvement of theoretical models. Moreover, since it is not feasible to manufacture instrumented tubes of the type used in the present work for all cases for which data may be required, the results presented in this paper may also be of value for assessing experimental methods, for example where vapor-side results are inferred

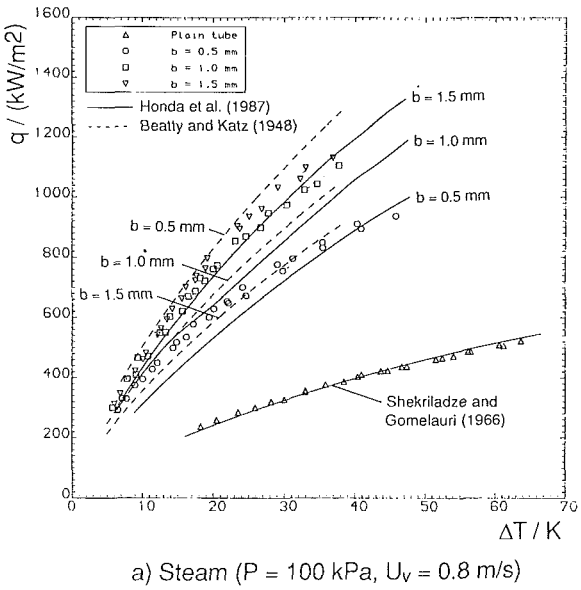

a) Steam (P = 100 kPa, U_V = 0.8 m/s)

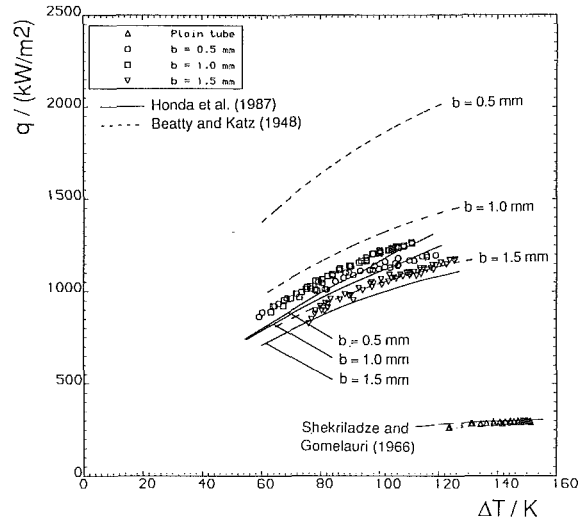

b) Ethylene Glycol (P = 100 kPa, U_V = 0.42 m/s)

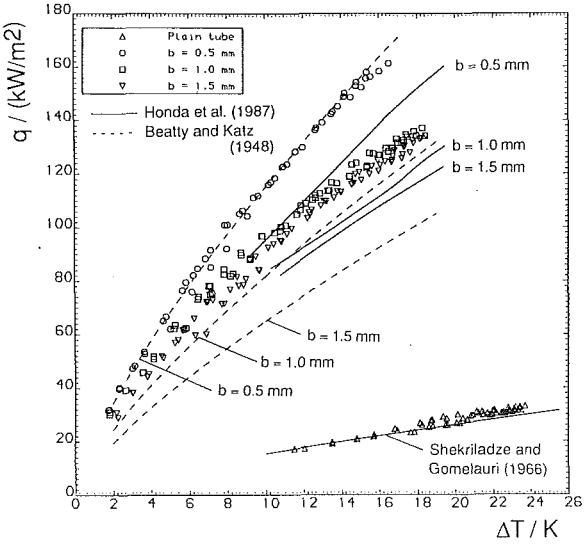

c) R-113 (P = 100 kPa, U_V = 0.28 m/s)

Fig. 7 Comparison of experimental data for smaller diameter tubes with theory ($d = 12.7$ mm, $t = 0.5$ mm, $h = 1.6$ mm)

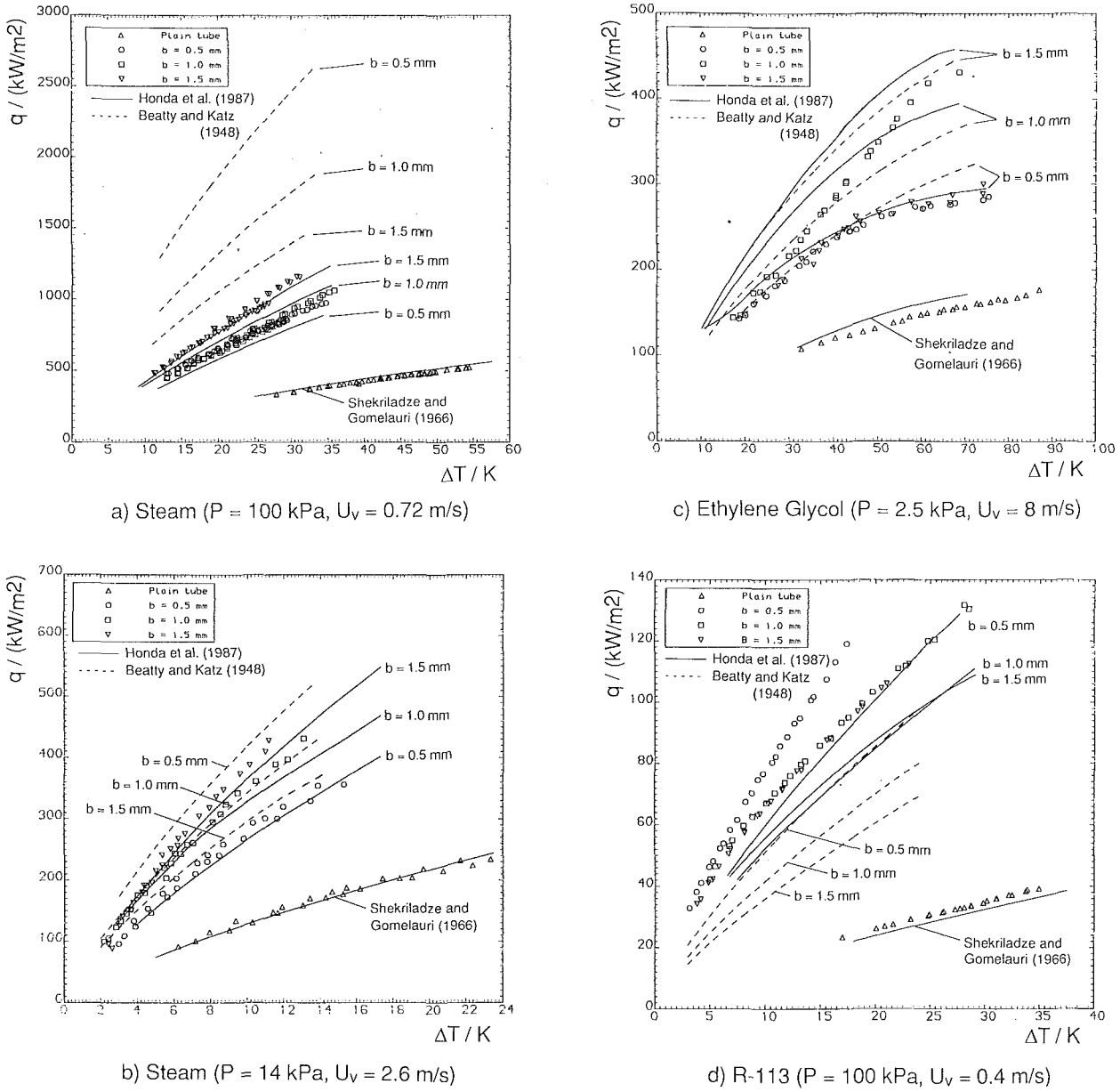

Fig. 8 Comparison of experimental data for larger diameter tubes with theory ($d = 19.1$ mm, $t = 1.0$ mm, $h = 1.0$ mm)

from overall heat transfer data. Comparisons with earlier work, where the same tube and fin geometry and test fluids have been used, show that indirect methods can give satisfactory results when extreme care is taken in the determination of heat flux and overall temperature difference. If such indirect methods are employed in future investigations, tests with one of the fluids and at least one finned tube, with geometry the same as in the present investigation, would serve to assess the reliability of the method.

Detailed comparisons with theory have shown the simple model of Beatty and Katz (1948) to be inadequate, although in some cases, where the beneficial and detrimental effects of surface tension cancel out, it can give fortuitously good results. The model of Honda et al. (1987) gave better overall agreement with the present experimental results.

Acknowledgments

The authors thank Professor H. Honda for providing the numerical results of his theoretical model.

References

Adamek, T., and Webb, R. L. 1990, Prediction of Film Condensation on Horizontal Integral Fin Tubes," *Int. J. Heat Mass Transfer*, Vol. 33, pp. 1721–1735.

Beatty, K. O., and Katz, D. L., 1948, "Condensation of Vapors on Outside of Finned Tubes," *Chem. Eng. Prog.*, Vol. 44, pp. 55–70.

Honda, H., Nozu, S., and Mitsumori, K., 1983, "Augmentation of Condensation on Horizontal Finned Tubes by Attaching a Porous Drainage Plate," *Proc. ASME-JSME Thermal Eng. Joint Conf.*, Vol. 3, pp. 289–296.

Honda, H., Nozu, S., and Uchima, B., 1987, "A Generalized Prediction Method for Heat Transfer During Film Condensation on a Horizontal Low-Finned Tube," *Proc. 2nd ASME-JSME Thermal Eng. Joint Conf.*, Vol. 4, pp. 385–392.

Honda, H., 1991, Private Communication.

Lee, W. C., Rahbar, S., and Rose, J. W., 1984, "Film Condensation of Refrigerant-113 and Ethanediol on a Horizontal Tube—Effect of Vapor Velocity," ASME JOURNAL HEAT TRANSFER, Vol. 106, pp. 524–530.

Marto, P. J., Zebrowski, D., Wanniarachchi, A. S., and Rose, J. W., 1988, "Film Condensation of R-113 on Horizontal Finned Tubes," *Fundamentals of Phase Change: Boiling and Condensation*, Proc. ASME Nat. Heat Transf. Conf., Vol. 2, pp. 583–592.

Masuda, H., and Rose, J. W., 1985, "An Experimental Study of Condensation

of Refrigerant-113 on Low Integral-Fin Tubes," *Proc. Int. Symp. on Heat Transfer*, Beijing, China, Vol. 2, Paper No. 32.

Masuda, H., and Rose, J. W., 1988, "Condensation of Ethylene Glycol on Horizontal Integral-Fin Tubes," ASME JOURNAL OF HEAT TRANSFER, Vol. 110, pp. 1019–1020.

Memory, S. B., and Rose, J. W., 1986, "Film Condensation of Ethylene Glycol on a Horizontal Tube at High Vapour Velocity," *8th Int. Heat Transf. Conf.*, Vol. 4, pp. 1607–1612.

Nusselt, W., 1916, "Die Oberflachenkondensation des Wasserdampfes," *Z. Vereines Deutsch, Ing.*, Vol. 60, pp. 541–546, 569–575.

Rose, J. W., 1984, "Effect of Pressure Gradient in Forced-Convection Film Condensation on a Horizontal Tube.," *Int. J. Heat Mass Transfer*, Vol. 27, pp. 39–47.

Shekriladze, I. G., and Gomelauri, V. I., 1966, "Theoretical Study of Laminar Film Condensation of Flowing Vapour," *Int. J. Heat Mass Transfer*, Vol. 9, pp. 581–591.

Sukhatme, S. P., Jagadish, B. S., and Prabhakaran, P., 1990, "Film Condensation of R-11 Vapor on Single Horizontal Enhanced Condenser Tubes," ASME JOURNAL OF HEAT TRANSFER, Vol. 112, pp. 229–234.

Wanniarachchi, A. S., Marto, P. J., and Rose, J. W., 1986, "Film Condensation of Steam on Horizontal Finned Tubes: Effect of Fin Spacing," ASME JOURNAL OF HEAT TRANSFER, Vol. 108, pp. 960–966.

Webb, R. L., Rudy, T. M., and Kedzierski, M. A., 1985, "Prediction of the Condensation Coefficient on Horizontal Integral-Fin Tubes," ASME JOURNAL OF HEAT TRANSFER, Vol. 107, pp. 369–376.

Yau, K. K., Cooper, J. R., and Rose, J. W., 1985, "Effect of Fin Spacing on the Performance of Horizontal Integral-Fin Condenser Tubes," ASME JOURNAL OF HEAT TRANSFER, Vol. 107, pp. 377–383.

An Experimental Study of Heat and Mass Transfer During Drying of Packed Beds

W. C. Lee

O. A. Plumb

L. Gong

Department of Mechanical and Materials Engineering, Washington State University, Pullman, WA 99164-2920

An experimental study has been conducted to provide a data base for drying packed beds of granular, nonhygroscopic materials. Experimental results for drying rate, saturation distribution, temperature distribution, and surface saturation are reported for drying glass beads under carefully documented drying conditions. Capillary pressure for both imbibition and drainage was measured for the glass beads, whose size ranged from 65 μm to 450 μm. The drying results demonstrate that, contrary to available model predictions, porous materials do not necessarily exhibit saturation gradients that always increase with distance from the drying surface. Under certain conditions the capillary potential is sufficient to create an internal drying front. The measurements of surface saturation are the first to be reported. They are utilized to speculate on the reasons for the failure of drying models to compare well with experiment without adjusting the convective heat or mass transfer coefficients.

Introduction

In the heat transfer literature there exists a large body of work on drying of porous materials. This work is for the most part theoretical or analytical. Models for the coupled transport phenomena that occur during various drying scenarios and numerical and analytical solutions for a variety of geometries, materials, and drying conditions are presented. The majority of these models are based on the work of Luikov (1966) and Whitaker (1977). Despite the significant theoretical attention to the problem, and the numerous natural and industrial applications, very few experimental data having sufficient detail to validate the theoretical models are available. This is particularly true for situations where the drying is initiated at near-saturated conditions.

The experimental data most frequently referenced are those of Ceaglske and Hougen (1937). These data have several shortcomings in terms of their utility in validating physical models for the drying process. First, only a very limited number of local saturation measurements were made during drying. These measurements were made by sectioning partially dried columns. Thus, the uncertainty in these measurements might be quite high. The necessary capillary pressure versus saturation data are also very minimal. Second, the drying air velocities are not reported, making it difficult for the modeler to estimate appropriate convective heat and mass transfer rates. Third, simultaneous measurement of temperature distributions, saturation distributions, etc., were not made in the Ceaglske and Hougen experiments.

Whitaker (1980, 1984) and Whitaker and Chow (1983) have attempted to make comparisons between model calculations and the Ceaglske and Hougen experiments and in doing so have pointed out some of the above shortcomings. Good agreement between measured saturation profiles and calculated results was achieved when the relative permeability and the capillary pressure were treated as adjustable functions. Both Plumb et al. (1985) and Whitaker (1984) have raised questions with regard to the appropriate heat and mass transfer coefficients for use in models for convective drying. Whitaker (1984) had to adjust the heat transfer coefficient in order to obtain good agreement between his model and the Ceaglske and Hougen results and Plumb et al. (1985) had to adjust the mass transfer coefficient to get agreement with drying data for wood. This points out the need for experimental results for temperature and saturation or moisture content at the surface.

The experimental results to be presented in this paper were undertaken with the objective of providing better experimental data for use in validating models for the drying process involving nonhygroscopic porous material. This work focuses on the high moisture content region where capillary transport plays the dominant role.

Experimental results are reported for three sizes of glass beads spanning the range from 65 μm to 450 μm. Measurements of local saturation, local temperature, and drying rate are reported along with the parameters related to the drying environment. These include air velocity, relative humidity, and temperature. In addition, the capillary pressure versus saturation functions were measured for both imbibition and drainage. The surface saturation was also measured in order to provide some insight on the convection mass transfer coefficient.

In what follows a brief summary of the theoretical background will be presented. This is followed by a detailed description of the experimental apparatus and procedures. The resulting measurements are then presented and discussed.

Theoretical Background

Whitaker (1980) has demonstrated that for low-intensity drying conditions the early stages of drying can be modeled as isothermal. Under these conditions the liquid transport is due to capillary action and the governing transport equation can be written in terms of the saturation:

$$\phi \frac{\partial S}{\partial t} = -\frac{\partial}{\partial x}\left[\frac{KK_{rl}}{\mu_l}\left(\frac{\partial p_c}{\partial S}\frac{\partial S}{\partial x} - \rho_l g\right)\right] \tag{1}$$

The appropriate boundary conditions would be a convective boundary condition for mass transfer at the surface and a no-flux condition at the bottom, depending on the drying geometry.

Knowledge of two transport properties is essential in order to solve Eq. (1). Both are strongly dependent on the liquid saturation. These are the relative permeability, K_{rl}, and the capillary pressure function, $\partial p_c/\partial S$. The liquid phase relative

Contributed by the Heat Transfer Division and presented at the 3rd ASME/JSME Joint Thermal Engineering Conference, Reno, Nevada, March 1991. Manuscript received by the Heat Transfer Division November 1990; revision received January 1992. Keywords: Geophysical Heat Transfer, Packed and Fluidized Beds, Porous Media.

permeability has traditionally been represented as a cubic function of the normalized saturation:

$$K_{rl} = S_e^3 \tag{2}$$

where

$$S_e = \frac{S - S_{ir}}{1 - S_{ir}} \tag{3}$$

In Eq. (3) S_{ir} is the irreducible saturation, defined as the saturation below which the liquid phase is no longer continuous and hence immobile. Equation (2) has been well documented experimentally, at least for granular materials consisting of particles of uniform size (Verma et al. 1985). Other models for the liquid phase relative permeability can be found from Brooks and Corey (1968), Mualem (1976), and van Genuchten (1980). The models of both Mualem and van Genuchten agree well with Eq. (2). Relative permeability was not pursued in detail in this study since functions very similar to Eq. (2) are well supported by experimental results.

An excellent summary of the available predictive tools for both relative permeability and capillary pressure can be found from Luckner et al. (1989). For granular materials of relatively uniform particle size, capillary pressure curves can be well represented empirically by expressions of the form

$$S_e = \left[\frac{1}{1 + (\alpha h)^n}\right]^m, \quad m = 1 - 1/n \tag{4}$$

where α and n are constants to be determined experimentally and S_e is given by Eq. (3) for drainage and $S_e = S$ for imbibition. In Eq. (4) the capillary pressure is expressed in terms of the hydrostatic head, $h = p_c/\rho_l g$. If experimental results are to be useful, the empirical constants α and n that appear in Eq. (4) as well as the irreducible saturation must be presented for the material in question. As will become apparent later, these constants must be determined for both imbibition and drainage because of hysteresis in the capillary pressure curve.

Equation (4) does not include a mechanism to account for variations in surface tension that result from changes in temperature during drying. This is generally done in the heat transfer and petroleum reservoir engineering literature using the functional relationship proposed by Leverett (1941):

$$p_c = \frac{\sigma f(S_e)}{\sqrt{K/\phi}} \tag{5}$$

It is of great importance to the modeling effort to determine whether Eq. (5) can be used for a broad range of materials and the resulting sacrifice in accuracy since hysteresis is not taken into account.

Experimental Apparatus and Procedures

The results to be reported involve convective drying of packed beds of 65 μm, 120 μm, and 450 μm glass beads. The uniformity and sphericity of the glass beads are reported in Table 1. Capillary pressure versus saturation was measured by wetting or draining a column of glass beads until hydrostatic equilibrium was reached. For imbibition or wetting a column of dry glass beads was exposed at its lower end to a pool of distilled water, which was maintained at a constant level. The top of the column was covered with a plate containing a pinhole, which allowed atmospheric pressure to be maintained above the column but prevented excessive evaporation. After achieving equilibrium, the columns were then allowed to drain by gravity to obtain the drainage curve. The local saturation as function of height was then measured using gamma attenuation.

Table 1 Properties of glass beads used in drying experiments

	450 μm	120 μm	65 μm
Density, g/cm^3	2.5	2.5	2.5
Size range—min	295	104	43
max	589	149	100
Sphericity, percent	>85	80–85	>85

Details of the design of the gamma attenuation system, which was used to make saturation measurements both for the capillary pressure curves and for the drying experiments, can be found from Spolek and Plumb (1981) and Plumb et al. (1984). A cylindrical 570 mCi Am-241 gamma source is collimated by placing it in brass shielding behind a slit. The slit is 2.8 cm wide and 0.5 mm high. Thus, local saturation measurements are averaged values over a slice of the material approximately 0.5 mm thick. The attenuated gamma energy emerging from the test sample is detected using an NaTl scintillation crystal integrally mounted to a photomultiplier tube. The detector is also shielded with a brass plate having a slit 0.5 mm high and 3.8 cm wide. This slit is aligned with the slit at the source and serves to minimize background radiation. The entire source/detector assembly is mounted on a traverse mechanism having a minimum vertical step of 0.44 mm.

Making saturation measurements using this system requires the measurement of the amount of attenuation that results due to the container, measurement of the amount of attenuation that results due to dry glass beads, and measurement of the mass attenuation coefficient for water. The uncertainty in the saturation measurements is estimated to be less than 5 percent at 90 percent saturation and 36 percent at 9 percent saturation. At an intermediate saturation of 30 percent it is approximately 12 percent. Fortunately, we are interested primarily in saturation above the irreducible saturation, which is between 10 and 15 percent.

Surface saturation measurements were made utilizing near-infrared reflectance (NIR). The NIR system assembled for this study utilizes the adsorption band for water, which is centered on 1.94 μm. Infrared light is produced by a 250 W quartz-halogen lamp with a tungsten filament. Light from the lamp is collimated by a 3.81-cm-dia, 35 mm focal length pyrex condensing lens. This produced a beam normal to a turret in which 1.9 μm and 1.7 μm narrow band filters are mounted. The 1.9

Nomenclature

D = particle diameter
f = capillary pressure saturation function defined in Eq. (5)
g = acceleration of gravity
h_{fg} = latent heat for evaporation
K = permeability
K_{rl} = liquid phase relative permeability
L = bed depth
m, n = empirical constants defined in Eq. (4)
Nu = Nusselt number
p_c = capillary pressure
p_o = reference pressure defined in Eq. (9)
p_v = vapor pressure
R = gas constant
Re = Reynolds number
S = saturation
S_e = normalized saturation defined in Eq. (3)
S_{ir} = irreducible saturation
T = temperature
T_o = reference temperature defined in Eq. (9)
x = Cartesian coordinate
α = empirical constant defined in Eq. (4)
κ = empirical constant defined in Eq. (6)
μ_l = liquid viscosity
ρ_l = liquid density
σ = surface tension
ϕ = porosity

Table 2 Calibration constants for the NIR surface saturation measurements

	$\kappa_{1.9}$	$\kappa_{1.7}$	C
65 μm	0.11410	2.0594	0.60086
120 μm	−0.23190	2.4748	0.78400
450 μm	0.00335	1.1096	0.09174

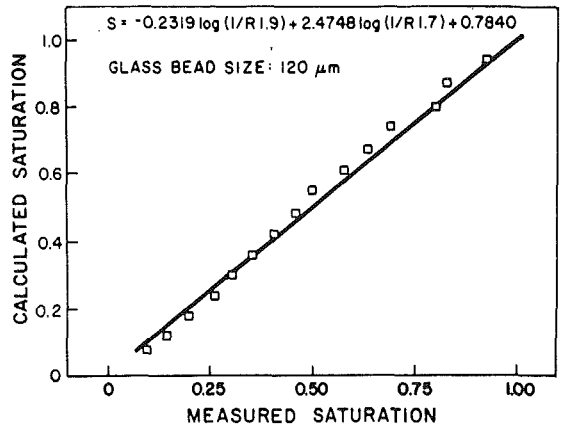

Fig. 1 Calibration curve for NIR surface saturation measurements for 120 μm glass beads

μm filter is near the center of a strong absorption band for water, whereas the 1.7 μm filter is in a much weaker absorption band. The basic operating principle is that the radiative properties of the glass beads will not vary significantly over this small difference in wave length. However, both are strongly dependent on the presence of water at the surface. A 90 deg light tube with a 50 mm focal length planoconvex lens was used to focus the filtered light on the sample surface. This resulted in a measuring area on the sample surface that was approximately 0.5 cm in diameter, thus providing the capability to make a local surface saturation measurement. The incident beam was directed normal to the surface. The reflected beam that was sensed by the detector was at 10 deg from the normal. The reflected light from the sample was sensed using a lead sulfide detector with a thermoelectric cooler to maintain constant temperature. In order to reduce background radiation and other noise, a chopper was placed between the filters and the condensing lens assembly.

The NIR system was calibrated by making measurements on packed beds of the glass beads used in the experiments. These beds were 3 mm thick to insure as closely as possible that they were of uniform saturation. The saturation level of these beds was established by weight. Distilled water was used in all the experimental measurements to be discussed. The calibration was completed using multiple linear regression analysis as suggested by Wetzel (1983) to fit the results with an expression of the form

$$S = \kappa_{1.9} \log \frac{1}{V_{1.9}} + \kappa_{1.7} \log \frac{1}{V_{1.7}} + C \tag{6}$$

The calibration constants for the three sizes of glass beads studied are listed in Table 2. Figure 1 presents the actual calibration data for the 120 μm beads. This figure is included to provide a quantitative picture of the uncertainty associated with this measurement.

The total weight loss as a function of time or drying rate was measured using an electronic balance. The uncertainty in this measurement was estimated to be 2.5 percent. Weight loss measurements will be compared with integrations of the local saturation measurements in the results section in order to provide further evidence of the performance of these two measurement systems.

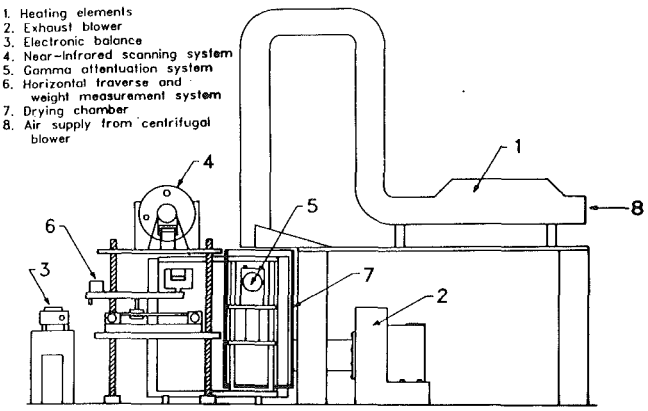

Fig. 2 Schematic of the experimental facility

Because of the desire to eliminate aerodynamic drag on the sample during weighing and because the optics for the NIR system would interfere with the air flow, it was necessary to remove the sample physically from the drying air stream for surface saturation measurements and weighing. To accomplish this, a traverse system designed around a print head career and drive mechanism was fabricated. This allowed both measurements to be made while removing the sample from the drying air stream for less than one minute. The uncertainty associated with this procedure is difficult to estimate. This measurement was typically made every ten minutes; thus, the sample was removed from the forced air drying environment for less than 10 percent of the total drying time, leading to the conclusion that the associated uncertainty is less than 10 percent.

The temperature distribution in the packed bed was measured using embedded thermocouples. The uncertainty in these measurements is estimated to be approximately ± 0.5°C. Since the drying is intended to be one-dimensional, care was taken to design a container for the packed bed that had minimal heat losses or gains. The container was constructed from plexiglass with a double wall to provide a 1 cm air gap on all four vertical sides. In addition, the bottom and the sides parallel to the gamma beam were insulated with 4 cm of rigid foam insulation. This insulation could not be placed on the sides normal to the gamma beam because of limited space between the source and detector. The heat transfer to the packed bed from sides and bottom was calculated to be a maximum of 5 percent of the total heat transfer at the drying surface for the entire drying period.

Since an extensive amount of data was to be acquired over a long period of time, the entire experiment was computer controlled and the data acquisition automated. Hence, once initiated the experiment could run unattended if desired. A schematic of the complete drying system is shown in Fig. 2.

Discussion of Results

The results for the capillary pressure measurements are shown in Figs. 3–5. Results are presented as head in cm versus the normalized saturation, S_e. The solid and dashed lines on the figures are the result of curve fits of the form given by Eq. (4). The constants for the curve fits are presented in Table 3. The general shape of the capillary pressure-saturation curves is typical. However, it is quite clear that the empirical constants in Eq. (4) are not universal. This is somewhat discouraging since it implies that capillary pressure measurements must be made for every material of interest.

In an attempt to develop a universal capillary pressure versus saturation function, the Leverett function given by Eq. (5) was tested. The Leverett equation scales the capillary pressure for

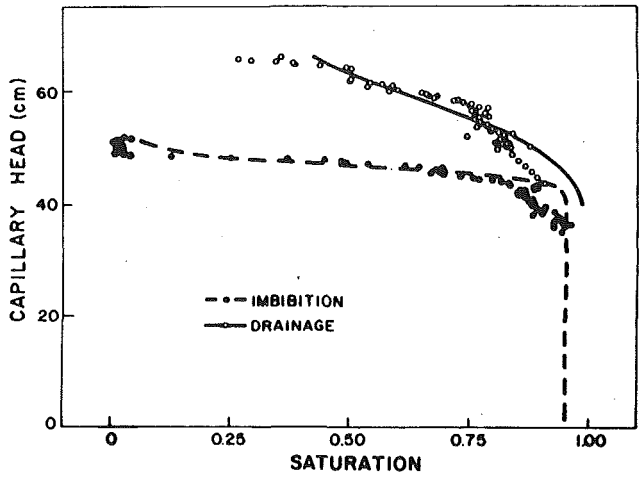

Fig. 3 Capillary pressure curves for 65 μm beads

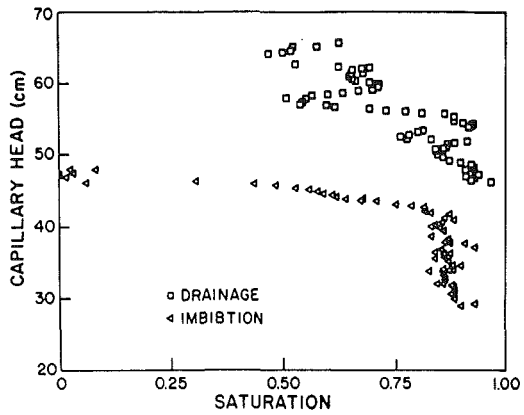

Fig. 4 Capillary pressure curves for 120 μm beads

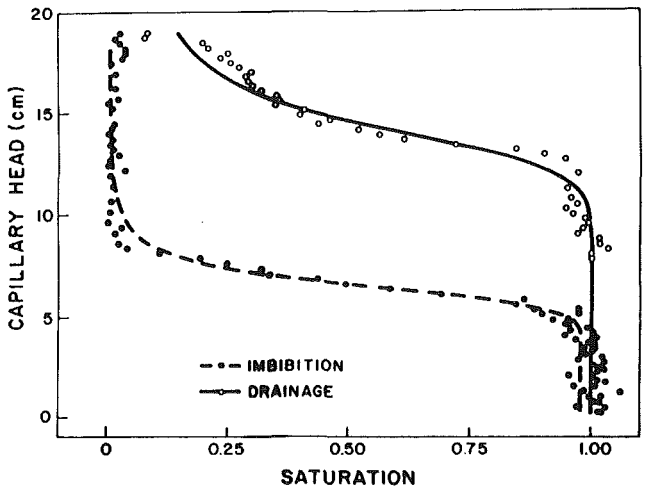

Fig. 5 Capillary pressure curves for 450 μm beads

particle size using the square root of the permeability, which is proportional to the square of particle diameter. In this case the saturated permeability was determined using the Blake–Kozeny equation, which is commonly used in modeling studies and has been verified experimentally (Ergun, 1952; Crawford and Plumb, 1986):

$$K = \frac{\phi^3 D^2}{150(1-\phi)^2} \tag{7}$$

Table 3 Constants determined by fitting Eq. (4) to the experimental results

	α	n	S_{ir}
65 μm imbibition	0.02191	50.39	—
65 μm drainage	0.01776	10.02	0.10
120 μm imbibition	0.02289	50.92	—
120 μm drainage	0.01734	8.162	0.10
450 μm imbibition	0.1656	14.34	—
450 μm drainage	0.07324	14.95	0.10

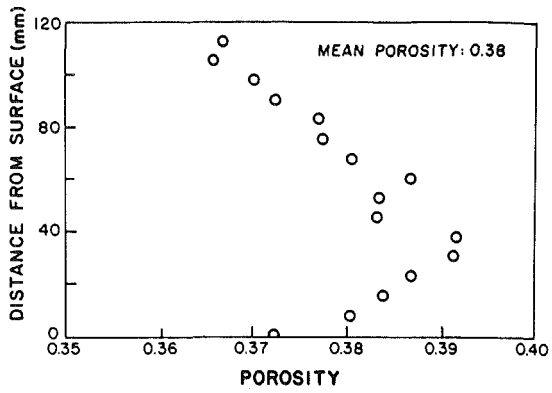

Fig. 6 Measured variation in porosity in a packed bed of 450 μm glass beads

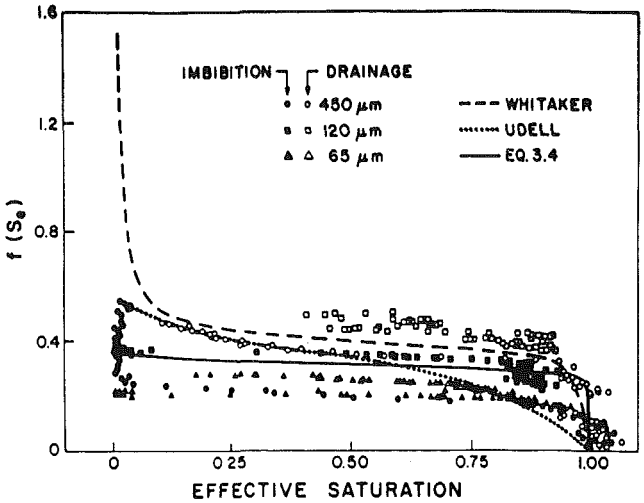

Fig. 7 Comparison of the experimental results for three sizes of glass beads with Eq. (5)

In Eq. (7) D is the mean particle diameter. The porosities of all of the packed beds were measured and varied from 0.35 to 0.38. An example of the variation in porosity measured using gamma attenuation for a typical bed is shown in Fig. 6. Figure 7 shows the experimental data for drainage and imbibition for the three sizes of glass beads compared to Eq. (5). In this case $f(S_e)$ has been fit to the functional form as given by Eq. (4), resulting in $\alpha = 3.25$, $n = 24$, and $S_{ir} = 0.10$. Hysteresis is accounted for only through the different definitions of S_e for drainage and imbibition. The imbibition function proposed by Udell (1985) and subsequently used in several other modeling studies is also shown on the figure. The conclusion is that this is not the best fit at least for the type of materials studied here even though it is a fit to some of the original data due to Leverett. Also shown on the figure is the function used by Whitaker (1980) in his modeling studies. This function originated from a fit to Ceaglske and Hougen's data. It appears to be a fairly good representation of the experimental data developed in this study.

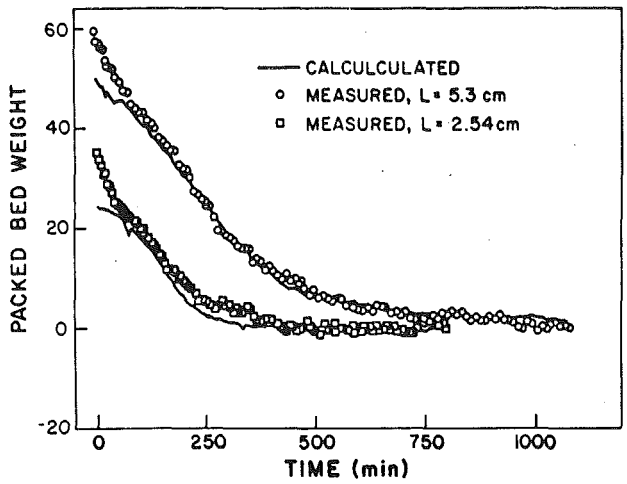

Fig. 8 Weight loss as a function of time for 65 μm beads from direct measurement and integration of saturation profiles

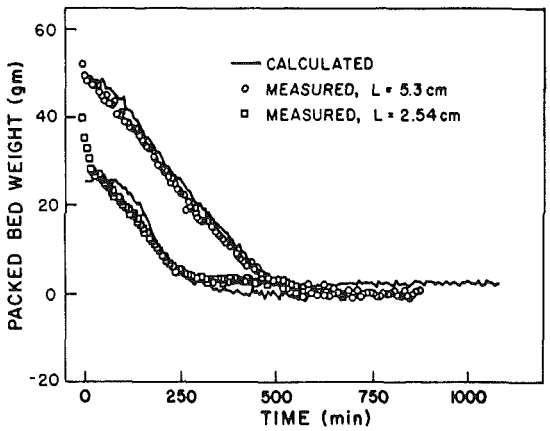

Fig. 9 Weight loss as a function of time for 450 μm beads from direct measurement and integration of saturation profiles

As indicated earlier, the cubic relationship between liquid phase relative permeability is fairly well accepted; thus, no attempts were made to make a direct measurement. Mualem (1976) has developed a method for estimating relative permeability from measurement of the capillary pressure curve. This relationship was simplified by van Genuchten (1980) to yield the following relationship in terms of the empirical constants defined in Eq. (4):

$$K_{rl} = S_e^{1/2}[1-(1-S_e^{1/m})^m]^2 \quad (8)$$

Equation (8) with constants from our data compares well with the cubic relation expressed in Eq. (2).

Weight loss for the 65 μm and 450 μm glass beads and for beds 2.54 cm and 5.3 cm deep is shown in Figs. 8 and 9. In these figures a comparison is made between the direct measurement of weight loss and the weight loss calculated by integrating the saturation profiles measured using gamma attenuation. The two methods of determining weight loss compare well and support our confidence in the reliability of both measurement systems. For all cases the drying air velocity is 4.8–4.9 m/s and the temperature 63–65°C. The dew point for the drying air varied from −1°C to 7°C and the porosity of the beds ranged from 0.35 to 0.37. Table 4 gives the details of the experimental conditions for all of the results presented. The drying rates during the constant drying rate period for all three sizes of glass beads are tabulated in Table 5. A typical drying rate curve for the 120 μm beads is shown in Fig. 10. Under the conditions studied a constant drying rate resulted

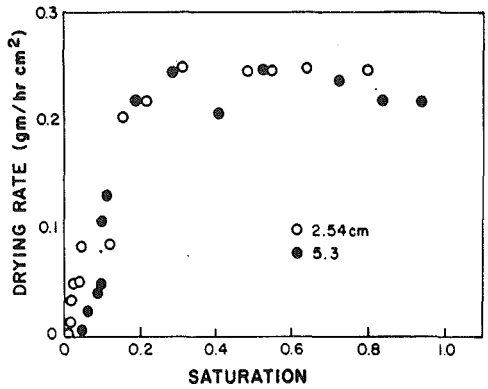

Fig. 10 Drying rate versus saturation for 120 μm beads (experiments No. 3 and 4)

Table 4 Drying conditions for the results presented

Exp No.	Bead size	Bed depth, cm	Porosity	Air velocity, m/s	Air temperature, °C	Dew point, °C
1	65 μm	2.54	0.375	4.8	63	7.0
2	65 μm	5.30	0.370	4.8	63	6.0
3	120 μm	2.54	0.355	4.9	65	−1.5
4	120 μm	5.30	0.370	4.9	65	−1.0
5	450 μm	2.54	0.346	4.8	65	5.0
6	450 μm	5.30	0.363	4.9	65	0.0

Table 5 Drying rates during the constant rate period (air velocity 4.8–4.9 m/s)

Bead Size	Drying rate, g/h cm²	
	2.54 cm bed	5.3 cm bed
65 μm	0.29	0.29
120 μm	0.25	0.22
450 μm	0.24	0.25

for all three sizes of glass beads down to a saturation of approximately 0.2 at which point the falling rate regime began. This is the point at which the saturation is approaching the irreducible saturation and capillary transport is no longer the dominant liquid transport mechanism. Throughout the constant rate period the drying process is externally limited by the transport in the boundary layer at the surface. As can be seen in the table, the 65 μm beads actually displayed a slightly higher drying rate than the larger beads. This is contrary to the data of Ceaglske and Hougen, in which the drying rate for smaller grain size was typically lower. This might be the expected result since the permeability is much less for the smaller beads. An explanation for this will develop later when the local saturation measurements are discussed.

Typical results for the surface saturation measurements are shown in Fig. 11 for experimental runs Nos. 1 and 5 involving 65 μm and 450 μm glass beads. The surface saturation drops quickly at the onset of drying as the surface heats up, and excess surface water is removed, establishing saturation gradients that drive the capillary transport of liquid. This is followed by an almost linear decrease in surface saturation with time during the constant drying rate period. When the surface saturation reaches the irreducible saturation a slight increase in the slope is observed. This increase in slope coincides with the end of the constant rate period. The 65 μm beads exhibit a wetter surface condition due to the greater capillary pressure. This is most likely the reason for the higher drying rates.

Results of local saturation measurements are shown in Figures 12–14. The results are presented as saturation as a function of position with time as a parameter. The 450 μm beads dry as would be expected and as would be predicted at least qual-

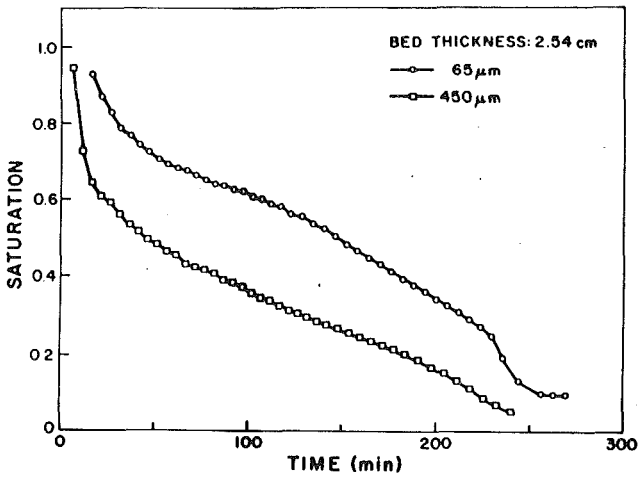

Fig. 11 Measured surface saturation as a function of time for 65 μm and 450 μm glass beads

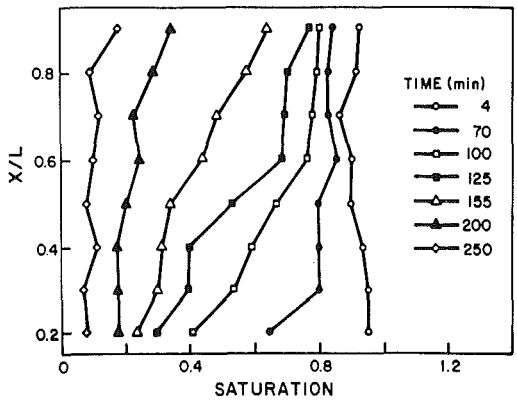

Fig. 12 Saturation distribution in the 65 μm glass beads

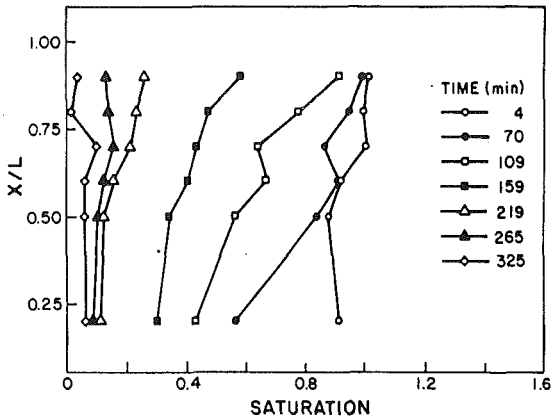

Fig. 13 Saturation distribution in the 120 μm glass beads

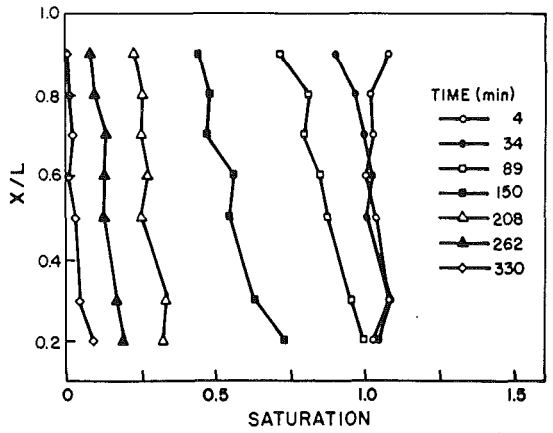

Fig. 14 Saturation distribution in the 450 μm glass beads

itatively by the models available in the literature. That is, a saturation gradient is established that provides liquid to the surface via capillary transport. The saturation always increases with distance from the drying surface. As the irreducible saturation is approached at the end of the constant rate period, the saturation is very uniform throughout the bed. This is the point at which capillary transport ceases and subsequent water removal is through diffusion in the vapor phase.

For the 65 μm and 120 μm glass beads a somewhat surprising phenomenon was observed. It is at least contrary to any of the model predictions that are available in the literature. In all cases these beds had the lowest saturation at the bottom and very close to the surface. In this case sufficient suction potential is developed near the surface to lift the entire water column in the packed bed. This implies that in model calculations the vapor phase pressure must be included, the gravitational term should not be neglected, as is most often the case, and careful attention must be paid to the bed depth and the boundary condition at the bottom. This phenomenon was verified in several ways to insure that the saturation measurements were correct. First, a bed of 65 μm glass beads was partially dried and sectioned vertically. This was done since we had learned that visual observation gives a qualitative indication of saturation. The drier beads appear lighter in color due to the increased reflection and scattering of light in the visible range. This exercise confirmed the measurements. In addition, one experiment using 65 μm beads was conducted with a pressure tap attached to a manometer inserted at the bottom of the bed. The pressure dropped very quickly to 0.305 cm (vacuum) of water as the bed began to dry but after a short period rose to atmospheric. This implies that air broke through from the surface of the bed even at very high liquid saturation. This result is not extremely surprising since the knee of the capillary pressure curves for the 65 μm and 120 μm beads is at roughly 60 cm and 40 cm of head, respectively, for imbibition, while that for the 450 μm beads is only about 12 cm. The relative permeability for the vapor phase should be expected to be nonzero at liquid phase saturation somewhere around 20 percent. Thus, the potential exists for the smaller beads to lift a large column of water and the air should be expected to penetrate at high saturations. Some further evidence of this phenomenon can be seen in the measured temperature distributions, although it is not conclusive.

Typical temperature profiles for the 65 and 450 μm sizes are shown in Fig. 15. As can be seen in the figure, the assumption of isothermal drying would not appear to be unreasonable for the conditions examined. In all cases the temperature quickly rose to the wet bulb temperature at the onset of drying. It then increased very slowly during the constant rate period where capillary transport is sufficient to supply liquid to the surface. When the surface reached the irreducible saturation, the temperature then increased rather quickly to the dry bulb temperature as the falling rate period began. This type of temperature behavior is indicative of low-intensity drying. For high-intensity drying the surface temperature would be expected to rise directly to the dry bulb temperature, eliminating the plateau at the wet bulb temperature. This is an important delineation since for many situations it is desirable to maintain the surface at the wet bulb temperature for as long as possible. Certain products—particularly food products—case harden if the surface is completely dry. This can impede further drying as well as produce an undesirable end product. Low-intensity

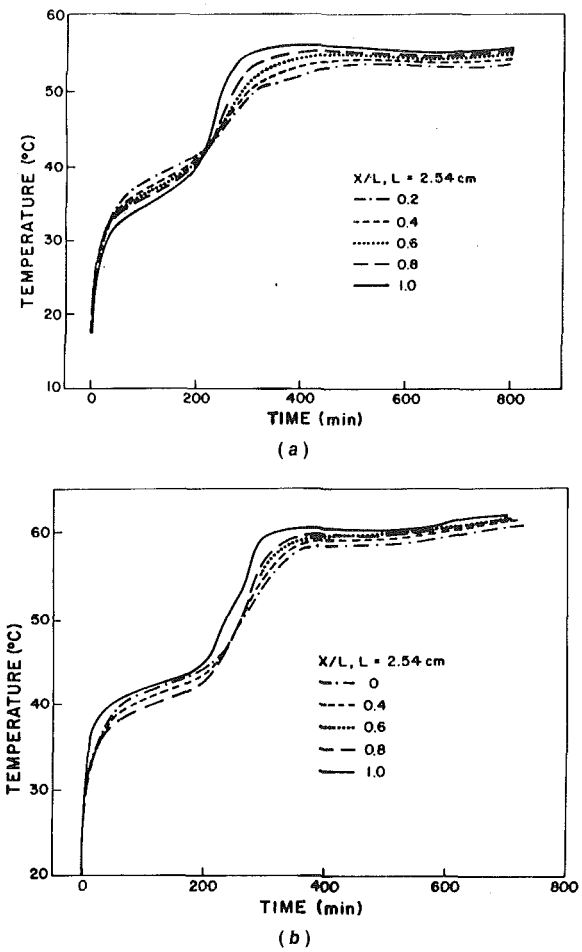

Fig. 15 Local temperature as a function of time for (*a*) 65 μm and (*b*) 450 μm glass beads

drying is also important for temperature sensitive materials and materials subject to drying stresses caused by sharp gradients in temperature and moisture content. For these reasons the ability to predict the drying environment for which low-intensity drying will prevail is highly desirable.

The measured temperature profiles are consistent with the saturation measurements in that for the large beads the temperature is highest at the drying surface throughout the drying process. However, for the 120 μm and 65 μm beads the highest measured temperatures were frequently in the lower regions of the bed during the constant rate period where the surface was near the wet bulb temperature. If thermal equilibrium is assumed to prevail, it can be expressed by the combination of the Clapeyron and Kelvin equations resulting in

$$T = T_o \frac{\left[1 + \frac{p_c}{h_{fg}\rho_l}\right]}{1 - T_o\left(\left(\frac{\overline{R}}{h_{fg}} \ln \frac{p_v}{p_o}\right)\right.} \tag{9}$$

Equation (9) demonstrates that high capillary pressure, which corresponds to low saturation, serves to elevate the equilibrium temperature. Equation (9) implies that at equilibrium the driest regions of the bed can exhibit higher temperatures. If the driest portion of the bed is at the bottom, as is the case for the smaller beads, there must be a source of heat transfer to the lower regions of the bed other than conduction from the top. This could result from heat carried by convection in the vapor phase when the air "breaks through" from the surface or perhaps more likely from heat gain from the ambient through the insulation to the lower portions of the bed.

As indicated earlier both Plumb et al. (1985) and Whitaker (1984) have encountered problems with the convective boundary conditions when attempting to make comparisons between experimental results and models. In the first case the convective mass transfer coefficient was altered from that calculated from analogy based on the postulation that analogy should hold only if the surfaces were completely covered with water resulting in the saturated vapor conditions at all points on the surface. If the surface is only partially wet, then the vapor pressure at the surface should be less than the saturated value, thus decreasing the driving potential for mass transfer. Whitaker (1984) had to alter the heat transfer coefficient calculated from analogy with the mass transfer in order to obtain agreement between his model and the experimental data of Ceaglske and Hougen. Thus, it is of interest to use our experimental data to explore the near surface physics. For the stagnation flow studied the predicted Reynolds number is on the order of 6000. The Nusselt number for a Prandtl number of 0.7 is then given by (Kays and Crawford, 1980)

$$\mathrm{Nu} = 0.496\mathrm{Re}^{1/2} \tag{11}$$

This leads to a Nusselt number of approximately 40 and an identical Sherwood number since the Lewis number is near unity. If this Sherwood number and the measured surface temperature in the constant drying rate region are used to calculate the mass transfer rate assuming saturated vapor at the surface, the result is higher than the measured drying rate by a factor of two. In contrast when the convective heat transfer coefficient is calculated using Eq. (11) and coupled with the measured surface temperature to predict the rate of heat transfer, the result is 30 percent less than that necessary to result in the measured drying rate assuming that all of the heat transfer at the surface goes into latent heat. This leads to the conclusion that for drying packed beds, the partial pressure of the water vapor at the surface is less than the saturated value for all surface saturations measured during the constant rate period, the mass transfer coefficient obtained from analogy is incorrect, or a combination of these two occurs. This has important implications from the modeling standpoint. This, coupled with the pressure-driven flow through the bed for the smaller beads, means that the transport of air by both diffusion and convection must be considered in the analysis in order to predict the partial pressure of the water vapor at the drying surface. This has not been done in most of the drying predictions available in the literature.

In order to present results having some practical value, we have, for the constant drying rate period, back calculated surface vapor pressure as a function of saturation. This calculation uses the measured drying rate and the convective mass transfer coefficient calculated using Eq. (11). These results are shown in Fig. 16. For the 450 μm glass beads the calculated partial pressure is 20 to 30 percent of the saturated value. In the case of the 120 μm beads this value is 40–50 percent. Our explanation for this is that for smaller beads the islands of water are smaller and larger in number for the same saturation. The results for the 65 μm glass beads fall in between. This appears to be a result of the fact that the surface temperature was higher for the smaller beads and the plateau at or near the wet bulb temperature was much shorter and less well defined. These results should be applied with great caution since they are expected to be, at the minimum, a function of Reynolds number or mass transfer boundary layer thickness, whether the flow is laminar or turbulent, drying rate, and Schmidt number if the vapor is other than water.

Conclusions

We have presented what is believed to be the most compre-

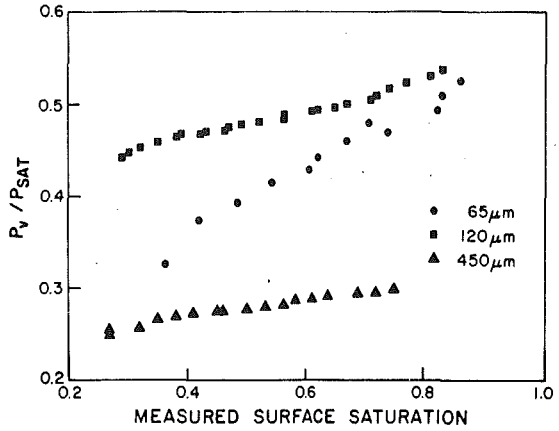

Fig. 16 Calculated water vapor partial pressure as a function of measured surface saturation

hensive set of drying data available for packed beds of glass beads. Results include capillary pressure curves for both drainage and imbibition, parameters that define the drying geometry and environment, drying rates as a function of time, surface saturation, saturation distribution, and temperature distribution. The following conclusions have been drawn:

1 The empirical expression for capillary pressure recommended by Luckner et al. (1989) provides a good fit to the experimental data for glass beads, although the empirical constants are not universal. The universal relationship of Leverett results in a good qualitative representation but lacks precision probably because hysteresis is not effectively modeled.

2 Under the same drying conditions, the data indicate that the drying rate for smaller bead sizes can be higher than that for larger beads despite the much lower permeability. This is presumed to be a result of the capillary pressure being sufficiently high to maintain high saturation near the drying surface.

3 Local saturation does not always increase with depth as predicted by previous model studies. When capillary pressure is sufficiently high the entire column of liquid can be lifted toward the surface, resulting in two drying fronts—one at the top of the bed and one at the bottom.

4 These results confirm the observations of others with regard to the convective mass transfer coefficient. The data indicate that the partial pressure of water vapor at the drying surface is less than the saturated value for the majority of the drying period or that the convective mass transfer coefficient calculated from analogy is incorrect or a combination of these two is prevalent.

It is hoped that these results will provide a useful tool for use in validating drying models for a variety of materials and drying scenarios.

Acknowledgments

This material is based in part upon work supported by the Cooperative State Research Service, U.S. Department of Agriculture, under Grant No. 87-FSTY-9-0244.

References

Brooks, R. H., and Corey, A. T., 1968, "Properties of Porous Media Affecting Fluid Flow," ASCE *J. Irrig. Drain*, Vol. 92(IR2), pp. 61–66.

Ceaglske, N. H., and Hougen, O. A., 1937, "Drying Granular Solids," *Ind. Eng. Chem.*, Vol. 29, pp. 805–817.

Crawford, C., and Plumb, O. A., 1986, "The Influence of Surface Roughness on Resistance to Flow Through Packed Beds," ASME *Journal of Fluids Engineering*, Vol. 108, pp. 343–347.

Ergun, S., 1952, "Fluid Flow Through Packed Columns," *Chemical Engineering Progress*, Vol. 43(2), pp. 89–94.

Kays, W. M., and Crawford, M. E., 1980, *Convective Heat and Mass Transfer*, 2nd ed., McGraw-Hill, New York.

Leverett, M. C., 1941, "Capillary Behavior in Porous Solids," *AIME Trans.*, Vol. 142, pp. 152–169.

Luckner, L., van Genuchten, M. Th., and Nielsen, D. R., 1989, "A Consistent Set of Parametric Models for the Two-Phase Flow of Immiscible Fluids in the Subsurface," *Water Resour. Res.*, Vol. 25(10), pp. 2187–2193.

Luikov, A. V., 1966, *Heat and Mass Transfer in Capillary-Porous Bodies*, Pergamon Press, Oxford, United Kingdom.

Mualem, Y., 1976, "A New Model for Predicting the Hydraulic Conductivity of Unsaturated Porous Media," *Water Resour. Res.*, Vol. 25(3), pp. 513–522.

Plumb, O. A., Brown, C. A., and Olmstead, B. A., 1984, "Experimental Measurements of Heat and Mass Transfer During Convective Drying of Southern Pine," *Wood Sci. Technol.*, Vol. 18, pp. 187–204.

Plumb, O.A., Spolek, G. E., and Olmstead, B. A., 1985, "Heat and Mass Transfer in Wood During Drying," *Int. J. Heat Mass Transfer*, Vol. 28, pp. 1669–1678.

Spolek, G. A., and Plumb, O. A., 1981, "Capillary Pressure in Softwoods," *Wood Sci. Technol.*, Vol. 15, pp. 189–199.

Udell, K. S., 1985, "Heat Transfer in Porous Media Considering Phase Change and Capillarity—the Heat Pipe Effect," *Int. J. Heat Mass Transfer*, Vol. 28(2), pp. 485–495.

van Genuchten, M. Th., 1980, "A Closed-Form Equation for Predicting the Hydraulic Conductivity of Unsaturated Soils," *Soils Sci. Soc. Am. J.*, Vol. 44, pp. 892–898.

Verma, A. K., Pruess, K., Tsang, C. F., and Witherspoon, P. A., 1985, "A Study of Two-Phase Concurrent Flow of Stream and Water in an Unconsolidated Porous Medium," in: *Heat Transfer in Porous Media and Particulate Flows*, L. S. Yao, ed., ASME HTD-Vol. 46, pp. 135–143.

Wetzel, D. L., 1983, "Near Infrared Reflectance Analysis-Sleeper Among Spectroscopic Techniques," *Analytical Chemistry*, Vol. 55, p. 1165A.

Whitaker, S., 1977, "Simultaneous Heat, Mass and Momentum Transfer in Porous Media: A Theory of Drying," in: *Advances in Heat Transfer*, T. J. Irvine and J. P. Hartnett, eds., Academic Press, New York, Vol. 3.

Whitaker, S., 1980, "Heat and Mass Transfer in Granular Porous Media," in: *Advances in Drying*, A. S. Mujumdar, ed., Hemisphere, Washington, DC, Vol. 1.

Whitaker, S., and Chow, W. T.-H., 1983, "Drying Granular Porous Media—Theory and Experiment," *Drying Tech.*, Vol. 1, pp. 3–33.

Whitaker, S., 1984, "Moisture Transport Mechanisms During the Drying of Granular Porous Media," *Proc. of the Fourth Intl. Drying Symposium*, Vol. 1, Kyoto, Japan, pp. 31–42.

A Three-Dimensional Analysis of Particle Deposition for the Modified Chemical Vapor Deposition (MCVD) Process

Y. T. Lin

M. Choi[1]

R. Greif

Department of Mechanical Engineering,
University of California at Berkeley,
Berkeley, CA 94720

A study has been made of the deposition of particles that occurs during the modified chemical vapor deposition (MCVD) process. The three-dimensional conservation equations of mass, momentum, and energy have been solved numerically for forced flow, including the effects of buoyancy and variable properties in a heated, rotating tube. The motion of the particles that are formed is determined from the combined effects resulting from thermophoresis and the forced and secondary flows. The effects of torch speed, rotational speed, inlet flow rate, tube radius, and maximum surface temperature on deposition are studied. In a horizontal tube, buoyancy results in circumferentially nonuniform temperature and velocity fields and particle deposition. The effect of tube rotation greatly reduces the nonuniformity of particle deposition in the circumferential direction. The process is chemical-reaction limited at larger flow rates and particle-transport limited at smaller flow rates. The vertical tube geometry has also been studied because its symmetric configuration results in uniform particle deposition in the circumferential direction. The "upward" flow condition results in a large overall deposition efficiency, but this is also accompanied by a large "tapered entry length."

Introduction

The Modified Chemical Vapor Deposition (MCVD) process is widely used for the manufacture of high-quality optical waveguides (MacChesney et al., 1974a, 1974b; Nagel et al., 1982; Simpkins et al., 1979; Walker et al., 1979). Studies of laser-enhanced MCVD have been carried out by Wang et al. (1985), DiGiovanni et al. (1985), and Morse et al. (1986). Variable property effects have been studied by Walker et al. (1980) and a study of chemical kinetics and silica aerosol dynamics has been carried out by Kim and Pratsinis (1988). Annulus MCVD has been proposed and studied experimentally and numerically by Fiebig et al. (1988). Three-dimensional variations of the temperature profiles have been studied utilizing a parabolic velocity profile (Choi et al., 1989). The effects of buoyancy and tube rotation have also been studied using a perturbation analysis (Choi et al., 1990). An earlier work studied the effects of variable properties with tube rotation for a fast-moving torch (Choi et al., 1987). The effects of buoyancy, tube rotation, and variable properties on the flow and heat transfer in respect to the MCVD process were studied by Lin et al. (1991).

In the present work the effects of tube rotation, torch speed, inlet flow rate, tube radius, and maximum surface temperature on particle deposition are studied in a three-dimensional flow field relative to the MCVD process. The vertical tube geometry is also included because for this configuration there is no circumferential variation (the surface temperature is assumed to be uniform in the angular direction, i.e., two-dimensional) and the resulting particle deposition is uniform in the circumferential direction. The motion of the particles is determined from the combined effects of thermophoresis and the forced and secondary flows, due to the effects of buoyancy and variable properties.

Analysis

The gas is flowing inside a circular tube, which is rotating about its axis (Fig. 1). A coordinate ξ defined by $\xi = x - V_{torch}t$, together with the polar coordinates r, θ (fixed in space, not rotating) results in the steady-state coordinate system (r, θ, ξ) with velocities (v, u, w). The torch is located at $\xi = 0$. The flow is considered to be three dimensional and laminar. The governing equations and boundary conditions are given by Burmeister (1982) and Lin et al. (1991). Information on the numerical solution is given by Lin et al. (1991). The effects of buoyancy and variable properties are included with the density, thermal conductivity, and viscosity being functions of the temperature. The wall temperature distribution is based on the measurements of Walker et al. (1980). It is assumed that the wall temperature is uniform in the circumferential direction. A study was carried out to determine the circumferential variation of the wall temperature. This included the effects of tube thickness, deposition layer, and tube rotation. The resulting inside wall temperature was shown to vary only slightly in the circumferential direction (Lin et al., 1992). At the entrance, $\xi = -L_t$, the temperature is equal to a constant value, T_l. The total length, L, is 0.6 m and the distance between the torch and the location where the velocity and temperature are specified L_t, is 0.275 m. In the region behind and away from

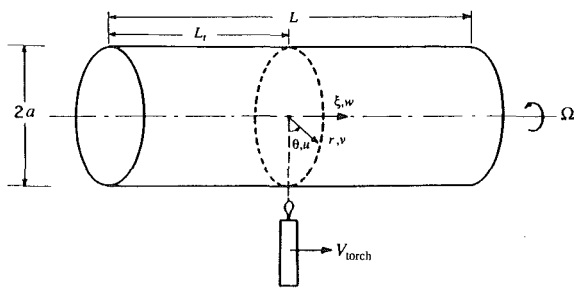

Fig. 1 Sketch of the system

[1]Seoul National University, Seoul, South Korea.

Contributed by the Heat Transfer Division for publication in the JOURNAL OF HEAT TRANSFER. Manuscript received by the Heat Transfer Division February 1991; revision received January 1992. Keywords: Forced Convection, High-Temperature Phenomena, Mixed Convection.

the torch, chemical reactions do not occur and the gas is comprised of $SiCl_4$, O_2, etc. In the region near the torch, chemical reactions occur and particles have formed. In this region it is assumed that particle mass loading does not strongly influence the flow field. A study of the effects of particle loading is given by Rosner and Park (1988). Particles are initiated (formed) at the locations, (r_i, θ_i, ξ_i), where the gas temperatures first exceed the reaction temperature, T_{rxn}, along the streamlines. The local particle formation rate per unit area is $|\rho(\mathbf{V}\cdot\mathbf{n})F|$, where F is the fraction of the reacting components, such as $SiCl_4$ and/or $GeCl_4$, of the gas, and $\mathbf{V}$ is the local gas velocity and $\mathbf{n}$ is the unit vector normal to the isothermal contour for $T = T_{rxn}$. It is assumed that the gas is uniformly mixed and that F is constant. The chemical reactions are assumed to be completed once the gas temperature reaches T_{rxn}. The motion of the particles is then determined from the combined effects resulting from thermophoresis and the forced and secondary flows.

The thermophoretic velocity is given by Talbot et al. (1980). Using a Lagrangian description for the particle motion, the following differential equations are obtained for the velocity of the particles:

$$\frac{d\xi}{dt} = w - \frac{K\nu}{T}\frac{\partial T}{\partial \xi};\quad \frac{dr}{dt} = v - \frac{K\nu}{T}\frac{\partial T}{\partial r};\quad r\frac{d\theta}{dt} = u - \frac{K\nu}{T}\frac{1}{r}\frac{\partial T}{\partial \theta} \qquad (1)$$

where $\frac{d\xi}{dt}$, $\frac{dr}{dt}$, $r\frac{d\theta}{dt}$ are the axial, radial, and angular velocities of the particles, respectively. A value of 0.9 for K is used in the present work (Walker et al., 1980). It is noted that for the MCVD process the effects of particle Brownian diffusion are negligible in comparison to the effects of thermophoresis (Walker et al., 1979; Simpkins et al., 1979). To determine the particle trajectories, Eqs. (1) were solved by using the second-order Runge-Kutta method after u, v, w, and T had been obtained from the solution of the conservation equations. The spatial deposition location, (ξ_d, θ_d), where the particle trajectory reaches the tube surface, $r = a$, can also be determined, provided that the particle is not convected out of the tube. Note that (ξ_d, θ_d) is the relative deposition location in the (r, θ, ξ) reference coordinate system. The particle formation percentage (from $SiCl_4$ (or $GeCl_4$) to SiO_2 (or GeO_2)) is obtained by summing all of the formation rates at all of the formation locations and dividing by the total incoming flow rate of $SiCl_4$ (or $GeCl_4$); i.e., Σ (formation rate/$\rho_l QF$) $\times$ 100 percent. The spatial deposition efficiency of the process, $E(\xi)$, is defined as the particle deposition rate over the axial distance extending from the inlet $\xi = -L_t$ to $\xi = \xi$ divided by the incoming flow rate of $SiCl_4$; i.e., $E(\xi) = \Sigma$ (deposition rate in $[-L_t, \xi]$/$\rho_l QF$) $\times$ 100 percent. The total deposition efficiency, E_T, is the total deposition rate over the entire tube divided by the inlet flow rate of $SiCl_4$ so that $E_T = E(\xi_{exit})$.

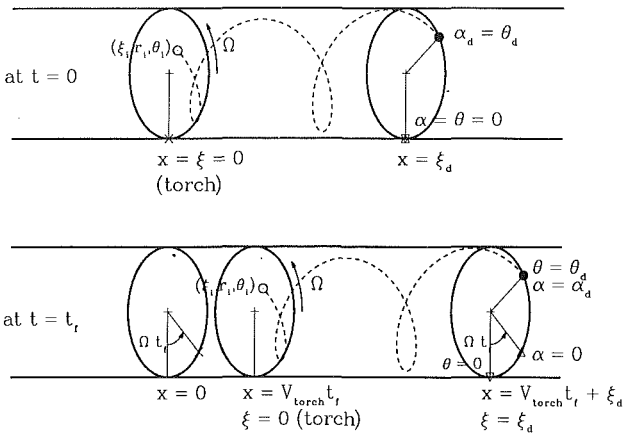

Fig. 2 Relationship between two coordinates (ξ, r, θ) and (x, r, α)

For the same particle formation location (r_i, θ_i, ξ_i), the actual particle deposition location on the tube surface, (x_d, α_d) depends on the torch movement and the tube rotation. The relationship is (Fig. 2)

$$x_d = \xi_d + V_{torch}t; \qquad \alpha_d = \theta_d - \Omega t. \qquad (2)$$

At time $t = 0$ the coordinate system (r, α, x) is chosen to coincide with (r, θ, ξ). For a given formation location (r_i, θ_i, ξ_i), the particle deposition locations for different times, t, form the spiral pattern on the tube surface (Fig. 3). Knowing all of the spatial formation locations, $(r_i, \theta_i \xi_i)$ and their particle formation rates per unit area permits the determination of the actual deposition locations on the tube surface, (x_d, α_d) and the deposition rate at each location (x_d, α_d) in any time interval $[0, t_f]$ for given values of V_{torch} and Ω. Therefore, the axial and angular distributions of the particle deposition on the tube

Nomenclature

A = area
a = tube radius
D = particle deposition (mass)
E = spatial deposition efficiency
E_T = total deposition efficiency
F = fraction of the reacting components of the gas
g = gravitational acceleration
K = thermophoretic coefficient
L = length of the tube
L_t = distance between the torch and the specified inlet
$\mathbf{n}$ = unit vector normal to the isothermal contour for $T = T_{rxn}$
Q = inlet flow rate
q = heat flux
r = radial coordinate
T = temperature
T_l = temperature at the inlet plane
T_{max} = maximum temperature on the tube wall
T_{rxn} = reaction temperature
t = time
t_f = end of time for calculating particle deposition
u = circumferential velocity
$\mathbf{V}$ = velocity of gas (vector)
V_{av} = average velocity of gas in the axial direction
V_{torch} = torch speed
v = radial velocity
w = axial velocity (in the steady-state reference coordinate system)
x = axial coordinate
α = angle $= \theta - \Omega t$
θ = angle
ν = kinematic viscosity
ξ = moving coordinate $= x - V_{torch}t$
ρ = density
ξ_{exit} = axial coordinate at the exit of the tube
Ω = angular velocity of tube

Subscripts

d = positions of particle deposition
i = locations where the particles are initiated (formed)
r = radial coordinate
θ = angle
ξ = moving coordinate $= x - V_{torch}t$

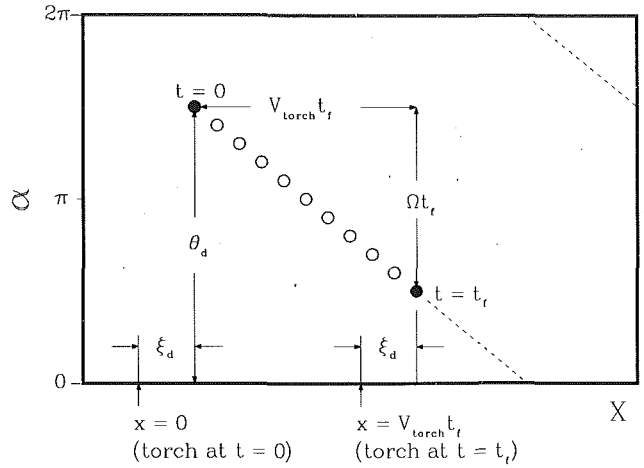

Fig. 3 Deposition locations from a specific formation location at different times

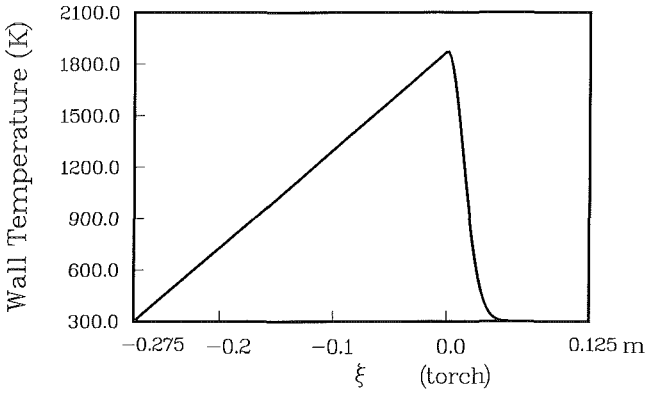

Fig. 4 Axial distribution of wall temperature

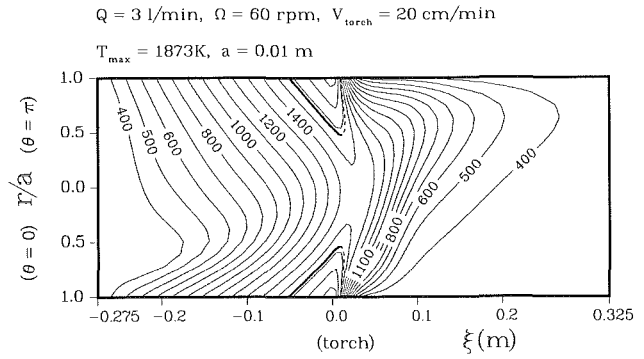

Fig. 5 Isothermal contours in the central vertical plane: Ω = 60 rpm, a = 0.01 m, Q = 3 l/min, V_{torch} = 20 cm/min, T_{max} = 1873 K

surface can be determined for one torch traverse. The effects of flow rate, buoyancy, rotation, tube diameter, torch speed, and maximum wall temperature on deposition have been studied.

Results and Discussion

Figure 4 shows the variation of the wall temperature (Walker et al., 1980). Figure 5 shows the isothermal contours in the vertical plane passing through the center of the horizontal tube for Ω = 60 rpm. The resulting nonsymmetric distribution (with respect to the centerline, $r = 0$) is due to the effects of buoyancy (Lin et al., 1991). The gas temperature exceeds the reaction

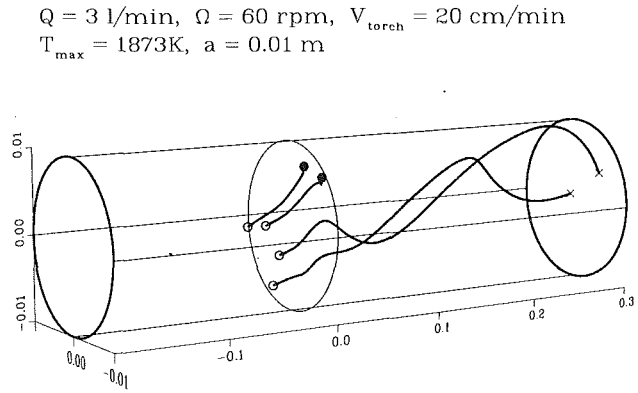

Fig. 6 Three-dimensional particle trajectories: Ω = 60 rpm, a = 0.01 m, Q = 3 l/min, V_{torch} = 20 cm/min, T_{max} = 1873 K

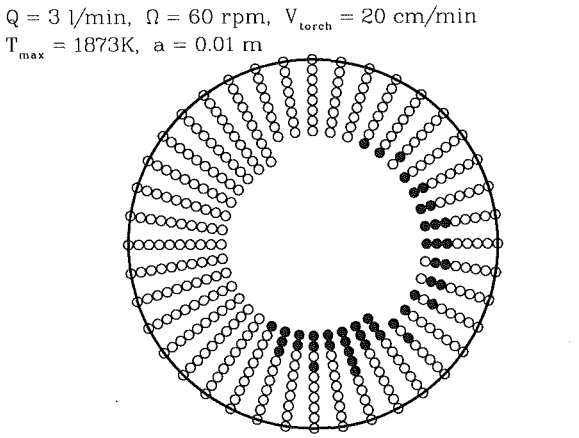

Fig. 7 Particle formation locations of the side view; solid points are convected out of the tube: Ω = 60 rpm, a = 0.01 m, Q = 3 l/min, V_{torch} = 20 cm/min, T_{max} = 1873 K

temperature, $T_{rxn} \approx 1573$ K (Walker et al., 1980), only in the small region near the tube surface and near the torch (for this case). Chemical reactions occur when the gas reaches the upstream portion of this region (as shown by the thicker curves in Fig. 5). It is assumed that the reactions are completed in this portion; i.e., no reactions occur downstream of this portion. Particles such as SiO_2 or GeO_2 form during the chemical reactions and then follow very complex trajectories (cf. Eqs. (1), Fig. 6). Most of the particles formed in the region near the surface will be deposited on the surface because the radial temperature gradients and the corresponding radial thermophoretic velocities (toward the wall) downstream are large (with only small axial velocities near the surface). However, particles that form in the core may be carried out of the tube (Fig. 7) because there the radial thermophoretic velocities are small and the axial velocities are large. About 55 percent (by mass) of the inlet $SiCl_4$ (and/or $GeCl_4$) is oxidized and about 83 percent (by mass) of the product SiO_2 (and/or GeO_2) deposit on the tube for this specific condition. The overall deposition efficiency, E_T, is approximately 46 percent ($= 0.55 \times 0.83 \times 100$ percent).

The distribution of the points of particle deposition on the tube surface (ξ_d, θ_d) is shown in Fig. 8*a* in the quasi-steady system; i.e., relative to the torch. Each circle in the figure represents a deposition location, $\xi = \xi_d$, $\theta = \theta_d$, that was initiated (formed) from the points (r_i, θ_i, ξ_i) that lie on the upstream portion of the contour whose temperature is equal to T_{rxn} (cf. the thicker curves in Fig. 5). Most of the particles are deposited over the axial distance extending from $\xi = 0.02$ to $\xi = 0.1$ m; i.e., the distribution density of the particles being deposited

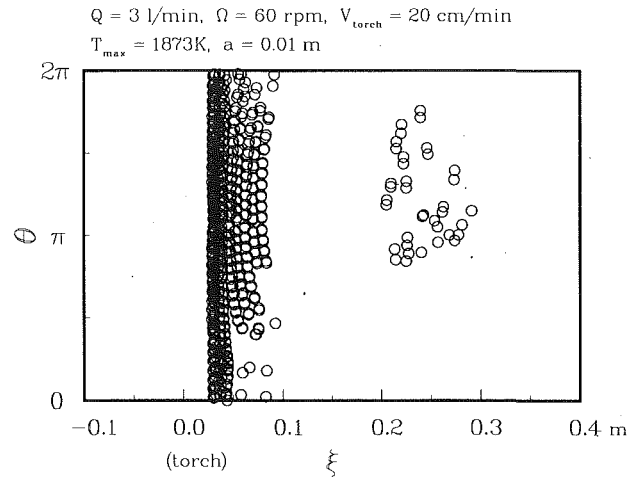

Fig. 8a Distribution of particle deposition locations: Ω = 60 rpm, a = 0.01 m, Q = 3 l/min, V_{torch} = 20 cm/min, T_{max} = 1873 K

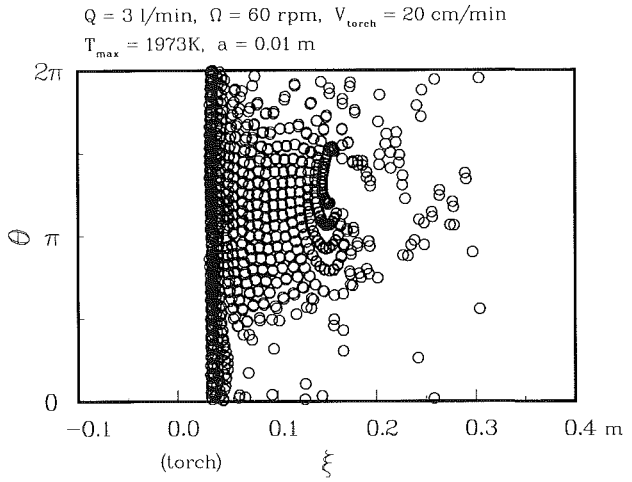

Fig. 8b Distribution of particle deposition locations: Ω = 60 rpm, a = 0.01 m, Q = 3 l/min, V_{torch} = 20 cm/min, T_{max} = 1973 K

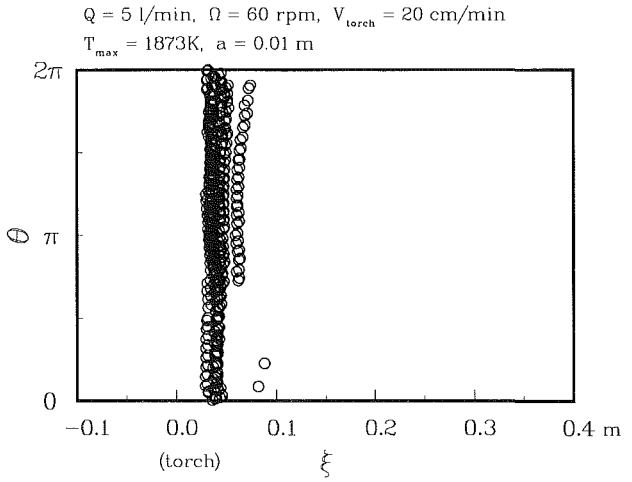

Fig. 8c Distribution of particle deposition locations: Ω = 60 rpm, a = 0.01 m, Q = 5 l/min, V_{torch} = 20 cm/min, T_{max} = 1873 K

in this region is high. It does not mean that there is no particle deposition in the regions where no circles appear. It only means that the distribution density of the particles being deposited there is very small. Note that even though the particles are

Table 1 Summary of formation percentage, overall deposition efficiency, and tapered length for different conditions

Condition	% of form.	% of dep.	E_T	Tapered-entry length
Horizontal flow				
1. standard	55%	84%	46%	8*cm*
2. Q = 1*l/min*	100%	73%	73%	~15*cm*
3. Q = 5*l/min*	22%	98%	22%	7*cm*
4. Ω = 0	54%	84%	45%	8*cm*
5. Ω = 30*rpm*	56%	79%	44%	8*cm*
6. Ω = 90*rpm*	55%	81%	44%	8*cm*
7. Ω = 120*rpm*	56%	79%	44%	8*cm*
8. T_{max} = 1973*K*	100%	68%	68%	>20*cm*
9. V_{torch} = 10*cm/min*	55%	83%	46%	8*cm*
10. V_{torch} = 30*cm/min*	55%	83%	46%	8*cm*
11. a = 0.6*cm*	45%	95%	43%	11*cm*
12. a = 0.8*cm*	50%	88%	45%	10*cm*
Vertical flow				
13. upward	64%	86%	55%	>20*cm*
14. downward	26%	100%	26%	5*cm*
With no gravity				
15. g = 0	45%	100%	45%	

The standard condition is Q = 3*l/min*, Ω = 60*rpm*, T_{max} = 1873*K*, V_{torch} = 20*cm/min*, a = 1*cm*.
% of form. = percentage of $SiCl_4$ is oxidized to form SiO_2
% of dep. = percentage of SiO_2 that is formed deposit on the surface
E_T = (% of form.) X (% of dep.)

formed in the region behind the torch, $\xi < 0$, they are deposited ahead of the torch, $\xi > 0.02$ m, where the radial thermophoretic velocities are toward the surface (from the hot gas to the cold wall) with some particles (most of them being formed near the central region) being deposited on the surface very far downstream (beyond $\xi = 0.2$ m) as shown in Fig. 8*a*. (Note that 17 percent of the particles are convected out of the tube.)

The distributions for other conditions are shown in Figs. 8(*b*) and 8(*c*). Figure 8(*b*) shows the distribution for a higher value of T_{max}, namely, 1973 K. For this specification, all of the inlet $SiCl_4$ ($GeCl_4$) (100 percent) is oxidized (i.e., the isothermal contour of $T = T_{rxn} = 1573$ K extends to the center of the tube) but only about 68 percent of the product SiO_2 is deposited. Therefore, the overall deposition efficiency is 68 percent. Those aerosols that are formed near the central region are convected out of the tube because in the core the radial thermophoretic velocities are small and the axial velocities are large. For this case there is (now) significant deposition from $\xi = 0.02$ to $\xi = 0.2$ m (particles formed farther away from the surface of the tube are carried further downstream). This effect will make the "tapered entry length" longer and is discussed later. Figure 8(*c*) shows the results for a specification of $T_{max} = 1873$ K at a higher flow rate, Q(= 5 l/min). At a higher flow rate, the gas temperature is lower and only in the small region very near the wall and the torch does it exceed T_{rxn}. Only about 22 percent of the inlet $SiCl_4$ ($GeCl_4$) is now oxidized (in the upstream portion of this small region) and almost all of the product SiO_2(GeO_2) (98 percent) is deposited in the region near the torch as shown in Fig. 8(*c*) (while the background gas exits almost free of particles). Thus, for the high flow rate condition, the process is chemical-reaction limited (Walker et al., 1980). It is pointed out that even though the region of particle formation is small and its overall deposition efficiency, E_T, is only about 22 percent, the corresponding deposition rate may be high due to the high inlet flow rate. (Note that for a further higher inlet flow rate the chemical reactions may be incomplete.) However, for this case a large amount of $SiCl_4$ or $GeCl_4$ flows out of the tube and equipment for recycling the expensive $SiCl_4$, especially the $GeCl_4$, may be

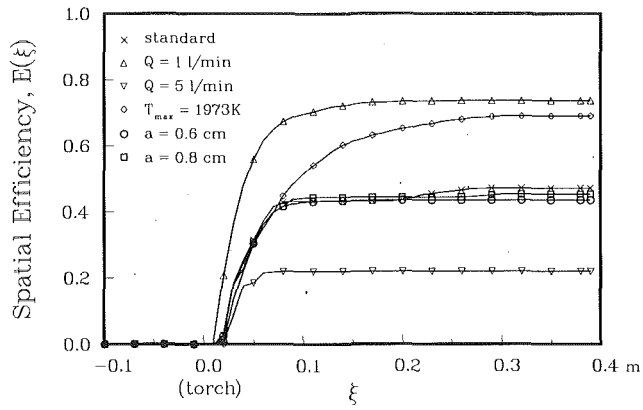

Fig. 9 Spatial efficiency, $E(\xi)$, for different conditions

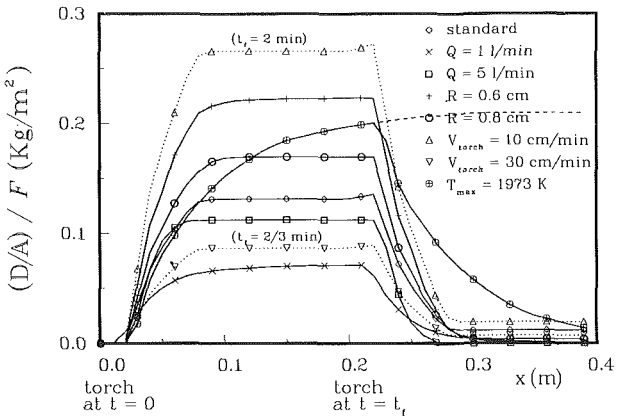

Fig. 10 Axial deposition curve (circumferentially lumped); torch moves from $x = 0$ to 0.2 m for $V_{torch} = 10$, 20, 30 cm/min, $t_f = 2$, 1, 2/3 min

appropriate. At a lower flow rate, e.g., $Q = 1$ l/min, and $T_{max} = 1873$ K, the results are similar to the case with $Q = 3$ l/min and $T_{max} = 1973$ K. The isothermal contour of $T = T_{rxn}$ extends to the center of the tube (figure not shown) and all of the inlet $SiCl_4$ ($GeCl_4$) (100 percent) is oxidized. About 73 percent of the particles that are formed are deposited on the tube surface and these particles are spread over a large axial distance. Note that the overall deposition efficiency is 73 percent and for the low flow rate condition the process is "particle-transport limited" (Walker et al., 1980). Even with this high efficiency the deposition rate may be low because of the low incoming flow rate. The percentage of particle formation (oxidization from $SiCl_4$ to SiO_2) and particle deposition (percent of the product SiO_2 deposited) and overall deposition efficiency, E_T (E_T = formation fraction × deposition fraction × 100 percent), are tabulated in Table 1 for different cases. For completeness, the case without gravity is included. For this case the particle deposition locations are uniformly distributed in the angular direction.

The deposition distributions for different tube rotational speeds are essentially similar; most particles deposit over the range from $\xi = 0.02$ to 0.1 m and the particle formation is between 54 and 56 percent and the overall deposition efficiency, E_T, is between 44 and 45 percent. Thus, tube rotation has only a slight effect on the deposition efficiency but it does indeed have a significant influence on the angular uniformity of particle deposition (discussed later). Different torch speeds, $V_{torch} = 10$ and 30 cm/min, for the same specified wall temperature boundary condition, have little effect on the particle deposition distribution and the overall deposition efficiency (the torch speeds are much smaller (< 1 percent) than the axial gas velocity). The results are similar to Fig. 8 (*a*). However, the actual axial and angular deposition distributions in the (x, α) coordinates over a specified time interval are different (discussed later). The effects of the value of the tube radius, a, have also been studied for a fixed inlet flow rate, $Q = 3$ l/min (the average gas velocity is proportional to $1/a^2$). The chemical reactions occur only in a small region very near the tube surface and the torch and less than 50 percent of the inlet $SiCl_4$ (or $GeCl_4$) is oxidized for tubes with radii $a = 0.6$ and 0.8 cm. The overall deposition efficiencies, E_T, vary only from 43 to 45 percent. However, a higher percentage of SiO_2 (or GeO_2) deposits on the surface with the smaller tube radii; i.e., 95, 88, and 84 percent for $a = 0.6$, 0.8, and 1 cm, respectively.

The spatial deposition efficiency, $E(\xi)$, is shown in Fig. 9 for different operating conditions. The results for different torch speeds and different rotation speeds for the same specified wall temperature differ only slightly from the standard results; that is, for $V_{torch} = 20$ cm/min and $\Omega = 60$ rpm and are not shown. The spatial efficiency for smaller tube radii deviates only slightly from the standard radius as described in the preceding paragraph. Most of the curves reach constant values before $\xi = 0.1$ m except for the $Q = 1$ l/min and $T_{max} = 1973$ K cases. For these two cases, many particles are deposited over a larger range in ξ as discussed above.

To determine the actual axial and angular deposition distribution on the tube surface (in (x, α) coordinates), Eqs. (2) are applied at every formation point (r_i, θ_i, ξ_i) over a time interval from $t = 0$ to $t_f = 1$ min. Recall that the deposition point (ξ_d, θ_d) depends only on its formation location (r_i, θ_i, ξ_i) and that (x_d, α_d) is a function of (ξ_d, θ_d) and time for specified Ω and V_{torch}. For this case, the torch moves a distance of 20 cm. It is assumed that the particles are formed and distributed uniformly within the control volumes in which the chemical reactions occur. The size of the control volumes is the same as specified in the size of the grids (Lin et al., 1991). Figure 10 shows the axial deposition distribution (circumferentially lumped) for different conditions; the initial location of the torch is at $x = 0$. Since almost all of the particles are deposited ahead of the torch, the curves start at positive values of x. The deposition develops until a fairly uniform axial deposition layer is obtained. The developing deposition profile near $x = 0$ will persist for several torch traverses even though the torch may start at different initial angles α for each traverse. This results in an undesirable tapered portion of the preform near the inlet, which would be cut off before the preform is drawn into a fiber. Therefore, a shorter tapered entry is preferred, which corresponds to having more of the particles being deposited near the torch rather than being spread out over a long distance. It is seen from Fig. 10 (cf. Table 1) that the $T_{max} = 1973$ K case results in a very long tapered entry length (over 20 cm). Note that with $V_{torch} = 10$ cm/min, the torch only moves to $x = 0.1$ m in $t_f = 1$ min and thus the particle deposition (kg) per unit area (m^2), D/A, is very large because the overall efficiency ($E_T = 46$ percent) is about the same as for the $V_{torch} = 20$ cm/min case ($E_T = 46$ percent). The deposition per unit area is very small for the $V_{torch} = 30$ cm/min case (again $E_T = 46$ percent) because the deposition zone is longer (the torch moves to $x = 0.3$ m in 1 min). The curve for $Q = 1$ l/min is also low because the incoming flow rate of $SiCl_4$ (or $GeCl_4$) is also small and the corresponding amount that can be oxidized (and deposited) is therefore small. Note that D/A for a higher flow rate, $Q = 5$ l/min, is larger than that for $Q = 1$ l/min because of its high flow rate of $SiCl_4$ (or $GeCl_4$). However, D/A is not larger than that for $Q = 3$ l/min (standard case) because of the low percentage of particle formation for $Q = 5$ l/min (due to the temperatures in the central region being lower than the reaction temperature for the 5 l/min condition). Thus, the deposition per unit area for the case $Q = 3$ l/min is higher than that for the cases $Q = 1$ and 5 l/min. Note that the particle deposition per unit area is larger for smaller tube radius, but less fiber is

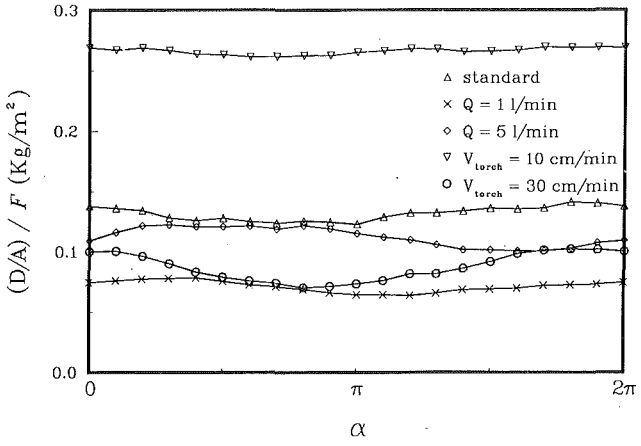

Fig. 11a Angular deposition distribution at $x = 0.180$ m

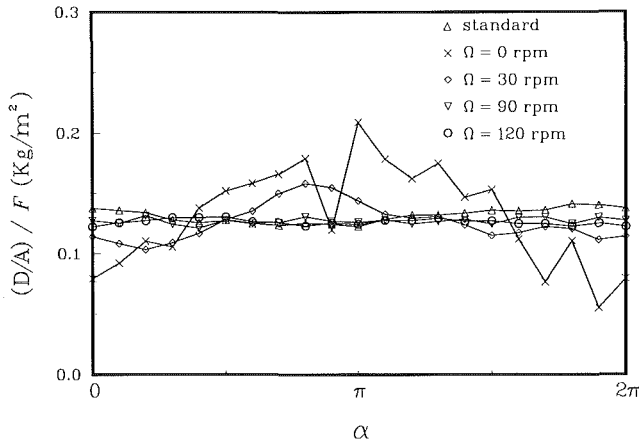

Fig. 11b Angular deposition distribution at $x = 0.180$ m

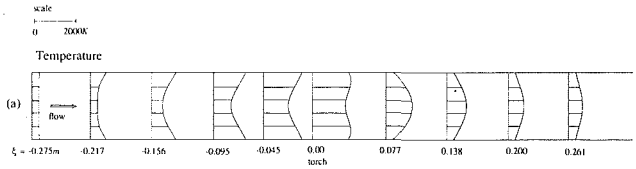

Fig. 12 (*a*) Isothermal distribution along a diameter

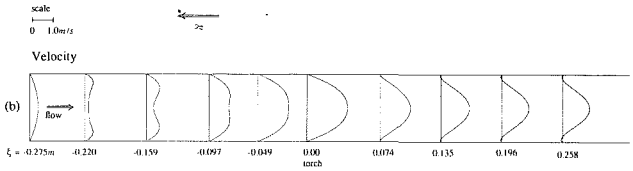

Fig. 12 (*b*) Axial velocity distribution along a diameter

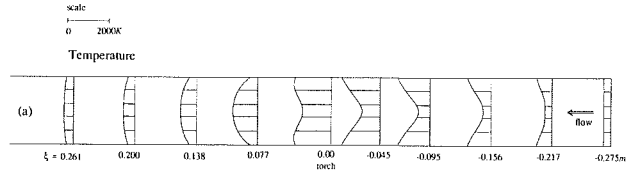

Fig. 13 (*a*) Isothermal distribution along a diameter

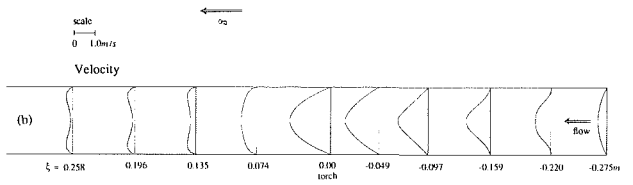

Fig. 13 (*b*) Axial velocity distribution along a diameter; for the "downward" flow: $a = 0.01$ m, $Q = 3$ l/min, $V_{torch} = 20$ cm/min, $T_{max} = 1873$ K

produced. The overall efficiencies for the cases with different tube radii differ by only a few percent (Table 1). With the same axial deposition length (the same torch speed), the tube with smaller radius (smaller surface area) has a larger value of particle deposition per unit area.

Figures 11(a) and 11(*b*) show the angular deposition distribution (in (x, α) coordinates) at $x = 0.180$ m for one torch traverse. At this location most of the axial deposition curves in Fig. 10 have reached their uniform values. After the torch moves beyond $x = 0.180$ m, the subsequent particle deposition at later times does not influence the distribution at that location. A small circumferential strip on the tube surface of width $\Delta x = 0.002$ m from $x = 0.180$ to 0.182 m is considered in detail. It is divided into 20 equally sized small widths, $2\pi/20$, in the angular direction. As the torch passes, the particle deposition is calculated, and the results are shown for $\Omega = 60$ rpm in Figs. 11 (*a*) and 11(*b*). The angular nonuniformity of the deposition results from the effects of buoyancy; without the effect of gravity there would be no angular nonuniformity for flow in a horizontal tube. Results for different V_{torch} and Q are shown in Fig. 11(*a*). For a large V_{torch}, e.g., 30 cm/min, the deposition extends over a larger axial length (Fig. 10) and results in greater nonuniformity in the angular direction. The effect of tube rotation is shown in Fig. 11(*b*). The deposition is strongly nonuniform for $\Omega = 0$ because of the dominant effect of buoyancy. As the rotational speed increases, the nonuniformity is greatly reduced.

The angular uniformity of the deposition is very important in the preform manufacturing process because it affects the quality of the fibers. The nonuniformity described above is due to the effects of buoyancy, which results in a complex, asymmetric secondary flow pattern and nonuniform deposition in a horizontal tube. Accordingly, a study was also carried out for deposition in a vertical tube where the velocity and temperature fields are two dimensional; i.e., $\partial/\partial\theta = 0$. Two situations were studied: inlet flow upward from the bottom of the tube, "upward" flow, and inlet flow downward from the top. In both cases the torch motion is in the flow direction and the specified wall temperature distribution is the same as for the horizontal tube. Figures 12(*a*, *b*) show the calculated temperature and axial velocity profiles along a diameter at different axial locations for $\Omega = 0$, "upward" flow. In the region behind the torch, $\xi < 0$, the gas is being heated and its temperature is lower than the surrounding wall temperature, as shown in Fig. 12(*a*). Near the wall, the decreased density of the gas in conjunction with the effect of gravity aids the axial velocity and the axial velocity there may be larger than that in the core (Fig. 12*b*). In the region ahead of the torch, $\xi > 0$, the wall temperature decreases rapidly to 300 K (Fig. 4). The heated gas flows ahead of the torch and has a higher temperature than the surrounding cold wall surface (Fig. 12*a*). The increased density of the gas near the wall with the effect of gravity retards the axial velocity and results in a flow reversal very close to the wall (Fig. 12*b*).

Figure 13(*a*, *b*) is for "downward" flow for $\Omega = 0$. In the region behind the torch, $\xi < 0$, near the wall, the decreased density of the gas opposes the downward flow and in the central region mass conservation results in larger axial velocities. Near the torch, the gas temperature is very high (low density) and the corresponding axial velocity is very large. Near the torch

the effects of buoyancy are therefore less important and the temperatures and axial velocities for both the upward and the downward flows are similar. Ahead of the torch, $\xi > 0$, in the central region the higher gas temperatures (lower densities) are accompanied by lower axial velocities (Fig. 13*b*). In addition to changes in the axial velocity, there is a strong outward radial flow for both "upward" and "downward" flows in the region near the torch where the gas temperatures are very high (there is a large volume expansion near the torch, Lin et al., 1991). This outward radial velocity near the torch would aid the thermophoretic velocity and enhance the rate of particle deposition. For "downward flow" (Fig. 13*a*) the gas temperature behind the torch, $\xi < 0$, is lower in the central region (than for "upward" flow, Fig. 12*a*) due to the larger axial velocity in the central region (which brings in the colder gas from the upstream region). Therefore, fewer particles form for "downward" flow. Indeed, for "downward flow," only about 26 percent of the inlet $SiCl_4$ ($GeCl_4$) is oxidized very near the torch and the wall and almost all (~ 100 percent) of the SiO_2 (GeO_2) that is formed deposits downstream near the torch (partly because the small axial velocity in the region ahead of the torch cannot carry the particles out of the tube (Fig. 13*b*)). Thus the overall deposition efficiency is about 26 percent and the tapered entry length is only 5 cm. For "upward" flow, however, much more of the gas, i.e., over a larger region, reaches the reaction temperature, T_{rxn}, and about 64 percent of the inlet $SiCl_4$ ($GeCl_4$) is oxidized. The particles formed away from the wall are carried out of the tube because of the large axial velocity there (the large axial velocity downstream of the torch also makes it easier for the particles to be convected downstream) (Fig. 12*b*). About 86 percent of the products are deposited on the tube surface and the overall efficiency, E_T is 55 percent. Since the particles are carried farther and deposited downstream, the deposition layer for one torch traverse will have a longer tapered length for "upward" flow (Table 1).

Tube rotation over a range from $\Omega = 0$ to 120 rpm has little effect on the axial velocity and temperature distributions for a vertical tube. The flow rate will affect the velocity and temperature fields and the corresponding particle deposition. For small Q the buoyancy effects will be more pronounced. The gas temperature may reach T_{rxn} over the entire cross section even for "downward" flow. For this case the small axial velocity ahead of the torch may result in more particles being deposited near the torch, thereby resulting in a shorter tapered length. For "upward" flow, the temperature will also reach T_{rxn} over the entire cross section. However, now the larger axial velocity downstream will allow more particles to be deposited farther downstream or be carried out of the tube and the tapered length will be longer. For higher flow rates, the gas temperatures can only reach T_{rxn} in a region very near the wall and the torch for both cases. Most of the particles will deposit on the surface near the torch and there is probably little difference between the two cases; i.e., the effects of buoyancy are less important at the higher flow rates.

Summary and Conclusions

Numerical solutions have been obtained for particle deposition in studies, which include the effects of variable properties and buoyancy for horizontal and vertical tubes, relative to the modified chemical vapor deposition (MCVD) process. Parameters include tube rotation, torch speed, flow rate, maximum wall temperature, and tube radius. The following conclusions are drawn:

1 Particles are formed near the torch, and for most of the cases studied, near the tube surface. However, for lower flow rates, e.g., $Q = 1$ l/min, or high maximum surface temperatures, e.g., $T_{max} = 1973$ K, particles are formed over the entire cross section (near the torch).

2 Particles formed near the surface are deposited in the region near (and ahead of) the torch. Particles that are formed in the central region are either deposited farther downstream or are convected out of the tube.

3 The deposition per unit area, D/A, for $Q = 3$ l/min is higher than that for $Q = 1$ and for 5 l/min. At the lower flow rates D/A is small because of the corresponding small flow rate of $SiCl_4$. For the higher flow rates, D/A is also small because of the small percentage of particle formation.

4 Higher maximum surface temperatures result in a higher percentage of particle formation and a higher deposition efficiency, but the tapered entry length becomes much longer.

5 In a horizontal tube nonuniform circumferential particle deposition arises from the nonuniform circumferential gas temperature distribution that is present due to buoyancy. Tube rotation has a significant effect on deposition uniformity. As the rotational speed increases, the nonuniformity is greatly reduced. However, tube rotation has only a small influence on the axial distribution of particle deposition.

6 At a fixed flow rate, changing the tube radius has only a slight effect on the overall deposition efficiency. The tube with a smaller radius has a larger particle deposition per unit area.

7 More torch traverses are needed for the case of faster torch speeds to obtain a specified amount of particle deposition. For a single traverse, a slower torch speed will result in more uniform deposition in the circumferential direction.

8 Particle deposition is uniform circumferentially for the vertical tube geometry. However, the effects of buoyancy result in temperature and velocity fields and deposition characteristics that depend on the direction of the flow. The effects of buoyancy in "upward" flow result in a smaller axial flow in the central region behind the torch and a larger axial flow ahead of the torch. The corresponding higher temperatures behind the torch result in more particle formation but the larger velocities ahead of the torch yield a smaller percentage of deposition (of the particles formed) and longer tapers. The opposite is true for "downward" flows; i.e., there is less particle formation, a greater percentage of deposition, and a shorter taper.

Acknowledgments

The interest of Dr. U. C. Paek, Korea Academy of Industrial Technology, in this research is greatly appreciated. Support from the National Science Foundation, the San Diego Supercomputer Center, and the Computing Center of the University of California at Berkeley is gratefully acknowledged.

References

Burmeister, L. C., 1982, *Convective Heat Transfer*, Wiley, New York.

Choi, M., Baum, H. R., and Greif, R., 1987, "The Heat Transfer Problem During the Modified Chemical Vapor Deposition Process," ASME JOURNAL OF HEAT TRANSFER, Vol. 109, pp. 642–646.

Choi, M., Greif, R., and Baum, H. R., 1989, "A Study of Heat Transfer and Particle Motion Relative to the Modified Chemical Vapor Deposition Process," ASME JOURNAL OF HEAT TRANSFER, Vol. 111, pp. 1031–1037.

Choi, M., Lin, Y. T., and Greif, R., 1990, "Analysis of Buoyancy and Tube Rotation Relative to the Modified Chemical Vapor Deposition Process," ASME JOURNAL OF HEAT TRANSFER, Vol. 112, pp. 1063–1069.

DiGiovanni, D., Wang, C. Y., Morse, T. F., and Cipolla, J. W., Jr., 1985, "Laser Induced Buoyancy and Forced Convection in Vertical Tubes," *Natural Convection: Fundamentals and Applications*, S. Kakac, W. Aung, and R. Viskanta, eds., Hemisphere, New York, pp. 1118–1139.

Fiebig, M., Hilgenstock, M., and Riemann, H.-A., 1988, "The Modified Chemical Vapor Deposition Process in a Concentric Annulus," *Aerosol Science and Technology*, Vol. 9, pp. 237–249.

Kim, K. S., and Pratisinis, S. E., 1988, "Manufacture of Optical Waveguide Preforms by Modified Chemical Vapor Deposition," *AIChE J.*, Vol. 34, No. 6, pp. 912–920.

Lin, Y. T., Choi, M., and Greif, R., 1991, "A Three-Dimensional Analysis of the Flow and Heat Transfer for the Modified Chemical Vapor Deposition Process Including Buoyancy, Variable Properties, and Tube Rotation," ASME JOURNAL OF HEAT TRANSFER, Vol. 113, pp. 400–406.

Lin, Y. T., Choi, M., and Greif, R., 1992, "Effect of Solid Layer Relative to the Modified Chemical Vapor Deposition Process," in preparation.

MacChesney, J. B., O'Connor, P. B., DiMarcello, F. V., Simpson, J. R., and Lazay, P. D., 1974a, "Preparational Low-Loss Optical Fibers Using Simultaneous Vapor Phase Deposition and Fusion," *Proc. 10th Int. Congr. Glass*, Kyoto, Japan, pp. 6-40–6-44.

MacChesney, J. B., O'Connor, P. B., and Presby, H. M., 1974b, "A New Technique for Preparation of Low-Loss and Graded Index Optical Fibers," *Proc. IEEE 62*, pp. 1278–1279.

Morse, T. F., DiGiovanni, D., Chen, Y. W., and Cipolla, J. W., Jr., 1986, "Laser Enhancement of Thermophoretic Deposition Process," *J. of Lightwave Technology*, LT-4, No. 2, pp. 151–155.

Nagel, S. R., MacChesney, J. B., and Walker, K. L., 1982, "An Overview of the Modified Chemical Vapor Deposition (MCVD) Process and Performance," *IEEE J. Quantum Electronics*, Vol. QE-18, No. 4, pp. 459–176.

Rosner, D. E., and Park, H. M., 1988, "Thermophoretically Augmented Mass-, Momentum- and Energy-Transfer Rates in High Particle Mass Loaded Laminar Forced Convection Systems," *Chem. Eng. Sci.*, Vol. 43, No. 10, pp. 2689–2704.

Simpkins, P. G., Kosinski, S. G., and MacChesney, J. B., 1979, "Thermophoresis: The Mass Transfer Mechanism in Modified Chemical Vapor Deposition," *J. Appl. Physics*, Vol. 50, pp. 5676–5681.

Talbot, L., Cheng, R. K., Schefer, R. W., and Willis, D. R., 1980, "Thermophoresis of Particles in a Heated Boundary Layer," *J. Fluid Mech.*, Vol. 101, part 4, pp. 737–758.

Walker, K. L., Homsy, G. M., and Geyling, F. T., 1979, "Thermophoretic Deposition of Small Particles in Laminar Tube Flow," *J. Colloid Interface Sci.*, Vol. 69, pp. 138–147.

Walker, K. L., Geyling, F. T., and Nagel, S. R., 1980, "Thermophoretic Deposition of Small Particles in the Modified Chemical Vapor Deposition (MCVD) Process," *J. Am. Ceram. Soc.*, Vol. 63, pp. 552–558.

Wang, C. Y., and Morse, T. F., and Cipolla, J. W., Jr., 1985, "Laser Induced Natural Convection and Thermophoresis," ASME JOURNAL OF HEAT TRANSFER, Vol. 107, pp. 161–167.

An Experimental Investigation of Free Surface Transport, Bifurcation, and Adhesion Phenomena as Related to a Hollow Glass Ampule and a Metallic Conductor

S. C. Chen

K. Vafai
Professor.
Fellow ASME

Department of Mechanical Engineering,
The Ohio State University,
Columbus, OH 43210

An experimental investigation of free surface transport and subsequent bifurcation and adhesion for a hollow glass ampule is presented in this work. Detailed phenomenological features of the process are displayed and discussed. This experimental investigation, which is generic in nature, provides the much needed phenomenological information on free surface transport, glass processing as related to optical fiber production, and glass-to-metal sealing processes. Detailed images of the actual sealing process provide valuable information on identifying and isolating the key regimes in the process and mapping out process defects, and contribute to a basic understanding of the physical mechanisms involved in the sealing process.

Introduction

Glass and ceramic materials have become extremely useful in a variety of applications over the past few decades, especially in the electronic industry. Glasses are best suited for forming mechanically reliable and vacuum-tight fusion seals (hermetic seals) with metals, ceramics and micas, due to their properties, durability, and formability. They also provide mechanical support and environmental protection. For electronic applications, there are two types of glass-to-metal seals that are widely used: matched seals in which the thermal coefficients of expansion of the glass and metal are similar, and compression seals in which the expansion coefficients are mismatched. Currently, a detailed knowledge of the manufacturing process for these seals does not exist and there is heavy reliance on empiricism. A practical need exists to reduce the empiricism in manufacturing hermetic seals by a better understanding of the physics involved in the sealing process so that the seal rejection and postmanufacturing problems can be minimized. This work also sheds some light in free surface glass processing, glass-to-metal contact, and bubble formation problems encountered in optical fiber production.

The glass-to-metal sealing process can be divided into three regimes as shown in Figs. 1, 2, and 3. To investigate the generic phenomenological information on free surface transport and glass-to-metal sealing processes, the glass ampule is heated by a laser heat source. For this generic arrangement, for the first regime, a glass ampule is heated by the laser beam from both radial directions of the outer surface of the glass tube. This regime is purely a conduction-dominated problem up to the point when the temperature of the glass reaches the melting point. After reaching the pseudo-melting point, it enters the second regime and conduction is no longer the dominant mode. Because of the pressure difference induced by the laser beam striking the outer surface (Eckert and Drake, 1972), the inner and outer surfaces start moving inward, up to the point where

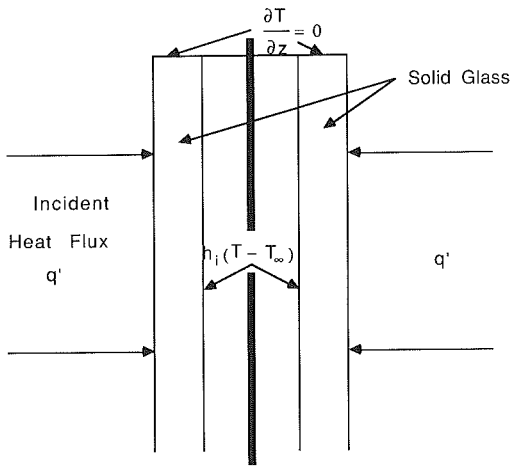

Fig. 1 Schematic diagram for the first regime of the sealing process

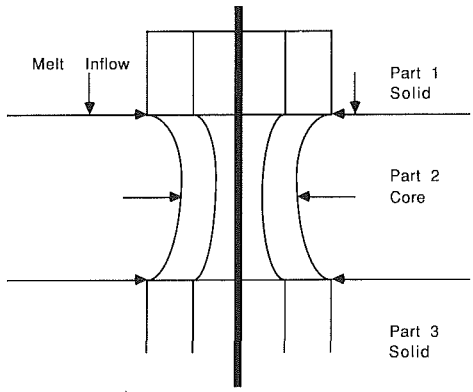

Fig. 2 Schematic diagram for the second regime of the sealing process

Contributed by the Heat Transfer Division for publication in the JOURNAL OF HEAT TRANSFER. Manuscript received by the Heat Transfer Division June 25, 1991; revision received December 19, 1991. Keywords: Materials Processing and Manufacturing Processes, Moving Boundaries, Thin-Film Flow.

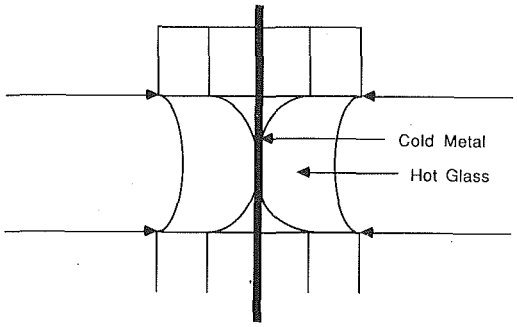

Fig. 3 Schematic diagram for the third regime of the sealing process

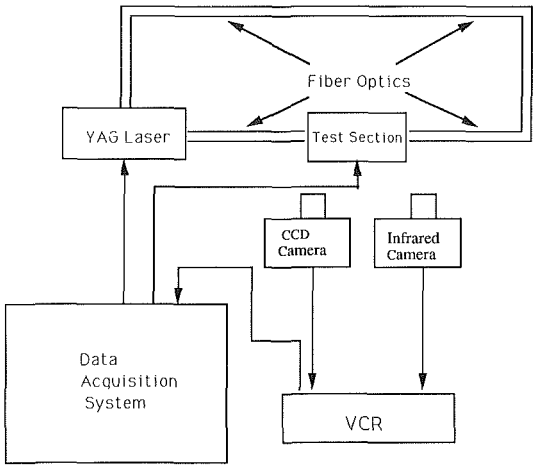

Fig. 4 Experimental setup for investigating the free surface transport and glass-to-metal sealing process

the inner surface touches the conductor. After the inner surface touches the conductor, it enters the third regime of the sealing process. During the third regime, glass material, which is right on the top of the core regime, feeds into the core regime. The third regime marks the bifurcation and adhesion leading to the complete sealing process.

Several aspects of the glass-to-metal seals have been under investigation for a long time. Buckley (1979) and Miska (1976) presented a general glass-to-metal seals application guide and described several types of seals available in the industry. Haim et al. (1982) discussed that adhesion, which involves solidified glass, must begin with the wetting of the metal surfaces by the glass melt, and also presented the experimental method for comparing the tendency of glass melts to wet metal surfaces. Wang et al. (1986) concluded that wetting and adherence between glass and metal can be improved by adding certain specific additives to the glass, and some preliminary aspects of glass-to-metal sealing were discussed by Vafai (1991). To this end, the formulation and numerical simulation of the free-surface transport within a hollow glass ampule were analyzed by Vafai and Chen (1992).

It is quite important to note that very little work has been done in the phenomenological understanding of the sealing process. Such an understanding will help in identifying and mapping out process defects and providing some basic information in the area of free surface transport. In the present study, we are aiming at a basic understanding of the formation of seals through an experimental investigation. This problem is generic in nature; therefore it will provide us with much

Table 1 Input information for cases 1 to 6

Case	Related Figures	Input Power (watt)	Heating Characteristics (Sec)	Incidence Location (mm) (from top end)	Observations
1	10I, 10II	34	10	2.54	Loose Seal and Single Bubble Formation
2	11I, 11II 11III	48	10	2.54	*Rupture of the Hollow Glass* Ampule and Asymmetrical Seal Formation
3	12I, 12II 12III	48	6 4 6	2.54	Single Bubble Formation and Asymmetrical Seal Formation *due to the Inclination of the* Metallic Conductor
4	13I, 13II 13III	34	14	2.54	No Bubble Formation
5	14I, 14II 14III	48	8 3 6	2.54	Small Diameter Bubble Formation
6	15I, 15II 15III	48	8 3 6	1.91	No Bubble Formation

needed information on free surface transport, bifurcation, and adhesion phenomena. Detailed images of the actual sealing process provide valuable information on identifying and isolating the key regimes in the process, and contribute to a basic understanding of the physical mechanisms involved in the sealing process.

Experimental Apparatus and Procedure

The apparatus used in our experimental investigation is depicted in Fig. 4. The hollow glass ampule used in the present study is made by the Schott Technical Glass Company (1982). Some glass products with part numbers such as 8512, 8515, 8516, 8530, and 8533 are commonly used for the glass-to-metal sealing processes. Thermal radiative absorption is desirable for these types of sealing processes, and for this reason, all the glasses have a special coating (doped with FeO), which enables them to absorb most of the thermal radiation in the infrared range. The type of glass tube used in the present experimental investigation is 8530 with $D_i = 0.2642$ cm, $D_o = 0.3353$ cm, and $H = 1.8136$ cm. The other types of glass tubes have displayed features similar to those presented for 8530. The wavelength of the YAG laser is 1.064 μm, which is in the infrared range. At this wavelength, the chosen glass tube absorbs 85 percent of the radiation striking its surface. Therefore, the radiative output from the YAG laser will mostly contribute to an increase in the temperature of the glass ampule. The metal conductor is made of a material with a thermal expansion coefficient similar to the glass ampule. This then corresponds to a matched sealing process. The surface of the metallic rod possesses certain degree of roughness which enhances the adhesion between the inner surface of the glass ampule and that of the metallic conductor.

The experimental setup, depicted in Fig. 4, consists of the laser system, transmitting system, testing section, image processing system, and control system. The diameter of the laser beam is 3.0 mm and its power distribution is Gaussian. The power of the laser beam from each of the fiberoptics couplers ranges from 0 to 64 W. Changing the output power can be done by adjusting the laser lamp current. In the present experimental setup, the lamp current can be adjusted either manually or by the central processing unit. In our experiments, the pulse mode for the laser can also be utilized. However, at this stage we are more interested in the effects of different types of continuous power supply from the YAG laser, shown in

Nomenclature

D_i = inner diameter of the glass ampule, cm
D_o = outer diameter of the glass ampule, cm
H = height of the glass ampule, cm
T = temperature, °C
T_e = inner surface temperature, °C
T_o = outer surface temperature, °C

Table 1. Control signals are sent out by the D/A converter within the data acquisition system. On receiving the command from the computer, the output power from the laser changes. It takes less than 100 ms to achieve steady output from the laser. In the present experiment, ramping or constant power control signals will be sent out from the computer, and the output from the laser will be varied during the process. The laser beam is transmitted through a fiber optics system. One of the important incentives behind our choice for a fiber optics system instead of a traditional optical system was to obtain a more uniform laser beam. The use of the fiber optical system tends to homogenize the laser beam in the fiber tube during the transmission process, resulting in a beam that is spatially more uniform. The main drawback for using a fiber optics system is the loss of power, which can be as high as 15 percent. However, this does not pose any problems since we have access to significantly more power than we need in our experiments.

The test section is composed of two major parts, the holding mechanism and the rotating mechanism. The mechanism used to hold the glass ampule is a bracket with a clamp to adjust the inside diameter. The glass ampule is placed inside the bracket and is then tightened up by the clamp. The position of the metal rod placed inside the glass tube is an important parameter in the third regime of the sealing process. So, three separate micropositioners are used to control the position of the metal rod more accurately. The output coupler of the fiber optics system is also an important mechanism, and is controlled by another micropositioner. This micropositioner controls the striking location of the laser beam on the glass tube and the subsequent amount of glass material fed into the core regime during the third regime of the sealing process. The other important purpose of this mechanism is to ascertain whether the laser beams are aligned on each other. The output coupler micropositioner is adjustable in the z direction; allowing the range of striking locations to be from the center to the very top of the glass ampule. The effects of the striking location on the glass ampule, the location and angle of the metallic conductor, the ramping up or down of the power level, and the magnitude of that power itself can be fully investigated by our present experimental setup.

Two pieces of equipment are involved in the images processing system: the CCD camera and the infrared imaging system. The movement of the free surface and temporal temperature distribution of the outer surface are captured and processed by our imaging processing system. The CCD camera is used to track the movement of the glass ampule, and the infrared camera tracks the temperature change of the outer surface of the glass tube during the sealing process. The CCD camera used in our experiment takes 30 frames per second. Images from the CCD camera are monitored in real time during the sealing process. A frame-grabber is used for transferring the images from the CCD camera to the computer. Images from the CCD camera are first digitized and stored in the frame-grabber's memory, and then transferred to the computer using a Rs-170 port.

The infrared imaging system (IIS) used in our experiment maps out the spatial domain over the outer free surface in real time. Color thermographs from the infrared imaging system are recorded and analyzed in the present investigation. The IIS also has the capability of zeroing in on a particular point, much like a thermocouple reading. Also, an area function associated with the IIS can be used to obtain the average temperature value for a sample area. Like other high-precision devices, the infrared camera needs to be calibrated. Images from the IIS were transferred via the RS-170 port to the frame-grabber for further analysis.

The control system for the experimental setup consists of the CPU unit, D/A board, IEEE-488 board, frame-grabber, HP-3458A used as a multimeter, and HP-3497A used as temperature measurements control unit. The CPU unit is the master control unit of the system. All the control signals are sent from the master control unit through a GPIB bus and the D/A board. Since the infrared imaging system can only display the temperature distribution for the outer free surface, a thermocouple temperature measurement setup shown in Fig. 5 measures the temperature of the inner free surface of the glass ampule. A thermocouple with a diameter of 0.001 in. and a response time of 0.05 s was used in our experiments. The thermocouple was connected to the HP3497 and the voltage signal from the thermocouple was processed by the HP3458A unit and sent to the CPU by the GPIB bus. At a sampling rate of ten measurements per second, 50–60 temperature measurements were taken during the sealing process. The thermocouple was positioned at the center of the inner surface of the glass ampule to measure the center temperature of the tube.

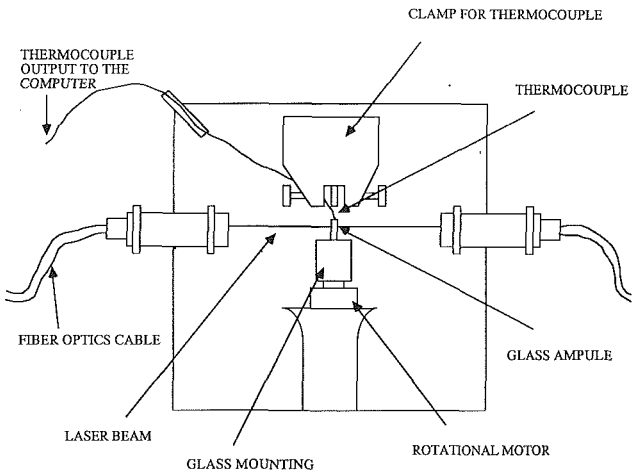

Fig. 5 Experimental setup for temperature measurement of a hollow glass ampule by a thermocouple

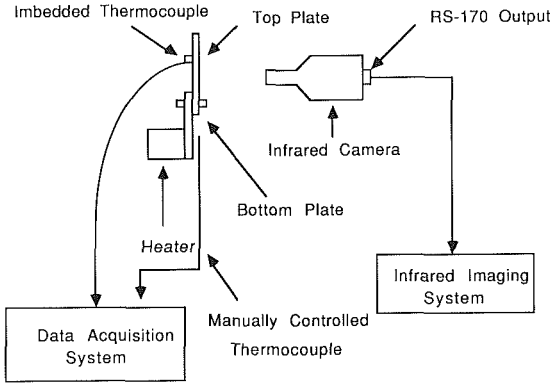

Fig. 6 Configuration of the setup for the calibration of the infrared image system

Proper background lighting is important in capturing details of the free surface transport and subsequent bifurcation and adhesion processes. Under normal background lighting, the glass ampule is almost invisible to our imaging system. After many preliminary tests, a 75 mm lens having a variable aperture combined with extension tubes and an X2 extender was found to give the clearest image. Also, after many tests, it was found that a combination of two 500 W lights, a piece of white paper attached right behind the glass tube, a lens assembly including a 75 mm lens with 5.6 f-stop, and an orange filter would eliminate the glare while providing the proper background lighting.

The calibration of the infrared imaging system was done through the setup in Fig. 6. The bottom plate shown in Fig. 6 is made of oxidized aluminum, and can be heated to 250°C.

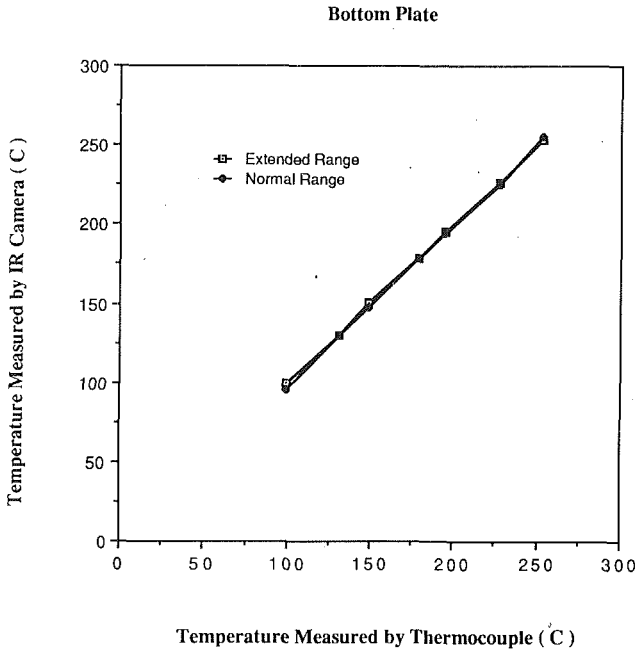

Fig. 7 Relationship between the temperatures measured by the infrared image system at normal and extended range and by the thermocouple for the bottom plate

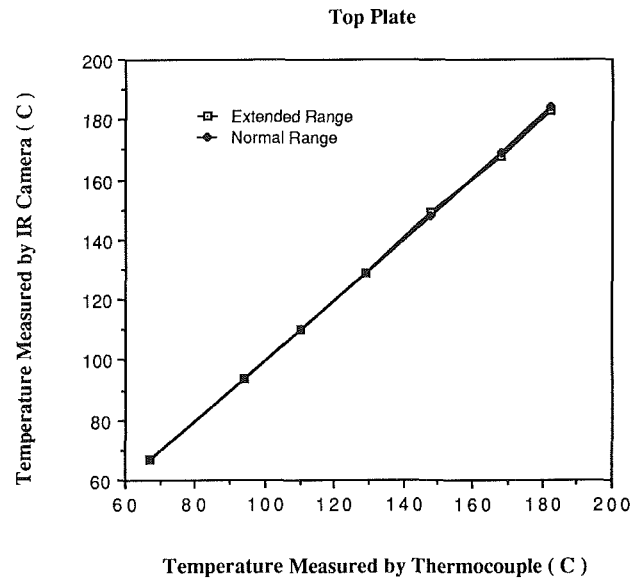

Fig. 8 Relationship between the temperatures measured by the infrared image system at normal and extended range and by the thermocouple for the top plate

The top plate made of aluminum with a black coating can be heated to 180°C. The temperature of the top at a known location is continuously monitored by an imbedded thermocouple connected to a digital thermometer, while the temperature of the bottom plate at a specified location is taken manually by another thermocouple. When the temperatures of both plates becomes stable based on the thermocouple reading, the IIS is focused on the location of the known temperatures. This process is repeated for a variety of temperature settings on the hot plates. The results are shown in Figs. 7 and 8. As can be seen, the results are accurate to within 1 percent. Both plates had a constant value of emissivity over the temperature range used in the calibration experiments. Also, the glass ampule used in the experiments had essentially a constant emissivity (Schott, 1982). As was mentioned earlier, the sealing

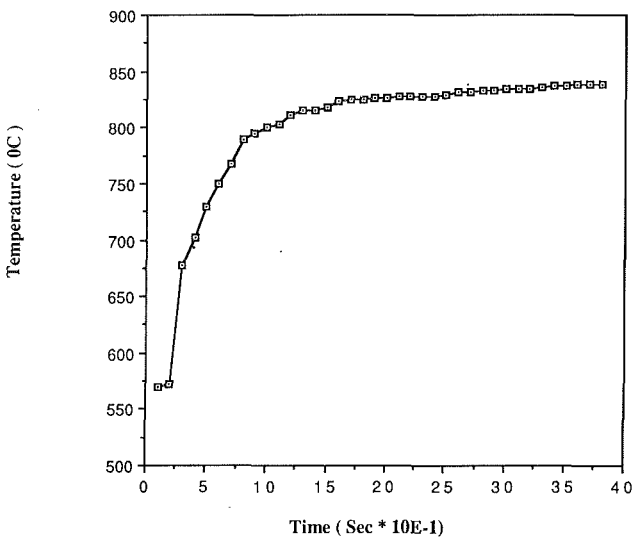

Fig. 9 Temporal temperature distribution for the inner surface for case 6

process can be divided into three regions. These are the first, second, and third regimes. As seen in Figs. 10–15, once the core regime reaches the pseudo-melting point, the inner and outer free surfaces move inward. The actual temperatures shown in Fig. 9 are temperatures of the center point of the inner surface for case 6, described in Table 1. These values were obtained by using the setup depicted in Fig. 5 during the sealing process. Figure 9 displays the temperature changes of the inner surface from the beginning of the sealing process for case 6. From 0 to 1 s, temperature increases are apparently confined to the first regime of the process. From 1 s to 4 s, temperature increases slowly with little fluctuation. This corresponds to the second regime of the sealing process.

The experimental procedure was done in the following sequence. First, the heating characteristics were specified. For a specified incidence location of the laser beam, the CCD and IIS would then be adjusted. Next, the image processing program would be initialized. Finally, the master control program would be initialized leading to the full execution of the experiment.

Results and Discussion

Figures 10 to 15 are images taken by the CCD camera and processed by our imaging system for six different cases. These cases were chosen such that they would reveal some pertinent information on the basic aspects of the free surface transport and bifurcation and adhesion phenomena for the glass ampule and the glass-to-metal seal formation. The heating input characteristics, the incidence locations, and the specific observations are displayed in Table 1. For case 1, the seal turned out to be loose with a single bubble formation. As seen in Fig. 10, the loose seal was caused by the low input power from the laser. This resulted in a low quantity of the glass material above the core region to reach the melting temperature. Enough of this glass material is needed for the proper seal formation. Therefore, a premature temperature drop resulted in the solidification of the glass material on the outer surface of the core region, preventing the upper part of the glass from feeding into the core region. This premature temperature drop is also responsible for the formation of the thermal crack within the seal as seen in Fig. 10(*e*).

Based on the outcome of case 1, the input power from the laser was increased for future cases using the same heating duration and incidence position as case 1. As seen in Fig. 11, the hollow glass ampule ruptures at $t = 3$ s, resulting in an

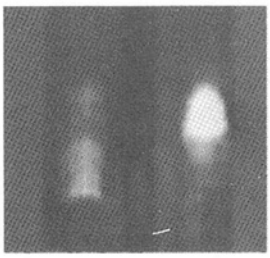

(a) t = 3 Sec

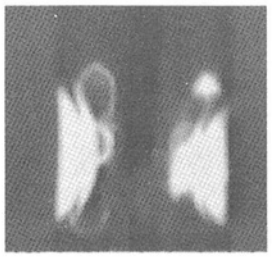

(b) t = 4 Sec

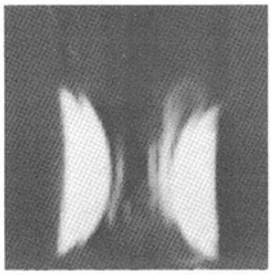

(c) t = 5 Sec

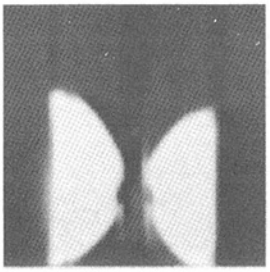

(d) t = 6 Sec

Fig. 10 I

(e) t = 7 Sec

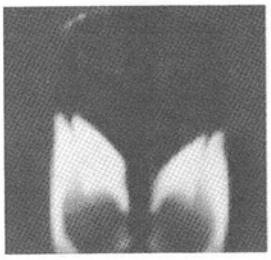

(f) t = 8 Sec

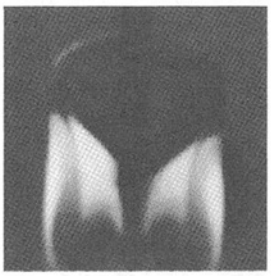

(g) t = 9 Sec

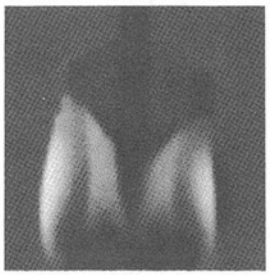

(h) t = 10 Sec

Fig. 10 II

Fig. 10 Images for the sealing process for case 1

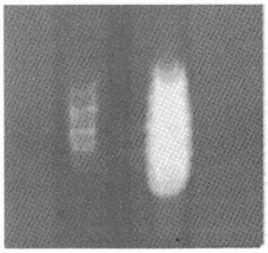

(a) t = 1 Sec

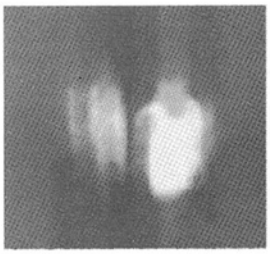

(b) t = 2 Sec

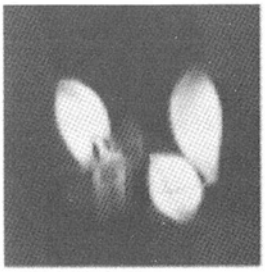

(c) t = 3 Sec

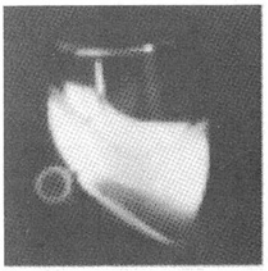

(d) t = 4 Sec

Fig. 11 I

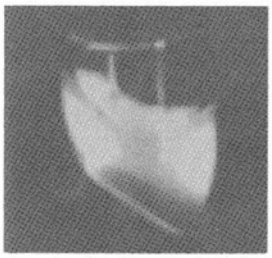

(e) t = 5 Sec

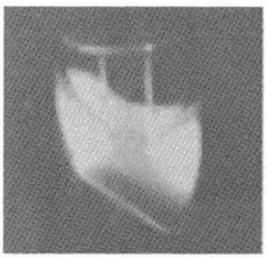

(f) t = 6 Sec

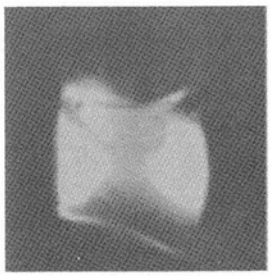

(g) t = 7 Sec

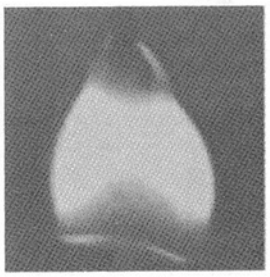

(h) t = 8 Sec

Fig. 11 II

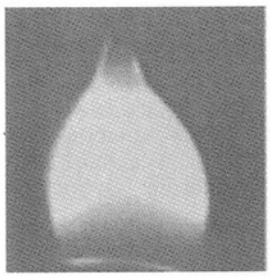

(i) t = 9 Sec

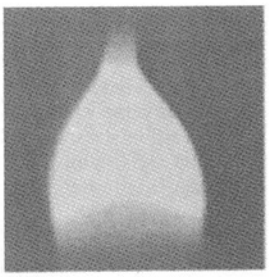

(j) t = 10 Sec

Fig. 11 III

Fig. 11 Images for the sealing process for case 2

asymmetric formation of the seal. This rupture phenomenon is most probably caused by the high input power. It is interesting to note that the final seal formation does not show any visible signs that it has endured a rapture. Yet, the intermediate rupture will significantly alter the final strength and durability of the seal.

The heating characteristic was changed from a constant heat supply to a ramp type based on the results obtained for case 2. The sealing characteristics for case 3 are listed in Table 1. The incentive for using a ramp type of heat input was based on physical considerations for decreasing the temperature gradient through the initial heat up and the final cool down of the process. This, in turn, reduces the chances for the occurrence of a thermal crack. As seen in Fig. 12, ramping of the

(a) t = 1 Sec

(b) t = 2 Sec

(c) t = 3 Sec

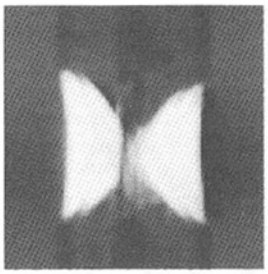

(d) t = 4 Sec

Fig. 12 I

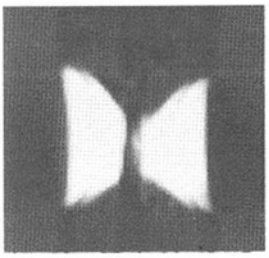

(e) t = 5 Sec

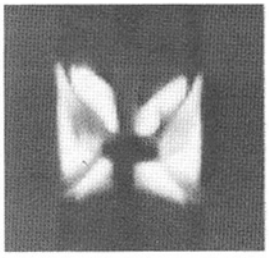

(f) t = 6 Sec

(g) t = 7 Sec

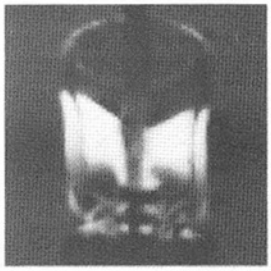

(h) t = 8 Sec

Fig. 12 II

(i) t = 9 Sec

(j) t = 10 Sec

(k) t = 11 Sec

(l) t = 12 Sec

Fig. 12 III

Fig. 12 Images for the sealing process for case 3

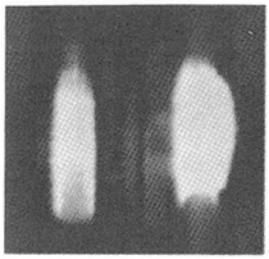

(a) t = 5 Sec

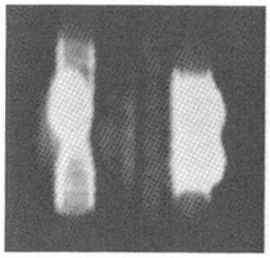

(b) t = 6 Sec

(c) t = 7 Sec

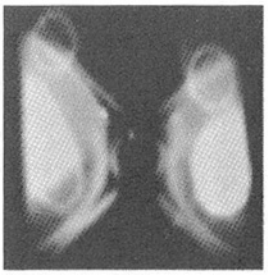

(d) t = 8 Sec

Fig. 13 I

heat supply eliminated the rupture phenomena. However, a relatively large size bubble was formed at the center of the seal. The mechanism for the formation of the bubble can be explained from a heating characteristics point of view. As seen in Fig. 12, a cavity is formed at $t = 10$ s, which gradually shrinks as the glass material from the upper part feeds into the cavity and fills the space that was earlier occupied by air. Therefore, it is plausible to expect no bubble if more glass material from the upper part would be fed into the cavity. As seen in Table 1 for case 3, the heat supply is decreased during the final 6 s. This results in a sharp drop in the overall temperature of the glass, which results in a significant increase in its viscosity. This higher viscosity literally stops the feeding glass material into the cavity, which results in the formation of the bubble.

To resolve this situation, a constant power heating was used again in case 4, to avoid the bubble formation. Also, to avoid the rupture phenomena (case 2), a lower input power level over a longer heating duration was used. Details of the heating characteristics and duration are listed in Table 1. As seen in Fig. 13, the quality of the seal for this case is much better than the former three cases. Cases 3 and 4 have made it amply clear that the lack of heat supply at the final stage is the major reason for the bubble formation. The ramping type heat supply was investigated again in case 5, since this type of heating is expected to exert the least amount of adverse thermal stresses during the critical start up and final stages of the process. A detailed description of the sealing parameters are listed in Table 1. This time, the ramp up duration has been increased based on the phenomenon occurring in case 3. As seen in Fig. 14, there is a bubble formation inside the seal; however, the diameter of the bubble becomes much smaller than that in case 3. This result clearly shows that the bubble formation is related

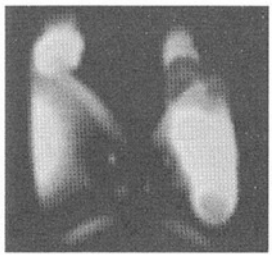

(e) t = 9 Sec

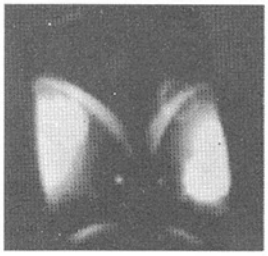

(f) t = 10 Sec

(g) t = 11 Sec

(h) t = 12 Sec

Fig. 13 II

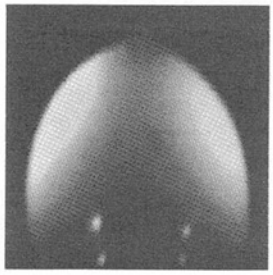

(i) t = 13 Sec

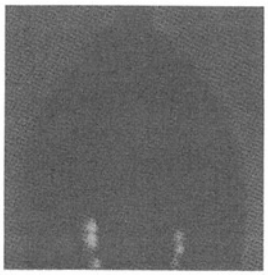

(j) t = 14 Sec

Fig. 13 III

Fig. 13 Images for the sealing process for case 4

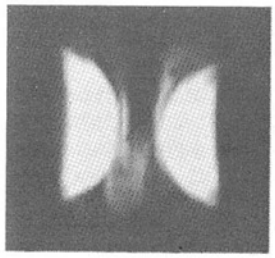

(e) t = 7 Sec

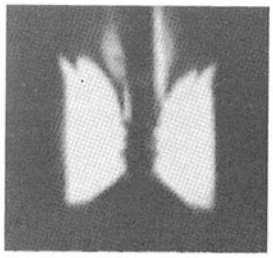

(f) t = 8 Sec

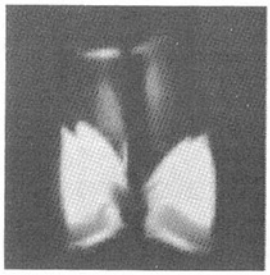

(g) t = 9 Sec

(h) t = 10 Sec

Fig. 14 II

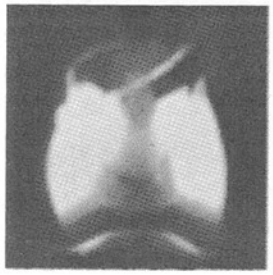

(i) t = 11 Sec

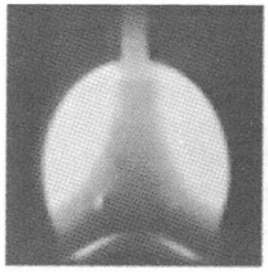

(j) t = 12 Sec

Fig. 14 III

Fig. 14 Images for the sealing process for case 5

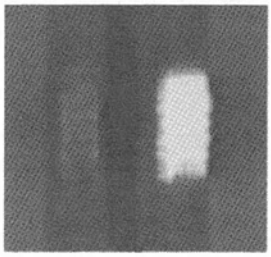

(a) t = 3 Sec

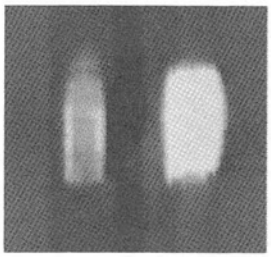

(b) t = 4 Sec

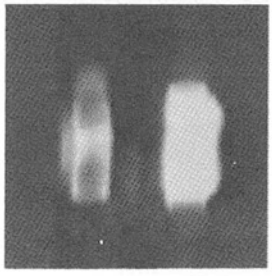

(c) t = 5 Sec

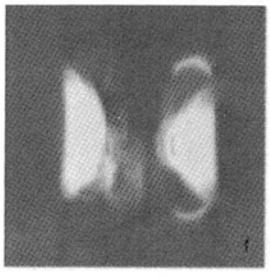

(d) t = 6 Sec

Fig. 14 I

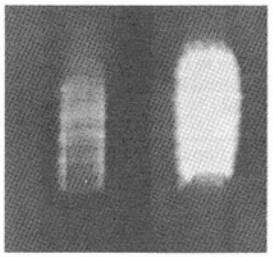

(a) t = 5 Sec

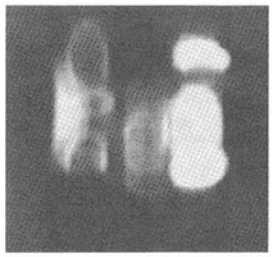

(b) t = 6 Sec

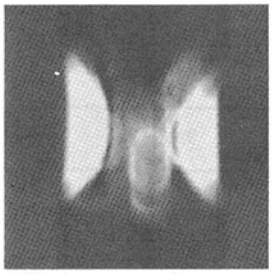

(c) t = 7 Sec

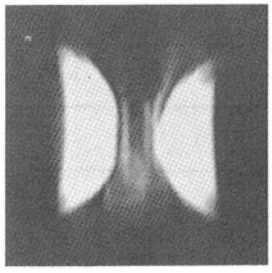

(d) t = 8 Sec

Fig. 15 I

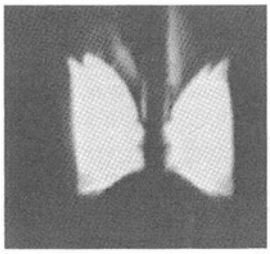

(e) t = 9 Sec

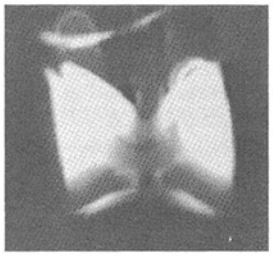

(f) t = 10 Sec

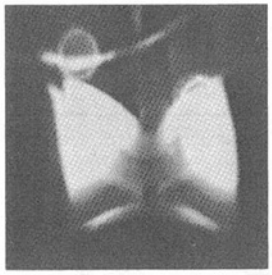

(g) t = 11 Sec

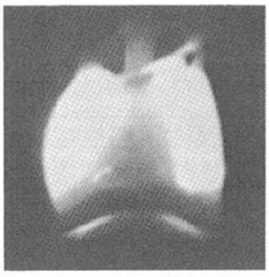

(h) t = 12 Sec

Fig. 15 II

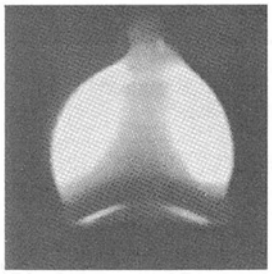

(i) t = 13 Sec

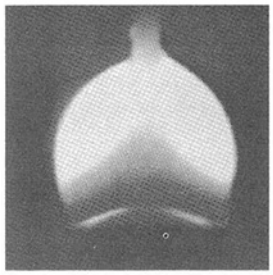

(j) t = 14 Sec

Fig. 15 III

Fig. 15 Images for the sealing process for case 6

Table 2 Quantitative information on the times related to the different regimes in the experimental runs

Case	Time for the Inner Surface Hitting the Metallic Conductor Within the Second Regime (Seconds)	Time for the Upper Solid Glass to be Fed into the Centeral Region of the Glass Tube. (Seconds)
1	1.7	Not Enough Energy to Melt the Upper Part of the Glass.
2	The Glass Ampule Ruptures	7.63
3	2.00	7.70
4	1.77	10.86
5	2.40	11.17
6	2.31	9.68

to the amount of heat supply, among other variables. Case 6 is based on the same power and heating characteristics as in case 5. The only difference is that in case 6, the incidence location was raised. This means that less glass material from the upper part is needed for the sealing process. Therefore,

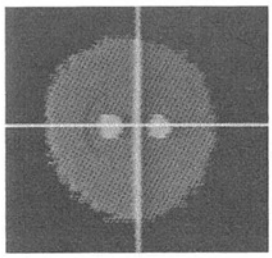

(a) t = 5 Sec

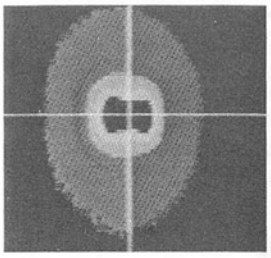

(b) t = 6 Sec

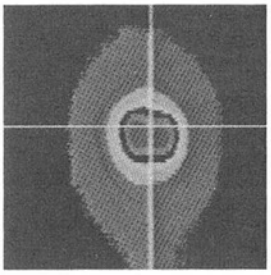

(c) t = 7 Sec

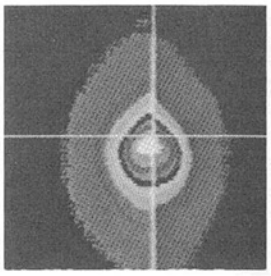

(d) t = 8 Sec

Fig. 16 I

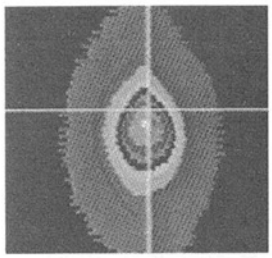

(e) t = 9 Sec

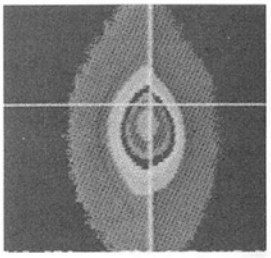

(f) t = 10 Sec

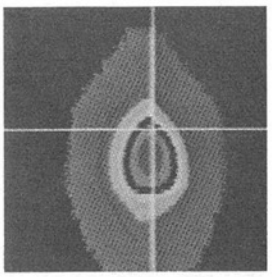

(g) t = 11 Sec

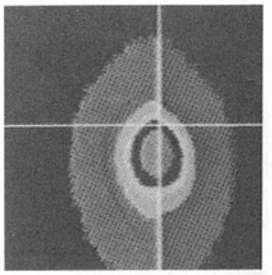

(h) t = 12 Sec

Fig. 16 II

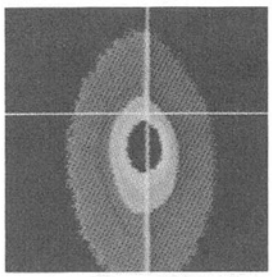

(i) t = 13 Sec

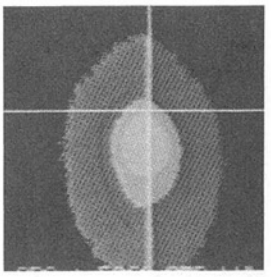

(j) t = 14 Sec

Fig. 16 III

Fig. 16 Thermographs for the sealing process for case 6

with the same heating characteristics as in case 5, we should be able either to decrease further the bubble size or to eliminate it altogether. This indeed turns out to be the case as seen in Fig. 15 for case 6, for which there is no bubble formation inside the seal. Quantitative information on the times related to the different regimes in the experimental runs are given in Table 2. These tables plus all the detailed relevant qualitative information on the free surface transport, bifurcation, and adhesion constitute an important source for benchmarking of various free surface numerical schemes and models.

Thermographs for the outer surface of the glass ampule captured by the infrared imaging system for case 6 are displayed in Fig. 16. It can be clearly seen that as the laser beam strikes the outer surface of the glass ampule, radiation energy is absorbed and temperature of the glass ampule increases. The cross-line seen in Fig. 16 describes the POINT function of IIS and is not related to the temperature field on and around the glass ampule. The movement of the free surface is clearly shown in Fig. 16 as the size of the thermographs continues to change during the sealing process. Figure 16 clearly establishes the fact that even for the processes that do not involve the rotation of the glass ampule, the temperature field is still quite symmetric around the z axis.

Based on the outcomes of cases 1 to 6, it can be seen that a systematic experimental investigation of various parameters involved in the glass-to-metal sealing process reveal some crucial phenomena on the free surface transport and bifurcation and adhesion processes. This information can have a significant effect in increasing the reliability, endurance, and quality of the seal.

Conclusion

Detailed phenomenological descriptions of the free surface transport, bifurcation, and adhesion characteristics related to glass-to-metal sealing processes were presented in this work. For the first time, process defects such as bubble formation were displayed and were related to the other physical attributes of the sealing phenomena. By analyzing detailed images of the sealing process, the effects of various other parameters, such as power distribution, heating duration, and striking location on the quality of the seal were established. The effects of the pertinent physical parameters have been discussed in detail and the governing mechanisms for properly understanding the observed phenomena have been discussed and shown to be intimately tied to the heat transfer characteristics. The results of the present work can have a significant impact in identifying and isolating the key regimes in the process, and contribute to a basic understanding of the physical mechanisms involved in the sealing process and the related free surface transport and bifurcation phenomena. The present work also clarifies various aspects such as free surface glass processing, glass-to-metal contact, and bubble formation problems as related to the production of the optical fibers.

Acknowledgments

Grants from National Science Foundation (CTS-8817747) and Edison Welding Institute (EES 312516) are acknowledged and greatly appreciated.

References

Buckley, R. G., 1979, "Glass-to-Metal Seals—What You Need to Know," *Ceramic Industry Magazine*, Vol. 112, pp. 20–23.

Eckert, E. R. G., and Drake, X. X., 1972, *Analysis of Heat and Mass Transfer*, McGraw-Hill, New York.

Haim, B. Z., Grodentizk, G., and Rigbi, Z., 1982, "The Wetting of Metal Surface by a Glass Melt," *Glass Technology*, Vol. 23, No. 3.

Miska, K. H., 1976, "How to Obtain Reliable Glass- and Ceramic-to-Metal Seals," *Materials Engineering*, Vol. 83, pp. 32–35.

Schott Product Catalog, 1982, "Schott Technical Glass, Schott Glass Company," West Germany.

Vafai, K., 1991, "Analysis of Heat Transfer Phenomena in Glass-to-Metal Seals," *International Communications in Heat and Mass Transfer*, Vol. 18, pp. 171–184.

Vafai, K., and Chen, S. C., 1992, "Analysis of Free-Surface Transport Within a Hollow Glass Ampule," *Numerical Heat Transfer*, Part A, in press.

Wang, M., Ge, Manzhen, Cheng, F., Yu, Z., and Tang, Y., 1986, "The Effect of a Small Amount of Oxide Additives on the Wetting Behavior of Glass on Metal," *Journal of Non-Crystalline Solids*, Vol. 80, pp. 379–386.

Journal of Heat Transfer

Technical Notes

This section contains shorter technical papers. These shorter papers will be subjected to the same review process as that for full papers.

Transient Response of Crossflow Heat Exchangers With Finite Wall Capacitance

H.-T. Chen[1] and K.-C. Chen[1]

Nomenclature

- A^* = heat transfer surface, m^2, also ratio of mass flow rate given in the appendix
- c = specific heat, J/kg K
- H = dimensionless total length parameter shown in Table 1
- h = heat transfer coefficient, W/m^2 K; also dimensionless space parameter given in the appendix
- L = exchanger length, m
- m = mass flow rate, kg/s
- M = mass of exchanger, kg
- N = dimensionless exchanger length
- R = heat transfer resistance ratio
- s = Laplace transform parameter
- t = dimensionless time variable
- T = dimensionless temperature
- $\bar{T}$ = dimensionless temperature in the transform domain
- u = fluid velocity, m/s
- V = heat capacity ratio
- x, y = dimensionless space variables
- β = constant value
- ξ, η = space variables, m
- τ = time variable, s
- ψ = primary fluid inlet temperature, K

Subscripts

- a = prime fluid
- b = secondary fluid
- w = solid wall

Introduction

Dusinberre (1959) proposed a finite difference method to obtain the transient behavior of crossflow heat exchangers with both fluids unmixed. Evans and Smith (1962) showed a detailed analysis for such problems and obtained their analytical solutions with arbitrary variation of time in the inlet temperatures of both fluids. However, in the work of Evans and Smith (1962), the heat capacity of the tube wall was not taken into account. Thus the governing differential equations were obtained only for the fluids. Tan and Spinner (1984) applied the method of characteristics in conjunction with the modified Euler's method to determine the numerical solution of continuous countercurrent processes in the nonsteady state. This method can also be applied to crossflow heat exchangers only with proper modification of the characteristic lines and boundary conditions. Spiga and Spiga (1987) presented analytical solutions to the transient temperature distributions of the core wall and both the unmixed gases with arbitrary initial and inlet conditions by using the threefold Laplace transform. Afterward, Spiga and Spiga (1988) applied the same method to determine the transient temperature distributions of the core wall and both fluids with a deltalike perturbation in the inlet temperature of the primary fluid.

The present work applies the Laplace transform method with respect to time to analyze the same problem given by Spiga and Spiga (1988). It can be found from the work of Chen (1991) that the results obtained from the present method are in good agreement with those given by Spiga and Spiga (1987, 1988). Details can be found in the work of Chen (1991). The main aim of this work is to develop a straightforward computer code for the transient response of crossflow heat exchangers with both fluids unmixed and finite wall heat capacity. The transformed temperatures of the core wall and both fluids expressed in the form of power series are specialized to describe arbitrary time varying inlet temperature of the primary fluid. These transformed temperatures expressed in the form of power series are so regular that they are easily written in a computational program. Moreover, it is not difficult to invert the transformed temperatures to the physical quantities by using the numerical inversion method of Honig and Hirdes (1984). For the problem of present method has considerable saving in the computer time because of a fast rate of convergence.

Analysis

The dynamic response of crossflow heat exchangers with walls separating the two fluid streams is investigated. Stream a flows through a set of tubes or plates arranged in a bank. Stream b threads its way through the spaces at right angles to the bank. The mathematical model has been developed resorting to the simplifying assumptions by Spiga and Spiga (1988). The dimensionless space and time-dependent variables are:

$$t = \frac{(hA^*)_a}{Mc_w}\tau \tag{1a}$$

$$x = \frac{(hA^*)_a \xi}{(mc)_a L_a} \tag{1b}$$

$$y = \frac{(hA^*)_b \eta^*}{(mc)_b L_b} \tag{1c}$$

On the basis of these assumptions and parameters, Spiga

[1] Department of Mechanical Engineering, National Cheng Kung University, Tainan, Taiwan 701.

Contributed by the Heat Transfer Division of THE AMERICAN SOCIETY OF MECHANICAL ENGINEERS. Manuscript received by the Heat Transfer Division January 1991; revision received January 1992. Keywords: Direct-Contact Heat Transfer, Heat Exchangers, Numerical Methods.

and Spiga (1988) applied the energy equation to both fluids and the wall to obtain three simultaneous partial differential equations.

$$\frac{\partial T_w}{\partial t}+(1+R)T_w=T_a+RT_b \tag{2a}$$

$$\frac{\partial T_a}{\partial x}+V_a\frac{\partial T_a}{\partial t}+T_a=T_w \tag{2b}$$

$$\frac{\partial T_b}{\partial y}+\frac{V_b}{R}\frac{\partial T_b}{\partial t}+T_b=T_w \tag{2c}$$

for $t>0$, $0\le x\le N_a$ and $0\le y\le N_b$.

The corresponding initial and inlet conditions are given as

$$T_w(x, y, 0)=T_a(x, y, 0)=T_b(x, y, 0)=0 \tag{3a}$$

$$T_a(0, y, t)=\varphi(t) \tag{3b}$$

$$T_b(x, 0, t)=0 \tag{3c}$$

The dimensionless physical parameters R, V_a, V_b, N_a, and N_b are

$$R=\frac{(hA^*)_b}{(hA^*)_a} \quad V_a=\frac{(mc)_a}{Mc_w}\frac{L_a}{u_a} \quad V_b=\frac{(mc)_b}{Mc_w}\frac{L_b}{u_b}$$

$$N_a=\frac{(hA^*)_a}{(mc)_a} \quad N_b=\frac{(hA^*)_b}{(mc)_b} \tag{4}$$

Mathematical Formulation

The Laplace transform of $T_\alpha(x, y, t)$ corresponding to t and its inversion formula are, respectively, defined as

$$\tilde{T}_\alpha(x, y, s)=L\{T_\alpha(x, y, t)\}=\int_0^\infty T_\alpha(x, y, t)e^{-st}dt \tag{5a}$$

$$T_\alpha(x, y, t)=L^{-1}\{\tilde{T}_\alpha(x, y, s)\} \tag{5b}$$

where $\alpha=w, a, b$.

Taking the Laplace transform of Eqs. (2), (3b), and (3c) with respect to t with initial condition (3a) yields:

$$\tilde{T}_w=\frac{1}{1+R+s}\tilde{T}_a+\frac{R}{1+R+s}\tilde{T}_b \tag{6a}$$

$$\frac{\partial \tilde{T}_a}{\partial x}+(V_as+1)\tilde{T}_a=\tilde{T}_w \tag{6b}$$

$$\frac{\partial \tilde{T}_b}{\partial y}+\left(\frac{V_bs}{R}+1\right)\tilde{T}_b=\tilde{T}_w \tag{6c}$$

and the transformed boundary conditions:

$$\tilde{T}_a(0, y, s)=\tilde{\varphi}(s)=\int_0^\infty \varphi(t)e^{-st}dt \tag{7a}$$

$$\tilde{T}_b(x, 0, s)=0 \tag{7b}$$

The substitution of Eq. (6a) into Eqs. (6b) and (6c) can reduce the problem to a set of first-order partial differential equations:

$$\frac{\partial \tilde{T}_a}{\partial x}+A\,\tilde{T}_a=B\,\tilde{T}_b \tag{8a}$$

$$\frac{\partial \tilde{T}_b}{\partial y}+C\,\tilde{T}_b=D\,\tilde{T}_a \tag{8b}$$

where

$$A=V_as+1-\frac{1}{1+s+R} \qquad B=\frac{R}{1+s+R}$$

$$C=\frac{V_bS}{R}+1-\frac{R}{1+s+R} \qquad D=\frac{1}{1+s+R} \tag{9}$$

It is seen that the problem has now been reduced to solving Eqs. (8) with conditions (7) for $\tilde{T}_a$ and $\tilde{T}_b$.

The function $\tilde{T}_a(x, y, s)$ can be expressed in the form of power series

$$\tilde{T}_a(x, y, s)=\tilde{\varphi}(s)+\sum_{k=1}^{\infty}a_k(y, s)x^k \tag{10}$$

Substituting Eq. (10) into Eq. (8a) gives

$$\tilde{T}_b(x, y, s)=\frac{1}{B}\left\{(a_1(y, s)+A\tilde{\varphi}(s))+\sum_{k=1}^{\infty}[(k+1)a_{k+1}(y, s)+Aa_k(y, s)x^k]\right\} \tag{11}$$

Equation (11) should satisfy the boundary condition (7b). Thus,

$$a_1(0, s)+A\tilde{\varphi}(s)=0$$

$$(k+1)a_{k+1}(0, s)+Aa_k(0, s)=0, \quad k\ge 1 \tag{12}$$

Substituting Eqs. (10) and (11) into Eq. (8b) and then collecting the coefficients of successive power of x produces the following form:

$$\left[\frac{da_1}{dy}+Ca_1-(BD-CA)\tilde{\varphi}(s)\right]+\sum_{k=1}^{\infty}(k+1)\left[\frac{da_{k+1}}{dy}+Ca_{k+1}-\frac{a_k}{k+1}(BD-CA)+\frac{A}{k+1}\frac{da_k}{dy}\right]x^k=0 \tag{13}$$

This implies that the coefficients of all powers of x must vanish independently. The vanishing of the coefficient of x^k, $k\ge 0$, gives the following recurrence formulas:

$$\frac{da_1}{dy}+Ca_1=(BD-CA)\tilde{\varphi} \tag{14a}$$

$$\frac{da_{k+1}}{dy}+Ca_{k+1}=\frac{a_k}{k+1}(BD-CA)+\frac{A}{k+1}\frac{da_k}{dy}, \quad k\ge 1 \tag{14b}$$

Next, we assume that the functions a_k, $k\ge 1$ can be expressed as

$$a_1(y, s)=f_1(s)+p_1(s)e^{-Cy}$$

$$a_2(y, s)=f_2(s)+(p_2(s)+q_2(s)y)e^{-Cy}$$

$$a_3(y, s)=f_3(s)+(p_3(s)+q_3(s)y+r_3(s)y^2)e^{-Cy} \tag{15}$$

By the direct substitution of Eq. (15) into Eqs. (14) with the condition (12), we obtain

$$f_1(s)=\frac{BD-CA}{C}\tilde{\varphi}$$

$$p_1(s)=-\frac{BD}{C}\tilde{\varphi} \tag{16a}$$

$$f_2(s)=\frac{1}{2!C^2}(BD-CA)^2\tilde{\varphi}$$

$$p_2(s)=\frac{1}{2!}A^2\tilde{\varphi}-f_2(s)$$

$$q_2(s)=\frac{1}{1\cdot 2}BDp_1(s) \tag{16b}$$

$$f_3(s)=\frac{1}{3!C^3}(BD-CA)^3\tilde{\varphi}$$

$$p_3(s)=-\frac{1}{3!}A^3\tilde{\varphi}-f_3$$

$$q_3(s)=\frac{1}{3}BDp_2-\frac{A}{3}q_2$$

$$r_3(s)=\frac{1}{2\cdot 3}BDq_2 \tag{16c}$$

$$\vdots$$

Substituting Eqs. (15) and (16) into Eq. (10) leads to the analytical form of $\tilde{T}_a(x, y, s)$ as

$$\tilde{T}_a(x, y, s) = \tilde{\varphi}(s)\left\{e^{\eta} - e^{-Ax-Cy}\left[\sum_{k=1}^{\infty}\left(\frac{BDx}{C}\right)^k \cdot \frac{1}{k!}\sum_{n=1}^{k-1}(Cy)^n\right]\right\} \tag{17}$$

where

$$\eta = \frac{BD - CA}{C}x \tag{18}$$

By the substitution of Eq. (17) into Eq. (8*a*), there follows

$$\tilde{T}_b(x, y, s) = \tilde{\varphi}(s)\frac{D}{C}\left\{e^{\eta} - e^{-Ax-Cy}\left[\sum_{k=0}^{\infty}\frac{1}{k!}\left(\frac{BDx}{C}\right)^k \times \sum_{n=0}^{k}(Cy)^n\right]\right\} \tag{19}$$

The analytical form of $\tilde{T}_w(x, y, s)$ can also be obtained by the insertion of Eqs. (17) and (19) into Eq. (6*a*) as

$$\tilde{T}_w(x, y, s) = D\tilde{\varphi}(s)\left\{e^{\eta} - e^{-Ax-Cy}\left[\sum_{k=1}^{\infty}\left(\frac{BDx}{C}\right)^k \cdot \frac{1}{k!}\sum_{n=1}^{k-1}(\mathrm{Cy})^n\right]\right\} + B\tilde{\varphi}(s)\frac{D}{C}\left\{e^{\eta} - e^{-Ax-Cy}\left[\sum_{k=0}^{\infty}\left(\frac{BDx}{C}\right)^k \cdot \frac{1}{k!}\sum_{n=0}^{k}(\mathrm{Cy})^n\right]\right\} \tag{20}$$

Inserting Eqs. (9) and (18) for A, B, C, and D leads to the following form:

$$\tilde{T}_\alpha(x, y, s) = \tilde{G}_\alpha(x, s)e^{-V_a xs} + \tilde{H}_\alpha(x, y, s)e^{-(V_a x + V_b y/R)s} \tag{21}$$

where $\alpha = a, b, w$.

Thus

$$T_\alpha(x, y, t) = G_\alpha(x, t - V_a x)U(t - V_a x) + H_\alpha(x, y, t - V_a x - V_b y/R)U(t - V_a x - V_b y/R) \tag{22}$$

where $U(t-\beta)$ is the unit step function defined as

$$U(t-\beta) = \begin{cases} 0 & t < \beta \\ 1 & t \geq \beta \end{cases} \tag{23}$$

It is evidently seen that there exists a wave front propagating in the x direction at a speed $1/V_a$ and the other wave front propagating in the y direction at a speed R/V_b. Equation (22) also implies that at any position (x, y) the temperatures of both fluids and the core wall are zero as long as $t < V_a x$. In the intermediate case, $V_a x \leq t < V_a x + V_b y/R$, the temperature T_α is independent of y. On the other hand T_α is only a function of t and x. However, for $t > V_a x + V_b y/R$, T_α is a function of t, x, and y.

Results and Concluding Remarks

The program for the present study is written in the FORTRAN language. All the numerical computations are performed on a personal computer with a 386-25 system. The present method can easily be applied to the works of Evans and Smith (1962) and Tan and Spinner (1984) only with proper modifications of initial and inlet conditions, parameters, and coordinates, etc. For example, the transient response of the countercurrent heat exchanger with a step change in the inlet temperature of stream a from 65 to 90°C given by Tan and Spinner (1984) is analyzed. Its model equations are given in the appendix. The current method compares within 99.99 percent of the calculations by Tan and Spinner (1984). The results are shown in Table 1.

The aim of the results presented here is to show the accuracy of the present method. Thus the present study deals only with the investigation of the exchanger temperature distributions following a deltalike perturbation in the inlet primary temperature, where the parameters $N_a = N_b = 2$ and $R = 1$ are assumed. Other results can be found in the work of Chen (1991). In addition, it can also be found from the work of Chen (1991) that the present method has good accuracy for such problems.

Table 1 Comparison of the outlet temperatures with $A^* = B^* = 1.25$ and $H = 1$

	$T_a(H, \theta)$		$T_b(0, \theta)$	
θ	Present work	Tan and Spinner (1984)	Present work	Tan and Spinner (1984)
0	41.883	41.883	38.897	38.897
0.5	41.883	41.883	43.967	43.967
1.0	53.116	53.116	47.358	47.358
1.5	54.800	54.800	49.736	49.736
2.0	55.695	55.695	51.477	51.478
2.5	56.132	56.132	51.806	51.806
3.0	56.299	56.299	51.949	51.949
3.5	56.347	56.347	52.004	52.004
4.0	56.365	56.365	52.002	52.002
4.5	56.371	56.371	52.028	—
5.0	56.374	56.374	52.030	—

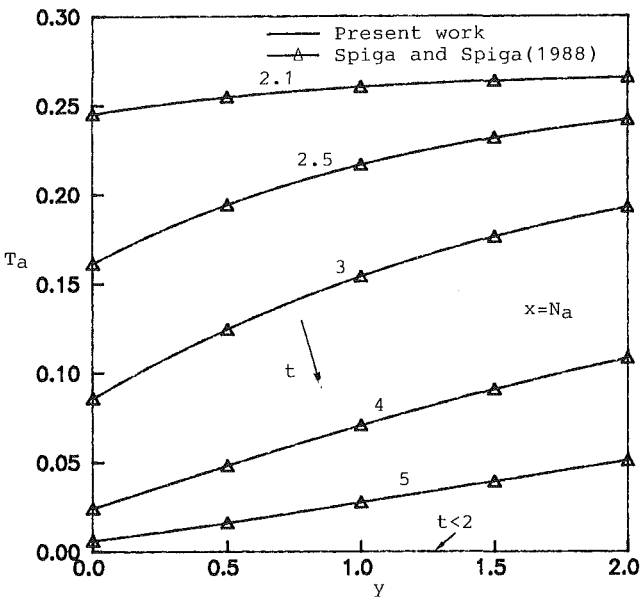

Fig. 1 Exit temperatures of the primary fluid for various times, V_a = 1, and V_b = 0.01

The numerical inversion of Laplace transforms proposed by Honig and Hirdes (1984) can be applied to invert the temperatures in the transform domain $\tilde{T}_a$, $\tilde{T}_b$, and $\tilde{T}_w$, as shown in Eqs. (17), (19), and (20), to the results in the physical quantities. For the present study the convergent rate of series expansions is fast. Thus only the first five terms of power series are required to obtain the present results.

As an example, the temperature distributions of both fluids in the exit sections are shown in Figs. 1 and 2. The results shown are in good agreement (within 0.01 percent) with those contained in Figs. 3 and 4 of Spiga and Spiga (1988) except for the result of Fig. 4 at $t = 0.1$. It is evident, however, that the result at $t = 0.1$ in Fig. 4 of Spiga and Spiga (1988) is wrong because the temperature distribution of T_b in the exit section is not a horizontal line. The perturbation reaches the exist section of the primary at $t = V_a N_a$ for arbitrary choices of $\varphi(t)$. When t is small enough, T_a is constant all over the length N_b.

To show the effect of the finite wall heat capacitance on the exit temperatures of both fluids, the results for the case of $V_a = 1$ and $V_b = 0.01$ are shown in Figs. 1 and 2. Under this circumstance the secondary fluid behaves like a gas and the secondary wave front is much faster than the primary one. A

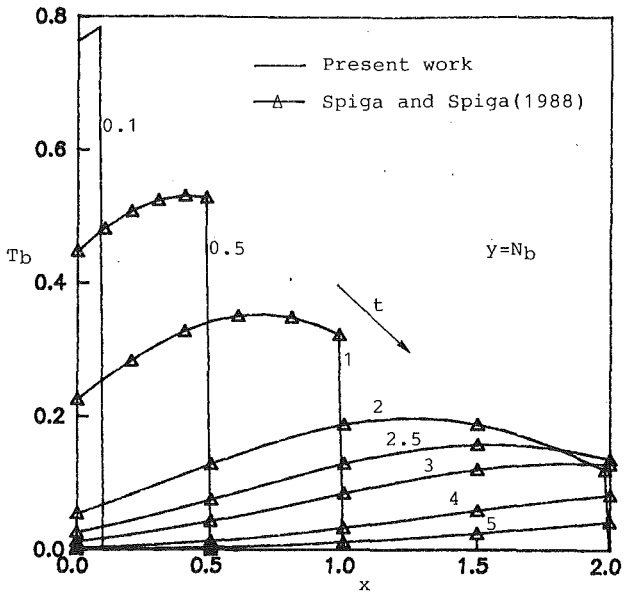

Fig. 2 Exit temperatures of the secondary fluid for various times, V_a = 1, and V_b = 0.01

consequence of these features is that the temperature distributions of the primary fluid in the exit section are affected by the inlet primary temperature earlier on, and T_b exhibits very sharp variations in a small neighborhood of $x = t/V_a$. However, the temperature variation of the primary fluid in the exit section is not very great.

Acknowledgments

This work was financially supported by the National Science Council, Taiwan, under Grant No. NSC 80-0401-E006-36.

References

Chen, K. C., 1991, "Two-Dimensional Transient Response of Crossflow Heat Exchangers," MS Thesis, Mech. Eng. Dept., National Cheng Kung University, Tainan, Taiwan.

Dusinberre, G. M., 1959, "Calculation of Transients in a Crossflow Heat Exchanger," ASME JOURNAL OF HEAT TRANSFER, Vol. 81, pp. 61-67.

Evans, F., and Smith W., 1962, "Cross-Current Transfer Processes in the Non-steady State," *Proc. Roy. Soc., London*, Vol. 272A, pp. 241-269.

Honig, G., and Hirdes, U., 1984, "A Method for the Numerical Inversion of Laplace Transforms," *Journal of Computational Applied Mathematics*, Vol. 9, pp. 113-132.

Spiga, G., and Spiga, M., 1987, "Two-Dimensional Transient Solutions for Crossflow Heat Exchangers With Neither Gas Mixed," ASME JOURNAL OF HEAT TRANSFER, Vol. 109, pp. 281-286.

Spiga, M., and Spiga, G., 1988, "Transient Temperature Fields in Crossflow Heat Exchangers With Finite Wall Capacitance," ASME JOURNAL OF HEAT TRANSFER, Vol. 110, pp. 49-53.

Tan, K. S., and Spinner, I. H., 1984, "Numerical Methods of Solution for Continuous Countercurrent Processes in the Nonsteady State," *AIChE Journal*, Vol. 30, pp. 770-786.

APPENDIX

The model equations for the transient response of the countercurrent heat exchanger are given as (Tan and Spinner, 1984)

$$A^* \frac{\partial T_a}{\partial h} + B^* \frac{\partial T_a}{\partial \theta} = T_b - T_a \tag{A1}$$

$$-\frac{\partial T_b}{\partial h} + \frac{\partial T_b}{\partial \theta} = T_a - T_b \tag{A2}$$

where A^* is the ratio of mass flow rate, B^* is the ratio of holdup in the two contacting phases, h is the dimensionless space parameter, and θ is the dimensionless time parameter. It was assumed that the system was initially at steady state with the following inlet conditions:

$$\overline{T}_a(0) = 65°\text{C} \text{ and } \overline{T}_b(H) = 10°\text{C} \tag{A3}$$

Experimental Study on Effect of Interwall Tube Cylinder on Heat/Mass Transfer Characteristics of Corrugated Plate Fin-and-Tube Exchanger Configuration

Q. Xiao,[1] B. Cheng,[1] and W. Q. Tao[1]

Nomenclature

- A = actual transfer area, used in Eq. (1)
- A_c = minimum flow area
- A_f = nominal transfer area, used in Eq. (5*a*)
- D = tube diameter
- D_h = hydraulic diameter
- $\mathfrak{D}$ = naphthalene-to-air diffusion coefficient
- H = fin spacing
- K = mass transfer coefficient
- L = streamwise length of test section
- Q = volumetric air flow rate
- Re = Reynolds number
- S = height of corrugation
- Sh = Sherwood number
- S_1 = spanwise distance between tube center
- S_2 = streamwise distance between tube center
- u = velocity
- W = width of test section
- x = ratio of naphthalene concentration at exit to that at wall
- α = corrugation angle
- ΔM = net sublimated mass, excluding the sublimation in auxiliary process
- $\Delta\rho_{n,m}$ = log-mean difference of naphthalene concentration in air flow
- ν = kinematic viscosity of air
- ρ_n = naphthalene concentration in air flow
- τ = run time duration

Subscripts

- e = exit
- i = inlet
- w = wall

Introduction

Plate fin-and-tube heat exchangers are widely used in air-conditioning equipment. In order to enhance the air side heat transfer, corrugated fins are often used instead of plane fins. The corrugated fins are, in essence, plates that have been fabricated with a periodic waviness in the streamwise direction. Although a number of research works have been performed to investigate the heat transfer and pressure drop performances of plate fin-and-tube heat exchangers, only a limited number of publications are related to the corrugated plate fin-and-tube heat exchangers (Goldstein and Sparrow, 1976, 1977; Giovannoni and Mattarolo, 1983; Poredos and Gaspersic, 1983;

[1]Department of Power Machinery Engineering, Xi'an Jiaotong University, Xi'an, Shaanxi 710049, The People's Republic of China.

Contributed by the Heat Transfer Division of the THE AMERICAN SOCIETY OF MECHANICAL ENGINEERS. Manuscript received by the Heat Transfer Division May 1991; revision received January 1992. Keywords: Finned Surfaces, Forced Convection, Heat Exchangers.

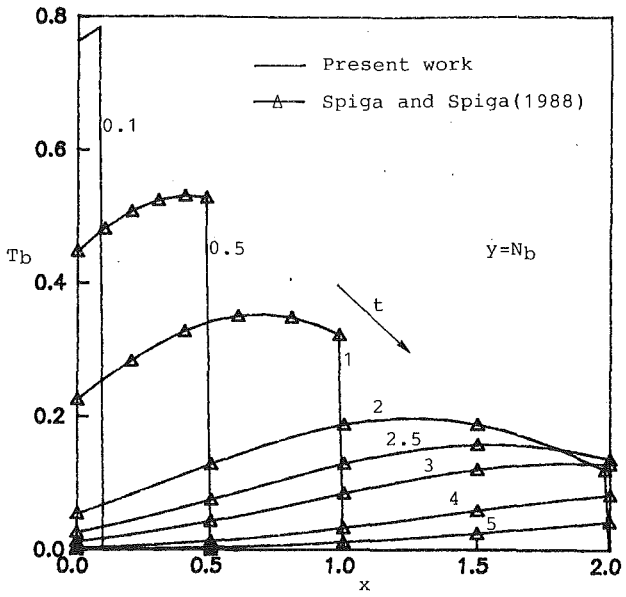

Fig. 2 Exit temperatures of the secondary fluid for various times, V_a = 1, and V_b = 0.01

consequence of these features is that the temperature distributions of the primary fluid in the exit section are affected by the inlet primary temperature earlier on, and T_b exhibits very sharp variations in a small neighborhood of $x = t/V_a$. However, the temperature variation of the primary fluid in the exit section is not very great.

Acknowledgments

This work was financially supported by the National Science Council, Taiwan, under Grant No. NSC 80-0401-E006-36.

References

Chen, K. C., 1991, "Two-Dimensional Transient Response of Crossflow Heat Exchangers," MS Thesis, Mech. Eng. Dept., National Cheng Kung University, Tainan, Taiwan.

Dusinberre, G. M., 1959, "Calculation of Transients in a Crossflow Heat Exchanger," ASME JOURNAL OF HEAT TRANSFER, Vol. 81, pp. 61-67.

Evans, F., and Smith W., 1962, "Cross-Current Transfer Processes in the Non-steady State," *Proc. Roy. Soc., London*, Vol. 272A, pp. 241-269.

Honig, G., and Hirdes, U., 1984, "A Method for the Numerical Inversion of Laplace Transforms," *Journal of Computational Applied Mathematics*, Vol. 9, pp. 113-132.

Spiga, G., and Spiga, M., 1987, "Two-Dimensional Transient Solutions for Crossflow Heat Exchangers With Neither Gas Mixed," ASME JOURNAL OF HEAT TRANSFER, Vol. 109, pp. 281-286.

Spiga, M., and Spiga, G., 1988, "Transient Temperature Fields in Crossflow Heat Exchangers With Finite Wall Capacitance," ASME JOURNAL OF HEAT TRANSFER, Vol. 110, pp. 49-53.

Tan, K. S., and Spinner, I. H., 1984, "Numerical Methods of Solution for Continuous Countercurrent Processes in the Nonsteady State," *AIChE Journal*, Vol. 30, pp. 770-786.

APPENDIX

The model equations for the transient response of the countercurrent heat exchanger are given as (Tan and Spinner, 1984)

$$A^* \frac{\partial T_a}{\partial h} + B^* \frac{\partial T_a}{\partial \theta} = T_b - T_a \tag{A1}$$

$$-\frac{\partial T_b}{\partial h} + \frac{\partial T_b}{\partial \theta} = T_a - T_b \tag{A2}$$

where A^* is the ratio of mass flow rate, B^* is the ratio of holdup in the two contacting phases, h is the dimensionless space parameter, and θ is the dimensionless time parameter. It was assumed that the system was initially at steady state with the following inlet conditions:

$$\overline{T}_a(0) = 65°\text{C} \text{ and } \overline{T}_b(H) = 10°\text{C} \tag{A3}$$

Experimental Study on Effect of Interwall Tube Cylinder on Heat/Mass Transfer Characteristics of Corrugated Plate Fin-and-Tube Exchanger Configuration

Q. Xiao,[1] B. Cheng,[1] and W. Q. Tao[1]

Nomenclature

- A = actual transfer area, used in Eq. (1)
- A_c = minimum flow area
- A_f = nominal transfer area, used in Eq. (5*a*)
- D = tube diameter
- D_h = hydraulic diameter
- $\mathfrak{D}$ = naphthalene-to-air diffusion coefficient
- H = fin spacing
- K = mass transfer coefficient
- L = streamwise length of test section
- Q = volumetric air flow rate
- Re = Reynolds number
- S = height of corrugation
- Sh = Sherwood number
- S_1 = spanwise distance between tube center
- S_2 = streamwise distance between tube center
- u = velocity
- W = width of test section
- x = ratio of naphthalene concentration at exit to that at wall
- α = corrugation angle
- ΔM = net sublimated mass, excluding the sublimation in auxiliary process
- $\Delta\rho_{n,m}$ = log-mean difference of naphthalene concentration in air flow
- ν = kinematic viscosity of air
- ρ_n = naphthalene concentration in air flow
- τ = run time duration

Subscripts

- e = exit
- i = inlet
- w = wall

Introduction

Plate fin-and-tube heat exchangers are widely used in air-conditioning equipment. In order to enhance the air side heat transfer, corrugated fins are often used instead of plane fins. The corrugated fins are, in essence, plates that have been fabricated with a periodic waviness in the streamwise direction. Although a number of research works have been performed to investigate the heat transfer and pressure drop performances of plate fin-and-tube heat exchangers, only a limited number of publications are related to the corrugated plate fin-and-tube heat exchangers (Goldstein and Sparrow, 1976, 1977; Giovannoni and Mattarolo, 1983; Poredos and Gaspersic, 1983;

[1]Department of Power Machinery Engineering, Xi'an Jiaotong University, Xi'an, Shaanxi 710049, The People's Republic of China.

Contributed by the Heat Transfer Division of the THE AMERICAN SOCIETY OF MECHANICAL ENGINEERS. Manuscript received by the Heat Transfer Division May 1991; revision received January 1992. Keywords: Finned Surfaces, Forced Convection, Heat Exchangers.

Xiao and Tao, 1990). Goldstein and Sparrow (1976) used a naphthalene sublimation technique to determine local air side heat transfer coefficients for one-row corrugated plate fin-and-tube heat exchangers. The same authors (1977) also examined a corrugated duct, which did not contain the interwall cylinders, while the other configurations were the same as those in 1976. They found that the flow in the corrugated duct could be regarded as laminar up to Reynolds number 1000–1200 (based on the hydraulic diameter $D_h = 2H$). This implies that the existence of corrugation makes some contribution to the onset of turbulence.

From the geometric point of view, the major characteristics of the corrugated plate fin-and-tube heat exchanger, as compared to the plain duct, are the existence of wall corrugation and the interwall tube cylinders, which serve as the passage for the in-tube fluid and also as the holder of the corrugated plate fins. The purpose of this work is to investigate experimentally the effect of the interwall tube cylinders on the heat/mass transfer characteristics of corrugated channel. To facilitate the test process, the naphthalene sublimation technique was used. In the study mass transfer measurements were done for the test section with interwall cylinders and for that without interwall cylinders, with other geometric dimensions remained the same.Mass transfer results may be converted to heat transfer results by application of the analogy between the two processes. Since the focus of this study is to make a relative comparison, this inversion will not be completed and the presentation is limited to mass transfer aspect.

Experimental Apparatus and Procedure

A schematic diagram of the fin surfaces tested is shown in Fig. 1. In view of the spanwise periodicity the mass transfer measurements were conducted for the typical unit ABCD. The dimensions of the tested configurations are:

$$S_1/D = 2.38, \quad S_2/D = 2.07, \quad \alpha = 15.5 \text{ (deg)}$$
$$H/D = 0.189, \quad 0.237, \quad 0.332, \text{ and } 0.379$$
$$\text{(i.e., } H/S = 1.326, \quad 1.658, \quad 2.231, \text{ and } 2.653\text{)}$$

The actual physical dimensions are $S_1 = 0.05$ m, $S_2 = 0.0435$ m, $D = 0.0211$ m, $H = 4$, 5, 7, and 8×10^{-3} m, and $W = 0.175$ m.

The experimental apparatus is presented in Figs. 2 and 3. The model of the corrugated plate fin-and-tube heat exchanger was composed of a pair of specially cast corrugated surfaces of naphthalene and two arrays of aluminum disks, which serve to simulate the heat tubes. The fin spacing was set by two pieces of bilateral parting bars and the disks. In the model of the corrugated duct (Fig. 1(*b*)), the interwall disks were moved away while all the others remained the same. Both the disks and the bilateral bars were made from aluminum and did not participate in the mass transfer process. Since the disk lateral surfaces were less than 10 percent of the total fin surface area, the minor difference in thermal boundary condition of disk surfaces may be thought of as being an insignificant factor affecting the transfer process.

The mold structure and the cast process were prescribed in detail in the paper by Xiao and Tao (1990) and will not be presented here.

The experimental procedure of the naphthalene sublimation technique is well documented in literature and may be found from Xiao and Tao (1990) and Sparrow et al. (1983). Only the following facts are mentioned here. An analytical balance having a resolution of 0.1 mg was used to weigh the test plates. The inlet air temperature was recorded from a laboratory thermometer with a resolution of 0.1°C. A stop watch capable of timing to 0.01 s was used to measure the run duration time.

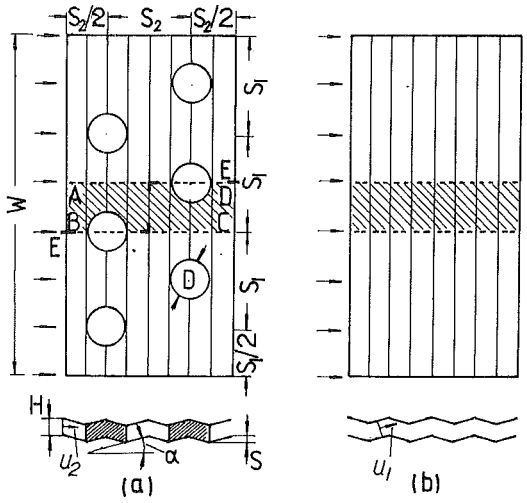

Fig. 1 Schematic diagram of tested surfaces

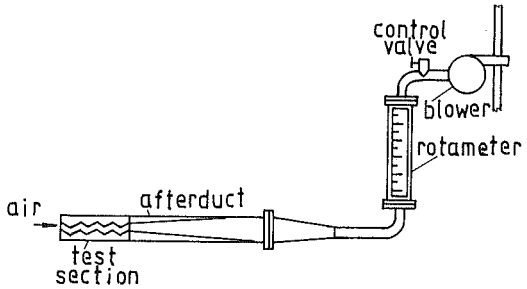

Fig. 2 Experimental apparatus

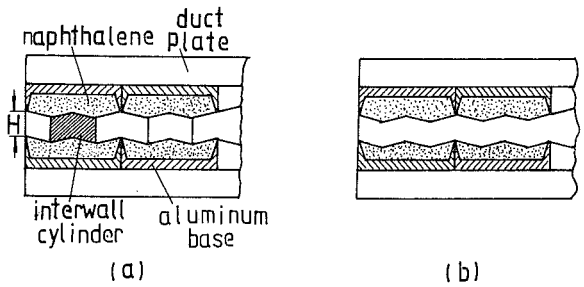

Fig. 3 Side view of tested sections: (*a*) model of corrugated plate fin-and-tube exchanger; (*b*) model of corrugated duct

Data Reduction

The average mass transfer coefficient was evaluated from the definition

$$K = \frac{\Delta M}{\tau A \Delta \rho_{n,m}} \tag{1}$$

The log-mean naphthalene concentration difference between the ones in the bulk and at wall was calculated from

$$\Delta \rho_{n,m} = \frac{(\rho_{n,w} - \rho_{n,i}) - (\rho_{n,w} - \rho_{n,e})}{\ln[(\rho_{n,w} - \rho_{n,i})/(\rho_{n,w} - \rho_{n,e})]} \tag{2}$$

where $\rho_{n,w}$ was evaluated from the Sogin vapor-pressure-temperature relation of naphthalene (1958) in conjunction with the perfect gas law. The inlet bulk naphthalene vapor density $\rho_{n,i}$ was equal to zero, and the exit one was obtained by the mass conservation equation

$$\rho_{n,e} = \rho_{n,i} + \Delta M/Q \tag{3}$$

The Reynolds number and the average Sherwood number were defined as:

$$\mathrm{Re} = uD_h/\nu, \quad \mathrm{Sh} = KD_h/\mathfrak{D} \tag{4}$$

The mass diffusion coefficient $\mathfrak{D}$ in Eq. (4) is related to the Schmidt number via the definition $\mathrm{Sc} = \nu/\mathfrak{D}$. For the naphthalene-air mixture, $\mathrm{Sc} = 2.5$ (Sogin, 1958). In addition, the concentration of naphthalene vapor in the mixture is so small that ν is equal to the kinematic viscosity of air.

As a characteristic length for the Reynolds number and Sherwood number, two definitions were tried:

1 The definition given by Kays and London (1984):

$$D_{h1} = 4A_cL/A_f \tag{5a}$$

where the minimum flow area A_c was calculated by

$$A_c = H \cos \alpha \, (s_1 - D)/2 \tag{5b}$$

and the transfer area A_f was evaluated using both the fin and the tube cylinder lateral surface area.

2 The hydraulic diameter as if the corrugated duct were of infinite aspect ratio and without interwall cylinders:

$$D_{h2} = 2H \tag{6}$$

It should be noted that these two definitions correspond to two different velocities in Reynolds number, $\mathrm{Re} = u_1D_{h1}/\nu$, $\mathrm{Re}_2 = u_2D_{h2}/\nu$. Here u_1 is the velocity at the minimum flow area, while u_2 corresponds to the channel cross-sectional area (see Fig. 1). For the purpose of comparison with literature (Goldstein and Sparrow, 1977), in the following presentation only the reduced data based on D_{h2} will be presented. Since the same characteristic length D_{h2} was used for both the corrugated plate fin-and-tube heat exchanger and the corrugated duct, the reduced data for these two test sections are fully comparable. For simplicity, the subscript 2 in D_{h2} will be omitted hereafter.

Results and Discussions

The experimental mass transfer data of the two test models for four fin spacings are shown in Figs. 4–7, where the average Sherwood number is plotted as a function of the Reynolds number. These figures reveal several important facts.

First, it is seen that the average Sherwood numbers of both models increase continuously as the Reynolds number increases. As it may be expected, at a given Reynolds number and a fin spacing, the Sherwood number of the corrugated plate fin-and-tube exchanger model is always higher than that of the corrugated duct model. This means that the interwall tube cylinders actually act as turbulators. The enchancement effect is more significant in the low Reynolds number region. For example, at $\mathrm{Re} = 1100$, the interwall cylinder can enhance the mass transfer about 70–90 percent, and at $\mathrm{Re} = 4800$ by about 11–30 percent. In the higher Reynolds number region, each pair of Sh versus Re curves tends to approach each other.

Second, for the four spacings investigated, the curves of $\mathrm{Sh} \sim \mathrm{Re}$ for the corrugated ducts continuously change their slopes in the low Reynolds number range (from about 1000 to about 2000), and then gradually approach straight lines. The continuous change in slope may be indicative of the transition from laminar flow to turbulent. Thus, these curves suggest that from a Reynolds number of about 2500–3000, the flow in a corrugated duct may be regarded as turbulent. This observation agrees quite well with the experimental results of Goldstein and Sparrow (1977). In their paper the upper limit of channel Reynolds number for laminar flow was taken as 1000–1200. The shape of the $\mathrm{Sh} \sim \mathrm{Re}$ curve and the Reynolds number range within which the curve slope continuously changes are quite agreeable with those shown in Fig. 10 of that paper.

The third important fact is that in the range of Reynolds

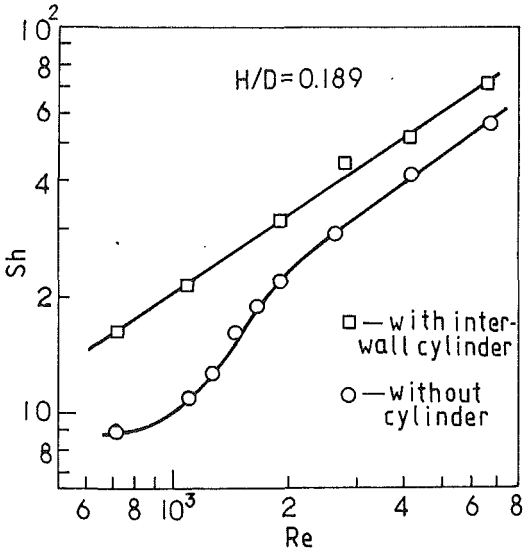

Fig. 4 Average mass transfer results for $H/D = 0.189$

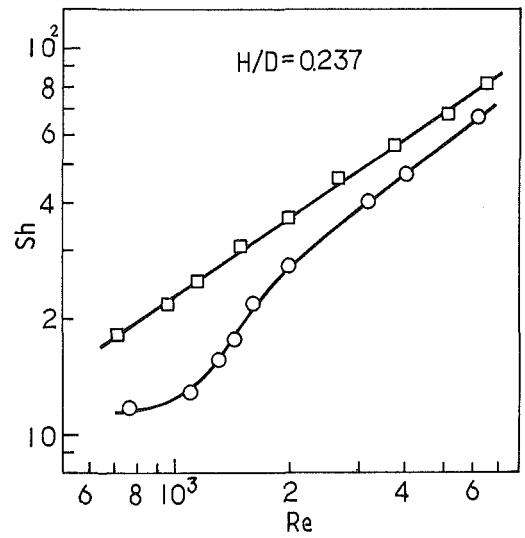

Fig. 5 Average mass transfer results for $H/D = 0.237$

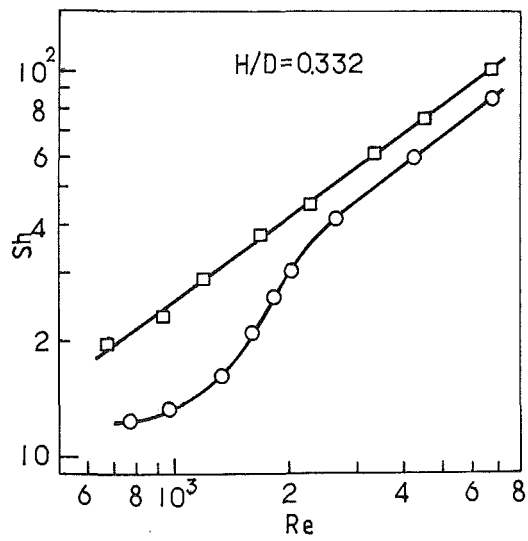

Fig. 6 Average mass transfer results for $H/D = 0.332$

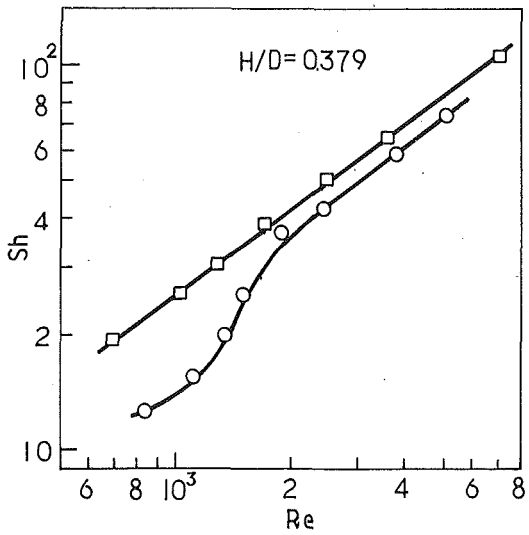

Fig. 7 Average mass transfer results for $H/D = 0.379$

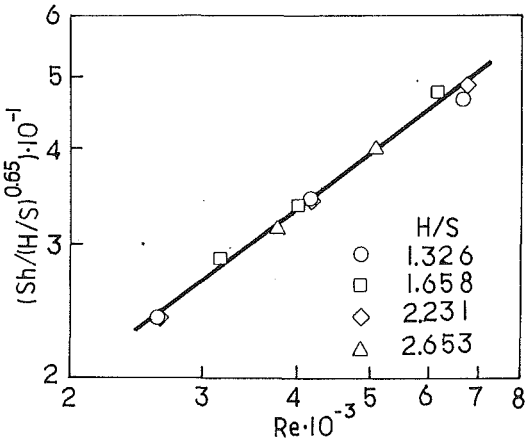

Fig. 8 Average mass transfer results of corrugated duct (turbulent flow)

number studied, the Sherwood number of the corrugated plate fin-and-tube exchanger model can be well correlated by a single equation for the four different spacing cases. This indicates that all these data are in the turbulent range, implying that the existence of the interwall cylinder makes the transition from laminar to turbulent occur at a lower Reynolds number. The authors presented a correlation in 1990, in which the Reynolds number and the Sherwood number were based on the hydraulic diameter given by Kays and London. Following is the revised version using $2H$ as a characteristic length in Sh and Re:

$$\mathrm{Sh} = 0.139\ \mathrm{Re}^{0.702}\ (H/S)^{0.42} \tag{7}$$

$$1.326 \le H/S \le 2.653, \quad 670 \le \mathrm{Re} \le 7000$$

The maximum deviation of Eq. (7) from the experimental data is 6.5 percent. This data scatter is a bit less than that of the equation presented in our previous paper (1990), of which the maximum deviation is 9 percent.

For the corrugated duct model in the turbulent region, the experimental results may be presented by the following equation:

$$\mathrm{Sh} = 0.061\ \mathrm{Re}^{0.76}\ (H/S)^{0.65} \tag{8}$$

$$1.326 \le H/S \le 2.653, \quad 2600 \le \mathrm{Re} \le 6700$$

The maximum deviation of Eq. (8) from experimental data is 4.65 percent. Equation (8) is shown in Fig. 8.

Here it is to be noted that the fin spacing has some effect on the enhancement function of the interwall tube cylinder. With the increase in fin spacing, the enhancement caused by the interwall tube cylinder become less significant.

Finally attention is turned to the analysis of uncertainty. The experimental data taken from the two models were reduced to give two primary variables, Re and Sh. The uncertainties in these two primary variables may be divided into two major types: (1) fluid property uncertainties and (2) experimental uncertainties. These uncertainty estimates are summarized as follows: fluid temperature $\pm 0.2°C$, sublimed mass ± 0.1 mg, naphthalene vapor pressure ± 3.5 percent, hydraulic diameter ± 1.1 percent (including the effect of sublimation on the change of channel cross section), surface area ± 0.7 percent, flow rate ± 2 percent, run duration time ± 0.5 percent, fluid viscosity ± 1.5 percent, and diffusion coefficient ± 2 percent. The uncertainty of the reduced variables Re and Sh due to the uncertainties in the properties and measurements are approximately calculated by the method of Kline and McClintock (1953). For example, the Sherwood number can be expressed by

$$\mathrm{Sh} = \frac{D_h}{\mathfrak{D}} \frac{\Delta M}{\tau A} \frac{\ln\left(\rho_{n,w}/(\rho_{n,w}-\rho_{n,e})\right)}{\rho_{n,e}} \tag{9}$$

Then the uncertainty in Sh is calculated by the following equation:

$$\frac{\delta(\mathrm{Sh})}{\mathrm{Sh}} = \left\{ \left(\frac{\delta(D_h)}{D_h}\right)^2 + \left(\frac{\delta(\Delta M)}{M}\right)^2 + \left(\frac{\delta\tau}{\tau}\right)^2 + \left(\frac{\delta A}{A}\right)^2 + \left(\frac{\delta\mathfrak{D}}{\mathfrak{D}}\right)^2 + \left(\frac{\delta(\rho_{n,e})}{\rho_{n,e}}\right)^2 \left(1 + \frac{1}{1/x-1} \cdot \frac{1}{\ln(1/(1-x))}\right)^2 + \left(\frac{\delta(\rho_{n,w})}{\rho_{n,w}}\right)^2 \left(\frac{1}{\ln(1/(1-x))} - \frac{1}{1-x} \cdot \frac{1}{\ln(1/(1-x))}\right)^2 \right\}^{1/2} \tag{10}$$

where x stands for $\rho_{n,e}/\rho_{n,w}$. In all data runs of this study, $\rho_{n,e}/\rho_{n,w} \le 0.1$. Substitution of the estimated uncertainties of the variables in the right-hand side of the above equation leads to an uncertainty interval of Sh ± 6.47 percent. The same analysis for Re yields an uncertainty of Re ± 2.99 percent.

Conclusions

The experimental result reported here is, seemingly, the first investigation of the effect of the interwall tube cylinder on the heat/mass transfer of the corrugated duct. It is found that the interwall cylinder serves as a turbulator and a turbulence promotor. It may significantly enhance the heat/mass transfer in the low Reynolds number region. The existence of the interwall cylinder also causes the transition from laminar to turbulent to occur at a lower Reynolds number.

Acknowledgments

This work was supported by the Research Foundation for Doctorate of Chinese Institutes and Universities.

References

Giovannoni, F., and Mattarolo, L., 1983, "Experimental Researches on the Finned Tube Heat Exchangers With Corrugated Fins," *Proceedings of the XVIth International Congress of Refrigeration*, Vol. 2, pp. 215–220.

Goldstein, L., Jr., and Sparrow, E. M., 1976, "Experiments on the Transfer Characteristics of a Corrugated Fin and Tube Heat Exchanger Configuration," ASME JOURNAL OF HEAT TRANSFER, Vol. 98, pp. 26–34.

Goldstein, L., Jr., and Sparrow, E. M., 1977, "Heat/Mass Transfer Characteristics for Flow in a Corrugated Wall Channel," ASME JOURNAL OF HEAT TRANSFER, Vol. 99, pp. 187–196.

Kays, W. M., and London, A. L., 1984, *Compact Heat Exchangers*, 3rd ed., McGraw-Hill, New York.

Kline, S. J., and McClintock, F. A., 1953, "The Description of Uncertainties in Single Sample Experiments," *Mechanical Engineering*, Vol. 75, pp. 3–9.

Poredos, A., and Gaspersic, B., 1983, "Influence of Parameters on Heat, Mass and Momentum Transport Coefficients in Dehumidifying Finned Heat Exchangers," *Proceedings of the XVIth International Congress of Refrigeration*, Vol. 2, pp. 221-226.

Sogin, H. H., 1958, "Sublimation From Disks to Air Stream Flowing Normal to Their Surfaces," *ASME Trans.*, Vol. 80, pp. 61-71.

Sparrow, E. M., Tao, W. Q., and Radiky, D., 1983, "Heat Transfer at an Array of Co-planar Slot-like Surfaces Oriented Normal to a Forced Convection Flow," *Int. J. Heat Mass Transfer*, Vol. 26, pp. 33-40.

Xiao, Q., and Tao, W. Q., 1990, "Effect of Fin Spacing on Heat Transfer and Pressure Drop of Two-Row Corrugated Fin-and-Tube Heat Exchangers," *Int. Comm. Heat Mass Transfer*, Vol. 17, pp. 577-586.

A New Formula for Calculating the Flow Temperature in a Gas Pipeline

A. A. Zaman[1]

Nomenclature

A_1 = constant in Eq. (9) = $(2a/Rc_p)\ (dP/dx)$, K^2/m
A_2 = constant in Eq. (9) = $(2U/\rho Vc_p r_i)$, m^{-1}
A_3 = constant in Eq. (9) = $(b/c_p)\ (dP/dx) - (2UT_g/\rho Vc_p r_i)$, m^{-1} K
A = pipe cross-sectional area, m^2
a = Van der Waals constant, (J m^3)/kg
b = Van der Waals constant, m^3/kg
c_p = specific heat of the gas, J/(kg K)
C = constant in Eq. (12)
e = energy = $h+gz+V^2/2$, J/kg
K_g = gas thermal conductivity, J/(m s K)
m = mass flow rate = ρVA, kg/s
P_1 = inlet gas pressure, Pa
p_2 = output gas pressure, Pa
p' = perimeter of the pipe, m
Q = gas volume flow rate at standard conditions, m^3/s
r_i = inside radius of the pipe, m
R = gas constant, J/(kg K)
T = gas temperature, K
T_g = ground (surrounding) temperature, K
U = total coefficient of heat transfer, J/(m^2 s K)
V = gas velocity at standard conditions, m/s
v = specific volume of the gas, m^3/kg
x = length of the pipeline, m
μ = Joule-Thompson coefficient, K/Pa
ρ = gas density at standard conditions, kg/m^3

Introduction

Calculation of the flowing temperature in a gas pipeline is necessary for the design of gas compressor stations, chilling systems after compressors, and for conditions in which gas flows are increased through existing lines.

The temperature of the gas pipeline must be controlled where either frost heaves or melting of unstable ices could be a problem.

Increased gas flows can raise gas temperature and require greater downstream compressor power unless energy input is balanced by heat loss to the surrounding ground and to Joule-Thompson cooling. The degree of gas cooling and compressor power required at each compressor power station depends on the temperature of the gas arriving at the station. Therefore, it is necessary to be able to calculate the gas temperature along a gas pipeline.

[1]Department of Chemical Engineering, University of Florida, Gainesville, FL 32611.

Contributed by the Heat Transfer Division of THE AMERICAN SOCIETY OF MECHANICAL ENGINEERS. Manuscript received by the Heat Transfer Division June 1991; revision received January 1992. Keywords: Forced Convection, Turbulence.

Previous Work

During the past forty years, various equations have been presented. The first equation for determining the temperature in a gas transmission line was presented by Charles E. Schorre (1954) and interpreted by Forrest (1978). Schorre considered a linearly increasing Joule-Thompson effect and a gas temperature that was due to conduction instead of actual temperature of the gas.

Coulter and Bardon (1979) considered a linearly increasing Joule-Thompson effect and actual temperature of the gas and presented an equation., Also Coulter (1979), by using an equation of state, evaluated the velocity changes of the gas along the line and obtained a new equation. Even though he considered the velocity changes and the actual temperature of the gas, the Joule-Thompson effect did not change.

The Joule-Thompson effect shows the changes in temperature with pressure at constant enthalpy. The effect is a function of the gas temperature and may be calculated at each point along the pipeline by considering a suitable equation of state.

Thermodynamic Analysis

By considering an element of the gas pipeline and assuming radially lumped heat transfer at steady-state conditions, the energy equation would be as follows:

$$\frac{\partial}{\partial x}(me)+\frac{\partial q_x}{\partial x}dx+q''p'dx=0 \tag{1}$$

By neglecting the changes in kinetic and potential energy and assuming constant density and cross-sectional area, Eq. (1) reduces to the following:

$$-k_g\frac{\partial^2 T}{\partial x^2}+\rho V\frac{\partial h}{\partial x}+\frac{q''p'}{A}=0 \tag{2}$$

Since

$$h=h(T,\ P),\ P'=2\pi r_i,\ A=\pi r_i^2$$

and

$$\mu=\left(\frac{\partial T}{\partial P}\right)_h=-\frac{v-T\left(\frac{\partial v}{\partial T}\right)}{C_p},$$

considering the enthalpy changes of the gas and substituting in Eq. (2), gives

$$k_g\frac{\partial^2 T}{\partial x^2}-\rho V\left[c_p\frac{dT}{dx}-\mu c_p\frac{dP}{dx}\right]-\frac{2q''}{r_i}=0 \tag{3}$$

The above equation is the total differential equation of energy in gas transmission lines.

In this investigation, we have used the Van der Waals equation of state to determine the Joule-Thompson coefficient and solved the above differential equation. From the Van der Waals equation of state, μ can be written as

$$\mu=-\frac{b-\frac{2a}{RT}}{c_p} \tag{4}$$

By substituting Eq. (4) in Eq. (3), we have

$$k_g\frac{\partial^2 T}{\partial x^2}-\rho V\left[c_p\frac{dT}{dx}+\left(b-\frac{2a}{RT}\right)\frac{dP}{dx}\right]-\frac{2q''}{r_i}=0 \tag{5}$$

Experimental results on heat transfer in gases show that conduction heat transfer in flowing gases is very small compared with convective heat transfer; therefore:

Poredos, A., and Gaspersic, B., 1983, "Influence of Parameters on Heat, Mass and Momentum Transport Coefficients in Dehumidifying Finned Heat Exchangers," *Proceedings of the XVIth International Congress of Refrigeration*, Vol. 2, pp. 221–226.

Sogin, H. H., 1958, "Sublimation From Disks to Air Stream Flowing Normal to Their Surfaces," *ASME Trans.*, Vol. 80, pp. 61–71.

Sparrow, E. M., Tao, W. Q., and Radiky, D., 1983, "Heat Transfer at an Array of Co-planar Slot-like Surfaces Oriented Normal to a Forced Convection Flow," *Int. J. Heat Mass Transfer*, Vol. 26, pp. 33–40.

Xiao, Q., and Tao, W. Q., 1990, "Effect of Fin Spacing on Heat Transfer and Pressure Drop of Two-Row Corrugated Fin-and-Tube Heat Exchangers," *Int. Comm. Heat Mass Transfer*, Vol. 17, pp. 577–586.

A New Formula for Calculating the Flow Temperature in a Gas Pipeline

A. A. Zaman[1]

Nomenclature

A_1 = constant in Eq. (9) = $(2a/Rc_p)\ (dP/dx)$, K^2/m
A_2 = constant in Eq. (9) = $(2U/\rho Vc_p r_i)$, m^{-1}
A_3 = constant in Eq. (9) = $(b/c_p)\ (dP/dx) - (2UT_g/\rho Vc_p r_i)$, m^{-1} K
A = pipe cross-sectional area, m^2
a = Van der Waals constant, (J m^3)/kg
b = Van der Waals constant, m^3/kg
c_p = specific heat of the gas, J/(kg K)
C = constant in Eq. (12)
e = energy = $h+gz+V^2/2$, J/kg
K_g = gas thermal conductivity, J/(m s K)
m = mass flow rate = ρVA, kg/s
P_1 = inlet gas pressure, Pa
p_2 = output gas pressure, Pa
p' = perimeter of the pipe, m
Q = gas volume flow rate at standard conditions, m^3/s
r_i = inside radius of the pipe, m
R = gas constant, J/(kg K)
T = gas temperature, K
T_g = ground (surrounding) temperature, K
U = total coefficient of heat transfer, J/(m^2 s K)
V = gas velocity at standard conditions, m/s
v = specific volume of the gas, m^3/kg
x = length of the pipeline, m
μ = Joule-Thompson coefficient, K/Pa
ρ = gas density at standard conditions, kg/m^3

Introduction

Calculation of the flowing temperature in a gas pipeline is necessary for the design of gas compressor stations, chilling systems after compressors, and for conditions in which gas flows are increased through existing lines.

The temperature of the gas pipeline must be controlled where either frost heaves or melting of unstable ices could be a problem.

Increased gas flows can raise gas temperature and require greater downstream compressor power unless energy input is balanced by heat loss to the surrounding ground and to Joule-Thompson cooling. The degree of gas cooling and compressor power required at each compressor power station depends on the temperature of the gas arriving at the station. Therefore, it is necessary to be able to calculate the gas temperature along a gas pipeline.

[1]Department of Chemical Engineering, University of Florida, Gainesville, FL 32611.

Contributed by the Heat Transfer Division of THE AMERICAN SOCIETY OF MECHANICAL ENGINEERS. Manuscript received by the Heat Transfer Division June 1991; revision received January 1992. Keywords: Forced Convection, Turbulence.

Previous Work

During the past forty years, various equations have been presented. The first equation for determining the temperature in a gas transmission line was presented by Charles E. Schorre (1954) and interpreted by Forrest (1978). Schorre considered a linearly increasing Joule-Thompson effect and a gas temperature that was due to conduction instead of actual temperature of the gas.

Coulter and Bardon (1979) considered a linearly increasing Joule-Thompson effect and actual temperature of the gas and presented an equation., Also Coulter (1979), by using an equation of state, evaluated the velocity changes of the gas along the line and obtained a new equation. Even though he considered the velocity changes and the actual temperature of the gas, the Joule-Thompson effect did not change.

The Joule-Thompson effect shows the changes in temperature with pressure at constant enthalpy. The effect is a function of the gas temperature and may be calculated at each point along the pipeline by considering a suitable equation of state.

Thermodynamic Analysis

By considering an element of the gas pipeline and assuming radially lumped heat transfer at steady-state conditions, the energy equation would be as follows:

$$\frac{\partial}{\partial x}(me)+\frac{\partial q_x}{\partial x}dx+q''p'dx=0 \tag{1}$$

By neglecting the changes in kinetic and potential energy and assuming constant density and cross-sectional area, Eq. (1) reduces to the following:

$$-k_g\frac{\partial^2 T}{\partial x^2}+\rho V\frac{\partial h}{\partial x}+\frac{q''p'}{A}=0 \tag{2}$$

Since

$$h=h(T,\ P),\ P'=2\pi r_i,\ A=\pi r_i^2$$

and

$$\mu=\left(\frac{\partial T}{\partial P}\right)_h=-\frac{v-T\left(\frac{\partial v}{\partial T}\right)}{C_p},$$

considering the enthalpy changes of the gas and substituting in Eq. (2), gives

$$k_g\frac{\partial^2 T}{\partial x^2}-\rho V\left[c_p\frac{dT}{dx}-\mu c_p\frac{dP}{dx}\right]-\frac{2q''}{r_i}=0 \tag{3}$$

The above equation is the total differential equation of energy in gas transmission lines.

In this investigation, we have used the Van der Waals equation of state to determine the Joule-Thompson coefficient and solved the above differential equation. From the Van der Waals equation of state, μ can be written as

$$\mu=-\frac{b-\frac{2a}{RT}}{c_p} \tag{4}$$

By substituting Eq. (4) in Eq. (3), we have

$$k_g\frac{\partial^2 T}{\partial x^2}-\rho V\left[c_p\frac{dT}{dx}+\left(b-\frac{2a}{RT}\right)\frac{dP}{dx}\right]-\frac{2q''}{r_i}=0 \tag{5}$$

Experimental results on heat transfer in gases show that conduction heat transfer in flowing gases is very small compared with convective heat transfer; therefore:

$$\frac{dT}{dx}+\frac{\left(b-\frac{2a}{RT}\right)}{c_p}\frac{dP}{dx}+\frac{2q''}{\rho V c_p r_i}=0 \tag{6}$$

The heat transfer rate per unit area between the gas and the surrounding is

$$q''=U(T-T_g) \tag{7}$$

So:

$$\frac{dT}{dx}-\frac{2a}{Rc_p}\frac{1}{T}\frac{dP}{dx}+\frac{2UT}{\rho V c_p r_i}+\frac{b}{c_p}\frac{dP}{dx}-\frac{2UT_g}{\rho V c_p r_i}=0 \tag{8}$$

For convenience, Eq. (8) can be written as follows:

$$\frac{dT}{dx}-\frac{A_1}{T}+A_2T+A_3=0 \tag{9}$$

The above equation is a nonlinear differential equation and must be solved by a mathematical or a numerical method. For obtaining a formula that will be applicable for determination of the gas temperature at each point of the line, we have solved it by an analytical method. Also, we have studied the temperature profile of the gas at various cross sections of the line by solving Eq. (5) numerically.

Analytical Solution

By introducing a new factor $T=1/Y$, and replacing the respective derivatives in Eq. (9), one can obtain the following ordinary differential equation:

$$\frac{dY}{A_2Y+A_3Y^2-A_1Y^3}=dx \tag{10}$$

Equation (10) can be solved analytically by partial fractions:

$$\left(\frac{1}{A_2Y}+\frac{\frac{A_1}{A_2}Y}{A_2+A_3Y-A_1Y^2}-\frac{\frac{A_3}{A_2}}{A_2+A_3Y-A_1Y^2}\right)dY=dx \tag{11}$$

By integrating the above equation, and substituting $1/T$ for Y, we have:

$$\frac{1}{A_2}\log_e\frac{1}{T}-\frac{1}{2A_2}\log_e\left(A_2+\frac{A_3}{T}-\frac{A_1}{T^2}\right)$$
$$-\frac{A_3}{2A_2\sqrt{A_3^2+4A_1A_2}}\log_e\frac{\frac{-2A_1}{T}+A_3-\sqrt{A_3^2+4A_1A_2}}{\frac{-2A_1}{T}+A_3+\sqrt{A_3^2+4A_1A_2}}+C=x \tag{12}$$

The nonlinear Eq. (12) is applicable for determining the temperature of the flowing gases and must be solved by a suitable computer method for solving nonlinear equations. We have solved it by the Regula-Falsi method for natural gas pipelines with 16 percent methane and 84 percent ethane, for Schorre's (1954) observed values at winter and summer conditions. The constant C can be calculated from the boundary conditions, $T=T_{in}$ at $x=0$.

The results of the new equation have been compared with Schorre's observed values and the results of the Coulter equation. Figure 1 shows the results for winter conditions and Fig. 2 shows the results for summer conditions. Conditions that have been considered for solving Eq. (12) are:

(A) Winter Condition

$Q=184.5883$ m^3/s; $r_i=0.381$ m; $P_1=5472331.389$ Pa;

$P_2=3121223.4035$ Pa; $x=126955.3$ m; $T_g=16.67$°C;

$U=2.8391$ J/(m^2 s K); $c_p=2089$ J/(kg K);

$R=455.8$ J/(kg K);

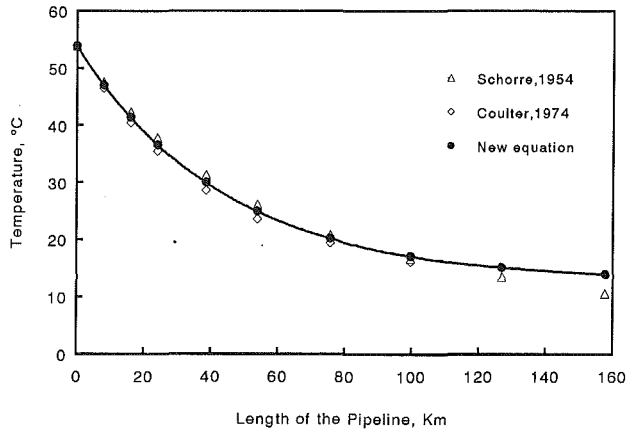

Fig. 1 Comparison between the results of Coulter, Schorre, and new equation for winter conditions

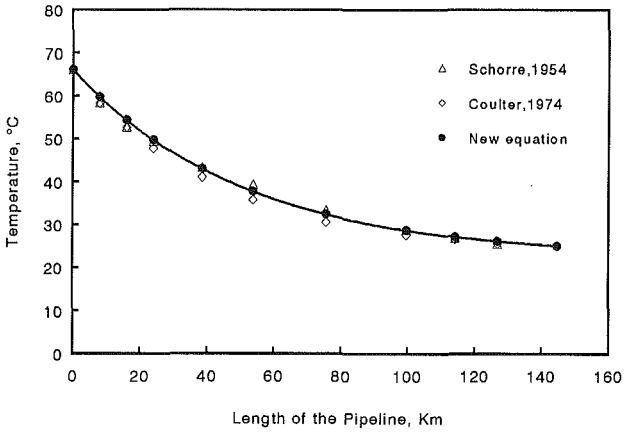

Fig. 2 Comparison between the results of Coulter, Schorre, and new equation for summer conditions

Van der Waals equation constants a and b would be equal to:

$a_{CH4}=229332.0572$ (J m^3)/kmole^2,

$a_{C2H6}=556069.5936$ (J m^3)/kmole^2

$a^{0.5}=\Sigma x_i a_i=0.84\ (229332.0572)^{0.5}+0.16\ (556069.5936)^{0.5}$

$a=272042.132$ (J m^3)/kmole^2

$b_{CH4}=0.04278$ m^3/kmole, $b_{C2H6}=0.0638$m^3/kmole

$b=\Sigma x_i b_i=0.84\ (0.04278)+0.16\ (0.0638)$

$b=0.0461432$ m^3/kmole

(B) Summer Condition

In this case, only Q, P_1, P_2 and T_g are different from the winter condition, the other conditions are the same.

$Q=213.667$ m^3/s; $p_1=5479226.1338$ Pa;

$p_2=3088845.6818$ Pa; $T_g=26.67$°C.

For the dP/dX term in A_1 and A_2, we have calculated it by using the Weymouth pressure drop formula. Also, we have used an average value for $\Delta p/x$. The calculations show that there is no major difference between the results.

Comparison and Conclusion

Schorre considered a linearly increasing Joule-Thompson effect and a gas temperature that was only due to conduction. This is a poor model since the heat transfer driving force is between the actual temperature and the ground. He defined the term J/A_2 as the temperature difference between the gas and the surroundings at equilibrium conditions, which would be necessary to hold the gas temperature constant, but his

equation shows a continuously decreasing gas temperature along the length of the pipeline and never reaches an equilibrium value, while the new equation does. In Coulter-Bardon and Coulter's equations, the Joule-Thompson effect has been considered constant. Figures 1 and 2 show the comparison between the results of the new equation and previous models. This formula is an improvement on previous equations considering the basic thermodynamic principles and the actual value of the Joule-Thompson coefficient and is applicable for obtaining the temperature of the various flowing gases.

Acknowledgments

The author wishes to thank Mr. Wolfgang Schmidl for his assistance in editing the manuscript.

References

Arpaci, V. S., 1966, *Conduction Heat Transfer*, Addison-Wesley Publishing Co., Reading, MA.

Carnahan, B., Luther, H. A., and Wilkes, J. O., 1969, *Applied Numerical Methods*, Wiley, New York.

Coulter, D. M., 1979, "New Equation Accurately Predicts Flowing Gas Temperatures," *Pipeline Industry*, Vol. 50, pp. 71-73.

Coulter, D. M., and Bardon, M. F., 1979, "Revised Equation Improves Flowing Gas Temperature Prediction," *The Oil and Gas Journal*, Vol. 77, pp. 107-108.

Edmister, W. C., 1984, *Applied Hydrocarbon Thermodynamics*, Gulf Publishing Co., Houston, TX.

Firoozabadi, A., 1977, "Gas Cooling Improves IGAT System Performance," *Pipeline Industry*, Vol. 47.

Forrest, J. A., 1978, "Interpreting the Schorre Gas Temperature Equation," *Pipeline Industry*, Vol. 48, pp. 58-60.

Katz, D. L., 1959, *Hand Book of Natural Gas Engineering*, McGraw-Hill, New York.

Prausnitz, J. M., Lichtenthaler, R. N., and Azevedo, E. G., 1986, *Molecular Thermodynamics of Fluid-Phase Equilibria*, Prentice-Hall, Englewood Cliffs, NJ.

Rawat, P. C., Agarwal, S. L., Malhorta, A. K., Gulhati, S. K., and Venkatappa, G., 1982, "Determination of Thermal Conductivity of Solids: A Need for Computing Heat Loss Through Buried Submarine Pipelines," *Society of Petroleum Engineering Journal*, Vol. 22, No. 4, pp. 558-562.

Robert, L. V., 1981, "Advantages of Pipelining Gas at Low Temperatures," *Pipeline Industry*, Vol. 55, pp. 49-56.

Schorre, C. E., 1954, "Flow Temperature in a Gas Pipeline," *The Oil and Gas Journal*, Vol. 53, pp. 64-68.

Zanker, A., 1980, "Nomograph Speed Calculation of Flowing Gas Temperatures," *Pipeline Industry*, Vol. 53, pp. 85-87.

A Time-Dependent Analysis of the Vortex Instability in the Thermal Entrance Region of an Inclined Parallel-Plate Channel

F. S. Lee[1,3] and G. J. Hwang[2,3]

Nomenclature

- a = wave number of longitudinal vortex = $2\pi h/\lambda$
- D = dimensionless continuity variable defined in Eq. (11)
- Gr_x = Grashof number based on streamwise onset distance = $\beta g(T_1 - T_0)x^3/\nu^2$
- h = distance between two parallel plates
- p = dimensionless amplitude function of perturbation pressure
- $\bar{p}$ = dimensionless basic pressure
- Pe = Peclet number = $U_m h/\kappa$
- Pr = Prandtl number = ν/κ
- Ra = Rayleigh number = $\beta g(T_1 - T_0)h^3/\nu\kappa$
- Re_x = Reynolds number based on streamwise onset distance = $U_m x/\nu$
- t = dimensionless time
- u, v, w = dimensionless amplitude functions of perturbation velocity in x, y, and z directions
- $\bar{u}, \bar{v}$ = dimensionless basic streamwise and normal velocities
- x, y, z = dimensionless streamwise, normal, and spanwise coordinates = X/h, Y/h, and Z/h
- x^* = dimensionless streamwise coordinate of onset position = $X/\mathrm{Pe}\cdot h$
- α = inclination angle of parallel-plate channel from the horizontal
- θ = dimensionless amplitude function of perturbation temperature
- $\bar{\theta}$ = dimensionless basic temperature
- λ = wavelength

Subscripts

- x = quantity based on streamwise distance
- 0 = upper plate
- 1 = lower plate

Superscripts

- * = critical condition
- 0 = initial state
- $\bar{}$ = basic flow quantity

Introduction

Using a linear stability theory, Hwang and Cheng (1973) studied the onset of longitudinal vortex rolls in the thermal entrance region of a horizontal parallel-plate channel heated from below. Hwang and Liu (1976) determined the onset of longitudinal vortices by flow visualization in the thermal entrance region of a horizontal parallel-plate channel heated from below. They observed that the critical Rayleigh number from flow visualization was 1.4 to 10 times higher than the theoretical predictions of Hwang and Cheng (1973). Kamotani and Ostrach (1976), and Kamotani et al. (1979) performed experiments for air flow in the thermal entrance region of a horizontal parallel-plate channel; the critical Rayleigh numbers agree reasonably with those of Hwang and Liu (1976). The effect of inclination on thermal instability has received relatively less attention in spite of its importance in practical application. Fukui et al. (1983) investigated the vortex instability in a fully developed laminar flow between horizontal and inclined parallel plates. The maximum inclination angle was 32.1 deg from the horizontal and the Rayleigh numbers were less than 9300. Maughan and Incropera (1987) performed experiments to study the effect of surface heat flux and channel orientation on the local Nusselt number in an inclined channel. The present investigation applies a time-dependent three-dimensional linear stability theory (Lee and Hwang, 1991a, 1991b) to study the effect of inclination on the onset of vortex instability in the thermal entrance region of a parallel-plate channel. The normalized transient perturbation equations in the normal and streamwise directions are derived, and then solved together with the basic flow equations for a changing Rayleigh number to determine the neutral stability condition by a criterion of $\partial/\partial t = 0$ with nonzero streamwise derivatives.

Theoretical Analysis

Consider a fully developed laminar flow of an incompressible viscous fluid in the thermal entrance region between inclined parallel plates with gap h, where the lower plate is heated isothermally with a temperature T_1 for $x \geq 0$. The inlet fluid temperature is constant and equal to the isothermal upper wall

[1]Ph.D. Candidate.

[2]Professor, Mem. ASME.

[3]Department of Power Mechanical Engineering, National Tsing Hua University, Hsinchu, Taiwan 30043.

Contributed by the Heat Transfer Division of THE AMERICAN SOCIETY OF MECHANICAL ENGINEERS. Manuscript received by the Heat Transfer Division February 1991; revision received October 1991. Keywords: Flow Instability, Mixed Convection, Numerical Methods.

equation shows a continuously decreasing gas temperature along the length of the pipeline and never reaches an equilibrium value, while the new equation does. In Coulter-Bardon and Coulter's equations, the Joule-Thompson effect has been considered constant. Figures 1 and 2 show the comparison between the results of the new equation and previous models. This formula is an improvement on previous equations considering the basic thermodynamic principles and the actual value of the Joule-Thompson coefficient and is applicable for obtaining the temperature of the various flowing gases.

Acknowledgments

The author wishes to thank Mr. Wolfgang Schmidl for his assistance in editing the manuscript.

References

Arpaci, V. S., 1966, *Conduction Heat Transfer*, Addison-Wesley Publishing Co., Reading, MA.

Carnahan, B., Luther, H. A., and Wilkes, J. O., 1969, *Applied Numerical Methods*, Wiley, New York.

Coulter, D. M., 1979, "New Equation Accurately Predicts Flowing Gas Temperatures," *Pipeline Industry*, Vol. 50, pp. 71-73.

Coulter, D. M., and Bardon, M. F., 1979, "Revised Equation Improves Flowing Gas Temperature Prediction," *The Oil and Gas Journal*, Vol. 77, pp. 107-108.

Edmister, W. C., 1984, *Applied Hydrocarbon Thermodynamics*, Gulf Publishing Co., Houston, TX.

Firoozabadi, A., 1977, "Gas Cooling Improves IGAT System Performance," *Pipeline Industry*, Vol. 47.

Forrest, J. A., 1978, "Interpreting the Schorre Gas Temperature Equation," *Pipeline Industry*, Vol. 48, pp. 58-60.

Katz, D. L., 1959, *Hand Book of Natural Gas Engineering*, McGraw-Hill, New York.

Prausnitz, J. M., Lichtenthaler, R. N., and Azevedo, E. G., 1986, *Molecular Thermodynamics of Fluid-Phase Equilibria*, Prentice-Hall, Englewood Cliffs, NJ.

Rawat, P. C., Agarwal, S. L., Malhorta, A. K., Gulhati, S. K., and Venkatappa, G., 1982, "Determination of Thermal Conductivity of Solids: A Need for Computing Heat Loss Through Buried Submarine Pipelines," *Society of Petroleum Engineering Journal*, Vol. 22, No. 4, pp. 558-562.

Robert, L. V., 1981, "Advantages of Pipelining Gas at Low Temperatures," *Pipeline Industry*, Vol. 55, pp. 49-56.

Schorre, C. E., 1954, "Flow Temperature in a Gas Pipeline," *The Oil and Gas Journal*, Vol. 53, pp. 64-68.

Zanker, A., 1980, "Nomograph Speed Calculation of Flowing Gas Temperatures," *Pipeline Industry*, Vol. 53, pp. 85-87.

A Time-Dependent Analysis of the Vortex Instability in the Thermal Entrance Region of an Inclined Parallel-Plate Channel

F. S. Lee[1,3] and G. J. Hwang[2,3]

Nomenclature

- a = wave number of longitudinal vortex = $2\pi h/\lambda$
- D = dimensionless continuity variable defined in Eq. (11)
- Gr_x = Grashof number based on streamwise onset distance = $\beta g(T_1 - T_0)x^3/\nu^2$
- h = distance between two parallel plates
- p = dimensionless amplitude function of perturbation pressure
- $\bar{p}$ = dimensionless basic pressure
- Pe = Peclet number = $U_m h/\kappa$
- Pr = Prandtl number = ν/κ
- Ra = Rayleigh number = $\beta g(T_1 - T_0)h^3/\nu\kappa$
- Re_x = Reynolds number based on streamwise onset distance = $U_m x/\nu$
- t = dimensionless time
- u, v, w = dimensionless amplitude functions of perturbation velocity in x, y, and z directions
- $\bar{u}, \bar{v}$ = dimensionless basic streamwise and normal velocities
- x, y, z = dimensionless streamwise, normal, and spanwise coordinates = X/h, Y/h, and Z/h
- x^* = dimensionless streamwise coordinate of onset position = $X/\mathrm{Pe}\cdot h$
- α = inclination angle of parallel-plate channel from the horizontal
- θ = dimensionless amplitude function of perturbation temperature
- $\bar{\theta}$ = dimensionless basic temperature
- λ = wavelength

Subscripts

- x = quantity based on streamwise distance
- 0 = upper plate
- 1 = lower plate

Superscripts

- $*$ = critical condition
- 0 = initial state
- $\bar{}$ = basic flow quantity

Introduction

Using a linear stability theory, Hwang and Cheng (1973) studied the onset of longitudinal vortex rolls in the thermal entrance region of a horizontal parallel-plate channel heated from below. Hwang and Liu (1976) determined the onset of longitudinal vortices by flow visualization in the thermal entrance region of a horizontal parallel-plate channel heated from below. They observed that the critical Rayleigh number from flow visualization was 1.4 to 10 times higher than the theoretical predictions of Hwang and Cheng (1973). Kamotani and Ostrach (1976), and Kamotani et al. (1979) performed experiments for air flow in the thermal entrance region of a horizontal parallel-plate channel; the critical Rayleigh numbers agree reasonably with those of Hwang and Liu (1976). The effect of inclination on thermal instability has received relatively less attention in spite of its importance in practical application. Fukui et al. (1983) investigated the vortex instability in a fully developed laminar flow between horizontal and inclined parallel plates. The maximum inclination angle was 32.1 deg from the horizontal and the Rayleigh numbers were less than 9300. Maughan and Incropera (1987) performed experiments to study the effect of surface heat flux and channel orientation on the local Nusselt number in an inclined channel. The present investigation applies a time-dependent three-dimensional linear stability theory (Lee and Hwang, 1991a, 1991b) to study the effect of inclination on the onset of vortex instability in the thermal entrance region of a parallel-plate channel. The normalized transient perturbation equations in the normal and streamwise directions are derived, and then solved together with the basic flow equations for a changing Rayleigh number to determine the neutral stability condition by a criterion of $\partial/\partial t = 0$ with nonzero streamwise derivatives.

Theoretical Analysis

Consider a fully developed laminar flow of an incompressible viscous fluid in the thermal entrance region between inclined parallel plates with gap h, where the lower plate is heated isothermally with a temperature T_1 for $x \geq 0$. The inlet fluid temperature is constant and equal to the isothermal upper wall

[1]Ph.D. Candidate.

[2]Professor, Mem. ASME.

[3]Department of Power Mechanical Engineering, National Tsing Hua University, Hsinchu, Taiwan 30043.

Contributed by the Heat Transfer Division of THE AMERICAN SOCIETY OF MECHANICAL ENGINEERS. Manuscript received by the Heat Transfer Division February 1991; revision received October 1991. Keywords: Flow Instability, Mixed Convection, Numerical Methods.

temperature T_0. The normalized governing equations of basic flow are:

$$\frac{\partial \bar{u}}{\partial x}+\frac{\partial \bar{v}}{\partial y}=0 \tag{1}$$

$$\left[\frac{\mathrm{Pe}}{\mathrm{Pr}}\right]\left(\bar{u}\frac{\partial \bar{u}}{\partial x}+\bar{v}\frac{\partial \bar{u}}{\partial y}\right)=-\frac{\partial \bar{p}}{\partial x}+\left[\frac{\mathrm{Ra}}{\mathrm{Pe}}\right]\bar{\theta}\sin\alpha+\left(\frac{\partial^2\bar{u}}{\partial x^2}+\frac{\partial^2\bar{u}}{\partial y^2}\right) \tag{2}$$

$$\left[\frac{\mathrm{Pe}}{\mathrm{Pr}}\right]\left(\bar{u}\frac{\partial \bar{v}}{\partial x}+\bar{v}\frac{\partial \bar{v}}{\partial y}\right)=-\frac{\partial \bar{p}}{\partial y}+\left[\frac{\mathrm{Ra}}{\mathrm{Pe}}\right]\bar{\theta}\cos\alpha+\left(\frac{\partial^2\bar{v}}{\partial x^2}+\frac{\partial^2\bar{v}}{\partial y^2}\right) \tag{3}$$

$$[\mathrm{Pe}]\left(\bar{u}\frac{\partial \bar{\theta}}{\partial x}+\bar{v}\frac{\partial \bar{\theta}}{\partial y}\right)=\left(\frac{\partial^2\bar{\theta}}{\partial x^2}+\frac{\partial^2\bar{\theta}}{\partial y^2}\right) \tag{4}$$

The associated boundary conditions are:

$$\begin{aligned}&\bar{u}=\bar{v}=\bar{\theta}-1=0 && \text{at } y=0\\ &\bar{u}=\bar{v}=\bar{\theta}=0 && \text{at } y=1\\ &\bar{u}-6\cdot(y-y^2)=\bar{v}=\bar{\theta}=0 && \text{at } x=0\\ &\frac{\partial \bar{u}}{\partial x}=\frac{\partial \bar{v}}{\partial x}=\frac{\partial \bar{\theta}}{\partial x}=0 && \text{at } x=\infty\end{aligned} \tag{5}$$

Perturbation Equations

Based on the same procedure as previous works (Lee and Hwang, 1991a, 1991b), governing equations of perturbation flow are stated as follows:

$$\frac{\partial u}{\partial x}+\frac{\partial v}{\partial y}-aw=0 \tag{6}$$

$$\frac{\partial u}{\partial t}+\left[\frac{\mathrm{Pe}}{\mathrm{Pr}}\right]\left(\bar{u}\frac{\partial u}{\partial x}+u\frac{\partial \bar{u}}{\partial x}+\bar{v}\frac{\partial u}{\partial y}+v\frac{\partial \bar{u}}{\partial y}\right)=-\frac{\partial p}{\partial x}+\nabla^2 u+\left[\frac{\mathrm{Ra}}{\mathrm{Pe}}\right]\theta\sin\alpha \tag{7}$$

$$\frac{\partial v}{\partial t}+\left[\frac{\mathrm{Pe}}{\mathrm{Pr}}\right]\left(\bar{u}\frac{\partial v}{\partial x}+u\frac{\partial \bar{v}}{\partial x}+\bar{v}\frac{\partial v}{\partial y}+v\frac{\partial \bar{v}}{\partial y}\right)=-\frac{\partial p}{\partial y}+\nabla^2 v+\left[\frac{\mathrm{Ra}}{\mathrm{Pe}}\right]\theta\cos\alpha \tag{8}$$

$$\frac{\partial w}{\partial t}+\left[\frac{\mathrm{Pe}}{\mathrm{Pr}}\right]\left(\bar{u}\frac{\partial w}{\partial x}+\bar{v}\frac{\partial w}{\partial y}\right)=-ap+\nabla^2 w \tag{9}$$

$$\frac{\partial \theta}{\partial t}+\left[\frac{\mathrm{Pe}}{\mathrm{Pr}}\right]\left(\bar{u}\frac{\partial \theta}{\partial x}+u\frac{\partial \bar{\theta}}{\partial x}+\bar{v}\frac{\partial \theta}{\partial y}+v\frac{\partial \bar{\theta}}{\partial y}\right)=-\left[\frac{1}{\mathrm{Pr}}\right]\nabla^2\theta \tag{10}$$

$$\nabla^2 p=-\frac{\partial D}{\partial t}+\nabla^2 D-\left[\frac{\mathrm{Pe}}{\mathrm{Pr}}\right]\left(\bar{u}\frac{\partial D}{\partial x}+\bar{v}\frac{\partial D}{\partial y}\right)-2\left[\frac{\mathrm{Pe}}{\mathrm{Pr}}\right]\left(\frac{\partial v}{\partial x}\frac{\partial \bar{u}}{\partial y}+\frac{\partial u}{\partial y}\frac{\partial \bar{v}}{\partial x}+\frac{\partial u}{\partial x}\frac{\partial \bar{u}}{\partial x}+\frac{\partial v}{\partial y}\frac{\partial \bar{v}}{\partial y}\right)-\left[\frac{\mathrm{Pe}}{\mathrm{Pr}}\right]\left\{u\left(\frac{\partial^2\bar{u}}{\partial x^2}+\frac{\partial^2\bar{v}}{\partial x\partial y}\right)+v\left(\frac{\partial^2\bar{v}}{\partial y^2}+\frac{\partial^2\bar{u}}{\partial x\partial y}\right)\right\}+\left[\frac{\mathrm{Ra}}{\mathrm{Pe}}\right]\left(\frac{\partial \theta}{\partial y}\cos\alpha+\frac{\partial \theta}{\partial x}\sin\alpha\right) \tag{11}$$

where

$$\nabla^2=\frac{\partial^2}{\partial x^2}+\frac{\partial^2}{\partial y^2}-a^2 \text{ and } D=\frac{\partial u}{\partial x}+\frac{\partial v}{\partial y}-aw.$$

The appropriate boundary conditions and initial conditions are:

$$u=v=w=\theta=0 \quad \text{at } y=0 \text{ and } 1, \text{ and } x=0$$

$$\frac{\partial u}{\partial x}=\frac{\partial v}{\partial x}=\frac{\partial w}{\partial x}=\frac{\partial \theta}{\partial x}=\frac{\partial p}{\partial x}=0 \quad \text{at } x=\infty \tag{12}$$

$$u=v=w=\theta-\theta^0=p=0 \quad \text{at } t=0 \tag{13}$$

where θ^0 is set at 1×10^{-10} in the present computation, following the same solution procedure as previous works (Lee and Hwang, 1991a, 1991b), except that the basic flow equations are solved iteratively for a varying Ra with the perturbation equations.

Results and Discussion

For a horizontal channel flow ($\alpha=0$), the maximum axial velocity is located near the center of channel; an adverse temperature gradient appears in the gravitational direction due to the heated bottom plate. For an upward inclined flow ($\alpha>0$), the maximum axial velocity shifts toward the heated wall due to free convection. The streamwise flow acceleration is mainly due to the buoyancy force parallel to the channel $[\mathrm{Ra/Pe}]\cdot\bar{\theta}\cdot\sin\alpha$ shown in Eq. (2), and partially due to induced pressure gradient from $[\mathrm{Ra/Pe}]\cdot\bar{\theta}\cdot\cos\alpha$ shown in Eq. (3). As the inclination angle is increased, a large fraction of fluid flows near the heated plate, so the flow must undergo a reversal near the upper plate to maintain mass conservation. For a downward inclined flow ($\alpha<0$), the term $[\mathrm{Ra/Pe}]\cdot\bar{\theta}\cdot\sin\alpha$ is negative, and a decelerated flow in the streamwise direction is shown. The deceleration is proportional to the basic flow temperature $\bar{\theta}$, and the location of maximum axial velocity shifts toward the upper plate.

Figure 1 shows the critical Rayleigh number Ra* marking the onset of longitudinal vortex instability along the streamwise direction with various inclination angles for Pr = 0.7 and 7.0. The previous theoretical and experimental data are also presented for comparison. The theoretical prediction for $\alpha = 0$ (Hwang and Cheng, 1973) underestimated the critical Ra* in comparison with experimental results. For the case of an upward inclined channel flow, the critical Ra* increases with an increase in inclination. It is understood that the basic flow is accelerated near the heated lower plate and the thickness of the thermal boundary layer is thinner for $\alpha>0$. These situations stabilize the upward inclined channel flow. This stabilizing effect is also demonstrated by experimental investigation (Maughan and Incropera, 1987). Among the experimental data shown in Fig. 1, the results of Maughan and Incropera (1987) present higher critical values than the others. Kamotani and Ostrach (1976), Kamotani et al. (1979), and Hwang and Liu

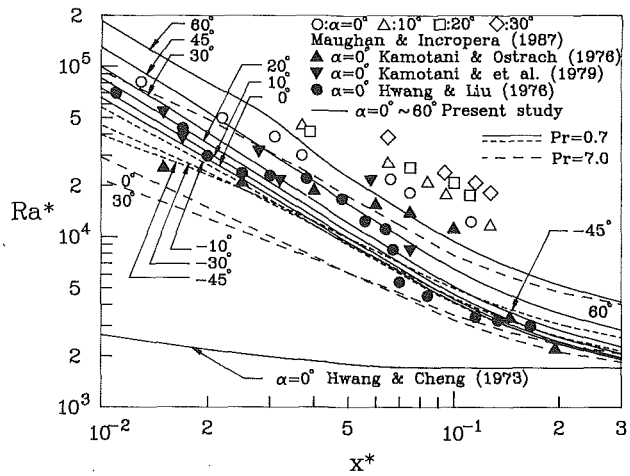

Fig. 1 Critical condition for inclined channel

(1976) determined the onset of thermal instability from flow visualization of secondary flow. On the other hand, Maughan and Incropera (1987) inferred the onset point from a sharp increase in heat transfer enhancement curves. Heat transfer enhancement occurs downstream of the onset position of an infinitesimal disturbance. The results of the present predictions for $Pr = 0.7$, $Pe = 175$, inclination angles 0 deg $\leq \alpha \leq$ 60 deg, and onset positions $0.01 \leq x^* \leq 0.30$ can be correlated within an average difference of 7.3 percent by the following equation:

$$\log\left[\frac{Ra^* \cdot \cos\alpha}{1+0.09\cdot\tan\alpha}\right] = 2.9274 - 0.4903\cdot\log x^* + 0.2487\cdot(\log x^*)^2 \quad (14)$$

It is clear that there are no theoretical predictions or experimental data concerning the instability of a downward inclined channel flow available in the literature. Figure 1 also shows that the critical Rayleigh numbers of downward inclined flow do not behave as those of the upward inclined flow. In the inlet region $x^* \leq 0.02$, the critical Ra* decreases as the inclination angle $|\alpha|$ increases. In downstream regions $x^* \geq 0.04$, the increase of inclination angle $|\alpha|$ presents an opposite effect on the critical Ra*. This behavior requires a more detailed interpretation of the effect of basic flow on the vortex instability. As shown in Eq. (2), the term $[Ra/Pe]\cdot\bar{\theta}\cdot\sin\alpha$ is negative for $\alpha < 0$, and gives a streamwise flow deceleration. The thicker the thermal boundary layer, the lower the critical Ra*. It is seen in Eq. (3) that the buoyancy force in the normal direction is weakened by a large inclination angle $|\alpha|$ through the term $[Ra/Pe]\cdot\bar{\theta}\cdot\cos\alpha$ in spite of upward or downward inclination. This stabilizes an inclined flow for a larger $|\alpha|$ for both $\alpha > 0$ and $\alpha < 0$. This demonstrates the opposite effect of inclination angle on the critical Ra* at $x^* \geq 0.04$.

It is observed that the flow is more unstable for $Pr = 7.0$ than that for $Pr = 0.7$. This may be explained by examining the inertia terms $\bar{u}\cdot\partial u/\partial x$, $\bar{u}\cdot\partial v/\partial x$, and $\bar{u}\cdot\partial w/\partial x$ with a coefficient [Pe/Pr] in Eqs. (7), (8), and (9), respectively. These terms suppress the disturbance and their values decrease with an increase in the Prandtl number. One may conclude that air is more stable than water in thermal instability in spite of channel inclination.

Figure 2 shows the variation of the critical wave number a^* along the streamwise direction with various inclination angles for $Pr = 0.7$ and 7.0. It is seen that the critical wave number a^* decreases monotonically along the streamwise direction. As the onset of instability moves upstream, the corresponding critical wave number increases due to a thinner thermal boundary layer near the inlet. When the inclination angle is increased from -45 deg to 30 deg, the a^* value increases monotonically. But when the inclination is increased from 30 to 60 deg, a^* is decreased in the region near the channel inlet. This may be because the thickness of the unstable region in the vertical direction (g direction) is increased when $\alpha \geq 30$ deg, giving a larger vortex size or a smaller a^*. It is clear that the critical wave number a^* is smaller for $Pr = 7.0$ than for $Pr = 0.7$. Due to less suppression force for $Pr = 7.0$ in the streamwise direction, a larger unstable region in the y direction is provided for larger vortex rolls. The larger vortex rolls give a smaller critical wave number.

In the region near the inlet of a parallel-plate channel, the thermal boundary layer is thin and the temperature field in this region may not be far from that of a single plate. Although the flow field is not the same, it is still interesting to compare the results for these two physical configurations. The previous studies for the onset of flow instability in the thermal boundary layer over an isothermal plate are shown in Fig. 3. The previous theoretical prediction of Chen et al., (1982) presents an underestimation about two orders of magnitude lower than the experimental investigations of Abu-Mulaweh et al. (1987), and

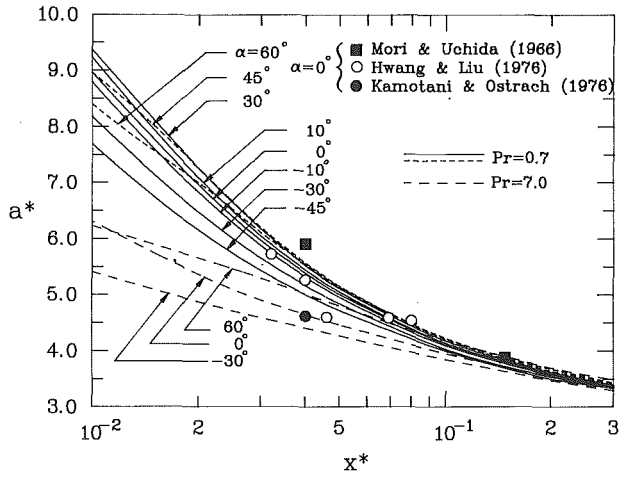

Fig. 2 Critical wave number a^* versus the streamwise coordinate for various inclination angles

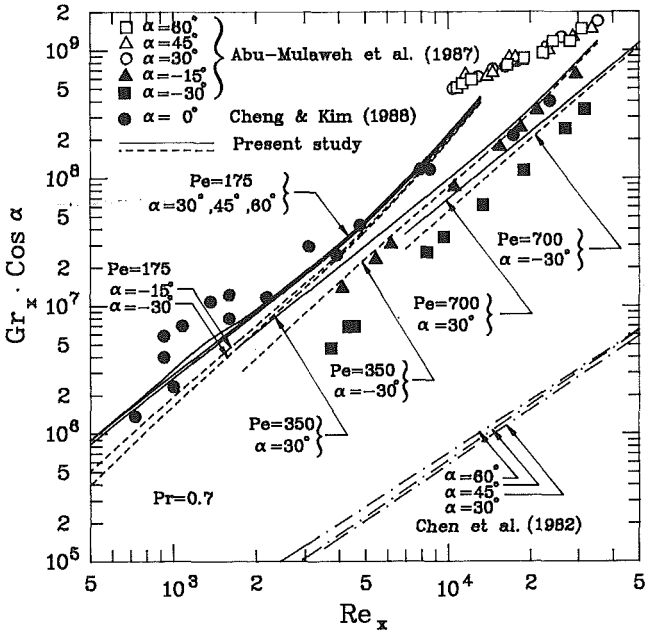

Fig. 3 Comparison of results on an isothermal inclined plate

Cheng and Kim (1988). For comparison, the value of Ra* and Pe in this study are changed to Gr_x and Re_x by

$$Re_x = \left(\frac{Pe}{Pr}\right)\cdot x \text{ and } Gr_x = \left(\frac{Ra^*}{Pr}\right)\cdot x^3 \quad (15)$$

The present result is much closer to the experimental data than that of the previous prediction (Chen et al., 1982). It is also interesting to see that the present theoretical prediction for $\alpha > 0$ fall on the same line as the experimental data of Abu-Mulaweh et al. (1987). It is also noted that the region for wave instability determined by Chen et al., 1982) is in the range of $Re_x > 8.5\times10^4$, which is beyond the scope of this figure.

Concluding Remarks

1 Inclination of the channel has a stabilizing effect on the flow for an upward inclined channel due to the streamwise acceleration in the basic flow. The stabilizing effect was also shown by the corresponding experimental data in the literature. For a downward inclined channel, the basic flow streamwise deceleration dominates the flow instability condition. The inclination destabilizes the flow near the inlet region, but stabilizes the flow in the downstream region.

2 In spite of the channel inclination, the increasing Prandtl number for a fixed Peclet number has a destabilizing effect on the flow along the streamwise direction, and gives a smaller critical wave number.

3 Although the flow field is not the same, it is interesting to compare the results between the data for a single plate and parallel plates by considering the thin thermal boundary layer in the thermal entrance region of the parallel-plate channel.

Acknowledgments

The authors would like to acknowledge the National Science Council, ROC, for its support of the present work through project NSC 79-0404-E007-07.

References

Abu-Mulaweh, H. I., Armaly, B. F., and Chen, T. S., 1987, "Instabilities of Mixed Convection Flows Adjacent to Inclined Plates," ASME JOURNAL OF HEAT TRANSFER, Vol. 109, pp. 1031-1033.

Chen, T. S., Moutsoglou, A., and Armaly, B. F., 1982, "Thermal Instability of Mixed Convection Flow Over Inclined Surfaces," *Numerical Heat Transfer*, Vol. 5, pp. 343-352.

Cheng, K. C., and Kim, Y. W., 1988, "Vortex Instability Phenomena Relating to the Cooling of a Horizontal Isothermal Flat-Plate by Natural and Forced Laminar Convection Flows," *Cooling Technology for Electronic Equipment*, W. Aung, ed., Hemisphere, Washington, DC, pp. 169-182.

Fukui, K., Nakajima, M., and Ueda, H., 1983, "The Longitudinal Vortex and Its Effects on the Transport Processes in Combined Free and Forced Laminar Convection Between Horizontal and Inclined Parallel Plates," *Int. J. Heat Mass Transfer*, Vol. 26, pp. 109-120.

Hwang, G. J., and Cheng, K. C., 1973, "Convective Instability in the Thermal Entrance Region of a Horizontal Parallel-Plate Channel Heated From Below," ASME JOURNAL OF HEAT TRANSFER, Vol. 95, pp. 72-77.

Hwang, G. J., and Liu, C. L., 1976, "An Experimental Study of Convective Instability in the Thermal Entrance Region of a Horizontal Parallel-Plate Channel Heated From Below," *Can. J. Chem. Eng.*, Vol. 54, pp. 521-525.

Kamotani, Y., and Ostrach, S., 1976, "Effect of Thermal Instability on Thermally Developing Laminar Channel Flow," ASME JOURNAL OF HEAT TRANSFER, Vol. 98, pp. 62-66.

Kamotani, Y., Ostrach, S., and Miao, H., 1979, "Convective Heat Transfer Augmentation in Thermal Entrance Regions by Means of Thermal Instability," ASME JOURNAL OF HEAT TRANSFER, Vol. 101, pp. 222-226.

Lee, F. S., and Hwang, G. J., 1991a, "Transient Analysis on the Onset of Thermal Instability in the Thermal Entrance Region of a Horizontal Parallel Plate Channel," ASME JOURNAL OF HEAT TRANSFER, Vol. 113, pp. 363-370.

Lee, F. S., and Hwang, G. J., 1991b, "The Effect of Asymmetric Heating on the Onset of Thermal Instability in the Thermal Entrance Region of a Parallel Plate Channel," *Int. J. Heat Mass Transfer*, Vol. 34, pp. 2207-2218.

Maughan, J. R., and Incropera, F. P., 1987, "Experiments on Mixed Convection Heat Transfer for Airflow in a Horizontal and Inclined Channel," *Int. J. Heat Mass Transfer*, Vol. 30, pp. 1307-1318.

Mori, Y., and Uchida, Y., 1966, "Forced Convective Heat Transfer Between Horizontal Flat Plates," *Int. J. Heat Mass Transfer*, Vol. 9, pp. 803-817.

Enhancement of Single-Phase Heat Transfer and Critical Heat Flux From an Ultra-High-Flux Simulated Microelectronic Heat Source to a Rectangular Impinging Jet of Dielectric Liquid

D. C. Wadsworth[1, 3] and I. Mudawar[2, 3]

Nomenclature

a = empirical constant
A_p = heat source planform area
A_T = heat source total wetted area
C = empirical constant
c_p = specific heat of liquid
H = height of confinement channel between chip surface and nozzle surface
h_{fg} = latent heat of vaporization
k = thermal conductivity of liquid based on mean liquid temperature
L = length (and width) of heat source (12.7 mm)
$\overline{\mathrm{Nu}}_A$ = average Nusselt number based on wetted area = $q(A_p/A_T)L/(T_s - T_f)k$
$\overline{\mathrm{Nu}}_L$ = average Nusselt number based on heater length = $qL/(T_s - T_f)k$
Pr = Prandtl number of liquid based on mean liquid temperature
q = mean heat flux based on heat source planform area
q_m = critical heat flux based on heat source planform area
q_{mA} = critical heat flux based on wetted area = $q_m(A_p/A_T)$
Re = Reynolds number based on mean jet velocity and orifice hydraulic diameter = $U(2W)/\nu$
T_f = liquid temperature at nozzle inlet
T_m = mean liquid temperature = $(T_s + T_f)/2$
T_s = mean surface temperature
T_{sat} = saturation temperature
ΔT_{sat} = $T_s - T_{\mathrm{sat}}$
ΔT_{sub} = $T_{\mathrm{sat}} - T_f$
U = mean jet velocity at orifice exit
W = width of rectangular orifice
ν = kinematic viscosity of liquid based on mean liquid temperature

Introduction

Jet impingement is encountered in numerous applications demanding high heating or cooling fluxes. Examples include annealing of metal sheets and cooling of turbine blades, x-ray medical devices, laser weapons, and fusion blankets. The attractive heat transfer attributes of jet impingement have also stimulated research efforts on cooling of high-heat-flux microelectronic devices. These devices are fast approaching heat fluxes in excess of 100 W/cm^2 (Ma and Bergles, 1983), which have to be dissipated using coolants that are both electrically and chemically compatible with electronic components. Unfortunately, fluids satisfying these requirements tend to possess poor transport properties, creating a need for significant enhancement in the heat transfer coefficient by such means as increased coolant flow rate and phase change. The cooling problem is compounded by a need to cool large arrays of heat sources in minimal volume, and to reduce the spacing between adjacent circuit boards. These requirements place severe constraints on the packaging of jet impingement cooling hardware.

Recently, the authors of this study presented a new concept for cooling multi-heat-source electronic circuit boards using jets of dielectric liquid issued from thin rectangular slots into channels confined between the surfaces of the chips and the opposite nozzle manifolding plate (Wadsworth and Mudawar, 1990). They demonstrated the predictability and uniformity of cooling for each of nine heat sources in a 3 × 3 heat source array and presented a correlation for the single-phase convective heat transfer coefficient as a function of jet width, length of heat source, flow velocity, and fluid properties.

The authors also examined the cooling performance of the multi-heat-source jet impingement module during phase change (Mudawar and Wadsworth, 1991). As in the case of single-phase cooling, cooling uniformity was demonstrated for each of the nine heat sources and guidelines were developed to preclude any degradation of cooling performance resulting from bubble generation within the confinement channels.

Despite being tested for a 3 × 3 heat source array only, the near perfect uniformity of cooling suggests this cooling concept

[1]Graduate Research Assistant.

[2]Associate Professor and Director of the Purdue University Boiling and Two-Phase Flow Laboratory.

[3]Boiling and Two-Phase Flow Laboratory, School of Mechanical Engineering, Purdue University, West Lafayette, IN 47907.

Contributed by the Heat Transfer Division of THE AMERICAN SOCIETY OF MECHANICAL ENGINEERS. Manuscript received by the Heat Transfer Division April 1991; revision received January 1992. Keywords: Boiling, Electronic Equipment, Jets.

2 In spite of the channel inclination, the increasing Prandtl number for a fixed Peclet number has a destabilizing effect on the flow along the streamwise direction, and gives a smaller critical wave number.

3 Although the flow field is not the same, it is interesting to compare the results between the data for a single plate and parallel plates by considering the thin thermal boundary layer in the thermal entrance region of the parallel-plate channel.

Acknowledgments

The authors would like to acknowledge the National Science Council, ROC, for its support of the present work through project NSC 79-0404-E007-07.

References

Abu-Mulaweh, H. I., Armaly, B. F., and Chen, T. S., 1987, "Instabilities of Mixed Convection Flows Adjacent to Inclined Plates," ASME JOURNAL OF HEAT TRANSFER, Vol. 109, pp. 1031–1033.

Chen, T. S., Moutsoglou, A., and Armaly, B. F., 1982, "Thermal Instability of Mixed Convection Flow Over Inclined Surfaces," *Numerical Heat Transfer*, Vol. 5, pp. 343–352.

Cheng, K. C., and Kim, Y. W., 1988, "Vortex Instability Phenomena Relating to the Cooling of a Horizontal Isothermal Flat-Plate by Natural and Forced Laminar Convection Flows," *Cooling Technology for Electronic Equipment*, W. Aung, ed., Hemisphere, Washington, DC, pp. 169–182.

Fukui, K., Nakajima, M., and Ueda, H., 1983, "The Longitudinal Vortex and Its Effects on the Transport Processes in Combined Free and Forced Laminar Convection Between Horizontal and Inclined Parallel Plates," *Int. J. Heat Mass Transfer*, Vol. 26, pp. 109–120.

Hwang, G. J., and Cheng, K. C., 1973, "Convective Instability in the Thermal Entrance Region of a Horizontal Parallel-Plate Channel Heated From Below," ASME JOURNAL OF HEAT TRANSFER, Vol. 95, pp. 72–77.

Hwang, G. J., and Liu, C. L., 1976, "An Experimental Study of Convective Instability in the Thermal Entrance Region of a Horizontal Parallel-Plate Channel Heated From Below," *Can. J. Chem. Eng.*, Vol. 54, pp. 521–525.

Kamotani, Y., and Ostrach, S., 1976, "Effect of Thermal Instability on Thermally Developing Laminar Channel Flow," ASME JOURNAL OF HEAT TRANSFER, Vol. 98, pp. 62–66.

Kamotani, Y., Ostrach, S., and Miao, H., 1979, "Convective Heat Transfer Augmentation in Thermal Entrance Regions by Means of Thermal Instability," ASME JOURNAL OF HEAT TRANSFER, Vol. 101, pp. 222–226.

Lee, F. S., and Hwang, G. J., 1991a, "Transient Analysis on the Onset of Thermal Instability in the Thermal Entrance Region of a Horizontal Parallel Plate Channel," ASME JOURNAL OF HEAT TRANSFER, Vol. 113, pp. 363–370.

Lee, F. S., and Hwang, G. J., 1991b, "The Effect of Asymmetric Heating on the Onset of Thermal Instability in the Thermal Entrance Region of a Parallel Plate Channel," *Int. J. Heat Mass Transfer*, Vol. 34, pp. 2207–2218.

Maughan, J. R., and Incropera, F. P., 1987, "Experiments on Mixed Convection Heat Transfer for Airflow in a Horizontal and Inclined Channel," *Int. J. Heat Mass Transfer*, Vol. 30, pp. 1307–1318.

Mori, Y., and Uchida, Y., 1966, "Forced Convective Heat Transfer Between Horizontal Flat Plates," *Int. J. Heat Mass Transfer*, Vol. 9, pp. 803–817.

Enhancement of Single-Phase Heat Transfer and Critical Heat Flux From an Ultra-High-Flux Simulated Microelectronic Heat Source to a Rectangular Impinging Jet of Dielectric Liquid

D. C. Wadsworth[1, 3] and I. Mudawar[2, 3]

Nomenclature

a = empirical constant
A_p = heat source planform area
A_T = heat source total wetted area
C = empirical constant
c_p = specific heat of liquid
H = height of confinement channel between chip surface and nozzle surface
h_{fg} = latent heat of vaporization
k = thermal conductivity of liquid based on mean liquid temperature
L = length (and width) of heat source (12.7 mm)
$\overline{\mathrm{Nu}}_A$ = average Nusselt number based on wetted area = $q(A_p/A_T)L/(T_s - T_f)k$
$\overline{\mathrm{Nu}}_L$ = average Nusselt number based on heater length = $qL/(T_s - T_f)k$
Pr = Prandtl number of liquid based on mean liquid temperature
q = mean heat flux based on heat source planform area
q_m = critical heat flux based on heat source planform area
q_{mA} = critical heat flux based on wetted area = $q_m(A_p/A_T)$
Re = Reynolds number based on mean jet velocity and orifice hydraulic diameter = $U(2W)/\nu$
T_f = liquid temperature at nozzle inlet
T_m = mean liquid temperature = $(T_s + T_f)/2$
T_s = mean surface temperature
T_{sat} = saturation temperature
ΔT_{sat} = $T_s - T_{\mathrm{sat}}$
ΔT_{sub} = $T_{\mathrm{sat}} - T_f$
U = mean jet velocity at orifice exit
W = width of rectangular orifice
ν = kinematic viscosity of liquid based on mean liquid temperature

Introduction

Jet impingement is encountered in numerous applications demanding high heating or cooling fluxes. Examples include annealing of metal sheets and cooling of turbine blades, x-ray medical devices, laser weapons, and fusion blankets. The attractive heat transfer attributes of jet impingement have also stimulated research efforts on cooling of high-heat-flux microelectronic devices. These devices are fast approaching heat fluxes in excess of 100 W/cm^2 (Ma and Bergles, 1983), which have to be dissipated using coolants that are both electrically and chemically compatible with electronic components. Unfortunately, fluids satisfying these requirements tend to possess poor transport properties, creating a need for significant enhancement in the heat transfer coefficient by such means as increased coolant flow rate and phase change. The cooling problem is compounded by a need to cool large arrays of heat sources in minimal volume, and to reduce the spacing between adjacent circuit boards. These requirements place severe constraints on the packaging of jet impingement cooling hardware.

Recently, the authors of this study presented a new concept for cooling multi-heat-source electronic circuit boards using jets of dielectric liquid issued from thin rectangular slots into channels confined between the surfaces of the chips and the opposite nozzle manifolding plate (Wadsworth and Mudawar, 1990). They demonstrated the predictability and uniformity of cooling for each of nine heat sources in a 3 × 3 heat source array and presented a correlation for the single-phase convective heat transfer coefficient as a function of jet width, length of heat source, flow velocity, and fluid properties.

The authors also examined the cooling performance of the multi-heat-source jet impingement module during phase change (Mudawar and Wadsworth, 1991). As in the case of single-phase cooling, cooling uniformity was demonstrated for each of the nine heat sources and guidelines were developed to preclude any degradation of cooling performance resulting from bubble generation within the confinement channels.

Despite being tested for a 3 × 3 heat source array only, the near perfect uniformity of cooling suggests this cooling concept

[1]Graduate Research Assistant.

[2]Associate Professor and Director of the Purdue University Boiling and Two-Phase Flow Laboratory.

[3]Boiling and Two-Phase Flow Laboratory, School of Mechanical Engineering, Purdue University, West Lafayette, IN 47907.

Contributed by the Heat Transfer Division of THE AMERICAN SOCIETY OF MECHANICAL ENGINEERS. Manuscript received by the Heat Transfer Division April 1991; revision received January 1992. Keywords: Boiling, Electronic Equipment, Jets.

is applicable to larger arrays of heat sources. For example, in a 10 × 10 heat source module, fluid exiting the heat source confinement channels could be routed laterally through passages separating rows of 10 heat sources. Alternatively, the fluid could be rejected from each of four 5 × 5 arrays separately before being routed to a single outlet.

Machining microstructures into the surface of the heat source is another means of enhancing cooling effectiveness both in the single-phase and two-phase regimes. One important measure for this effectiveness is critical heat flux (CHF), which defines the upper limit on heat flux achievable with any electronic cooling system. In the case of electronic cooling, microstructures can be formed either directly on the chip surface by such techniques as chemical etching or laser cutting, or by bonding a micro-machined metallic attachment to the chip surface. The latter approach produces an additional contact resistance, which can be minimized with the use of a high thermal conductivity solder.

The CHF enhancement potential of microstructures has been successfully demonstrated in a variety of cooling configurations. Nakayama et al. (1984) and Mudawar and Anderson (1989) achieved, respectively, over 450 and 700 percent enhancement in CHF in the pool boiling of FC-72, a dielectric fluid made by 3M, by bonding onto the heat source studs covered with miniature structures. Grimley et al. (1988) tested microstructured surfaces to enhance CHF in an FC-72 liquid film flowing over a vertically mounted heat source. Surfaces with rectangular microgrooves machined in the direction of fluid flow produced the highest CHF compared to those with smooth or square microstud finish. Similar surfaces were tested by Mudawar and Maddox (1990) in the boiling of FC-72 flowing parallel to the surface of a heat source mounted on one wall of a rectangular flow channel. CHF increased with increasing microfin height, reaching values of 262 and 317 W/cm^2 for the microstud and microgroove surfaces, respectively.

The focus of the present paper is to examine means of boosting the power dissipation of electronic heat sources via a combination of jet impingement, subcooled phase change, and low-profile surface enhancement using the jet-impingement cooling concept described in the paper by Wadsworth and Mudawar (1990).

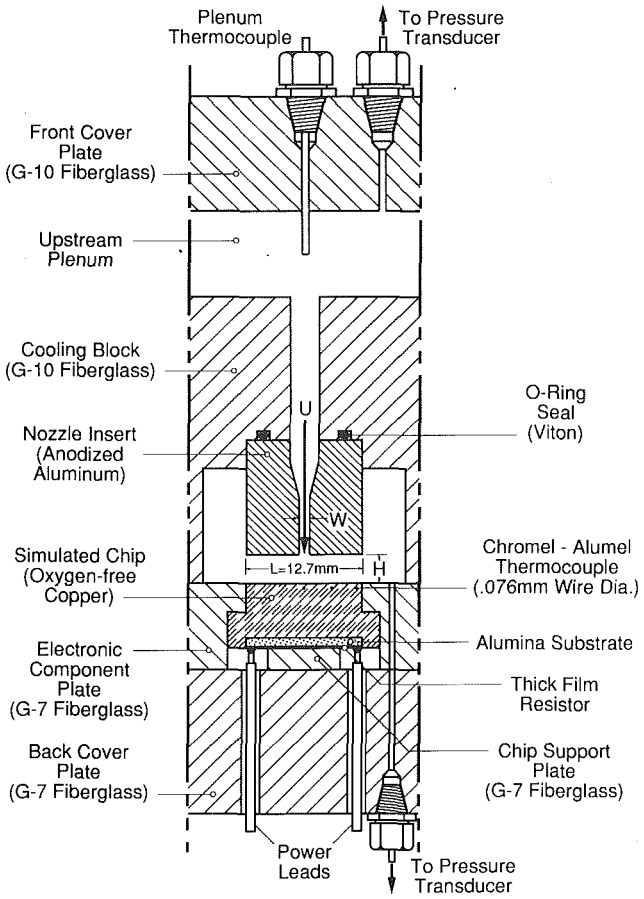

Fig. 1 Sectional diagram of cooling module; heat source (simulated chip) is shown without surface enhancement

Experimental Methods

Experiments were performed with a single 12.7 mm × 12.7 mm heat source housed in a cooling module as shown in Fig. 1. The module consisted of four parallel attachments: a front cover plate, cooling block, heat source plate, and back cover. Fluorinert FC-72, a dielectric coolant having a boiling point of 56°C at atmospheric pressure, was supplied into a plenum chamber formed between the front cover plate and the cooling block, where liquid temperature and pressure were measured, and impinged upon the surface of the heat source. Following impingement, the flow was confined to two channels (one on each side of the impingement zone) formed between the surfaces of the heat source and nozzle insert, and routed to the module exit port through relatively large channels (perpendicular to the plane of Fig. 1) on either side of the nozzle insert. A differential pressure transducer measured the pressure drop between the nozzle upstream and the confinement channel downstream. Other details of the flow loop and module construction are available elsewhere (Wadsworth and Mudawar, 1990).

The heat source consisted of a resistive heating element vapor-deposited onto an alumina substrate. The back side of the substrate was soldered to an oxygen-free copper block, which transmitted the heat to the impinging fluid. Three type-K thermocouples were embedded within the copper block, as illustrated in Fig. 1, allowing for determination of an area-weighted average of surface temperature corrected for the conduction resistance between the thermocouple plane and the surface. Heat loss from the heat source was simulated numerically by assuming zero contact resistances with the mating plastic substrate. This analysis determined a maximum of 4 percent of the electrical power input was lost during the single-phase regime decreasing to less than 1 percent for most boiling data; therefore, the heat flux was determined as the measured electrical power input divided by the planform area of the heat source. Measurements of average surface temperature were made with a maximum uncertainty of 0.1°C. Complete details concerning these issues can be found elsewhere (Wadsworth and Mudawar, 1990).

Two structurally enhanced surfaces, microgroove and microstud, were tested and their performances compared to those of a smooth surface. All three surfaces were blasted prior to testing with a slurry of air, water, and silica particles at high pressure, resulting in a fairly homogeneous and consistent microstructure having 10 to 15 μm radius cavities. The geometry of the microstructures used was based on previous surface enhancement work by Nakayama et al. (1984), Grimley et al. (1988), Mudawar and Anderson (1989), and Mudawar and Maddox (1990) involving boiling in FC-72. A maximum fin height of 1.02 mm was established based on the considerations of machinability and fin structural strength.

The microgroove surface, Fig. 2, was fabricated by machining 0.305-mm-wide grooves to a depth of 1.02 mm into the copper surface at 0.610 mm centers, effectively creating a surface flush mounted at the base with the insulating substrate shown in Fig. 1, with 21 longitudinal fins protruding from the base.

The microstud surface, Fig. 2, was fabricated by cutting grooves identical to those of the microgroove surface but in

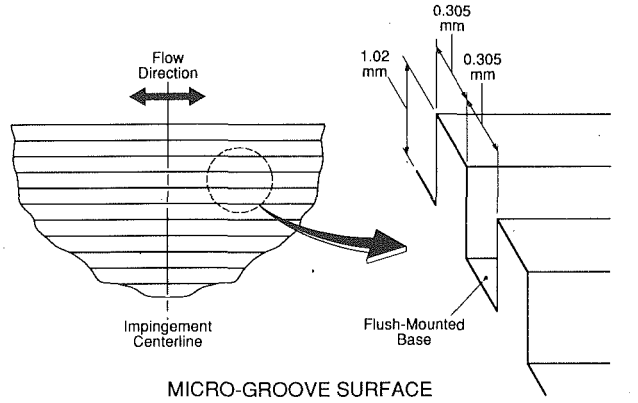

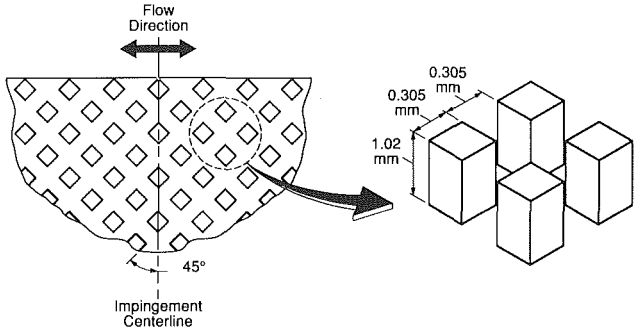

Fig. 2 Microgroove and microstud enhancement geometries

two perpendicular directions. The studs protruded 1.02 mm from the base and measured 0.305 mm on the side. The side walls of the studs were oriented at 45 deg with respect to the flow direction, creating a serpentine path for the fluid between adjacent stud rows. One benefit that was sought in forming rows of individual studs compared to a single continuous longitudinal fin was the establishment of a large number of thin boundary layer regions at the leading edges of the studs downstream from the jet-impingement zone. A total of 421 studs were fabricated on a single 12.7 mm × 12.7 mm base surface.

Experimental Results

Single-Phase Results. In the previous study by Wadsworth and Mudawar, involving smooth surfaces, a correlation was developed for the single-phase heat transfer coefficient subject to large variations in jet geometry (W and H) and jet velocity. The jet parameters in the present study were set at $W = 0.254$ mm and $H = 2.54$ mm while the Reynolds number was varied from 2000 to 30,000. Data for the microgroove and microstud surfaces were correlated individually using the form

$$\overline{\mathrm{Nu}}_L/\mathrm{Pr}^{1/3} = C\ \mathrm{Re}^a \qquad (1)$$

where the coefficient, C, and exponent, a, were determined from a least-square fit to the data, and heat flux was based on the heat source planform area, 1.61 cm^2. The overall uncertainties in Re and $\overline{\mathrm{Nu}}_L/\mathrm{Pr}^{1/3}$ are estimated at 4.5 and 1.0 percent, respectively (Wadsworth and Mudawar, 1990).

As shown in Fig. 3(*a*), both the microgroove and microstud surfaces outperformed the smooth surface, with the microgroove yielding the highest heat transfer coefficient of the three surfaces. Enhancement for the microgroove and microstud surfaces ranged, respectively, from 240 and 230 percent for Re = 1000 to 406 and 316 percent for Re = 30,000. Remarkably, the microgroove enhancement provided a *nearly isothermal* heat source surface, with less than 0.8°C variation

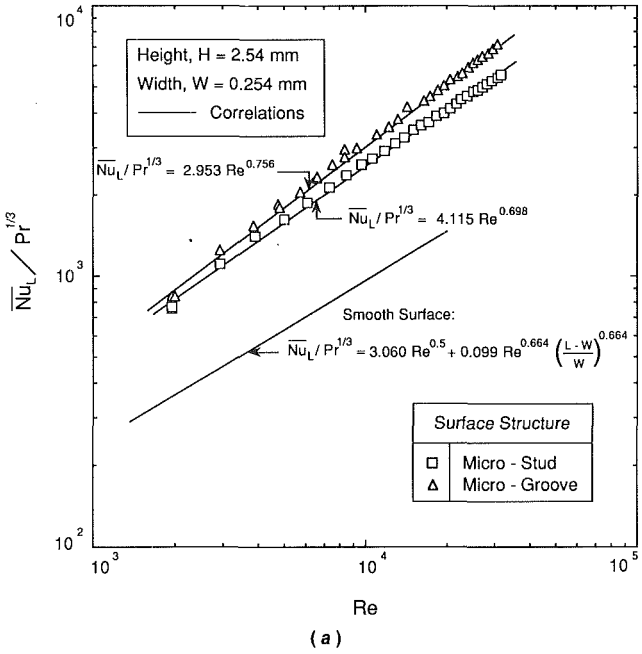

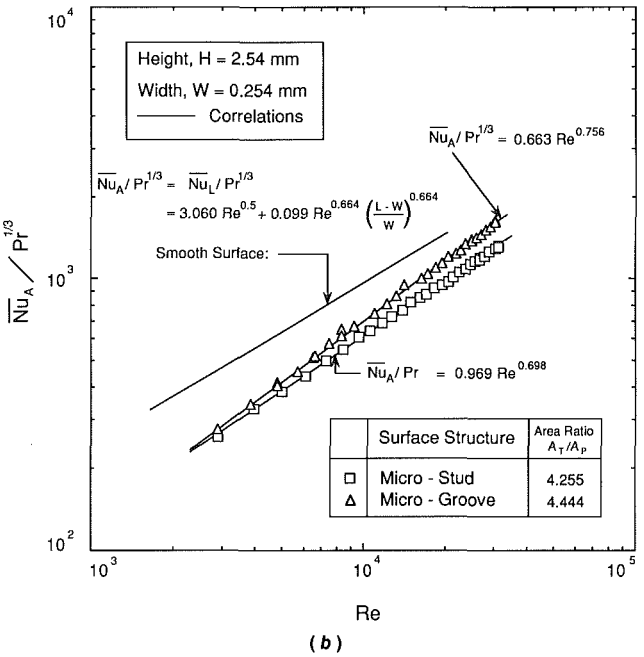

Fig. 3 Comparison of single-phase heat transfer performances for the smooth and enhanced surfaces based upon (a) planform area and (b) wetted area

for a flux of 61.8 W/cm^2, and increased pressure drop very slightly, less than 0.5 psi at the highest jet velocity as compared to the smooth surface. Temperature uniformity was less evident with the microstud surface, with spatial variation in surface temperature of 3.2°C at a heat flux of 52.6 W/cm^2, and the associated increase in pressure drop was approximately 1.0 psi. It should be noted that temperature uniformity is a primary concern in the implementation of jet impingement in the field of electronic cooling.

Figure 3(*b*) shows a comparison of the heat transfer performances of the three surfaces based upon total wetted area. The decrease in heat transfer coefficients for the enhanced surfaces may be attributed to the reduced fin effectiveness away from the base, the disturbances created by the microstructures near the impingement zone, and the reduced effective velocity of fluid along the fin and stud surfaces as compared to a smooth

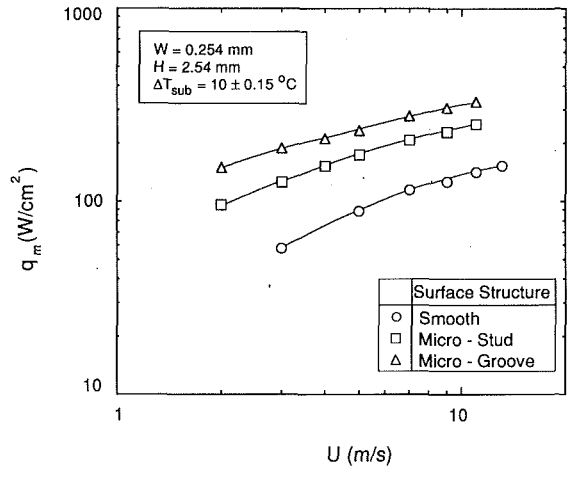

(a)

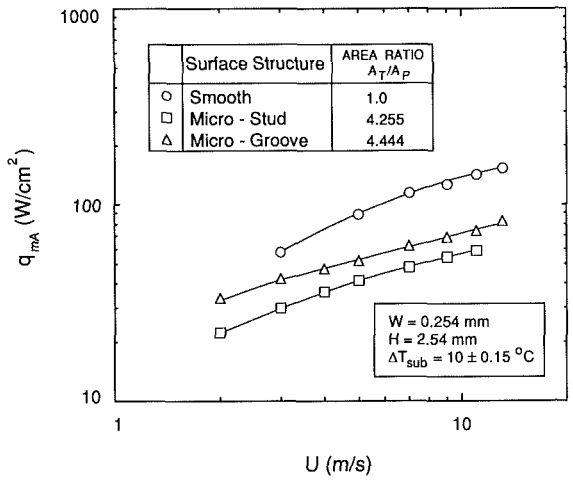

(b)

Fig. 4 CHF dependence on jet velocity for the three surfaces based upon (*a*) planform area and (*b*) wetted area

surface. It is important to note that enhancement with respect to planform area, Fig. 3(*a*), is the true measure for cooling performance for microelectronic chips.

Two-Phase Results. Figure 4(*a*) shows the exponential dependence of CHF on velocity is virtually the same for all three surfaces, i.e., $q_m \propto U^{0.7}$. As was found in the single-phase study, the microgroove enhancement resulted in a virtually isothermal surface and surpassed the smooth and microstud surfaces in heat flux based on planform area. CHF enhancement with the microgroove and microstud surface, were, respectively, 214 and 186 percent for the lowest velocity and 233 and 178 percent for the highest velocity. Plotting CHF based upon wetted area, Fig. 4(*b*), shows the attractive performances of the enhanced surfaces were primarily the result of increased heat transfer area. Figure 4(*a*) shows that fluxes well in excess of 160 W/cm^2 can be easily achieved with the microgroove surface at jet velocities as small as 1 m/s (i.e., minimal flow rate), a feature that is important for electronic cooling.

Figure 5 shows CHF increasing monotonically for the microstud surface with increasing subcooling as is commonly expected in most boiling systems. The microgroove surface, on the other hand, followed two different regimes. Below a transition point corresponding to $\Delta T_{sub} \cong 23°C$, increasing subcooling actually *decreased* CHF. This unexpected trend was verified for other velocities as well with the microgroove surface. This phenomenon was investigated by visual observation of the flow inside a transparent tube, which was connected to the outlet from the test module. A two-phase mixture with a

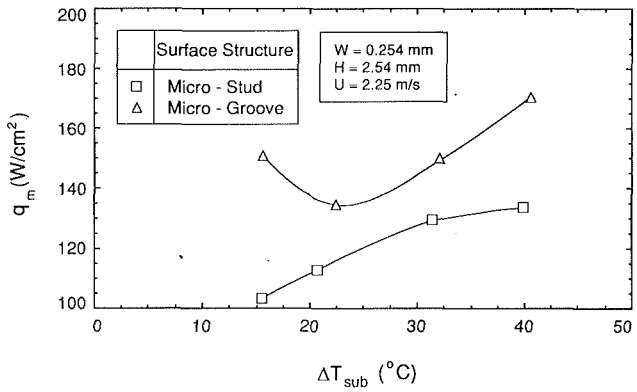

Fig. 5 CHF dependence on subcooling for the microgroove and microstud surfaces

large void ratio was observed for low subcooling conditions. Increasing subcooling above 23°C resulted in smaller bubbles and a significant suppression of vapor production.

Prior to CHF, the heat source power is dissipated only to liquid from the bulk flow, which is capable of making contact with the heated surface. If the mass flow rate of that liquid is $\dot{m}_l$ and its subcooling is $\Delta T_{sub,l}$, where $\Delta T_{sub,l} \leq 1$, then a fraction of the heat source power, $\dot{m}_l\, c_p\, \Delta T_{sub,l}$, goes into increasing the temperature of that liquid to saturation, while the balance of the power, $\dot{m}_l\, h_{fg}$, will be consumed by vaporization. One hypothesis for the increase in CHF with decreasing subcooling below $\Delta T_{sub} = 23°C$ is the acceleration of the flow in the confinement channel caused by the larger rate of vapor generation produces a significant increase in $\dot{m}_l$. Furthermore, the strong mixing induced by bubble agitation increases the value of $\Delta T_{sub,l}/\Delta T_{sub}$.

On the other hand, significant condensation of vapor bubbles for $\Delta T_{sub} > 23°C$ produces negligible acceleration of the flow and reduces $\dot{m}_l$ considerably. This results in the usual increase in CHF with increasing subcooling dominated by the increase in sensible energy of the bulk fluid. Since the CHF values for the microstud surface were significantly smaller than for the microgroove surface, the void ratio and corresponding acceleration were apparently too small to reverse the trend of increasing CHF with increasing subcooling for the microstud surface.

The CHF data base obtained with the smooth and enhanced surfaces demonstrated that CHF increases with increasing jet velocity, U, increasing nozzle width, W, and increasing subcooling, ΔT_{sub} (except for the low subcooling regime of the microgroove surface). These three parameters were maximized in an attempt to determine the maximum value for CHF and highest level of enhancement attainable under a combination of the most favorable conditions within the limitations of the present study. Only the smooth and microgroove surfaces were used in this test. The microgroove surface was preferred over the microstud surface due to the proven superior effectiveness of the former for all other conditions. Figure 6 shows boiling curves for the smooth and microgroove surfaces. A complete smooth surface boiling curve was measured up to and including the CHF condition; however, physical burnout of the resistive heating element precluded reaching CHF for the microgroove surface. The heating element failed at 411 W/cm^2 without experiencing the sharp temperature overshoot of CHF. This curve is evidence that jet impingement is capable of removing extremely high fluxes. Figure 6 also shows that fluxes in excess of 275 W/cm^2 can be dissipated even without phase change.

Results and Conclusions Experiments were performed to investigate single-phase and boiling heat transfer from smooth and microstructured (microgroove and microstud) surfaces having an equal planform area of 12.7 × 12.7 mm^2, to jets

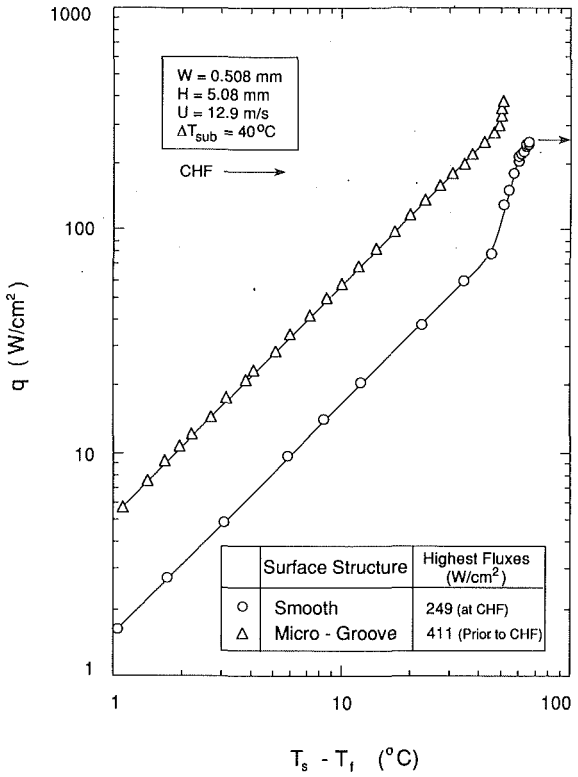

Fig. 6 Maximum heat fluxes attained in the present study for the smooth and microgroove surfaces

of dielectric Fluorinert FC-72 liquid issued from thin rectangular slots into channels confined between the surfaces of the heat source and the nozzle. Specific findings from the study are as follows:

1 The microgroove and microstud enhanced surfaces augmented the single-phase heat transfer coefficient and CHF substantially. This enhancement was a direct result of the increased surface area. The microgroove surface outperformed the other two surfaces, reaching CHF values well in excess of 160 W/cm^2 at jet velocities as small as 2 m/s.

2 The microgroove structure provided a virtually isothermal heat source surface under single-phase as well as boiling conditions.

3 CHF dependence on subcooling for the microgroove surface exhibited a transition from decreasing to increasing CHF with increasing subcooling.

4 Fluxes in excess of 400 W/cm^2 were achieved with the microgroove surface with a combination of high jet velocity and large subcooling.

In summary, the use of a jet-impingement cooling scheme and structurally enhanced surfaces coupled with phase change can quite easily and reliably remove very high heat fluxes such as those anticipated with future microelectronic devices.

Acknowledgments

This material is based upon work supported by the National Science Foundation under Grant No. CBT-8618949. The authors greatly appreciate this support and thank the Industrial Chemical Products Division of 3M for supplying test fluid (FC-72) for this study.

References

Grimley, T. G., Mudawar, I., and Incropera, F. P., 1988, "CHF Enhancement in Flowing Fluorocarbon Liquid Films Using Structured Surfaces and Flow Deflectors," *Int. J. Heat Mass Transfer*, Vol. 31, pp. 55–65.

Ma, C. F., and Bergles, A. E., 1983, "Boiling Jet Impingement Cooling of Simulated Microelectronic Chips," *Heat Transfer in Electronic Equipment*, ASME HTD-Vol. 28, pp. 5–12.

Mudawar, I., and Anderson, T. M., 1989, "High Flux Electronic Cooling by Means of Pool Boiling—Part II: Optimization of Enhanced Surface Geometry," *Heat Transfer in Electronics*, R. K. Shah, ed., ASME HTD-Vol. 111, pp. 35–50.

Mudawar, I., and Maddox, D. E., 1990, "Enhancement of Critical Heat Flux From High Power Microelectronic Heat Sources in a Flow Channel," ASME *Journal of Electronic Packaging*, Vol. 112, pp. 241–248.

Mudawar, I., and Wadsworth, D. C., 1991, "Critical Heat Flux From a Simulated Chip to a Confined Rectangular Impinging Jet of Dielectric Liquid," *Int. J. Heat Mass Transfer*, Vol. 34, pp. 1465–1479.

Nakayama, W., Nakajima, T., and Hirasawa, S., 1984, "Heat Sink Studs Having Enhanced Boiling Surfaces for Cooling of Microelectronic Components," ASME Paper No. 84-WA/HT-89.

Wadsworth, D. C., and Mudawar, I., 1990, "Cooling of a Multichip Electronic Module by Means of Confined Two-Dimensional Jets of Dielectric Liquid," ASME JOURNAL OF HEAT TRANSFER, Vol. 112, pp. 891–898.

Natural Convection Heat Transfer From Cylinders of Arbitrary Cross Section

A. V. Hassani[1]

Nomenclature

A = heat transfer surface area of the body, m^2
A_h = horizontal downward-facing surface of the body, m^2
$\overline{C}_l$ = function of Pr given by Eq. (5)
$\overline{C}_t$ = mean turbulent coefficient given by Eq. (11)
$\hat{C}_t$ = $\overline{C}_t(P_i/H)$
G = quantity given by Eq. (6) or Eq. (10)
H = characteristic length defined by Eq. (16), m
k = thermal conductivity of fluid, W/mK
l = length of the cylinder, m
L = characteristic dimension, m
m = exponent used in Churchill–Usagi fit equal to 10 for two-dimensional shapes
Nu = Nusselt number = $QL/A\Delta Tk$
Nu_L = Nusselt number based on L
Nu_{P_i} = Nusselt number based on P_i
P_i = perimeter of the inner cylinder, m
Pr = Prandtl number = $\mu C_p/k$
Ra_H = Rayleigh number based on H, $g\beta\Delta TH^3/\nu\alpha$
Ra_L = Rayleigh number based on L, $g\beta\Delta TL^3/\nu\alpha$
S = conduction shape factor, m
T_a = fluid temperature, K
T_b = body temperature, K
ΔT = temperature difference between the body and the fluid far from the body, K
z_f = total height of the cylinder cross section, Fig. 1, m
z = spatial coordinate, elevation of a point above a reference level, m
α = thermal diffusivity of fluid, m^2/s
$\overline{\Delta}$ = area-weighted harmonic mean of the local thickness, m
$\overline{\Delta}_l$ = conduction layer thickness when the flow around the body is completely laminar, m
$\overline{\Delta}_t$ = conduction layer thickness when the flow around the body is completely turbulent, m

[1]National Renewable Energy Laboratory (formerly Solar Energy Research Institute), Thermal, Fluid, & Optical Sciences Branch, Golden, CO 80401.

Contributed by the Heat Transfer Division of THE AMERICAN SOCIETY OF MECHANICAL ENGINEERS. Manuscript received by the Heat Transfer Division January 1991; revision received January 1992. Keywords: Natural Convection. Associate Technical Editor: J. R. Lloyd.

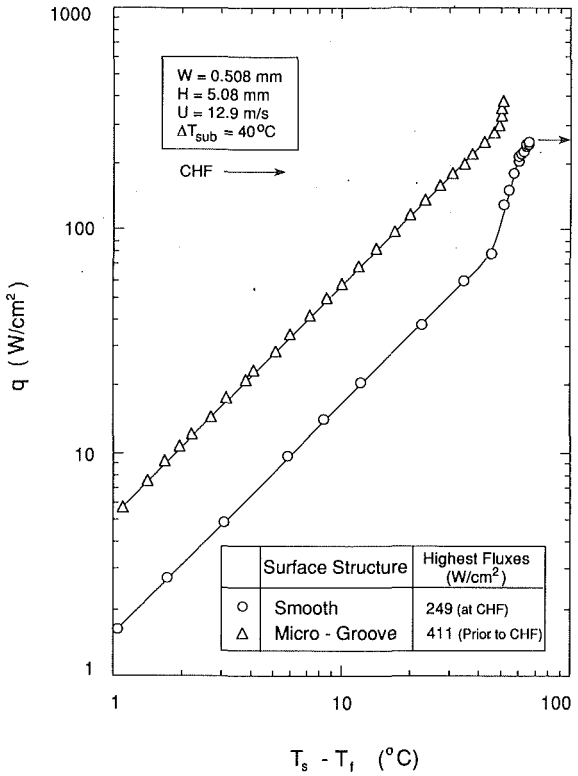

Fig. 6 Maximum heat fluxes attained in the present study for the smooth and microgroove surfaces

of dielectric Fluorinert FC-72 liquid issued from thin rectangular slots into channels confined between the surfaces of the heat source and the nozzle. Specific findings from the study are as follows:

1 The microgroove and microstud enhanced surfaces augmented the single-phase heat transfer coefficient and CHF substantially. This enhancement was a direct result of the increased surface area. The microgroove surface outperformed the other two surfaces, reaching CHF values well in excess of 160 W/cm^2 at jet velocities as small as 2 m/s.

2 The microgroove structure provided a virtually isothermal heat source surface under single-phase as well as boiling conditions.

3 CHF dependence on subcooling for the microgroove surface exhibited a transition from decreasing to increasing CHF with increasing subcooling.

4 Fluxes in excess of 400 W/cm^2 were achieved with the microgroove surface with a combination of high jet velocity and large subcooling.

In summary, the use of a jet-impingement cooling scheme and structurally enhanced surfaces coupled with phase change can quite easily and reliably remove very high heat fluxes such as those anticipated with future microelectronic devices.

Acknowledgments

This material is based upon work supported by the National Science Foundation under Grant No. CBT-8618949. The authors greatly appreciate this support and thank the Industrial Chemical Products Division of 3M for supplying test fluid (FC-72) for this study.

References

Grimley, T. G., Mudawar, I., and Incropera, F. P., 1988, "CHF Enhancement in Flowing Fluorocarbon Liquid Films Using Structured Surfaces and Flow Deflectors," *Int. J. Heat Mass Transfer*, Vol. 31, pp. 55–65.

Ma, C. F., and Bergles, A. E., 1983, "Boiling Jet Impingement Cooling of Simulated Microelectronic Chips," *Heat Transfer in Electronic Equipment*, ASME HTD-Vol. 28, pp. 5–12.

Mudawar, I., and Anderson, T. M., 1989, "High Flux Electronic Cooling by Means of Pool Boiling—Part II: Optimization of Enhanced Surface Geometry," *Heat Transfer in Electronics*, R. K. Shah, ed., ASME HTD-Vol. 111, pp. 35–50.

Mudawar, I., and Maddox, D. E., 1990, "Enhancement of Critical Heat Flux From High Power Microelectronic Heat Sources in a Flow Channel," ASME *Journal of Electronic Packaging*, Vol. 112, pp. 241–248.

Mudawar, I., and Wadsworth, D. C., 1991, "Critical Heat Flux From a Simulated Chip to a Confined Rectangular Impinging Jet of Dielectric Liquid," *Int. J. Heat Mass Transfer*, Vol. 34, pp. 1465–1479.

Nakayama, W., Nakajima, T., and Hirasawa, S., 1984, "Heat Sink Studs Having Enhanced Boiling Surfaces for Cooling of Microelectronic Components," ASME Paper No. 84-WA/HT-89.

Wadsworth, D. C., and Mudawar, I., 1990, "Cooling of a Multichip Electronic Module by Means of Confined Two-Dimensional Jets of Dielectric Liquid," ASME JOURNAL OF HEAT TRANSFER, Vol. 112, pp. 891–898.

Natural Convection Heat Transfer From Cylinders of Arbitrary Cross Section

A. V. Hassani[1]

Nomenclature

A = heat transfer surface area of the body, m^2
A_h = horizontal downward-facing surface of the body, m^2
$\overline{C}_l$ = function of Pr given by Eq. (5)
$\overline{C}_t$ = mean turbulent coefficient given by Eq. (11)
$\hat{C}_t$ = $\overline{C}_t(P_i/H)$
G = quantity given by Eq. (6) or Eq. (10)
H = characteristic length defined by Eq. (16), m
k = thermal conductivity of fluid, W/mK
l = length of the cylinder, m
L = characteristic dimension, m
m = exponent used in Churchill–Usagi fit equal to 10 for two-dimensional shapes
Nu = Nusselt number = $QL/A\Delta Tk$
Nu_L = Nusselt number based on L
Nu_{P_i} = Nusselt number based on P_i
P_i = perimeter of the inner cylinder, m
Pr = Prandtl number = $\mu C_p/k$
Ra_H = Rayleigh number based on H, $g\beta\Delta TH^3/\nu\alpha$
Ra_L = Rayleigh number based on L, $g\beta\Delta TL^3/\nu\alpha$
S = conduction shape factor, m
T_a = fluid temperature, K
T_b = body temperature, K
ΔT = temperature difference between the body and the fluid far from the body, K
z_f = total height of the cylinder cross section, Fig. 1, m
z = spatial coordinate, elevation of a point above a reference level, m
α = thermal diffusivity of fluid, m^2/s
$\overline{\Delta}$ = area-weighted harmonic mean of the local thickness, m
$\overline{\Delta}_l$ = conduction layer thickness when the flow around the body is completely laminar, m
$\overline{\Delta}_t$ = conduction layer thickness when the flow around the body is completely turbulent, m

[1]National Renewable Energy Laboratory (formerly Solar Energy Research Institute), Thermal, Fluid, & Optical Sciences Branch, Golden, CO 80401.

Contributed by the Heat Transfer Division of THE AMERICAN SOCIETY OF MECHANICAL ENGINEERS. Manuscript received by the Heat Transfer Division January 1991; revision received January 1992. Keywords: Natural Convection. Associate Technical Editor: J. R. Lloyd.

μ = dynamic viscosity, kg/ms
ν = kinematic viscosity, m^2/s
φ = angle measured between vertical direction and surface tangent, Fig. 1
χ = coordinate along the streamline measured from the leading edge of the cross section, Fig. 1, m
χ_f = value of χ at trailing edge of the cross section

Introduction

Analytical, numerical, and experimental studies of free convection heat transfer from the external surface of isothermal two-dimensional bodies, especially circular cylinders and vertical flat plates, have been conducted by many investigators. In the interest of brevity, only that material directly relevant to the derivations herein will be reviewed in detail.

Early investigations of natural convection heat transfer from horizontal long circular cylinders were undertaken by Petavel (1901), Langmuir (1911), and Nusselt (1929). Langmuir (1911), following his extensive study of free convection heat transfer from thin wires, concluded that viscosity played an important role in the flow field near the wire surface. He introduced a simple model known as "film theory" for analyzing the convection heat transfer around cylinders. In this model, he suggested that the convection heat transfer in the boundary layer could be replaced by a process of conduction through a stationary fluid layer that surrounds the cylinder. Later investigators such as Rice (1923) improved upon "film theory" and Elenbaas (1937), Eckert and Soehngen (1952), and Sparrow (1956) used this theory on free and forced convection heat transfer analysis around horizontal and vertical cylinders. In later years, McAdams (1954) correlated the existing experimental data for horizontal circular cylinders over the range of $10^{-4} < \mathrm{Ra} < 10^9$. A wider range of Ra was covered by the experiments of Kutateladze (1963) performed in air and other fluids. Hesse and Sparrow (1974) used thin wires in their experiments and reported results for $10^{-4} < \mathrm{Ra} < 10^2$. In 1975, Morgan, after a comprehensive study and review of the existing experimental data, proposed a correlation over a wide range of Rayleigh numbers $10^{-10} < \mathrm{Ra} < 10^{12}$.

While others were focusing on experimental results, Chiang and Kaye (1962), Saville and Churchill (1967), and Lin and Chao (1974) developed analytical solutions for the conditions in which the boundary layer thickness was small compared to the cylinder's local radius of curvature. In some cases, those solutions (referred to as "thin layer" solutions) were developed for cylinders of fairly arbitrary shape. Raithby and Hollands (1975, 1976, 1985), following the "film theory" of Langmuir, introduced an approximate method for predicting heat transfer from various two- and three-dimensional shapes. They applied their method to elliptic cylinders, with a vertical plate and a horizontal circular cylinder as limiting cases. Kuehn and Goldstein (1976) also presented a correlation equation for circular cylinders. Their correlation could predict heat transfer over a wide range of $10^{-13} < \mathrm{Ra} < 10^{13}$, and that showed very good agreement with predictions of Raithby and Hollands (1976). Fujii et al. (1979) and Kuehn and Goldstein (1980) performed numerical analysis of the laminar region from isothermal horizontal cylinders for $10^{-3} < \mathrm{Ra} < 10^3$ and $1 < \mathrm{Ra} < 10^7$, respectively.

A review of the existing literature shows that most workers have focused mainly on experimental data of circular cylinders and vertical plates with air ($\mathrm{Pr} \approx 0.71$) as working fluid. The results of these studies have been empirical correlations restricted either to some simple geometries or to a narrow range of Rayleigh numbers. Only a few scientists have carried out numerical techniques, which, unfortunately, are also restricted to simple geometries such as circular cylinders. There are a few analytical solutions for cylinders of fairly arbitrary cross section, but, unfortunately, those solutions are restricted to a very narrow range of Rayleigh where the boundary layer is thin compared to the local radius of curvature of the cylinder. The approximate method suggested by Raithby and Hollands (1975), however, is capable of predicting heat transfer from cylinders of various cross sections and for wide ranges of Prandtl and Rayleigh numbers. Unfortunately, following the steps of their approximate method is complex, and engineers might be discouraged from using it. Therefore it is the goal of this study to simplify this approximate method and introduce an expression for predicting natural convection heat transfer from isothermal two-dimensional bodies of arbitrary cross section over a wide range of Rayleigh and Prandtl numbers.

Simplified Method

According to Langmuir (1911), the convected heat transfer from a body can be approximated by the conducted heat transfer through a stationary fluid layer surrounding the body. Therefore the convection problem is reduced to a simpler conduction problem. Raithby and Hollands (1975, 1976, 1985) adopted Langmuir's idea and suggested an approximate integral technique for obtaining the convected heat transfer from a body. Their technique consisted of calculating the local thickness Δ_x of the stationary fluid layer of variable thickness (called the conduction layer) surrounding the body and then solving for the conduction heat transfer through this layer. Recently Hassani and Hollands (1989a), following Chamberlain et al. (1985), simplified the Raithby–Hollands method by replacing the conduction layer of variable thickness by one of uniform thickness $\bar{\Delta}$ equal to the area-weighted harmonic mean of the local thickness Δ_x. Hassani and Hollands (1989a) proposed further simplifications to the integral expressions of the Raithby–Hollands method and introduced an expression for natural convection heat transfer from three-dimensional bodies of various shape. They also extended this work to cover a wide range of Prandtl numbers, namely $0.7 < \mathrm{Pr} < 2000$ (see Hassani and Hollands, 1989b).

In this paper, following a similar procedure to that outlined by Hassani and Hollands (1989a), an expression for predicting the convection heat transfer from two-dimensional bodies (cylinders of different convex cross sections) is derived. Hassani and Hollands (1989a) showed that the thickness of the uniform conduction layer $\bar{\Delta}$ can be obtained by first determining the average thickness of the boundary layer when the flow is everywhere laminar and then when the flow is everywhere turbulent. Solutions for these two special cases are given by Raithby and Hollands (1985) as

$$\bar{\Delta} = \bar{\Delta}_l = \frac{L}{G\bar{C}_l \mathrm{Ra}_L^{1/4}} \tag{1}$$

and

$$\bar{\Delta} = \bar{\Delta}_t = \frac{L}{\bar{C}_t \mathrm{Ra}_L^{1/3}}, \tag{2}$$

respectively. Then using the Churchill–Usagi (1972) interpolation technique, which blends laminar and turbulent solutions, an expression for $\bar{\Delta}$ was obtained:

$$\frac{1}{\bar{\Delta}} = \left[\left(\frac{1}{\bar{\Delta}_l}\right)^m + \left(\frac{1}{\bar{\Delta}_t}\right)^m \right]^{1/m} \tag{3}$$

where m is the exponent of Churchill–Usagi fit. Substituting for $\bar{\Delta}_l$ and $\bar{\Delta}_t$ from Eqs. (1) and (2) results in

$$\frac{1}{\bar{\Delta}} = \frac{1}{L} \left[(G\bar{C}_l \mathrm{Ra}_L^{1/4})^m + (\bar{C}_t \mathrm{Ra}_L^{1/3})^m \right]^{1/m}. \tag{4}$$

Equation (4) combines laminar and turbulent solutions neglecting the transition regime, which is of limited importance for cylinders. The average laminar flow coefficient $\bar{C}_l$ is a

function of Prandtl number and is given by Churchill and Usagi (1972):

$$\overline{C}_l = 0.671\left(1+\left(\frac{0.492}{\mathrm{Pr}}\right)^{9/16}\right)^{-4/9}. \tag{5}$$

The coefficient G for a two-dimensional body is given by Raithby and Hollands (1985):

$$G = \frac{L^{1/4}}{\chi_f}\left[\int_0^{\chi_f}(\cos\varphi)^{1/3}d\chi\right]^{3/4} \tag{6}$$

where L is the characteristic length, χ_f is the distance from the lowest part of the cross section of the cylinder, and φ is the angle between the body and vertical direction as shown in Fig. 1. Assuming that

$$\cos\varphi \approx \overline{\cos\varphi} = \frac{1}{\chi_f}\int_0^{\chi_f}(\cos\varphi)d\chi = \frac{z_f}{\chi_f} \tag{7}$$

where z_f is the total height of the cross section as shown in Fig. 1, Eq. (6) can be reduced to a simpler form:

$$G = \frac{L^{1/4}}{\chi_f}\left[(\overline{\cos\varphi})^{1/4}\chi_f^{3/4}\right] = \left(\frac{Lz_f}{\chi_f^2}\right)^{1/4}. \tag{8}$$

To further simplify the expression for G, one can assume that

$$\chi_f \approx \frac{P_i}{2} \tag{9}$$

where P_i is the perimeter of the cross section of the cylinder. This assumption becomes exact when the cylinder cross section is symmetric. Using Eq. (9), the expression for G reduces to

$$G = \left(\frac{4Lz_f}{P_i^2}\right)^{1/4}. \tag{10}$$

Hassani and Hollands (1989a) developed a simple expression for the mean turbulent flow coefficient $\overline{C}_t$ for three-dimensional bodies. Following a similar procedure and employing the same assumptions, $\overline{C}_t$ for two-dimensional bodies can be expressed in terms of purely geometric properties of the body

$$\overline{C}_t = a + (b-a)\frac{A_h}{A} + e\frac{2z_f}{P_i} \tag{11}$$

where A is the total surface area, P_i is the perimeter of the cross section of the cylinder, and A_h represents all the horizontal downward-facing surfaces for a heated body ($T_b > T_a$) for which $\varphi = -\pi/2$. For a cooled body ($T_b < T_a$), A_h represents all the horizontal upward-facing surfaces for which $\varphi = \pi/2$. The coefficients a, b, and e are functions of Prandtl number and are given by Hassani and Hollands (1989b).

Expression for Nusselt Number

It was shown earlier that the thickness of the uniform conduction layer $\overline{\Delta}$ can be calculated from Eq. (4), where the coefficients $\overline{C}_l$, G, and $\overline{C}_t$ are given by Eqs. (5), (10), and (11), respectively. The next step is to calculate the heat conducted through this uniform layer. Langmuir et al. (1913), in a comprehensive study, suggested approximate expressions for conduction shape factor of several configurations. Following their work, Hassani et al. (1992) developed an expression, given by Eq. (12), for the conduction shape factor of a uniform layer surrounding a cylinder of arbitrary cross section:

$$\frac{S}{l} = \frac{2\pi}{\ln(1+(2\pi\overline{\Delta}/P_i))}. \tag{12}$$

This expression was developed under the assumption that the cylinder and the surface of the surrounding layer were kept at uniform temperatures T_i and T_o, respectively. $\overline{\Delta}$ in Eq. (12) is the thickness of the uniform layer surrounding the cylinder, P_i is the cylinder's cross-sectional perimeter, and l is the length of the cylinder. Readers are encouraged to refer to Nakai and Okazaki (1975) for derivation of exact asymptotic solution to conduction problem. Substituting from Eqs. (4) and (10) into Eq. (12), the expression for S becomes

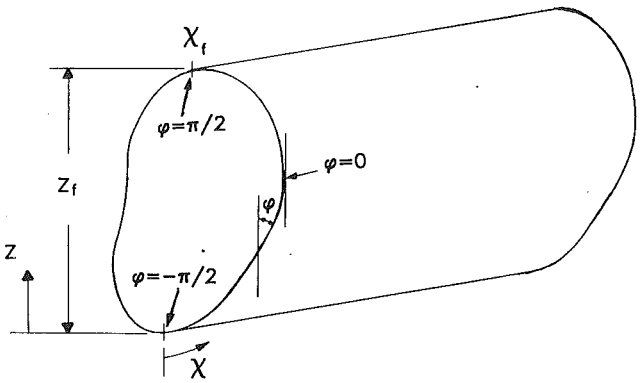

Fig. 1 Surface coordinate system for cylinder with arbitrary cross section

$$\frac{S}{l} = \frac{2\pi}{\ln\left[1+\dfrac{2\pi L}{P_i\left(\left(\left(\dfrac{4Lz_f}{P_i^2}\right)^{1/4}\overline{C}_l\mathrm{Ra}_L^{1/4}\right)^m+(\overline{C}_t\mathrm{Ra}_L^{1/3})^m\right)^{1/m}}\right]} \tag{13}$$

The average Nusselt number in terms of the conduction shape factor is given by

$$\overline{\mathrm{Nu}}_L = \frac{SL}{A} \tag{14}$$

where L is the characteristic dimension and $A = P_i l$ is the surface area of the cylinder. Substituting for S from Eq. (13), the expression for $\overline{\mathrm{Nu}}_L$ becomes

$$\overline{\mathrm{Nu}}_L = \frac{2\pi L}{P_i\ln\left[1+\dfrac{2\pi L}{P_i\left(\left(\left(\dfrac{4Lz_f}{P_i^2}\right)^{1/4}\overline{C}_l\mathrm{Ra}_L^{1/4}\right)^m+(\overline{C}_t\mathrm{Ra}_L^{1/3})^m\right)^{1/m}}\right]}. \tag{15}$$

This expression can be used for isothermal two-dimensional bodies of convex cross section. To further simplify this expression, it is suggested here that a new characteristic dimension for Ra be defined as

$$H = (4z_f P_i^2)^{1/3} \tag{16}$$

and Nu be based on P_i instead of L. This choice of characteristic dimensions reduces Eq. (15) to a more compact form:

$$\overline{\mathrm{Nu}}_{P_i} = \frac{2\pi}{\ln\left[1+\dfrac{2\pi}{((\overline{C}_l\mathrm{Ra}_H^{1/4})^m+(\hat{C}_t\mathrm{Ra}_H^{1/3})^m)^{1/m}}\right]} \tag{17}$$

where

$$\hat{C}_t = \overline{C}_t(P_i/H). \tag{18}$$

This expression is easy to use, and its coefficients depend solely on simple geometric properties of the body and the Prandtl number. The exponent m of Eq. (17) for two-dimensional bodies is empirically found to be about 10 ($m = 10$).

Comparison With Experimental Results and Other Correlations

The predictions of Eq. (17) were compared to experimental data and correlations gathered from several sources. The coef-

Table 1 Coefficients of Eq. (17)

Cross Section	Pr	$\overline{C}_l$ Eq.(5)	$\hat{C}_l$ Eq.(18)
Circular cylinder	0.71	0.515	0.095
Vertical flat plate	0.71	0.515	0.084
Vertical flat plate	55	0.651	0.081
Triangular, Fig. 3	5.0	0.618	0.100
Square orientation 1, Fig. 3	5.0	0.618	0.101
Square orientation 2, Fig. 3	5.0	0.618	0.098
Fig. 5, L/D = 1, $\Theta = \pi/2$	0.71	0.515	0.093
Fig. 5, L/D = 1, $\Theta = \pi/4$	0.71	0.515	0.086
Fig. 5, L/D = 2, $\Theta = \pi/2$	0.71	0.515	0.087
Fig. 5, L/D = 4, $\Theta = \pi/2$	0.71	0.515	0.085
Fig. 5, L/D = 4, $\Theta = 0$	0.71	0.515	0.127
Fig. 5, L/D = 2, $\Theta = 0$	0.71	0.515	0.106

Table 2 $\overline{Nu_{P_i}}$ of Eq. (17) and other sources for circular cylinder in air

Ra_H	Morgan (1975)	Kyte et al. (1953)	Churchill-Chu (1975)	Eq.(17)	Kuehn-Goldstein (1976)	Hesse-Sparrow (1974)	McAdams (1954)
3.97×10^{-12}			1.140	0.693	0.691		
3.97×10^{-11}			1.143	0.740	0.738		
3.97×10^{-10}			1.150	0.794	0.792		
3.97×10^{-9}	0.559		1.156	0.856	0.851		
3.97×10^{-8}	0.638		1.169	0.929	0.924		
3.97×10^{-7}	0.729		1.187	1.015	1.012		
3.97×10^{-6}	0.833	0.793	1.215	1.120	1.110		
3.97×10^{-5}	0.952	0.888	1.255	1.246	1.240		
3.97×10^{-4}	1.088	1.010	1.316	1.405	1.397		
3.97×10^{-3}	1.243	1.170	1.407	1.608	1.598	1.379	1.540
3.97×10^{-2}	1.420	1.388	1.546	1.878	1.864	1.568	1.728
3.97×10^{-1}	1.621	1.704	1.763	2.246	2.230	1.775	2.080
3.97×10^{0}	2.279	2.190	2.110	2.760	2.740	2.340	2.640
3.97×10^{1}	3.204	3.010	2.670	3.550	3.510	3.090	3.401
3.97×10^{2}	4.505	4.520	3.610	4.760	4.701	4.110	4.740
3.97×10^{3}	6.347	6.820	5.250	6.740	6.630	6.280	6.621
3.97×10^{4}	9.790	10.38	8.210	10.08	9.890		9.922
3.97×10^{5}	15.08	16.70	13.74	15.84	15.51		16.88
3.97×10^{6}	26.82	28.04	24.48	26.02	25.40		29.30
3.97×10^{7}	47.68	48.60	45.68	44.28	42.98		50.90
3.97×10^{8}	84.12	85.96	88.78	79.48	76.78		90.48
3.97×10^{9}	181.06	153.90	177.76	156.34	154.35		161.16
3.97×10^{10}	389.82	277.50	363.75	327.75	327.61		293.11
3.97×10^{11}	839.20		756.10	700.60	702.10		
3.97×10^{12}	1806.6		1589.0	1505.2	1508.9		
3.97×10^{13}	3889.2		3365.4	3239.0	3247.1		
3.97×10^{14}	8372.7		7166.2	6974.6	6992.1		

ficients of Eq. (17) for all those cases are listed in Table 1. First the case of long horizontal circular cylinder was considered. The predictions of present work were compared to the correlations of other workers such as Kyte et al. (1953), McAdams (1954), Hesse and Sparrow (1974), Morgan (1975), Churchill and Chu (1975), and Kuehn and Goldstein (1976). The results for this comparison are listed in Table 2. In general Eq. (17) compares very well with the correlation of Kuehn and Goldstein (1976) for the whole range of Rayleigh numbers. For Ra > 1, the agreement between Eq. (17) and the correlations of other workers is very good, and for Rayleigh numbers as low as 10^{-6}, it compares very well with the correlation

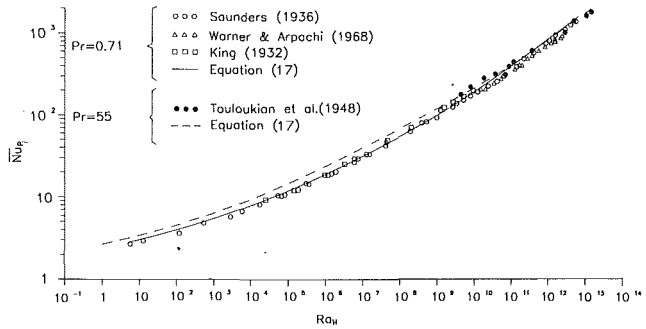

Fig. 2 Heat transfer coefficient for vertical plate at Pr ≈ 0.71 and Pr ≈ 55

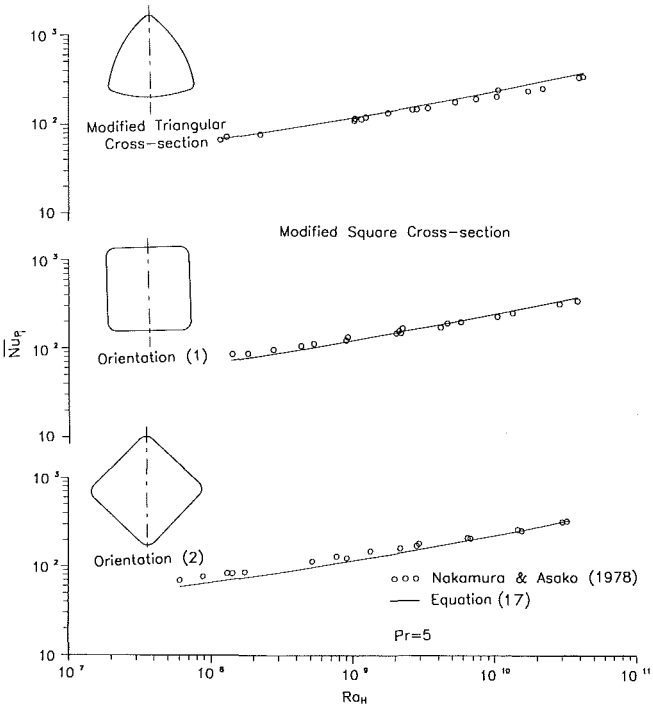

Fig. 3 Heat transfer coefficient for cylinders with modified triangular and square cross section

suggested by Churchill and Chu (1975). For Ra < 10^{-6}, predictions of this work lie between the correlations of Morgan (1975) and Churchill and Chu (1975).

Predictions of this work were next compared to existing data for a vertical flat plate of height L_p. The characteristic lengths P_i and H for this case are equal to $2L_p$ and $2.52L_p$, respectively. Comparisons were made to the experimental results of King (1932), Saunders (1936), and Warner and Arpaci (1968) for air (Pr ≈ 0.71) and to the experimental data of Touloukian et al. (1948) for ethylene glycol (Pr ≈ 55) over a Rayleigh number range of 10^{-1} < Ra < 10^{12}. As shown in Fig. 2, the agreement between the predictions and the experimental data is very good, with rms differences of less than 10 percent for air and 8.5 percent for ethylene glycol.

Nakamura and Asako (1978) carried out experiments in water (Pr ≈ 5) on long cylinders of modified triangular and square cross section as shown in the inset of Fig. 3. The comparison between the predictions of this work and experimental results of Nakamura and Asaka are plotted in Fig. 3. The coefficients of Eq. (17) for these cases are listed in Table 1. The agreement between the experimental data and predictions for modified triangular cross section is very good, with an rms difference of 9.5 percent. The comparison between the experiments and

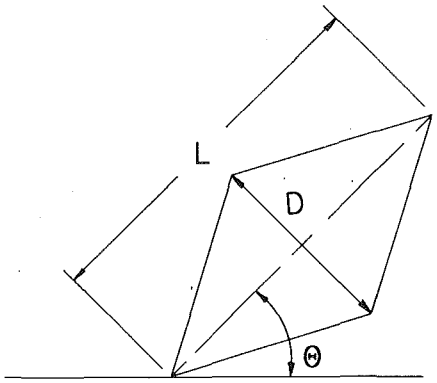

Fig. 4 Cross section of cylinder tested by Oosthuizen and Paul (1984)

predictions for a cylinder with modified square cross section in orientation 1 showed an rms difference of 8.4 percent. The results for the next case, a cylinder with modified square cross section in orientation 2, showed an rms difference of 12 percent. This orientation is more streamlined and has a smaller turbulence coefficient $\hat{C}_t$, which means that the laminar flow regime is the dominant regime.

Oosthuizen and Paul (1984) performed experiments on cylinders of prism cross section with L/D ranging from 1.0 to 4.0 (see Fig. 4), in air (Pr $\approx$ 0.71). Their data were obtained for different orientations of these cylinders only at a single Rayleigh number. The single data point for each orientation with the corresponding predicted result is shown in Fig. 5. Agreement between the predictions and the data is very good for the aspect ratio of one (cylinder with square cross section) with maximum difference of 5.4 percent. The other aspect ratios showed maximum deviations as high as 22.7 percent. In total, 76 percent of the experimental data lie within 15 percent of predictions. Although good agreement has been observed with this limited data, more experimental data are required on these shapes for further verification of Eq. (17). The author has access to data from a recent experimental study on five cylinders of different cross section carried out by Blair Clemes (1990). The comparison between Eq. (17) and the experimental data of Clemes (1990) show very good agreement. Since Clemes' data have not been officially published in any technical journal, the author will refrain from presenting them here. Reporting the comparison between that set of data and Eq. (17) is left to Blair Clemes.

In general, the predictions of this work and the existing experimental data for cylinders of various cross sections, with finite length vertical plate as limiting case, gathered from several sources agree very well over a wide range of Rayleigh and Prandtl numbers.

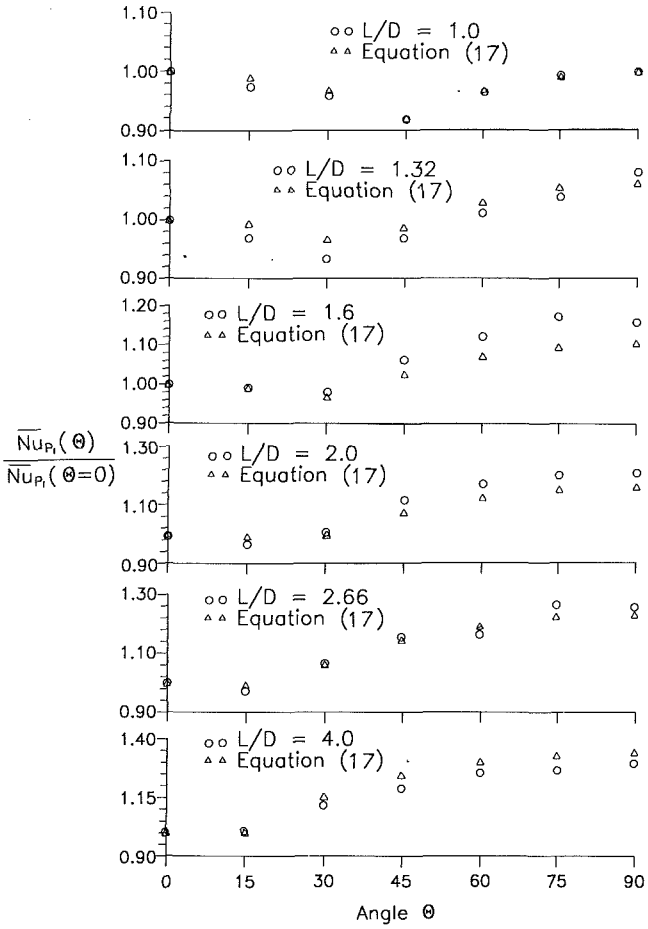

Fig. 5 Normalized $\overline{Nu}_{P_i}$ for various orientations and aspect ratios of cylinder with prismatic cross section tested by Oosthuizen and Paul (1984)

Conclusions

Natural convection heat transfer from two-dimensional bodies of arbitrary cross section can be easily and closely calculated over a wide range of Rayleigh and Prandtl numbers by using Eq. (17). The predictions of this equation for a variety of two-dimensional shapes immersed in air, water, and ethylene glycol were compared to available experimental data. The agreement was generally very good for most of the cases considered in this study.

The experimental data and correlations of several researchers on circular cylinders compared well to the predictions of this work for Ra > 1. For Ra < 1, predicted results showed very good agreement with the correlations suggested by Churchill and Chu (1975) and Kuehn and Goldstein (1976). Predictions of Eq. (17) also agreed well with the experimental data of several workers who studied natural convection heat transfer from vertical flat plates in air and in ethylene glycol.

Good agreements were also observed between predictions of this work and experimental data gathered from several sources on cylinders with modified square and triangular cross sections and cylinders with prism cross section of various aspect ratio.

An important advantage of Eq. (17) over the existing correlations is its broad applicability to cylinders of convex cross section over a wide range of Rayleigh and Prandtl numbers. Other correlations found in the literature are restricted to either a particular geometry (cross section) or a limited Ra and Pr range.

References

Chamberlain, M. J., Hollands, K. G. T., and Raithby, G. D., 1985, "Experiments and Theory on Natural Convection Heat Transfer From Bodies of Complex Shape," ASME JOURNAL OF HEAT TRANSFER, Vol. 107, pp. 624–629.

Chiang, T., and Kaye, J., 1962, "On Laminar Free Convection From Horizontal Cylinders," *Proceedings of the 4th National Congress of Applied Mechanics*, pp. 1213–1219.

Churchill, S. W., and Usagi, R., 1972, "A General Expression for the Correlation of Rates of Transfer and Other Phenomena," *AIChE J.*, Vol. 18, pp. 1121–1128.

Churchill, S. W., and Chu, H. H. S., 1975, "Correlating Equations for Laminar and Turbulent Free Convection From a Horizontal Cylinder," *Int. J. Heat Mass Transfer*, Vol. 18, p. 1049–1053.

Clemes, B., 1990, "Free Convection Heat Transfer From Two Dimensional Bodies," M.S. Thesis, University of Waterloo, Waterloo, Ontario, Canada.

Eckert, E. R. G., and Soehngen, E., 1952, "Distribution of Heat Transfer

Coefficient Around Circular Cylinders in Cross-flow at Reynolds Numbers From 20 to 500," *Transactions of ASME*, Vol. 74, pp. 343.

Elenbaas, W., 1937, "On a Combination of the Hydrodynamical Theory of Heat Transfer and Langmuir's Theory—Parts 1 and 2," *Physica Grav.*, Vol. 4, p. 761.

Fujii, T., Fujii, M., and Matsunaga, T., 1979, "A Numerical Analysis of Laminar Free Convection Around an Isothermal Horizontal Circular Cylinder," *Numerical Heat Transfer*, Vol. 2, pp. 329–344.

Hassani, A. V., and Hollands, K. G. T., 1989a, "On Natural Convection Heat Transfer From Three-Dimensional Bodies of Arbitrary Shape," ASME JOURNAL OF HEAT TRANSFER, Vol. 111, pp. 363–371.

Hassani, A. V., and Hollands, K. G. T., 1989b, "Prandtl Number Effect on External Natural Convection Heat Transfer From Irregular Three-Dimensional Bodies," *Int. J. Heat Mass Transfer*, Vol. 32, No. 11, pp. 2075–2080.

Hassani, A. V., Hollands, K. G. T., and Raithby, G. D., 1992, "Conduction Shape Factor for Two-Dimensional Layer of Uniform Thickness Surrounding a Cylinder of Arbitrary Cross Section," in press.

Hesse, G., and Sparrow, E. M., 1974, "Low Rayleigh Number Natural Convection Heat Transfer From High-Temperature Horizontal Wires to Gases," *Int. J. Heat Mass Transfer*, Vol. 17, pp. 796–798.

King, W. J., 1932, "The Basic Laws and Data of Heat Transmission," *Mech. Eng.*, Vol. 54, pp. 347–353.

Kuehn, T. H., and Goldstein, R. J., 1976, "Correlating Equation for Natural Convection Heat Transfer Between Horizontal Circular Cylinders," *Int. J. Heat Mass Transfer*, Vol. 19, pp. 1127–1134.

Kuehn, T. H., and Goldstein, R. J., 1980, "Numerical Solution to the Navier–Stokes Equations for Laminar Natural Convection About a Horizontal Isothermal Circular Cylinder," *Int. J. Heat Mass Transfer*, Vol. 23, pp. 971–979.

Kutateladze, S. S., 1963, *Fundamentals of Heat Transfer*, Academic Press, New York, pp. 288–297.

Kyte, J. R., Madden, A. J., and Piret, E. L., 1953, "Natural Convection Heat Transfer at Reduced Pressure," *Chem. Eng. Prog.*, Vol. 49, pp. 653–662.

Langmuir, I., 1911, "Thermal Conduction and Convection in Gases at Extremely High Temperatures," *Trans. Am. Electrochem. Soc.*, Vol. 20, pp. 225–242; see Vol. 2, Chap. 1.

Langmuir, I., Adams, E. Q., and Meikle, G. S., 1913, "Flow of Heat Through Furnace Walls: The Shape Factor," *Trans. Am. Electrochem. Soc.*, Vol. 23, p. 299.

Lin, F. N., and Chao, B. T., 1974, "Laminar Free Convection Over Two-Dimensional and Axisymmetric Bodies of Arbitrary Contour," ASME JOURNAL OF HEAT TRANSFER, Vol. 96, pp. 435–442.

McAdams, W. H., 1954, *Heat Transmission*, McGraw-Hill, New York.

Morgan, V. T., 1975, "The Overall Convective Heat Transfer From Smooth Circular Cylinders," *Advances in Heat Transfer*, Vol. 11, Academic Press.

Nakai, S., and Okazaki, T., 1975, "Heat Transfer From a Horizontal Circular Wire at Small Reynolds and Grashof Numbers—Pure Convection," *Int. J. Heat Mass Transfer*, Vol. 18, pp. 387–396.

Nakamura, H., and Asako, Y., 1978, "Laminar Free Convection From a Horizontal Cylinder With Uniform Cross Section of Arbitrary Shape," *Bull. JSME*, Vol. 21, No. 153, pp. 471–478.

Nusselt, W., 1929, *Zeitschrift des Vereins Deutscher Ingenieure fuer Maschinenbau und Metallbearbeitung*, Vol. 73, p. 1475.

Oosthuizen, P. H., and Paul, J. T., 1984, "An Experimental Study of Free Convective Heat Transfer From Horizontal Non-circular Cylinders," *The 22nd National Heat Transfer Conference*, Niagara Falls, New York, ASME Heat Transfer Division, Vol. 32, pp. 91–97.

Petavel, J. E., 1901, "On the Heat Dissipation by a Platinum Surface at High Temperatures. Part 4: Thermal Emissivity in High Pressure Gases," *Phil. Trans. Roy. Soc. London A*, Vol. 197, pp. 229–254.

Raithby, G. D., and Hollands, K. G. T., 1975, "A General Method of Obtaining Approximate Solutions to Laminar and Turbulent Free Convection Problems," *Advances in Heat Transfer*, Academic Press, Vol. 11; see also *Int. J. Heat Mass Transfer*, Vol. 17, pp. 1620–1622.

Raithby, G. D., and Hollands, K. G. T., 1976, "Laminar and Turbulent Free Convection From Elliptic Cylinders, With a Vertical Plate and Horizontal Circular Cylinder as Special Cases," ASME JOURNAL OF HEAT TRANSFER, Vol. 98, pp. 72–80.

Raithby, G. D., and Hollands, K. G. T., 1985, *Handbook of Heat Transfer Fundamentals*, 2nd ed., W. M. Rohsenow, J. P. Hartnett, and E. N. Ganic, eds., McGraw-Hill, New York, Chap. 6.

Rice, C. W., 1923, "Free and Forced Convection of Heat in Gases and Liquids," *Journal of American Institute of Electronic Engineers*, Vol. 42, pp. 1288–1289.

Saunders, O. A., 1936, "The Effect of Pressure on Natural Convection in Air," *Proc. Royal Soc.*, series A, Vol. 157, pp. 278–291.

Saville, D. A., and Churchill, S. W., 1967, "Laminar Free Convection in Boundary Layers Near Horizontal Cylinders and Vertical Axisymmetric Bodies," *Journal of Fluid Mechanics*, Vol. 29, pp. 391–399.

Sparrow, E., 1956, "Laminar Free Convection Heat Transfer From the Outer Surface of a Vertical Circular Cylinder," *Trans. ASME*, Vol. 78, pp. 1823–1829.

Touloukian, Y. S., Hawkins, G. A., and Jakob, M., 1948, "Heat Transfer by Free Convection From Heated Vertical Surfaces to Liquids," *Trans. ASME*, Vol. 70, pp. 13–18.

Warner, C. Y., and Arpaci, V. S., 1968, "An Experimental Investigation of Turbulent Natural Convection in Air at Low Pressure on a Vertical Heated, Flat Plate," *Int. J. Heat Mass Transfer*, Vol. 11, pp. 397–406.

Numerical Study of Natural Convection in a Differentially Heated Cavity With Internal Heat Generation: Effects of the Aspect Ratio

T. Fusegi,[1] J. M. Hyun,[2] and K. Kuwahara[3]

Introduction

Flows in an enclosure that are generated by both internal and external heating are found in several important thermal engineering applications. Examples include heat removal from postaccident nuclear reactors and thermal control of nuclear waste stored underground. There exists a large body of previous studies on natural convection in cavities in which either internal heat generation or external heating is present (Lambha et al., 1978; Kulacki and Richards, 1985; Ostrach, 1988). However, analysis of flows that involve both modes of heating has attracted far less attention in the past.

In the present paper, systematically organized high-resolution numerical calculations of natural convection in a differentially heated rectangular cavity with internal heat generation are reported. Referring to Fig. 1, the two vertical sidewalls of the cavity are maintained at temperatures of T_H ($x=0$) and T_C ($x=L$), where $T_H \geq T_C$, while the horizontal walls ($y=0$ and H) are insulated. The aspect ratio of the cavity, A ($=H/L$), varies in range of $0.3 \leq A \leq 5.0$. The Prandtl number of the fluid is set equal to 5.85. A uniform volumetric heat generation of Q is present throughout the cavity interior. Under these conditions, two principal flow parameters, each of which characterizes either internal or external heating, evolve. They are termed the internal Rayleigh number: Ra_I ($=g\beta c_p \rho^2 L^5 Q/\mu k^2$); and the external Rayleigh number: Ra_E ($=g\beta c_p \rho^2 L^3 (T_H - T_C)/\mu k$); where g is the gravitational acceleration, β is the thermal expansion coefficient, c_p is the specific heat at constant pressure, μ is the viscosity, and k is the thermal conductivity of the fluid. In the present investigation, the external and internal Rayleigh numbers range $4.0 \times 10^5 \leq \mathrm{Ra}_E \leq 5.0 \times 10^7$ and $4.0 \times 10^7 \leq \mathrm{Ra}_I \leq 5.0 \times 10^9$, respectively.

For a differentially heated square cavity with internal heat generation, Acharya and Goldstein (1985) performed numerical computations in lower Rayleigh number cases: namely, $10^3 \leq \mathrm{Ra}_E \leq 10^6$ and $10^4 \leq \mathrm{Ra}_I \leq 10^7$. They also investigated the cases of inclined cavities, and the effects of the cavity aspect ratio were documented by Acharya (1984). The major finding for the case of the sidewall-heated cavity (the configuration shown in Fig. 1) was that, when Ra_I was significantly greater than Ra_E, the flow was directed downward along both the heated and cooled sidewalls. Wang and Wang (1988) conducted a combined experimental and numerical investigation in the range of $10^4 \leq \mathrm{Ra}_I \leq 10^6$ and $\mathrm{Ra}_E \approx 5.0 \times 10^4$ for an enclosure of the aspect ratio of 3.2. The heat transfer rate calculated from Mach-Zehnder interferograms was in satisfactory agreement with numerically determined data. However, no measurements of the flow fields were undertaken.

Of much interest would be cases for which Ra_E and Ra_I are

[1]Institute of Computational Fluid Dynamics, Meguro, Tokyo 152, Japan; present address: Energy Technology Research Institute, Tokyo Gas Co., Ltd., Minato, Tokyo 105, Japan; Mem. ASME.

[2]Department of Mechanical Engineering, Korea Advanced Institute of Science and Technology, Chong Ryang, Seoul 131, Korea.

[3]Institute of Space and Astronautical Science, Sagamihara, Kanagawa 229, Japan.

Contributed by the Heat Transfer Division of THE AMERICAN SOCIETY OF MECHANICAL ENGINEERS. Manuscript received by the Heat Transfer Division January 1991; revision received January 1992. Keywords: Enclosure Flows, Natural Convection.

Coefficient Around Circular Cylinders in Cross-flow at Reynolds Numbers From 20 to 500," *Transactions of ASME*, Vol. 74, pp. 343.

Elenbaas, W., 1937, "On a Combination of the Hydrodynamical Theory of Heat Transfer and Langmuir's Theory—Parts 1 and 2," *Physica Grav.*, Vol. 4, p. 761.

Fujii, T., Fujii, M., and Matsunaga, T., 1979, "A Numerical Analysis of Laminar Free Convection Around an Isothermal Horizontal Circular Cylinder," *Numerical Heat Transfer*, Vol. 2, pp. 329–344.

Hassani, A. V., and Hollands, K. G. T., 1989a, "On Natural Convection Heat Transfer From Three-Dimensional Bodies of Arbitrary Shape," ASME JOURNAL OF HEAT TRANSFER, Vol. 111, pp. 363–371.

Hassani, A. V., and Hollands, K. G. T., 1989b, "Prandtl Number Effect on External Natural Convection Heat Transfer From Irregular Three-Dimensional Bodies," *Int. J. Heat Mass Transfer*, Vol. 32, No. 11, pp. 2075–2080.

Hassani, A. V., Hollands, K. G. T., and Raithby, G. D., 1992, "Conduction Shape Factor for Two-Dimensional Layer of Uniform Thickness Surrounding a Cylinder of Arbitrary Cross Section," in press.

Hesse, G., and Sparrow, E. M., 1974, "Low Rayleigh Number Natural Convection Heat Transfer From High-Temperature Horizontal Wires to Gases," *Int. J. Heat Mass Transfer*, Vol. 17, pp. 796–798.

King, W. J., 1932, "The Basic Laws and Data of Heat Transmission," *Mech. Eng.*, Vol. 54, pp. 347–353.

Kuehn, T. H., and Goldstein, R. J., 1976, "Correlating Equation for Natural Convection Heat Transfer Between Horizontal Circular Cylinders," *Int. J. Heat Mass Transfer*, Vol. 19, pp. 1127–1134.

Kuehn, T. H., and Goldstein, R. J., 1980, "Numerical Solution to the Navier–Stokes Equations for Laminar Natural Convection About a Horizontal Isothermal Circular Cylinder," *Int. J. Heat Mass Transfer*, Vol. 23, pp. 971–979.

Kutateladze, S. S., 1963, *Fundamentals of Heat Transfer*, Academic Press, New York, pp. 288–297.

Kyte, J. R., Madden, A. J., and Piret, E. L., 1953, "Natural Convection Heat Transfer at Reduced Pressure," *Chem. Eng. Prog.*, Vol. 49, pp. 653–662.

Langmuir, I., 1911, "Thermal Conduction and Convection in Gases at Extremely High Temperatures," *Trans. Am. Electrochem. Soc.*, Vol. 20, pp. 225–242; see Vol. 2, Chap. 1.

Langmuir, I., Adams, E. Q., and Meikle, G. S., 1913, "Flow of Heat Through Furnace Walls: The Shape Factor," *Trans. Am. Electrochem. Soc.*, Vol. 23, p. 299.

Lin, F. N., and Chao, B. T., 1974, "Laminar Free Convection Over Two-Dimensional and Axisymmetric Bodies of Arbitrary Contour," ASME JOURNAL OF HEAT TRANSFER, Vol. 96, pp. 435–442.

McAdams, W. H., 1954, *Heat Transmission*, McGraw-Hill, New York.

Morgan, V. T., 1975, "The Overall Convective Heat Transfer From Smooth Circular Cylinders," *Advances in Heat Transfer*, Vol. 11, Academic Press.

Nakai, S., and Okazaki, T., 1975, "Heat Transfer From a Horizontal Circular Wire at Small Reynolds and Grashof Numbers—Pure Convection," *Int. J. Heat Mass Transfer*, Vol. 18, pp. 387–396.

Nakamura, H., and Asako, Y., 1978, "Laminar Free Convection From a Horizontal Cylinder With Uniform Cross Section of Arbitrary Shape," *Bull. JSME*, Vol. 21, No. 153, pp. 471–478.

Nusselt, W., 1929, *Zeitschrift des Vereins Deutscher Ingenieure fuer Maschinenbau und Metallbearbeitung*, Vol. 73, p. 1475.

Oosthuizen, P. H., and Paul, J. T., 1984, "An Experimental Study of Free Convective Heat Transfer From Horizontal Non-circular Cylinders," *The 22nd National Heat Transfer Conference*, Niagara Falls, New York, ASME Heat Transfer Division, Vol. 32, pp. 91–97.

Petavel, J. E., 1901, "On the Heat Dissipation by a Platinum Surface at High Temperatures. Part 4: Thermal Emissivity in High Pressure Gases," *Phil. Trans. Roy. Soc. London A*, Vol. 197, pp. 229–254.

Raithby, G. D., and Hollands, K. G. T., 1975, "A General Method of Obtaining Approximate Solutions to Laminar and Turbulent Free Convection Problems," *Advances in Heat Transfer*, Academic Press, Vol. 11; see also *Int. J. Heat Mass Transfer*, Vol. 17, pp. 1620–1622.

Raithby, G. D., and Hollands, K. G. T., 1976, "Laminar and Turbulent Free Convection From Elliptic Cylinders, With a Vertical Plate and Horizontal Circular Cylinder as Special Cases," ASME JOURNAL OF HEAT TRANSFER, Vol. 98, pp. 72–80.

Raithby, G. D., and Hollands, K. G. T., 1985, *Handbook of Heat Transfer Fundamentals*, 2nd ed., W. M. Rohsenow, J. P. Hartnett, and E. N. Ganic, eds., McGraw-Hill, New York, Chap. 6.

Rice, C. W., 1923, "Free and Forced Convection of Heat in Gases and Liquids," *Journal of American Institute of Electronic Engineers*, Vol. 42, pp. 1288–1289.

Saunders, O. A., 1936, "The Effect of Pressure on Natural Convection in Air," *Proc. Royal Soc.*, series A, Vol. 157, pp. 278–291.

Saville, D. A., and Churchill, S. W., 1967, "Laminar Free Convection in Boundary Layers Near Horizontal Cylinders and Vertical Axisymmetric Bodies," *Journal of Fluid Mechanics*, Vol. 29, pp. 391–399.

Sparrow, E., 1956, "Laminar Free Convection Heat Transfer From the Outer Surface of a Vertical Circular Cylinder," *Trans. ASME*, Vol. 78, pp. 1823–1829.

Touloukian, Y. S., Hawkins, G. A., and Jakob, M., 1948, "Heat Transfer by Free Convection From Heated Vertical Surfaces to Liquids," *Trans. ASME*, Vol. 70, pp. 13–18.

Warner, C. Y., and Arpaci, V. S., 1968, "An Experimental Investigation of Turbulent Natural Convection in Air at Low Pressure on a Vertical Heated, Flat Plate," *Int. J. Heat Mass Transfer*, Vol. 11, pp. 397–406.

Numerical Study of Natural Convection in a Differentially Heated Cavity With Internal Heat Generation: Effects of the Aspect Ratio

T. Fusegi,[1] J. M. Hyun,[2] and K. Kuwahara[3]

Introduction

Flows in an enclosure that are generated by both internal and external heating are found in several important thermal engineering applications. Examples include heat removal from postaccident nuclear reactors and thermal control of nuclear waste stored underground. There exists a large body of previous studies on natural convection in cavities in which either internal heat generation or external heating is present (Lambha et al., 1978; Kulacki and Richards, 1985; Ostrach, 1988). However, analysis of flows that involve both modes of heating has attracted far less attention in the past.

In the present paper, systematically organized high-resolution numerical calculations of natural convection in a differentially heated rectangular cavity with internal heat generation are reported. Referring to Fig. 1, the two vertical sidewalls of the cavity are maintained at temperatures of T_H ($x=0$) and T_C ($x=L$), where $T_H \geq T_C$, while the horizontal walls ($y=0$ and H) are insulated. The aspect ratio of the cavity, A ($=H/L$), varies in range of $0.3 \leq A \leq 5.0$. The Prandtl number of the fluid is set equal to 5.85. A uniform volumetric heat generation of Q is present throughout the cavity interior. Under these conditions, two principal flow parameters, each of which characterizes either internal or external heating, evolve. They are termed the internal Rayleigh number: Ra_I ($=g\beta c_p \rho^2 L^5 Q/\mu k^2$); and the external Rayleigh number: Ra_E ($=g\beta c_p \rho^2 L^3 (T_H - T_C)/\mu k$); where g is the gravitational acceleration, β is the thermal expansion coefficient, c_p is the specific heat at constant pressure, μ is the viscosity, and k is the thermal conductivity of the fluid. In the present investigation, the external and internal Rayleigh numbers range $4.0 \times 10^5 \leq \mathrm{Ra}_E \leq 5.0 \times 10^7$ and $4.0 \times 10^7 \leq \mathrm{Ra}_I \leq 5.0 \times 10^9$, respectively.

For a differentially heated square cavity with internal heat generation, Acharya and Goldstein (1985) performed numerical computations in lower Rayleigh number cases: namely, $10^3 \leq \mathrm{Ra}_E \leq 10^6$ and $10^4 \leq \mathrm{Ra}_I \leq 10^7$. They also investigated the cases of inclined cavities, and the effects of the cavity aspect ratio were documented by Acharya (1984). The major finding for the case of the sidewall-heated cavity (the configuration shown in Fig. 1) was that, when Ra_I was significantly greater than Ra_E, the flow was directed downward along both the heated and cooled sidewalls. Wang and Wang (1988) conducted a combined experimental and numerical investigation in the range of $10^4 \leq \mathrm{Ra}_I \leq 10^6$ and $\mathrm{Ra}_E \approx 5.0 \times 10^4$ for an enclosure of the aspect ratio of 3.2. The heat transfer rate calculated from Mach-Zehnder interferograms was in satisfactory agreement with numerically determined data. However, no measurements of the flow fields were undertaken.

Of much interest would be cases for which Ra_E and Ra_I are

[1]Institute of Computational Fluid Dynamics, Meguro, Tokyo 152, Japan; present address: Energy Technology Research Institute, Tokyo Gas Co., Ltd., Minato, Tokyo 105, Japan; Mem. ASME.

[2]Department of Mechanical Engineering, Korea Advanced Institute of Science and Technology, Chong Ryang, Seoul 131, Korea.

[3]Institute of Space and Astronautical Science, Sagamihara, Kanagawa 229, Japan.

Contributed by the Heat Transfer Division of THE AMERICAN SOCIETY OF MECHANICAL ENGINEERS. Manuscript received by the Heat Transfer Division January 1991; revision received January 1992. Keywords: Enclosure Flows, Natural Convection.

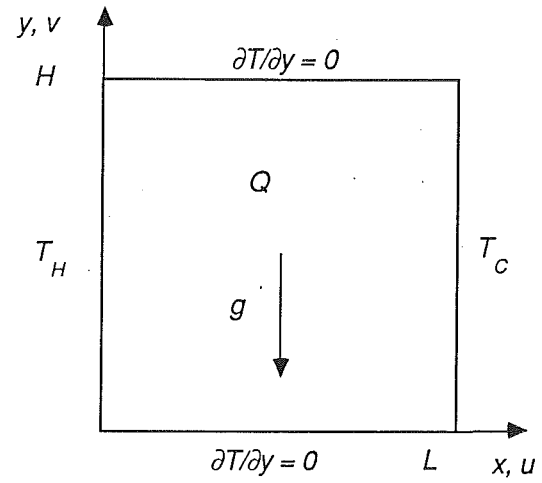

Fig. 1 Schematic of the flow configuration

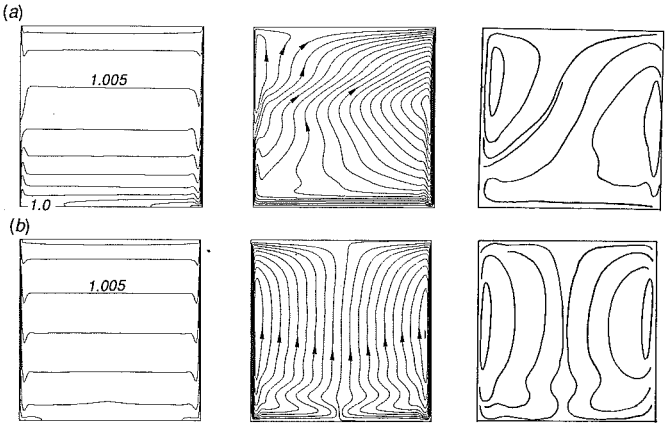

Fig. 2 The computed results of isotherms (left) and stream function contours (center) at $A = 1.0$. Representative flow lines of the flow visualization (Kawara et al., 1990) (right) are also included. The temperature of the sidewalls is: (*a*) 1.005 at $x/L = 0$ and 0.995 at $x/L = 1$, (*b*) 1.0 at $x/L = 0$ and 1; the increment of the isotherms is: $\Delta T = 0.001$ for both cases. (*a*) Computation: $Ra_I = 5.0 \times 10^9$, $Ra_E = 5.0 \times 10^7$ [$\Delta\psi = 0.680 \times 10^{-3}$]; experiment: $Ra_I = 5.4 \times 10^9$, $Ra_E = 5.2 \times 10^7$; (*b*) computation: $Ra_I = 5.0 \times 10^9$, $Ra_E = 0$ ($\Delta\psi = 0.528 \times 10^{-3}$); experiment: $Ra_I = 5.4 \times 10^9$, $Ra_E = 0.0$.

sufficiently high so that boundary layers formed near the isothermal walls have significance in the flow structure. These situations will be examined in the present numerical study. As experimental counterparts, Kawara et al. (1990) have recently carried out an extensive series of flow visualizations. In the experiments, the uniformly distributed internal heat generation was simulated by passing electric current through a dilute potassium chloride aqueous solution ($Pr = 5.85$). The ranges of parameters were: $10^6 \le Ra_E \le 10^8$ and $10^8 \le Ra_I \le 10^{10}$, and for the enclosure aspect ratio, A, $0.3 \le A \le 5.0$. The observed flow structure illustrated qualitatively different patterns as the ratio Ra_I/Ra_E was altered. An important aspect of the present problem is the effect of the cavity aspect ratio on flow features.

One principal objective of the present study is to verify the steady-state experimental observations of Kawara et al. by performing a critical assessment of the numerical and experimental results. In addition, further details of flow and heat transfer characteristics will be secured. These numerical results will be complementary to the preceding experiments (Kawara et al., 1990). It should be emphasized that the numerical data will furnish the local information of the flow field as well as the spatial structure of the heat transfer rate throughout the cavity boundary walls.

The flow is governed by the two-dimensional, time-dependent, incompressible Navier–Stokes and energy equations. They are solved by a control volume-based finite difference technique. The complete mathematical formulation and a detailed description of the numerical method can be found elsewhere (Fusegi et al., 1992) and, hence, they are not repeated here. It suffices to mention that the convective terms are discretized by the QUICK scheme modified for nonuniform grids (Freitas et al., 1985) and that the iterative solution algorithm is based on the well-known SIMPLE type (Patankar, 1980) and the Strongly Implicit Procedure (Stone, 1968). The constructed numerical code has been validated by a set of benchmark solutions proposed by de Vahl Davis (1983) for natural convection in a differentially heated square cavity ($Ra_I = 0$). The entire enclosure constitutes the full computational domain.

Results and Discussion

In the actual computations, four values of the aspect ratio are considered, namely, $A = 0.3$, 1.0, 2.0, and 5.0. For a given value of A, the Rayleigh numbers are specified such that their ratio, Ra_I/Ra_E, is equal to 100. This allows a systematic assessment of the effects of the aspect ratio on the field characteristics. For reference purposes, parallel computations are performed by selectively turning off the internal heat generation (i.e., $Ra_I = 0.0$) or the temperature difference of the sidewalls ($Ra_E = 0.0$). The number of grid points in the x direction for the finite difference mesh network is fixed at 122, while that in the y direction varies depending on the aspect ratio: It is 62 for $A = 0.3$, 122 for $A = 1.0$, and 242 for $A = 2.0$ and 5.0. A nonuniform grid system is utilized. The spacing ratio, Δ (the ratio of the smallest mesh distance located adjacent to the sidewall to the largest spacing in the center), is set equal to 3.0. A 10 percent decrease in the average heat flux, $\overline{q}$, at the sidewall is found compared to the case of the uniform meshes. When Δ is further increased, changes in $\overline{q}$ are less than 2 percent of the value for $\Delta = 3.0$.

In all the results presented here, steady state has been attained. No indication of transition to unsteady flows is detected in the computations. The critical value of Ra_I is considered to be beyond the range used in the present study.

The changes in the global structure of the thermal and flow fields due to the internal heat generation are examined first. Figure 2 illustrates the numerically constructed isotherms and streamline contours at $A = 1.0$. The results of the flow visualization (Kawara et al., 1990) are also included for comparison. In this and also in what follows, the temperature, T, and the stream functions, ψ, are normalized with respect to $(T_C + T_H)/2 (= T_0)$ and u_0/L, respectively, where u_0 is a reference velocity defined as $[g\beta L(T_H - T_C)]^{1/2}$. The temperature difference is set equal to 1 percent of the reference temperature, T_0, in order to simulate closely the experimental conditions of Kawara et al.

In Fig. 2(*a*), the results of $Ra_I = 5.0 \times 10^9$ and $Ra_E = 5.0 \times 10^7$ are depicted. At this relatively high Rayleigh number, thin thermal and velocity boundary layers are present near the isothermal vertical walls. If there is no internal heat generation ($Ra_I = 0$), the fields would exhibit centro-symmetry with respect to the cavity center ($x/L = y/H = 0.5$). However, in the present case, the symmetry is not found due to the internal heat generation. A counterrotating vortex of smaller size appears near the heated wall ($x = 0$). The temperature of this smaller vortex is higher than the temperature of the heated wall. In this zone, the heated wall acts as a source of *negative* buoyancy, which drives the flow downward near this surface. This downward flow meets the upward flow, which originates from the lower portion of the heated wall; consequently, the downward flow turns sharply upward afterward. This flow pattern can also be inferred from the isotherms. The numerical prediction of the flow field is consistent with the flow visu-

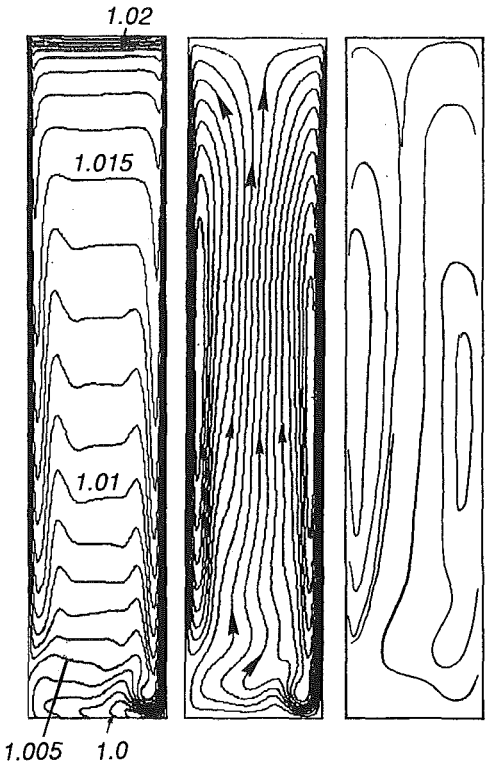

Fig. 3 The computed results of isotherms (left) and stream function contours (center) at $A = 5.0$. Representative flow lines of the flow visualization (Kawara et al., 1990) (right) are also included. The temperature of the sidewalls is: 1.005 at $x/L = 0$ and 0.995 at $x/L = 1$; the increment of the isotherms is: $\Delta T = 0.001$. Computation: $Ra_I = 4.0 \times 10^7$, $Ra_E = 4.0 \times 10^5$ ($\Delta\psi = 0.146 \times 10^{-1}$); experiment: $Ra_I = 1.4 \times 10^7$, $Ra_E = 3.8 \times 10^5$.

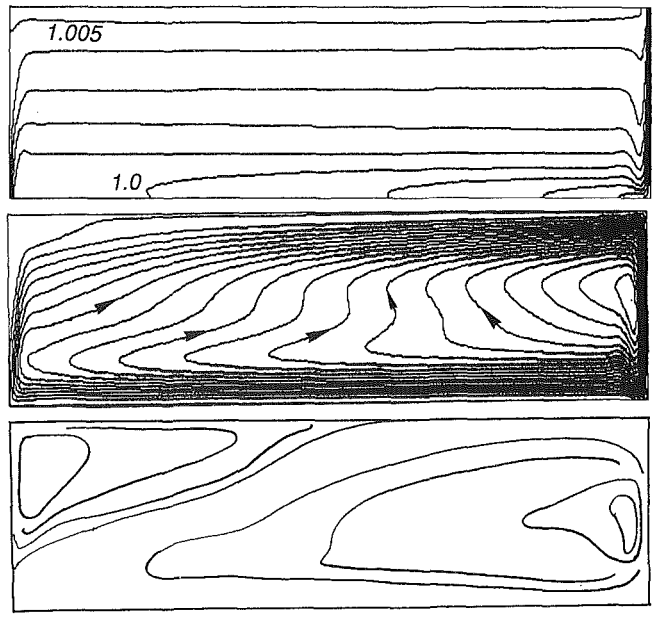

Fig. 4 The computed results of isotherms (top) and stream function contours (center) at $A = 0.3$. Representative flow lines of the flow visualization (Kawara et al., 1990)) (bottom) are also included. The temperature of the sidewalls is: 1.005 at $x/L = 0$ and 0.995 at $x/L = 1$; the increment of the isotherms is: $\Delta T = 0.001$. Computation: $Ra_I = 5.0 \times 10^9$, $Ra_E = 5.0 \times 10^7$ [$\Delta\psi = 0.242 \times 10^{-3}$]; experiment: $Ra_I = 8.3 \times 10^9$, $Ra_E = 6.3 \times 10^7$.

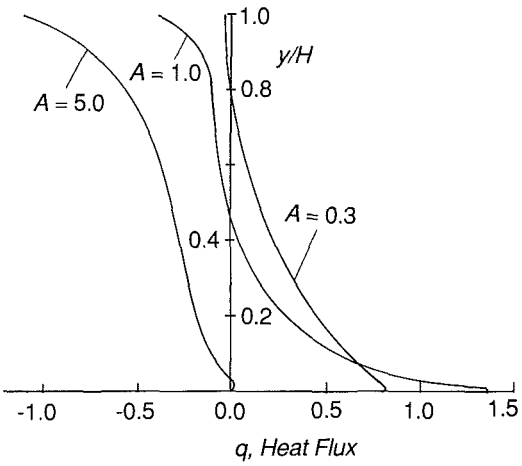

Fig. 5 The local heat flux distribution at the externally heated sidewall ($x/L = 0$) for various aspect ratios with $Ra_I/Ra_E = 100.0$. For $A = 0.3$ and 1.0, $Ra_I = 5.0 \times 10^9$ and $Ra_E = 5.0 \times 10^7$; for $A = 5.0$, $Ra_I = 4.0 \times 10^7$ and $Ra_E = 4.0 \times 10^5$.

alization result (Kawara et al., 1990). These flow patterns are clearly captured in the experiment, although the size of the experimentally observed smaller vortex appears to be larger than that of the computed prediction.

Figure 2(*b*) shows the results when there is no differential heating of the sidewalls ($Ra_E = 0.0$) and the convection is due to the internal heat generation only. As expected, the fields are symmetric with respect to the centerline ($x/L = 0.5$). The major features of the field structure are the presence of the boundary layers near the isothermal vertical walls (with $T = 1.0$) and the thermally stratified central part, in which a slow upward flow is conspicuous. The particle path pattern of the measurements (Kawara et al., 1990) are in close agreement with the computed flow field.

A tall cavity of $A = 5.0$ is considered next. In this case, the Rayleigh numbers are set equal to $Ra_E = 4.0 \times 10^5$ and $Ra_I = 4.0 \times 10^7$, to allow direct comparisons with the measurements (Kawara et al., 1990). The bottom edge of the counterrotating cell near the heated wall is extended further down compared with the case of $A = 1.0$ [Fig. 2(*a*)]. Actually, the bulk of the heated plate is seen to be covered with the downward boundary layer. The isotherm, the temperature of which is at the same value as that of the externally heated sidewall ($x = 0$) is located slightly above the bottom corner. The flow field of the present computation is in reasonable qualitative agreement with the experiment (Kawara et al., 1990). The global features of the fields at $A = 2.0$ are consistent with the present results and, hence, they are not shown here.

The results for a shallow enclosure with the aspect ratio $A = 0.3$ are illustrated in Fig. 4. The values of Ra_I and Ra_E used for the present computations are the same as those for the square cavity. A very weak counterrotating vortex appears near the top-left corner. The upflow is still predominant in the vicinity of the heated wall, as indicated by both streamlines and isotherms. In the experiment (Kawara et al., 1990), a counterrotating cell is observed near the top-left corner. The size of this cell appears to be substantially different from the computational results. The heat transfer through the horizontal walls in the actual experiments may have a comparatively strong impact on the flow patterns.

As described earlier, downward flows may be observed near the externally heated sidewall ($x = 0$) due to generation of the negative buoyancy when the internal heat source is intense. In such circumstances, of much interest is the heat transfer at the heated sidewall located at $x = 0$. The distribution of the local heat flux is plotted in Fig. 5 for different aspect ratios. The nondimensional heat flux, q, is defined as $q^* (Ra_E Pr)^{1/2}/\rho c_p u_0 T_0$ where q^* stands for the dimensional value. Negative values imply that heat is transferred from the fluid to the wall.

Table 1 The average heat flux, $\bar{q}$, at the isothermal walls for various aspect ratios, A. The left and right columns, respectively, indicate values at the walls at $x/L = 0$ and 1.0.

Ra_I/Ra_E $A=$	0.3	1.0	2.0	5.0
0.0	0.640 −0.641	0.547 −0.537	0.265 −0.249	0.112 −0.114
∞	−0.460 −0.463	−0.391 −0.393	−0.428 −0.428	−0.456 −0.454
100.0	0.228 −1.18	0.152 −0.938	−0.119 −0.743	−0.311 −0.619
Percent error*	3.0	0.26	0.70	2.2

*$|(\bar{q}_{\text{at } x/L=0} + \bar{q}_{\text{at } x/L=1}) - C|/C \times 100.0$ where $C = |\bar{q}_{\text{at } x/L=0} + \bar{q}_{\text{at } x/L=1}|$ for $Ra_I/Ra_E = \infty$

Table 2 The net heat input across the boundary [$\times 10^2 \int q_{in}$] at various aspect ratios, A

Ra_I/Ra_E $A=$	0.3	1.0	2.0	5.0
0.0	0.662	0.533	0.776	2.63
100.0	0.229	0.204	0.0875	0.0433
η (percent) =	34.6	38.3	11.3	1.65

For a fixed value of Ra_I/Ra_E, patterns of the local heat flux at the externally heated isothermal wall ($x=0$) are dramatically different depending on the aspect ratio. In the case of the square cavity ($A=1.0$) at $Ra_I = 5.0 \times 10^9$ and $Ra_E = 5.0 \times 10^7$, the direction of heat flow changes its sign at around $y/H = 0.5$. Positive q occurs below that height, i.e., the fluid near the region is actually heated by the wall. However, q turns negative above $y/H \approx 0.5$, indicating that heat escapes from the fluid of higher temperatures to the surroundings due to the internal heat generation. This result is compared with those of $A = 5.0$ and 0.3. In the case of a tall cavity ($A = 5.0$), heat leaves from the fluid toward the surroundings over the entire length of the externally heated wall, except in very small portions near the bottom wall ($y=0$). On the contrary, for a shallow cavity ($A=0.3$), heat enters into the fluid through the isothermally heated wall over much of the whole height of the cavity. Heat leaves from a small region due to the internal heat generation.

Computed values of the average heat flux at the isothermal walls are summarized in Table 1. If the fluid is heated by either the temperature difference of the sidewalls only or the internal heat generation only, the heat transfer in the cavity is symmetric. However, at $Ra_I/Ra_E = 100.0$, when both modes of heating are present simultaneously, the direction of the overall heat transfer at $x = 0$ reverses depending on the aspect ratio. The wall acts as the energy supply if $A \le 1.0$, while it serves to remove heat from the fluid when $A > 1.0$ Errors in $\bar{q}$ are estimated from the solutions for $Ra_I/Ra_E = 100.0$ and ∞, and they are indicated in Table 1.

From a practical viewpoint of heat removal from the cavity walls, the information concerning how much heat enters into the system from the surroundings is of primary importance. The total heat input across the boundary, $\int q_{in}$ ($= \int_0^y q dy$ for which $q > 0$) is presented in Table 2 for various aspect ratios. It has to be stressed that $\int q_{in}$ indicates the heat transfer from the surroundings to the cavity interior across the externally heated sidewall. At each A, two situations are considered: the case of no internal heat generation and the case of $Ra_I/Ra_E = 100.0$. For $A > 1.0$, the heat input from the surroundings into the system increases as A becomes larger when there is no internal heat generation; on the contrary, $\int q_{in}$ is reduced considerably for large values of A, when the internal heat generation is present. For example, at $A = 5.0$, the net heat input from the surroundings to the cavity interior across the system boundary is negligibly small.

This trend can be better illustrated by the ratio, η, defined as

$$\eta = \frac{\int q_{in} \text{ for } Ra_I/Ra_E = 100.0}{\int q_{in} \text{ for } Ra_I = 0.0} \times 100.0 \qquad (1)$$

This parameter measures how much reduction in the heat input across the boundary from the surroundings to the cavity interior is realized by the presence of the internal heat generation. The peak value of η occurs when the aspect ratio is close to unity. When the aspect ratio is small, the thermal boundary layer becomes thin, since the cavity height is small. There is not enough room for the downward flow near the externally heated wall ($x=0$) to develop, although the upflow near the major portion of the heated surface is of substantial strength (see also Fig. 4). For larger values of A, the downward flow extends to the locations near the bottom surface, as seen in Fig. 3. Consequently, the net heat transfer across the system boundary becomes very small when the aspect ratio is large.

Concluding Remarks

Natural convection in a differentially heated rectangular cavity with internal heat generation is examined numerically. The computed results of the temperature and flow characteristics are consistent with the experimental measurements (Kawara et al., 1990). The qualitative changes in the flow patterns, when the internal heat generation is appreciable, are captured successfully in the present analysis.

As the aspect ratio increases, a larger portion of the heated wall is covered by the downward flow. When the aspect ratio is large, the heat transport across the externally heated sidewall is directed from the fluid to the surroundings over much of the height of the wall. When the cavity is shallow ($A < 1.0$), the inward heat transport across the isothermally heated wall is approximately one third that of the case in which no internal heat generation exists.

Acknowledgments

The authors are grateful to Dr. Zensaku Kawara of Kyoto University for providing the details of the experimental investigations.

References

Acharya, S., 1984, "The Influence of Aspect Ratio on Natural Convection in Internally Heated Inclined Layers Which Are Heated or Cooled From Below," *Proceedings, SECTAM XII*, Vol. II, p. 393.

Acharya, S., and Goldstein, R. J., 1985, "Natural Convection in an Externally Heated Vertical or Inclined Square Box Containing Internal Energy Sources," ASME JOURNAL OF HEAT TRANSFER, Vol. 107, pp. 855–866.

de Vahl Davis, G., 1983, "Natural Convection of Air in a Square Cavity: a Bench Mark Solution," *International Journal for Numerical Methods in Fluids*, Vol. 3, pp. 249–264.

Freitas, C. J., Street, R. L., Findikakis, A. N., and Koseff, J. R., 1985, "Numerical Simulation of Three-Dimensional Flow in a Cavity," *International Journal for Numerical Methods in Fluids*, Vol. 5, pp. 561–575.

Fusegi, T., Hyun, J. M., and Kuwahara, K., 1992, "Natural Convection in a Differentially Heated Square Cavity With Internal Heat Generation," *Numerical Heat Transfer*, Part A, Vol. 21, pp. 215–229.

Kawara, Z., Kishiguchi, I., Aoki, N., and Michiyoshi, I., 1990, "Natural Convection in a Vertical Fluid Layer With Internal Heating," *Proceedings, 27th National Heat Transfer Symposium of Japan*, Vol. II, pp. 115–117.

Kulacki, F. A., and Richards, D. E, 1985, "Natural Convection in Plane Layers and Cavities With Volumetric Energy Sources," *Natural Convecion*, S. Kakac et al., eds., pp. 197-255, Hemisphere, Washington, DC.

Lambha, N. K., Korpera, S. A., and Kulacki, F. A., 1978, "Thermal Convection in a Cylindrical Cavity With Uniform Volumetric Energy Generation," *Proceedings, 6th International Heat Transfer Conference*, Vol. 2, pp. 311-316.

Ostrach, S., 1988, "Natural Convection in Enclosures," ASME JOURNAL OF HEAT TRANSFER, Vol. 110, pp. 1175-1190.

Patankar, S. V., 1980, *Numerical Heat Transfer and Fluid Flow*, Chap. 6, Hemisphere, Washington, DC.

Stone, H. L., 1968, "Iterative Solution of Implicit Approximations of Multidimensional Partial Differential Equations," *Journal of Numerical Analysis*, Vol. 5, pp. 530-558.

Wang, H. S., and Wang, Q. J., 1988, "Natural Convection in an Externally Heated Vertical Rectangular Enclosure Containing Internal Energy Sources," *Proceedings, Experimental Heat Transfer, Fluid Mechanics, and Thermodynamics*, R. K. Shah et al., eds., pp. 709-714.

Heat Transfer in Power Cables Packaged Inside Trays

Z. Zhao,[1] Z. Ren,[2] and D. Poulikakos[1]

Nomenclature

b = thickness of enclosure wall, m
B = ratio of radiation heat transfer rate to total rate of heat transfer
D = diameter, m
g = gravitational acceleration, m/s^2
Gr = Grashof number = $g\beta q_t D^3/\pi k\nu^2$
h = convection heat transfer coefficient, W/m^2
$\bar{h}$ = average convection heat transfer coefficient, W/m^2
H = height of the enclosure, m
I = electric current intensity of power cable laid in the tray, A
I_∞ = electric current intensity of power cable suspended in an infinite space of air, A
k = fluid thermal conductivity, W/m·K
L = length of the cylinder or length of the enclosure
n_∞ = index of refraction of ambient air
Nu = Nusselt number, Eq. (4)
$\overline{\text{Nu}}$ = average Nusselt number, Eq. (5)
N_w = fringe order number at the wall
N_{w+k} = fringe order number of the kth fringe away from the wall
$\overline{\text{Nu}}_\infty$ = average Nusselt number of cylinder in an infinite air
Pr = Prandtl number for air
q_c = rate of convection heat transfer per unit length, W/m
$q_{c,\infty}$ = rate of convection heat transfer per unit length of cylinder in an infinite air space, W/m
q_r = rate of radiation heat transfer per unit length, W/m
q_t = total heat transfer rate per unit length, W/m
s = cylinder spacing, m, Fig. 1
T = temperature of air, K
T_w = wall temperature, K
T_{w+k} = temperature of air at the kth fringe away from the wall, K
T_∞ = ambient temperature, K
W = width of the enclosure, m
β = volumetric expansion coefficient, K^{-1}
ΔN_k = $N_{w+k} - N_{w+k-1}$
$\Delta\xi_w$ = normal distance between the first fringe and the wall
$\Delta\xi_{w+1}$ = normal distance between the N_{w+1} fringe and the N_{w+2} fringe
ϵ = emissivity
η = capacity decreasing factor of power cable, I/I_∞
θ = angle, deg, Fig. 1
λ_o = wavelength of laser beam, μm
ν = kinematic viscosity, m^2/s
ξ = distance normal to the wall, m

1 Introduction

Cooling of large power cables is of paramount importance to the power industry. In this paper, the results of a fundamental study on the cooling of electrically heated cylinders that models indirectly such cables laid in an enclosed tray are reported. Cooling of the cylinders occurs by combined natural convection between the cylinders and the surrounding air and radiation between the cylinders and the tray in which they are enclosed. Relevant to the present work are studies of heat transfer between "inner" bodies and their surrounding enclosure. In the following paragraphs representatives of such studies are reviewed.

Warrington and Crupper (1981) investigated the phenomenon of natural convection heat transfer between a bundle of tubes and a cubic enclosure surrounding the tubes. They showed that cell formation between the inner bodies (tubes) intensified the natural convection in the enclosure. Babus'Haq et al. (1984, 1985) studied pipeline arrangements in underground tunnels in district heating applications. They reported that the heat losses were affected by the relative position of the high and low temperature tubes in the tunnel. Sparrow and co-workers have carried out several studies on the heat transfer between an enclosure and the inner bodies that it surrounds. For example, Sparrow et al. (1984) investigated the phenomenon of natural convection in enclosures with off-center inner bodies. Sparrow and Charmchi (1983) carried out experiments on natural convection in an enclosure formed between eccentric and concentric vertical cylinders of different height and diameter.

The experimental methods used in the present study are holographic interferometry and Schlieren interferometry. Details on the experimental apparatus are presented in the next section.

2 Experimental Apparatus and Methodologies

A schematic of the cross section of the experimental apparatus is shown in Fig. 1. Three brass cylinders of diameter $D = 50$ mm and length $L = 690$ mm are placed parallel to each other at the bottom of a rectangular enclosure. The enclosure is made out of plexiglass of thickness $b = 5$ mm. Its height is $H = 236$ mm, its width $W = 356$ mm and its length $L = 700$ mm, only slightly longer than the brass cylinders. Three identical cartridge heaters were installed inside the brass tubes. Direct current was supplied to the heaters with the help of three power supplies. The power input to the heaters was measured with three Watt meters accurate within 0.5 percent. The power input to the three cylinders was identical. The temperature of the surface of each cylinder was monitored with the help of type-T thermocouples. Six thermocouples per cylinder were used spaced at 60 deg increments around the periphery. Their leads were buried inside small channels parallel to the cylinder axis to minimize "fin" effects. The azimuthal temperature variation of the cylinders was found to be small (of the order 1°C) because of the high thermal conductivity of the brass tubes. In addition, this variation did not affect the accuracy of the measurements of the local heat transfer rate at the cylinder surface since holographic interferometry was utilized to calculate these gradients on the air side. Steady state was obtained about 4 h after the power to the heaters was turned on. The

[1] Mechanical Engineering Department, University of Illinois at Chicago, Chicago, IL 60680.

[2] Thermal Engineering Department, Qinghua University, Beijing 100084, People's Republic of China.

Contributed by the Heat Transfer Division of the THE AMERICAN SOCIETY OF MECHANICAL ENGINEERS. Manuscript received by the Heat Transfer Division November 1990; revision received December 1991. Keywords: Natural Convection, Radiation, Thermal Packaging.

Kulacki, F. A., and Richards, D. E, 1985, "Natural Convection in Plane Layers and Cavities With Volumetric Energy Sources," *Natural Convecion*, S. Kakac et al., eds., pp. 197–255, Hemisphere, Washington, DC.

Lambha, N. K., Korpera, S. A., and Kulacki, F. A., 1978, "Thermal Convection in a Cylindrical Cavity With Uniform Volumetric Energy Generation," *Proceedings, 6th International Heat Transfer Conference*, Vol. 2, pp. 311–316.

Ostrach, S., 1988, "Natural Convection in Enclosures," ASME JOURNAL OF HEAT TRANSFER, Vol. 110, pp. 1175–1190.

Patankar, S. V., 1980, *Numerical Heat Transfer and Fluid Flow*, Chap. 6, Hemisphere, Washington, DC.

Stone, H. L., 1968, "Iterative Solution of Implicit Approximations of Multidimensional Partial Differential Equations," *Journal of Numerical Analysis*, Vol. 5, pp. 530–558.

Wang, H. S., and Wang, Q. J., 1988, "Natural Convection in an Externally Heated Vertical Rectangular Enclosure Containing Internal Energy Sources," *Proceedings, Experimental Heat Transfer, Fluid Mechanics, and Thermodynamics*, R. K. Shah et al., eds., pp. 709–714.

Heat Transfer in Power Cables Packaged Inside Trays

Z. Zhao,[1] Z. Ren,[2] and D. Poulikakos[1]

Nomenclature

b = thickness of enclosure wall, m
B = ratio of radiation heat transfer rate to total rate of heat transfer
D = diameter, m
g = gravitational acceleration, m/s^2
Gr = Grashof number = $g\beta q_t D^3/\pi k\nu^2$
h = convection heat transfer coefficient, W/m^2
$\bar{h}$ = average convection heat transfer coefficient, W/m^2
H = height of the enclosure, m
I = electric current intensity of power cable laid in the tray, A
I_∞ = electric current intensity of power cable suspended in an infinite space of air, A
k = fluid thermal conductivity, W/m·K
L = length of the cylinder or length of the enclosure
n_∞ = index of refraction of ambient air
Nu = Nusselt number, Eq. (4)
$\overline{\text{Nu}}$ = average Nusselt number, Eq. (5)
N_w = fringe order number at the wall
N_{w+k} = fringe order number of the kth fringe away from the wall
$\overline{\text{Nu}}_\infty$ = average Nusselt number of cylinder in an infinite air
Pr = Prandtl number for air
q_c = rate of convection heat transfer per unit length, W/m
$q_{c,\infty}$ = rate of convection heat transfer per unit length of cylinder in an infinite air space, W/m
q_r = rate of radiation heat transfer per unit length, W/m
q_t = total heat transfer rate per unit length, W/m
s = cylinder spacing, m, Fig. 1
T = temperature of air, K
T_w = wall temperature, K
T_{w+k} = temperature of air at the kth fringe away from the wall, K
T_∞ = ambient temperature, K
W = width of the enclosure, m
β = volumetric expansion coefficient, K^{-1}
ΔN_k = $N_{w+k} - N_{w+k-1}$
$\Delta\xi_w$ = normal distance between the first fringe and the wall
$\Delta\xi_{w+1}$ = normal distance between the N_{w+1} fringe and the N_{w+2} fringe
ϵ = emissivity
η = capacity decreasing factor of power cable, I/I_∞
θ = angle, deg, Fig. 1
λ_o = wavelength of laser beam, μm
ν = kinematic viscosity, m^2/s
ξ = distance normal to the wall, m

1 Introduction

Cooling of large power cables is of paramount importance to the power industry. In this paper, the results of a fundamental study on the cooling of electrically heated cylinders that models indirectly such cables laid in an enclosed tray are reported. Cooling of the cylinders occurs by combined natural convection between the cylinders and the surrounding air and radiation between the cylinders and the tray in which they are enclosed. Relevant to the present work are studies of heat transfer between "inner" bodies and their surrounding enclosure. In the following paragraphs representatives of such studies are reviewed.

Warrington and Crupper (1981) investigated the phenomenon of natural convection heat transfer between a bundle of tubes and a cubic enclosure surrounding the tubes. They showed that cell formation between the inner bodies (tubes) intensified the natural convection in the enclosure. Babus'Haq et al. (1984, 1985) studied pipeline arrangements in underground tunnels in district heating applications. They reported that the heat losses were affected by the relative position of the high and low temperature tubes in the tunnel. Sparrow and co-workers have carried out several studies on the heat transfer between an enclosure and the inner bodies that it surrounds. For example, Sparrow et al. (1984) investigated the phenomenon of natural convection in enclosures with off-center inner bodies. Sparrow and Charmchi (1983) carried out experiments on natural convection in an enclosure formed between eccentric and concentric vertical cylinders of different height and diameter.

The experimental methods used in the present study are holographic interferometry and Schlieren interferometry. Details on the experimental apparatus are presented in the next section.

2 Experimental Apparatus and Methodologies

A schematic of the cross section of the experimental apparatus is shown in Fig. 1. Three brass cylinders of diameter $D = 50$ mm and length $L = 690$ mm are placed parallel to each other at the bottom of a rectangular enclosure. The enclosure is made out of plexiglass of thickness $b = 5$ mm. Its height is $H = 236$ mm, its width $W = 356$ mm and its length $L = 700$ mm, only slightly longer than the brass cylinders. Three identical cartridge heaters were installed inside the brass tubes. Direct current was supplied to the heaters with the help of three power supplies. The power input to the heaters was measured with three Watt meters accurate within 0.5 percent. The power input to the three cylinders was identical. The temperature of the surface of each cylinder was monitored with the help of type-T thermocouples. Six thermocouples per cylinder were used spaced at 60 deg increments around the periphery. Their leads were buried inside small channels parallel to the cylinder axis to minimize "fin" effects. The azimuthal temperature variation of the cylinders was found to be small (of the order 1°C) because of the high thermal conductivity of the brass tubes. In addition, this variation did not affect the accuracy of the measurements of the local heat transfer rate at the cylinder surface since holographic interferometry was utilized to calculate these gradients on the air side. Steady state was obtained about 4 h after the power to the heaters was turned on. The

[1] Mechanical Engineering Department, University of Illinois at Chicago, Chicago, IL 60680.

[2] Thermal Engineering Department, Qinghua University, Beijing 100084, People's Republic of China.

Contributed by the Heat Transfer Division of the THE AMERICAN SOCIETY OF MECHANICAL ENGINEERS. Manuscript received by the Heat Transfer Division November 1990; revision received December 1991. Keywords: Natural Convection, Radiation, Thermal Packaging.

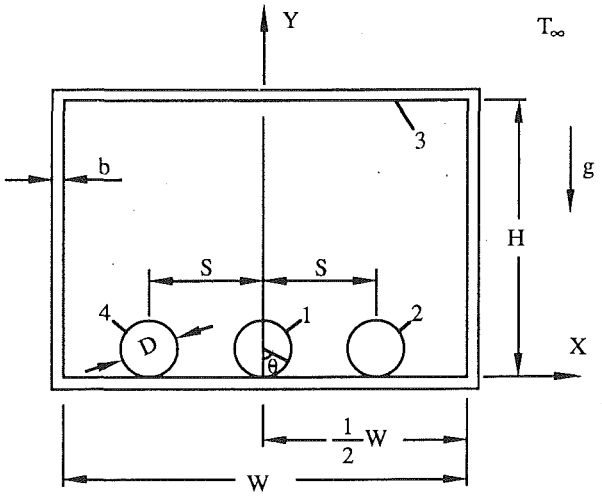

Fig. 1 Schematic of the system of interest

cooling of the system (necessary for steady state to be reached) was provided by the natural convection interaction between the enclosure and the room air. No additional cooling was provided. All measurements and observations reported in this study were obtained at steady-state conditions.

The holographic interferometry setup used in this study is standard (Vest, 1979) and will not be described in detail. Briefly, a HeNe laser beam is split into an object beam and a reference beam. The object beam is expanded and passed through the test section before it strikes the holographic film. The reference beam is expanded and meets the object beam at the holographic film.

To be able to measure temperatures with holographic interferometry, reference temperatures are needed. To this end, six temperature measurements of each cylinder wall surface were taken with the help of thermocouples. With the wall temperature known, it can be shown (Zhao, 1988) that the temperature field in the enclosure and the temperature gradients at the wall of the cylinder are given by the following expressions:

$$T_{w+1}=\frac{1}{\frac{1}{T_w}+\frac{\Delta\xi_w}{\Delta\xi_{w+1}}\frac{\lambda_o}{L(n_\infty-1)T_\infty}} \tag{1}$$

$$T_{w+k}=\frac{1}{\frac{1}{T_w}+\frac{\Delta N_k\lambda_o}{L(n_\infty-1)T_\infty}} \tag{2}$$

$$\left(\frac{dT}{d\xi}\right)_w=-\frac{1}{\Delta\xi_{w+1}}\frac{\lambda_o T_w^2}{L(n_\infty-1)T_\infty} \tag{3}$$

The index of refraction at the temperature of the environment (n_∞) can be found from Vest (1979). The temperature of the first fringe away from the wall can now be calculated directly from Eq. (1). Equation (2) yields the temperature of all fringes for $k>1$. The wall temperature gradient is obtained from Eq. (3). Note that as Gr increases the thermal boundary layer is expected to become sharper, bringing up the issue of fringe definition in the holograms to allow for accurate fringe interpretation. Indeed, in all cases reported in this paper, the temperature gradients were evaluated from clear holograms with sharply defined fringes. In addition, as mentioned earlier, Schlieren interferometry was used to check the findings for Nu, and it yielded identical results. We did not encounter particular difficulties in fringe interpretation for the values of Gr used in this study.

It is worth noting that in Eq. (1) the ratio $\Delta\xi_w/\Delta\xi_{w+1}$ is measured from the holographic interferograms and has a magnitude 0 (1). In addition, if a consistent error occurs in the measurements of $\Delta\xi_w$ and $\Delta\xi_{w+1}$, the effect of this error is "reduced" in the ratio $\Delta\xi_w/\Delta\xi_{w+1}$. On the other hand, $\Delta\xi_{w+1}$ is a small number and it appears alone in the denominator of Eq. (3) for the wall temperature gradient measurement. Experimental errors in the measurement of $\Delta\xi_{w+1}$ may affect the result for $(dT/d\xi)_w$ in a manner that may not be negligible. Based on the above, while we deem Eqs. (1) and (2) reliable in obtaining temperature measurements, we feel that the accuracy of Eq. (3) for the wall temperature gradients needs to be checked. To circumvent this difficulty, Schlieren interferometry was used to double check the temperature gradients at the wall. The optical setup for the Schlieren is standard (Merzkirch, 1987) and will not be described here, for brevity. In all cases reported in this study the difference between the values obtained with holographic interferometry and the values obtained with Schlieren interferometry was less than 5 percent. To establish the accuracy of the temperature measurements we obtained the temperature of the right cylinder by using Eqs. (1) and (2), starting from the center cylinder, and calculating the temperatures of all fringes until we reached the surface of the right cylinder. We also measured the surface of the right cylinder with the help of thermocouples. The difference between the two measurements was indeed negligible. For example, for $\mathrm{Gr}=1.995\times10^6$, Eq. (2) yielded a surface temperature of 30.2°C while the thermocouples measured 30.5°C. The relative error was less than 1 percent. Note that the room temperature ($T_\infty\approx24$°C) was *not* used as the reference temperature for the data reduction.

3 Results and Discussion

The results on the local convective heat transfer from the cylinders are reported with the help of the local Nusselt number, defined as

$$\mathrm{Nu}=\frac{hD}{k}=-\frac{D}{T_w-T_\infty}\left(\frac{\partial T}{\partial\xi}\right)_w \tag{4}$$

In the above equation T_∞ is the ambient temperature outside the enclosure, T_w the wall temperature, and $(\partial T/\partial\xi)_w$ the wall temperature gradient. Equation (3) can be used to obtain the wall temperature gradient from the holographic interferograms. It is worth clarifying that the conduction heat loss from the cylinders to the underlying plexiglass wall is indeed small since the contact area is practically zero (a straight line). In addition, this loss does not affect any of the results since the convective heat transfer coefficient (Nusselt number) is obtained utilizing holographic interferometry and not by subtracting the heat loss from the total heat input to the cylinder.

Figure 2(*a*) reports the dependence of the local Nusselt number of the central and the right cylinders for $\mathrm{Gr}=1.33\times10^6$ and $\mathrm{Gr}=4\times10^6$, respectively. The properties of the air used in the evaluation of both the Grashof and the Nusselt number throughout this study were taken at room temperature. In both cases (but more so for $\mathrm{Gr}=4\times10^6$), the values of Nu for the right cylinder are higher than the values of Nu for the central cylinder indicating better heat transfer. The dependence of Nu on θ is nonmonotonic, featuring a maximum for both the central and the right cylinder (Fig. 2*a*). Increasing Gr increases Nu for both the central and the right cylinders.

A convection-based average Nusselt number for the central cylinder is defined as follows:

$$\overline{\mathrm{Nu}}=\frac{\bar{h}D}{k} \tag{5}$$

The dependence of $\overline{\mathrm{Nu}}$ on Gr is shown in Fig. 2(*b*). The points indicate the experimental data and the solid line the equation

$$\overline{\mathrm{Nu}}=0.240\ \mathrm{Gr}^{1/6} \tag{6}$$

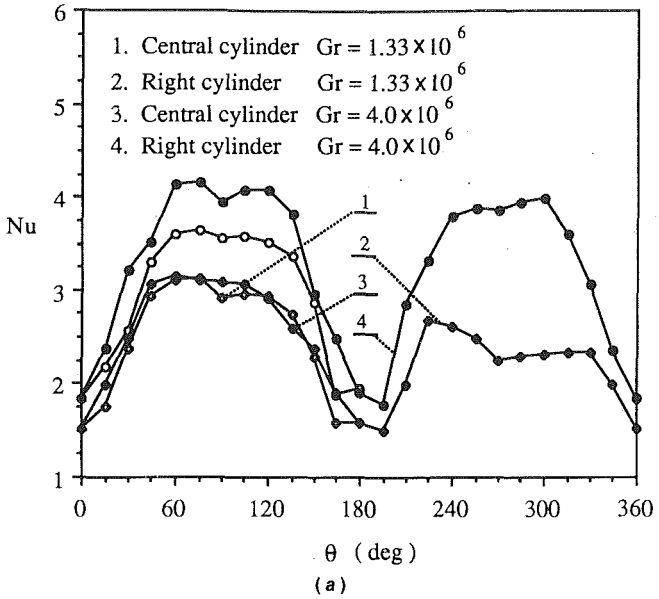

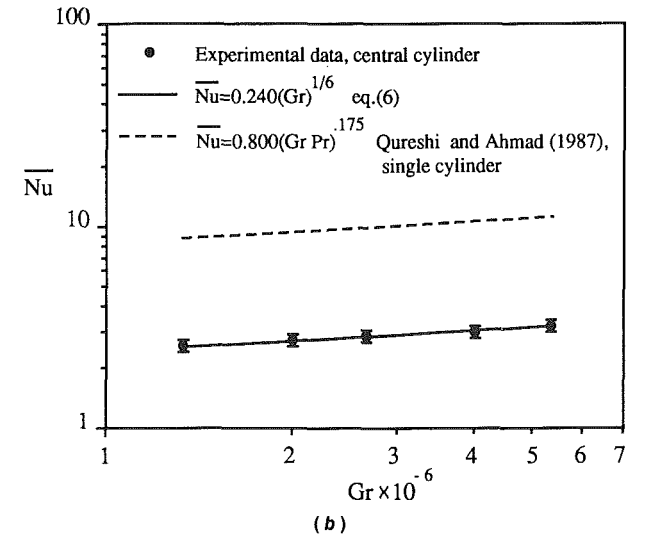

Fig. 2 (*a*) **Local Nusselt number of the center and right cylinders for representative values of Gr;** (*b*) **dependence of the average Nusselt number of the central cylinder on Gr**

by which these data were correlated. The error bars represent the overall error associated with evaluation of $\overline{Nu}$. This error is approximately no more than 15 percent of the reported values of $\overline{Nu}$. Clearly, $\overline{Nu}$ increases monotonically with Gr. The dashed line represents the correlation of the numerical investigation by Qureshi and Ahmad (1987) for natural convection from a single cylinder in an infinite space. Figure 2(*b*) clearly indicates that placing the cylinders in a tray drastically reduces the convective heat transfer rate. In addition, at the suggestion of an anonymous reviewer of this paper, we attempted to compare Eq. (6) to an approximate correlation for $\overline{Nu}$ for natural convection from a single cylinder inside a finite enclosure published in Warrington et al. (1988). These authors recommend that their correlation should be used to estimate the effect of the enclosure on the natural convection heat transfer only if it yields values of $\overline{Nu}$ lower than an upper bound corresponding to natural convection from a cylinder in an infinite medium. For the parametric domain of our study the correlation of Warrington et al. (1988) yielded values of $\overline{Nu}$ slightly higher (by about 5 percent) than those of Qureshi and Ahmad (1987), indicating that our parametric domain is outside its range of applicability.

Radiation Heat Transfer. An evaluation of the contribution of the radiative heat transfer mechanism to the heat removal from the cylinders simulating the power cables is necessary to put into proper perspective the convective heat transfer results reported earlier. The emissivity of the cylinders was $\epsilon_1 = \epsilon_2 = \epsilon_4 = 0.92$ and of the enclosure (tray) walls $\epsilon_3 = 0.84$. A simple "network" model was employed to estimate the radiation heat transfer (Siegel and Howell, 1981). The subscript 1 was used to denote the central cylinder, subscript 2 to denote the right cylinder, subscript 3 to denote enclosure walls, and subscript 4 to denote the left cylinder (Fig. 1). Note that the temperatures and properties of the right and left cylinders (surfaces 2 and 4) are identical. Each surface was assumed to be at a constant (average) temperature for simplicity. This approximation does not have a serious effect on the accuracy of the results. Even in the case of the container (surface 3) the average temperature of its bottom wall was measured to be not higher than about 5°C compared to the temperature of the side and the top walls. The average surface temperatures are obtained with thermocouple measurements and the view factors from Siegel and Howell (1981). No details of the model are shown here, for brevity.

The ratio of radiative heat transfer to the total heat transfer (denoted by B) from the central cylinder is shown in Fig. 3(*a*) as a function of the Grashof number. This ratio does not vary monotonically with Gr. Instead, at small values of Gr it decreases as Gr increases, then it reaches a minimum value, and thereafter it increases with Gr. The abovedescribed behavior indicates that natural convection is not very effective at small values of Gr.

The impact of the cylinder spacing, s, on the ratio of the radiation heat transfer to the total heat transfer, B, for the central cylinder and for the right cylinder is shown in Fig. 3(*b*). As s increases, B decreases monotonically for the central cylinder, indicating that the role of convection is enhanced and the role of radiation is reduced as the spacing between cylinders increases. The same is true for the side cylinder as well, except for the very large values of the spacing ($s = 130$ mm) where B increases with s. The reason for this fact is that for large values of s the right cylinder is placed very close to the side wall of the cavity, thus restricting the buoyancy-driven flow.

Estimation of the Power Cable Capacity Decreasing Factor. Since this study aims at modeling heat transfer from power cables in trays, it is important to provide estimates of the effect of the heating of the cables on the current intensity capacity of the cables. Such estimates are necessary for the correct spacing of the cables. To this end, the capacity decreasing factor (η) is defined as the ratio of the electric current intensity that yields the maximum allowable temperature at the surface of the center cylinder (cable) of the present study, divided by the electric current intensity that yields the maximum allowable surface temperature of this cylinder (cable) when it is suspended alone in an infinite air space. For the present numerical example a ZQ type cable will be used. This cable is described in Table 1, which is constructed out of data contained in the *Handbook of Electrical Wires and Power Cables* published by the Department of Industry of PRC (1978). It can be rather easily shown (Zhao, 1988) that

$$\eta \le \left[\frac{q_c + q_r}{q_{c,\infty} + q_r}\right]^{1/2} = \frac{1}{\left[\dfrac{\overline{Nu}_\infty}{\overline{Nu}} + \left[1 - \dfrac{\overline{Nu}_\infty}{\overline{Nu}}\right] B\right]^{1/2}} \qquad (7)$$

Based on the data of Table 1, the maximum allowable heat generation for a single cable is 6.03 W/m. The resulting Grashof number is $Gr \approx 1.08 \times 10^6$. Utilizing the correlation of Qureshi

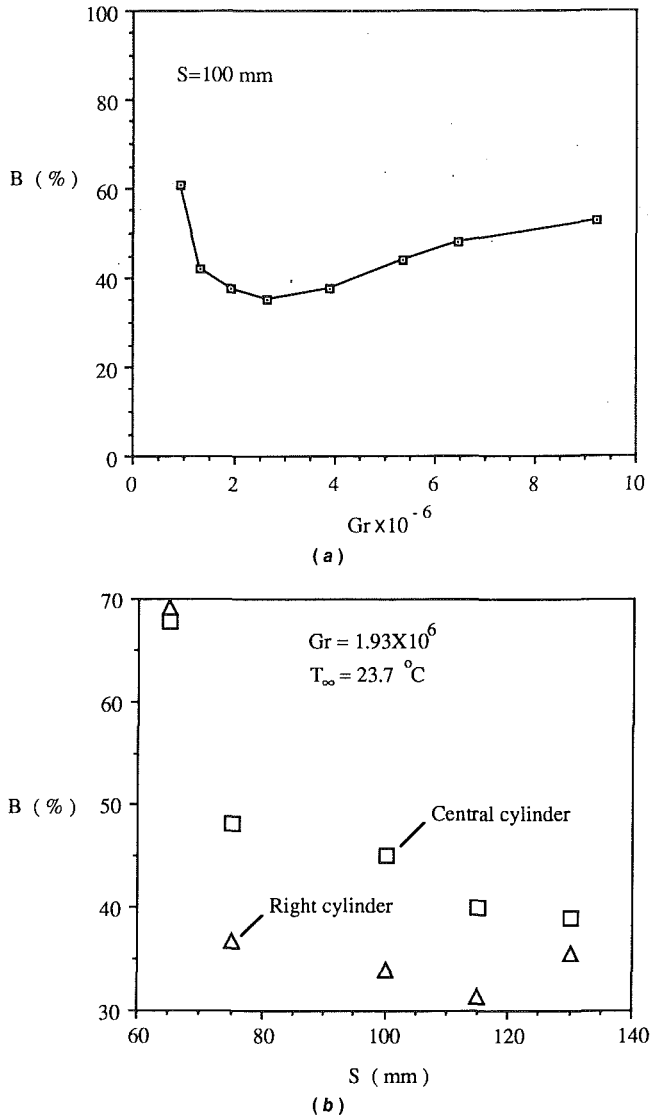

Fig. 3 (*a*) Dependence of the parameter *B* on Gr; (*b*) dependence of parameter *B* on the cylinder spacing

and Ahmad (1987) for the average Nusselt number from a single cylinder in an infinite air space, we obtain $\overline{\mathrm{Nu}}_\infty = 8.547$. On the other hand, the central cylinder in the present experiments reached a surface temperature of 54°C (equal to the maximum allowable temperature) for $\mathrm{Gr} \approx 7 \times 10^6$. For this value of Gr, Eq. (6) yields $\overline{\mathrm{Nu}} = 3.32$, and from Fig. 3(*a*), $B \approx 0.48$. With the above quantities known, criterion (7) results in the estimate $\eta \leq 0.74$. Therefore, the current carrying capacity of the center cylinder in the enclosed tray is at least 26 percent less than the current carrying capacity of a single cylinder suspended in air, a result that underlines the great importance of the proper heat removal from large power cables placed in trays and the necessity for a thorough heat transfer analysis and design before these cables are positioned in the trays.

4 Conclusions

In this paper, an experimental study was reported on the problem of heat transfer from three electrically heated cylinders, resting at the bottom of a rectangular enclosure. The experiment aimed at indirectly simulating heat transfer from large power cables placed inside trays. The main findings of the study are as follows:

Table 1 Description of a single ZQ type power cable in air

Cable outer diameter	50 mm
Conductor material	Cu or Al
Capacity for Cu	380 A
Capacity for Al	295 A
Maximum allowable outer surface temperature	54°C
Maximum allowable heat generation for the surface temperature not to exceed 54°C	6.30 W/m
Resistance	4.177×10^{-5} Ohm/m

- The effect of interaction between the cylinders as well as between the cylinders and the enclosure was significant. To this end, utilizing single cylinder correlations to estimate the heat transfer rate from the cylinders (local as well as total) is *not* recommended. An engineering correlation (Eq. (6)) for the dependence of $\overline{\mathrm{Nu}}$ on Gr obtained in this study yields values of $\overline{\mathrm{Nu}}$ markedly lower than those for a single cylinder in an infinite space (Qureshi and Ahmad, 1987).
- Thermal radiation was a significant contributor to the total heat removal from the cylinders, more so for small spacings. A "critical" value of Gr existed for which the contribution of thermal radiation to the total heat transfer from the central cylinder reached a minimum.
- It was estimated that the ineffective cooling because of cable-to-cable and cable-to-tray thermal interaction seriously affects the current carrying capacity of power cables and needs to be taken into account seriously before the cables are placed into the tray.

References

Aihara, T., Yamada, Y., and Endo, S., 1972, "Free Convection Along the Downward-Facing Surface of a Heated Horizontal Plate," *Int. J. Heat Mass Transfer*, Vol. 15, pp. 2535–2549.

Babus'Haq, R. F., Probert, S. D., Shilston, M. J., and Talati, A., 1985, "Design Improvements Concerning District Heating Pipeline Configurations," *Applied Energy*, Vol. 17, pp. 77–96.

Babus'Haq, R. F., Probert, S. D., and Shilston, M. J., 1985, "Natural Convection Across Cavities: Design Advice," *Applied Energy*, Vol. 20, pp. 161–188.

Department of Industry, 1978, *Handbook of Electrical Wires and Power Cables*, Beijing, People's Republic of China.

Eckert, E. R. G., and Carlson, W. D., 1961, "Natural Convection in an Air Layer Enclosed Between Two Vertical Plates With Different Temperatures," *Int. J. Heat Mass Transfer*, Vol. 2, pp. 106–120.

Kuehn, T. H., and Goldstein, R. J., 1976, "An Experimental and Theoretical Study of Natural Convection in the Annulus Between Horizontal Concentric Cylinders," *J. Fluid Mech.*, Vol. 74, pp. 695–719.

Merzkirch, W., 1987, *Flow Visualization*, 2nd ed., Academic Press, Orlando, FL.

Ostrach, S., 1953, "Analysis of Laminar Free Convection Flow and Heat Transfer About a Flat Plate Parallel to the Direction of the Generating Body Force," NACA Rep., No. 11.

Qureshi, Z. H., and Ahmad, R., 1987, "Natural Convection From a Uniform Heated Flux Horizontal Cylinder at Moderate Rayleigh Numbers," *Numerical Heat Transfer*, Vol. 11, pp. 199–212.

Siegel, R., and Howell, J. R., 1981, *Thermal Radiation Heat Transfer*, 2nd ed., McGraw-Hill, New York.

Sparrow, E. M., Stryker, P. C., and Ansri, M. A., 1984, "Natural Convection in Enclosures With Off-Centre Innerbodies," *Int. J. Heat Mass Transfer*, Vol. 27, pp. 49–56.

Sparrow, E. M., and Charmchi, M., 1983, "Natural Convection Experiments in an Enclosure Between Eccentric and Concentric Vertical Cylinders of Different Height and Diameter," *Int. J. Heat Mass Transfer*, Vol. 26, No. 1, pp. 133–143.

Vest, C. M., 1979, *Holographic Interferometry*, Wiley, New York.

Warrington, R. O., and Crupper, G., 1981, "Natural Convection Heat Transfer Between Cylindrical Tube Bundles and a Cubical Enclosure," ASME JOURNAL OF HEAT TRANSFER, Vol. 103, pp. 103–107.

Warrington, R. O., Smith, S., Powe, R. E, and Mussulman, R. L., 1988, "Boundary Effects on Natural Convection Heat Transfer for Enclosures," *Int. J. Heat Mass Transfer*, Vol. 31, pp. 1322–1325.

Zhao, Z., 1988, "Natural Convection Combined With Radiation in an Enclosure With Power Cables," M.S. Thesis, Qinghua University, Beijing, People's Republic of China.

Effect of Index of Refraction on Radiation Characteristics in a Heated Absorbing, Emitting, and Scattering Layer

R. Siegel[1] and C. M. Spuckler[2]

Nomenclature

a = absorption coefficient of layer, m^{-1}
D = thickness of plane layer, m
E_1, E_2, E_3 = exponential integral functions, $E_m(x) = \int_0^1 \mu^{m-2} \exp(-x/\mu) d\mu$
n = index of refraction
q = heat flux, W/m^2
T = absolute temperature, K
T_{s1}, T_{s2} = temperatures of surrounding radiating regions, K
x = coordinate normal to boundary of plane layer, m; $X = x/D$
κ = optical depth, $(a+\sigma_s)x$; κ_D, optical thickness, $(a+\sigma_s)D$
σ = Stefan–Boltzmann constant, $W/m^2 \cdot K^4$
σ_s = scattering coefficient of layer, m^{-1}
ρ^i = reflectivity of interface for internally incident radiation
τ^o = transmissivity of surface for externally incident radiation
Φ = dimensionless temperature distribution
Ψ = dimensionless radiative heat flux

Subscripts

i, o = incoming and outgoing radiation
r = radiative quantity
1, 2 = the hotter and cooler surroundings of the layer

Introduction

The index of refraction can considerably influence the temperature distribution and radiative heat flow in semitransparent materials such as some ceramics. For external radiant heating, the refractive index influences the amount of energy transmitted into the interior of the material. Emission within a material depends on the *square* of its refractive index, and hence this emission can be many times that for a blackbody radiating into a vacuum. Since radiation exiting through an interface into a vacuum cannot exceed that of a blackbody, there is extensive reflection at the internal surface of an interface, mostly by total internal reflection. This redistributes energy within the layer and tends to make its temperature distribution more uniform.

The purpose of the present analysis is to show that, for radiative equilibrium in a gray layer with diffuse interfaces, the temperature distribution and radiative heat flux for any index of refraction can be obtained very simply from the results for an index of refraction of unity. For the situation studied here, the layer is subjected to external radiative heating incident on each of its surfaces. The material emits, absorbs, and isotropically scatters radiation. For simplicity the index of refraction is unity in the medium surrounding the layer.

The surfaces of the layer are assumed diffuse. This is probably a reasonable approximation for a ceramic layer that has not been polished. When transmitted radiation or radiation emitted from the interior reaches the inner surface of an interface, the radiation is diffused and some of it thereby placed into angular directions for which there is total internal reflection. This provides a trapping effect for retaining energy within the layer and tends to equalize its temperature distribution.

An analysis of temperature distributions in absorbing-emitting layers, including index of refraction effects, was developed by Gardon (1958) to predict cooling and heat treating of glass plates. The interfaces were optically smooth; the resulting specular reflections were computed from the Fresnel reflection laws. This provides a somewhat different behavior than for diffuse interfaces. A similar application was for heating that occurs in a window of a re-entry vehicle (Fowle et al., 1969). A number of recent papers (Rokhsaz and Dougherty, 1989; Ping and Lallemand, 1989; Crosbie and Shieh, 1990) further examined the effects of Fresnel boundary reflections and nonunity refractive index. Other examples of analyses of both steady and transient heat transfer to single or multiple plane layers (Amlin and Korpela, 1979; Tarshis et al., 1969) have used diffuse assumptions at the interfaces as in the present study.

Analysis

A plane layer of ceramic material has thickness D as shown in Fig. 1. It absorbs, emits, and isotropically scatters radiation. The limiting case is considered here where the layer temperature distribution is dominated by radiation so heat conduction is neglected. The material has a constant index of refraction; it is the effect of the index of refraction that is investigated here. Because of the large amount of scattering in many ceramic materials, the interfaces between the ceramic and the surrounding air or vacuum are assumed to be diffuse. The refractive index of the surroundings is unity. As shown in Fig. 1, the layer is subjected to radiation from the surroundings at T_{s1} and T_{s2} on the two sides $x=0$ and $x=D$. It is assumed that the surroundings act as black environments so the incident energies on the two sides are $q_{r1}(0) = \sigma T_{s1}^4$ and $q_{r2}(D) = \sigma T_{s2}^4$. Inside the layer there are outgoing and incoming fluxes, q_o and q_i, at each interior surface, as shown on the figure. Since scattering is included, the local optical depth is related to the x coordinate by $\kappa = (a+\sigma_s)x$.

The temperature distribution inside the layer is governed by the integral equation given by Siegel and Howell (1981), modified with the index of refraction factor as

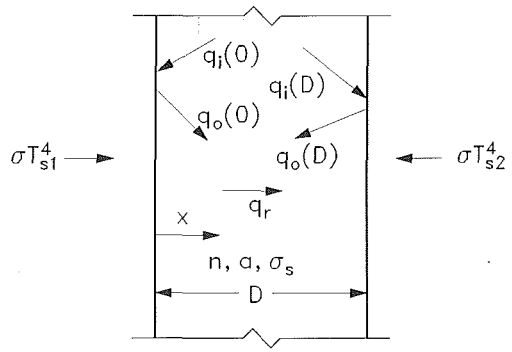

Fig. 1 Layer geometry, coordinate system, and nomenclature of heat fluxes at boundaries

[1]Research Scientist, Lewis Research Academy, NASA Lewis Research Center, Cleveland, OH 44135; Fellow ASME.
[2]Research Scientist, Heat Transfer Branch, Lewis Research Center, Cleveland, OH 44135; Assoc. Mem. ASME.

Contributed by the Heat Transfer Division of THE AMERICAN SOCIETY OF MECHANICAL ENGINEERS. Manuscript received by the Heat Transfer Division August 1991; revision received January 1992. Keywords: Radiation.

$$n^2\sigma T^4(\kappa)=\frac{1}{2}\left[q_o(0)E_2(\kappa)+q_o(\kappa_D)E_2(\kappa_D-\kappa)\right]+\frac{n^2}{2}\int_0^{\kappa_D}\sigma T^4(\kappa^*)E_1(|\kappa-\kappa^*|)d\kappa^* \quad (1)$$

The radiative flux, which is a constant through the layer for the present conditions of radiative equilibrium, can be found from the temperature distribution as (Siegel and Howell, 1981),

$$q_r=q_o(0)-2q_o(\kappa_D)E_3(\kappa_D)-2n^2\int_0^{\kappa_D}\sigma T^4(\kappa)E_2(\kappa)d\kappa \quad (2)$$

The following dimensionless groups are now defined:

$$\Phi(\kappa)=\frac{n^2\sigma T^4(\kappa)-q_o(\kappa_D)}{q_o(0)-q_o(\kappa_D)}; \quad (3a)$$

$$\Psi=\frac{q_r}{q_o(0)-q_o(\kappa_D)} \quad (3b)$$

Equations (1) and (2) then become (note that $X=x/D=\kappa/\kappa_D$)

$$\Phi(X)=\frac{1}{2}E_2(\kappa_D X)+\frac{1}{2}\kappa_D\int_0^1\Phi(X^*)E_1(\kappa_D|X-X^*|)dX^* \quad (4)$$

$$\Psi=1-2\kappa_D\int_0^1\Phi(X)E_2(\kappa_D X)dX \quad (5)$$

In Eqs. (4) and (5) Φ and Ψ are not functions of n. Hence to obtain Φ and Ψ for all $n\geq 1$ it is necessary to solve Eq. (4) only once for each κ_D and use each result to evaluate Eq. (5). For the special case when the index of refraction of the layer is 1, there are no reflections at the interfaces so that $q_o(0)=\sigma T_{s1}^4$, $q_o(\kappa_D)=\sigma T_{s2}^4$, and the dimensionless groups become

$$\Phi(\kappa)=\frac{T^4(\kappa)-T_{s2}^4}{T_{s1}^4-T_{s2}^4}; \quad (6a)$$

$$\Psi=\frac{q_r}{\sigma T_{s1}^4-\sigma T_{s2}^4}; \quad (6b)$$

For $n>1$, however, the Φ and Ψ in Eq. (3) contain the outgoing boundary fluxes $q_o(0)$ and $q_o(\kappa_D)$ that are unknown, so the solution has not yet provided $T(\kappa)$ and q_r for the cases when $n>1$. In order to find these quantities the $q_o(0)$ and $q_o(\kappa_D)$ must be obtained in terms of known quantities. This is accomplished by looking at the boundary conditions in detail.

At the diffuse interfaces the internal fluxes are related to the transmission of external flux and the reflection of internal flux by

$$q_o(0)=\sigma T_{s1}^4\tau^o+q_i(0)\rho^i \quad (7a)$$

$$q_o(\kappa_D)=\sigma T_{s2}^4\tau^o+q_i(\kappa_D)\rho^i \quad (7b)$$

At the inside surfaces of the two boundaries there are the following relations between the radiative flux and the outgoing and incoming fluxes:

$$q_r(0)=q_o(0)-q_i(0) \quad (8a)$$

$$q_r(\kappa_D)=-q_o(\kappa_D)+q_i(\kappa_D) \quad (8b)$$

Equations (7a) and (8a) are combined to eliminate $q_i(0)$ and similarly for Eqs. (7b) and (8b) to eliminate $q_i(\kappa_D)$. This yields

$$q_o(0)=\frac{1}{1-\rho^i}\left(\tau^o\sigma T_{s1}^4-q_r\rho^i\right) \quad (9a)$$

$$q_o(\kappa_D)=\frac{1}{1-\rho^i}\left(\tau^o\sigma T_{s2}^4+q_r\rho^i\right) \quad (9b)$$

These relations are substituted into Eq. (3b) to eliminate the q_o's. This yields the radiative flux for any index of refraction in terms of the value of Ψ. Use is also made of the relation at an interface (Richmond, 1963) that $\tau^o=(1-\rho^i)n^2$. The result for q_r *for any* n is,

$$\frac{q_r}{\sigma(T_{s1}^4-T_{s2}^4)}=\frac{n^2\Psi}{1+\frac{2\rho^i}{1-\rho^i}\Psi} \quad (10)$$

Following the same procedure, the temperature distribution is found by starting with Eq. (3a), using Eq. (9) to eliminate the q_o's and then using Eq. (10) to eliminate q_r. This yields the $T(X)$ *for any* n as

$$\frac{T^4(X)-T_{s2}^4}{T_{s1}^4-T_{s2}^4}=\frac{\Phi(X)+\frac{\rho^i}{1-\rho^i}\Psi}{1+\frac{2\rho^i}{1-\rho^i}\Psi} \quad (11)$$

To use these relations values of ρ^i are needed for various refractive indexes. The externally incident radiation is diffuse. Although the interfaces are probably not optically smooth, it is assumed that each bit of roughness acts as a smooth facet so that the reflectivity can be obtained from the usually used interface relations for a nonabsorbing dielectric medium. Then by integrating the reflected energy over all incident directions the relation for $\rho^i(n)$ is (Richmond, 1963),

$$\rho^i(n)=1-\frac{1}{n^2}\left\{\frac{1}{2}-\frac{(3n+1)(n-1)}{6(n+1)^2}-\frac{n^2(n^2-1)^2}{(n^2+1)^3}\ln\left(\frac{n-1}{n+1}\right)+\frac{2n^3(n^2+2n-1)}{(n^2+1)(n^4-1)}-\frac{8n^4(n^4+1)}{(n^2+1)(n^4-1)^2}\ln(n)\right\} \quad (12)$$

As discussed by Cox (1965), in the fairly transparent spectral regions of ceramic materials, the extinction coefficient in the complex index of refraction is usually not large enough to affect the surface reflectivity significantly, so Eq. (12) for nonattenuating dielectrics gives good results. The extinction

Table 1 Dimensionless temperature distribution, Φ

	Optical Thickness, κ_D						
X	0.1	0.3	1.0	3.0	10	30	100
0	.5710	.6419	.7582	.8693	.9495	.9819	.9948
.05	.5619	.6229	.7230	.8211	.8966	.9304	.9456
.10	.5541	.6072	.6946	.7819	.8511	.8828	.8974
.20	.5397	.5786	.6429	.7088	.7627	.7876	.7994
.30	.5262	.5517	.5942	.6384	.6750	.6920	.6999
.40	.5130	.5257	.5468	.5690	.5874	.5961	.6002
.50	.5000	.5000	.5000	.5000	.5000	.5000	.5000
.60	.4870	.4743	.4532	.4310	.4125	.4038	.4002
.70	.4738	.4483	.4058	.3616	.3249	.3079	.3004
.80	.4603	.4214	.3571	.2912	.2372	.2123	.2007
.90	.4459	.3928	.3054	.2181	.1488	.1171	.1026
.95	.4382	.3771	.2770	.1789	.1034	.0695	.0543
1.0	.4290	.3581	.2419	.1307	.0505	.0181	.0052

Table 2 Dimensionless heat flux, Ψ

Optical Thickness κ_D	Ψ
0.1	.9157
0.3	.7936
1.0	.5534
3.0	.3017
10	.1168
30	.0419
100	.0122

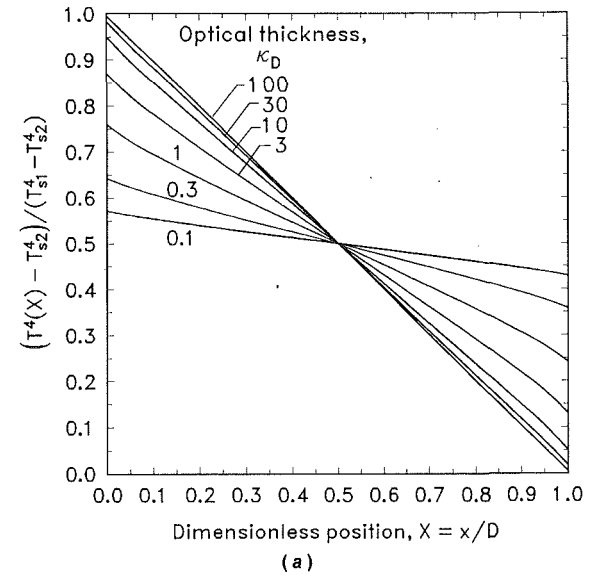

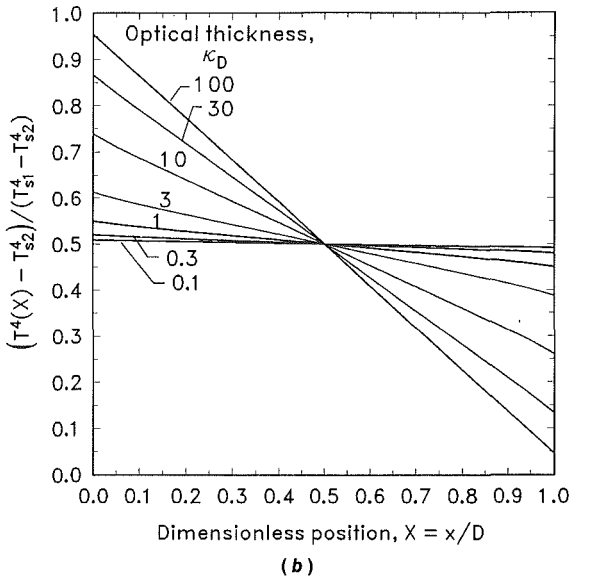

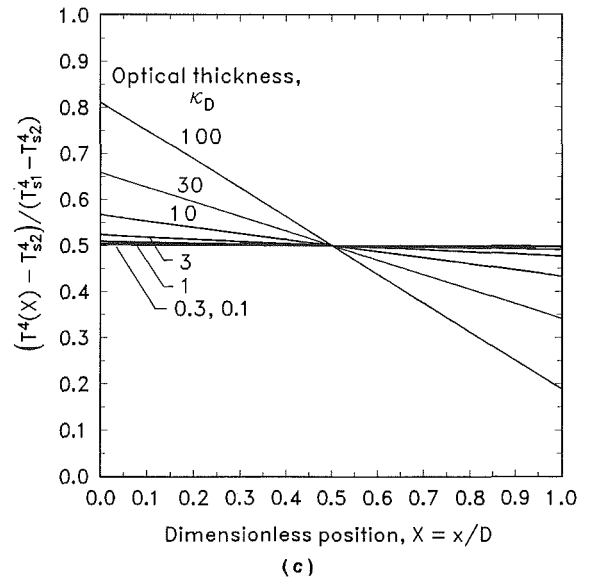

Fig. 2 Effect of index of refraction on dimensionless temperature distributions for various optical thicknesses: (*a*) index of refraction, $n = 1$; (*b*) index of refraction, $n = 2$; (*c*) index of refraction, $n = 4$

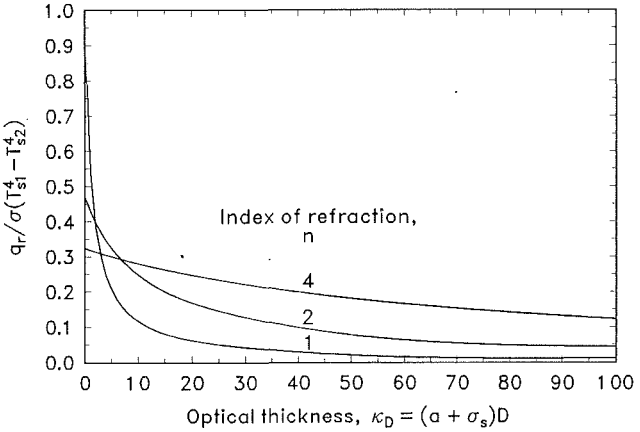

Fig. 3 Effect of index of refraction on radiative heat flux through the layer as a function of optical thickness

effect can be important in highly absorbing wavelength bands. General property relations as given by Hering and Smith (1968) would then be required to estimate average surface properties for use in the present gray analysis.

Equations (10)–(12) provide the means for obtaining the temperature distributions and radiative heat fluxes for a layer with $n > 1$ from the results for $n = 1$. The solutions of Eqs. (4) and (5) for Φ and Ψ were obtained in another context by Heaslet and Warming (1965). In connection with some of our work (Siegel, 1987), a computer program was available; solutions were obtained from that program to have results in a convenient tabular form for the desired optical thicknesses. As discussed in that work the program uses a Gaussian integration subroutine, and 80 grid points were used across the layer. Cubic spline interpolation is used to obtain the irregularly spaced integration points for the Gaussian routine. To deal with the singularity $E_1(0) \to \infty$, the integral in Eq. (4) was evaluated analytically for X^* very close to X by assuming $\Phi(X^*) \approx \Phi(X)$ so that $\Phi(X)$ could be taken out of the integral for very small $|X - X^*|$ (see Siegel, 1987). The results were in agreement with those of Heaslet and Warming (1965).

Results and Discussion

The Φ and Ψ were evaluated from Eqs. (4) and (5). The results are in excellent agreement with the plotted values of Heaslet and Warming (1965) and are given for convenience in Tables 1 and 2 for $0.1 \le \kappa_D \le 100$. Equations (10) and (11) were then used to obtain dimensionless radiative heat fluxes and temperatures for $n > 1$. The required ρ^i were obtained from Eq. (12).

Figure 2 shows the dimensionless temperature distributions for $n = 1, 2$, and 4. For small optical thickness the dimensionless distribution approaches 0.5, and as $\kappa_D \to \infty$ the profile becomes linear extending from 1.0 to 0. The effect of increasing n is to decrease the range of the temperature distributions, and for a fixed κ_D they move closer to 0.5 as n is made larger. The dimensionless profiles are all rather linear. The fact that the profiles become more uniform with increasing n is the result of increasing internal reflections within the absorbing and scattering layer and decreasing transmission into the layer. Since each element in the layer is in radiative equilibrium all locally absorbed radiation must be reemitted. Since scattering is assumed isotropic, local scattering is added to the local emission. The large amount of internal reflection tends to equalize the energy throughout the layer and flatten the temperature distributions. The effect of n is calculated very easily from the simple relation given by Eq. (11), where ρ^i is a function of n.

The effect of n and κ_D on the dimensionless radiative heat flux through the layer is in Fig. 3. The heat flux decreases as

the optical thickness increases, and the effect of n is quite pronounced in altering the heat flux. The curve becomes very flat for $n=4$. This is because interface reflections and increased internal emission (as a result of the n^2 factor) have become quite strong in regulating the heat transfer. The effect of optical thickness is thereby suppressed. At large optical thicknesses this increases the radiative flux as compared with the results for $n=1$. As the layer becomes transparent $\kappa_D \to 0$, $\Psi \to 1$ and the dimensionless flux from Eq. (10) approaches $n^2(1-\rho^i)/(1+\rho^i)$.

References

Amlin, D. W., and Korpela, S. A., 1979, "Influence of Thermal Radiation on the Temperature Distribution in a Semi-transparent Solid," ASME JOURNAL OF HEAT TRANSFER, Vol. 101, pp. 76–80.

Cox, R. L., 1965, "Fundamentals of Thermal Radiation in Ceramic Materials," in: *Thermal Radiation in Solids*, S. Katzoff, ed., NASA SP-55, pp. 83–101.

Crosbie, A. L., and Shieh, S. M., 1990, "Three-Dimensional Radiative Transfer for Anisotropic Scattering Medium With Refractive Index Greater Than Unity," *Journal of Quantitative Spectroscopy and Radiative Transfer*, Vol. 44, No. 2, pp 299–312.

Fowle, A. A., Strong, P. F., Comstock, D. F., and Sox, C., 1969, "Computer Program to Predict Heat Transfer Through Glass," *AIAA Journal*, Vol. 7, No. 3, pp. 478–483.

Gardon, R., 1958, "Calculation of Temperature Distributions in Glass Plates Undergoing Heat-Treatment," *Journal of the American Ceramic Society*, Vol. 41, No. 6, pp. 200–209.

Heaslet, M. A., and Warming, R. F., 1965, "Radiative Transport and Wall Temperature Slip in an Absorbing Planar Medium," *International Journal of Heat and Mass Transfer*, Vol. 8, No. 7, pp. 979–994.

Hering, R. G., and Smith, T. F., 1968, "Surface Radiation Properties From Electromagnetic Theory," *International Journal of Heat and Mass Transfer*, Vol. 11, pp. 1567–1571.

Ping, T. H., and Lallemand, M., 1989, "Transient Radiative-Conductive Heat Transfer in Flat Glasses Submitted to Temperature, Flux, and Mixed Boundary Conditions," *International Journal of Heat and Mass Transfer*, Vol. 32, No. 5, pp. 795–810.

Richmond, J. C., 1963, "Relation of Emittance to Other Optical Properties," *Journal of Research of the National Bureau of Standards*, Vol. 67C, No. 3, pp. 217–226.

Rokhsaz, F., and Dougherty, R. L., 1989, "Radiative Transfer Within a Finite Plane-Parallel Medium Exhibiting Fresnel Reflection at a Boundary," *Heat Transfer Phenomena in Radiation, Combustion and Fires*, ASME HTD-Vol. 106, pp. 1–8.

Siegel, R., and Howell, J. R., 1981, *Thermal Radiation Heat Transfer*, 2nd ed., Hemisphere, Washington, DC.

Siegel, R., 1987, "Transient Radiative Cooling of a Droplet-Filled Layer," ASME JOURNAL OF HEAT TRANSFER, Vol. 109, No. 1, pp. 159–164.

Tarshis, L. A., O'Hara, S., and Viskanta, R., 1969, "Heat Transfer by Simultaneous Conduction and Radiation for Two Absorbing Media in Intimate Contact," *International Journal of Heat and Mass Transfer*, Vol. 12, pp. 333–347.

The Prandtl Number Effect on Melting Dominated by Natural Convection

J. S. Lim[1] and A. Bejan[1,2]

Nomenclature

B = constant, Eq. (13)
c_P = liquid specific heat
Fo = Fourier number $=\alpha t/H^2$
g = gravitational acceleration
Gr = Grashof number $=g\beta\Delta TH^3/\nu^2$
h_{sf} = latent heat of melting
H = height
k = liquid thermal conductivity
Nu = Nusselt number $= q'/(k\Delta T)$
Pr = Prandtl number $=\nu/\alpha$
q' = overall heat transfer rate, W/m
Ra = Rayleigh number $=g\beta\Delta TH^3/(\alpha\nu)$
Ra_z = Rayleigh number $=g\beta\Delta Tz^3/(\alpha\nu)$
s = thickness of conduction zone
Ste = Stefan number $=c_P\Delta T/h_{sf}$
T_h = temperature of isothermally heated wall
T_m = melting point
ΔT = temperature difference $=T_h-T_m$
z = height of convection zone
α = liquid thermal diffusivity
β = liquid coefficient of volumetric thermal expansion
δ = thermal boundary layer thickness
ν = kinematic viscosity
$()_c$ = critical

Objective

In a recent paper, Gobin and Benard (1990) considered the task of correlating the heat transfer data for melting in the presence of natural convection when the Pr value of the liquid phase is considerably smaller than 1. Earlier correlations were reported by Webb and Viskanta (1986), and Beckermann and Viskanta (1989). Additional low-Pr studies were conducted by Webb and Viskanta (1985), Gau and Viskanta (1986), Wolff and Viskanta (1987), and Beckermann (1989). To correlate the low-Pr data is an important and timely task, especially in view of the voluminous work that has been dedicated to situations in which Pr is greater than 1.

For the convection-dominated regime known also as quasi-stationary melting, Gobin and Benard (1990) correlated their low-Pr numerical data with the formula:

$$\mathrm{Nu}=0.29\mathrm{Ra}^{0.27}\mathrm{Pr}^{0.18} \tag{1}$$

They noted that this correlation does not agree with the $\mathrm{Nu}\sim(\mathrm{RaPr})^{1/4}$ trend that might be expected from the single-phase natural convection scales for low Prandtl numbers (Bejan, 1984). They concluded that:

1 The relevance of the group (RaPr) is not verified by their numerical results for convection-dominated melting, and

2 Further work is required to determine the scaling laws that govern the transition from the initial (conduction) regime to the final (convection) regime of the process of melting by side heating.

These two conclusions defined the work presented in this note. In it we report the correct scales of natural convection melting when the Prandtl number is small. We then construct a scaling-correct heat transfer correlation that spans the entire range of Prandtl numbers.

Scale Analysis

The scales of the natural convection melting process can be determined by extending Jany and Bejan's (1988) high-Pr theory to the range of low Prandtl numbers represented by liquid metals. The theory is based on the geometric fact that during the transition from conduction to convection-dominated melting the melt region contains two distinct zones. As shown in Fig. 1, the upper zone of height z is ruled by convection (namely, distinct boundary layers, δ), while the lower zone of uniform thickness s and height $(H-z)$ is governed by horizontal conduction. It is assumed that the flow is laminar, and that $\mathrm{Ste}\ll 1$.

The conduction thickness is well known,

$$s\sim H(\mathrm{SteFo})^{1/2} \tag{2}$$

[1]Department of Mechanical Engineering and Materials Science, Duke University, Durham, NC 27706.

[2]J. A. Jones Professor of Mechanical Engineering; Fellow ASME.

Contributed by the Heat Transfer Division of THE AMERICAN SOCIETY OF MECHANICAL ENGINEERS. Manuscript received by the Heat Transfer Division April 1991; revision received December 1991. Keywords: Liquid Metals, Natural Convection, Phase-Change Phenomena.

the optical thickness increases, and the effect of n is quite pronounced in altering the heat flux. The curve becomes very flat for $n=4$. This is because interface reflections and increased internal emission (as a result of the n^2 factor) have become quite strong in regulating the heat transfer. The effect of optical thickness is thereby suppressed. At large optical thicknesses this increases the radiative flux as compared with the results for $n=1$. As the layer becomes transparent $\kappa_D \to 0$, $\Psi \to 1$ and the dimensionless flux from Eq. (10) approaches $n^2(1-\rho^i)/(1+\rho^i)$.

References

Amlin, D. W., and Korpela, S. A., 1979, "Influence of Thermal Radiation on the Temperature Distribution in a Semi-transparent Solid," ASME JOURNAL OF HEAT TRANSFER, Vol. 101, pp. 76–80.

Cox, R. L., 1965, "Fundamentals of Thermal Radiation in Ceramic Materials," in: *Thermal Radiation in Solids*, S. Katzoff, ed., NASA SP-55, pp. 83–101.

Crosbie, A. L., and Shieh, S. M., 1990, "Three-Dimensional Radiative Transfer for Anisotropic Scattering Medium With Refractive Index Greater Than Unity," *Journal of Quantitative Spectroscopy and Radiative Transfer*, Vol. 44, No. 2, pp 299–312.

Fowle, A. A., Strong, P. F., Comstock, D. F., and Sox, C., 1969, "Computer Program to Predict Heat Transfer Through Glass," *AIAA Journal*, Vol. 7, No. 3, pp. 478–483.

Gardon, R., 1958, "Calculation of Temperature Distributions in Glass Plates Undergoing Heat-Treatment," *Journal of the American Ceramic Society*, Vol. 41, No. 6, pp. 200–209.

Heaslet, M. A., and Warming, R. F., 1965, "Radiative Transport and Wall Temperature Slip in an Absorbing Planar Medium," *International Journal of Heat and Mass Transfer*, Vol. 8, No. 7, pp. 979–994.

Hering, R. G., and Smith, T. F., 1968, "Surface Radiation Properties From Electromagnetic Theory," *International Journal of Heat and Mass Transfer*, Vol. 11, pp. 1567–1571.

Ping, T. H., and Lallemand, M., 1989, "Transient Radiative-Conductive Heat Transfer in Flat Glasses Submitted to Temperature, Flux, and Mixed Boundary Conditions," *International Journal of Heat and Mass Transfer*, Vol. 32, No. 5, pp. 795–810.

Richmond, J. C., 1963, "Relation of Emittance to Other Optical Properties," *Journal of Research of the National Bureau of Standards*, Vol. 67C, No. 3, pp. 217–226.

Rokhsaz, F., and Dougherty, R. L., 1989, "Radiative Transfer Within a Finite Plane-Parallel Medium Exhibiting Fresnel Reflection at a Boundary," *Heat Transfer Phenomena in Radiation, Combustion and Fires*, ASME HTD-Vol. 106, pp. 1–8.

Siegel, R., and Howell, J. R., 1981, *Thermal Radiation Heat Transfer*, 2nd ed., Hemisphere, Washington, DC.

Siegel, R., 1987, "Transient Radiative Cooling of a Droplet-Filled Layer," ASME JOURNAL OF HEAT TRANSFER, Vol. 109, No. 1, pp. 159–164.

Tarshis, L. A., O'Hara, S., and Viskanta, R., 1969, "Heat Transfer by Simultaneous Conduction and Radiation for Two Absorbing Media in Intimate Contact," *International Journal of Heat and Mass Transfer*, Vol. 12, pp. 333–347.

The Prandtl Number Effect on Melting Dominated by Natural Convection

J. S. Lim[1] and A. Bejan[1,2]

Nomenclature

B = constant, Eq. (13)
c_P = liquid specific heat
Fo = Fourier number $=\alpha t/H^2$
g = gravitational acceleration
Gr = Grashof number $=g\beta\Delta TH^3/\nu^2$
h_{sf} = latent heat of melting
H = height
k = liquid thermal conductivity
Nu = Nusselt number $=q'/(k\Delta T)$
Pr = Prandtl number $=\nu/\alpha$
q' = overall heat transfer rate, W/m
Ra = Rayleigh number $=g\beta\Delta TH^3/(\alpha\nu)$
Ra_z = Rayleigh number $=g\beta\Delta Tz^3/(\alpha\nu)$
s = thickness of conduction zone
Ste = Stefan number $=c_P\Delta T/h_{sf}$
T_h = temperature of isothermally heated wall
T_m = melting point
ΔT = temperature difference $=T_h-T_m$
z = height of convection zone
α = liquid thermal diffusivity
β = liquid coefficient of volumetric thermal expansion
δ = thermal boundary layer thickness
ν = kinematic viscosity
$()_c$ = critical

Objective

In a recent paper, Gobin and Benard (1990) considered the task of correlating the heat transfer data for melting in the presence of natural convection when the Pr value of the liquid phase is considerably smaller than 1. Earlier correlations were reported by Webb and Viskanta (1986), and Beckermann and Viskanta (1989). Additional low-Pr studies were conducted by Webb and Viskanta (1985), Gau and Viskanta (1986), Wolff and Viskanta (1987), and Beckermann (1989). To correlate the low-Pr data is an important and timely task, especially in view of the voluminous work that has been dedicated to situations in which Pr is greater than 1.

For the convection-dominated regime known also as quasi-stationary melting, Gobin and Benard (1990) correlated their low-Pr numerical data with the formula:

$$\mathrm{Nu}=0.29\mathrm{Ra}^{0.27}\mathrm{Pr}^{0.18} \tag{1}$$

They noted that this correlation does not agree with the $\mathrm{Nu}\sim(\mathrm{RaPr})^{1/4}$ trend that might be expected from the single-phase natural convection scales for low Prandtl numbers (Bejan, 1984). They concluded that:

1 The relevance of the group (RaPr) is not verified by their numerical results for convection-dominated melting, and

2 Further work is required to determine the scaling laws that govern the transition from the initial (conduction) regime to the final (convection) regime of the process of melting by side heating.

These two conclusions defined the work presented in this note. In it we report the correct scales of natural convection melting when the Prandtl number is small. We then construct a scaling-correct heat transfer correlation that spans the entire range of Prandtl numbers.

Scale Analysis

The scales of the natural convection melting process can be determined by extending Jany and Bejan's (1988) high-Pr theory to the range of low Prandtl numbers represented by liquid metals. The theory is based on the geometric fact that during the transition from conduction to convection-dominated melting the melt region contains two distinct zones. As shown in Fig. 1, the upper zone of height z is ruled by convection (namely, distinct boundary layers, δ), while the lower zone of uniform thickness s and height $(H-z)$ is governed by horizontal conduction. It is assumed that the flow is laminar, and that $\mathrm{Ste}\ll 1$.

The conduction thickness is well known,

$$s\sim H(\mathrm{SteFo})^{1/2} \tag{2}$$

[1]Department of Mechanical Engineering and Materials Science, Duke University, Durham, NC 27706.

[2]J. A. Jones Professor of Mechanical Engineering; Fellow ASME.

Contributed by the Heat Transfer Division of THE AMERICAN SOCIETY OF MECHANICAL ENGINEERS. Manuscript received by the Heat Transfer Division April 1991; revision received December 1991. Keywords: Liquid Metals, Natural Convection, Phase-Change Phenomena.

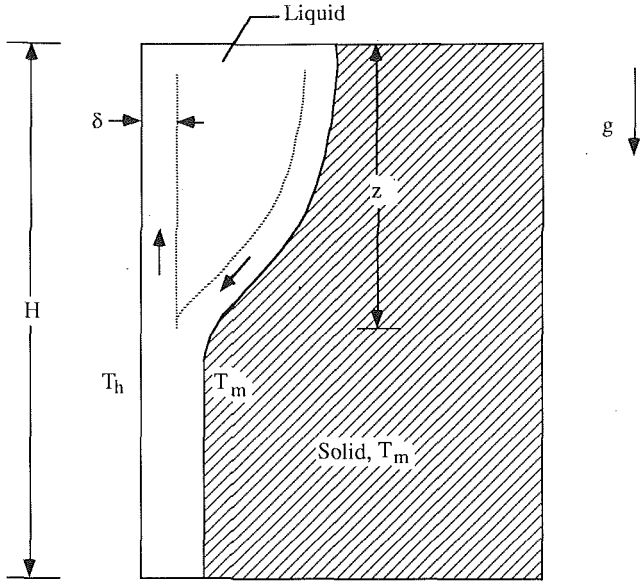

Fig. 1 Two-zone model for the transition from the conduction regime to the convection regime in melting due to heating from the side

where (SteFo) is the dimensionless time defined in the Nomenclature. In the case of low-Pr liquids, the outer boundary layer thickness δ is the thermal thickness (e.g., Bejan, 1984)

$$\delta \sim z(\mathrm{Ra}_z \mathrm{Pr})^{-1/4} \tag{3}$$

where $\mathrm{Ra}_z = g\beta\Delta T z^3/(\alpha\nu)$, and $\Delta T = T_h - T_m$. Expressed in terms of the Rayleigh number based on the height H, $\mathrm{Ra} = g\beta\Delta T H^3/(\alpha\nu)$, the δ scale reads

$$\delta \sim z^{1/4} H^{3/4} (\mathrm{RaPr})^{-1/4} \tag{4}$$

The upper and lower zones meet at the depth z where

$$\delta \sim s \tag{5}$$

Combined with Eqs. (2) and (4), this last relation pinpoints the size (depth) of the convection-dominated zone,

$$z \sim H\mathrm{RaPr}(\mathrm{SteFo})^2 \tag{6}$$

We define the overall Nusselt number in the same way as Gobin and Benard (1990), $\mathrm{Nu} = q'/(k\Delta T)$, and note the additivity (through a constant C_1 of order 1) of the heat transfer contributions made by the two zones of the melt region

$$q' \sim k(H-z)\frac{\Delta T}{s} + kz\frac{\Delta T}{\delta} \tag{7}$$

$$\mathrm{Nu} = \frac{q'}{k\Delta T} \sim (\mathrm{SteFo})^{-1/2} + C_1 \mathrm{Ra\ Pr}(\mathrm{SteFo})^{3/2} \tag{8}$$

The first term on the right side represents the contribution due to pure conduction, while the second term accounts for the incipient convection effect. The validity of Eq. (8) expires at that time when z is as large as H; by setting $z \sim H$ in Eq. (6) we conclude that the critical time of transition to convection over the entire height H is

$$(\mathrm{SteFo})_c \sim (\mathrm{RaPr})^{-1/2} \tag{9}$$

The overall heat transfer rate in the postcritical convection regimes $\mathrm{SteFo} > (\mathrm{SteFo})_c$ is obtained by replacing z with H in Eq. (7)

$$\mathrm{Nu} \sim (\mathrm{RaPr})^{1/4},\ \mathrm{Pr} < 1 \tag{10}$$

In summary, the scale analysis of melting with natural convection in low-Pr liquids yields not only the time-dependent heat transfer scale [Eqs. (8) and (10)] but also the critical time of transition to the convection-dominated (quasi-steady) regime, Eq. (9).

Correlation for Convection-Dominated Melting and Arbitrary Prandtl Number

It is known that the corresponding Nu scale for convection-dominated melting when $\mathrm{Pr} > 1$ is $\mathrm{Nu} \sim \mathrm{Ra}^{1/4}$. As in the preceding section, it is assumed that $\mathrm{Ste} \ll 1$, i.e., that the convection-dominated melting regime is quasi-steady. Jany and Bejan (1988) developed the following correlation for the convection-dominated regime:

$$\mathrm{Nu} \cong 0.35\ \mathrm{Ra}^{1/4},\ \mathrm{Pr} > 1 \tag{11}$$

There is no controversy about convection-dominated melting when $\mathrm{Pr} \gtrsim 1$. This is why as $\mathrm{Pr} \gtrsim 1$ asymptote for our correlation [Eq. (12)] we adopted Eq. (11), which agrees within percentage points with $\mathrm{Pr} \gtrsim 1$ correlations proposed by others. These similarities, i.e., the reliability of Eq. (11), are amply documented by Jany and Bejan (1988).

A scaling-correct correlation that covers the entire Pr range must have Eqs. (10) and (11) as asymptotes. Our choice is

$$\mathrm{Nu} = \frac{0.35\ \mathrm{Ra}^{1/4}}{\left[1 + (B/\mathrm{Pr})^{9/16}\right]^{4/9}} \tag{12}$$

because Churchill and Chu (1975) showed that the expression in the denominator captures very well the Pr dependence in boundary-layer natural convection over a vertical surface. We determined the empirical constant B by fitting Eq. (12) to a total of 17 experimental data: the nine Nu data reported graphically by Gobin and Benard (1990, Fig. 7), three additional Nu data from Webb and Viskanta (1986, Fig. 10), and five Nu data from Beckermann and Viskanta (1989, Fig. 5). Our graphic deduction (measurement) of those data is reported in Table 1, along with the numbering scheme (1, ..., 17) employed in Fig. 2. The best fit is obtained by setting

$$B = 0.143 \tag{13}$$

when the standard deviation is 3.5 percent.

Figure 2 shows that the agreement between Eq. (12) and the data of Table 1 is excellent. In fact, the standard deviation turned out comparable with the error that we would have assigned to our graphic procedure of reading the Nu data off Gobin and Benard's, Webb and Viskanta's, and Beckermann and Viskanta's figures. It is also comparable with the 2-percent error within which Gobin and Benard's correlation (1) reproduces their numerical data. Figure 2 further shows that the Gobin-Benard, Webb-Viskanta, and Beckermann-Viskanta data sets are fitted equally well by the present correlation.

The scaling-correct correlation (12) agrees also with the correlation reported for gallium by Webb and Viskanta (1986)

$$\mathrm{Nu} = 0.157\ \mathrm{Ra}^{0.263},\ \mathrm{Pr} = 0.021 \tag{14}$$

and the correlation developed by Beckermann and Viskanta (1989),

$$\mathrm{Nu} = 0.5\ (\mathrm{RaPr})^{1/4},\ \mathrm{Pr} = 0.011\text{-}0.021 \tag{15}$$

The agreement between the correlation (12) and Eqs. (14) and (15) occurs in the limited Pr range in which Eqs. (14) and (15) are valid. Note that Eq. (14) does not account for the Pr effect, and that in the $\mathrm{Pr} \to 0$ limit Eq. (15) underestimates by 12 percent the Nu values recommended by the general correlation (12).

The older correlations, Eqs. (1), (14), and (15), illustrate the difficulty that was encountered in correlating the low-Pr Nusselt number data. The difficulty stemmed from the fact that the Pr range in which data were available ($\mathrm{Pr} = 0.01\text{-}1$) is situated at the intersection (at the "knee") between the asymptotes $\mathrm{Pr} \gtrsim 1$ and $\mathrm{Pr} \lesssim 1$. The new correlation (12) covers the entire range of Prandtl numbers.

Table 1 Overall Nu data for convection-dominated melting: Points 1-9 are deduced from Fig. 7 of Gobin and Benard (1990), points 10-12 from Fig. 10 of Webb and Viskanta (1986), and points 13-17 from Fig. 5 of Beckermann and Viskanta (1989)

Point	Pr	Ra	Nu
1	0.01	10^5	2.77
2	0.0184	10^5	3.16
3	0.04	10^5	3.78
4	0.1	10^5	4.20
5	0.02	2×10^4	2.17
6	0.02	9×10^4	3.20
7	0.02	2×10^5	4.12
8	0.02	6.24×10^5	5.29
9	0.02	9×10^5	6.04
10	0.021	2.2×10^4	2.26
11	0.021	2.2×10^5	3.91
12	0.021	2.2×10^6	7.33
13	0.0208	3.28×10^5	4.43
14	0.0208	3.28×10^5	4.53
15	0.0208	3.28×10^5	4.63
16	0.0208	1.67×10^5	4.28
17	0.0208	4.88×10^5	4.99

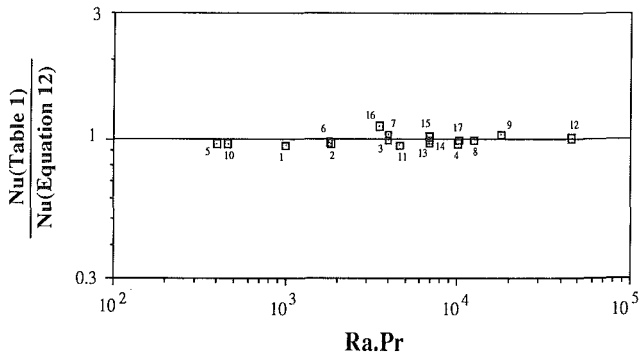

Fig. 2 The agreement between the correlation (12), (13) and the numerical low-Pr melting data compiled in Table 1

The Critical Time of Transition to Convection-Dominated Melting (Pr < 1)

Additional backing for the scale analysis that led to correlation (12) is presented in Fig. 3. Plotted on the ordinate is the time of transition to convection-dominated melting deduced from Gobin and Benard's (1990) Figs. 4 and 6, and Webb and Viskanta's (1986) Fig. 10. We determined the ten SteFo values

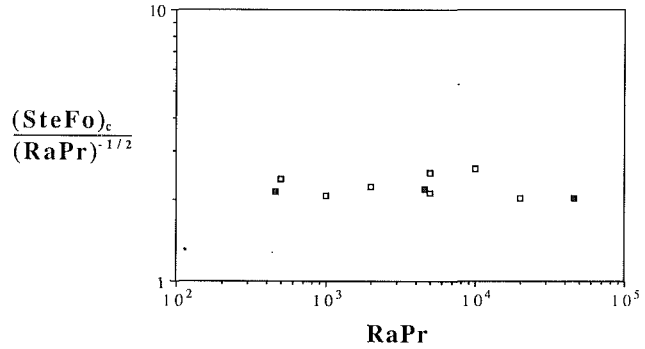

Fig. 3 The time $(SteFo)_c$ for the conduction-convection transition deduced from Gobin and Benard's (1990) data (white squares), and Webb and Viskanta's (1986) data (black squares), showing the correctness of the scaling law (9)

graphically, by intersecting the horizontal Nu asymptotes (convection) with the solid Ra = 0 curve (pure conduction). Our Fig. 3 shows that the critical time $(SteFo)_c$ varies as RaPr raised to the power $-1/2$, i.e., in accordance with the scaling law (9). Furthermore, Fig. 3 confirms that the numerical coefficient in the proportionality $(SteFo)_c \sim (RaPr)^{-1/2}$ is a number of order 1.

Conclusion

The Nu correlation developed in this note, Eq. (12) with $B = 0.143$, reproduces not only Gobin and Benard's low-Pr data [i.e., as done by Eq. (1)], but also

(*a*) Webb and Viskanta's (1986) data
(*b*) Beckermann and Viskanta's (1989) data
(*c*) The correct scaling trend in the $Pr \ll 1$ limit
(*d*) The correct scaling trend and in the $Pr \gg 1$ limit
(*e*) The empirical Nu correlation for the $Pr \gtrsim 1$ domain

The case for using the correlation (12), (13) is supported further by the success of Churchill and Chu's (1975) correlation for boundary-layer natural convection, and by the tests presented here in Figs. 2 and 3.

It is tempting to extrapolate Eq. (12) to the limit $Pr \to 0$, and to regard

$$Nu = 0.565\ (RaPr)^{1/4},\ Pr \to 0 \qquad (16)$$

as the low-Pr counterpart of the high-Pr asymptote (11). The invocation of the $Pr \to 0$ limit requires special care in view of the recent discovery (Bejan and Lage, 1990) that the transition to turbulence occurs at $Gr \sim 10^9$ for all Prandtl numbers (i.e., not at $Ra \sim 10^9$). By rewriting RaPr as $GrPr^2$ we see that when the flow is laminar ($Gr < 10^9$) and $Pr \to 0$, the (RaPr) domain covered by Eq. (16) decreases to zero. Said another way, the laminar-flow correlation (12) holds for Pr values higher than approximately $Ra/10^9$, or when Ra does not exceed approximately $10^9 Pr$.

Acknowledgments

This work was supported by the Electric Power Research Institute contract No. RP 8006-4 under the management of Dr. Jong H. Kim.

References

Beckermann, C., 1989, "A General Correlation for Melting in Rectangular Enclosures," ASME JOURNAL OF HEAT TRANSFER, Vol. 111, pp. 1111-1115.

Beckermann, C., and Viskanta, R., 1989, "Effect of Solid Subcooling on Natural Convection Melting of a Pure Metal," ASME JOURNAL OF HEAT TRANSFER, Vol. 111, pp. 417-424.

Bejan, A., 1984, *Convection Heat Transfer*, Wiley, New York, p. 118.

Bejan, A., and Lage, J. L., 1990, "The Prandtl Number Effect on the Transition in Natural Convection Along a Vertical Surface," ASME JOURNAL OF HEAT TRANSFER, Vol. 112, pp. 787–790.

Churchill, S. W., and Chu, H. H. S., 1975, "Correlating Equations for Laminar and Turbulent Free Convection From a Vertical Plate," *International Journal of Heat and Mass Transfer*, Vol. 18, pp. 1323–1329.

Gau, C., and Viskanta, R., 1986, "Melting and Solidification of a Pure Metal on a Vertical Wall," ASME JOURNAL OF HEAT TRANSFER, Vol. 108, pp. 174–181.

Gobin, D., and Benard, C., 1990, "Influence of the Prandtl Number on the Melting of Metals," ASME HTD-Vol. 143, pp. 75–81.

Jany, P., and Bejan, A., 1988, "Scaling Theory of Melting With Natural Convection in an Enclosure," *International Journal of Heat and Mass Transfer*, Vol. 31, pp. 1221–1235.

Webb, B. W., and Viskanta, R., 1985, "On the Characteristic Length Scale for Correlating Melting Heat Transfer Data," *International Communications in Heat and Mass Transfer*, Vol. 12, pp. 637–646.

Webb, B. W., and Viskanta, R., 1986, "Analysis of Heat Transfer During Melting of a Pure Metal From an Isothermal Vertical Wall," *Numerical Heat Transfer*, Vol. 9, pp. 539–558.

Wolff, F., and Viskanta, R., 1987, "Melting of a Pure Metal From a Vertical Wall," *Experimental Heat Transfer*, Vol. 1, pp. 17–30.